UNIVERSITY OF MALTA
Faculty of Engineering
Department of Metallurgy and Materials Engineering (DMME)

Doctor of Philosophy (Ph.D.) Thesis

Surface Engineered Titanium Nitride for Implantable, Soft-Surface Neural Interfacing Electrodes

By Jeanelle Arpa
B.Eng. (Hons.) Melit., M.Sc. (Strath.)

Supervised by: Prof. Ing. Bertram Mallia
B.Eng. (Hons.) Melit., Ph.D. (Leeds)

Co-Supervised by: Prof. Pierre Schembri Wismayer, M.D.
Ph.D. (Glas.)

A dissertation submitted in partial fulfilment of the requirements of the award of Doctor of Philosophy at the University of Malta

February 2023

L-Università ta' Malta

FACULTY/INSTITUTE/CENTRE/SCHOOL OF ENGINEERING

DECLARATION OF AUTHENTICITY FOR DOCTORAL STUDENTS

(a) Authenticity of Thesis/Dissertation

I hereby declare that I am the legitimate author of this Thesis/Dissertation and that it is my original work.

No portion of this work has been submitted in support of an application for another degree or qualification of this or any other university or institution of higher education.

I hold the University of Malta harmless against any third party claims with regard to copyright violation, breach of confidentiality, defamation and any other third party right infringement.

(b) Research Code of Practice and Ethics Review Procedure

I declare that I have abided by the University's Research Ethics Review Procedures. Research Ethics & Data Protection form code 7105_17112020 and 4954_11052020.

☒ As a Ph.D. student, as per Regulation 66 of the Doctor of Philosophy Regulations, I accept that my thesis be made publicly available on the University of Malta Institutional Repository.

□ As a Doctor of Sacred Theology student, as per Regulation 17 (3) of the Doctor of Sacred Theology Regulations, I accept that my thesis be made publicly available on the University of Malta Institutional Repository.

□ As a Doctor of Music student, as per Regulation 26 (2) of the Doctor of Music Regulations, I accept that my dissertation be made publicly available on the University of Malta Institutional Repository.

☒ As a Professional Doctorate student, as per Regulation 55 of the Professional Doctorate Regulations, I accept that my dissertation be made publicly available on the University of Malta Institutional Repository.

02.2023

Publications

Parts of the work in this thesis have been presented in the following publications and conferences:

Journal Publications

J. Arpa, K. Rechendorff, P. S. Wismayer, and B. Mallia, “Ultra-porous titanium nitride as a dual-action supercapacitor for implantable neural interfacing electrodes,” *Mater. Chem. Phys.*, vol. 289, no. June, p. 126435, 2022, doi: 10.1016/j.matchemphys.2022.126435.

Conference Poster Presenations

J. Arpa, K. Rechendorff, P. S. Wismayer, and B. Mallia, “Surface Engineered Implantable Neural Interfacing Electrodes based on Titanium Nitride (TiN); Towards better functionality, compatibility, and longevity,” *NECABIO (Emerging Biomaterials and Regenerative Cardiology and Neurology) Conference*, July 2021, Prague, Czechia.

Abstract

Implantable neural interfacing electrodes are conduits for the flow of uni- or bi-directional information between the nervous system and an electrically-active device. Many electrodes, including those in widespread clinical use and those currently under investigation, suffer from three prominent limitations, these being poor electrochemical properties, susceptibility towards fibrous encapsulation, and lack of neural interfacing. Such factors are heavily influenced by the chemistry, morphology, and mechanical properties of the electrode material. This work focuses on a variety of surface engineering techniques applied systematically to titanium nitride (TiN) electrodes with the aim of improving the limiting aspects described.

When compared to more established alternatives like platinum (Pt), platinum/iridium (Pt/Ir) alloys, and iridium oxide (IrO_x), TiN is a relatively recent addition to the repertoire of suitable materials for chronic neural interfacing electrodes. In its porous and over-stoichiometric form, the transition metal nitride has demonstrated superior electrochemical properties to Pt-based devices, and is broadly described in literature as an electrochemical double-layer capacitor. However, through exclusionary experiments in protonated and non-protonated electrolytes, the porous TiN electrodes in this work were shown to engage in both pseudocapacitance and double-layer capacitance, the former of which constitutes the majority of capacitive action at ~79%. The reversible faradaic reactions were linked to oxygen vacancies in the surface oxide (TiO_2) and their cyclic regeneration through nitrogen dopants in the overstoichiometric TiN. This mechanism allowed the electrodes to retain their electrochemical properties (i.e., impedance and charge storage capacity (CSC_C)) even with 10,000 charge/discharge cycles at 1 Vs^{-1}.

A prominent issue with porous TiN electrodes, fibrous encapsulation *in vivo*, was addressed by increasing the surface roughness of the Ti6Al4V alloy prior to PVD. Increasing the root mean square roughness (R_q) of the TiN surface from 0.2 to 4.0 µm was effective in this regard, successfully mitigating the proliferation of fibroblasts and effectively reducing the number of viable cells by 62%. This result was achieved without any adverse effects to the electrochemical behaviour. The TiN electrodes deposited on the roughened substrates exhibited identical impedance and CSC_C measurements to the original. Despite the improved fouling resistance and superior electrochemistry as compared to traditional electrode materials (Pt, Pt/Ir, etc.), the properties of TiN could not compete with new, frontier electrode designs.

To tackle this shortcoming, a layer of conductive polymer PEDOT:PSS (poly(3,4-ethylenedioxythiophene) polystyrene sulfonate) was electrodeposited onto the roughened TiN electrodes. At the maximum permissible thickness of ~ 9 µm, the polymer successfully reduced the impedance at 1 Hz ($|Z|_{1Hz}$) by 77% and increased the CSC_C at 1 Vs^{-1} by 52% as compared to the TiN. These improvements were attributed to the porous, nodular structure of the polymer which effectively enlarged the electrochemical surface area of the electrode. Moreover, the large intrinsic pseudocapacitance exhibited by PEDOT:PSS and its wide water window further served to set the TiN/PEDOT:PSS electrodes apart from other materials presently being evaluated for their application in chronic neural interfacing. The electrodes even exhibit superior performance in comparison to frontier materials like carbon nanotubes and to the gold standard within the field, IrO_x. The electrochemical properties, namely high capacitance and low impedance, were even retained with 10,000 charge/discharge cycles at a scan rate of 1 Vs^{-1}, with 20 minutes of ultrasonication at 45 kHz, and in protein-containing electrolytes over 24 hours of immersion

The electrodes were made more resistant to fouling and simultaneously more hospitable to neural growth via the electrodeposition of a calcium alginate hydrogel layer. Using a process of anodic electrogelling, thin, bioresorbable gels were successfully grown onto the PEDOT:PSS surface. Following the gradual dissolution of the hydrogel in physiological liquid, the original electrochemical properties of the electrode were almost completely regained. This outcome revealed that the adopted processing procedure of the gel had minimal impact on the characteristics of PEDOT:PSS. Through cell culture experiments, the alginate-coated electrodes were shown to impede both fibroblast attachment and proliferation, resulting in 72% less viable cells on the surfaces after 72 hours as compared to the PEDOT:PSS.

Furthermore, both PEDOT:PSS and alginate-coated electrodes were observed to support the adhesion and differentiation of SH-SY5Y cells into neuron-type cells having fusiform morphologies and process extensions. In contrast, TiN surfaces did not allow this differentiation to occur, despite many adherent and proliferating SH-SYFY cells observed on the electrodes. This behaviour was attributed to the stiffness mismatch between the flexible cells and the rigid ceramic, highlighting the importance of soft-surface neural interfacing. The PEDOT:PSS and alginate-coated electrodes thus have significant potential for bio-integration in addition to the benefits of excellent electrochemical properties and resistance to fibrous fouling.

Acknowledgements

The author would like to express gratitude towards their supervisor Prof. Ing. Bertram Mallia and to their co-supervisor Prof. Pierre Schembri Wismayer for providing guidance, support, and opportunities for growth within the field.

This work would not have been possible without the input of Dr Kristian Rechendorff and the Danish Technological Institute, who provided the equipment and expertise for sand blasting and physical vapour deposition.

The author would like to thank all the DMME staff for their help throughout the years, including Ing. James Camilleri, Ing. Mary Grace Micallef, Mr. Nicholas Gingell, Mr. Daniel Dimech, Mr. Noel Tonna, Mr. Andrew Agius, and Ms. Sarah Morales Ballesteros. Gratitude is also extended to the staff at the anatomy department of the faculty of medicine and dental surgery, especially Dr Sherif Suleiman and Dr Lucienne Vassallo Gatt.

The author would like to thank Ms. Giulia Vassallo Eminyan for supplying the SH-SY5Y neuroblastoma cell line used in this work, as well as for her assistance in executing biological protocols and procedures. Gratitude is also extended to fellow researchers Ms. Janet Attard, Mr. Lian Bonnici, and Mr. Antonio Polidano Vella for their support in familiarisation with the biological sphere.

I would also like to show appreciation to my fellow researchers and labmates Ms. Christabelle Tonna, Mr. Dylan Abela, Ms. Luana Bonnici, Mr. Clayton Farrugia, Dr Eleanor Saliba, Dr Leonardo Fanton, and Dr Bonnie Attard for their encouragement, help, and collaboration. Special thanks go to Ms. Lisa Asciak at the University of Strathclyde for her valuable input and remote support. Thanks are also extended to Mr. John Gabarretta and Dr Gabriella Borg Balzan M.D. for sharing their chemistry and medical knowledge, respectively.

Miscellaneous gratitude is also given to Jodie and Баба Яга for their companionship, and to mom and dad for their patience.

The research work disclosed in this publication is partially funded by the Endeavour Scholarship Scheme (Malta). Project part-financed by the European Social Fund - Operational Programme II – European Structural and Investment Funds 2014-2020 "*Investing in human capital to create more opportunities and promote the well-being of society*".

Operational Programme II - European Structural and Investment Funds 2014-2020
"Investing in human capital to create more opportunities and promote the well-being of society"
Project part-financed by the European Social Fund
Co-financing rate: 80% European Union; 20% National Funds

Surface Engineered Titanium Nitride for Implantable, Soft-Surface Neural Interfacing Electrodes

Table of Contents

List of Figures

List of Tables

List of Abbreviations

AC	Alternating Current
AD	Alzheimer's Disease
ADSC	Adipose-derived Stem Cells
AIROF	Activated Iridium Oxide
AN	Acetonitrile
ATP	Adenosine Triphosphate
ATRA	All-Trans Retinoic Acid
BBXRD	Bragg-Brentano X-Ray Diffraction
BDD	Boron-doped Diamond
BDNF	Brain-derived Neurotrophic Factor
β-N	Substitutional Nitrogen
BSA	Bovine Serum Albumin
CA	Calcium Alginate
CE	Counter Electrode
C_{dl}	Double-Layer Capacitance
CIC	Charge Injection Capacity
CNF	Carbon Nanofiber
CNS	Central Nervous System
CNT	Carbon Nanotube
CP	Conductive Polymer
CPE	Constant Phase Element
C_{pseu}	Pseudocapacitance
CSC_C	Cathodic Charge Storage Capacity
CSF	Cerebrospinal Fluid
CV	Cyclic Voltammetry
DBS	Deep Brain Stimulation
DC	Direct Current
DEX	Dexamethasone
DI	Deionized
DMEM	Dulbecco's Modified Eagle Medium

DMEM:F12	Dulbecco’s Modified Eagle Medium:F12 1:1 Mixture
DMSO	Di-methyl Sulfoxide
ECM	Extracellular Matrix
ED	Electrodeposited
EDLC	Electrochemical Double-Layer Capacitor
EDS	Energy Dispersive Spectroscopy
EHT	Electron High Tension
EIROF	Electrodeposited Iridium Oxide
EIS	Electrochemical Impedance Spectroscopy
EMEM	Eagle’s Minimum Essential Medium
ESA	Electrochemical Surface Area
Et_4NBF_4	Tetraethylammonium Tetrafluoroborate
FBGC	Foreign Body Giant Cells
FBR	Foreign Body Response
FBS	Foetal Bovine Serum
FCC	Face Centred Cubic
$f_{cut\text{-}off}$	Cut-off Frequency
FINE	Flat Interface Nerve Electrode
FITC	Fluorescein Isothiocyanate-conjugated
GDNF	Recombinant Glial-derived Neurotrophic Factor
GDL	D-glucono-δ-lactone
GFAP	Glial Fibrillary Acidic Protein
GSA	Geometric Surface Area
ICF	Intercellular Fluid
IPA	Isopropyl Alcohol
IPSC	Induced Pluripotent Stem Cells
LA	Longitudinal Acoustic
LFP	Local Field Potential
MRI	Magnetic Resonance Imaging
MS	Magnetron Sputtering
MTT	3-(4,5-Dimethylthiazol-2-yl)-2,5-Diphenyltetrazolium Bromide
MW	Molecular Weight
NB	Neurobasal Media

NHDF	Normal Human Dermal Fibroblasts
NPS	Neural Progenitor Cells
NSC	Neural Stem Cells
OCP	Open Circuit Potential
PANi	Polyaniline
PBS	Phosphate Buffered Saline
PD	Parkinson's Disease
PEDOT:PSS	Poly(3,4-ethylenedioxythiophene) Polystyrene Sulfonate
PNS	Peripheral Nervous System
PP	PEDOT:PSS Electrodes
PP_N	Nitrogen Partial Pressure
P/S	Penicillin-Streptomycin
PSC	Post-synaptic Current
PTFE	Polytetrafluoroethylene
PVD	Physical Vapour Deposition
R_a	Roughness Average
RE	Reference Electrode
R_f	Faradaic Resistance
RGD	Arginine-Glycine-Aspartic Acid
rGO	Reduced Graphene Oxide
ROS	Reactive Oxygen Species
R_p	Maximum height of peak
R_q	Root Mean Square Roughness
R_s	Solution Resistance
R_t	Maximum total height of the profile
R_v	Maximum depth of valley
SC	Spin-coated
SCE	Saturated Calomel Electrode
SCI	Spinal Cord Injury
SD	Standard Deviation
SEM	Scanning Electrode Microscopy
SH-SY5Y	Neuroblastoma Cell Line
SIROF	Sputtered Iridium Oxide

SNR	Signal-to-Noise Ratio
TA	Transverse Acoustic
TBI	Traumatic Brain Injury
TCP	Tissue Culture Polystyrene
TiN	Titanium Nitride
TMN	Transition Metal Nitride
TMO	Thermanox
TO	Transverse Optical
UV	Ultraviolet
v	Sweep Rate
WE	Working Electrode
WW	Water Window
XRD	X-Ray Diffractogram
|Z|	Absolute Impedance
Z’	Real Impedance
Z’’	Imaginary Impedance

1 Introduction

Neural interfacing is a relatively young field of medical therapy that involves electrical exchange between the patient's nervous system and a surgically implanted device [1]. Medtronic kickstarted this branch of therapeutics in the 1960's with their commercial launch of the first implantable neuromodulator for easing chronic pain [2]. The scope of neural interfacing has since widened broadly and is now applied for the treatment and management of various disorders, diseases, and injuries resulting from trauma. Bioelectronics has improved prognostics for highly debilitating conditions such as Parkinson's and Huntington's disease, epilepsy, diabetes, recurrent myocardial infarction and severe depression [3], [4]. As of 2020, it is estimated that approximately 200,000 patients worldwide have received deep brain stimulating electrodes for the treatment of Parkinson's Disease [4], around 700,000 have been fitted with inner ear implants to overcome deafness [5], and around 350 retinal prosthesis have been implanted to restore sight [6]. Moreover, an estimated 50,000 patients suffering from chronic pain receive spinal cord stimulation electrodes every year to help manage their symptoms [7]. Progress in the past decade in particular has been substantial, having come so far as to restore major functions such as walking and sensation to paralysed patients [8].

The demand for neural interfacing electrodes is only projected to intensify in the coming years [9]. The current rate of population ageing, where the expected lifetime grows with each passing year, has increased the incidence of geriatric-associated neurological disorders in the general population [10]. Diseases like Alzheimer's and Parkinson's, both of which can benefit from neuromodulation, are thus on the rise [11]. Correspondingly, so is the demand for effective neural interfacing electrodes. Other conditions for which evidence of treatment efficacy via neuromodulation is starting to emerge, like diabetes [12] and major depression [13], are also experiencing unprecedented growth [14], [15]. In developed countries this phenomenon is even affecting young individuals (< 25 years of age), placing greater strain on the healthcare system as those affected become 'lifelong patients' [14]. The crucial role that neural interfacing electrodes play in global wellbeing thus cannot be understated.

Despite the many outstanding developments seen within the field, neural interfacing electrodes exhibit a number of limiting factors that hinder their efficacy and longevity

[16]. A vexing problem with such devices is the incongruency between projected performance and practical operation [17]. A host of issues, including but not limited to device rejection, tissue damage, scarring, material breakdown, electric signal attenuation, and device migration can all contribute to redundancy, underperformance, or in severe cases, great hazard to the patient [18]. This is especially problematic when considering the great levels of associated risk tied to these devices [12]. Patients consenting to high-risk surgeries, the insertion of a several-centimetres-long shaft into their brains while conscious for example, expect significant improvements to their quality-of-life. This is understandable considering that neural injury, seizures, strokes, paralysis and infection to the nervous system are all potential complications of the device and its placement surgery [18], [19]. In many cases however, this risk-to-benefit ratio skews unfavourably, as some electrodes have reported rates of removal or replacement as high as 34% [19]. Apart from the physical and mental stress that is placed on the patient, failed electrodes are also a huge financial burden on an already struggling healthcare system [20].

Much work has been done with the aim of mitigating these issues [13], [21]–[23]. The library of applicable electro-materials has grown considerably, with revolutionary new compounds, alloys, and multi-material systems offering superior characteristics as compared to traditional alternatives [3]. Moreover, materials conventionally unrelated with electrical systems like polymers have also found their footing in this sector [24]. Surface engineering, a process by which the surface of an electrode may be modified whilst retaining the properties of the bulk, offers a unique opportunity to combine the strengths of various materials whilst offsetting their drawbacks [25]. Traditionally reserved for well-established industrial applications like thermal spraying and anodizing, the term “surface engineering” has come a long way in its adaptation to meet the needs of contemporary electrode designers [26]. Novel surface engineering techniques can now incorporate materials of biological origin, pharmaceuticals, and even live organisms [27]–[31]. This has opened the door for new, more effective solutions towards electrode functionality.

This work aims to apply different surface engineering techniques to biomedical grade titanium alloy to tackle three facets of neural interfacing electrodes: (i) their electrochemical properties; (ii) their susceptibility to surface fouling, and; (iii) their poor capacity for neural integration. A combination of surface roughening, physical vapour

deposition, electropolymerisation, and electrogelling were used towards these ends. A thorough review of the literature identified a research gap, leading to the development of an electrode with a unique combination of materials, these being sand-blasted titanium alloy, a porous transition metal nitride ceramic, a conducting polymer, and an antifouling hydrogel. These techniques were applied in a stepwise manner, leading to sub-categories of electrodes that were also novel in their own right. The electrodes were then thoroughly characterised for their chemical makeup, defect content, crystallographic phases, surface roughness, and layer thickness. Measurements in simulated body fluids and non-protonated electrolytes would then be applied to determine electrochemical properties and resistance to cyclic and mechanical degradation. Moreover, the electrodes would also be assessed in a series of *in vitro* cell culture experiments for their resistance to fouling with fibroblasts and for their ability to support the growth of neural cells.

The hypotheses this work endeavoured to prove were thus as follows:

1. That the transition metal nitride electrode is capable of both double-layer capacitance and pseudocapacitance, as opposed to the leading theory in the field of neural interfacing where it is classed as a pure double-layer capacitor;
2. That by surface roughening the titanium alloy prior to ceramic deposition, its morphology would change significantly so as to mitigate fibrous fouling without negatively affecting the electrochemical properties;
3. That a conductive polymer could be successfully electrodeposited onto the ceramic, establish a strong adhesive bond, and improve the electrochemical properties of the electrode;
4. That a bioresorbable and antifouling hydrogel layer could be grown onto the polymer with precise and repeatable dimensions whilst having minimal effects on the electrochemical properties of the electrode, and provide a platform for neural growth and bio-integration.

This research therefore seeks to address a gap that exists in the application of transition metal nitrides in the field of neural interfacing. Specifically, in the untapped potential they have for biofunctionality and in supporting multi-layered systems that can benefit electrochemical performance. In doing so, this work provides a bridge between the mechanical, electrical, and biological performance of such devices, resulting in electrodes that are at the forefront of neuromodulation technology in all three of these aspects.

2 Literature Review

2.1 The Nervous System

The specific requirements of implantable neural electrodes necessitate an understanding of the human nervous system. The following sections will provide an overview of its cellular components and their functions, the mechanisms of electrical conduction, its anatomical organisation, and prominent physiological processes relevant to neural interfacing. The ‘nervous system’ is a collective term used to describe the body’s neural cells as well as the connective tissue and blood vasculature that support them. Anatomically, the nervous system may be divided into the central nervous system (CNS), comprising of the brain and spinal cord, and the peripheral nervous system (PNS), constituting of cranial and spinal nerves that connect to the brain and spinal cord, respectively [32], [33].

2.1.1 Cells of the Nervous System

In both the CNS and PNS, the fundamental active units are distinct cells called neurons that are responsible for receiving, computing, and transferring electrical information around the human body. Although there exist four structural classifications of neurons (based on the number of processes in relation to the cell body), a representative multipolar neuron is shown in Figure 2.1. The cell body, or soma, (typically 5-10 μm in diameter) houses the nucleus of the cell and is surrounded by cytoplasm [34]. Emerging from the cell body are a number of dendrites that further branch into multiple processes known as dendritic spines. An axon (which can be up to 1m in length) connects the cell body to telodendrons, branching processes that end in axon terminals. A selectively permeable membrane containing various channels surrounds the entire cell and is responsible for maintaining its resting electrochemical potential with respect to the extracellular fluid [32], [35], [36].

Neuroglia, or simply glia, are homeostatic cells that provide support, including developmental, immunological, physiological, and metabolic functions, to the neurons [34]. Different glia have different functions. One of the most important roles of neuroglia is the myelination of axons. Oligodendrocytes in the CNS and Schwann cells in the PNS surround the axon and form electrically insulative wrapped segments surrounded by a

myelin sheath, while the non-myelinated gaps found between the segments are known as the Nodes of Ranvier [37]. In the CNS, microglia conduct phagocytic processes, consuming pathogens, cellular waste, and debris, while ependymal cells form lining tissue and produce cerebrospinal fluid. Environmental regulatory processes (monitoring levels of dissolved gases, nutrients, and other chemicals) are carried out by satellite cells in the PNS, and by astrocytes in the CNS. Moreover, astrocytes also participate in the process of glial scarring following injury to the CNS, providing an essential dual role in its pathology by both protecting the injury site and inhibiting axonal regeneration [38], [39].

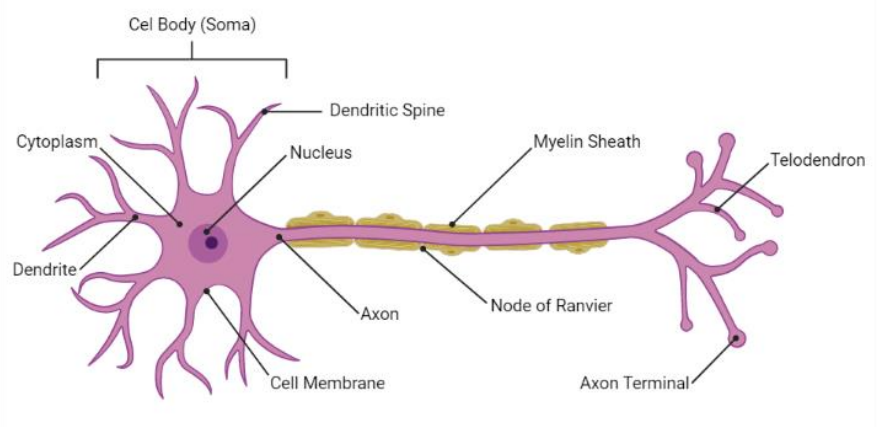

Figure 2.1: A representative multipolar neuron with labelling of prominent structures. Diagram created with BioRender.com and labelled in line with the text of Martini *et al.* [32].

2.1.2 Electrical Conduction in the Nervous System

Electric current is transmitted through individual neurons following a stimulus that can generate what is referred to as an action potential [40]. When at rest, a neuron contains higher concentrations of potassium ions and a lower concentration of sodium ions within the cell membrane as compared to the extracellular space. This electrochemical gradient across the boundary results in a negative membrane potential (~ -70 mV) [41]. When an external stimulant is strong enough to open various gated channels (voltage-gated, ligand-gated, or mechanically-gated channels) residing on the membrane, ions diffuse along their concentration gradient to disrupt the rest potential [32], [40]. If the threshold potential (~ -55 mV) is reached, an action potential is initiated and cannot be stopped. At this potential, voltage-gated Na^+ channels are opened, and sodium ions enter the cell and depolarise the membrane. When reaching the maximum overshoot potential (~ +30 mV), the Na^+ channel becomes inactivated, and influx of sodium ions is halted. Simultaneously, voltage-gated K^+ channels also open to allow potassium ions to exit the

cell, repolarising the membrane and dropping its potential back to negative values. Owing to the slow response of the K^+ channels, excess potassium ions escape the cell to cause a brief period of hyperpolarisation where the membrane potential drops below the resting potential [42]. At this point the K^+ channels close and sodium-potassium pumps restore the membrane potential to its resting state by moving ions in and out of the cell against their concentration gradient. During the repolarisation process, the inactivated Na^+ channels are unable to respond to any external stimulus, pushing the neuron into an absolute refractory period where it is prohibited from firing another action potential. During hyperpolarisation the Na^+ channels return to the closed position, initiating the relative refractory period [43]. At this stage, the neuron may fire another action potential if a large- enough stimulus is received. The process is reset once the resting potential is regained [32], [44]. Figure 2.2 a summarizes the action potential in terms of its voltage/time plot.

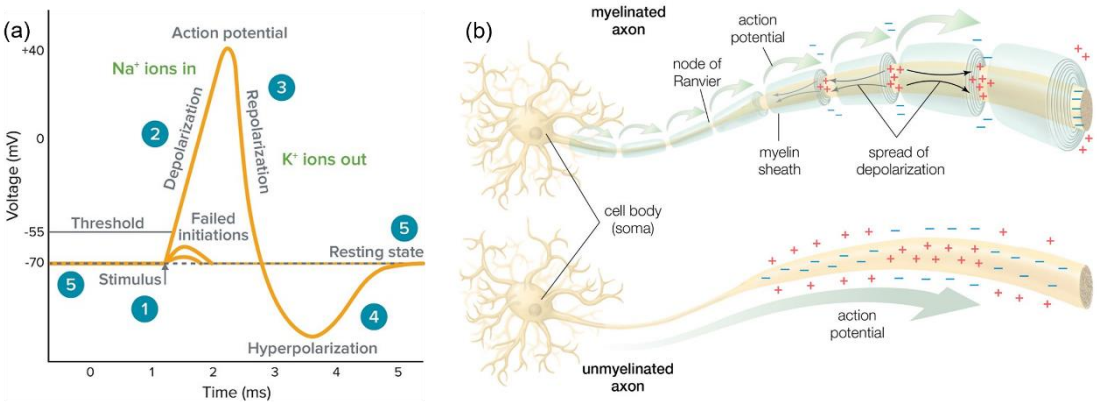

Figure 2.2: (a) The action potential summarized in terms of its voltage/time plot, from [45]; (b) Propagation of an action potential along a myelinated axon versus an unmyelinated axon, from [46].

It is important to note that neuron firing is an all-or-nothing event. Weak stimuli that fail to push the membrane potential to threshold will not result in an action potential [43], [47]. These graded potentials are simply rectified by the sodium-potassium pumps until rest potential is regained. Similarly, stronger stimuli will not result in a larger action potential, as the maximum overshoot potential for a specific neuron is capped [32]. However, the frequency of neural firing can vary, where the maximum rate depends on the individual neuron's refractory periods, and is affected by such properties as synaptic capacity, cell membrane geometry, and number of available ion channels [48], [49]. Most neurons have a dynamic firing range, and the mean frequency at any given time is dependent on the subject's physiological conditions, their state of alertness (for example,

being asleep versus awake), and their age, amongst other factors [50]. Table 2.1 summarizes the typical firing frequencies of different neurons.

Once an action potential is initiated in the cell, the impulse is conducted along the axon by sequential depolarization events caused by local currents. The refractory period ensures that action potential transmission is unidirectional, while myelination permits high-speed propagation in a process known as saltatory conduction [51]. Since voltage-gated ion channels are not located along the myelinated sections, these areas experience a simultaneous reduction in membrane capacitance and increase in its resistance. Conversely, these ion channels are abundant at the Nodes of Ranvier, and so the action potential appears to 'jump' from one node to another [32]. In the absence of myelin, either through intentional design or as a consequence of demyelinating diseases, action potential propagation down the axon is much slower. In these scenarios, the voltage-gated ion channels would have to regenerate the action potential along the entire length of the axon, rather than regenerating it only at interspaced points [32], [36], [51]. This is shown in Figure 2.2 b.

Table 2.1: Average and maximum recorded firing frequencies (in Hz) for different types of neurons. For context of neuron placement, refer to Figure 2.3.

Neuron Type	Average Firing Frequency (Hz)	Maximum Firing Frequency (Hz)	Reference
Enteric viscerofugal neurons of the gut	1-2	/	[52]
Dorsal root ganglion (DRG) neurons (nociceptors)	5.4	/	[40]
Neurons of the suprachiasmatic nucleus in the hypothalamus	7 (daytime) 2 (night-time)	/	[53]
Neurons of the Vagus nerve	1-10	/	[54]
Dopaminergic neurons of the midbrain	2-8	10	[55]
Cortical (temporal) fast-spiking neurons	/	453	[43]
Purkinje neurons of the cerebellum	1 (complex spikes) 2-200 (simple spikes)	500 (spikelets)	[49]
Neurons of the medial nucleus of the trapezoid body (MNTB)	10-250 (in absence of sound)	800 (during auditory simulation)	[56]
Mossy fibre contacts with the cerebellum	800	1000	[57]

Once the action potential reaches the axon terminus, interneural propagation can occur at neuronal junctions, called synapses, that exist between adjacent cells. The most prominent junction within the human body is axodendritic, where a synapse is formed at the axon

terminal of a pre-synaptic neuron (the transmitting cell) and the dendrites of a post-synaptic neuron (the receiving cell) [58]. Synaptic transmissions can occur either through the direct flow of electrical current, through chemical pathways, or through a combination of both mechanisms within the same synapse. Chemical synapses are the most abundant and occur across a nanometric gap between the cells known as the synaptic cleft. When the pre-synaptic axon terminal receives an action potential, voltage-gated Na^+ channels present along the cell membrane are opened following depolarization. The sudden influx of sodium ions further depolarises the membrane, resulting in voltage-gated Ca^{2+} channels to open and initiate calcium ion intake. This triggers a signalling cascade that results in neurotransmitters being released into the synaptic cleft and diffuse across to the post-synaptic membrane. Here, they bind to ligand-gated ion channels and cause them to open. Depending on the neurotransmitter released and the associated gate opened, the post-synaptic neuron can either be locally depolarised (neuron firing likely) or hyperpolarised (neuron firing unlikely). Inter-neural conduction via chemical synapses is strictly unidirectional, and subject to a small delay arising from the intermediary steps between pre-synaptic depolarisation and post-synaptic triggering [59], [60].

On the other hand, electrical synapses comprise of mechanical connections between neurons, termed gap junctions, that control the flow of ions and small metabolites directly between two cells. At the interface, intercellular channel proteins connect the cytoplasm of two neurons and are electrically analogous to ohmic resistors, providing a pathway for the flow of electric current. Electrical synapses, though not as abundant as their chemical counterparts, provide rapid intercellular communications owing to the absence of intermediary messengers. This quasi-instantaneous transmission is very advantageous in time-sensitive biological systems, notably in the execution of reflex actions [59], [61].

2.1.3 Anatomy of the Nervous System

The nervous system is anatomically divided into the CNS and the PNS. The CNS, comprising of the brain and spinal cord, is encased in three layers of non-neuronal tissue known as the meninges, and further protected by the bony structure of the skull and spinal column, respectively. The brain is a mass of tissue amassed from billions of neurons and glial cells, weighing approximately 1.27 kg for the average adult human [62]. When viewed in cross-section it is possible to identify two optically diverse sections of the brain, these being the outer grey matter, containing cell bodies and their unmyelinated axons,

and the inner white matter, which contains predominantly myelinated axons. In this arrangement, the grey matter is the hub for information processing, while white matter is charged with communicating information between sections of grey matter, and between the grey matter and other sections of the CNS [34], [36]. The brain stem connects the two main sections of the CNS (i.e., the brain and spinal cord) and is responsible for relaying information between them [32], [33]. The spinal cord then extends from the brainstem down along the back to terminate at the first or second lumbar vertebra of the spinal column [32], [63].

Circulating through the two innermost meningeal layers of the brain and spinal cord, as well as the ventricular and perivascular spaces of the brain, is a clear and colourless liquid known as cerebrospinal fluid (CSF). Containing a mixture of water, ions, glucose, neurotransmitters and protein, the CSF plays a vital role in maintaining CNS homeostasis, provides cushioning and mechanical support to the brain and spinal cord, and permits communication between the CNS, the PNS, and numerous other systems within the body [64]. The typical constituents of CSF are given in Table 2.2, along with those of interstitial fluid (ISF) and blood plasma for comparison. The electrical conductivity of CSF has been reliably measured using a variety of techniques, most notably through direct current application inside brain tissue via electrodes, and through the conversion of magnetic flux density collected via MRI (magnetic resonance imaging) during non-invasive current injection. Non-pathological CSF exhibits a conductivity of ~ 1.7 S/m [65], which is comparable to that of extracellular fluid (~ 1.6 S/m) [66], both of which are relatively high when compared to blood plasma (~ 0.8 S/m) [67].

Table 2.2: Constituents of the CSF as compared to ISF and blood plasma [68]–[70].

	CSF	**ISF**	**Blood Plasma**
Na^+ (mEq/L)	140-145	139	135-147
K^+ (mEq/L)	3	4	3.5-5.0
Ca^{2+} (mEq/L)	2.0-2.5	1.2	1.3
Mg^{2+} (mEq/L)	2.0-2.5	0.7	0.8
Cl^- (mEq/L)	115-120	105	95-105
HCO_3^- (mEq/L)	20-25	28.3	22-28
HPO_4^{2-}, $H_2PO_4^-$ (mEq/L)	0.3	2	2
Glucose (mg/dL)	50-75	66-135	70-110
Protein (g/dl)	0.05-0.07	2-3	6.0-7.8
pH	7.3	7.3-7.5	7.35-7.45

The PNS adjoins to the CNS via pairs (left and right) of cranial and spinal nerves that connect to the brain and spinal cord, respectively. Twelve pairs of nerves emerge from the brain, and a further 31 pairs from the spinal cord. Each nerve connects to the spinal cord via dorsal and ventral roots, each carrying afferent and efferent signals, respectively (Figure 2.3) [33], [71]. Sensory information regarding a spectrum of intrinsic and environmental signals (temperature, pain, muscle extension, etc) is carried via afferent neurons to the spinal cord. Efferent neurons at the ventral root transmit either autonomic signals, involuntary messages that control visceral functions lying outside conscious control (heart rate, glandular processes, etc), or somatic signals that terminate at skeletal muscles, and allow voluntary actions or involuntary reflex actions. Contrastingly, the cranial nerves do not connect at dorsal or ventral roots, may be dominantly afferent or efferent, and may contain none or several ganglia [36], [72]. Figure 2.3 illustrates the general outline of the nervous system, showing anatomical placement of brain, spinal cord, and the body's nerves.

Regarding the structural anatomy of individual nerves in the PNS, a sectioned, representative view is given in Figure 2.4, showing the tibial nerve of a cadaver after fixing and staining. Each nerve is superficially encased by a protective layer of collagenous tissue known as the epineural sheath. Perineurial sheaths surrounding axonal bundles (Figure 2.4 b) separate individual fascicles within interfascicular epineurium. Branching vasculature also runs along the length of the nerve within this interfascicular space (Figure 2.4 e), along with segments of adipose tissue. Within each fascicle, endoneurium tissue separates individual axons, wherein myelinated neurons may be readily identified by their dark, prominent outlines (Figure 2.4 c). As these nerves extend away from the CNS, they subdivide, branch, and interconnect to innervate the entire body. The sciatic nerve, the largest nerve in the human body, has many division points along its path down the leg. Several small branches split off to innervate muscles in the thigh, while the main segment divides into the tibial and peroneal nerves. The former then further divides into the medial and lateral planter nerves, while the peroneal nerve branches into the superficial peroneal and the deep peroneal [32], [33], [37]. It can thus be appreciated that the nervous system is a very complex web of interdependent and interconnected networks, totalling to a length of over 150,000 km for an adult [73]. This highlights the challenge that arises when dealing with any anomalies that may result from injury, disease, or senescence .

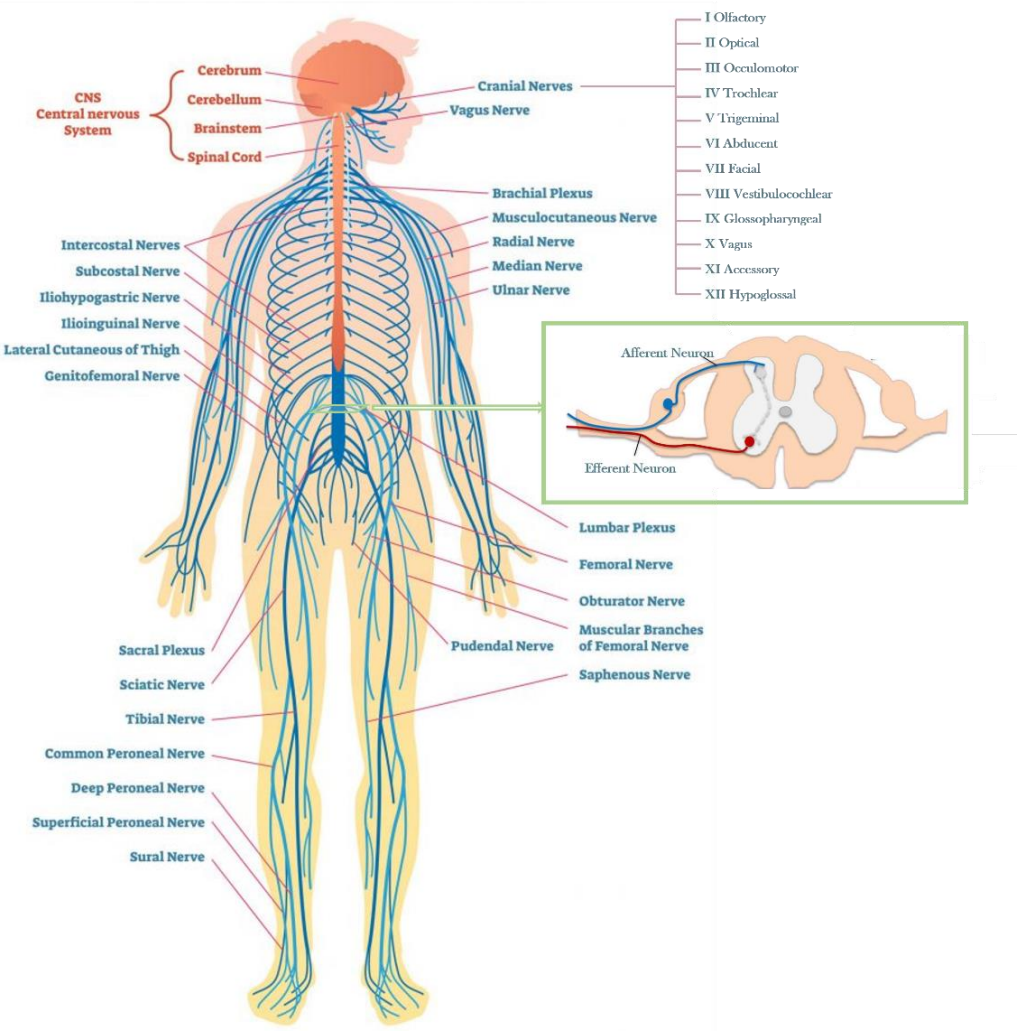

Figure 2.3: Labelled diagram of the body's nerves adapted from [74]. Diagram of spinal cord cross section adapted from [75].

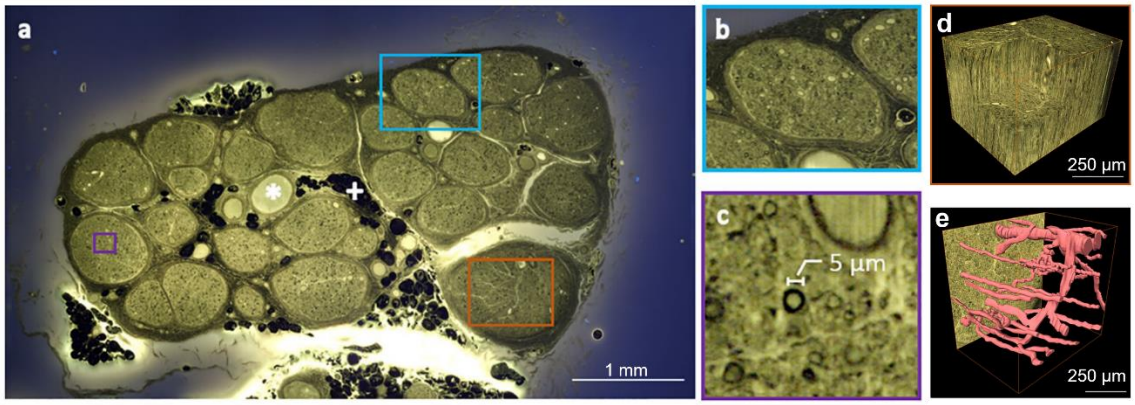

Figure 2.4: Cadaver tibial nerve fixed with osmium tetroxide and stained with rhodamine B. (a) Cross sectional image of the nerve, showing adipose cells (+), venule (*), and several fascicles; (b) Close up image of an individual fascicle; (c) High magnification image of a myelinated axon; (d) Volume rendering of fascicle section, and; (e) Intraneural vasculature obtained from the segment shown in (d). From [37].

2.1.4 Central and Peripheral Neuropathy

Damage or dysfunction of the nervous system, termed neuropathy, differs substantially when presenting in the brain, spinal cord, or peripheral nerves. Although rarely life threatening, peripheral neuropathy can manifest in a variety of symptoms, ranging from discomforting to severely disabling. As nerves carry sensory, motor, and autonomic neurons, effects may include localised numbness, pain, poor muscle strength, and even disruptions to basic functions like waste removal, digestion, and blood circulation [76]. In their analysis, Lehmann *et al.* [77] identify some of the most common sources of peripheral neuropathy to be diabetes, chemical toxicity, thyroid and kidney dysfunctions, B12 deficiencies, and immune system dysregulations.

By far the most frequent cause of severe peripheral neuropathy is physical trauma, as the PNS lacks any rigid, bony protection, and thus presents in ~3% of all patients admitted to accident and emergency centres [78]. With the consequences often being de-emphasized, especially in comparison to central neuropathy, extensively damaged peripheral nerves seldom fully recover. This is despite their capacity to regenerate, where the extent of recovery depends on a combination of factors [79], [80]. Age and general health of the patient, type of injury, as well as location can have a major impact on the outcome. Crush injuries are much more likely to recover than transections, and injuries occurring distally have a higher chance of reconnecting to their target tissue. Another important consideration is medical intervention, and critically, the delay between injury and intervention. A critical time window seems to exist in which axonal regeneration and tissue reinnervation is possible, and beyond which Schwann cells permanently degenerate and can no longer support fresh axonal growth [76].

Traumatic injury to a peripheral nerve will also inevitably trigger the wound healing process. Pro-inflammatory cytokines, growth factors, and inflammatory cells (neutrophils, macrophages, and lymphocytes) sequentially migrate to the wound site to control bleeding and eradicate cellular debris. Macrophages then experience phenotypic transition, stimulating the arrival of fibroblasts to the area. These collagen-producing cells rapidly proliferate, creating an extracellular matrix (ECM) that supports granulation tissue and scar formation [81]. Excessive scarring may completely impede nerve recovery, preventing the regenerating axon from traversing the injury site and reconnecting with its target tissue. Moreover, scar tissue can also compress regrowing

axons, compromising the microvasculature of the injured nerve and triggering secondary axon degeneration [82].

Injuries, diseases, and disorders of the CNS are substantially more complex, both in their physiology and potential treatment [83]. Neurodegenerative diseases, in which the neurons of the CNS progressively experience dysfunction or degeneration, are exceedingly common in the elderly population, with some conditions affecting up to 8% of people aged 65 and over [11]. Alzheimer's disease (AD), the most prevalent neurodegenerative disease, produces dementia (cognitive dysfunction) and eventually leads to death. The second most prevalent disease in this category, Parkinson's disease (PD), manifests in tremors, rigidity, and bradykinesia, and is caused by mass cellular loss in the brain. Concurrently, neurological disorders like epilepsy, which causes seizures triggered by hypersynchronous neural signals, and essential tremor, caused by erratic signalling between the CNS and PNS, are also widespread in the younger population [84].

The CNS, despite its many protective barriers, is also susceptible to injury. Besides being the second leading cause of global mortality, strokes of ischemic and haemorrhagic origin leave half of survivors with serious lifelong disabilities. Infarction and compressive damage of brain tissue caused by blood flow interruption and rising intracranial pressure results in mass neuronal death, lowering the patient's health-related quality of life as neural pathways are destroyed or compromised [85]. Neuronal damage is also commonly caused by pathogenic attack, such as infection with *Streptococcus pneumoniae,* the bacterium that causes bacterial meningitis and leaves half of recovered patients with neurological dysfunction [86].

However, much like the PNS, physical trauma is the cause most often associated with severe motor and cognitive impairment following injury [87]. Commonly arising from road vehicle accidents, armed violence, and work-and-sport-related activities, traumatic injury to the brain and spinal cord (TBI and SCI, respectively) can result in a wide variety of disabling conditions depending on the site of injury. Impaired spatial perception, language and speech disruption, muteness, behavioural disturbances, poor coordination and motor control, respiratory issues, dysphagia, and locked-in syndrome are some of many potential life-altering effects of TBI. Lesions and transections of the spinal cord also result in partial or complete paralysis and sensory loss, the extent of which is dependent on the segmented level of the cord affected [88], [89].

The biggest challenge in tackling neuropathies of the CNS is that mature neurons, being post-mitotic cells, lack the ability to proliferate, thus severely limiting the capacity for self-healing [38]. A very small number of neural stem cells are located within the adult brain, differentiating into mature neurons and glial cells to sustain memory and learning-associated functions. However, the large volume of neuronal loss associated with most injuries and conditions of the CNS cannot be replenished by this process [71]. As such, loss of neurons in the CNS is widely considered permanent without external intervention. Although in its infancy, the field of neural regeneration has made substantial steps in the recent decade, illustrating the potential for minimising, or even reversing damage done to the CNS through injury or disease. Transplantation of neural stem cells (NSCs) into the brain of AD-model (Alzheimer's disease-model) animals has been shown to attenuate inflammation, improve neurogenesis, and even restore learning and memory function to the subjects [90]. Neuronal regrowth has also been observed with NSC transplantation in the brain following ischemic stroke, as freshly injected NSCs were shown to differentiate into mature neurons and replace lost neural tissue in rats [91]. The capacity to repopulate the spinal cord following severe injury has also been demonstrated, with human trials involving autologous neural stem/progenitor cells (NPCs) derived from induced pluripotent stem cells (IPSCs) having shown some success [83].

Another deterrent to substantial recovery is the process of glial scarring, widely regarded as the primary reason axonal regrowth of damaged neurons is prohibited [92]. Injuries that disrupt the meninges become porous to non-CNS molecules and cells, notably macrophages and fibroblasts, that invade the site and participate in the scarring process. Reactive astrocytes come into contact with arriving fibroblasts and divert them to the epicentre of the injury, forming a dense astrocytic wall around a fibrotic mass. During this process, the astrocytes continuously produce proteoglycans that act as inhibitory axon guidance molecules, while macrophages maintain a highly inflammatory environment. Damaged axons that come into contact with this environment form sterile dystrophic endbulbs, permanently losing their ability to regenerate through the body's endemic processes. The glial scar is thus both physically and chemically inhibitive to axonal regrowth, and despite its crucial role in supporting the fragile injured tissue, broadly inhibits functional recovery [92]–[94].

2.2 Neural Interfacing Electrodes

2.2.1 What is a Neural Interfacing Electrode?

Implantable neural interfacing electrodes are Class III medical implants (as stipulated by council directive 93/42/EEC of the European Union and the Council of Europe [95]), that are conduits for the flow of uni- or bi-directional information between the nervous system and an electrically-active device. Although many different electrode designs have been implemented over the years [21], [96]–[99], some universal basic features may be identified. These comprise of an electrically conductive material having its active sites defined by an insulating component, and insulated leads that connect the electrode to the active device. When implanted in the human body, the electrodes are intended to achieve one of three forms of neuromodulation, these being stimulation, blocking, or recording [18], [100].

The goal in electrical stimulation is to trigger neural membrane depolarization and initiate a self-replicating action potential capable of eliciting the desired response. For most applications, this is achieved through periodic injection of a biphasic current pulse having charge balanced (net zero charge) cathodic and anodic phases. Cathodic current initiates electron flow from electrode to tissue, with a reducing effect taking place at the electrode. Anodic current moves in the opposite direction, resulting in an oxidative effect. Cathodic-first pulses are considered standard for stimulation to match the physiological process of generating an action potential [12], [101]. Some examples of typical stimulation pulses are given in Figure 2.5, each being charge-balanced to ensure no irreversible redox reactions can occur on the electrode surface [101]. Unlike the waveforms shown in Figure 2.5 a and b, Figure 2.5 c shows a pulse that is monophasic, where the charge balance is achieved by a capacitor discharge circuit rather than a separate anodic pulse. Owing to the wide variability in the physiology and anatomy of different sections of the nervous system, different electrical thresholds exist to evoke useful functional responses. These thresholds are heavily dependent on the target neuron and electrode placement, and are very sensitive to chemical and physical changes to the surrounding environment [101], [102].

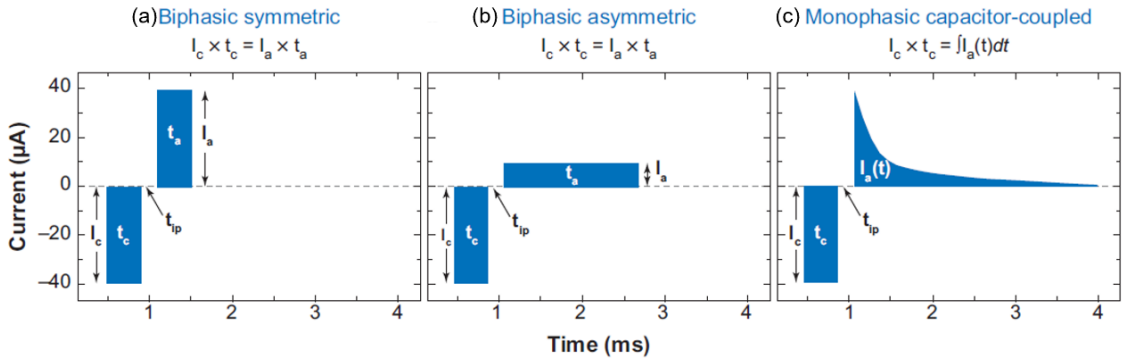

Figure 2.5: Three examples of charge-balanced current stimulation pulses, being (a) Biphasic symmetric; (b) Biphasic asymmetric, and; (c) Monophasic capacitor-coupled. The waveforms are characterised by the parameters of I_c (cathodic current), t_c (time for cathodic phase), t_{ip} (time for interphase dwell), and t_a (time for anodic phase), which vary based on the electrode and intended application. From [101].

Stimulating electrodes make up the majority of neural interfacing devices in widespread clinical use, finding application in the management and treatment of various neurological conditions [21], [99], [100], [103]. Perhaps the most well-known application is that of deep brain stimulation (DBS), where electric pulses are used to deliver charge-based therapy to different areas of the brain. Patients suffering from PD have seen great benefits from both high frequency (~130-185 Hz) and low frequency (~20-60 Hz) stimulation, mitigating the effects of bradykinesia and tremors primarily through stimulation of the subthalamic nucleus [104]. Other movement disorders such as dystonia and essential tremor have also been successfully treated with DBS, while its application in treating neurological conditions like epilepsy, treatment-resistant depression, and Tourette's Syndrome is also being explored [84], [105]. The restoration of auditory perception is another common application for stimulation electrodes, involving the delivery of depolarizing pulses to spiral ganglia in the cochlea[1]. On the other hand, stimulation of peripheral nerves has proven successful in restoring motor and sensory functions to patients suffering from SCI-induced paralysis [106].

Despite seemingly being antipodal, electrodes that perform blocking actions have essentially identical modes of operation to those of stimulating electrodes. While stimulating electrodes depolarise the membrane for neuron firing, blocking disrupts the neuron's membrane potential to either decrease its likelihood of firing or prevent it completely. This may be achieved either by pushing the neuron into its refractory period through hyperpolarization, inactivating the membrane channels through repetitive

[1] A hollow, spiral bone located in the inner ear.

subthreshold depolarization events, or through field modulation via high frequency pulses [101], [107], [108].

Blocking electrodes are employed for the management of conditions characterised by overactivated neurons, most notably neuropathic pain, muscle spasms, and urge incontinence [18]. Patients suffering from failed back surgery syndrome and complex regional pain syndrome are frequent recipients of blocking electrodes, wherein kilohertz frequency (~10 kHz) pulses are delivered to spinal dorsal horns to inhibit pain sensory processing [42], [103]. Research is also ongoing to determine the applicability of Vagus-blocking for appetite suppression in morbid obesity, with positive results indicating increased weight-loss associated with device usage [108]. For some applications, blocking and stimulation may be applied simultaneously along the same nerve to elicit the desired response via selective targeting. Concomitant efferent stimulation and afferent blocking on the Vagus nerve has successfully reduced glycemia in mouse models, demonstrating its potential for the management of type II diabetes [107]. Examples of typical parameters (amplitude, pulse width, and pulsing frequency) used for different stimulation and blocking electrodes are given in Table 2.3.

Table 2.3: Typical parameters used in stimulation and/or blocking electrodes. Values obtained from literature.

Electrode Type	**Organism/ Model**	**Stimulating/ Blocking**	**Current (mA)**	**Voltage (V)**	**Pulse Width (μs)**	**Freq. (Hz)**	**Ref.**
Cochlear	Cochlea Model	Stimulating	1.25	/	200	250	[109]
Deep Brain Stimulation	Human	Stimulating	/	1.5-4.1	60	60 and 130	[104]
Femoral Nerve Electrode	Human	Stimulating	0.1-2.0	/	1-225	20	[106]
Spinal Cord Stimulation	Human	Blocking	1-5	/	30	10k	[110]
Vagus Nerve Electrode	Human	Blocking	6	/	90	5k	[108]
Combination Vagus Nerve Electrodes	Rat	Stimulating	0-2	/	200	15	[107]
		Blocking	4	/	10	26k	

Recording electrodes measure neural firing on high-frequency bands as the voltage ‘spikes’ of individual neurons immediately adjacent to the device, and on low-frequency signals as the summation of action potentials occurring within ~350 μm of the electrode

[111]. These electrodes are very sensitive to noise, where useful measurements can only be achieved with a signal-to-noise ratio (SNR) of 5:1 or larger. Successfully maintaining this ratio with chronic implantation is complicated by several factors, most critically by the background noise of surrounding, non-targeted neurons, and by sources of impedance that provide obstacles to signal transmission. In the PNS, further interference is produced by muscle activity, the electric signals of which are orders of magnitude larger than those of neurons [18]. In terms of clinical application, recording electrodes are fundamental to all emerging functional prosthetics such as artificial retinas and bionic limbs, completing the closed-loop circuitry required for their smooth operation [99], [112].

2.2.2 Different Types of Neural Interfacing Electrodes

Implantable neural interfacing electrodes are typically categorised by their site of application, whether that be the CNS or the PNS. When considering devices for the CNS, the classification is based on whether the tissue of the cortex or spinal cord is penetrated by the electrode [113], and may be described as:

1. **Intracortical/ Intraspinal electrodes –** devices that penetrate the cortex or spinal cord, respectively. The electrodes may come in a variety of configurations, most notably as arrayed, rigid probes like the Utah Array (Figure 2.6 a), as microwire probes like the Michigan electrode (Figure 2.6 b), or as deep-penetrating shafts such as those used for DBS (Figure 2.6 c) [113].
2. **Intracranial (surface) electrodes –** do not penetrate the brain or spinal cord but are placed superficial to the tissue. May be subdural or epidural when applied to the brain [23]. When applied to the spinal cord they are typically inserted into the epidural space between the meninges and vertebral ligament. The device may be cylindrical or paddle-shaped, and have many electrically-active sites arranged throughout [114]. These electrodes achieve best results when having high conformity to the organ's external morphology, such as the flexible subdural device developed by Oribe *et al.* [115] shown in Figure 2.6 d.

For interfacing with the PNS, Russell *et al.* [116] outline four classifications of electrodes, listed hereunder from least to most invasive:

1. **Extra-neural electrodes** – similar in concept to surface electrodes in the CNS. These devices maintain the physical integrity of the epineurium as they are placed superficial to the nerve. However, they typically suffer from poor selectivity and have the highest interfacial impedance of the four electrode types. These electrodes are also poor at distinguishing between sensory and motor neurons within the nerve [97]. The flat interface nerve electrode (FINE) developed by Schiefer *et al.* [117] (shown in Figure 2.6 e) mitigates these problems by locally reshaping the nerve, allowing the electrode contacts to selectively interface with different axonal bundles. Assessments on the femoral nerves of 7 human patients demonstrated selective activation of distinct muscle groups when different contacts on the electrode were engaged.
2. **Interfascicular electrodes** – these electrodes are inserted into the nerve, penetrate the epineural sheath, and rest within the interfascicular space, adjacent to the axonal bundles. Tyler and Durand [118] developed the landmark 'slow penetrating interfascicular electrode' in 1997, capable of triggering distinct dorsiflexion and plantarflexion of the ankle with the same electrode.
3. **Intrafascicular electrodes** – like interfascicular electrodes, these devices are inserted into the nerve, but also breach the perineural sheath. This provides the highest possible resolution and least interfacial impedance, as electric signals are exchanged directly within the fascicle of interest. The transverse intrafascicular multichannel electrode (TIME) developed by Boretius *et al.* [119] is an example of such a device, demonstrating highly selective stimulation resulting in the activation of different muscle groups. The electrode is shown intersecting the sciatic nerve of a rat in Figure 2.6 f.
4. **Regenerative electrodes** – requiring an intersected nerve, the electric contacts are arranged in a mesh-like architecture through which axons are expected to regrow. MacEwan *et al.* [120] successfully demonstrated rat sciatic nerve regeneration through their sieve-like design (Figure 2.6 g), achieving significantly higher axonal growth as compared to the control group. In theory, these devices should also provide excellent selectivity, with the ability to record or stimulate individual axons. However, the degree to which this may be achieved is dependent on the placement of electrical contact with respect to the nodes of Ranvier. As regeneration is an integral part of this device operation, it is difficult to predict

where the nodes will form, and so its efficiency in this regard is subject to variation [116].

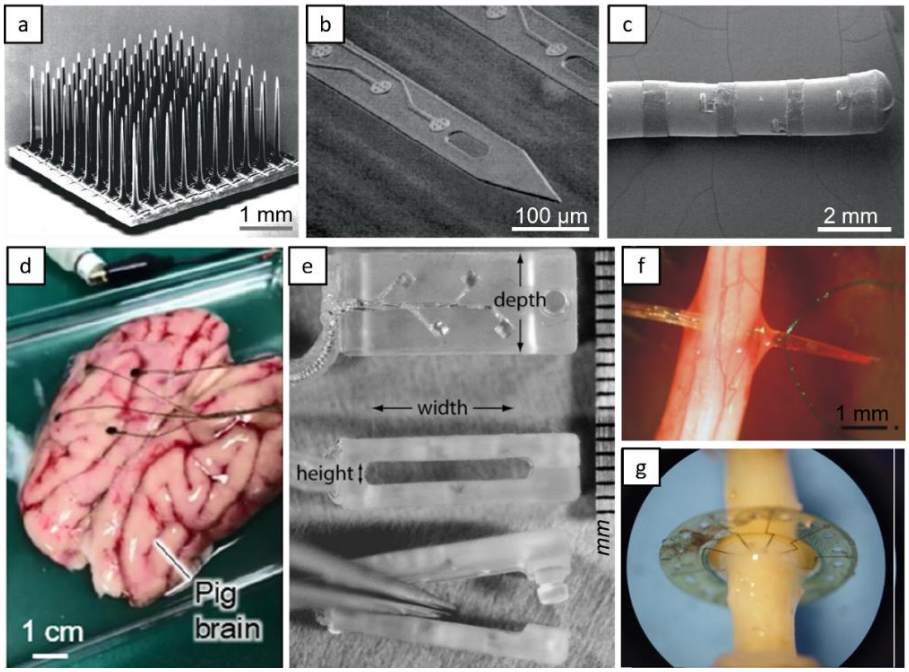

Figure 2.6: Implantable neural interfacing electrodes: (a) The Utah Array [121]; (b) The Michigan electrode [121]; (c) Shaft of a DBS electrode [121]; (d) Subdural electrode by Oribe *et al.* [115]; (e) FINE electrode by Schiefer *et al* [117]; (f) TIME electrode by Boretius *et al.* [119], and; (g) Regenerative electrode by MacEwan *et al.* [120].

2.2.3 Requirements of Implantable Neural interfacing Electrodes

Given the sensitivity of the tissues they interact with and the criticality of the functions they perform, implantable neural electrodes are naturally subject to a long list of stringent requirements. Meeting these criteria ensures a balanced risk-to-benefit ratio for the patient, delivering a device that is both safe and effective for chronic use [18], [101]. Hereunder, these requirements are categorised into three classifications and discussed accordingly.

2.2.3.1 Compatibility Requirements

An implantable neural electrode must be biocompatible. This means that any external surface of the device, including the electrical contact, insulation, lead, and electronic housing, must be strictly non-toxic and non-immunogenic to neural cells or to other surrounding tissue [122]. Moreover, the device must not leach or break down into chemicals or components that break biocompatibility or cause systemic issues, a

condition that must be maintained throughout the implant's entire lifetime [29], [123]. Fulfilling these requirements necessitates that electrode materials have a high level of biostability, as the environment within the human body provides a challenge for the longevity of implanted devices. This ensures the electrode can withstand physical and chemical degradation, maintain its structure as intended, and minimise the breakdown of its electrochemical characteristics throughout its lifetime [105], [122].

These requirements are in service of mitigating the foreign body response (FBR) that directly follows electrode implantation. The process of electrode implantation generates tissue damage at the site of insertion, triggering the body's wound healing response as described in section 2.1.4. While the acute stages of the FBR are synonymous with those of regular wound healing, the trajectories diverge when transitioning to the chronic stage [124]. The difference stems from the sustained presence of the implant (including any particulates it may produce), which macrophages try and fail to digest in a process known as phagocytosis. The continuous failure of macrophages to fulfil this role results in frustrated phagocytosis, triggering additional macrophage recruitment to the site that in turn causes the upregulation of pro-inflammatory and pro-fibrotic cytokines [1], [123]. Multinucleated giant cells, predominantly foreign body giant cells (FBGC), form through the fusion of mass-migrated macrophages and surround the implant. Subsequently, fibroblasts recruited to the ECM receive mechanical cues from the stiff surface of the electrode and become activated into myofibroblasts. With time, these cells encapsulate the implant, isolating it from the surrounding environment as the fibrous capsule matures; a process known as implant fibrosis [124] (Figure 2.7 a). When this process occurs in the CNS, additional cells, mainly astrocytes, are activated and migrate to the site of implantation, building a dual-layered scar (fibrous and glial) around the electrode (Figure 2.7 b) [121], [124], [125].

If the use of biocompatible materials is assured, then the stiffness of the electrode is one of the largest contributing factors to encapsulation [122], [126]. This problem continues to self-propagate even once the initial capsule has formed due to micromotions that the electrode is subjected to. These include seemingly minute movements such as those caused by the patient's breathing and blood pumping through adjacent vasculature [102]. Neural interfacing devices, the vast majority of which have rigid assembly designs based on materials with very high moduli of elasticity, cannot deform sufficiently to match the

movement of surrounding tissue [122]. This is due to the stiffness mismatch that exists between biological tissue and the materials used for constructing electrodes, a difference that can be several orders of magnitude. In addition to exacerbating the FBR, this stiffness mismatch can also damage targeted neurons through constant exposure to sliding and compressive forces, negating the electrode's therapeutic benefits. Even more recent flexible electrode designs, most of which are based on poly(dimethylsiloxane), are only able to mimic the mechanical properties of nerves and the spinal cord when including collagenous and meningeal layers, and as such are only matched for surface contact (refer to Table 2.4) [122]. Although this form of biomimicry is still effective at reducing the FBR, even in penetrating electrode types, it cannot be relied upon exclusively to manage electrode isolation [93], [94], [122], [127], [128].

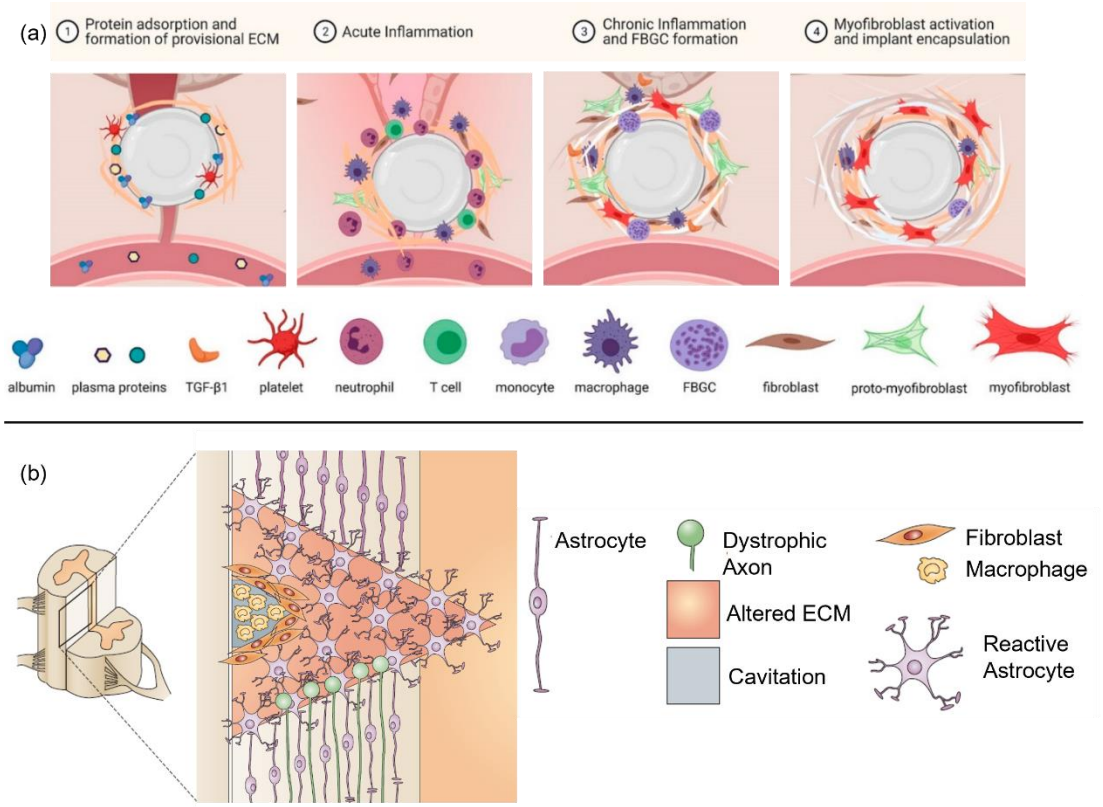

Figure 2.7: (a) Progression of the foreign body response (FBR) and fibrous encapsulation in the PNS. Adapted from [124]; (b) Formation of a glial scar in CNS (spinal cord) following a disruption to the meningeal layers, resulting in fibroblast and macrophage infiltration. Adapted from [93].

2.2.3.2 Physical Requirements

The most demanding physical requirement governing electrode design in the current age is miniaturisation [105], [129]–[131]. Driven by a compulsion to improve the human condition, research in the field of bionic technologies has been advancing at an

accelerated pace. Many devices emerging from this movement have operations contingent on high neural selectivity and signal resolution, specifically targeting the micrometric structures detailed in section 2.2.22.1.3. This coincides with a push for electrode miniaturisation in all applications of stimulating, blocking, and recording, requiring micro-electrodes with geometric surface areas (GSAs) less than 0.01 mm^2 [18], [101].

Table 2.4: The Young's Modulus (Pa) of human tissue relevant to neural interfacing, of electrodes in current use, and of flexible electrode arrays developed by different research groups.

	Reference	**Tissue/ Material**	**Young's Modulus (Pa)**
Human Tissue	[39]	Neurons	(2-4) x 10^2
		Glia	(1-10) x 10^3
	[132]	Brain	5.5 x 10^3
	[133]	Spinal Cord	4 x 10^4
	[134]	Peroneal Nerve	3.8 x 10^6
		Tibial Nerve	4.4 x 10^6
Electrodes in Current Use	[118], [135]	FINE Electrode (Silicone Rubber)	~ 6 x 10^6
	[119], [136]	TIME Electrode (Polyimide)	~ 3 x 10^9
	[22], [137]	Utah Array Electrode and Michigan Probe (Silicon)	~ 190 x 10^9
Flexible Electrode Array by Pul *et al.*	[138]	Parylene-C	(2-4) x 10^9
Flexible Electrode Array by Shur *et al.*	[139]	poly(dimethylsiloxane) (PDMS)	5 x 10^4
Flexible Electrode Array by Jeong *et al.*	[140]		

When considering electrodes for the CNS, the geometric limitations posed by the complex structures of the brain and spinal cord, as well as the criticality of their functions are appreciated even by those without medical backgrounds. However, this rarely extends to the PNS, where the limitations are often overlooked by electrode developers [71], [99]. Although nerves in general tend to grow adjacent to organs and blood vessels, all of which are vital in maintaining bodily functions, some nerves have placements that are exceptionally precarious. A fitting example is the vagus nerve, located within the sheath of the carotid artery, a major blood vessel that delivers oxygenated blood to the head and brain, that if penetrated or transected constitutes a surgical crisis. It follows then that

electrode size should be restricted, minimising disruption to the carotid sheath and by extension, the risk of fatal injury to the patient [18].

Besides making the case for electrode miniaturisation, this example may also be used to highlight another requirement, ease of implantation [13]. Regrettably, miniaturised electrodes are not conducive to easy insertion techniques, as device handling is complicated as its size diminishes. This issue is compounded by the rising use of flexible electrode materials, and particularly affects penetrating electrodes by mechanically inhibiting their capacity for self-supported penetration. Several techniques have been described to facilitate implant placement whilst maintaining a small surgical footprint, the aim being to reduce implantation trauma and mitigate the subsequent FBR [111]. The use of a rigid shuttle to deliver a decoupling electrode to its intended location is a popular choice, consisting mainly of stainless steel needles such as those used by Zhang *et al.* [141] and Boretius *et al.* [119] in the brain and sciatic nerve of rats, respectively. Alternatively, stiff bioresorbable materials may also be employed, being implanted into the tissue along with the device itself and then degrading with time. Pas *et al.* [142] adopted this technique in the form of hydrolytically degradable polymer shuttles, while Cointe *et al.* [143] developed a temporary electrode stiffener made of bioresorbable silk fibroin. By implementing these or similar approaches, electrode miniaturisation and flexibility can be maintained without compromising implantability.

Like any other implantable device, neural electrodes should also be capable of withstanding effective sterilisation procedures. Sterilisation is defined as the total destruction or elimination of microbial organisms and may be integrated into the device's production process (aseptic processing) or be carried out once the device has been finalised (terminal sterilisation). The most widespread sterilisation techniques include gamma-irradiation (γ), ultraviolet-irradiation (UV), pressurised steam (autoclaving), and ethylene oxide (EtO) exposure [144]. Sterilisation often presents a challenge for contemporary electrode developers, owing to the increased use of heat- and radiation-sensitive materials such as polymers and biological tissue. The issue is compounded in that such devices may contain a combination of materials, each with their own specific, and possibly inter-conflicting, technique incompatibilities. Undesired effects such as physical warping, loss of mechanical properties, altered degradation rates, decreased biocompatibility, and incomplete sterilisation may all result from poor technique

selection [144], [145]. Zada *et al.* [145] observed a 33% decrease in the molecular weight of PLCL (poly-L-lactide-co-ε-caprolactone) polymeric devices following 25 kGy (2.5 Mrad) of γ-irradiation. This was associated with scission of the polymer chains, and significantly shortened the implant's projected lifetime due to accelerated degradation kinetics. Conversely, no chemical or physical change was observed in implants sterilised via EtO exposure. Thus, the importance of designing devices that can withstand these sterilisation treatments, or that incorporate compensatory measures to account for these effects, cannot be understated.

2.2.3.3 Functional Requirements

2.2.3.3.1 Low Interfacial Impedance and High Charge Injection Capacity

Fundamentally, an electrode must be capable of transmitting an electrical current between the active device and the neurons of interest. It must do so whilst converting between its own electronic charge and the ionic charge generated by hydrated anions and cations in the body. Resistance to this conversion, i.e. resistance to the flow of current, creates impedance across the electrode/electrolyte interface [44]. Impedances that are strictly of electrochemical origin are highly undesirable, and being generally of certain and predictable nature, should be characterised and optimised at the early stages of electrode development. This is due to the compounding effect that electrochemical impedance will have when introduced into the biological environment, where additional impeding factors (predominantly fibrous growth) arise to obstruct current flow. In recording electrodes, where the amplitudes of neural signals are in the order of a few tens of microvolts, high interfacial impedance raises thermal noise. Distinguishing these minute signals from the general electrical noise of ionic fluctuations thus becomes impossible, as demonstrated in Figure 2.8 [101], [146].

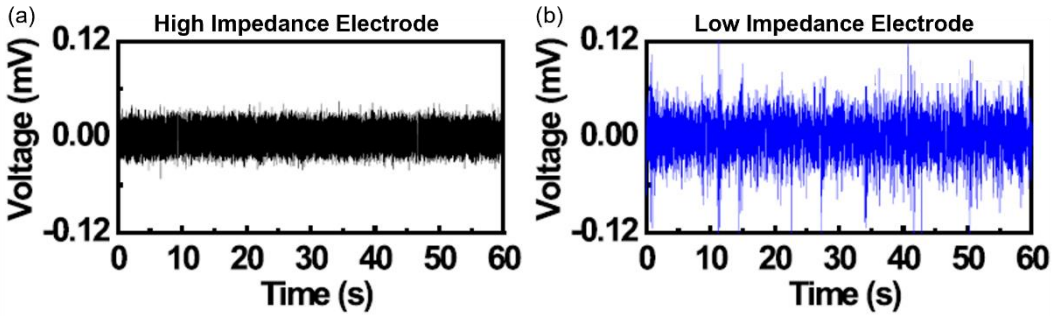

Figure 2.8: Spontaneous neural signals recorded in the brain of a Sprague-Dawley rat from (a) an electrode with high interfacial impedance, and; (b) an electrode with low interfacial impedance. From [146].

On the other hand, stimulating and blocking electrodes that must meet threshold voltages for operation are also held back by interfacial impedance. To compensate for the voltage drop caused by this resistance, higher current densities are injected through the electrode to meet the required minimum, risking damage to both tissue and electrode [147]. This damage comes in the form of irreversible faradaic reactions, most commonly through the electrolysis of water. When charge injection surpasses this polarising threshold, water molecules on the electrode surface are either reduced or oxidised, corresponding to excessive negative or positive polarisation, respectively. Cathodic polarisation results in the evolution of hydrogen gas along with hydroxyl ions (Equation 2.1), while anodic polarization evolves oxygen gas and hydrogen ions (Equation 2.2) [101].

$$2H_2O + 2e^- \rightarrow 2OH^- + H_2 \tag{2.1}$$

$$2H_2O \rightarrow O_2 + 4H^+ + 4e^- \tag{2.2}$$

The danger of electrolysis comes about from resulting localised pH changes, the formation of bubbles that have the potential to embolize, and the production of reactive oxygen species (ROS). The latter process, triggered by the metabolism of oxygen, produces super oxides that dismutate in the presence of hydrogen into hydrogen peroxide (H_2O_2) [148]. As demonstrated by Whittemore *et al.* [149], neurons are easily harmed by excessive peroxide formation, where *in vitro* tests demonstrate its capacity of inducing cell death through the pathway of apoptotic suicide in as little as 3 hours. The brain, having a very high oxygen demand, is exceptionally prone to oxidative stress, where its composition of unsaturated lipids readily undergo oxidative change and peroxidation [148].

In addition to tissue damage, the electrode itself is also invariably affected by irreversible faradaic reactions. In the case of metal electrodes, transpassive corrosion and pitting are common, and, especially in the case of platinum, soluble complexes evolving from the oxidative processes lead to dissolution of the electrode [101]. Shepherd *et al.* [150] observed this effect in platinum electrodes when stimulation was carried out at charge densities outside the established safety window. The electrodes, which were implanted in the cochlea of adult male cats for 6 months, exhibited significant degradation compared to controls, producing particulates that concentrated around the device and even reached the kidneys. When considering electrodes that feature some form of coating, this problem is further exacerbated, as irreversible faradaic reactions may also trigger blistering and delamination of the coated layer in addition to dissolution [101]. Negi *et al.* [151]

observed this effect in Utah Electrode Arrays coated with activated iridium oxide, when pulsing at charge densities that pushed the potential outside the safety window. The film was shown to lose its coherence and become dislodged from the underlying substrate in whole sections. It is therefore apparent that tissue damage is also instigated by the electrode's response to excessive polarisation in of itself, as by-products of implant degradation are well recorded to cause local and systemic problems *in vivo* [152]–[155].

For these reasons, it is imperative that all charge injection occurs within the respective material's electrolysis limits, commonly referred to as the water window. The amount of charge that can be safely and reversibly injected within this window is known as the charge injection capacity (CIC). The advantage of materials with large water windows is therefore evident, as higher current amplitudes may be administered without pushing the potential beyond the electrolysis limit [21].

2.2.3.3.2 Capacitive-Based Charge Transfer

In view of the hazards of irreversible faradaic reactions, charge transfer across neural electrodes must be achieved through alternate means. When considering an ideal electrode surface, the desired form of charge transfer may be broadly described as capacitive, comprising either double-layer capacitance, pseudocapacitance, or simultaneous operation of both [39].

The first classification, double-layer capacitance, relies on the alternating process of charging and discharging an electrochemical capacitor that forms on the electrode surface. When polarised, an implanted electrode will accumulate electrical charge on its surface, constituting the first 'plate' of an electrochemical double layer capacitor (EDLC). The second 'plate', comprising of ionic charge from the solvated ions in tissue fluid, is separated from the first by a dielectric layer of polarised water molecules adsorbed on the electrode surface. In this mechanism, charge transfer is achieved without the generation or consumption of chemical species, and thus faradaic reactions, being kinetically and thermodynamically unfavourable, are supressed [156], [157].

The charge stored on an electrode with double-layer capacitance C_{dl} may be calculated from Equation 2.3:

$$C_{dl} = \frac{Q}{V} \tag{2.3}$$

where Q is the amount of charge transferred for a given potential V. Assuming that the C_{dl} of a given electrode is constant, then the evolving current I may be derived from equation 2.3 to give:

$$I = \frac{dQ}{dt} = C_{dl}\frac{dV}{dt} \tag{2.4}$$

where t is time. For a voltage that changes linearly with time at a sweep rate of v (in Vs^{-1}), the relationship between current and rate of change of voltage may be described by equation 2.5:

$$I = C_{dl}v \tag{2.5}$$

It may thus be deduced that current should theoretically vary linearly with voltage sweep rate, a strong indicator of a true EDLC [158].

The concept of an EDLC in its most referenced form is illustrated in Figure 2.9 a. The model shown was developed by Stern, combining Helmholtz's initial contributions to the theory of EDLC (the rigid, inner Helmholtz plane) and Gouy-Chapman's theory of a diffused, outer layer (making up the outer Helmholtz plane). The Stern layer represents an area of linear potential drop from the electrode surface, which then changes to an exponential drop in the diffuse layer. Most researchers refer to this double-layer as a 'Helmholtz double layer', despite making reference to the Stern Model. For simplicity, most diagrams also depict a basic two-layer approach [157], [159].

From this perspective, the double-layer capacitance, C_{dl} may described using the basic equation for a parallel-plate capacitor, given in Equation 2.6:

$$C_{dl} = \varepsilon\frac{A}{d} \tag{2.6}$$

where ε is the electric permittivity of the dielectric, A is the surface area of the electrode, and d is the distance between the electrode surface and the outer Helmholtz plane. Although not useful in any practical sense to determine the capacitance of neural electrodes, Equation 2.6 demonstrates the relationship of direct proportionality between double layer capacitance and area, i.e., that a larger electrode area results in larger capacitance [158].

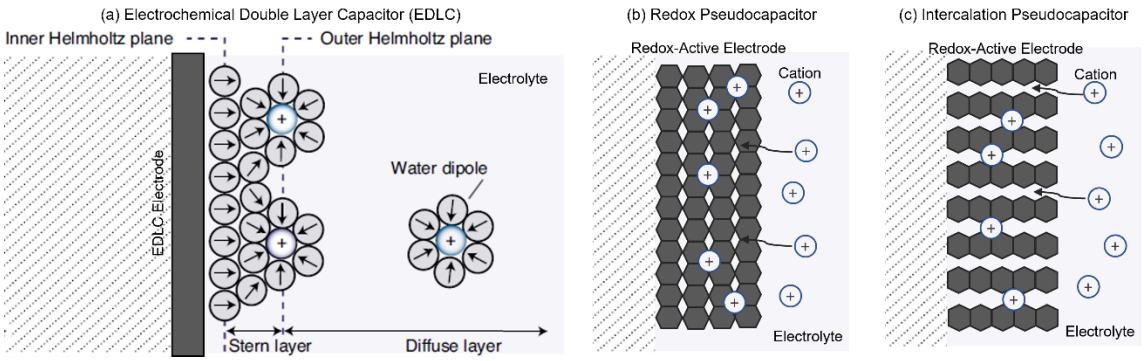

Figure 2.9: Charge transfer mechanisms of: (a) An electrochemical double layer capacitor (EDLC), showing the Stern model; (b) A redox pseudocapacitor, and; (c) An intercalation pseudocapacitor. (a) adapted from [157], (b) and (c) adapted from [160].

The second type of charge transfer is pseudocapacitance. As the name 'pseudocapacitance' suggests, electrodes that transfer charge via this mechanism exhibit *false*-capacitive behaviour, performing kinetically fast, reversible faradaic reactions on their surface or near-surface, whilst still retaining most of the electrochemical signatures associated with EDLCs. Namely, pseudocapacitors display a quasi-linear relationship between current and sweeping potential, a behaviour more closely associated with traditional capacitance rather than the battery-type devices that usually perform faradaic reactions[2] [161].

Pseudocapacitance in neural electrodes can occur via two mechanisms, either through redox reactions, so-called intrinsic pseudocapacitance (Figure 2.9 b), or through intercalation, known as extrinsic pseudocapacitance (Figure 2.9 c). In the first case, charge is transferred via ions that are electrochemically adsorbed onto and desorbed out of the surface of the electrode during its reduction and oxidation, respectively. Materials that fall in this category demonstrate pseudocapacitive behaviour irrespective of their morphology or particle size, hence the term 'intrinsic'. Additionally, this process is theoretically independent of diffusion-control, and the current should broadly have a linear relationship with the voltage sweep rate as per Equation 2.5. Although redox pseudocapacitance is largely a bulk phenomenon, a positive linear correlation also exists between its value and the electrolyte-accessible surface area [162], [163].

[2] For batteries, evolving current has a linear relationship with the square-root of changing potential.

Conversely, extrinsic pseudocapacitance involves the intercalation and deintercalation of ions in and out of an electrode's layered or tunnelled structure without any crystallographic phase change taking place. By this definition, extrinsic pseudocapacitors derive their charge transfer properties from their morphology and particle size, and do not necessarily retain them if these factors are altered. In particular, intercalation pseudocapacitors are more prone to diffusional limitations unless these characteristics are optimised (i.e., minimising the ion diffusion pathway), and as such benefit greatly from structural features that increase surface area [164]:

2.2.3.3.3 Large Electrochemical Surface Area

When considering a sinusoidal input, the relationship between capacitance and impedance Z_C is described by Equation 2.7:

$$Z_C = -j\frac{1}{\omega C} \tag{2.7}$$

where Z_C is the impedance across the capacitor in Ω, j is a complex number given by the square root of -1, ω is the frequency of the sinusoid in rads^{-1}, and C is the capacitance in F. It is evident from this equation that increasing electrode capacitance, whether it stems from double layer formation or through reversible faradaic reactions, is beneficial in reducing interfacial impedance [101], [157].

Given the inverse relationship between electrode area and interfacial impedance, enlarging the geometric surface area (GSA) to improve charge transfer seems intuitive. However, this directly contradicts the requirement for miniaturisation as outlined in section 2.2.3.2, where larger electrodes decrease selectivity and increase invasiveness to the detriment of device operation. Moreover, Wellman *et al.* [102] specifically oppose this approach for recording electrodes due to the signal attenuation that occurs across large distances. Figure 2.10 a compares a small electrode, which may be electrically modelled as a single RC (resistance-capacitor) circuit, with a larger one, modelled as several RC circuits connected in parallel. The more distant the parallel element is from the voltage source (the firing neuron), the smaller the voltage detected. Since the voltage across a parallel circuit is computed as the mean of the parallel elements, high voltages detected proximal to the source are averaged with smaller ones recorded distally, effectively weakening the measured signal.

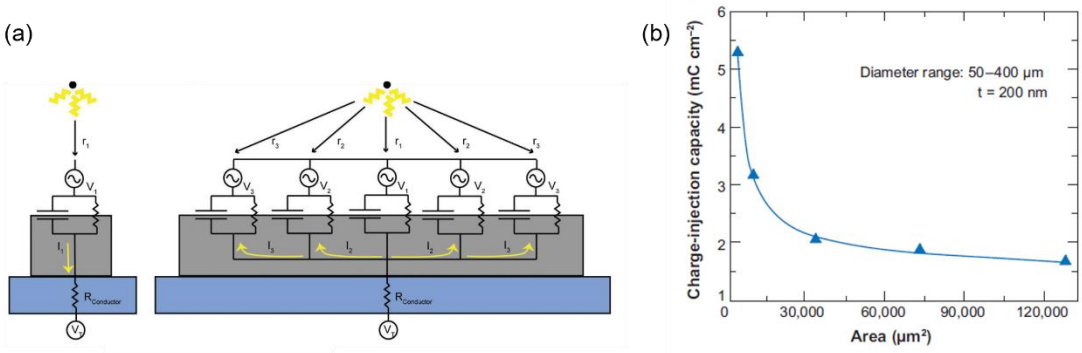

Figure 2.10: (a) Electrodes used for neural recording with a small GSA (left) and a large GSA (right), modelled using RC circuits connected in parallel. Signal attenuation ($I_1 > I_2 > I_3$) across distance r (where $r_1 < r_2 < r_3$) means that larger electrodes record smaller voltage amplitudes from a firing neuron due to averaging across parallel circuits [102]; (b) CIC decreases as the area of a stimulating electrode increases, from [101].

Cogan [101] further demonstrates the fault in this ideology when applied to stimulating electrodes. Considering circular electrodes sputter-coated with iridium oxide, the measured charge transfer capacity per cm^2 decreases as the electrode's diameter increases from 50 to 400 µm, despite an identical coating thickness of 200 nm throughout (Figure 2.10 b). This is attributed to non-uniform current distribution across large surfaces, resulting in charge-injection localised at the perimeter (or tips) of the electrode and an underutilised central region. Moreover, larger surfaces are highly susceptible to transport rate restrictions due to increased diffusion lengths, contributing to the reduced charge transfer capacity observed. For these reasons, solutions for impedance reduction should not depend on increasing the GSA.

Rather than increasing the GSA, this issue may instead be tackled by increasing the electrochemical surface area (ESA) of the electrode. Introducing roughness and/or porosity to the electrode surface on the micro- and nano-scale can increase the electrolyte-interfacing area by several orders of magnitude whilst maintaining the benefits of miniaturised geometry. By reducing the interfacial impedance, the required charge may thus be transferred across the electrode surface using pulses of smaller amplitudes. In the case of stimulating and blocking electrodes, the desired physiological response is achieved without causing damage to tissue or device, while recording electrodes benefit from a reduction in impedance-generated noise [101].

This approach has generated great success and achieved widespread implementation across several electrode-types. Lee *et al.* [165] increased the ESA of stainless steel

recording electrodes via electrochemical etching, creating a surface texture comprising of pores 1-1.3 µm in diameter. The modified electrodes exhibited significantly lowered impedance across a frequency spectrum of 0.05-200,000 Hz as compared to identical electrodes without etching (Figure 2.11 a). Additionally, local field potentials (LFPs) recorded in the cortex of Sprague-Dawley rats were consistently measured with higher amplitudes and lower noise for the textured electrodes. Chung *et al.* [146] achieved similar electrochemical improvements when using CF_4 (tetrafluoromethane) plasma to texture the surface of gold neural probes. As the surface roughness was increased from the original R_a of 1.7 nm to 16 and 22 nm, the measured interfacial capacitance was increased by factors of 3.4 and 42.4, respectively. Moreover, the amplitudes of action potentials induced via 200 and 1000 µA stimulation pulses demonstrated a clear upward trend with increased surface roughness. As shown in Figure 2.11 b, the R_a= 22 nm electrodes induced LFP pulses with larger voltage peaks than the R_a= 16 nm electrodes at both stimulation amplitudes, whereas both electrodes generated pulses larger than the original electrode, the measurements of which were too small to detect in the rat cortex.

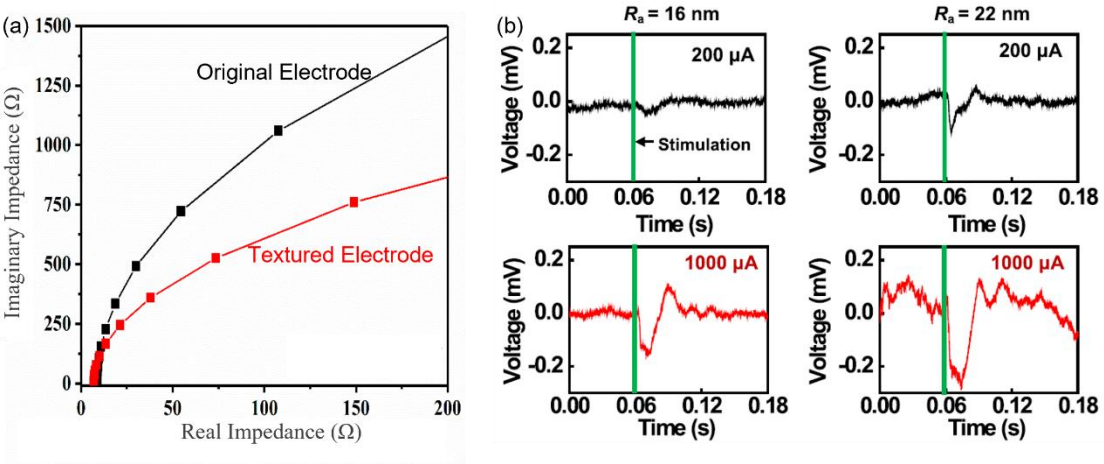

Figure 2.11: (a) A plot of the imaginary impedance (y-axis) versus real impedance (x-axis) measured as a response to an AC voltage pulse of amplitude 10 mV. Readings were taken within the frequency range of 0.05-200,000 Hz. Adapted from [165]. (b) Induced LFPs following stimulation pulses with current amplitudes of 200 µA (black) and 1000 µA (red) for gold electrodes textured to an R_a of 16 nm (left) and 22 nm (right). Adapted from [146].

However, this methodology is not without its restrictions, as the emergence of pore resistance places a geometric limit on its effectiveness. Charge transfer through porous structures becomes negatively impacted as their length is increased and their radius decreased. The resulting effect is illustrated in Figure 2.12 a, showing a pore inundated

with electrolyte resistance (R1, R2, etc), which when combined with the material's interfacial capacitance (C1, C2, etc) gives rise to a delay line with a large time constant. Large impedances result when the electrode is subjected to high frequency pulses, as the surface area at the lower part of the pore becomes ineffective. An equation derived by Song *et al.* [166] describes the maximum height of a pore with a given radius beyond which further increase in height becomes redundant. For a sinusoidal wave, the limiting height of a pore, λ may be given by Equation 2.8:

$$\lambda = \frac{1}{2}\sqrt{\frac{kr}{C\omega}} \tag{2.8}$$

where k is the conductivity of the electrolyte in $\Omega^{-1}cm^{-1}$, r is the radius of the pore in cm, C is the interfacial capacitance of the pore in Fcm^{-2}, and ω is the angular frequency of the sinusoid in $rads^{-1}$.

Achour *et al.* [167] provide a very effective demonstration of the relationship between pore geometry, testing frequency, and charge transfer capacity in their work on porous titanium nitride electrodes. The areal capacitance of electrodes having pores of identical diameters but different heights (180 and 980 nm, referred to respectively as E_{180} and E_{980}) was measured at increasing voltage scan rates. The E_{180} electrode, having a shorter pore length and thus a smaller ESA, has a low measured areal capacitance (~1.5 $mFcm^{-2}$), a value that undergoes little change as the scan rate is increased from 0.002 Vs^{-1} to 5 Vs^{-1}. The delay line that forms within the pores is inconsequential due to their shallow structure, and hence the loss in capacitance is minimal. By comparison, the E_{980} electrode, having an ESA that is ~ 5.4 times higher than that of the E_{180}, has a measured capacitance (~9.5 $mFcm^{-2}$) of approximately similar magnitude at a scan rate of 0.002 Vs^{-1}. However, this value drops significantly as the scan rate is increased, with a final areal capacitance (~1 $mFcm^{-2}$) very similar to that of to E_{180} electrode (~0.5 $mFcm^{-2}$) at 5 Vs^{-1}, a behaviour the authors attribute to increased pore resistance. These results are shown in Figure 2.12 b.

In the same study [167], the limiting effect of porosity is further demonstrated through the comparison of electrodes E_{670} and $E_{780,}$ having pore lengths of 670 and 780 nm respectively, and pore radii $E_{670} >> E_{780}$. Although the areal capacitances of both electrodes drop from ~4 $mFcm^{-2}$ to ~1 $mFcm^{-2}$ as the scan rate is increased from 0.002

Vs^{-1} to 5 Vs^{-1}, the electrochemical response differs between them throughout this range. The E_{780} electrode, evidently limited by its pore geometry even at slow scan rates despite its enlarged ESA, experiences a steep drop in capacitance and then plateauing as the rate is increased. On the other hand, the capacitance of the E_{670} electrode undergoes a much more gradual decrease, resulting in consistently higher values compared to E_{780} before matching again at 5 Vs^{-1}. These results are shown in Figure 2.12 c. The disadvantage of excessively long and narrow pores is thus effectively demonstrated, going beyond redundancy, and actively contributing to higher impedances.

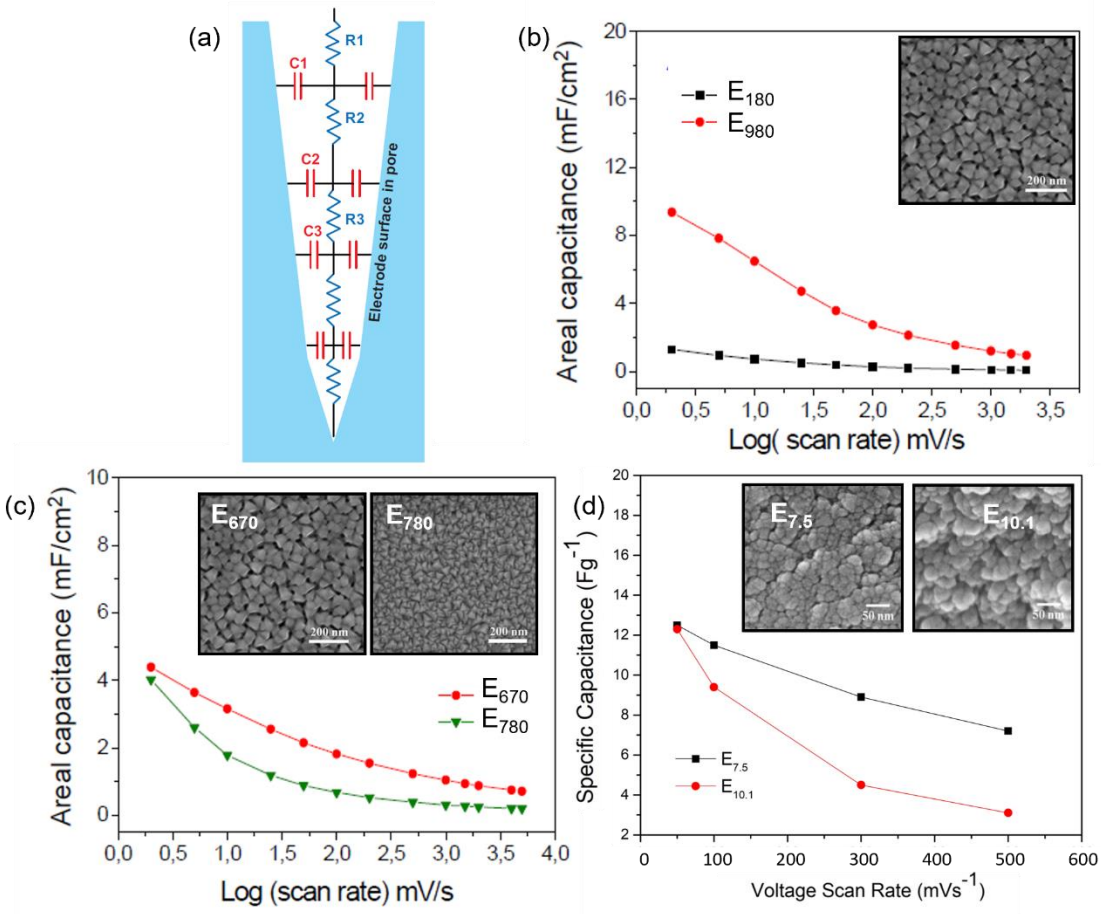

Figure 2.12: (a) Delay-line formation in a pore, the phenomenon behind pore resistance. From [101]; (b) Plot of areal capacitance versus log(scan rate) for electrodes with identical pore diameter but different pore lengths: 180 nm and 980 nm for E_{180} and E_{980}, respectively. Adapted from [167]; (c) Plot of areal capacitance versus log(scan rate) for electrodes with similar pore lengths (670 nm and 780 nm for electrodes E_{670} and E_{780}, respectively) but different pore heights, where the heights have the relationship $E_{670} >> E_{780}$. Adapted from [167]; (d) Plot of specific capacitance versus scan rate for electrodes with identical pore length but different radii: 7.5 nm and 10.1 nm for electrodes $E_{7.5}$ and $E_{10.1}$, respectively. Adapted from [168].

Conversely, Yang *et al.* [168] observed an opposite trend when studying carbon aerogel capacitors. The specific capacitance of electrodes with identical pore height (40 µm) but different radii (7.5 ± 0.1 nm versus 10.1 ± 0.2 nm, referred to as $E_{7.5}$ and $E_{10.1}$, respectively) was measured at different voltage scan rates. As shown in Figure 2.12 d, while both electrodes displayed a capacitance of ~12 Fg^{-1} at a scan rate of 50 mV/s, the capacitance of $E_{10.1}$ dropped below that of $E_{7.5}$ at a scan rate of 500 mV/s, measuring 3.1 Fg^{-1} and 7.2 Fg^{-1}, respectively. This is contrary to the predicted behaviour of porous electrodes, where wider pores are expected to produce comparatively less ionic resistance than their narrow counterparts at high frequencies. However, the authors observed that the $E_{10.1}$ electrodes had a sparse and poorly interconnected 3D structure when compared to the $E_{7.5}$. This inevitably leads to high electronic resistances in the material, eclipsing the benefits of lowered ionic resistance gained from larger pores. For this reason, the trade-off between pore diameter and electronic conduction should also be considered when designing for increased ESA.

2.3 Electrochemical Methods for Assessing Neural Electrodes

As evidenced by frequent reference to chemical reactions and electronic circuitry in the preceding section, the functional requirements of neural interfacing electrodes are discussed in terms of their electrochemistry. This section will outline the techniques most frequently employed to characterise the electrochemical properties of neural electrodes.

2.3.1 The Electrochemical Set-Up

Techniques to assess these properties rely on the ability to isolate electrochemical processes in a controlled environment and monitor them using highly sensitive equipment. As such, most experimentation takes the form of an electrochemical circuit made up of the electrode under test (referred to as the working electrode, WE), an electrolytic solution with ionic species of known molarity, and a counter electrode (CE) made of some inert material (usually platinum or carbon). This set-up is intended to mimic the two-electrode system of an implanted electrode, illustrated for stimulating and recording intracortical electrodes in Figure 2.13 a. When testing the electrodes *in vitro*, a third electrode is frequently added to the circuit to provide a reference against which voltage is measured (Figure 2.13 b) [169]. Although electrochemical measurements may be made without a reference electrode (RE), prominent research groups within the field

[157], [170], [171] recommend its inclusion to provide voltage measurements exclusive of the current generated between the WE and CE. Finally, the three electrodes are all wired to a potentiostat/galvanostat that drives and monitors the testing procedure.

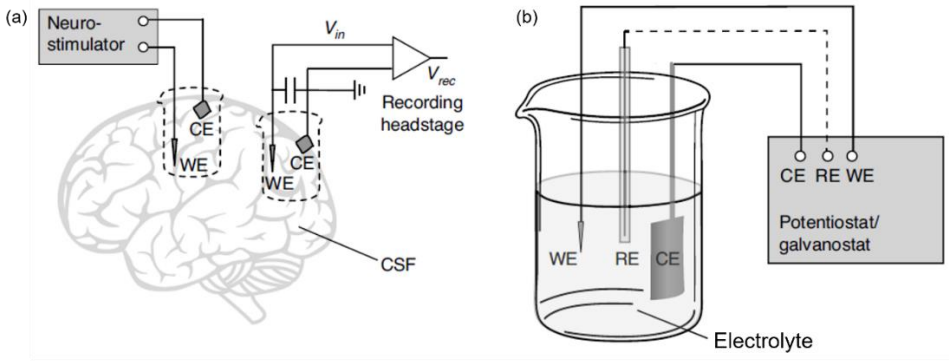

Figure 2.13: (a) Working and counter electrodes (WE and CE respectively) arranged in a two-electrode system to emulate intracortical stimulating and recording devices, and; (b) A three-electrode system comprising of working, counter, and reference electrodes (RE) immersed in electrolyte and connected to a potentiostat/galvanostat. From [157].

2.3.2 Electrochemical Impedance Spectroscopy (EIS)

The implementation of electrochemical impedance spectroscopy (EIS) as a testing procedure is crucial for thoroughly characterising an electrode's interfacial impedance [157]. The technique is based on the injection of a small-amplitude sinusoidal voltage[3] between the WE and CE at a fixed frequency. Measurements are made of the current passing through the circuit and of the WE's potential with respect to the reference, computing the electrode's impedance (|Z|) and phase angle (^{o}) at a given frequency. This process is repeated at different frequencies across a range that can span from as low as 0.01 Hz up to 1 MHz, populating an impedance spectrum known as a Bode Plot [170]. A Nyquist Plot, which plots the complex (Z") and real (Z') components of the measured impedance, is also produced from the same collected data. Figure 2.14 shows Bode and Nyquist plots that are typical for high-conductivity electrodes with a high ESA/GSA ratio. A notable drawback of the Nyquist plot is that frequency is represented only as an implicit variable, whereby only the direction of frequency increase may be determined, as marked on Figure 2.14 c. For this reason, Nyquist and Bode plots are typically presented together for context. When assessing electrodes for neural recording, low frequency measurements between 1 and 100 Hz are of most interest, whereas for stimulation or blocking,

[3] Although potentiostatic EIS is its most common form, the technique may also be performed in galvanostatic mode.

researchers typically quote impedance values measured at 1 kHz [170], [172]. However, Boehler *et al.* [157] emphasise the importance of the cut-off frequency, $f_{cut\text{-}off}$ (marked on Figure 2.14 a), beyond which the dominant contributing factor towards impedance is the electrolyte resistance. As such, better comparisons may be made between different electrode materials by assessing this value, as materials that reach $f_{cut\text{-}off}$ at lower frequencies indicate better performance.

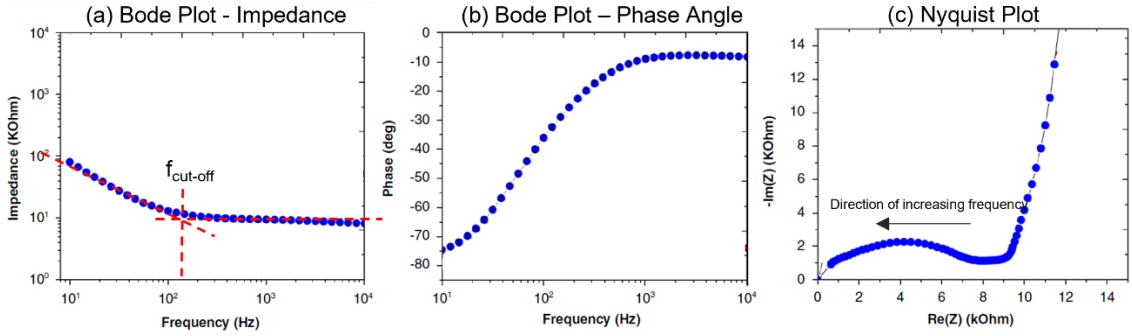

Figure 2.14: (a) Impedance Bode plot with the cut-off frequency indicated; (b) Phase angle Bode Plot, and; (c) Nyquist Plot with direction of increasing frequency indicated. Plots are representative, for an electrode with high ESA/GSA ratio. Adapted from [143].

Although values of the interfacial impedance are readily obtained from Bode and Nyquist plots, the strength of EIS as a characterisation technique comes from the ability to determine the impedance contribution of different influencing factors. This is achieved through the development of equivalent circuits which model the electrode's behaviour and assign values to the circuit elements as they correspond to physico-chemical phenomena [170]. The most basic model used to this end was originally developed by Randles, involving a simple -R-R‖C- circuit as depicted in Figure 2.15 a. The first element, R_S, features in all electrochemical models and represents the solution resistance, a stand-in for the tissue impedance when testing *in vitro*. The other elements of the circuit feature the double-layer capacitance, C_{dl}, placed in parallel with the electrode's resistance to faradaic charge transfer, R_F. Although adequate in representing very simple electrochemical systems, the Randles circuit has limited applicability when it comes to modelling neural interfacing electrodes and their complex behaviours. The circuit, therefore, must be expanded to account for other influencing factors [129], [173].

Foremost, Boehler *et al.* [157] draw attention to the use of ideal capacitors with an impedance as defined by Equation 2.7. Due to many contributing effects, notably the electrode's topography, current leakage, and non-uniform current distribution, physical

double-layer formation is rarely ever ideal. For these reasons, the traditional capacitor is often replaced by a constant phase element (CPE), a mathematical construct having an impedance defined by:

$$Z_{CPE} = \frac{1}{Y_o(j\omega)^{\alpha}} \tag{2.9}$$

where Y_o has units of Ss^{α} rather than F, and the exponent α is an empirical constant that ranges from 0.5 to 1. The value of α represents deviation from ideal electrode behaviour, and for most applications lies between 0.8 and 1, with 1 being the case for an ideal capacitor where $Y_o = C$. The CPE is included in Figure 2.15 a, where it replaces the traditional double-layer capacitor in a Randles model. Representative Bode and Nyquist plots of electrodes that can be modelled by this circuit are also given.

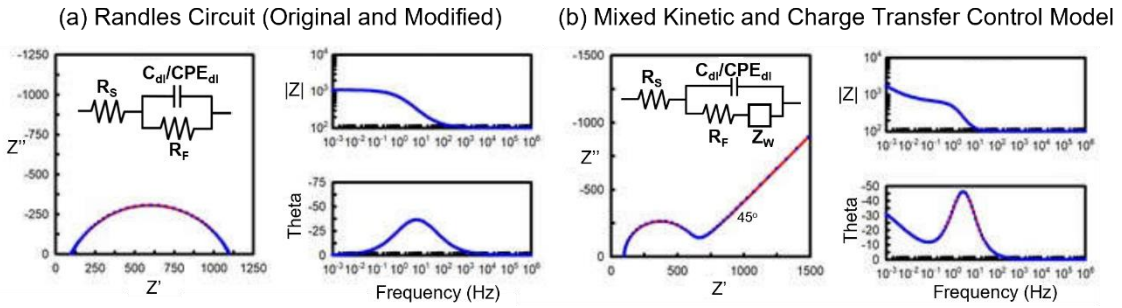

Figure 2.15: (a) Representative Bode and Nyquist plots that can be modelled with a Randles circuit; (b) Representative Bode and Nyquist plots that can be modelled using the mixed kinetic and charge transfer control model. Adapted from [174].

In the pursuit of large ESAs, many neural interfacing electrodes now feature highly porous structures, providing obstacles to ionic species diffusing to and from the current collector [173], [175]–[177]. When diffusion dominates the rate of electrochemical reactions, specifically driven by gradients in ionic composition as opposed to an electric field, a related impedance arises in the low-frequency domain. This phenomenon is modelled in equivalent circuits as a Warburg Impedance, Z_W, another mathematical construct whose impedance may be defined similarly to that of a CPE (Equation 2.9) with α fixed at a value of 0.5. A representative model that includes Z_W placed in series with R_F in the original Randles circuit, widely identified as the mixed kinetic and charge transfer control model, is given in Figure 2.15 b [173], [178]. Bode and Nyquist plots corresponding to the model are also given, where the most recognizable feature of a

Warburg impedance, the 45° phase angle in the low-frequency domain of the Nyquist plot, may be observed.

The sweeping use of a Warburg impedance to model any conditions where diffusion limitations are expected is often criticised. Huang [173] takes particular issue with the blind application of the element to porous electroactive materials, where behaviours arising from their multi-scale structures and multi-phasal diffusion elements might be overlooked through its use. In their work, Cooper *et al.* [178] observe that pore geometry has a strong influence on the shape of the resulting Nyquist plot. Figure 2.16 a, showing simulated plots for five different 2D pore configurations, illustrates how variation in pore cross-sectional geometry along the direction of ionic diffusion distorts the impedance data away from the typical 45° angle. Song *et al.* [179], observing similar trends in electrodes with nanoparticulate geometry, attributed a steep slope in the low-frequency domain to vertical capacitive behaviour, where the active material is sequentially filled and depleted of ionic species with the alternating current of EIS measurement. This quasi-90-degree phase angle recorded is quite contrary to the expected diffusion-limited response seen in other porous electrodes. Similar results were achieved by Brezesinski *et al.* [180], where nano-porous, redox-active electrodes demonstrated a steep, capacitive curve at low frequencies. Here, the equivalent circuit was deviated from the mixed-control model shown in Figure 2.15 b, and the Warburg resistance is replaced by a CPE. In this way, the model is used to distinguish between double-layer capacitance and pseudo-capacitance as shown in Figure 2.16 b [161].

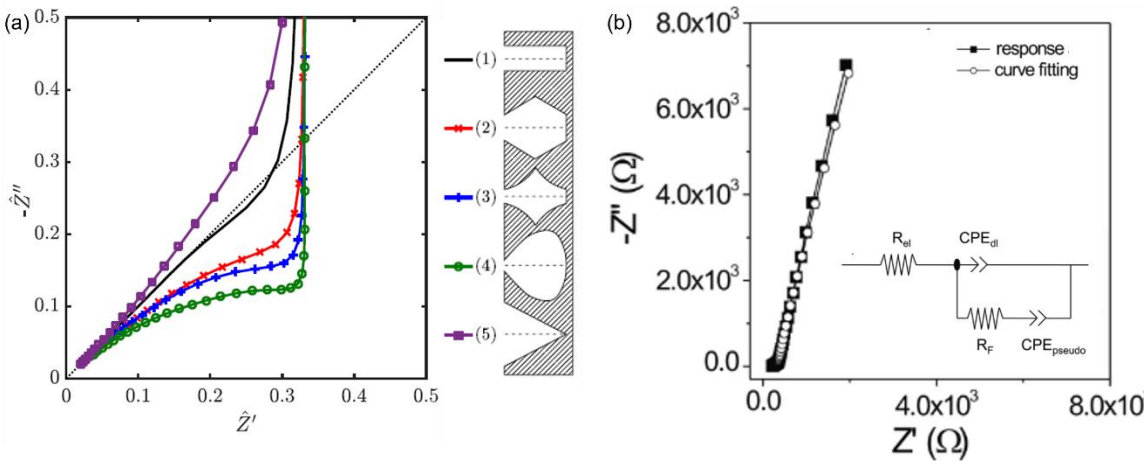

Figure 2.16: (a) Pore geometry has a strong influence on the resulting Nyquist plot, deviating away from the 45° response most typically associated with diffusion. Adapted from [178]; (b) Nyquist plot obtained from a redox-active electrode. The mixed control model is modified to include a CPE instead of a Warburg element, to allow distinction between EDLC and pseudo-capacitance. Adapted from [180].

2.3.3 Cyclic Voltammetry (CV)

Another electrochemical technique employed for the characterization of neural electrodes is cyclic voltammetry (CV), in which an electrode's potential is cycled between its electrolysis limits at a pre-defined scan rate (v in Vs^{-1}) while the current is measured. Scanning from negative to positive potentials is generally regarded as a forward sweep (charging) while the reverse is termed a backward sweep (discharging) [157]. The resulting current versus potential plot, the voltammogram, displays features that are characteristic of the electrode under test, and are collectively termed electrochemical signatures. EDLCs with the linear relationship $I = C_{dl}v$ generate rectangular voltammograms symmetric about the 0 mA current line (marked in blue in Figure 2.17 a), free of any redox peaks due to suppression of faradaic reactions [160]. Conversely, pseudocapacitors display redox peaks in their voltammograms, (shown in Figure 2.17 c). These can either be subtle or obvious, having broad and/or distributed shapes mirrored across the forward and backward sweeps. Shifting peak position in these electrodes is expected to be negligible with changing scan rate, and tends to happen only at higher values of v as a consequence of ohmic losses [156].

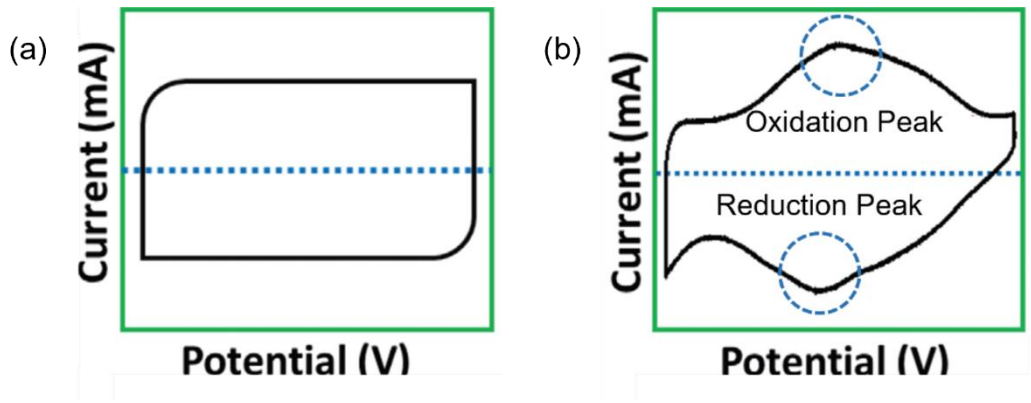

Figure 2.17: Representative cyclic voltammetry curves for (a) an EDLC; (b) a pseudocapacitor. Adapted from [160].

Of course, in practice the CV response is seldom as straightforward to interpret. Even the simplest curve for a pure EDLC distorts away from the ideal rectangular shape due to electrolyte resistance [156]. Moreover, multiple capacitive mechanisms tend to occur within the same electrode, especially in composite or multi-layered designs that utilise a combination of materials and morphologies to boost electrochemical properties. Obvious redox peaks might thus be muted and hard to distinguish, might overlap onto adjacent ones, be absent completely from a system in which they were anticipated, or vice versa

[160], [161]. It is for these reasons that CV is paired with EIS when assessing charge transfer mechanisms in neural electrodes, as the voltametric electrochemical signatures alone are not sufficient for accurate characterization.

The quantitative value of CV experiments is the calculation of an electrode's charge storage capacity (CSC), being the total charge transferred in one cyclic sweep. Within the field of neural interfacing, it has become the norm to consider only the cathodic CSC (CSC_C), derived by integrating the area bounded by the cathodic sweep and the 0-current line as per Equation 2.10:

$$CSC_C = \frac{1}{v}\int I_C \, dV \tag{2.10}$$

where I_C is the cathodic current density [181]. This value provides an indication of the electrode's charge transfer capacity for a given change in voltage and should be quoted along with the sweep rate at which it was measured. The great majority of studies perform this analysis with relatively slow scan rates, in the tune of 100 mVs^{-1} or lower [182]–[185]. Although there is merit in the use of slow scan rates (<500 mV^{-1}), primarily for observing the capacitive mechanisms at play, it is somewhat misleading to equate the CSC_C measured from these experiments with the CIC. In particular, Boehler *et al.* [157] argue that for neural stimulation and blocking, in which pulses with very short durations are used, a reflective value for charge transfer cannot be derived from such sweep rates. Affecting most strongly electrodes with high porosity, this is due to the kinetic limitations of faradaic reactions and the aforementioned pore resistance, whereby only the superficial surface area of the structure will be accessible for charge transfer. Characterisation is thus better served by including CV measurements at higher sweep rates where these phenomena can be observed [170].

When applied sequentially, CV is also useful to estimate an electrode's cycling lifetime. By subjecting the electrode to several thousand (>5000) charge/discharge cycles, one can monitor the reversibility of any faradaic reactions and evaluate the effect on charge retention capacity. Such assessments are of particular importance for pseudocapacitive electrodes. Being purely a physical process, the charge transfer mechanism behind EDLCs is virtually inexhaustible, and can withstand hundreds of thousands of cycles with negligible decay. Pseudocapacitors on the other hand have mechanisms intrinsically tied

to their unique properties and are thus much more susceptible to capacitive decay [161], [164]. Liu and Li [186] outline the possible pitfalls of pseudocapacitive degradation, and identify the main contenders as structural disintegration, loss of electrical conduction, dissolution of active components, and gas formation. Assessing the endurance of such properties in the context of chronic application is thus of utmost importance. Moreover, Hou *et al.* [187] draw attention to the scan rates used when assessing cycling stability, and recommend the application of two or more contrasting values of v (i.e., comparatively fast and slow sweep rates such as 1 and 0.1 Vs^{-1}, respectively) to better characterise arising behaviours.

2.4 Electrode Materials for Neural Interfacing

The most important component of a neural interfacing device is the interfacing site itself [3]. Hereunder is a review of the most prominent materials in the field, encompassing those that are in widespread clinical use, those under current academic scrutiny, as well as new and emerging contenders. Unless otherwise stated, all descriptions of a material's electrochemistry are considered within the context of a 3-electrode system and using PBS at a temperature of 37 ^{o}C as the test electrolyte. Figures showing electrochemical results are either normalised to 1cm^2 or the electrode area is given (if specified in the source publication). Table 2.8 summarizes notable electrode materials discussed in this section, outlining their $|Z|_{1Hz}$, $f_{cut\text{-}off}$, CSC_C at the reported value of v, as well as the water window it was measured at, when available.

2.4.1 Noble Metals and their Alloys

The materials with the longest history in neural interfacing are the noble metals and their alloys. Highly conductive, mechanically stable, and reliably corrosion resistant within safe parameters, these materials have core characteristics that have favoured their use over the decades. Platinum (Pt), Platinum-Iridium (Pt-Ir) alloys, and Gold (Au), are at the forefront of this category, and despite some critical drawbacks that have been made apparent with recent developments, are still the subject of many modern research initiatives [17], [102].

2.4.1.1 Platinum and Platinum-Iridium Alloys

Platinum is perhaps the most widely studied of all electrode materials, and certainly makes up the bulk of devices in current practical use [3], [101], including the Utah array [188], the DBS [189] and peripheral nerve cuff electrodes [190] by NeuroNexus, the TIME design by Boretius *et al.* [119], and innumerable others. Its charge transfer mechanisms have been described as being a mixture of EDLC and redox pseudocapacitance, carrying out reversible faradaic reactions based on the adsorption and desorption of hydrogen [101]. These reactions create platinum's characteristic redox peaks (Figure 2.18 c, f, and i), where PtO forms on the forward sweep between the approximate potentials of -0.2 to 0.2 V vs Ag/AgCl and is then reduced again on the backwards sweep [184].

Although reliably biocompatible and biostable [23], [101], smooth Pt has only modest charge transfer capacity and comparatively high impedances when juxtaposed against other alternatives. Its CSC_C at $\nu = 0.1$ Vs^{-1} has been measured at 0.55 $mCcm^{-2}$ for rolled sheets [191], 1 $mCcm^{-2}$ for sputtered layers [184], and 1.5 $mCcm^{-2}$ for electrodeposited coatings [192], despite a modest water window spanning from ~ -0.6 to 0.8 V vs Ag/AgCl. Impedances at 1 Hz, $|Z|_{1Hz}$, have been reported from hundreds to thousands of Ohms per cm^2, and cut-off frequencies, $f_{cut\text{-}off}$, lie outside the range of clinical relevance (>10 kHz) [162], [193]. Pt electrodes with low ESA/GSA ratios are thus of little clinical use going forward, and the bulk of research effort is directed towards improving this ratio.

Electroless deposition of a conformal Pt film onto titania (TiO_2) nanotube arrays by Wu *et al.* [184] successfully reduced $|Z|_{1Hz}$ down to ~ 70 Ωcm^2 and increased the CSC_C by an order of magnitude. Although brief, a 1000-cycle lifetime test at 0.1 Vs^{-1} further showed no significant change in the measured impedance, demonstrating the stability of the charge transfer mechanisms (Figure 2.18 a-c). Boehler *et al.* [162] achieved even greater properties through the electrochemical growth of nanoscale Pt 'grass', dropping $|Z|_{1Hz}$ down to ~20 Ωcm^2, shifting the cut-off frequency to ~300 Hz, and enlarging the CSC_C by a factor of 40 at $\nu = 0.1$ Vs^{-1} (Figure 2.18 d-f). More recently, Zeng *et al.* [193] electrodeposited nano-crystalline Pt 'flowers' that reduced $|Z|_{1Hz}$ to ~15 Ωcm^2 and increased the CSC_C to ~100 $mCcm^{-2}$ at $\nu = 0.05$ Vs^{-1}. A low cut-off frequency of 50 Hz was also measured (Figure 2.18 g-i).

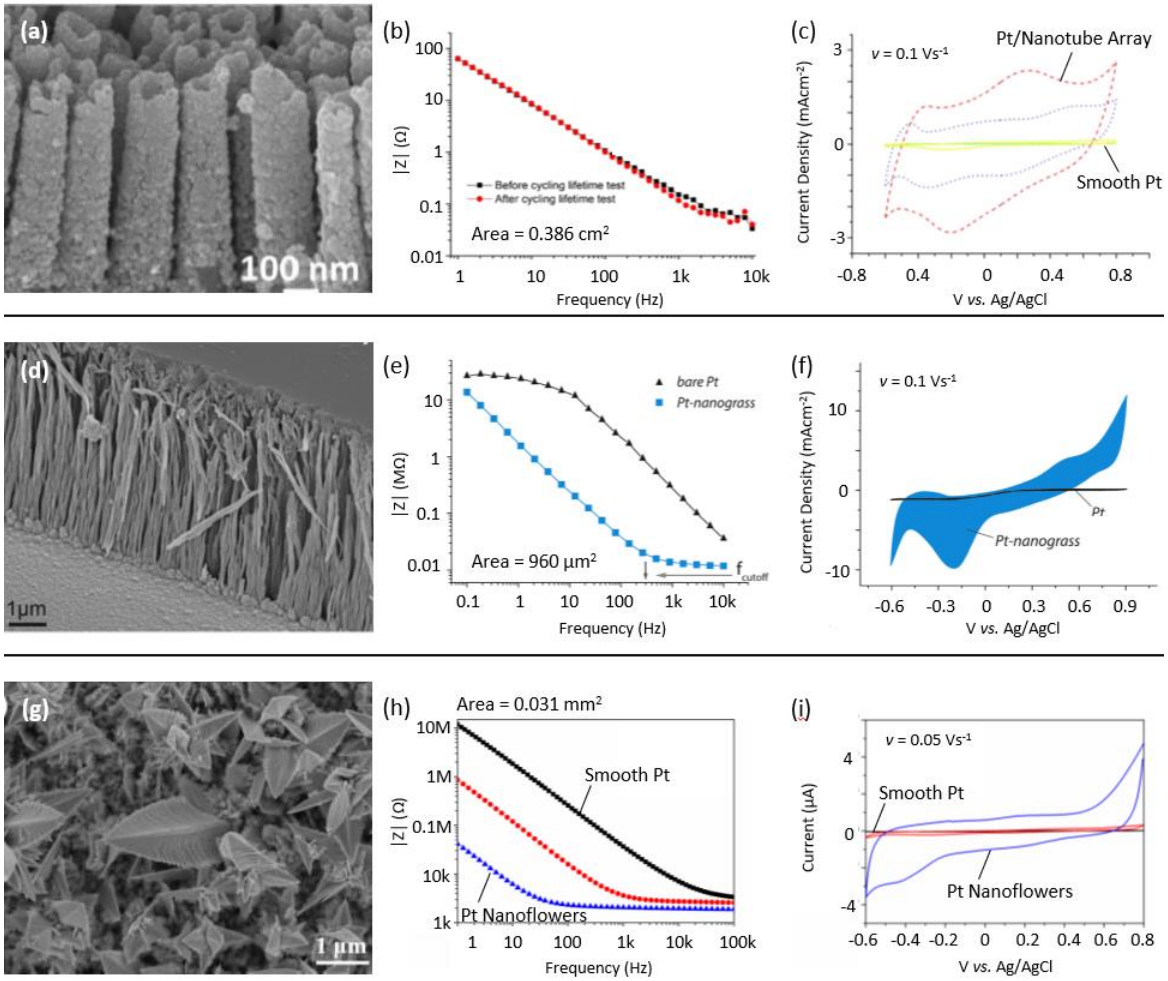

Figure 2.18: (a) Conformal Pt electrodeposited on titania nanotubes resulting in (b) lowered $|Z|_{1Hz}$ that is maintained with 1000 charge/discharge cycles, and (c) a higher CSC_C compared to smooth platinum. Adapted from [184]. (d) Nano-structured Pt grass which (e) lowers $|Z|_{1Hz}$ and shifts $f_{cut\text{-}off}$, and (g) increases the CSC_C as compared to smooth Pt. Adapted from [162]. (g) Electrodeposited Pt nano-flowers which (h) lower $|Z|_{1Hz}$ and shift $f_{cut\text{-}off}$, and (i) increase the CSC_C compared to smooth Pt. Adapted from [193].

A common variation of pure Pt electrodes are those composed of a Platinum-Iridium alloy (compositions as specified by the ASTM standard for Platinum-Iridium electrical contact materials, typically 10-30% Iridium [194]). A great many electrodes today make use of this alloy, including the Sensight^{TM} Directional DBS leads by Medtronic [195], a variety of Probes by Plextron [196] and some variations of the Utah array [188]. Its charge transfer mechanisms are similar to those of pure Pt, involving a combination of EDLC and hydrogen adsorption-desorption redox pseudocapacitance [191]. When electrodeposited, Pt-Ir films feature high electrochemical surface areas, delivering superior electrochemical properties when compared to smooth Pt electrodes [101], [182].

Dalrymple *et al.* [197] demonstrate this effect through the electrodeposition of a Pt-Ir alloy onto cochlear electrode arrays. When tested *in vitro*, the alloy's $|Z|_{1Hz}$ was measured at ~ 50 Ωcm^2, more than a magnitude of order lower than that of the Pt electrodes. Conversely, the cut-off frequency did not appear to change with alloy deposition, whereas the CSC_C at $v = 0.15$ Vs^{-1} was increased to 6 $mCcm^{-2}$ (Figure 2.19). It is worth noting that while Pt-Ir alloys improve upon the electrochemical properties of smooth Pt, they cannot compete with the nano-structured Pt electrodes discussed previously (Figure 2.18).

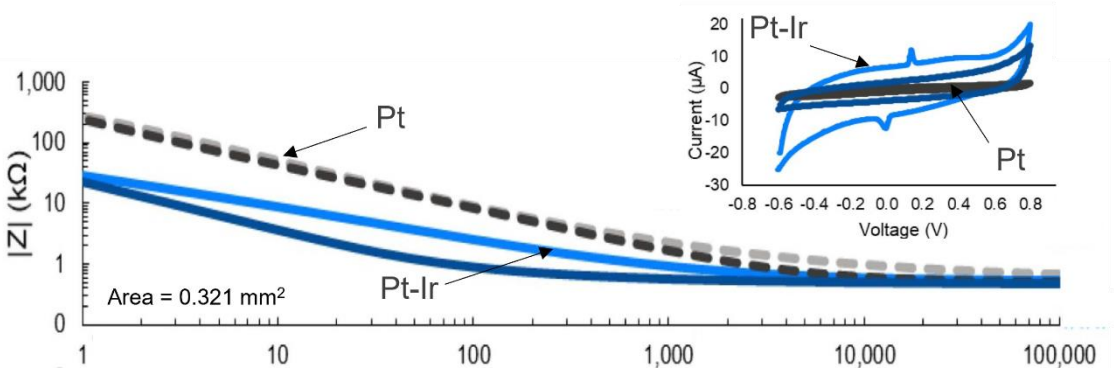

Figure 2.19: Bode plot for Pt electrodes with and without an electrodeposited layer of Pt-Ir alloy. Inset shows the voltammograms for the same electrodes obtained at a sweep rate of $v = 0.15$ $Vs^{-}1$. Adapted from [197].

The referenced studies omit CV measurements at clinically relevant scan rates ($v \geq 1$ Vs^{-1}), and so it is unknown whether the porous structures are accessible to the electrolyte at high charge/discharge rates. Moreover, no equivalent circuit modelling was used to analyse the impedance spectra, with the exception of Boehler *et al.* [162], who model the system as a Randles circuit with ideal capacitance. Therefore, no further in-depth observations can be made on the charge transfer mechanisms of nanostructured Pt electrodes.

2.4.1.2 Gold

Although very popular in the infancy of neural interfacing, the associated high impedances and low charge transfer capacities of gold (Au) have limited its clinical application [3]. Smooth Au electrodes have a measured $|Z|_{1Hz}$ that can be tens of thousands of ohms per cm^2, with cut-off frequencies higher than 10 kHz, and a CSC_C comparable to that of smooth Pt (~2 $mCcm^{-2}$ at $v = 0.2$ Vs^{-1}) [143], [198]. However, unlike Pt, efforts to increase the ESA of Au electrodes have not resulted in clinically relevant electrochemical improvements, despite significant reductions in impedance. Decataldo *et*

al. [199] report on micro-cracked Au electrodes that maintain a conduction pathway even when subjected to light bending, and are hence suited for flexible electrode arrays. Nevertheless, impedance measurements returned a $|Z|_{1Hz}$ value of 800 Ωcm^2 and a cut-off frequency of 2 kHz, which despite being a large improvement over the original values (20 $k\Omega cm^2$ and 10 kHz for $|Z|_{1Hz}$ and $f_{cut\text{-}off}$, respectively), are still inadequate for use in micro-electrodes.

Frommhold and Tarte [183] achieved much more favourable properties with sputtered gold electrodes, growing a nanometric columnar morphology as shown in Figure 2.20 a. By varying the deposition time and argon pressure during deposition, a $|Z|_{1Hz}$ value of 150 Ωcm^2 was achieved, with a negative shift of the cut-off frequency down to 30 Hz (Figure 2.20, b). The cyclic voltammetry scan of the electrodes at $v = 0.1$ Vs^{-1} is given in Figure 2.20 c, showing the distinct faradaic peaks associated with formation and consumption of gold oxide. Despite reducing the impedance by more than two orders of magnitude, nano-columnar Au still exhibits inferior electrochemical performance compared to all iterations of Pt electrodes, as well as all electrodes that will be discussed in the subsequent sections.

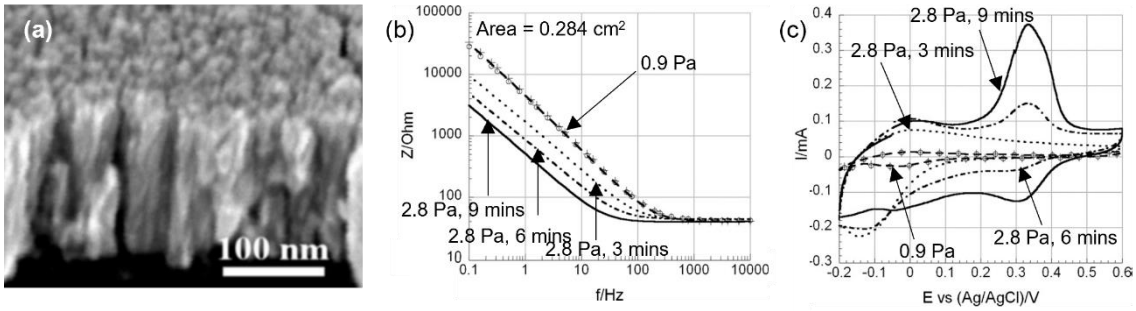

Figure 2.20: (a) SEM image, showing the morphology of sputter-deposited nano-columnar Au coating; (b) Bode plot of Au coatings deposited under different parameters (pressure and time), and; (c) The voltammograms of Au coatings deposited under different parameters, measured at a scan rate of $v = 0.1$ Vs^{-1}. Adapted from [183].

2.4.2 Iridium Oxide

Iridium Oxide (IrO_x) is a material with exceptionally high electroactivity stemming from its four oxidation states and easy transition between the valences of Ir^{3+} and Ir^{4+}. These qualities make IrO_x a strong intrinsic pseudocapacitor, whereby the formation of a hydrated porous oxide on the surface of iridium metal dramatically increases the ESA and thus its electrochemical properties [101], [200], [201]. Having shown no significant issues with regards to biocompatibility in a variety of cellular interactions *in vitro* and *in vivo*

[200], [202], [203], IrO_x is considered one of the best choices for neural interfacing electrodes. The same material may be developed with three distinct surface morphologies depending on the processing method used, these being activated IrO_x (AIROF), electrodeposited IrO_x (EIROF), and sputtered IrO_x (SIROF) [101].

The first variation of IrO_x involves the activation of bulk iridium by directly transforming it into $IrO(OH)_2$, hence the term AIROF. This is achieved either through square wave potential pulsing or through linear sweep cycling. In both cases, the activation is carried out between the water window limits of the material in a saline solution at low frequencies (~0.05 Hz) until all the metal has been activated into Ir(IV) [204], [205]. In their work, Frederick *et al.* [205] demonstrate the effect of pulsing number on AIROF's electrochemical properties, where $|Z|_{1Hz}$ is reduced by an order of magnitude to 8 Ωcm^2 over 1000 pulses, and CSC_C at $v = 0.05$ Vs^{-1} increases up to 28 $mCcm^{-2}$ (Figure 2.21 a and b). The cyclic voltammograms show four peaks associated with two redox pair reactions for AIROF electrodes, these being the transition between Ir^{3+}/Ir^{4+} and Ir^{4+}/Ir^{5+} valence states. Through the application of linear sweep cycling, Kang *et al.* [204] produced AIROF films with rough and porous microstructure (Figure 2.21 c) that, whilst maintaining the same low $|Z|_{1Hz}$ value of 8 Ωcm^2, increased the CSC_C at $v = 0.1$ Vs^{-1} to 40 $mCcm^{-2}$.

The second variation of IrOx, EIROF films, are grown through a process of anodic electrodeposition from a buffered solution containing an iridium precursor and oxalic acid. The iridium and oxygen atoms then combine to produce IrO_2 and deposit onto the current collector. In the work of Lu *et al.* [206], EIROF films are grown on the tips of platinum microwires and assessed with respect to different deposition times. The maximum CSC_C value of 37 $mCcm^{-2}$ at $v = 0.05$ Vs^{-1} was delivered by the nodular morphology shown in Figure 2.21 d where the IrO_2 particles measured 200-500 nm in diameter. However, the lowest impedance values ($|Z|_{1Hz}$ = 8 Ωcm^2) were obtained for thinner films, with numerous small particles only 50 nm in diameter (Figure 2.21 e). The CSC_C of these electrodes was only 15 $mCcm^2$, highlighting the fact that charge storage capacity and impedance do not necessarily scale in the same way with coating thickness. Conversely, Kang *et al.* [204] succeeded in improving the electrochemical properties of EIROF to obtain a balance between low impedance and high CSC_C. By subjecting EIROF films to 100 CV 'activation' cycles at $v = 0.1$ Vs^{-1}, a CSC_C of 68 $mCcm^{-2}$ was obtained

for a $|Z|_{1Hz}$ of 16 Ωcm^2. In this way, the CSC_C is more than 4.5 times larger[4] for only double the impedance (Figure 2.21 f and g).

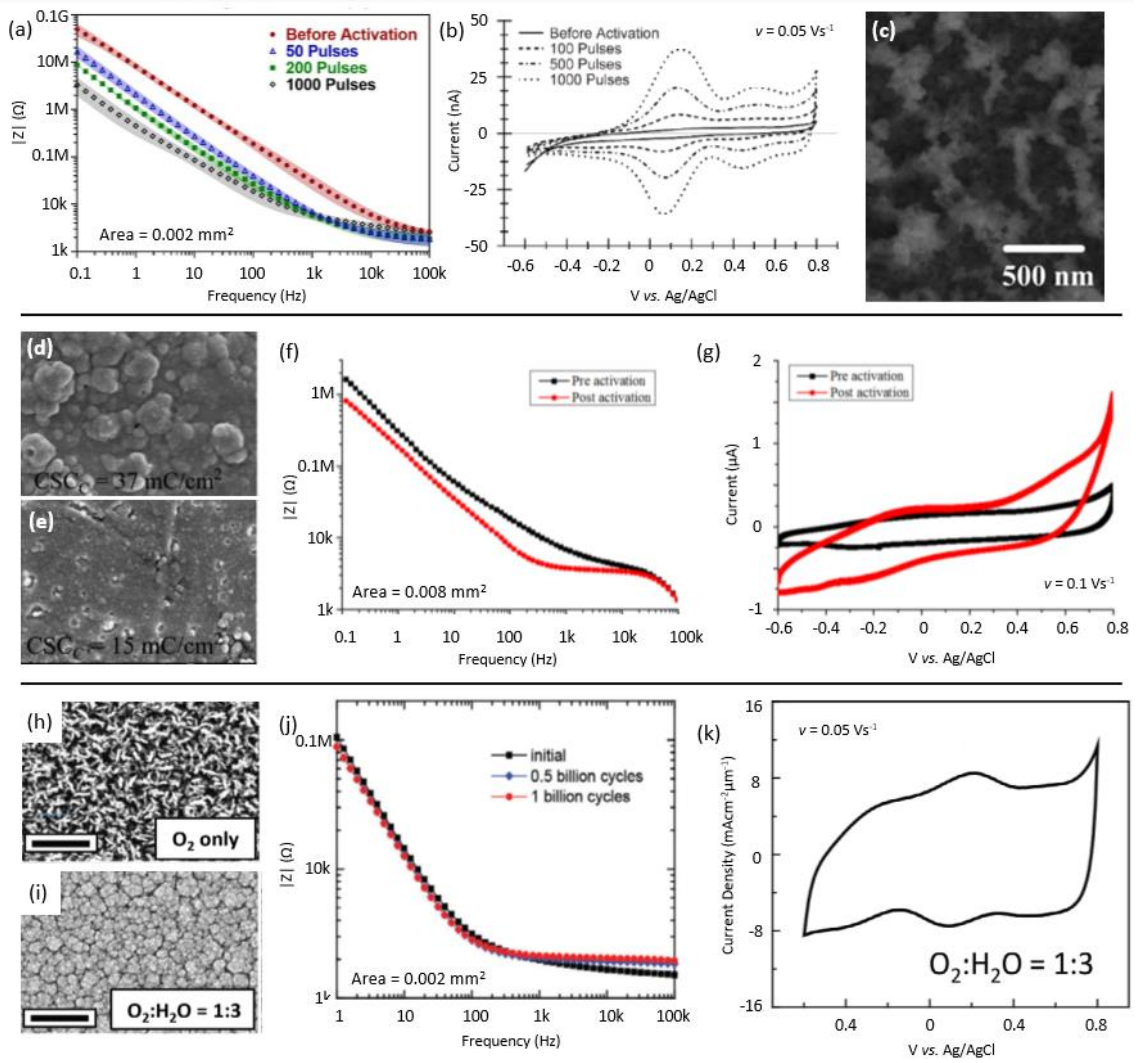

Figure 2.21: (a) Bode plots and (b) voltammograms obtained at a sweep rate of $v = 0.05$ Vs^{-1} for AIROF electrodes after different number of activation pulses. Adapted from [205]; (c) The porous microstructure of an AIROF electrode. From [204]; (d,e) EIROF films of different morphology produced by varying the deposition times. From [206]; (f) Bode plots and (g) voltammograms obtained at a sweep rate of $v = 0.1$ Vs^{-1} for EIROF electrodes before and after activation. From [204]; (h,i) Morphology of SIROF films obtained under different O_2:H_2O ratios; (j) Bode plots for SIROF films after different number of stimulation pulses, and; (k) The voltammogram for AIROF obtained at a sweep rate of $v = 0.05$ Vs^{-1}. From [200].

Typically, SIROF films are sputtered in a dry environment constituting O_2 and Ar gas plasma, such as those developed by Kang *et al.* [204] and Negi *et al.* [207]. These processing conditions produce IrO_x with dendritic microstructures that lack H_2O

[4] Different sweep rates are being compared (0.05 vs 0.1 Vs^{-1}) and CSC_C tends to increase as v decreases.

molecules, such as the example given in Figure 2.21 h. As a result of the reduced electrolyte permeability in these electrodes, the electrochemical properties for SIROF films are markedly inferior to those typically obtained for EIROF and AIROF. The notable advantage of SIROF films produced in this way is stronger adhesion to the substrate as compared to AIROF and EIROF, and hence higher stability of electrode structure and its electrochemical properties.

However, this perspective has shifted in recent years with modified sputtering techniques that incorporate H_2O molecules. Notably, Maeng *et al* [200] report excellent electrochemical properties for SIROF electrodes, achieving optimal CSC_C and impedance values by varying the gas blending ratios of O_2 and H_2O (water vapour) during deposition. The application of blending ratio $O_2 : H_2O = 1 : 3$ resulted in a porous, nodular morphology as shown in Figure 2.21 i, with a $|Z|_{1Hz}$ value of 5 Ωcm^2 and CSC_C of 60 $mCcm^{-2}$ at $v = 0.05$ Vs^{-1}. Moreover, these properties were retained with 1 billion stimulation cycles delivering 8 nC per phase at a frequency of 200 Hz, with no adverse effects on either the impedance or CSC_C (Figure 2.21 j and k). Therefore, not only are the SIROF films of comparable charge transfer capacity to AIROF and EIROF whilst having lower impedance, but also retain the excellent stability that was previously their sole advantage.

2.4.3 Titanium Nitride

Transition metal nitrides (TMNs), are a class of interstitial alloys where nitrogen atoms occupy the interstitial sites of a parent metal crystal, and have been steadily gaining traction in the field of electro-materials within recent years [208]. TMNs are characterised by a number of desired properties, including high electrical conductivity, extensive redox chemistry, and excellent resistance to corrosion and wear [209]. These compounds have a long history of successful application in other industries, notably as tool coatings, electrocatalysts, fuel cells, and electrical storage [210]. As such, the literature pertaining to their electrochemical performance is extensive within the scope of these sectors. Considered to be the most viable TMN for neural interfacing, Titanium Nitride (TiN) has the additional benefit of being well-established in the field of biomaterials. As a nano- or micro-metric thin film, TiN has been used as a tribocorrosion-resistant surface in joint replacements, as an anchoring aid in the abutments of dental implants, as an anti-

haemolysis coating for ventricular assist devices, and perhaps most significantly, as an electrode in cardiac pacemaker leads [211]–[213].

TiN's relevance to electrical conduction stems from its unusual combination of ionic, covalent, and metallic bonding. In the formation of stoichiometric TiN, each Ti atom bonds with N in a 1:1 ratio, giving up three of its four valence electrons in the process. Now having only a weak attraction to the nucleus, the fourth electron easily detaches itself from the Ti atom, corresponding to a shallow donor level in TiN's band gap. Very small amounts of activation energy are thus needed for the electron to jump to the conduction band. The amount of conduction electrons is also directly proportional to the number of Ti atoms, and hence exist in abundance. Moreover, the Ti atom becomes a positively charged ion on the lattice after giving up its electron, facilitating the metallic bond between it and other electrons. Metallic and semiconductor-type electrical conduction are thus possible simultaneously [214], [215].

In its most recognizable form, TiN has a lustrous gold colour that reflects its dense microstructure and extremely high hardness (up to 30 GPa, depending on the processing method and its parameters) [212]. Whilst clearly advantageous in the context of a protective coating, this iteration of TiN is of little value for neural interfacing with its low ESA/GSA ratio. Widely characterised as an EDLC, dense TiN has a very low charge transfer capacity and a corresponding high impedance when manufactured as smooth films. Meijs *et al*. [176] measured the electrochemical properties of such electrodes, growing a layer of TiN onto Ti6Al4V surfaces via physical vapour deposition (PVD). EIS measurements revealed a $|Z|_{1Hz}$ value of 1.5 $k\Omega cm^2$ and an $f_{cut\text{-}off}$ of ~1 kHz. It is interesting to note that even with a comparably low ESA/GSA ratio, smooth TiN still has lower impedance measurements than the noble metals Pt and Au. On the other hand, the CSC_C at $v = 0.05\ Vs^{-1}$ was found to be $0.36\ mCcm^{-2}$, indicative of the small area available for double-layer formation. Naturally, such a low charge transfer capacity is unacceptable for micro-electrode applications.

As the charge transfer of TiN relies on double-layer capacitance, research efforts over the years have focused on increasing the ESA to improve its electrochemical performance. One of the tactics employed towards this end involves transforming easily-produced titanium oxide (TiO_2) structures into TiN. Chen *et al.* [216] developed a porous TiN electrode by nitriding highly ordered titania nanotubes grown via anodizing. The pores,

which were produced with a variety of diameters to determine optimum geometry, are shown in Figure 2.22 a and b. When tested for their CSC_C, the best-performing electrodes (having 40 nm diameter nanotubes versus 60 or 80 nm) were only able to deliver 2.8 $mCcm^{-2}$ of charge for a sweep rate of $v = 0.1$ Vs^{-1}. Despite constituting an almost 5-fold increase over smooth TiN (measured at 0.6 $mCcm^{-2}$ for the same v), the nano-porous electrode still exhibits poor electrochemical properties for its stated intended use as a neural stimulator. Although CV is not performed at any higher sweep rates, CSC_C is expected to decrease as v increases due to pore resistance [101].

Canillas *et al.* [217] achieved marginally better results when nitriding rutile TiO_2 pellets produced via a cold-press and sintering procedure. Quasi-complete TiN conversion was confirmed via colour change (grey to golden brown) as well as Bragg-Brentano X-ray diffraction (BBXRD), where intense peaks associated with Osbornite TiN (rocksalt-type crystal structure) appeared alongside diminished TiO_2 peaks (Figure 2.22 c-e). The rough TiN surfaces as shown in Figure 2.22 c were attributed to oxygen released during the nitridation process, contributing to a higher ESA/GSA ratio. CV carried out at a sweep rate of $v = 0.02$ Vs^{-1} yielded a CSC_C of 15.3 $mCcm^{-2}$ in PBS and 8.4 $mCcm^{-2}$ in neurobasal media (NB). This value difference was attributed to the compositional discrepancies of PBS and NB media and was confirmed via EIS measurements. Using the equivalent circuit shown in Figure 2.22 f, the extracted value of R_s in PBS was found to be ~1.7 times larger than for NB media, likely due to the larger number of ions in solution available for charge transfer (content of NB media is given in Appendix A). The values for R_S, R_F, Y_{DL} and α_{DL} obtained from model-fitting in PBS were 30 Ωcm^2, 36 k Ωcm^2, 0.3 $mFcm^{-2}$, and 0.83, respectively. The authors justify the use of Farads (F) for Y_{DL} instead of $S*s^{\alpha}$ by describing the value of α_{DL} as high. Although it is possible to approximate Y_{DL} as C_{DL}, most experts within the field discourage this practice, especially since the α_{DL} value is below what is considered a high value for α (>0.9) [157], [218]. Units notwithstanding, it is clear from the values obtained that the electrode's performance is not ideal for use in neural interfacing, with values for R_F and Y_{DL} being too high and too low, respectively. Sait *et al.* [219] achieved comparable values for nitrided TiO_2 nanorods, establishing a clear trend of poor electrochemical performance for titania-derived TiN electrodes.

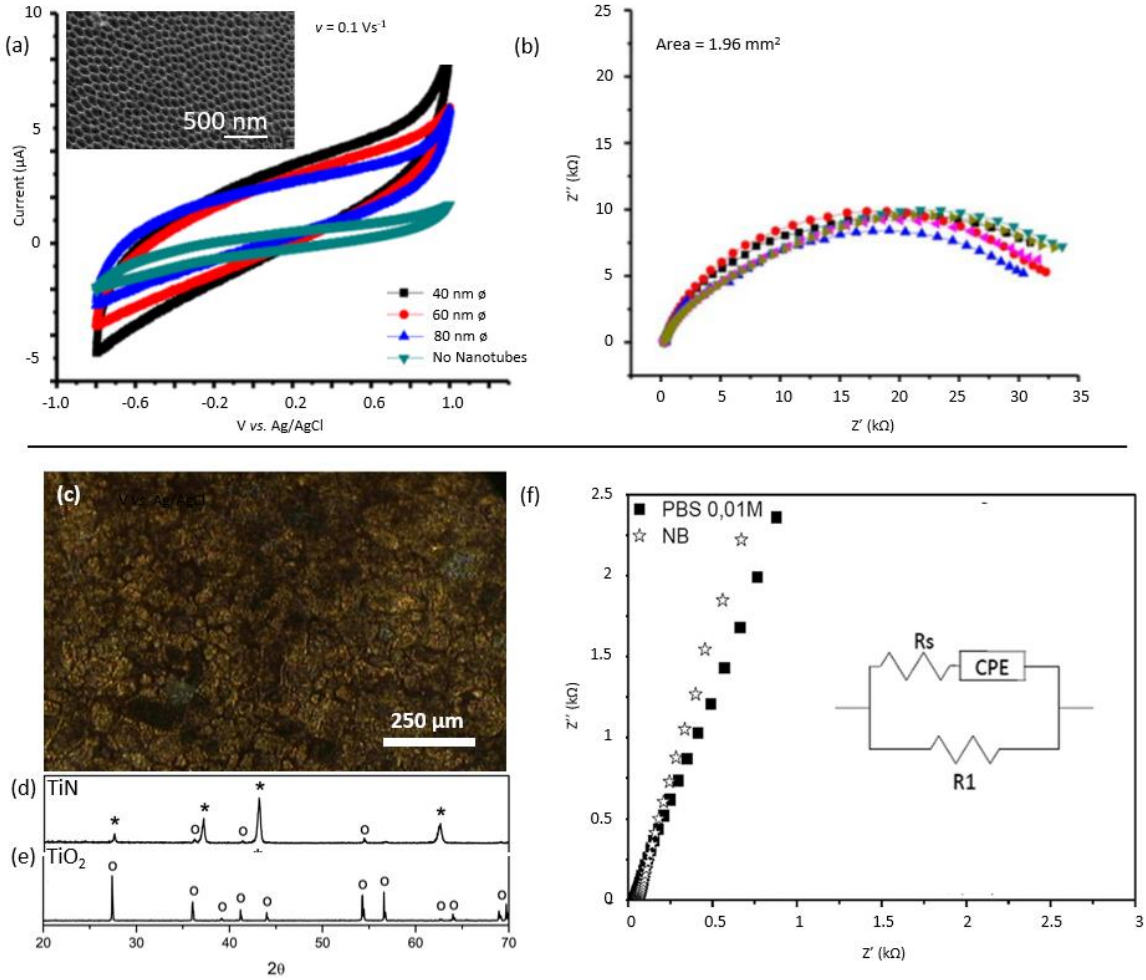

Figure 2.22: (a) The morphology of nitrided titania nanotubes, along with the voltammograms for different sized nanotubes, obtained at a sweep rate of $v = 0.1$ Vs^{-1}; (b) The Nyquist plots for TiN electrodes (30 nm diameter nanotubes), obtained periodically during immersion in PBS up to 60h. From ; (c) Bulk-nitrided TiO_2 (TiN); XRD scans for (d) TiN and (e) original TiO_2. * Indicate peaks associated with TiN while ° indicate peaks associated with TiO_2; (f) Nyquist plot for TiN measured in PBS and neurobasal media, showing the equivalent circuit model. From [217].

Conversely, large improvements in the impedance and charge transfer capacity of TiN have been made using PVD (physical vapour deposition) processes. The term PVD is used describe a variety of vacuum processes used to grow thin films or coatings onto an atomically clean surface. Physical techniques are employed to vaporise material from a mounted target, creating a supersaturated vapour which is then transported, nucleated, and deposited onto a substrate. In the case of TiN, targets usually comprise of commercially pure Ti material, while the atmosphere consists of an Ar and N_2 gas mixture. The deposition time, N_2 partial pressure, process temperature and substrate bias voltage may all be precisely controlled to achieve very different coatings [176], [220]–[222]. The most commonly used PVD processes include evaporation and sputtering

techniques, where the latter is preferred for neural electrodes due to the superior bonding strength generated between substrate and coating [223].

The primary intention of using PVD to produce TiN electrodes is to develop highly porous columnar microstructures without needing a pre-existing porous template. The topography and corresponding section of such a coating are shown in Figure 2.23 a and b, respectively. Immediately apparent is the distinct pyramidal shape of the grains, which are revealed to be the tops of high-aspect ratio columns growing perpendicular to the substrate. This quasi-unidirectional growth indicates a highly textured coating where the majority of grains grow in one planar direction. In this instance, the coating is dominated by growth in the (111) plane, a highly desirable microstructure for neural interfacing electrodes due to its large and accessible ESA [167].

One of the major contributing factors towards (111)-dominated growth is the coating thickness, where coatings in excess of 150 nm are expected to be textured in this way. Being the orientation of lowest strain energy, the (111) texture develops in thick coatings (where strain energy is larger than surface energy, i.e., $E_{strain} > E_{surface}$) to lower the system's overall energy. Liang *et al.* [177] demonstrate this phenomenon through a series of TiN films with varying thicknesses grown via DC reactive MS. Film thickness was varied by increasing the deposition time from 0.5 to 20 minutes while the other parameters were kept constant (temperature 350 ^{o}C, voltage 0.69 kV). Low incident angle XRD (0.8^{o}) was used to obtain the diffraction spectra within the range of $35^{o}<2\theta<65^{o}$, the results of which are shown in Figure 2.23 c. A clear cut-off was observed for (111) dominated growth, whereby thicknesses of 212 nm and over exhibited this texture[5], with the relative intensity of the (111) peak increasing with thickness. The advantage of this texturing (the high ESA/GSA ratio) may be evidenced in the atomic force microscopy (AFM) profiles shown in Figure 2.23 d and e. The 140 nm thick coating, being (200)-dominated, is low in roughness with a root mean square (RMS) value of 2.7 nm, whereas the 212 nm thick coating has a high RMS roughness value of 7.2 nm due to its (111) texture.

[5] Texturing is typically assessed using Bragg-Brentano XRD rather than glancing angle XRD [495]. The authors of the source publication [177] justify this deviation on the basis of very thin coatings, thus rendering the Bragg-Brentano set-up ineffective.

Another parameter that may be altered to maximise porosity is substrate temperature. In the work of Penilla and Wang [224], a series of TiN films were grown on Si substrates using sputtering PVD. Three different substrate temperatures were used (15, 200, and 400 ^{o}C) while the other parameters were kept constant (voltage 466 V, deposition time 105 minutes, deposition pressure 0.26 Pa). The resultant topographies and corresponding XRD spectra, shown in Figure 2.24, highlight a clear trend between (111) texturing and substrate temperature. Crystallographic orientations other than the pyramidal (111) begin to show as the temperature rises, most clearly at 400 ^{o}C where rectangular (200) and parallelogram-shaped crystals (200), (311) may be observed. Despite the reduced intensity of the (111) peak, the coating texture is still dominated by this crystallographic phase even at the highest temperature. The open, porous microstructure is however lost, once again demonstrating correlation between a (111) texture and large ESA.

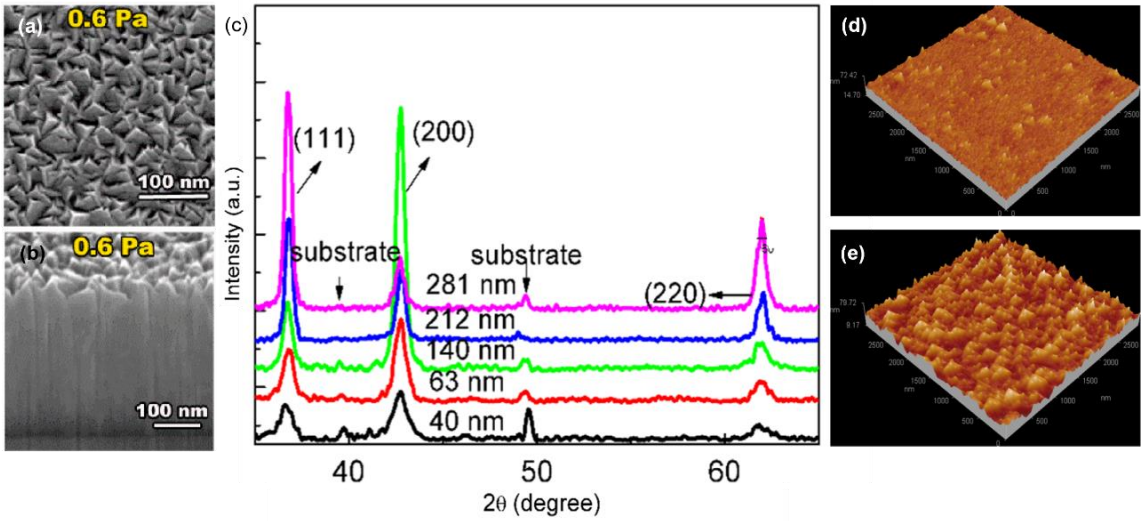

Figure 2.23: (a) Top and (b) cross-section views of a magnetron sputtered, porous TiN film with a (111) texture. From [225]; (c) Low incident angle XRD scans for DC reactive MS TiN films of different thicknesses; AFM profiles for a (d) 140 nm thick film and a (e) 212 nm thick film. Adapted from [177].

By far the most influential factor governing growth of porous TiN is the N_2 partial pressure in the chamber (PP_N). This is due to its influence on stoichiometry, where increasing the PP_N increases the value of x in TiN_x films. Over-stoichiometric films (ie, x>1) consist of highly strained grains that originate from an over-saturation of N atoms distorting the crystal lattice. In cases of strain-dominated growth, a porous film with a (111) texture is thus likely to develop. Cunha *et al.* [226] observed a quasi-linear relationship between PP_N, (111) texturing, and stoichiometry when depositing TiN films via reactive DC magnetron sputtering (temperature 200 ^{o}C, bias voltage -50V) , as shown

in Figure 2.25 a. Films deposited with a PP_N higher than 0.035 Pa developed an over-stoichiometric crystal structure with strong (111) texturing up to a value of x=1.34. The corresponding microstructure provides a stark contrast against films grown at lower PP_N, where stoichiometric TiN is shown with its dense, compact surface and weak texturing (Figure 2.25 b and c). Moreover, the high concentration of N-atoms in high PP_N depositions lowers the mean free path of sputtered atoms, decreasing the deposition rate and allowing the grains to grow larger in over-stoichiometric films. This trend has been replicated by numerous research groups [167], [176], [220], [224], [227], highlighting the prominent role that PP_N plays in determining TiN microstructure.

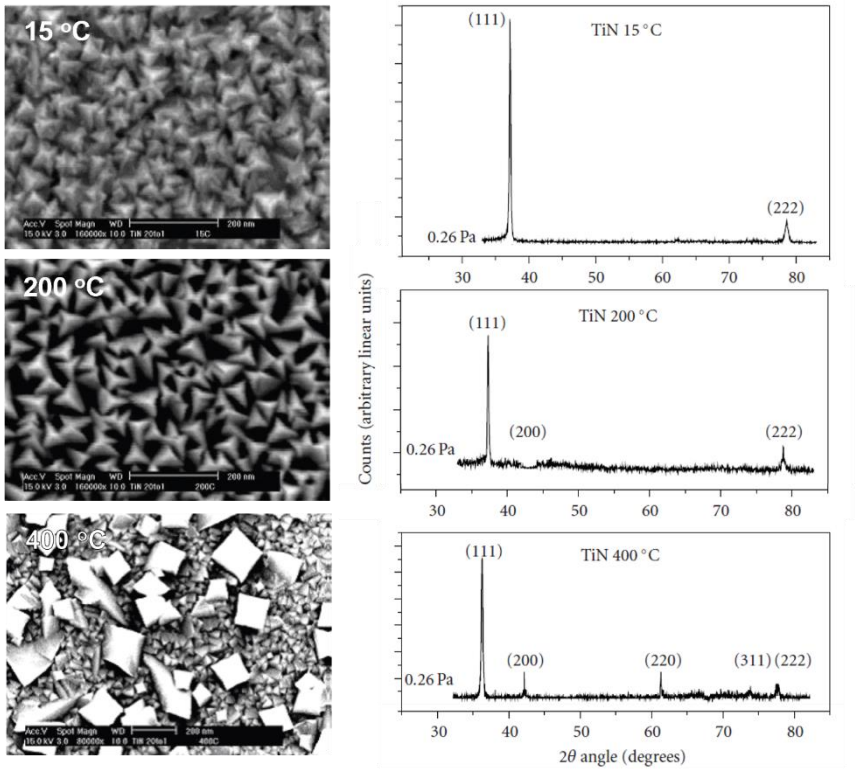

Figure 2.24: The effect of altering substrate temperature on resultant TiN morphology and crystallographic orientation. Topographical SEM images on the left correspond to the Bragg-Brentano XRD scans on the right for each temperature. Adapted from [224].

Cunha *et al.* [226] demonstrate the impact of stoichiometry on the electrochemistry of TiN by assessing the impedance of sub-, near-, and over-stoichiometric TiN_x films. The different values of x (0-1.34) were achieved by varying the PP_N from 0 to 0.29 Pa whilst keeping the substrate at a temperature of 200 °C and applying a bias voltage of -50 V. All coatings were grown to an approximate thickness of 1.3 µm. As shown in Figure 2.25 d, there is a clear downward trend in measured electrode impedance with increasing value

of x, where the lowest impedance is achieved by the over-stoichiometric TiN film for x=1.34. Using the equivalent circuit shown in the inset, the interfacial capacitance (modelled as CPE_{el}) was found to increase from $1.5x10^{-3}$ $S*s^{\alpha}cm^2$ to $4.2x10^{-3}$ $S*s^{\alpha}cm^2$ for near- and over-stoichiometric TiN respectively. The coefficient of α also increases, from a very poor 0.79 in x=1.15 to a value of 0.86 in x=1.34, indicating better double layer formation. Although the values of CPE_i and W are more favourable for x=1.15 (refer to Table 2.5), their circuit placement diminishes their impact, and hence the higher value of CPE_{el} in x=1.34 results in a lower overall impedance for the over-stoichiometric film.

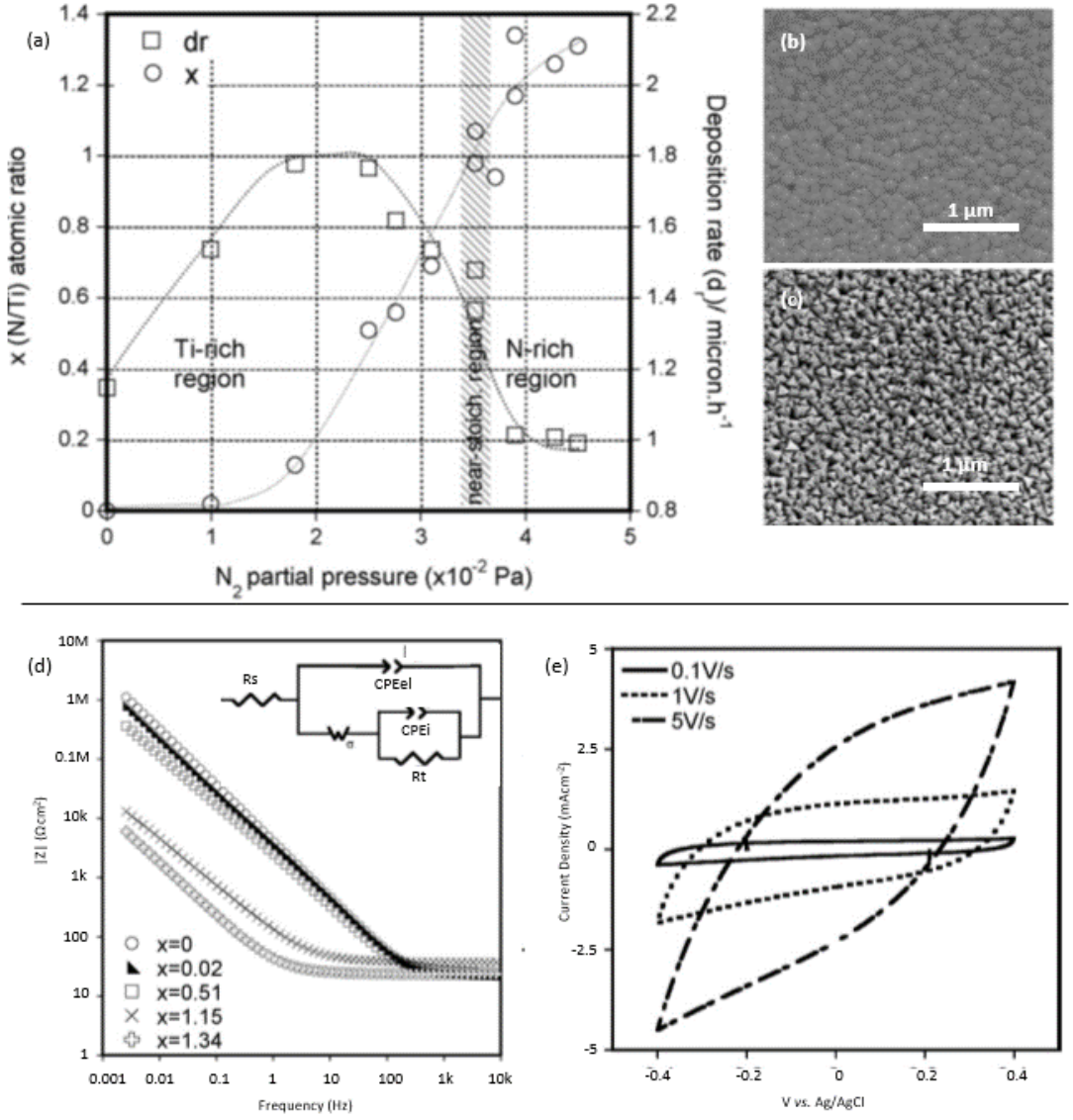

Figure 2.25: (a) The relationship between stoichiometry, PP_N, and deposition rate when using PVD to deposited TiN films; SEM images of TiN films produced under (b) low PP_N and (c) high PP_N; (d) Bode plots for TiN films of differing stoichiometry, showing also the equivalent circuit model, and; (e) The effect that scan rate has on the voltammogram's shape when testing over-stoichiometric (porous) TiN. Adapted from [226].

In addition to EIS, Cunha *et al.* [226] also record the CV response of the over-stoichiometric films when subjected to different values of v (0.1, 1, and 5 Vs^{-1}). Although the CSC_C is not computed, Figure 2.25 e is effective in demonstrating the relationship between pore resistance and sweep rate. The quasi-rectangular shape associated with capacitive performance, while apparent at v =0.1 Vs^{-1}, is lost as the rate is increased, transitioning to the diagonal response associated with ohmic conductors.

Table 2.5: Results of fitting the equivalent circuit to the impedance spectra obtained Figure 2.25 d by Cunha *et al.* [226].

x=N/Ti	Y_{el} ($S*s^{\alpha}cm^2$)	α_{el}	Y_i ($S*s^{\alpha}cm^2$)	α_i	Y_W ($S*s^{\alpha}cm^2$)	R_t (MΩ)
0.51	$43x10^{-6}$	0.93	$115x10^{-6}$	0.95	$5.4x10^{-5}$	2.9
1.15	$1.5x10^{-3}$	0.79	$8.2x10^{-3}$	0.95	0.06	0
1.34	$4.2x10^{-3}$	1	$2.8x10^{-3}$	1	0.01	0

Meijs *et al.* [228], who've been at the forefront of porous TiN-based research for the past decade, have done much to advance the relevance of TiN to neural interfacing. The variety of TiN electrodes produced are able to compete with other leading materials such as IrOx with similarly low impedances and high CSC_C's [176], [229]–[232]. Near- and over-stoichiometric TiN films approximately 1.5 µm thick were grown via reactive DC magnetron sputtering in an Ar/N_2 atmosphere, where the Ar flow rate was maintained at 180 sccm. Near- and over-stoichiometry were achieved by using N_2 flow rates of 180 and 300 sccm, respectively. Cyclic voltammetry measurements carried out at a sweep rate of $v = 0.05$ Vs^{-1} resulted in a higher CSC_C for over-stoichiometric TiN (58 $mCcm^{-2}$) than for near-stoichiometric TiN (32 $mCcm^{-2}$), despite having very similar growth morphology [176]. In another study [229], similar over-stoichiometric TiN films were grown (thickness not disclosed) and assessed for their charge retention capacity with 53 days of immersion in PBS. The CSC_C at $v = 0.05$ Vs^{-1} for electrodes kept passively submerged experienced only a marginal drop from 75 to 69 $mCcm^{-2}$ over the immersion period (Figure 2.26 a). The improved impedance response as compared to smooth TiN was also reported in other work [230], achieving a $|Z|_{1Hz}$ value of 24 Ωcm^2 and an $f_{cut\text{-}off}$ of ~50 Hz (Figure 2.26 b).

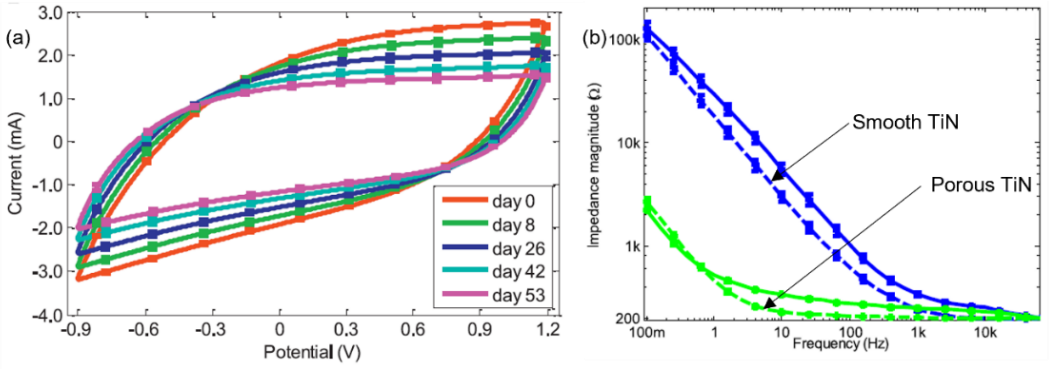

Figure 2.26: (a) Voltammograms for over-stoichiometric TiN electrodes immersed in PBS for 53 days, measured at a sweep rate of $v = 0.05$ Vs^{-1}. From [229]; (b) Bode plots for smooth and porous TiN. From [230].

As has been indicated thus far, the charge transfer properties of TiN are often attributed exclusively to double-layer capacitance, the rectangular voltammogram and accompanying lack of faradaic peaks providing the basis for this theory (refer to Figure 2.25 e and Figure 2.26 a). While this view appears to be the norm among researchers in the field of neural interfacing, other sectors, mainly those concerning energy storage, dispute this assertion [233]–[236]. In particular, the pseudo-capacitive behaviour of over-stoichiometric TiN has been demonstrated through a series of exclusionary electrochemical experiments. Hasegawa *et al.* [236] performed CV measurements on porous TiN electrodes using protonated aqueous electrolyte (1M NaCl) and non-protonated organic electrolyte (1M tetraethylammonium tetrafluoroborate (Et_4NBF_4) in acetonitrile). Having the large ionic size of 0.674 nm, the Et_4N^+ cation is largely restricted from participating in pseudocapacitance, but may still contribute to double-layer capacitance. Conversely, smaller cations like Na^+ with a diameter of 0.204 nm can contribute to both mechanisms in tandem. It is therefore expected that charge transfer be consistently higher in protonated electrolyte. Accordingly, the electrodes delivered larger capacitance values in the aqueous NaCl solution across all the scan rates tested (0.05, 0.1, 0.2, 0.5, and 1 Vs^{-1}), despite a larger testing window in organic electrolyte, effectively demonstrating their dual capacitive nature. Achour *et al.* [235] observed the same trend when testing over-stoichiometric TiN in protonated (aqueous 0.5 M K_2SO_4) versus non-protonated (1M Et_4NBF_4 in acetonitrile) electrolytes.

Over-stoichiometric TiN's ability to engage in pseudocapacitive charge transfer is theorised to originate from its susceptibility to oxidation. Given the abundance of loosely bound N atoms, reaction of TiN with ambient O_2 is thermodynamically favourable, and

has even been shown to occur at room temperature [237], [238]. In the work of Logothetidis *et al.* [237], it is hypothesised that upon exposure to air, rapid oxygen diffusion occurs along the grain boundaries, first forming transitional oxides and finally TiO_2. X-ray photoelectron spectroscopy (XPS) has been used extensively to characterise TiN surfaces, identifying a variety of oxides including TiO_x, NO_x, Ti_xO_y, and TiO_xN_y, which stabilize to form anatase TiO_2 [167], [234], [239]. Moreover, Raman analysis, being a subsurface characterisation technique, has revealed the presence of nitrogen vacancies within the bulk of oxidised, over-stoichiometric TiN. Concomitantly, a similar number of substitutional nitrogen (β-N) atoms were detected in the oxide via XPS. Achour *et al.* [235] thus suggest that excess N-atoms act as substitutional dopants in anatase TiO_2, a phenomenon that is widely reported to generate oxygen vacancies in the oxide [160], [167], [215], [234].

Figure 2.27 a shows the micro-Raman spectrum collected by Achour *et al.* [234] for oxidised over-stoichiometric TiN. Three major peaks may be identified, these being the first-order Transverse Acoustic (TA), Longitudinal Acoustic (LA), and Transverse Optical (TO). In accordance with multiple other research groups [236], [240], peaks occurring in the acoustic range (~150-350 cm^{-1}) are linked to heavy Ti cation vibrations, while those emerging in the optical range (~500-650 cm^{-1}) are associated with vibrations of the lighter N anions. It is understood that first order scattering is prohibited in perfect crystal structures like stoichiometric TiN due to its inversion symmetry. When this symmetry is disrupted, as is the case for over-stoichiometric TiN, atomic displacements have non-zero derivatives that are first-order polarizable. Peaks detected thus represent defects in the lattice, which in the case of TA and TO, correspond to nitrogen and titanium vacancies, respectively. A qualitative analysis of the elemental vacancy ratio may be obtained by comparing the intensities of TO and TA peaks, I_{TO} and I_{TA}, respectively. For the case shown, $I_{TO}/I_{TA} < 1$, indicating that N-vacancies are the most-frequently occurring defect in the sub-surface. The authors posit that this abundance of N-vacancies, an ostensible anomaly for over-stoichiometric TiN, represent N-atoms that outwardly diffused as dopants into the oxide. Another study by Achour *et al.* [235] using similar TiN samples provides support for this theory is the detection of peaks associated with N-doped TiO_2 (henceforth referred to as N-TiO_2, marked ‘a’ in Figure 2.27 b) that occur only at an excitation wavelength of 514 nm. Corresponding to an energy of ~ 2.41 eV, this value approximates the band gap of N-TiO_2 (2.2-2.4 eV), resulting in a resonance

effect that enables the peaks' detection. Interestingly, these peaks are absent when other excitation wavelengths are used, as only TiN-associated peaks emerge in these instances.

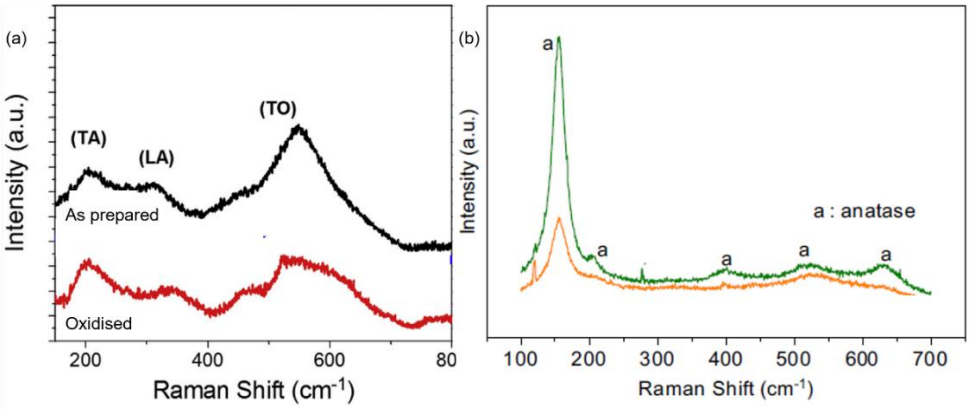

Figure 2.27: (a) Raman spectra for as-prepared (black) and oxidised (red) over-stoichiometric TiN films collected using a laser wavelength of 514 nm. Vibrations TA, LA, and TO are indicated on the figure. Adapted from [234]; (b) Raman spectrum for 500 nm over-stoichiometric TiN coating (green) collected using a laser wavelength of 514 nm. Peaks that are associated with N-TiO_2 are marked with 'a'. Adapted from [235].

These observations tie in with the emergence of pseudocapacitive charge transfer, where reversible faradaic reactions occur at the sites of O-vacancies either through redox reactions or intercalation. Considering the high capacitive retention of this material over tens of thousands of charge/discharge cycles (as tested by numerous research groups, examples given in Figure 2.28 a and b), the mechanism behind this stability comes into question. Towards this end, Achour *et al.* [235] put forward the following hypothesis, illustrating the theory by means of Figure 2.28 c. During one of these cycles, cations in solution interact with the N-TiO_2 and a number of O-vacancies are oxidised. Atomic oxygen is produced and diffuses away from the surface and into the bulk. Concomitantly, excess N-atoms diffuse outward and become incorporated into the oxide, acting as dopants and generating new O-vacancies in amounts roughly equivalent to the ones priorly consumed. In this way, the amount of available redox-active sites remains constant across numerous cycles, and the capacitive function does not decay significantly.

All these factors combined; the low impedance, high charge storage capacity, and excellent capacitive retention, make over-stoichiometric TiN a very attractive choice for chronic neural interfacing. Despite this, there exist several gaps in the literature with regards to this material, particularly regarding its pseudocapacitive behaviour in the context of this application. As TiN is often treated as a pure double-layer capacitor, electrochemical models lack any element that accounts for faradaic charge transfer.

Overlooking pseudocapacitance in physiological electrolytes may thus lead to over-estimation of the C_{DL}, inaccurate ESA/GSA ratio calculations, invalid lifetime projections, and possibly provide an erroneous basis on which further improvements may be made. Thorough characterization that takes into account TiN's dual capacitive nature is thus still required.

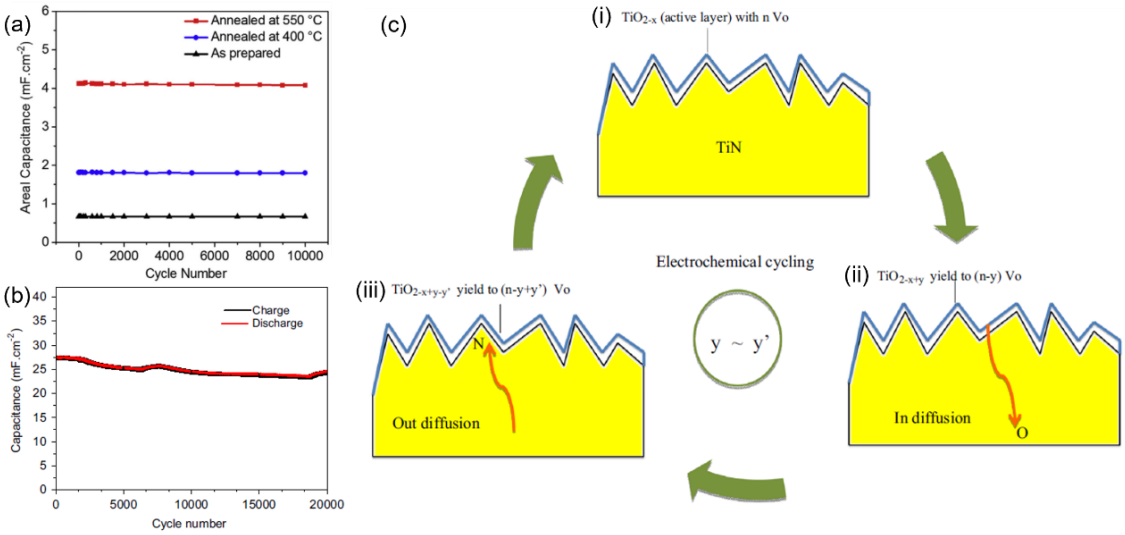

Figure 2.28: (a) As-prepared and annealed over-stoichiometric TiN retain their capacitance with 10,000 CV cycles at a scan rate of $v = 0.1$ Vs^{-1}. Test conducted in 0.5 M K_2SO_4. From [234]; (b) Oxidised over-stoichiometric TiN experiences only a minor drop in capacitance with 20,000 CV cycles at a scan rate of $v = 0.1$ Vs^{-1}. Test conducted in 0.5 M K_2SO_4; (c) An illustration summarizing the process of oxide vacancy consumption and renewal through N-dopants during a charge/discharge cycle. From [235].

2.4.4 Conductive Polymer PEDOT:PSS

Conductive polymers (CPs) have been steadily gaining traction as essential components in a variety of different applications, providing an alternative to noble metals and conductive oxides [127], [175], [241]. Owing to their low density, high flexibility, facile synthesis, and abundance of precursor materials, CPs have been explored for use in supercapacitors, catalytic converters, wearable electronics, sensors, and more [242]–[244]. Among the vast repertoire of CPs, encompassing materials such as polypyrrole (PPy), polyaniline (PANI), and polythiophene (PT), poly(3,4-ethylenedioxythiophene) (PEDOT) has received the most attention in both research and industry [245], [246]. High conductivity and chemical stability relative to its competitors has set it apart from other CPs, placing it at the forefront of polymeric materials for electrical contacts [241], [245].

While PEDOT is highly suited to most industrial devices, its applicability to the field of neural interfacing is limited despite its excellent qualities. The first issue is the inherent lack of biofunctionality of PEDOT films, which while not cytotoxic, are highly hydrophobic and thus unable to support any extensive form of cellular growth [247]. For a field that is heavily engaged in the promotion of close neural interaction between tissue and device, such a material presents an overt drawback. The second issue affiliated with the production of pristine PEDOT is its insolubility, radically complicating its deposition onto micro-sized electrodes [247], [248].

Both problems may be simultaneously resolved through a process of primary doping, whereby a hydrophilic counter-ion is added to PEDOT, usually in the form of poly(sodium-4-styrenesulfonate) (PSSNa). The resulting p-type semiconducting polymer, PEDOT:PSS (poly(3,4-ethylenedioxythiophene):poly(styrenesulfonate)), is made up of cationic PEDOT and anionic PSS, and may be dispersed in polar solvents as a homogeneous colloidal solution. Figure 2.29 shows the schematic of ionically-bonded PEDOT:PSS along with its core-shell structure and aggregated arrangement when processed into a film (a and b, respectively) [249]. These two physically distinct regions in the material lead to multi-scale phase separation, whereby the PEDOT-rich area conducts electricity via hole-transportation and the PSS-rich area conducts via ionic transport (Figure 2.29 c). A solid state double-layer capacitance forms between these two regions, allowing effective electrical conduction through the material [250].

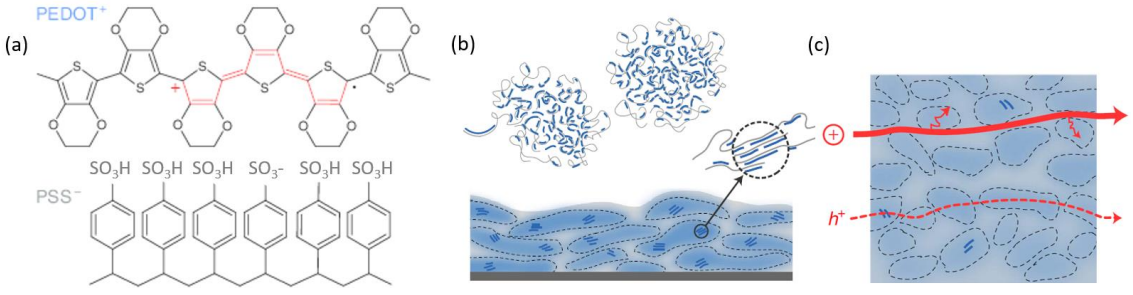

Figure 2.29: (a) The chemical structure of ionically cross-linked PEDOT:PSS polymer; (b) The spherical arrangement of the polymer, consisting of a PEDOT-rich core and a PSS-rich shell, and the consequential formation of two physically-distinct regions, and; (c) regions of hole (h^+) and ionic (+) transport through PEDOT and PSS, respectively. Adapted from [250].

The two most prominent techniques through which PEDOT:PSS films may be developed for neural interfacing are electrospinning [30], [251] and electrodeposition [98], [143], [252], [253]. In electrospinning, droplets of PEDOT:PSS precursor solution are

electrified into a jet, forming nanofibers that deposit onto a rotating current collector. The resulting morphology resembles a mesh of spun fibres in accordance with the process' namesake [254]. Although electrospun PEDOT:PSS has been well-characterised and shown to deliver very good electrochemical properties [241], [251], [255], it has a number of limitations that may be resolved by opting for electropolymerisation instead. Notably, as spinning is a line-of-sight process, it cannot produce films that closely follow the surfaces of long and narrow porous structures [254]. Conversely, electrodeposition requires that the electrode be submerged in a precursor solution, and if optimum wettability is achieved, the polymer may be grown even within the pores themselves.

In electropolymerisation, the precursor solution is made up of EDOT monomer and PSSNa salt dissolved in a protonated solvent, typically de-ionized water. A three-electrode setup such as the one described in section 2.3.1 is used, where the material to be coated acts as the working electrode. PEDOT:PSS is then polymerised from the solution using either a constant voltage, constant current, or dynamic voltage process. Since a galvanostatic process offers more direct control over the charge delivered during deposition, coatings developed in this way tend to have more uniform morphology, and as such this technique is generally preferred [98], [256]. A selection of polymer molarities, electrical parameters, and deposition conditions derived from a variety of research groups is given in Table 2.6.

Beyond the method and amount of charge applied during electropolymerisation, processing conditions such as solution agitation can also have significant effects on the resulting films. Solution agitation via stirring or ultrasonication produces rapid molecule movement, improving the mixing efficiency and thus altering the deposited morphology. Li *et al.* [257] observed very different PEDOT films deposited with and without 20 kHz ultrasonic-derived turbulence. A highly-porous structure with large ESA was obtained for turbulent depositions, with a specific capacitance of 100 F/g at a scan rate of $v = 0.005$ Vs^{-1}. Comparatively, films produced in the absence of ultrasonication had a dense and layered structure with a lower capacitance of 72 F/g under identical conditions. Solution agitation is thus highly encouraged in the production of CP films with high ESA/GSA ratios that translate into superior electrochemical performance.

Table 2.6: Processing parameters for electropolymerisation of PEDOT:PSS films in potentiostatic (PS), galvanostatic (GS), or potentiodynamic (PD) mode, obtained from literature.

Reference	EDOT (M)	PSS (M)	Mode	Q Density ($mCcm^{-2}$)	Voltage (V) *vs* Ag/AgCl	I Density ($mAcm^{-2}$)	Time (s)/ Scan Rate (Vs^{-1})
Chikar *et al.*[252]	0.007	0.017	GS	~ 7 - 200	/	/	/
Guex *et al.*[98]	0.007	0.017	GS	75-600	/	0.75	100 – 800 s
Pranti *et al.*[198]	0.01	0.17	GS	50 - 250	/	0.5	100 – 500 s
Siuzdak *et al.*[258]	0.015	0.1	PS	100 - 300	1.2	/	/
Mandal *et al.*[253]	0.01	0.1	PS	/	1.3	/	60 s
Cointe *et al.*[143]	0.01	0.034	PD	/	-0.7 to 1.0	/	0.01 Vs^{-1}
Boehler *et al.*[259]	0.01	0.04	PS	200	0.9	/	/
Leal *et al.*[260]	0.01	0.04	PS	200	0.9	/	/

Similar emphasis in literature is placed on solution de-oxygenation for the production of films with minimal physical defects. Multiple works have reported on the detrimental effects of soluble oxygen, whereby polymerisation reactions are drastically retarded or inhibited due to competing reactions [261], [262]. A side reaction of the polymerisation reaction is the transformation of dissolved oxygen into peroxide radicals. As styrene has a much higher propensity for reacting with peroxide radicals than it does for participating in polymerisation, polymeric chain propagation is disrupted. This leads to the formation of highly defective films that are characterised by a high frequency of uncoated areas [263]. For this reason, precursor solutions are often bubbled with inert gases such as Nitrogen or Argon prior to and during the polymerization process [252], [258], [264], [265].

Once deposited, PEDOT:PSS is classified as an intrinsic pseudocapacitor that can undergo reversible faradaic reactions through a process of doping (oxidation) and de-doping (reduction) [101]. This occurs via ion exchange with the electrolyte according to the reaction:

$$\mathrm{PEDOT^{+}{:}\,PSS^{-}} + \mathrm{Y^{+}} + \mathrm{e^{-}} \leftrightarrow \mathrm{PEDOT} + \mathrm{Y^{+}{:}\,PSS^{-}} \qquad (2.11)$$

where Y^+ are cations in solution [128]. Acting in tandem with double-layer capacitance, this mechanism results in a material with exceptionally low impedance and high charge storage capacity. Chikar *et al.* [252] developed PEDOT:PSS coatings on Pt-Ir cochlear electrodes using galvanostatic deposition. SEM analysis revealed the typical nodular

texture for the polymer, where aggregated micelles measured approximately 10-100 nm in diameter (Figure 2.30 a). The $|Z|_{1Hz}$ value obtained from EIS was lowered by two orders of magnitude, dropping from 6 $k\Omega cm^2$ for Pt-Ir down 20 Ωcm^2. The $f_{cut\text{-}off}$ also demonstrated a substantial shift, from >10 kHz to <100 Hz, owing to the radically different phase angle behaviour (Figure 2.30 b and c). In a similar way. Guex *et al.* [98] successfully improved the electrochemical performance of Pt electrodes through the application of PEDOT:PSS, increasing the CSC_C up to 35 $mCcm^{-2}$ at $v = 0.05$ Vs^{-1} (Figure 2.30 d and e). Through a CV deposition process, Cointe *et al.* [143] observed comparable increases in the CSC_C of PEDOT:PSS-coated Au electrodes, as well as a reduced impedance (Figure 2.30 f-h). All the parameters for depositions discussed in this paragraph are outlined in Table 2.6.

A very interesting behaviour observed in PEDOT:PSS films is volumetric capacitance, whereby the electrode's electrochemical performance (CSC_C and impedance) is observed to improve linearly with film thickness [244]. This has been attributed to effective film hydration, whereby electrolyte penetration into the material's porous architecture enables full use of its existing ESA, up to an observable saturation point. Bianchi *et al.* [266] provide a good demonstration of this phenomenon, measuring the impedance and capacitance of spin-coated PEDOT:PSS films varying in thickness from 100 to 400 nm (labelled A to E). The impedance was shown to decrease as film volume was increased, whereas the capacitance, as determined both from EIS and CV measurements at $v = 0.1$ Vs^{-1}, increased linearly with volume before plateauing (Figure 2.31). The authors attribute this saturation effect to incomplete film hydration, whereby the deep portions of the PEDOT:PSS architecture were inaccessible to the electrolyte ions.

Chikar *et al.* [252] observed similar improvements in the CSC_C of electro-deposited PEDOT:PSS films (parameters given in Table 2.6), where the value was observed to increase following a positive polynomial trend rather than a linear regression. The value of $|Z|_{1Hz}$ was also decreased by an order of magnitude, while the $f_{cut\text{-}off}$ experienced negative shifts as deposition time was lengthened (Figure 2.31 b and c). These findings indicate the benefit of exploring different film thicknesses for optimum electrochemical performance, where electrolyte penetration and structural integrity of the porous architecture act as capping limits.

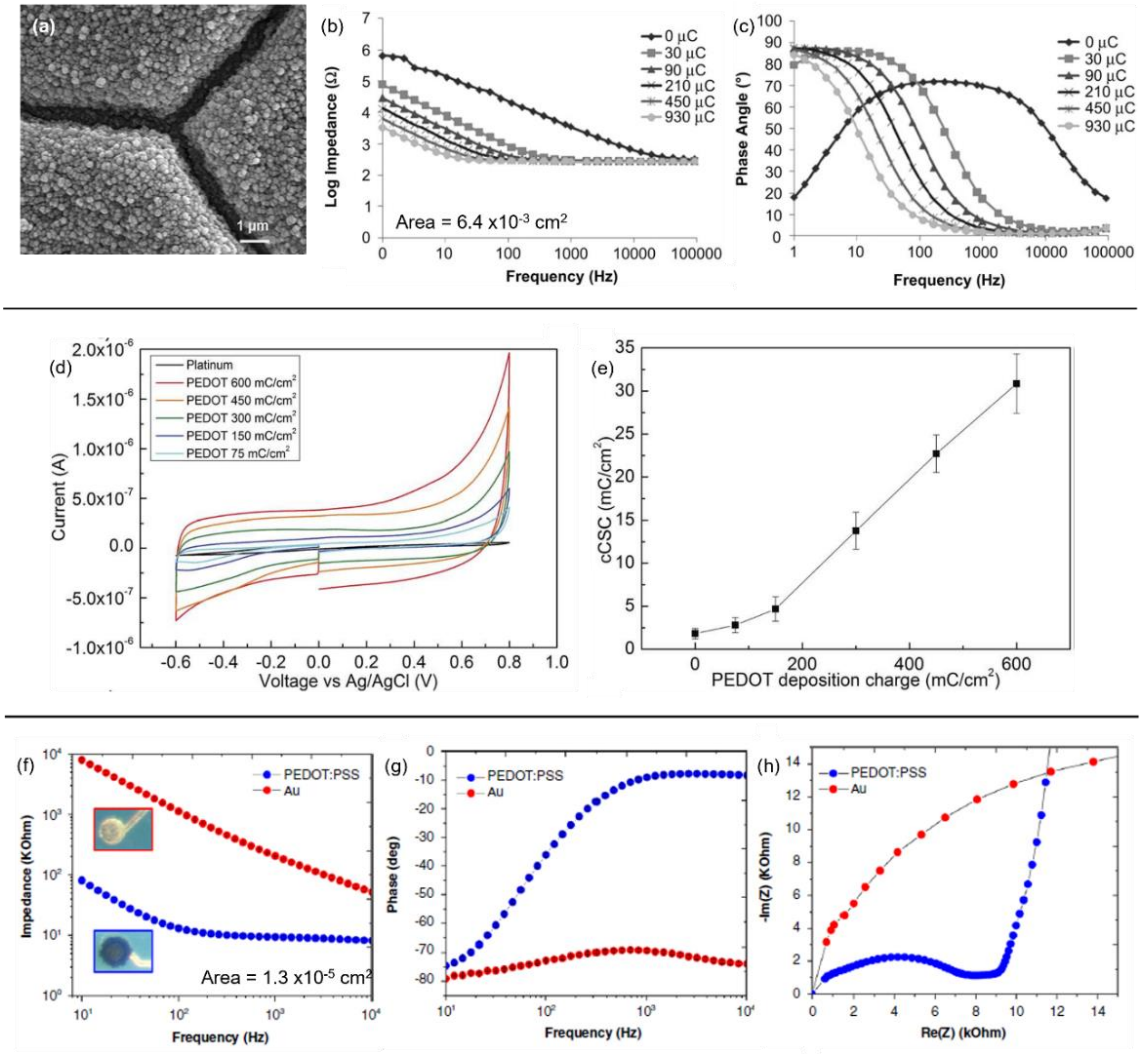

Figure 2.30: (a) SEM image of the PEDOT:PSS coating on the cochlear electrode; (b, c) Impedance and Phase angle Bode plots for PEDOT:PSS coatings deposited under different charges (longer deposition time). From [252]; (d, e) The CSC_C of PEDOT:PSS increases as deposition time increases, following a positive polynomial trend. From [252]; (f-h) Bode and Nyquist plots for Au electrodes with and without a PEDOT:PSS coating. From [143].

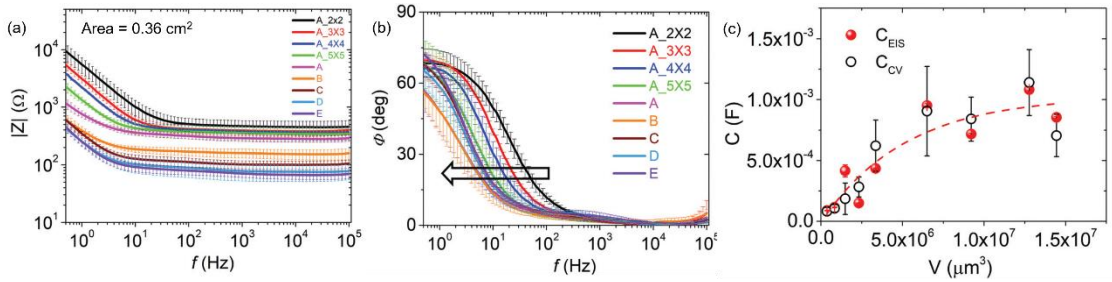

Figure 2.31: (a) Impedance and (b) phase Bode plots show the change in electrochemical properties as the thickness of PEDOT:PSS film is increased (labelled A-E on figure); (c) Plot of capacitance as determined from EIS (C_{EIS}) and CV (E_{CV}) versus PEDOT:PSS volume. From [266].

One of the main issues facing PEDOT:PSS-coated electrodes is in fact the structural integrity of the film's porosity. Mandal *et al.* [253] assessed the stability of electrodeposited PEDOT:PSS films (parameters outlined in Table 2.6) by subjecting them to a 75-day accelerated aging test carried out at 60 ^{o}C. EIS spectra gathered on days 1 and 75 are shown in Figure 2.32, where a marked increase in impedance and a positive shift of $f_{cut\text{-}off}$ are apparent. The values obtained from fitting the equivalent circuit model shown in the inset are outlined in Table 2.7 where R_s and R_{poly} represent the resistance of solution and faradaic charge transfer respectively, C_d indicates the double-layer capacitance, and Y_{poly} and α are elements of the CPE describing the polymer's capacitance. R_{poly}, which increases by several orders of magnitude over the immersion period, is identified as the main contributor towards electrochemical degradation. This was corroborated via scanning electron microscope (SEM), where the polymer's structure was found to have collapsed and compacted, decreasing the surface area available for charge transfer. The authors attribute this to the material's low crystallinity, producing low-strength structures that are unable to maintain their porous architecture for extended periods of time.

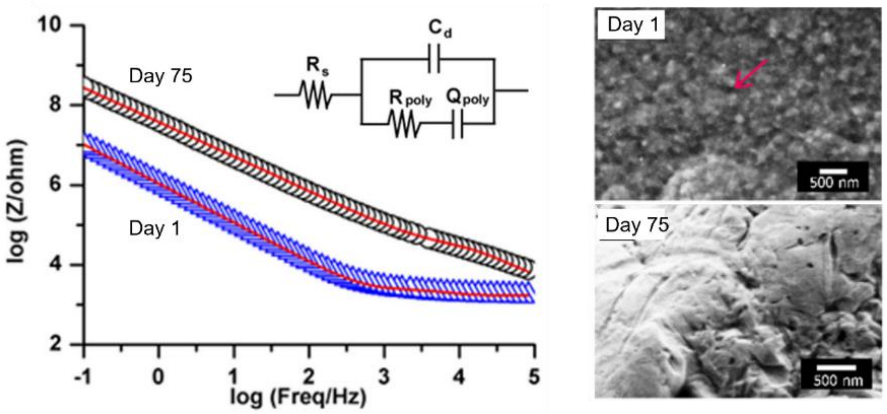

Figure 2.32: The impedance Bode plots for PEDOT:PSS electrodes on day 1 and day 75 of immersion in PBS kept at 60 ^{o}C. The equivalent circuit model and accompanying SEM images of the electrode surfaces on both days are also included. Red arrow points to evident porous structure. From [253].

Table 2.7: Results from fitting the EIS spectra to the circuit model given in Figure 2.32. From [253].

	R_s (kΩ)	**C_d (µF)**	**R_{poly} (kΩ)**	**Y_{poly} (µS*s^α)**	**α**
Day 1	1.98	3.16	2.47	0.91	0.654
Day 75	3.24	1.82	5.18×10^6	0.02	0.759

There have been many successful reports of PEDOT:PSS crystallisation, a process that simultaneously improves structural integrity and electrical conductivity. Most strategies rely on the post-deposition removal of PSS, largely considered to make up the less conductive regions of the material, through such techniques as UV irradiation [267],

exposure to sulfuric acid (H_2SO_4) [246], or high temperature annealing (~ 140-160 ^oC) [250]. Although successful, these processes result in a reduction of the PEDOT to PSS ratio, severely impacting the material's biofunctionality as indicated previously [268]. Rather than PSS-removal, a process of slow, low-temperature curing ($\leq$ 120 ^oC) may be employed to achieve polymer chain reorientation, and thus crystallisation, without significant PSS burn-off [269]–[271]. This process creates regions of ordered PEDOT crystallites with π–π stacking between the layered chains as shown in Figure 2.33, facilitating faster hole transport [241], [272].

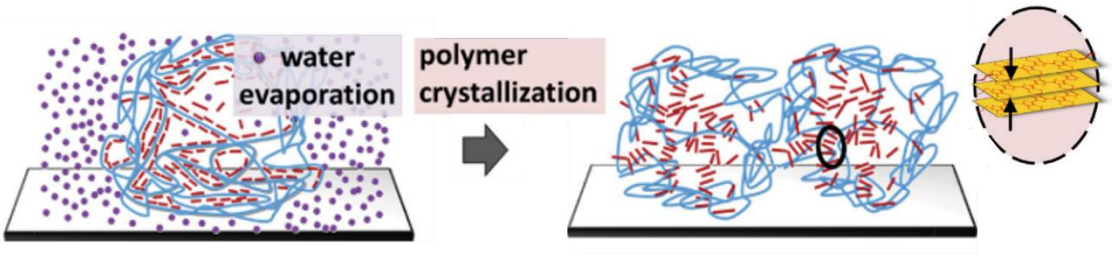

Figure 2.33: Polymer chain re-orientation and the formation of ordered PEDOT crystallite regions with π–π stacking. Adapted from [241].

The retention of PSS following baking may be confirmed via presence of PSS-related vibrations in Raman spectroscopy. The typical spectrum for pristine PEDOT:PSS is given in Figure 2.34 a, where Chang *et al.* [273] identify seven prominent peaks in accordance with the findings of many other research groups [274]–[276]. With reference to the labelled structures provided in Figure 2.34 b, the peaks at 1000 cm^{-2}, 1110 cm^{-2}, and 1575 cm^{-2} are attributed to C-C, SO_3^-, and C-C-H bonds of PSS, respectively. On the other hand, PEDOT-associated peaks were detected at 1272 cm^{-2}, 1383 cm^{-2}, 1452 cm^{-2}, and 1524 cm^{-2}. As per Figure 2.34 c, these peaks may be respectively assigned to C_α- $C_{\alpha'}$ inter-ring stretching, C_β - $C_{\beta'}$ stretching, symmetrical $C_\alpha = C_\beta$, and asymmetrical $C_\alpha = C_\beta$ vibrations of the benzoid PEDOT chain (Figure 2.34 d) [277], [278].

Noormohammadi *et al.* [279] achieved excellent electrochemical properties after baking drop-cast PEDOT:PSS films at 80 ^oC for 1 hr in air. Capacity retention in excess of 92.3% was achieved after aggressive CV cycling in 3M KOH at $v = 0.05$ Vs^{-1} for 50 cycles. Moreover, 99.4% of the material's capacitance was retained after 5000 galvanostatic charge-discharge cycles at 1 A/g. Shur *et al.* [139] use a similar low-temperature curing procedure (80 ^oC for 20 minutes) for neural interfacing electrodes, producing PEDOT:PSS films with a $|Z|_{1Hz}$ value of 25 Ωcm^2 and a CSC_C value of 11 $mCcm^{-2}$ at $v = 0.1$ Vs^{-1}. Low-temperature curing thus provides a viable alternative to harsher

crystallisation techniques which, in addition to stripping the PSS and lowering biofunctionality, may be incompatible with other materials in the electrode assembly [241].

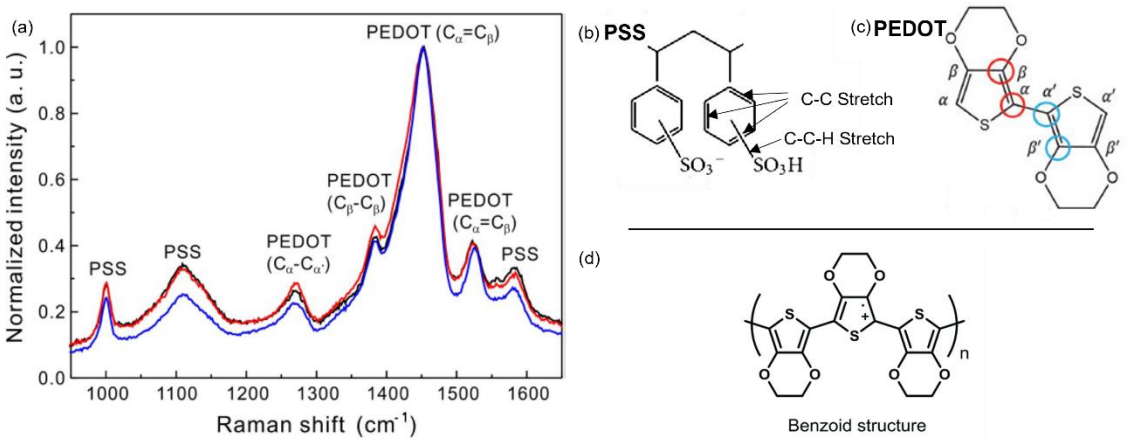

Figure 2.34: (a) Raman spectra for pristine PEDOT:PSS (black), from [273]; (b) labelled bonds of PSS, from [280]; (c) labelled bonds of PEDOT, from [281], and; (d) the benzoid structure of PEDOT, from [278].

Another prevalent issue with PEDOT:PSS films is weak adherence to the underlying substrate. Delamination is frequently reported, especially when the polymer is deposited onto non-textured metal surfaces such as Pt or Au [282], [283]. Many potential solutions for improved adhesion have been explored across PEDOT:PSS's diverse fields of application, notably the process of substrate functionalization using amines and the inclusion of adhesion layers with rich -OH groups like D-sorbitol [284], [285]. A widely successful technique in the field of neural interfacing is the promotion of mechanical adhesion via substrate texturing, doubly beneficial by way of increasing the electrode's ESA. Pranti *et al.* [282] demonstrated the enhanced adhesion of electropolymerized PEDOT:PSS films on Au electrodes (parameters outlined in Table 2.6) with and without a 0.05 mol/L iodine etching treatment. Film adhesion was assessed by subjecting the electrodes to ultrasonication at a frequency of 35 kHz and carrying out sequential impedance measurements every 2 minutes. Figure 2.35 a shows the average $|Z|_{1Hz}$ of the electrodes for a total testing time of 11 minutes. A negligible change in $|Z|_{1Hz}$ was measured for etched electrodes by the end of the test, whereas the value for non-etched electrodes increased by a factor of 30. Imaging revealed that 60% of the PEDOT:PSS coating had peeled off the non-etched substrates after only 5 minutes of ultrasonication, whereas no such delamination was observed for etched electrodes (Figure 2.35 b and c).

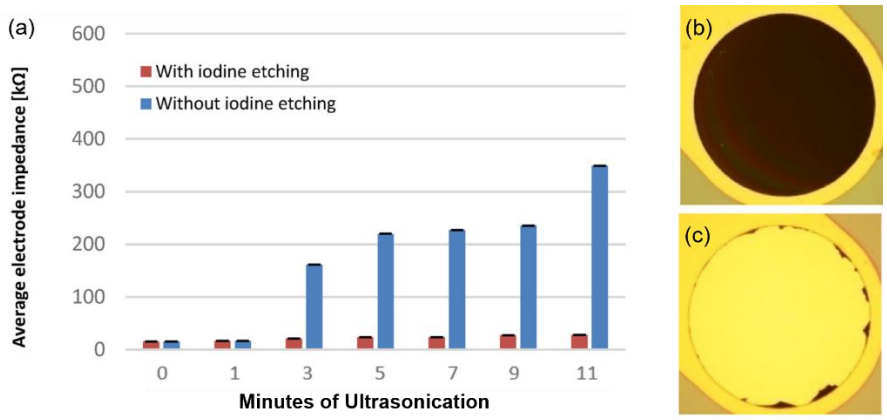

Figure 2.35: (a) The average $|Z|_{1Hz}$ for etched and non-etched Au electrodes with an electrodeposited coating of PEDOT:PSS following ultrasonication in PBS; Images of the (b) etched and (c) non-etched electrodes after 5 minutes of testing. From [198].

Beyond the problems discussed thus far is the Achilles' heel of all CPs, as aptly termed by Liu and Li [186], that takes the form of cyclic degradation. As their pseudocapacitive action relies on repetitive doping and de-doping of ionic species, the material undergoes a process of volumetric expansion and contraction with each cycle (Figure 2.36 a). This constant physical deformation subjects the polymer to internal osmotic stress, gradually degrading its structural integrity [187]. This occurs especially at interfaces of contrasting elasticity, such as for polymers deposited onto metals or their derivatives, wherein the CP is observed to crack, crumble, and delaminate after a number of cycles [186], [284]. For this reason, cyclic stability assessments are imperative when considering CPs for chronic neural interfacing, particularly for stimulation or blocking [186], [187].

Literature indicates that PEDOT:PSS films have better cycling stability when deposited onto rough and porous surfaces, likely due to the improved mechanical adhesion it permits. Boehler *et al.* [259] tested the cycling endurance of PEDOT:PSS films deposited onto Pt electrodes modified with SIROF. Sequential CV cycles at a scan rate of $v = 0.1$ Vs^{-1} were applied within the water window limits until >20% coating delamination was observed via optical microscopy. Variations in impedance were monitored via EIS measurements taken after every 20 cycles. The results, shown in Figure 2.36 b, demonstrate the excellent cyclability of PEDOT:PSS, where only a marginal increase in the value of $|Z|_{1Hz}$ was recorded after 10,000 cycles, increasing from ~ 18 Ωcm^2 to ~ 30 Ωcm^2, accompanied by a negligible shift in $f_{cut\text{-}off}$. Optical imaging (example given in the inset of Figure 2.36 b) revealed no instances of PEDOT:PSS delamination, but some cracking was observed by the end of the cycling regiment. Leal *et al.* [260] demonstrated

similarly high stability of PEDOT:PSS films electrodeposited onto SIROF as compared to Pt. High-charge, long-term DC stimulation (0.7 $mAcm^{-2}$) caused complete delamination of PEDOT:PSS from Pt after only 12 minutes, whereas SIROF/PEDOT:PSS electrodes withstood 60 minutes of stimulation before clear damage could be observed (Figure 2.36 c). Such a high resistance to cyclic degradation is exceptional among conductive polymers, where most films experience significant delamination before 100 cycles, and very few exceed 1000 cycles [187], [259], [283]. All the parameters for depositions discussed in this paragraph are outlined in Table 2.6.

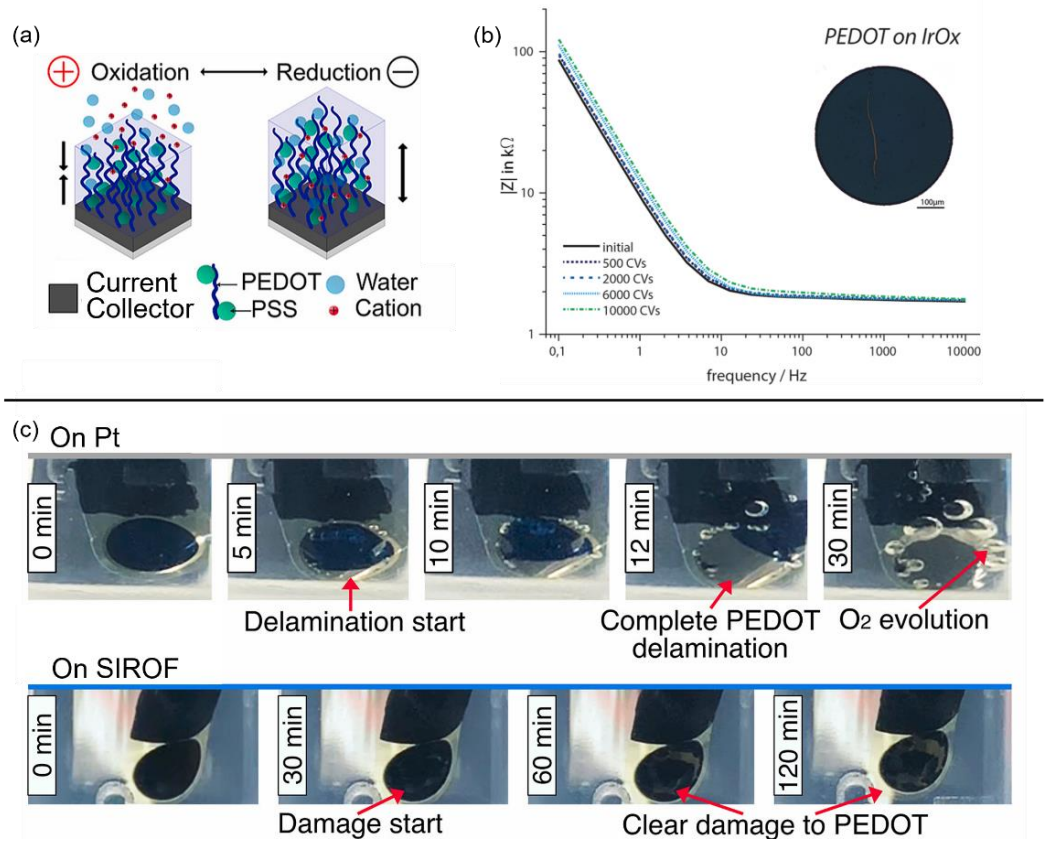

Figure 2.36: (a) The contraction and expansion of PEDOT:PSS during an oxidation-reduction cycle, adapted from [260]; (b) PEDOT:PSS deposited on sputtered IrOx can withstand 10,000 CV cycles at $v = 0.1\ Vs^{-1}$ with minimal effect on impedance and minor film damage, from [259]; (c) PEDOT:PSS deposited onto smooth Pt can only withstand 12 minutes of DC stimulation before complete delamination, whereas PEDOT:PSS/SIROF only starts to exhibit clear damage after 60 minutes, from [260].

All these characteristics; the ease of production, low impedance, large CSC_C, strong mechanical adherence to textured substrates, and high resistance to cyclic degradation, make deposited PEDOT:PSS films a highly advantageous surface engineering technique to improve electrochemical properties [98], [131], [255]. While the bulk of existing research has focused on the application of PEDOT:PSS to noble metals and IrOx, there

has thus far been no report of its development onto columnar TiN. Wang *et al.* [129] have described an electrode comprising of PEDOT:PSS electro-deposited onto sputtered TiN. Although no details are provided about the ceramic's deposition parameters, analysis of the cross-section and roughness measurements given in Figure 2.37 reveals a dense morphology with minimal topographic features. Nevertheless, the electrode still delivered acceptable $|Z|_{1Hz}$ and $f_{cut\text{-}off}$ values, ~ 80 Ωcm^2 and 100 Hz, respectively. While the impedance is not as low as other PEDOT:PSS electrodes [198], [252], [259], [260], and no investigation was made regarding its adhesion and cycling lifetime capabilities, the CP still improved the impedance measurement over smooth TiN by 2 orders of magnitude. This highlights the potential benefits that might be gained from depositing PEDOT:PSS onto porous TiN, a gap in the literature that has yet to be addressed.

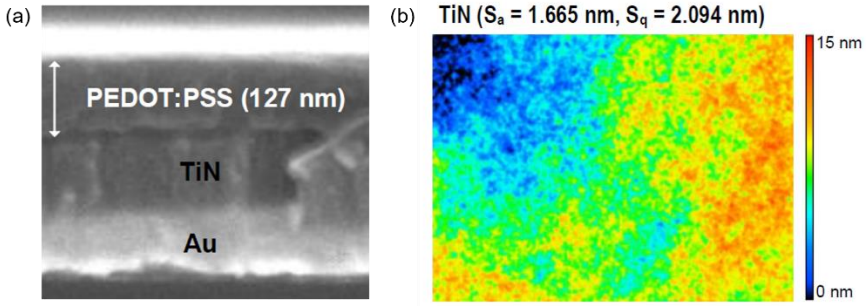

Figure 2.37: (a) Cross-section of the PEDOT:PSS film deposited onto sputtered TiN, with an Au adhesion layer, and; (b) light interferometry surface roughness measurement of sputtered TiN, where S_a and S_q are the average and RMS roughness of the surface, respectively. From [129].

2.4.5 Emerging and Composite Materials

The materials mentioned thus far have an established presence within the field of neural interfacing, whether they be in wide-spread clinical use or heavily researched. However, the materials discussed hereunder have only recently been placed under consideration for chronic, active implantation, and are thus still in the early stages of characterisation.

Most of the materials within this category are carbon-related, such as graphene and its derivatives. Having a single-layered, two-dimensional structure, graphene is highly conductive with a large electrolysis window, where its main point of interest lies in its transparency. Light-sensitive applications such as the optoelectronic devices used to restore vision thus stand to benefit greatly from graphene [29], [112]. Although the charge storage capacity of flat graphene electrodes is not up to par with other materials such as

IrOx or PEDOT:PSS, different processing techniques have been explored to produce (opaque) porous, three-dimensional structures that can be used for neural stimulation and blocking. Yichen *et al.* [286] developed doped porous graphene electrodes via laser pyrolysis, achieving $|Z|_{1Hz}$ and $f_{cut\text{-}off}$ values of ~ 60 Ωcm^2 and 1 kHz, respectively. The CSC_C at a scan rate of $v = 0.1$ Vs^{-1} was measured at 50 mCcm^{-2}, comparable to the other high-charge capacity materials discussed previously (Figure 2.38 a-c).

Reduced graphene oxide, rGO, has also been explored as a possible element in a CP composite electrode. Wang *et al.* [265] electrodeposited such a film using a mixture of heat-reduced graphene oxide and EDOT/PSSNa solution onto sputtered Au sites (Figure 2.38 d). The $|Z|_{1Hz}$ was measured at ~ 80 Ωcm^2, while the $f_{cut\text{-}off}$ occurred at ~ 200 Hz. Moreover, an impressive CSC_C of 80 mCcm^{-2} was observed at a scan rate of $v = 0.1$ Vs^{-1}, for a water window of only 1.4 V, which is much smaller than that of doped graphene. The coating adhesion, tested via ultrasonication in agarose gel, was satisfactory, with only an 8% increase at $|Z|_{100Hz}$ by the end of the 60-minute test (Figure 2.38 e). However, 1000 CV scans at a sweep rate of $v = 1$ Vs^{-1} (an approximate total charge transferred of 13 Ccm^{-2}) resulted in a 25% impedance increase at $|Z|_{100Hz}$. This is despite the relatively small amount of ionic dopants engaging the material with each cycle at such a high scan rate (Figure 2.38 f). In addition to the obvious drawbacks of decreasing charge capacity, the accompanying physical degradation due to osmotic stress limits the use of such an electrode, as the biocompatibility of bulk graphene is still under scrutiny, with much heavier scepticism directed towards particulates that could induce systemic problems [112], [155], [287].

Nanosized carbon structures have also been gaining traction in this field, notably as a primary dopant to PEDOT. Vajrala *et al.* [288] used oxidised carbon nanofibers (CNF) to develop the conjugated polymer PEDOT:CNF. When electrodeposited onto Au sites, the material delivered a CSC_C of 48 mCcm^{-2} at a sweep rate of $v = 0.2$ Vs^{-1} and had a remarkably low $|Z|_{10Hz}$ value of 1 Ωcm^2. Unlike the PEDOT:PSS/Graphene electrode, the PEDOT:CNF samples were able to withstand chronic charge-discharge cycling (an approximate total charge transferred of 250 Ccm^{-2}) without any delamination or osmotic stress cracking (Figure 2.39). The same issue however persists with such carbonaceous materials, in that their long-term biocompatibility, even when non-particulated, is still uncertain, especially since CNFs are already associated with the emergence of oxidative stress, cellular apoptosis, and mesothelioma [289]–[291].

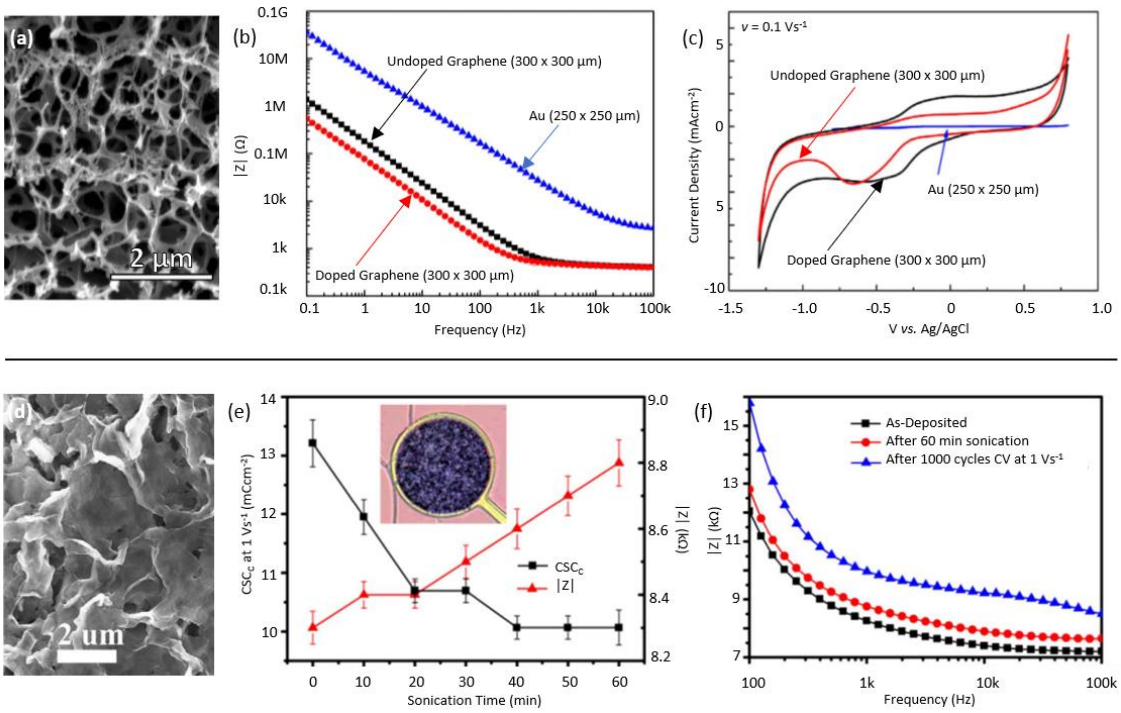

Figure 2.38: (a) SEM image of doped porous graphene produced using laser pyrolysis; (b) Impedance bode plots for electrodes of Au, undoped graphene, and doped graphene; (c) Voltammograms for the same three electrodes measured at a sweep rate of $v = 0.1$ Vs^{-1}. From [286]; (d) SEM image of PEDOT:PSS-rGO; (e) The change in $|Z|_{100Hz}$ and CSC_C measured at 1 Vs^{-1} with 60 minutes of ultrasonication, and; (f) The impedance Bode plots for the PEDOT:PSS-rGO electrodes as-deposited, after ultrasonication, and after lifetime cycling at v =1 Vs^{-1}. From [265].

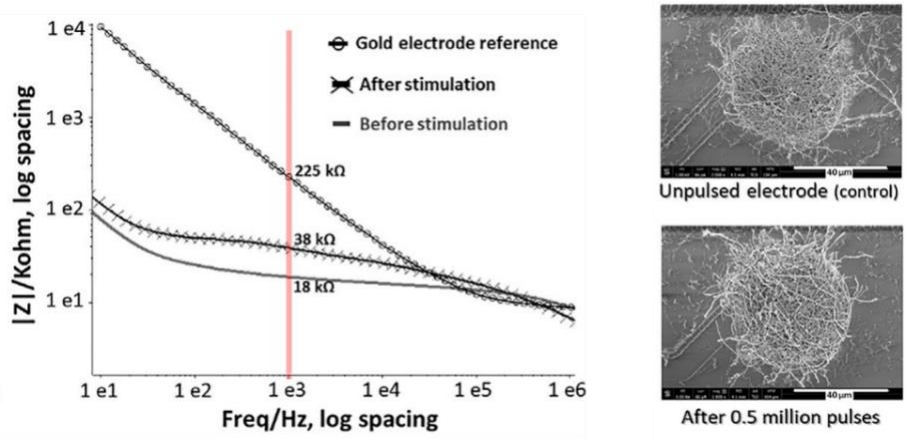

Figure 2.39: The impedance Bode plot for a reference Au electrode and PEDOT:CNF electrodes before and after stimulation. SEM images of control and PEDOT:CNF electrodes after stimulation are also included. From [288].

The final material of note in this category is nanocrystalline boron-doped diamond (BDD), usually grown via a process of chemical vapour deposition (CVD) onto a surface pre-conditioned with diamond solution [181], [292], [293]. Although on its own the

material has only modest electrochemical properties, its deposition onto a surface with high ESA/GSA ratio can dramatically increase its charge transfer capabilities. Meijs *et al.* [176] report a CSC_C of 253 Ccm^{-2} at a sweep rate of $v = 0.05$ Vs^{-1} when depositing BDD onto porous TiN. This large value is primarily attributed to the material's extended water window, spanning from -1.3 to 1.2 V *vs* Ag/AgCl (Figure 2.40 a). No significant improvement was made regarding the value of $|Z|_{1Hz}$, with the trend rather being to slightly increase the impedance at low frequencies (Figure 2.40 b). While BDD does not suffer from the same level of concern regarding its chronic toxicity as graphene or nanoscale carbon structures, studies regarding long-term mechanical stability, charge retention, and resistance to osmotic stress are still lacking [292], [294].

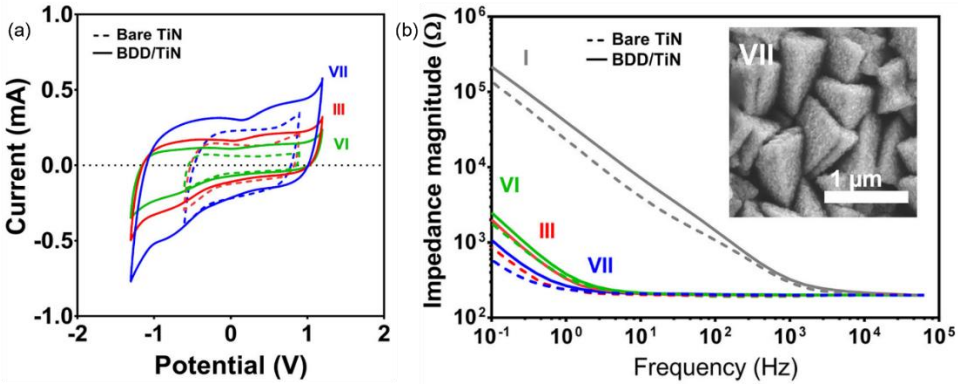

Figure 2.40: (a) Voltammograms of various different porous TiN electrodes coated with BDD, measured at a sweep rate of $v = 0.05$ Vs^{-1}; (b) Impedance Bode plots for the same electrodes. Inset shows an SEM image of BDD-coated TIN pyramidal grains. I, III, VI, and VII refer to different TiN coatings. From [176].

2.4.6 Comparisons

Table 2.8 presents a collection of notable electrode materials discussed in section 2.4, outlining their $|Z|_{1Hz}$, $f_{cut\text{-}off}$, CSC_C at the reported value of v, as well as the water window it was measured at, when available. All reported tests were carried out in PBS solution kept at physiological temperature, and using a three-electrode system where the reference electrode was either silver/silver chloride (Ag/AgCl) or saturated calomel (SCE). All EIS measurements were made at the open circuit potential (OCP) with a perturbation of ~10 mV. The materials are tabulated in order of reference in the text.

Table 2.8: Summary of the electrochemical properties of notable electrodes, derived from literature.

Electrode Material	$\|Z\|_{1Hz}$ (Ωcm^2)	$f_{cut\text{-}off}$ (Hz)	CSC_C ($mCcm^{-2}$)				Water Window (V *vs* Ref)	References
			0.05 Vs^{-1}	0.1 Vs^{-1}	0.15 Vs^{-1}	0.2 Vs^{-1}		
Smooth Pt	300-3000	>10,000	/	0.55-1.5	/	/	-0.6 to 0.8 V *vs* Ag/AgCl	[162], [184], [191]
Pt on TiO_2 Nanotube Array	70	2000	/	28	/	/	-0.6 to 0.8 V *vs* Ag/AgCl	[184]
Nanostructured Pt Grass	20	300	/	/	/	/	-0.6 to 0.9 V *vs* Ag/AgCl	[162]
Nanocrystalline Pt Flowers	15	50	100	/	/	/	-0.6 to 0.8 V *vs* Ag/AgCl	[295]
Pt-Ir Alloy	50	1000	/	/	6	/	-0.6 to 0.8 V *vs* Ag/AgCl	[197]
Smooth Au	20,000	>10,000	/	/	/	2	-0.6 to 0.6 V *vs* Ag/AgCl	[143], [198]
Micro-cracked Au	800	2000	/	/	/	/	/	[199]
Columnar Au	150	30	/	/	/	/	-0.2 to 0.6 V *vs* Ag/AgCl	[183]
AIROF	8	30	/	40	/	/	-0.6 to 0.8 V *vs* Ag/AgCl	[205]
EIROF	16	400	/	68	/	/	-0.6 to 0.8 V *vs* SCE	[206]
SIROF	5	200	60	/	/	/	-0.6 to 0.8 V *vs* Ag/AgCl	[200]
Smooth TiN	1500	1000	0.36	/	/	/	-0.6 to 0.9 *vs* Ag/AgCl	[176]
Bulk TiN (Nitrided TiO_2)	/	/	/	/	/	15	-0.6 to 0.8 *vs* Ag/AgCl	[217]
Porous TiN	24	50	58	/	/	/	-0.6 to 0.9 *vs* Ag/AgCl	[176], [230]
PEDOT:PSS on Pt-Ir	20	10 - 100	/	15	/	/	-0.6 to 0.8 V *vs* Ag/AgCl	[252]
PEDOT:PSS on Etched Au	30	100	/	/	/	/	-0.9 to 0.6 V *vs* Ag/AgCl	[198]
PEDOT:PSS on SIROF	18	10	/	40	/	/	-0.6 to 0.9 V vs Ag/AgCl	[259], [260]
PEDOT:PSS on TiN	80	100	/	/	/	/	/	[129]
Porous Graphene	60	1000	/	50	/	/	-1.5 to 0.8 V *vs* Ag/AgCl	[286]
PEDOT:PSS-rGO Composite	80	200	/	80	/	/	-0.6 to 0.8 V *vs* Ag/AgCl	[265]
PEDOT-CNF	/	200	/	/	/	48	-0.85 to 0.6 V *vs* Ag/AgCl	[288]
BDD on Porous TiN	25	150	253	/	/	/	-1.3 to 1.2 V *vs* Ag/AgCl	[176]

2.5 Issues arising *in vivo*

While assessing a material's electrochemistry in salt-containing solutions is a crucial and necessary step towards its characterisation, it alone is not sufficient to predict performance *in vivo*. Even when excluding materials of dubious biocompatibility (i.e., graphene and nanostructured carbon), a variety of biological factors persist, that through their interactions with the implanted device might completely alter the projected outcome.

2.5.1 Fouling and Encapsulation

One of the biggest issue facing chronically implanted electrodes is surface fouling and encapsulation. As outlined in section 2.2.3.2, triggering the inflammation cascade is largely unavoidable, even with mitigating factors like device flexibility in place. This presents an obvious drawback, as the conductivity of fibrous tissue is well below that of interstitial fluid, CSF, and even blood plasma, introducing a large source of impedance that may counter electrochemical improvements brought about through alloying, porosity, or oxidation [122], [228], [230].

Dalrymple *et al.* [197] provide a clear example of this phenomenon when assessing Pt and Pt-Ir cochlear implants. Five electrodes each of the two materials were implanted into the scala tympani (ST) of 10 Sprague Dawley rats (n=5) for 5 weeks. Histological analysis after the period of implantation revealed similar levels of fibrous tissue growth for both materials (~10-16 %), bar one of the Pt-Ir electrodes which experienced exceedingly high growth, generating ~60% coverage (Figure 2.41 a and b). As a consequence, no significant difference was observed in the measured impedance of both materials after 5 weeks (Figure 2.41 c), effectively negating the advantages of alloying.

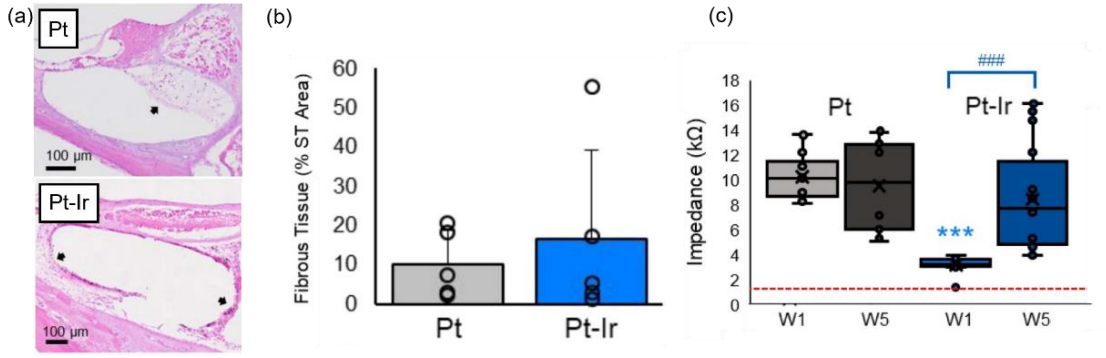

Figure 2.41: (a) Fibrous capsule (black arrows) on Pt and Pt-Ir electrodes after 5 weeks implantation in the ST; (b) % of ST covered by fibrous tissue after electrode explantation, and; (c) change in impedance from time of surgery to end of implantation. Adapted from [197].

Although most electrode materials develop fibrous attachment to some extent, different physicochemical characteristics can manifest in varying degrees of encapsulation [13], [102], [125]. One of the leading factors governing fibrous growth is surface roughness, where both micro- and nano-topographical features can have an influence. In the absence of other effects, smooth 2D surfaces typically encourage fibroblast attachment, where cells proliferate easily, are well-spread with a flattened morphology and a defined actin cytoskeleton, and possess many focal adhesions with multiple stress fibres [296]–[298]. Pennisi *et al.* [299] observed a reduction in the number of primary human fibroblasts growing on Pt surfaces when nano-texturing was introduced using e-gun evaporation. As seen in Figure 2.42, a significant difference in both the number of cells/mm^2 as well as their morphology is evident as the RMS-value was increased from 1.47 ± 0.03 nm to 26.30 ± 0.13 nm.

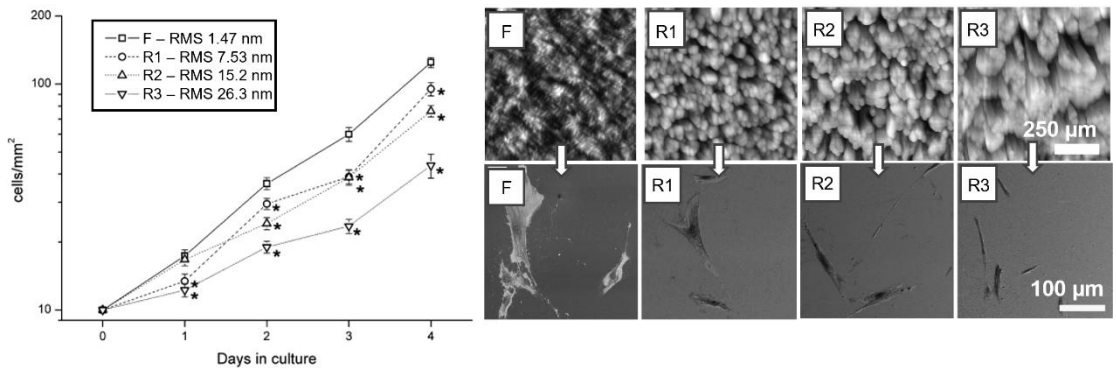

Figure 2.42: Plot of cell number per mm^2 versus days in culture for flat (F) and roughened substrates (R1-R3) of increasing RMS value. SEM images of the substrate topography are also given, along with images of the fibroblasts growing on the surfaces after culturing. Fibroblasts are notably smaller as roughness increases, and cell spreading is restricted. From [299].

The work of Bourkoula *et al.* [296] suggests the existence of a roughness threshold when it comes to discouraging fibroblast growth. Poly(methyl methacrylate) (PMMA) substrates were modified using oxygen plasma to produce 5 different surface textures having RMS roughness as shown in Figure 2.43 a. Human skin fibroblasts cultured on the samples for 3 days revealed a critical threshold RMS_{CR} of ~20 nm for the existing test conditions, with the cells demonstrating insensitivity to changes below this point. It is theorised that this threshold is related to the fibroblasts' elastic modulus, where increasing the height and inter-distance length of the texturing features causes the cell to stretch and sag as it tries to grow (Figure 2.43 b). While providing a large area for adhesion, threshold values are reached when the cell is stretched beyond its capacity, and thus the surface morphology becomes hostile to cell growth.

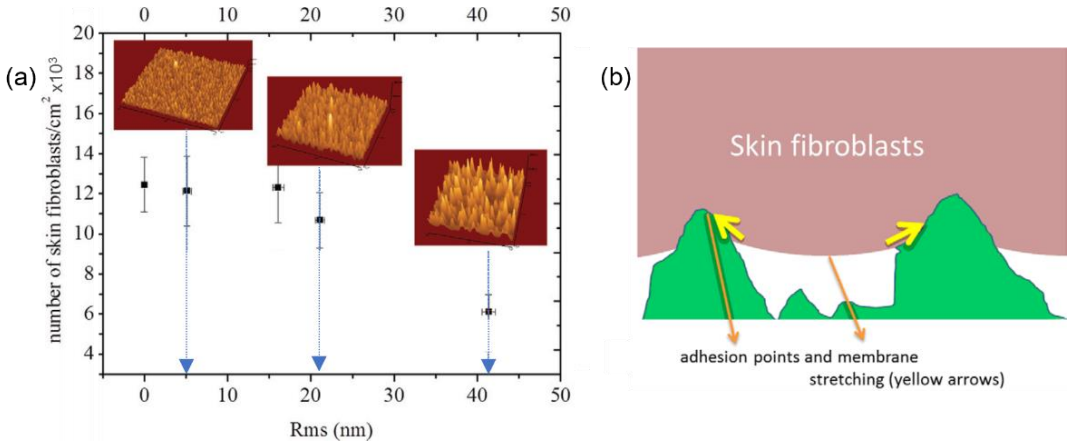

Figure 2.43: (a) Number of skin fibroblasts growing on PMMA substrates with different RMS roughness after 3 days of incubation. Insets show AFM images of surfaces with different textures; (b) Illustration of a skin fibroblast stretching over texture features, showing increased area of adhesion with simultaneous stretching. From [296].

It is possible that a threshold value was not reached by Meijs *et al.* [230] when testing the fouling resistance of dense and porous TiN electrodes in Wistar rats. Although measurements of surface roughness are not made for either electrode in this publication, it can be observed from Figure 2.44 a that the porous TiN has a consistent columnar microstructure with protrusions < 1 µm in diameter, and pores stated to measure 100 nm across on average. In contrast, the dense TiN mostly has a regular, smooth surface that is interrupted only occasionally by growth defects that were attributed to grinding edges on the substrate (Figure 2.44 b). Impedance measurements made after surgery and after 6 weeks of implantation were used to assess the level of fibrous growth. The $|Z|_{1kHz}$, which may be used as an approximation for tissue impedance, was observed to increase

for both smooth and porous electrodes by ~30 and ~43% over the testing period, respectively. Therefore, increased surface roughness did not discourage fibrous growth on porous TiN, and their response is instead described as being similar.

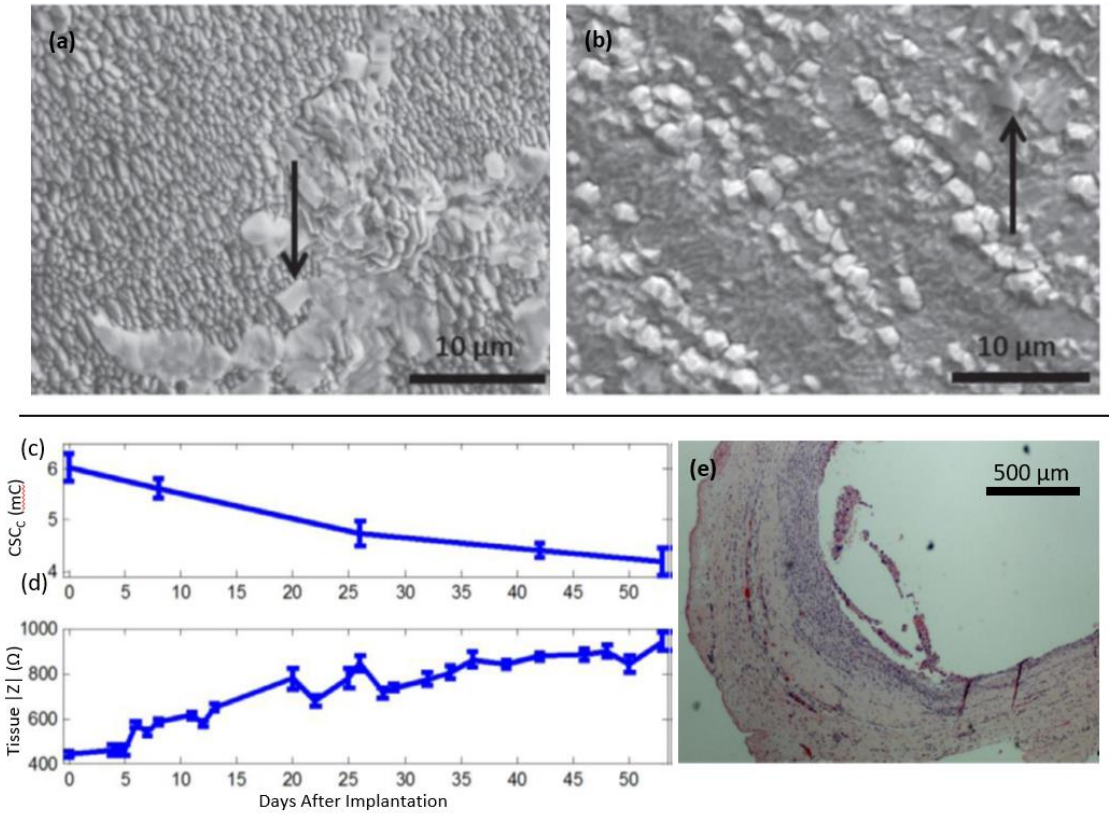

Figure 2.44: (a) Porous and (b) smooth TiN electrodes explanted from Wistar rats after 6 weeks of implantation. Arrows indicate salt crystals adhered to the surface. From [230]; (c) Average drop in CSC_C and (d) increase in the tissue impedance with time of implantation, measured for porous TiN electrodes in minipigs, while (e) shows the thick fibrous capsule that formed around one of the implants. From [229].

In a separate publication, Meijs *et al.* [229] confirmed the susceptibility of porous TiN to encapsulation whilst providing corroborating histological analysis. Electrodes of similar morphology to those in Figure 2.44 a were implanted in Gottingen minipigs for 55 days, with regular EIS and CV measurements made to monitor fibrous encapsulation. As shown in Figure 2.44 c and d, the CSC_C decreased throughout the period of implantation, while the tissue impedance increased drastically by 150%. The histological sample given in Figure 2.44 e provides context for the electrodes' deteriorated performance, showing a continuous fibrous capsule more than 500 µm thick in some places. Despite its excellent electrochemical properties *in vitro*, porous TiN in its current form is thus poorly suited for chronic implantation unless an antifouling strategy is developed.

Conversely, the surface morphology of some materials appears to have diminished influence on fibroblast attachment in contrast to other factors. PEDOT:PSS is one such example, as demonstrated by Marzocchi *et al.* [300] when comparing films of varying RMS roughness. Human dermal fibroblasts (HDF) cultured for 72 hours onto electrodeposited and spin-coated PEDOT:PSS surfaces (RMS roughness varying from 6 ± 1 to 33 ± 2 nm) produced a similar cellular response, with no significant differences observed. Electrochemical biasing of the CP films in PBS via reduction and oxidation at -0.9 V and 0.8 V *vs* SCE respectively did however induce a different response. Namely, oxidised samples exhibited much higher rates of fibroblast growth than their non-biased and reduced counterparts (Figure 2.45).

Amorini *et al.* [41] suggest that oxidised PEDOT:PSS influences cellular adhesion primarily due to membrane depolarization. Subjecting the polymer to a process of oxidation reduces the amount of electrons in PEDOT, creating strong electrostatic interactions with PSS. Concomitantly, a competing process termed over-oxidation creates neutral sulfoxides within PEDOT, requiring cations to migrate inwards and neutralise the emerging negative charge on PSS. Once placed in electrolyte, the material attempts to equalise its state and remove its potential bias, releasing adsorbed cations back into solution. Sufficient ion expulsion disrupts the cell's rest potential and causes membrane depolarization (similar to the process described in section 2.1.2), a process known to trigger actin polymerization and the formation of stress fibres. Cellular adhesion is thus encouraged on oxidised surfaces, leading to higher rates of fibrous growth. The theorised mechanism behind this process is illustrated in Figure 2.45 b.

Oxidation of PEDOT:PSS is typically established either through electrochemical means, by the application of UV radiation, or through the addition of p-dopants (secondary doping) with the aim of enhancing conductivity [242], [301]–[303]. While successful in this respect, the propensity for electrode encapsulation is also increased as a consequence. However even in the absence of oxidation, PEDOT:PSS surfaces are still open to fouling due to their hydrophilic surfaces, and degradation of electrochemical properties is expected to some extent when testing *in vivo*. Kozai *et al.* [304] developed electrodeposited PEDOT:PSS films on Au electrodes without any such oxidative treatments in place and implanted them in the visual cortex of mice. A rise in the tissue impedance was observed over the time of assessment, as shown in Figure 2.46 a (blue).

Filho *et al.* [305] used histological staining to view activated microglia around PEDOT:PSS electrodes implanted in the cortex of Wistar rats. Figure 2.46 b shows GFAP staining of recruited astrocytes that surround the electrically active sites, indicative of glial scarring and electrode isolation.

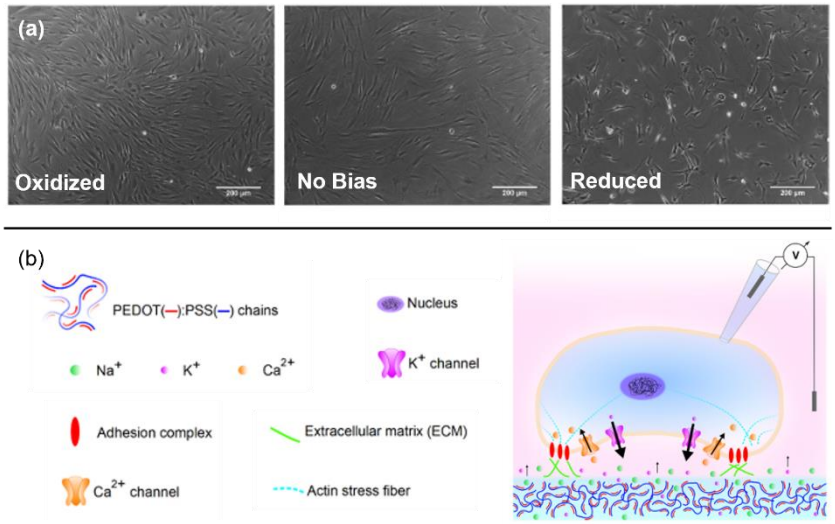

Figure 2.45: (a) HDF cells cultured on PEDOT:PSS substrates of identical RMS roughness. Oxidised samples (subject to 0.8 V *vs* SCE) encouraged higher rates of cell growth as compared to pristine and reduced (subject to -0.9 V *vs* SCE) substrates. From [300]; (b) A schematic illustrating the theory of Amorini *et al.* [41] regarding the role of PEDOT:PSS oxidation on cell membrane depolarization and subsequent adhesion. From [41].

It should be noted that despite their propensity for fouling, PEDOT:PSS electrodes tend to fare better than other commercially available electrode materials *in vivo*. Venkatraman *et al.* [283] assessed the stability of Pt-Ir electrodes with and without the addition of an electrodeposited PEDOT:PSS film in the somatosensory cortex of Sprague Dawley rats. As can be seen in Figure 2.46 c, EIS measurement made on day 6 post-implantation returned significantly lower impedance values for the CP electrode as compared to the alloy. Hsu *et al.* [306] suggest that this is due to reduced protein adsorption onto the polymer surface, as the negatively charged PSS ions repel similarly charged protein molecules. A 30% reduction in protein adsorption was in fact observed when compared to 316L stainless steel, a material that is well known to support extensive fibroblast growth (Figure 2.46 d) [307], [308]. Moreover, PEDOT:PSS electrodes do not appear to generate a stronger fibrotic response when compared to PEDOT-based electrodes doped with other materials. Kozai *et al.* [304] in fact noted a similar increase in the impedance of implanted PEDOT:CNT electrodes, seen in Figure 2.46 a (black). Therefore, although PEDOT:PSS films can stand to benefit from further

development of antifouling strategies, the absence of an environment that is hostile to cellular growth can be beneficial for reasons that will be explained in the next section.

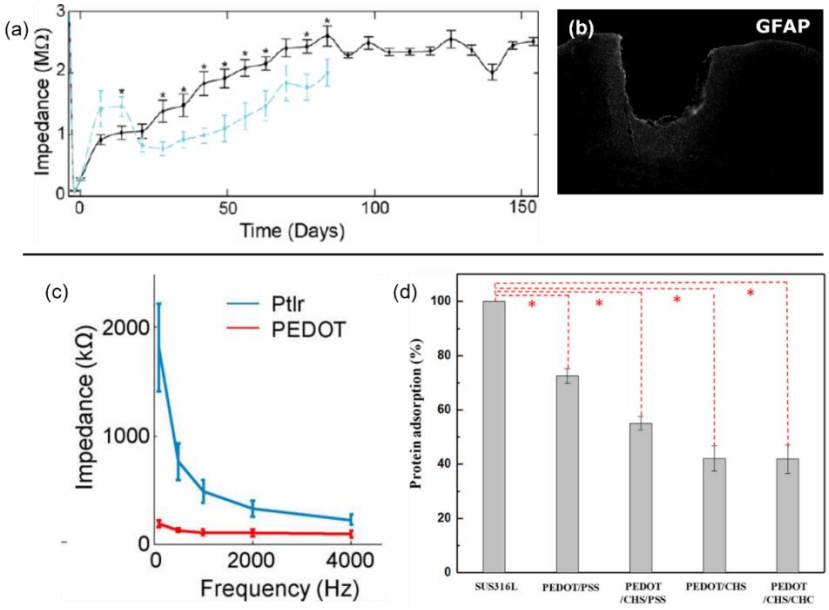

Figure 2.46: (a) Plot of $|Z|_{1kHz}$ for PEDOT:PSS (blue) and PEDOT:CNT (black) electrodes versus time of implantation in the visual cortex of mice. From [304]; (b) Fluorescent imaging of electrode implantation site in histological sample, from the cortex of rat. GFAP staining reveals activated microglia around the PEDOT:PSS surface. From [305]; (c) Impedance Bode plots for PtIr electrodes with and without a PEDOT:PSS coating, after 6 days of implantation in rat cortex. From [283]; (d) PEDOT:PSS adsorbs 30% less protein onto its surface as compared to AISI 316L stainless steel. From [306].

Finally, amongst the electrode materials currently under consideration, BDD is considered to have one of the highest resistances to fibrotic growth [309]. A combination of strong covalent bonds, low instance of crystalline defects, tuneable levels of doping, and variable surface terminations can all be employed to mitigate fibrous attachment. Moreover, its surface topography can be additionally exploited to produce super-hydrophobic surfaces, disrupting cellular attachment and preventing growth [310]. This was demonstrated by Alcaide *et al.* [294] when comparing the extent of fibrous encapsulation between BDD and smooth TiN electrodes (Figure 2.47 a and b) implanted subcutaneously in Wistar rats. After 4 weeks, the capsules surrounding TiN electrodes were found to be significantly thicker (~25 µm) than for the BDD electrodes (~15 µm).

In a separate study making use of similar electrodes, Meijs *et al.* [292] assessed levels of protein adsorption using fluorescein isothiocyanate-conjugated bovine serum albumin (FITC-BSA). The results, shown in Figure 2.47 c, indicate significantly higher adsorption on TiN as compared to BDD, which the authors credit as the underlying

mechanism behind the superior antifouling properties for the latter material. Moreover, while the CSC_C of TiN decreased when moving from PBS to albumin-containing electrolyte (50 gL^{-1} BSA in PBS), no such effect was observed for BDD (Figure 2.47 d). Thus, in addition to being an indicator for fouling, protein adsorption is also shown to have a negative impact on the electrochemical properties. It should be however noted that despite improved resistance to fouling *in vivo*, the electrochemical properties of BDD outlined in this work are very poor ($|Z|_{1Hz}$ = 48 kΩcm^2) and are not related to those detailed in Table 2.8, for which no comparable study involving animal models has yet been conducted.

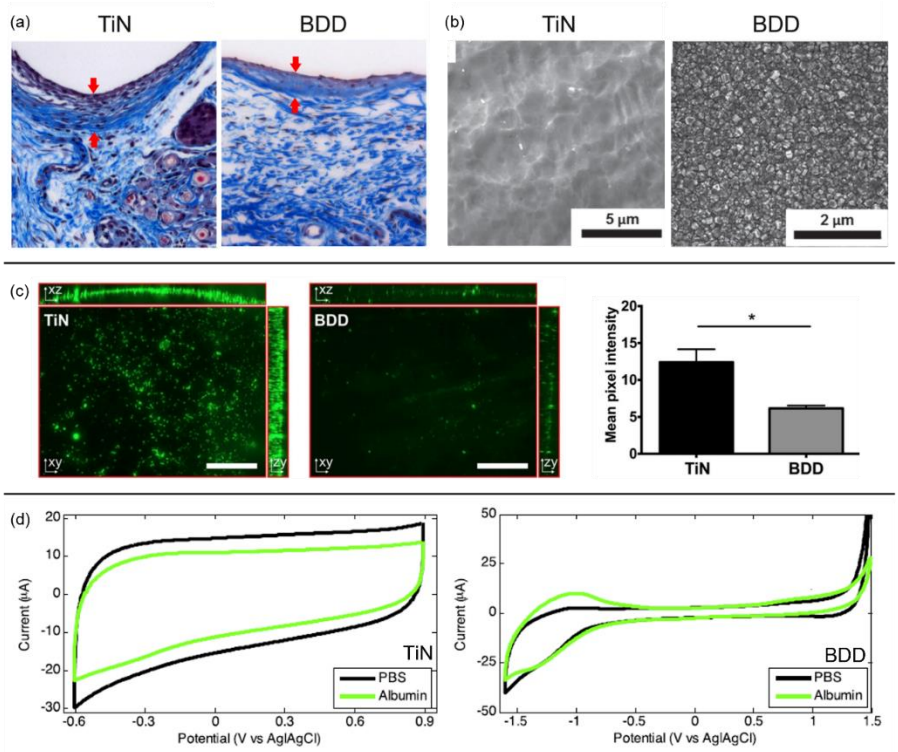

Figure 2.47: (a) The fibrous capsule surrounding smooth TiN and BDD electrodes, and (b) SEM images showing the surface morphology of the two materials. From [294]; (c) Fluorescent imaging of adsorbed FITC-BSA on smooth TiN and BDD electrodes with bar graph showing higher rates of adsorption on TiN; (d) Voltammograms measured at a sweep rate of of v = 0.1 Vs^{-1} for TiN (left) and BDD (right) in PBS (black) and 50 gL^{-1} BSA in PBS (green). From [292].

In fact, the anti-fouling advantage that BDD has over other materials comes into question when the assessment is based on electrodes having topographies and ESA's that are relevant to neural interfacing. Torres-Martinez *et al.* [311] compared the effect of implantation in swine brain on nano-structured Pt-Ir alloy with and without a film consisting of CNT's coated with BDD (Figure 2.48 a). Despite improving the electrochemical properties *in vitro*, BDD electrodes showed worse performance with

respect to encapsulation, having higher $|Z|_{1Hz}$ than Pt-Ir and identical $|Z|_{1kHz}$ (tissue impedance) after 12 weeks (Figure 2.48 b). Histological evaluation using GFAP staining in fact revealed very similar levels of astrocyte recruitment, representative of glial scar formation around the electrode (Figure 2.48 c). Thus, BDD electrodes have still not resolved the issue of balancing encapsulation resistance with high electrochemical performance.

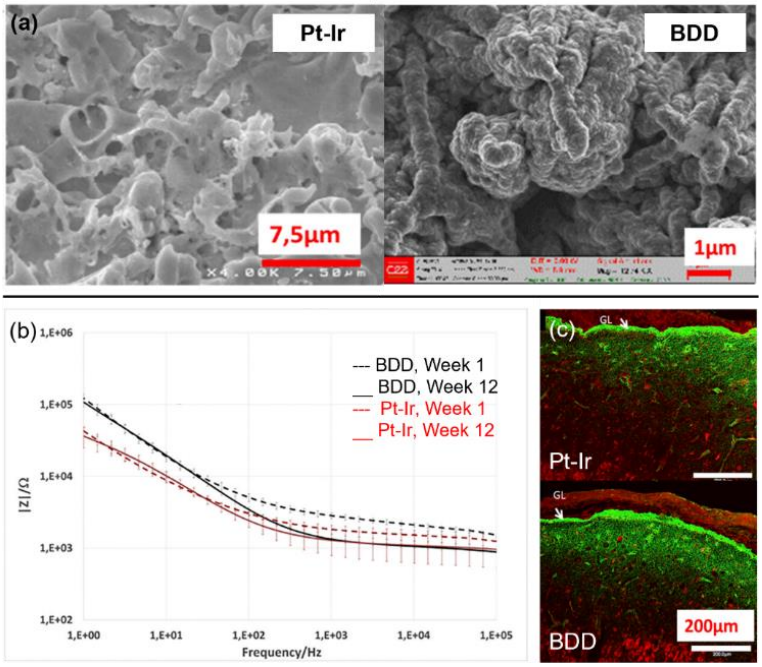

Figure 2.48: (a) Pt-Ir electrodes with (right) and without (left) a layer of BDD-coated CNTs; (b) Impedance Bode plots for both types of electrodes (Pt-Ir in red, BDD in black) after 1 and 12 weeks of implantation in the cortex of swine; (c) Fluorescent imaging of GFAP stained histological samples indicate similar amounts of recruited astrocytes for both electrodes. From [311].

2.5.2 Lack of Direct Neural Interfacing

Another challenge facing the development of new generation electrodes is intimately tied with that of encapsulation and deals with a lack of direct physical interfacing between device and neural tissue. The ultimate goal, which sees neurons growing directly on the surface and/or into the porous architecture of an electrode, is no easy feat. This is especially true when dealing with the CNS, where direct neural interfacing is most desired, since self-regeneration and growth of native damaged neurons is virtually impossible [90], [93]. A lot of emphasis is therefore placed on making the electrode surface as hospitable to neural growth as possible [1], [23], [99].

Recently, research has indicated that it is possible to control neural growth on a surface via the introduction of topographical features, providing the cells with spatial and physical cues. Ding *et al.* [312] demonstrate the effect that multi-scale topographical control can have on neural survivability. Using a nano-particle coating of silicon dioxide, the surface area of neural electrodes was enhanced beyond the scale typically considered by conventional RMS roughness, increasing the number of contact points along which a neuron can interact with adsorbed proteins and peptides. Neurite outgrowth was compared between coated and non-coated electrodes using primary neurons isolated from rat foetuses, with the latter demonstrating significantly higher values at an average of 3684 ± 294 versus 1096 ± 77 μm/mm^2. Dominguez-Bajo *et al.* [313] observed similar positive effects induced via nanotopographical (nanowires, NW) Au, where dissociated hippocampal cultures from the pups of Wistar rats were grown on electrodes with and without template-induced electrochemical texturing. In addition to promoting neural growth, the nanotopography was found to support diminished astrocyte cell density in significant amounts as compared to flat Au and control glass substrates, indicating potential for suppression of glial scar formation. Positive results were also achieved by Chen *et al.* [202] on nanopatterned IrOx, and by Chapman *et al.* [314] on nanoporous Au.

Despite these results, chronic *in vivo* demonstrations of the success of such electrodes are lacking. Many researchers now assert the criticality of matching the elasticity of electrode surfaces with that typically measured for the ECM of neural tissue. This is due to the high mechano-sensitivity observed in cells like neurons, astrocytes, and mesenchymal stem cells, which contrary to most other cell groups prefer soft rather than stiff substrates [79], [126], [315], [316]. When considering the elastic moduli of electrode materials both in current use and those under consideration (refer to Table 2.9), the challenge of finding a material that simultaneously boasts good electrochemical properties and low stiffness becomes apparent. Unsurprisingly, the lowest young's modulus belongs to CPs, of which PEDOT:PSS has demonstrated leading electrochemical capacity for neural interfacing [127], [139], [241].

As expected, PEDOT:PSS has therefore been the subject of many research endeavours where neural integration is an explicit goal, particularly because its topography may also be engineered into multi-scale features. In the work of Cellot *et al.* [317], PEDOT:PSS

electrodes were shown to support the development of neurons from hippocampal rat cultures whilst simultaneously reducing glial cell density as compared to poly-ornithine[6]-conditioned control surfaces (glass) (Figure 2.49 a). Moreover, the cultured neurons were demonstrated to produce spontaneous synaptic activity (postsynaptic currents, PSC), indicating that the polymer also promoted the formation of functional synaptic networks similar to control surfaces.

Table 2.9: The Young's Modulus for different electrode materials. Values obtained from literature.

Material	**~ Young's Modulus, E (Pa)**	**Reference**
Graphene	$1x10^{12}$	[318], [319]
BDD	700-800 $x10^{9}$	[320]
TiN	200-500 $x10^{9}$	[321], [322]
IrOx	200 $x10^{9}$	[323]
Noble Metals	10-200 $x10^{9}$	[324], [325]
PEDOT:PSS	200-500 $x10^{6}$	[326], [327]

Pisciotta *et al.* [328] determined that PEDOT:PSS could be used to promote the neurogenic commitment of neural crest derived stem cells (human dental pulp stem cells, hDPSC), where cells were shown to have excellent adhesion, proliferation, and maintenance over 7 days. In addition, comparisons made between spin-coated and electrodeposited films demonstrated significantly larger cell densities, higher levels of neuronal markers, and a more pronounced neural morphology for electrodeposited samples (Figure 2.49 b). Neural stem cells (NSC) also demonstrated good adhesion to crosslinked PEDOT:PSS electrodes pre-conditioned with laminin[7] in the work of Pires *et al.* [329]. NSC stretching, one of the key indicators for differentiation into large populations of well-spread neurons, was further enhanced when a DC pulsed electric field (1 V, 100 Hz) was applied through the PEDOT:PSS. These results are shown in Figure 2.49 c where they were quantified using cell elongation aspect ratio (AR) measurements. *In vivo,* Ferlauto *et al.* [330] demonstrated satisfactory behaviour of PEDOT:PSS electrodes following chronic implantation in the visual cortex of mice. NeuN staining and imaging of brain slices at the site of insertion following 1 and 2 months of implantation revealed no statistically significant difference in the number of neurons growing around the electrode as compared to a control sample located away from the site (Figure 2.49 d).

[6] Poly-ornithine is a synthetic amino acid that promotes the preferred differentiation of neural cells.
[7] Laminin is an ECM glycoprotein frequently used in neural stem cell culture studies to promote adhesion.

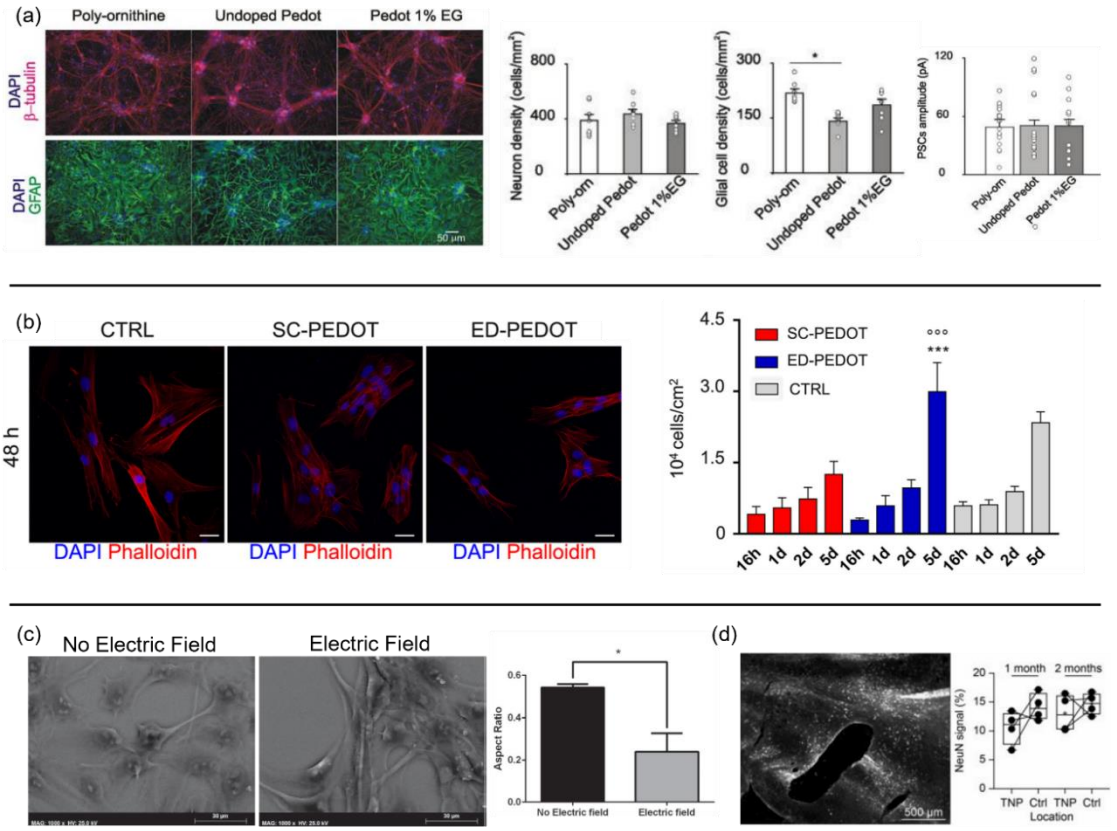

Figure 2.49: (a) PEDOT:PSS substrates (labelled undoped PEDOT in figure) support the growth of neurons at the same rate as poly-ornithine conditioned substrates (as determined by the neuronal marker β-tubulin), whilst supporting significantly less glial cell density (as determined by GFAP staining). The amplitude of PSCs recorded from neurons grown on poly-ornithine substrates and on undoped PEDOT substrates are similar. From [317]; (b) Spin-coated (SC) and electrodeposited (ED) PEDOT:PSS substrates show similar stem cell growth at 48 hours of culture as compared to control surface (shown in the DAPI and Phalloidin stained images). After 5 days, ED PEDOT:PSS supports a statistically significant (***) larger number of cells/cm^2 than the other 2 surfaces. From [328]; (c) DC pulsing through PEDOT:PSS substrates encourages stem cell spreading and neuronal differentiation. From [329]; (d) NeuN staining of histological site of PEDOT:PSS neural implant shows no statistically significant difference in number of neurons at implantation site as compared to control site. From [330].

Of course, the apparent contradiction of making a surface hospitable for the growth of one cell, *i.e.*, neurons, whilst simultaneously inhibiting the adhesion and proliferation of others, namely astrocytes and fibroblasts, presents a very significant obstacle. Although PEDOT:PSS has indeed been shown to mitigate the growth of glial cells as discussed above, it remains permissible to fibroblasts, cells which are extremely abundant in the PNS and which migrate to the site of tissue disturbance in the CNS to make up the core of a glial scar [38], [94], [283]. For this reason, the employment of PEDOT:PSS on its own is not a viable solution when considering highly demanding applications where direct neural interfacing is integral to device operation.

2.6 Hydrogels as a Potential Solution

2.6.1 Hydrogels Defined

Hydrogels are super-hydrophilic materials that consist of 3D polymeric networks capable of absorbing thousands of times their dry weight in water [331]. The polymer network is obtained from a hydrosol, a water-based solution containing dissolved polymers that can gel when subjected to certain stimuli. These stimuli can take the form of a physical, chemical, or biochemical trigger that induces crosslinking to produce the hydrogel [1], [332]. The resulting polymer is highly elastic, with physical characteristics that are easily controlled by degree of cross-linking, and which can be made to resemble those of soft, biological tissue [333], [334]. Hydrogels can be either of natural origin, such as hyaluronic acid, collagen, and dextran, or produced synthetically, of which poly(ethylene glycol) (PEG), and poly(lactic acid) (PLA) are typical examples [331].

Physical hydrogels, often termed ‘reversible’ hydrogels, are held together by entanglements in the molecular chain, and/or through secondary bonding forces like hydrogen and ionic bonds [332]. These materials are expected to degrade when disruptive conditions arise. Changes in the surrounding pH, molarity, or temperature, the application of physical stress, or the introduction of ionic species that compete with cross-linking ions for polymeric bonding are all sources of hydrogel disassociation [335]. Conversely, chemical hydrogels are gelled via covalent bonds, and are thus much more resistant to degradation than physical hydrogels. Production methods include click chemistry, grafting, or the introduction of a chemical crosslinker (acids, catalysts, etc.) to a solution of precursor molecules [334]. Neither physical or chemical hydrogels are considered homogenous materials, containing regions of irregular crosslinking density and variations in degree of swelling [331], [336].

Hydrogels have a good performance history in applications of biomedical engineering and pharmaceutical technology, with drug capsules, wound dressings, and contact lenses being popular examples of their use [331], [337]. In particular, their successful employment as porous scaffolds for the restoration of missing or diseased tissue in regenerative medicine has recently generated interest within the field of neural interfacing. This, coupled with demonstrably strong antifouling properties, have made

hydrogels attractive contenders as functional coatings for implantable electrodes [71], [336].

2.6.2 Calcium Alginate Hydrogels

Among the most frequently contended hydrogels for neural interfacing are those derived from alginate, anionic polysaccharides extracted from the cell walls of brown algae *Phaeophyceae*. Alginic acid salts like sodium alginate, the precursor material to hydrogel formation, are built from linear polymers containing blocks of (1,4)-linked β-D-mannuronate and α-L-guluronate, so-called M and G residues, respectively (Figure 2.50 a). Blocks can be one of three types, containing either consecutive G or M residues, or an arrangement of alternating G and M residues. As cross-linking occurs only at the site of G-blocks on the polymer chain, the physical and mechanical properties of the resulting gel are heavily dependent on their characteristics, namely the block length, compositional ratio with respect to M blocks, and molecular weight [332], [338].

Although alginate hydrogels are frequently produced via chemical covalent means, especially in the production of alginate-PEG or other co-polymers, physical methods of gelation involving ionic bonds are generally preferred in the context of neural interfacing. The factors governing this preference are wide-ranging, and include the involvement of simpler reagents, the absence of toxic chemical cross-linkers that must be thoroughly washed away after gelling, and facile methods of production requiring little to no specialist equipment. Moreover, many of the potential functions of alginates on implantable electrodes stand to benefit from reversibility, and as such degradation is a desirable corollary [132], [334], [339].

Ionic gelation is initiated through the introduction of divalent ions, typically Ca^{2+}, that interact with G-blocks on the alginate chain [340]. Junctions formed between adjacent G-blocks then produce a gel with a structure reminiscent of an eggbox, as shown in Figure 2.50 b. $CaCl_2$, $CaSO_4$, and $CaCO_3$ are all routinely employed as cross-linking agents, and are listed here in order of decreasing gelling rate [332]. Having the highest solubility, $CaCl_2$ induces the fastest gelation and hence also the poorest uniformity and lowest structural integrity. Gelation may be retarded considerably through the use of phosphate buffers that compete for reaction with Ca ions [332], or by lowering the reaction temperature and thus decreasing reactivity of ionic species [331]. However in

spite of these measures, bulk gelation using $CaCl_2$ still produces highly irregular structures, and as such is seldom employed for neural interfacing [332]. To mitigate this issue, researchers like Kim *et al.* [24] and Chikar *et al.* [252] adopted a dip-process where the electrode is alternatingly submerged in a solution of sodium alginate and then in a $CaCl_2$ solution. In this way, the hydrogel coating is developed layer by layer, improving its homogeneity and allowing closer control over its thickness.

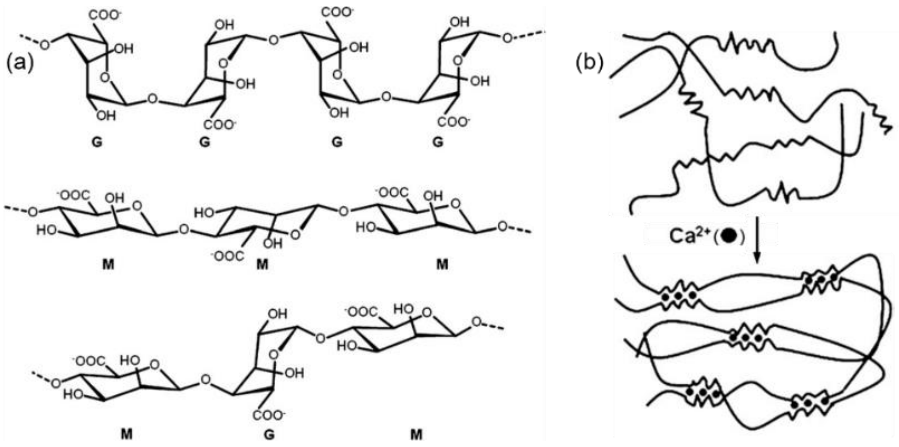

Figure 2.50: (a) G-Block, M-Block, and alternating MGM-Block of alginate; (b) Ionic cross-linking via Ca^{2+} ions which interact with G-blocks to create an alginate hydrogel with an eggbox structure. Adapted from [332].

The slowest gelation is achieved through $CaCO_3$ as it is insoluble in water at pH 7. Hydrogel formation may thus only be initiated through an acidic shift, gradually disassociating the Ca^{2+} ions and making them available for interaction with G-blocks. In this way, a homogenous suspension of sodium alginate and $CaCO_3$ can be achieved by physical mixing, while the catalyst, usually an acidulant like D-glucono-δ-lactone (GDL), can be introduced at a later stage [332], [341]. Nunamaker *et al.* [342] compared the physical and mechanical characteristics of alginate hydrogels produced via $CaCl_2$ and GDL-$CaCO_3$. Slow-gelling alginates consistently formed denser gels capable of absorbing larger amounts of water for the same amount of polymer: crosslinker ratio. Moreover, the complex modulus G^* (describes resistance to deformation as measured by rheology) was found to be significantly higher for GDL-$CaCO_3$ gels, indicating a larger amount of ionic bonds as compared to their $CaCl_2$ counterparts.

One of the most pertinent challenges in the application of hydrogels to neural interfacing deals with the method of deposition. While creating gels on the macro scale is simple enough and frequently undertaken using basic laboratory equipment, achieving

homogeneous films with repeatable, precise dimensions has proven to be an issue on the micro scale [31], [335]. This is especially problematic when the limits of the film are to be defined by the perimeter of the electrode site itself, rather than encompass the entire device, insulator and all. High-precision deposition techniques for hydrogels are not widespread, with 3D printing being the most well-documented. Many research groups [139], [333], [335] have successfully developed complex structures using alginate bioinks, creating porous scaffolds for applications in tissue engineering. This is however a costly process, requiring additional considerations for ink viscosity, shear resistance, and shape fidelity [334], [337].

A more cost-effective technique that offers high precision and reproducibility without requiring further insight into the mechanical properties of the precursor solution is electro-deposition [31], [343]. The process requires a homogenous solution of sodium alginate and $CaCO_3$, while excluding the need for GDL. Using a 3-electrode system, an anodic current is applied to induce water electrolysis at the working electrode (site of hydrogel formation), triggering the release of H^+ protons and creating a pH gradient:

$$2H_2O \rightarrow O_2 + 4H^+ + 4e^- \tag{2.11}$$

The protons then interact with the $CaCO_3$ particles, releasing Ca^{2+} ions that are free to form bonds with the G-blocks of alginate and trigger cross-linking [31], [344]:

$$H^+ + CaCO_3 \rightarrow Ca^{2+} + HCO_3^- \tag{2.12}$$

$$H^+ + HCO_3^- \rightarrow H_2CO_3 + H_2O + CO_2 \tag{2.13}$$

This process is summarised in the illustration given in Figure 2.51. The processing details for all the calcium alginate gels discussed in detail hereunder are summarised in Table 2.10.

Cheng *et al.* [31] conducted a thorough investigation of the mechanism behind electro-gelling, using a 1% w/v sodium alginate solution mixed with different concentrations of $CaCO_3$ (0, 0.05, 0.15, 0.25, and 0.5% w/v). Under a positive current of 0.5 $mAcm^{-2}$, droplet-shaped calcium alginate films were gelled onto a WE. When a universal pH indicator was mixed in with the deposition solution (50 µL per 1ml precursor solution), the pH gradient could be readily observed within the gelling area. Figure 2.52 a shows the varying colours in a hydrogel specimen whilst gelling at 160s. Mirroring the schematic in Figure 2.51 d, the lowest pH, pH 4, occurs closest to the site of proton

generation, gradually rising to a neutral pH 7 as distance from the WE increases. Figure 2.52 b plots the pH gradients for different concentrations of $CaCO_3$. As expected, the smallest drift from neutrality occurred at the highest $CaCO_3$ concentration, as generated protons are immediately consumed by the abundantly available carbonate particles. This directly correlates to Figure 2.52 c, where the thickness of alginate gels produced is plotted against $CaCO_3$ content. As more carbonate is available per cm^3 at higher concentrations, protons are consumed closer to the WE before outward diffusion occurs, creating thinner gels with a higher density of crosslinking as compared to lower $CaCO_3$ gels. A calcium ion indicator (Oregon Green, 488 BAPTA-1 hexapotassium salt at 4 µM, 20 µL per 1 ml precursor solution) was then added to alginate solution with 0.25% w/v $CaCO_3$. Fluorescence imaging was used to assess the amount of free calcium ions generated with different gelling times. As seen in Figure 2.52d, the highest concentration of Ca^{2+} is located closest to the WE, with a migrating dissolution front evident as gelling time is increased.

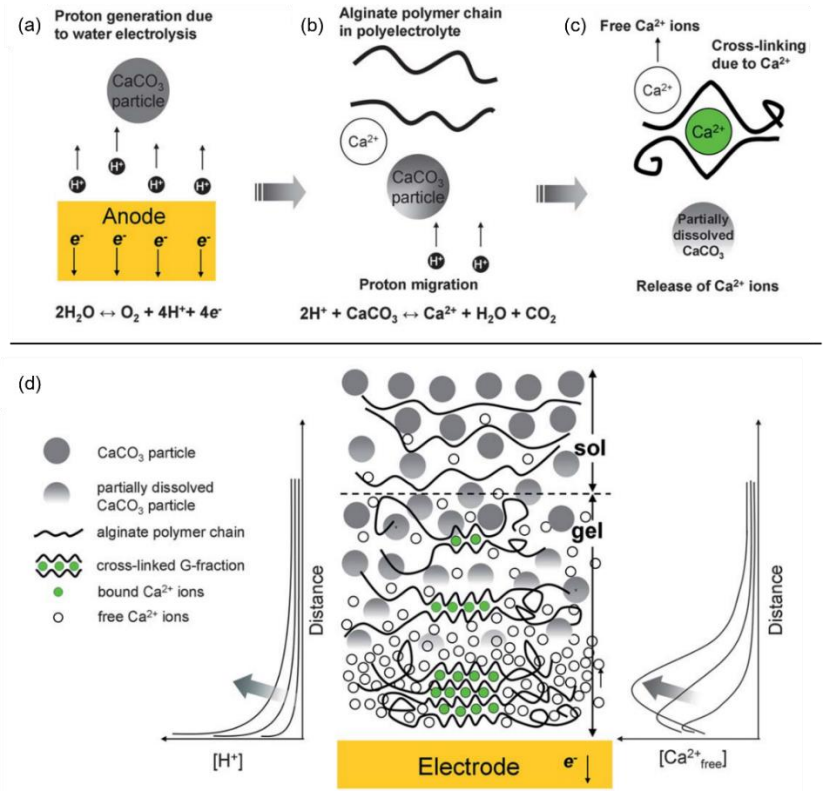

Figure 2.51: A schematic illustration the mechanism behind electrochemical gelling of calcium alginate: (a) Anodic currents cause water splitting and generation of H^+ protons, dropping the pH; (b) The protons diffuse away from the anode, creating a pH gradient and interacting with $CaCO_3$ powder to liberate Ca^{2+} ions; (c) The Ca^{2+} ions interact with the G-blocks of alginate and initiate ionic cross-linking to form the hydrogel; (d) A macroscopic view of the process, showing how crosslink density, H^+ protons, and free Ca^{2+} varies with distance. From [31].

Chemical characterization of hydrogels developed with a carbonate content of 0.25% w/v was also carried out using 632 nm Raman spectroscopy. The spectra, shown in Figure 2.52 e, were collected from samples of $CaCO_3$ powder, from areas of hydrogel specimens having undissolved $CaCO_3$ powder, and from transparent areas where carbonate powder had been almost completely solvated via water electrolysis. Peaks associated with $CaCO_3$ (at 283, 713, 1087, 1437, and 1749 cm^{-1}) are present in all three samples, although their intensity is significantly diminished when measurements are made in the gel's clear sections. In accordance with the works of Schmid *et al.* [345] and Campos-Vallette *et al.* [341], the major peaks that make up the fingerprint region of calcium alginate were identified at ~ 433, 814, 887, 957, 1419, and 1617 cm^{-1}. Raman shifts below 700 cm^{-1} are assigned to deformations of the pyranosyl rings[8] and vibrations in the C-O-C glycosidic bonds[9], whereas deformations and skeletal stretching accompanied by ring breathing generate the peaks between 700 and 950 cm^{-1}. The emergent peaks between 950 and 1400 cm^{-1} are attributed to stretching vibrations of C-O and C-C bonds, and deformations in the C-H, C-O-H, and C-C-H bonds. The most important peaks, containing the bulk of structural information about an alginate hydrogel, occur between Raman shifts of 1400 and 1800 cm^{-1}, and represent COO^- stretching vibrations and stretching of the C=O bond.

2.6.3 Alginate Hydrogels as Antifouling Coatings

Owing to the ease with which an alginate coating may be applied to neural electrodes (i.e., via dip coating or electrodeposition), a large body of work has evolved around the application of calcium alginate as a barrier to fibrous encapsulation. Very low rates of protein adsorption can occur due to the gel's super-hydrophilicity, creating a hydration barrier that prevents this first crucial step in cell adhesion. Coupled with a lack of cell-interactive domains, this prevents cells from developing specific attachment with calcium alginate, making adhesion and proliferation very difficult [338].

Machida *et al.* [346] demonstrated this phenomena by comparing the growth of normal human dermal fibroblasts (NHDF) on calcium alginate films versus tissue culture polystyrene (TCP). Seeding at a density of 4000 cells cm^{-2}, the NHDFs were cultured in

[8] A pyranosyl ring is a chemical structure containing 5 carbon atoms and 1 oxygen atom in a 6-ring arrangement.
[9] A glycosidic bond is a covalent bond between the hydroxyl group of an organic compound and a saccharide molecule.

MEM (minimum essential medium, contents detailed in Appendix A) and cell numbers were counted every 3 days for a total of 18 days. Very little cell attachment (~ 18%) was observed on the calcium alginate films in the first 4 hours, as can be seen in Figure 2.53 a, with no spreading or proliferation even after 18 days in culture. Rather, the number of fibroblasts decreased to less than half the initial value by day 3, a clear indication of the hydrogel's inability to support fibrous growth. Conversely, ~76% of seeded fibroblasts had adhered to TCP in the first 4 hours, where they spread and proliferated by a factor of 14 over the 18-day test period (Figure 2.53 b). Very similar results were obtained by Singh *et al.* [347] when assessing the adhesion of NHDFs cultured in DMEM (Dulbecco's modified Eagle's medium, contents detailed in Appendix A) onto calcium alginate films and TCP. Fluorescent imaging following calcein staining reveals the stark difference between a permissible surface (TCP) and a non-adherent material (calcium alginate), as shown in Figure 2.53 c.

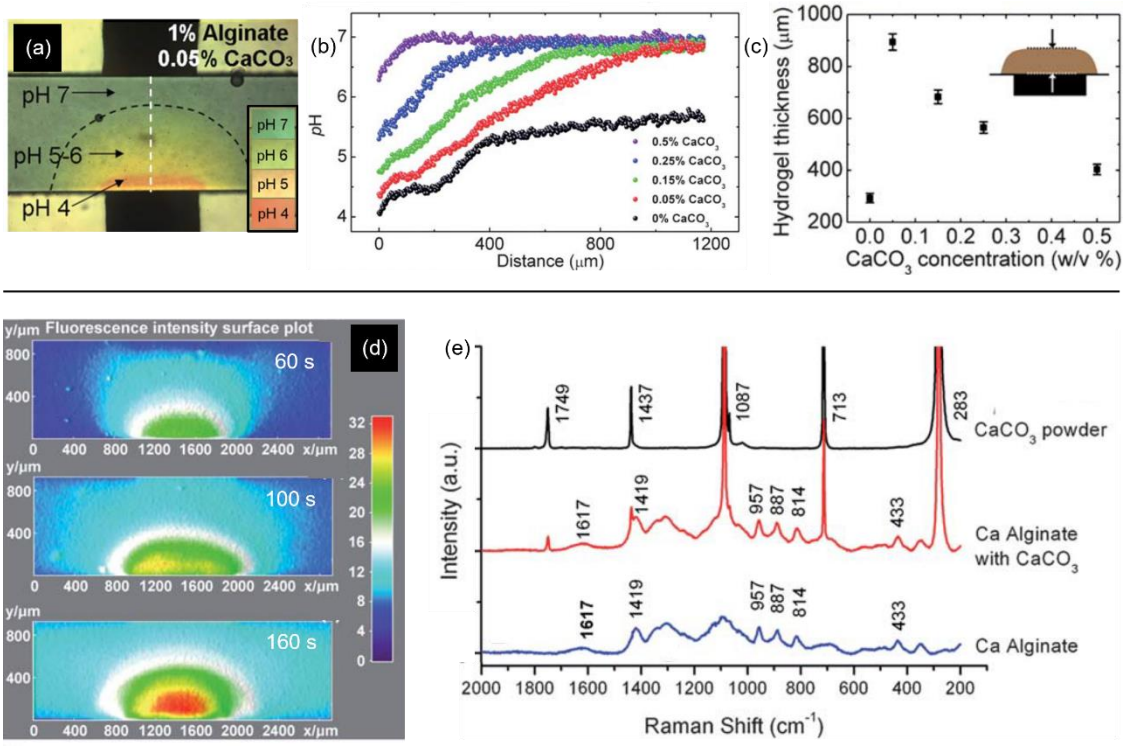

Figure 2.52: (a) Image showing calcium alginate gelling via anodic current injection. Universal pH indicator added to the precursor solution reveals the pH gradient that develops across a radial distance from the anode; (b) pH gradients for hydrogels developed with different $CaCO_3$ content, indicating that lower contents generate a steeper gradient and more acidic pH at the anode; (c) The variation of hydrogel thickness with different $CaCO_3$ concentrations; (d) Fluorescence imaging of unbound calcium ions when gelling with a 0.25 % w/v $CaCO_3$ content, showing the migrating dissolution front; (e) Raman spectra collected using 632 nm laser wavelength for $CaCO_3$ powder (black), Alginate with residual undissolved powder (red), and clear alginate with little to no undissolved powder (blue). From [31].

Chikar *et al.* [252] assessed Pt-Ir electrodes modified with PEDOT:PSS and a calcium alginate hydrogel functionalised with an RGD adhesion ligand to promote neural attachment. When implanted in the cochlea of guinea pigs, EIS measurements made over a period of months revealed consistently higher values of $|Z|_{1kHz}$ for the bare electrode as compared to the coated ones (Figure 2.53 d). Being indicative of tissue impedance, these values suggest a higher incidence of fibrous encapsulation for bare electrodes, positing the efficacy of alginate as a deterrent to fouling. However, no histological evaluation was conducted to correlate tissue reaction with the electrochemical results.

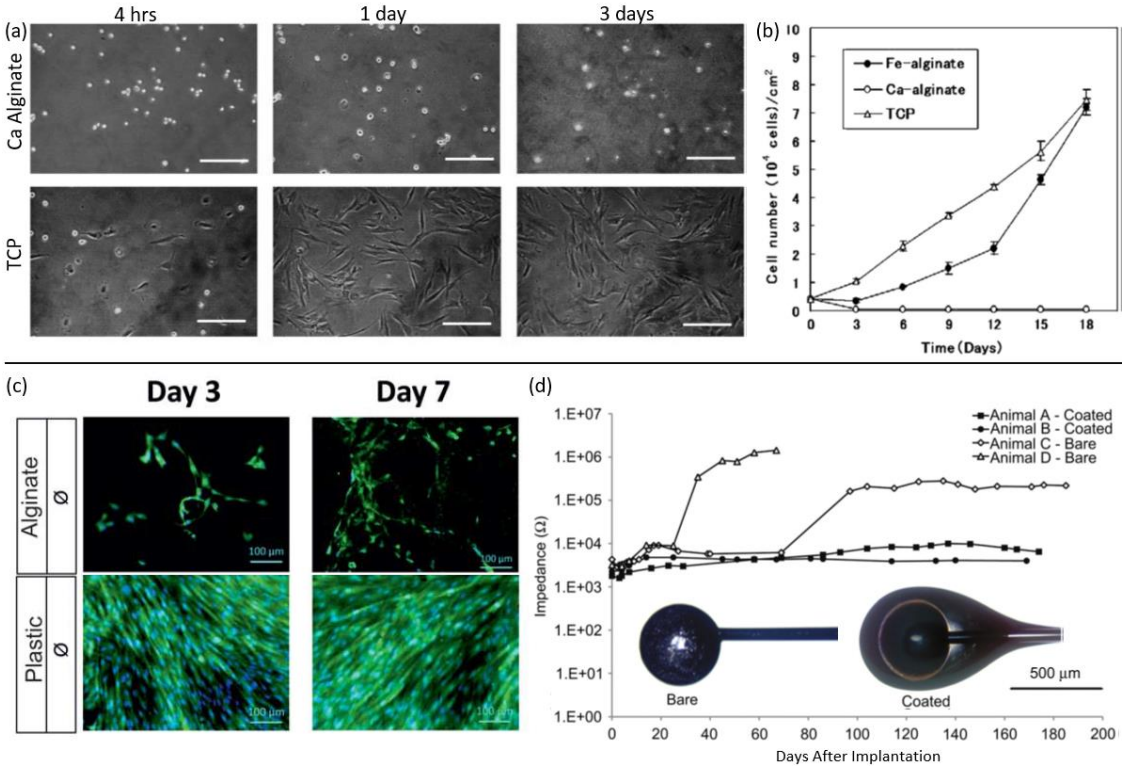

Figure 2.53: (a) Images of NHDFs cultured onto Ca Alginate gels and TCP after 4 hrs, 1 day and 3 days; (b) A plot of cell number (10^4 cells/cm^2) versus number of days in culture. From [346]; (c) Fluorescent images of calcein stained NHDFs cultured on calcium alginate gel and cell culture wells after 3 and 7 days. From [347]; (d) Plot of $|Z|_{1kHz}$ versus days of implantation in cochlea of guinea pigs, for Pt-Ir electrodes (marked Bare on figure) and PEDOT:PSS coated electrodes with a film of calcium alginate (labelled coated on figure). Insets show images of sample electrodes. Adapted from [252].

The work of Zhang *et al.* [348] may provide some corroboratory insight into this phenomenon, in which calcium alginate discs (1 cm diameter) were implanted subcutaneously in the dorsal region of mice. Masson's trichome staining of tissue samples, shown in Figure 2.54 a after 1 week, 4 weeks, and 3 months of implantation, reveal a very thin fibrous capsule. An approximate thickness of 50 µm was measured at the latter two timepoints, less than half that reported for Pt and Pt-Ir alloys (compare to

Figure 2.41) for similar durations *in vivo* [197]. Strand *et al.* [349] obtained even more favourable results when implanting calcium alginate capsules (0.4 mm diameter) into the peritoneal cavity of mice. Following 40 days *in vivo*, ~91% of retrieved spheres had no detectable fibrous growth on the surface.

Moreover, alginate hydrogels have also shown promise when applied as a deterrent to glial scarring. Skousen *et al.* [123] successfully reduced the activation of microglia in the cortex of Sprague-Dawley rats when assessing dip-coated Michigan electrodes over a course of 16 weeks. GFAP staining on the bare and coated electrodes revealed significantly diminished astrogliosis (-50%) at the biotic/abiotic interface for probes coated in alginate (Figure 2.54 b). The authors theorise that the hydrogel acts as a diffusional sink, passively reducing the presence of pro-inflammatory cytokines at the device/tissue barrier through absorption and eventual silencing. In this way the FBR is supressed, and device encapsulation is minimised.

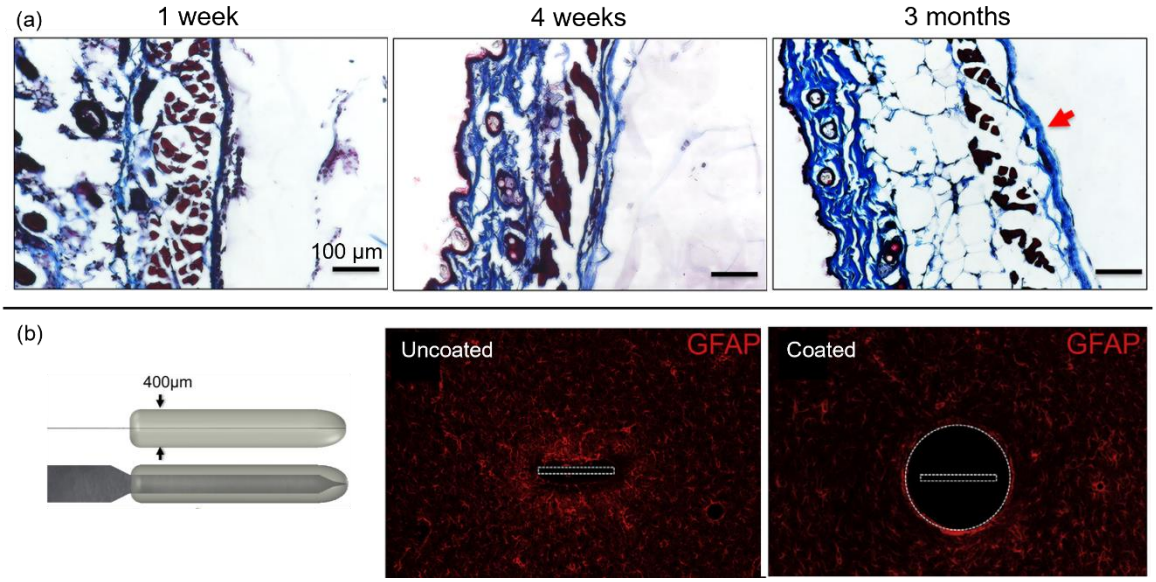

Figure 2.54: (a) Masson's trichome staining of histological sample around site of implant (1 cm diameter calcium alginate discs) after 1 week, 4 weeks, and 3 months. Red arrow indicates fibrous capsule. From [348]; (b) Michigan electrode array dip-coated with calcium alginate implanted in the cortex of rats along with uncoated control. Fluorescent imaging of GFAP-stained histological sample shows less astrogliosis around coated implant. From [123].

Another avenue of benefit derived from reversible hydrogels like calcium alginate is the release of anti-inflammatory drugs during their dissolution. Being of non-mammalian origin, the human body has no enzymatic process (i.e., alginase) available to cleave the polymer chains of calcium alginate, and hence the material is inherently non-degradable.

However, in the presence of ample Na^+ ions, as is the case in vivo, $Ca2^+$ ions are released from the polymer due to preferential bonding with monovalent species. In this way the hydrogel gradually dissolves, a process which fortuitously evades the inflammation response [132], [332]. Kim *et al.* [27] developed a calcium alginate coating on Michigan-style silicon probes containing PLGA (Polylactic-co-glycolic acid) nanoparticles loaded with Dexamethasone[10] (DEX). Implantation in the auditory cortex of guinea pigs over 25 days revealed sustained drug release over 3 weeks, accompanied by no significant rise in the $|Z|_{1kHz}$ value. In contrast, probes without the hydrogel coating displayed a 3-fold increase in impedance. It must however be acknowledged that the individual impact of DEX cannot be isolated from this work, as no control group was investigated in which a hydrogel coating was applied without drug loading. Nevertheless, multiple other studies in which DEX is administered through alternative means have demonstrated its efficacy in reducing the inflammation response to implanted devices. Notable examples include loose DEX-loaded PLGA microspheres at the site of a subcutaneous implant [350], drug delivery through intracortical retrodialysis of implanted probes [351], and via subcutaneous injection at the implantation site of a sciatic nerve electrode [352].

2.6.4 Alginate Hydrogels as Scaffolds for Neural Growth

Besides acting as a deterrent to fibrous encapsulation, calcium alginate hydrogels have also shown potential as permissible surfaces for neural adhesion, and as bioresorbable scaffolds for the growth and restoration of neural tissue.

Matyash *et al.* [353] assessed the impact of alginate crosslinking density on the adhesion and growth of foetal rat-derived neurons. A 1% w/v sodium alginate sol was gelled with $CaCl_2$ solutions of 1.8 mM (provided by Neurobasal medium), 2 mM, 0.1 M, and 1 M concentration. Large amounts of neural growth were recorded on the 1.8 and 2 mM films, forming confluent layers consisting of cell bodies with a network of long neurites (Figure 2.55 a and b). Moreover, the neurites were observed to penetrate down into the hydrogel matrix, forming a 3D mesh by the 6^{th} day of culture. In contrast, neurons could not adhere to gels made with $CaCl_2$ concentrations higher than 0.1M, and instead re-aggregated and formed spheroids (Figure 2.55 c and d). The authors note that despite not adhering to the stiffer hydrogels, the neuron spheroids remained viable for a number

[10] DEX is an anti-inflammatory an immunosuppressant drug in widespread clinical use.

of weeks *in vitro*. In fact, neurite outgrowth was observed within 3h when the spheroids were re-cultured onto the 1.8 and 2 mM $CaCl_2$ alginates (Figure 2.55 e and f).

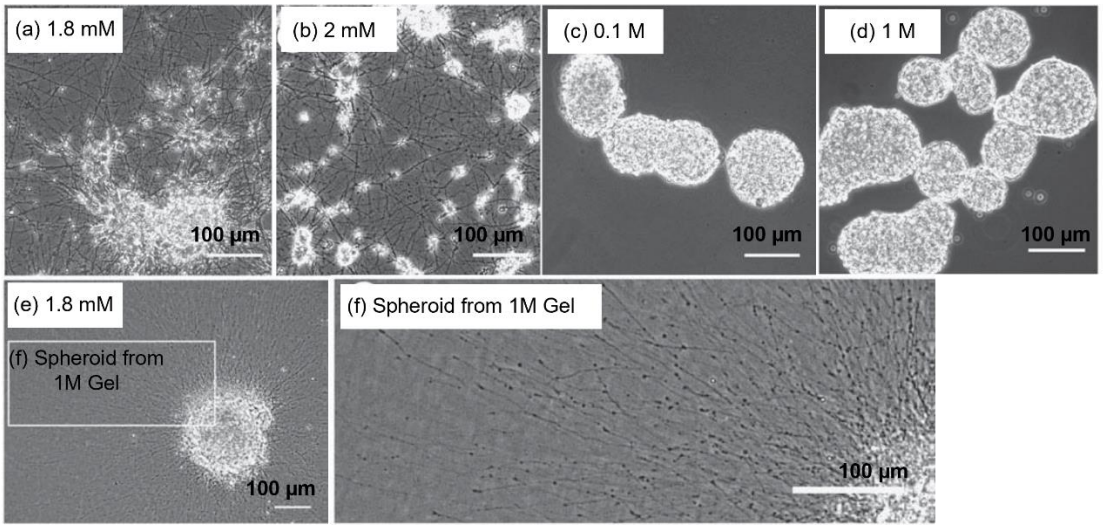

Figure 2.55: Images of foetal rat neurons cultured onto calcium alginate gels crosslinked with $CaCl_2$ solutions of (a) 1.8 mM, (b) 2 mM, (c) 0.1 M, and (d) 1M concentration. Images were taken after 7 days in culture; (e) Image of neuron sphere previously growing on 1M hydrogels re-cultured onto a 1.8 mM gel, displaying ample neurite outgrowth after just 3h of culture (f). From [353].

Banerjee *et al.* [354] carried out similar work, testing the survival and differentiation rate of NSCs that were mixed in with the precursor solution prior to the initiation of gelling (via $CaCl_2$). Four different hydrogel compositions were investigated, comprising alginate (wt%): $CaCl_2$ concentration (mM) ratios of 1:100, 0.25:100, 0.25:50, and 0.25:10. After culturing for 7 days in DMEM:F12 medium (composition given in Appendix A), a viability rate exceeding 80% was recorded, and the cell populations had multiplied on all hydrogels (approximately 15-fold on the 0.25:10 gel, and 2-fold on the 1:100 gel). The largest rate proliferation rate also corresponded to the largest relative increase in the neuronal marker β-tubulin III, indicating a high degree of differentiation in the softest gel (modulus G^* =183 Pa). These results are shown in Figure 2.56.

Both these studies serve to highlight the influence of crosslinking density on neural growth, where the main predictor of success is evidently tied to lowering stiffness. However, this approach is not without its limitations, as reducing the cross-linking density in pursuit of neural adhesion also weakens the hydrogel, threatening its structural integrity and reducing its lifetime. Alginate hydrogels with a lower crosslinking ratio necessarily degrade faster than their stiffer counterparts as they have less ionic bonds to reverse. When considering an electrode coating of calcium alginate as a tool for anti-

fouling and neural regeneration, the lifetime of the gel must be prolonged in such a way as to achieve these goals before its complete disintegration [334], [355]. Ayar *et al.* [356] drew attention to this issue when fabricating calcium alginate hydrogels (1 wt% sodium alginate) with crosslinker molarities below 10 mM. Despite widespread reporting of similar gels being ideal for neural growth, the authors note their poor structural integrity, as they would disassociate before the end of cell culture tests.

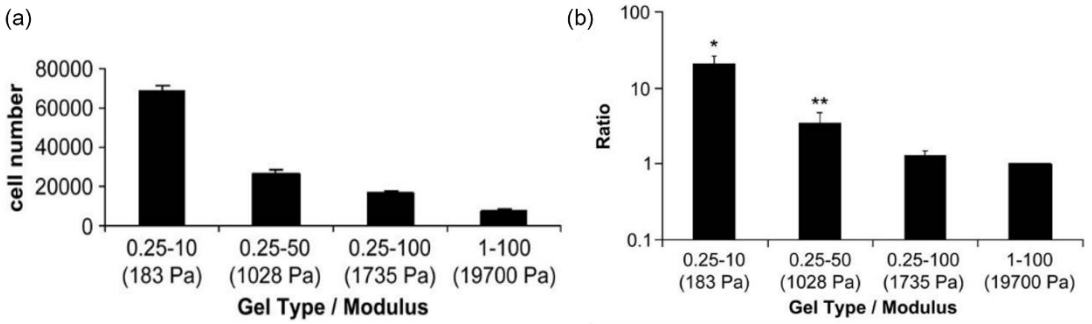

Figure 2.56: (a) Bar graph showing the number of NSC cells growing on calcium alginate gels with different $CaCl_2$ concentrations and Youngs modulus. Measurements were made after 7 days in culture; (b) Bar graph showing the relative increase in β-tubulin detection for the same hydrogels after the same timepoint. From [354].

Instead, alginates of higher crosslinking density may be functionalized in a variety of ways to boost neural adhesion and support tissue regeneration. Ayar *et al.* [356] cultured neonatal rat Schwann cells onto calcium alginate tablets ($CaCl_2$ concentration 10 mM) which were treated with ascorbic acid to stimulate secretion of ECM. The decellularized gels were then compared against non-functionalized alginate for their ability to support the differentiation of rat ADSCs (adipose-derived stem cells) into neural cells. While both supported higher rates of differentiation as compared to cell culture plates, a significant increase was also observed on the functionalised alginate versus the unmodified gel. Ansorena *et al.* [357] developed calcium alginate hydrogels loaded with human GDNF (recombinant glial-derived neurotrophic factor) with the aim of inducing recovery in hemisectioned rat spinal cord. GAP43 quantification, a protein indicative of neural growth cone numbers, was consistently higher for rats with alginate implants than those without at both 6-week and 3-month timepoints. Similarly, more neurofilaments were detected in rats receiving alginate gels at the same sampling points. Other research groups have likewise reported positive effects when functionalising alginate with RGD[11]

[11] Arginine glycine aspartic acid (RGD) is a recognition sequence for protein attachment [496].

adhesion ligands [252], BDNF (brain-derived neurotrophic factor) [358], and laminin [359] amongst others.

2.6.5 The Impact of Alginate Hydrogels on the Electrochemical Performance of Neural Electrodes

In addition to striking a balance between low stiffness, structural integrity, and coating lifetime, it is also desirable for the hydrogel layer to have minimal impact on the electrode's electrochemical properties [269], [335]. Since hydrogels efficiently absorb the liquid in which they are immersed, their ionic conductivity tends to acclimate towards that of the surrounding fluid [28], [360]. As such they are expected to contribute towards a minimal increase in electrode impedance when crosslinking density is low (< 0.01 M) [252]. However, cross-linking densities that are relative to the application at hand (~0.01-0.5 M) tend to produce a more complex response due to the increased number of polymer links impeding ionic movement [360], [361].

Ferlauto *et al.* [269] developed a multi-layer electrode system consisting of a PEDOT:PSS film on a Pt electrode. A calcium alginate layer was then electrodeposited onto the CP using a mixture of 1 wt% sodium alginate and 0.5 wt% $CaCO_3$. An adhesion layer was electropolymerized onto the PEDOT:PSS prior to hydrogel deposition and consisted of 0.1 wt% EDOT monomer and 4 wt% PSS dissolved in the sodium alginate/$CaCO_3$ solution. The PEDOT:PSS layer was electrodeposited from a precursor solution containing the same concentration of EDOT and PSS in DI water. The processing steps are summarised in Figure 2.57 a. When impedance measurements were made in PBS (sinusoidal amplitude of 50 mV), the alginate layer did not affect the high-frequency response (>10 kHz). Additionally, significantly lower impedance was recorded at frequencies below 100 Hz following alginate deposition (Figure 2.57 b). Although this phenomenon is not addressed by the authors, it is possible that this improved performance originates from the adhesion layer, where additional PEDOT:PSS is polymerised onto the electrode surface. This is also reflected in the increased CSC_C ($v = 0.05$ Vs^{-1}), observable in the voltammograms shown in Figure 2.57 d. Mid-range frequency measurements (100 – 10 kHz) reveal a section of increased impedance, corresponding to a capacitive shift marked by the phase angle change in Figure 2.57 c.

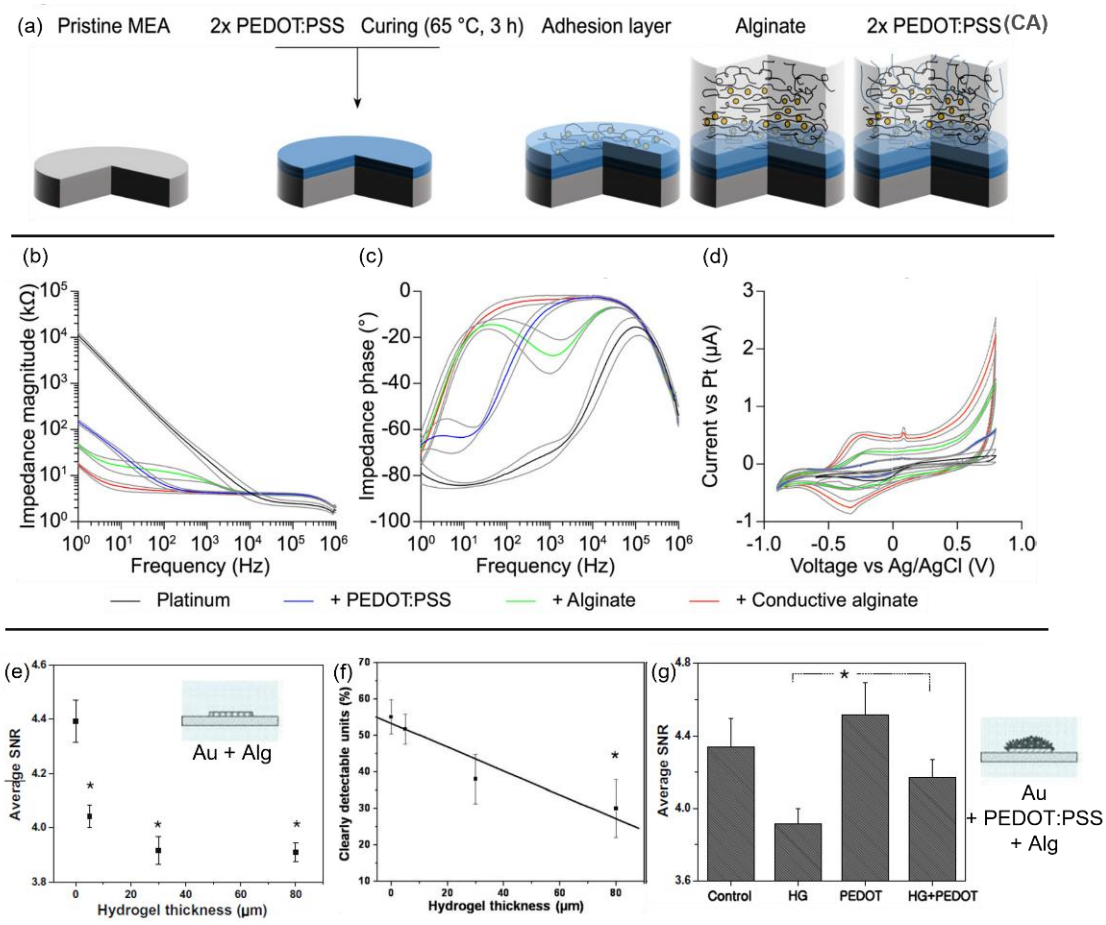

Figure 2.57: (a) Schematic showing the different steps involved to produce a multi-layer electrode. From [269]; (b) Impedance and (c) phase angle Bode plots for the different electrodes under test, and (d) voltammograms for the same electrodes measured at a sweep rate of $v = 0.05$ Vs^{-1}. Measurements were made *in vitro*. From [269]; Plots of (e) average signal-to-noise ratio (SNR) and (f) % of clearly detectable units versus hydrogel thickness; (g) Bar graph of the average SNR for Au, Au + hydrogel, Au + PEDOT:PSS, and Au + PEDOT:PSS + hydrogel electrodes, marked control, HG, PEDOT, and HG+PEDOT in figure, respectively. Measurements for (e-g) made in the auditory cortex of guinea pigs at acute stage of implantation. From [24].

A solution to lower electrode impedance across the entire frequency range is proposed in the form of a conductive alginate (CA). Following an identical production process, the electrodes were immersed in the CP precursor solution and PEDOT:PSS was electropolymerized within the porous hydrogel (last step shown in (Figure 2.57 a)). The improvements to electrochemical performance are apparent, with increased CSC_C, a reduced impedance, and elimination of the mid-range capacitive phase shift. However, despite these promising results, the issue of calcium alginate's reversibility is not addressed in this latter approach. It is unclear how the structural integrity of the PEDOT:PSS mesh is to be maintained following the hydrogel's inevitable dissolution,

and whether any adverse tissue response may be generated as a result of polymer break-off.

Another problem that may arise from a hydrogel layer is the physical separation of the electrode surface from the target neurons. In the work of Kim *et al.* [24], hydrogel coatings were applied to Au electrodes via a dip-coating method and implanted into the auditory cortex of guinea pigs. Acute neural readings were performed, from which the SNR was calculated for electrodes with different hydrogel thicknesses. While no significant impedance increase was measured for alginate layers up to 100 µm thick, the SNR drops as hydrogel thickness is increased *in vivo* (Figure 2.57 e). This was correlated with a drop in clearly detectable units after subjecting the test subjects to a 200 ms noise burst (Figure 2.57 f). Since the amplitude of an extracellular spike decreases with increasing distance from the cell body, the electrode is no longer able to differentiate between the signal and the background noise. However, the authors note that when a PEDOT:PSS film was electrodeposited onto the Au sites before a 30 µm hydrogel coating was applied, the SNR improved (Figure 2.57 g). Due to the exceptionally low impedance of PEDOT:PSS as compared to Au, an almost equivalent number of clearly detectable units were measured for Alg-PEDOT:PSS and bare Au. Therefore, despite the evident drop in the SNR between PEDOT:PSS and Alg-PEDOT:PSS, the hydrogel-coated electrode was still able to delivery satisfactory neural recordings.

These works bring to attention a pertinent question, namely whether a slight increase in electrode impedance is worth addressing in the context of reversible hydrogels. When calcium alginate is intended to mitigate fibrous encapsulation and permit neural integration, the effects of increased impedance are expected to diminish over time. As such, the electrode's electrochemical properties should be theoretically restored at the end of this process. Studies assessing this hypothesis are notably absent from literature, especially when considering alginate gels produced via electrodeposition. Work comparing the chemical state of electrode materials before and after hydrogel deposition, as well as following alginate dissolution, has thus far not been published. Such investigations are essential to instruct more productive strategies for electrode improvement, and may also serve to highlight flaws in existing propositions.

Table 2.10: The constituents for the production of calcium alginate hydrogels as described by notable research groups in literature. The method used for gelation are given as DC (dip-coating), ED (electrodeposition), or BM (bulk mixing). Details are tabulated in order of reference in the text.

Reference	**Substrate**	**Method**	**Alginate (%w/v)**	**Cross-linker**		**I Density / V**
				Content	**Type**	
Kim *et al.* [24]	Au/PEDOT:PSS	DC	1	0.5 M	$CaCl_2$	/
Chikar *et al.* [252]	PEDOT:PSS	DC	1	2% w/v	$CaCl_2$	/
Cheng *et al.* [31]	Au	ED	1	0.05-0.5% w/v	$CaCO_3$	0.5 $mAcm^{-2}$
Machida *et al.* [346]	TCP	BM	1	0.5 M	$CaCl_2$	/
Singh *et al.* [347]	TCP	BM	2	0.1 M	$CaCl_2$	/
Zhang *et al.* [348]	/	BM	1	10% w/v	$CaCl_2$	/
Strand *et al.* [349]	/	BM	1.8	0.05 M	$CaCl_2$	/
Skousen *et al.* [123]	Michigan Probe	DC	1.5	0.002 M	$CaCl_2$	/
Kim *et al.* [27]	Michigan Probe	DC	1	0.5 M	$CaCl_2$	/
Ansorena *et al.* [357]	/	BM	0.5	0.05 M	$CaCl_2$	/
Matyash *et al.* [353]	TCP	BM	1	0.0018, 0.002, 0.1, 1 M	$CaCl_2$	/
Banerjee *et al.* [354]	TCP	BM	1	0.1 M	$CaCl_2$	/
			0.25	0.01, 0.05, 0.1M		
Ayar *et al.* [356]	TCP	BM	1	0.01 M	$CaCl_2$	/
Ferlauto *et al.* [269]	Pt	ED	1	0.5 wt%	$CaCO_3$	2 V

3 Materials and Methods

3.1 Electrode Development

3.1.1 Electrode Identification

A total of 10 electrodes were explored in this work. For ease of identification, an illustrated guide is given in Figure 3.1. The electrodes are split into the following 3 categories:

1. The TiN electrodes – TiN_I, TiN_{II}, TiN_{III}, and TiN_{IV}
2. The TiN_{IV}/PEDOT:PSS electrodes – $PP_{12.5}$, PP_{15}, and $PP_{17.5}$
3. The $TiN_{IV}/PP_{17.5}$/Alginate electrodes – CA_{60s}, CA_{90s}, and CA_{120s}

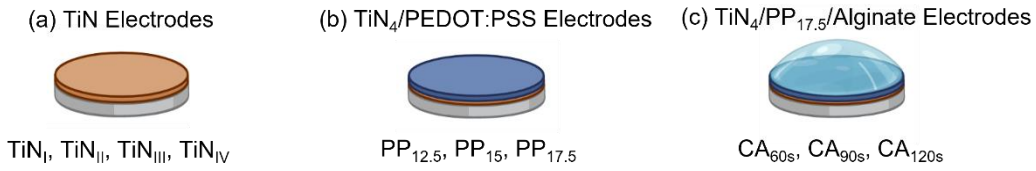

Figure 3.1: Schematic showing the 3 categories of electrodes explored in this work: (a) The TiN electrodes, (b) The TiN_{IV}/PEDOT:PSS electrodes, and (c) The $TiNI_V/PP_{17.5}$/Alginate electrodes. Diagram created on Biorender.com.

3.1.2 Preparation of Titanium Alloy Substrates

All electrodes developed in this work were based on a substrate of extra-low interstitial Grade 5 Ti6Al4V alloy (Brindley Metals, UK). The material was supplied in its annealed state as rods with diameters of 10 mm and 25 mm, and its certificate is provided in Appendix B. The rods were cut down to discs using silicon carbide (SiC) wheels (Metprep, UK) mounted on an Accutom-10 precision cut-off machine (Struers, Denmark). One surface of the discs was then ground and polished to a mirror finish using a Tegramin-25 automatic polisher (Struers, Denmark). The adopted procedure was in line with the manufacturer's recommendations and is summarized in Table 3.1. Coupons that did not meet the minimum height or diameter requirements for use in the polisher were first mounted in LevoFast heat-curing resin (Struers, Denmark). After polishing, the discs were reclaimed by applying pressure in a vice until the resin cracked

or the disc popped out. All coupons were cleaned by sequential ultrasonication for 5 minutes in acetone, IPA (isopropyl alcohol), and DI (de-ionized) water.

Discs intended for the development of TiN_I electrodes were used as-is. For development of the modified TiN electrodes (TiN_{II}, TiN_{III}, and TiN_{IV}), the discs were surface-blasted at the Danish Technological Institute (Aarhus, Denmark). Details are given in Table 3.2. Blasting was maintained until the desired values of R_q were reached. Morphology of the blasting media is shown in the optical micrographs of Figure 3.2.

Table 3.1: Summary of the material preparation procedure for Ti6Al4V discs.

Step	Grinding Paper/ Polishing Cloth	Solution
Grinding	SiC Grinding Paper (Grit sizes P400, P600, P800, and P1200) (MetPrep, UK)	Water
Fine Grinding	MD-Largo Cloth (Struers, Denmark)	Polycrystalline Diamond Suspension, Water Base (9 µm) (MetPrep, UK)
Polishing	MD-Chem Polishing Cloth (Struers, Denmark)	1:9 by volume mixture of H_2O_2 and OPS colloidal Silica Suspension (0.02 µm) (Struers, Denmark)

Table 3.2: Details of the surface-blasting process applied to titanium discs for the development of modified TiN electrodes.

Electrode Type	TiN_{II}	TiN_{III}	TiN_{IV}
Specification of Media (Sonnimax A/S, Denmark)	Glasperler AQ 00-50 MY	Normalkorund NK F 70	Normalkorund NK F 46
Diameter of Media (µm)	< 50	180-250	300-425
Equipment Used	HGH 7050 Microblasting Unit (HGH, Germany)	HGH 7050 Microblasting Unit (HGH, Germany)	ECO-80P Blast Cabinet (Contracor, Germany)
Final R_q of Surface (µm)	0.5	2.3	3.9

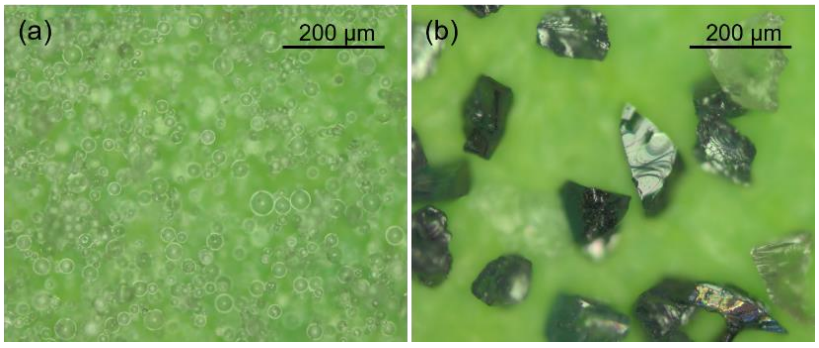

Figure 3.2: Optical micrographs showing the morphology of the blasting media used for roughening: (a) Glasperler AQ 00-50 MY; (b) Normalkorund NK F 70 (Normalkorund NK F 46 has identical morphology but larger particle size.)

3.1.3 Physical Vapour Deposition (PVD) Process

The discs were coated with a layer of over-stoichiometric titanium nitride (TiN) using a DC reactive magnetron sputtering physical vapour deposition (PVD) process. A CC800/9 SiNOx industrial PVD coating unit (CemeCon AG, Germany) was used, equipped with 4 sputtering targets (88 x 200 mm) made of 99.5% purity titanium. The atmosphere consisted of an Ar/N_2 gas mixture (99.999% purity) with a flow ratio of 400/350 sccm. The titanium discs were mounted onto jigs within the chamber that placed the surfaces of the targets and discs parallel to one another. All depositions were carried out at the Danish Technological Institute in Aarhus, Denmark.

3.1.4 Electrode Handling

Four types of electrodes having different dimensions (Figure 3.3) were used during this work. Type I electrodes were used for general electrochemistry measurements and imaging and could be handled as-is. The testing area was limited by means of a PTFE mask (Gamry, USA) that had the circle of desired diameter cut out (Figure 3.3 a).

Type II electrodes were used for mechanical adhesion assessments. They were placed in stainless steel hose clamps along with an insulated Cu wire that had its end stripped away. The hose clamp was then tightened to ensure electrical contact between electrode and wire. The assembly was then cast in room temperature curing EpoSet epoxy resin (Metprep, UK), leaving the electrode surface exposed for testing (Figure 3.3 b).

Type III electrodes were used for cell culture experiments and alginate dissolution assessments. No modifications were required for cell culture. For dissolution assessment, the testing area was limited by means of a mask (Gamry, USA) that had the circle of desired diameter cut out (Figure 3.3 c).

Type IV electrodes were used for cell culture experiments. They were placed in stainless steel hose clamps that were tightened to ensure electrical contact. The assembly was then cast in Leonardo Mold Making Silicone (Algaplay, Italy). Once cured, a scalpel was used to cut away part of the silicone and expose the screw of the clamp. A crocodile clip could then be used to make electrical contact for electrodeposition procedures (Figure 3.3 d). After deposition, the silicone could be cut away and the electrode liberated from the hose clamp.

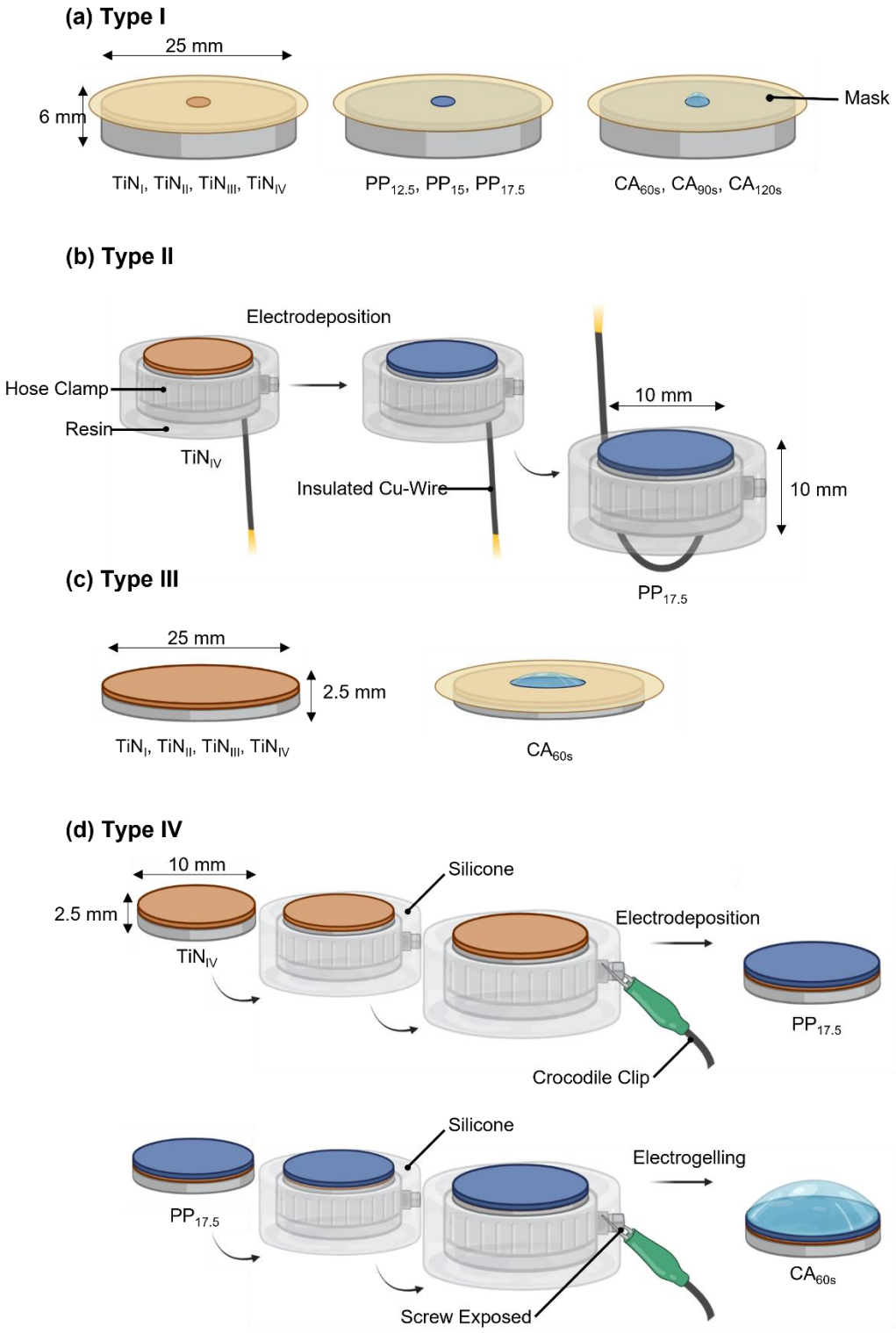

Figure 3.3: (a) Type I electrodes for general electrochemistry and imaging. Testing area defined by mask PTFE. (b) Type II electrodes for mechanical adhesion assessments. Electrode and Cu wire tightened in hose clamp and moulded in epoxy resin. (c) Type III electrodes for cell culture (no modification necessary) and for calcium alginate (CA) degradation assessment (area defined by mask). (d) Type IV electrodes for cell culture experiments. Electrode placed in hose clamp and moulded in silicone. Part of silicone is cut away to expose screw for electrical contact. Silicone is removed after deposition. Diagram created on Biorender.com.

3.1.5 Electrodeposition of PEDOT:PSS on TiN_{IV}

An electropolymerisation process was adopted to deposit a layer of PEDOT:PSS conductive polymer onto TiN_{IV}. A precursor solution was made containing 2 g/dl of PSS (poly(styrene sulfonic acid) sodium salt, MW = 70000) (Alfa Aesar, USA) and 107 µL/dl of EDOT monomer (2,3-Dihydrothieno[3,4-B]-Dioxene) (Apollo Scientific, UK) dissolved in DI water. The solution was mixed until a homogeneous liquid was achieved and was stored at a temperature of 3±1 ^{o}C when not in use. To impregnate the TiNIV electrode with precursor solution, 10 ml would be placed in a small vessel and bubbled for 1.5 minutes with Ar gas (flow rate 500 cc/minute) through a silicone tube (inner diameter 2 mm). A clean electrode (1 minute of ultrasonication at 45 kHz in IPA) would then be submerged in solution and placed in a CitoVac vacuum impregnation unit (Struers, Denmark) at 0.1 bar for 10 minutes.

Excess solution was wiped off the non-targeted areas and the electrode was mounted into the electropolymerisation jig as shown in Figure 3.4. A rubber O-ring, Type I electrode, wired Cu-disc, and insulated platform (rigid rubber) were aligned with the through-hole as shown in the diagram. A screw was then used to pressure-fit the sample against the PTFE bottom to create a water-tight seal. The Cu-disc was eliminated in the case of Type II and Type IV samples, as electrical contact was established directly through a crocodile clip (Figure 3.5 a and b, respectively).

100 ml of solution were poured into the vessel and bubbled with the Ar gas for 15 minutes. Galvanostatic electropolymerisation was then initiated by applying a current density of 1.3 $mAcm^{-2}$ for 12.5, 15, and 17.5 minutes to produce the $PP_{12.5}$, PP_{15}, and $PP_{17.5}$ electrodes, respectively. A three-electrode system was used for this process, in which the TiN_{IV} constituted the working electrode (WE), a 25 cm length of coiled Pt wire with 0.4 mm diameter (99.95% purity) (Advent Research Materials, UK) served as the counter electrode (CE), and an Ag/AgCl electrode (Ossila, UK) was used as a reference electrode (RE). The process was controlled by a computer-driven Reference600 Potentiostat/Galvanostat (Gamry, USA). During polymerisation, the solution was agitated by means of a custom-made motor-driven stirrer turning at a rate of 60 rpm. Argon bubbling was also maintained for the entire duration of the process. This process was optimized through a sequence of trial experiments in which the current density and deposition time were varied.

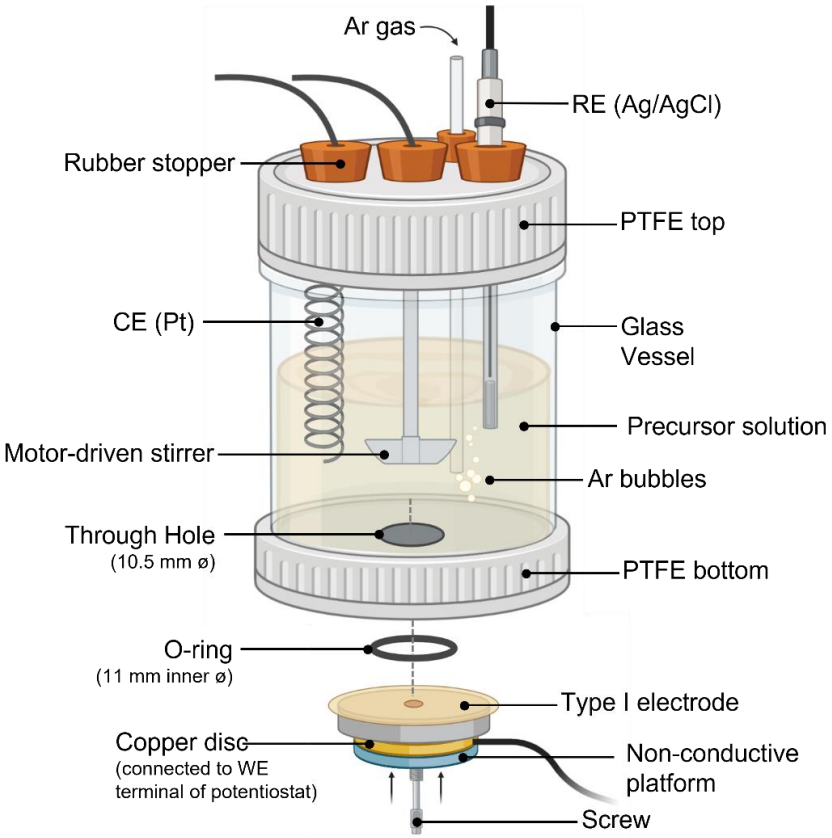

Figure 3.4: Illustration of the electrochemical set-up used to electrodeposit PEDOT:PSS films onto TiNIV electrodes. The set-up is shown with a Type I electrode in the process of being mounted. Diagram created on Biorender.com.

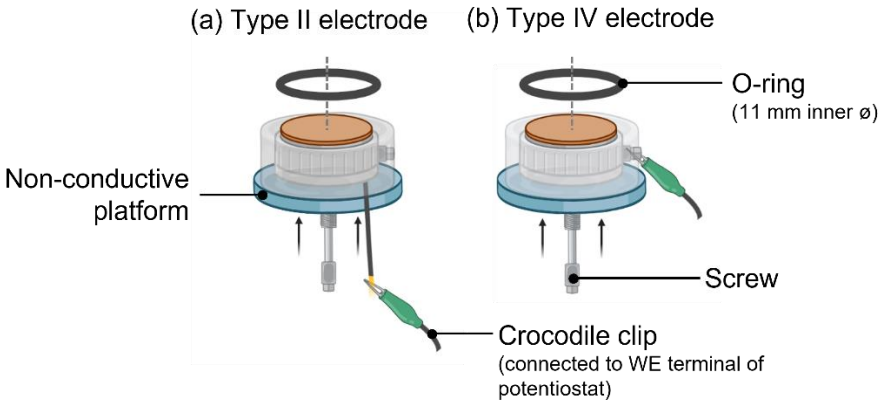

Figure 3.5: Illustrations of (a) Type II and (b) Type IV electrodes being mounted into the electrodeposition set-up shown in Figure 3.4. The copper disc is here eliminated as electrical contact is established directly by means of a crocodile clip. Diagram created on Biorender.com.

After polymerisation the electrode was dismounted from the electrochemical cell and cleaned via ultrasonication in DI water for 1 minute. In the case of Type IV samples, the electrode was carefully cut out of the silicone using a scalpel and taken out of the hose

clamp prior to cleaning. Cleaned electrodes were then transferred to an LT24/12/P330 muffle furnace (Nabertherm, Germany) where the temperature was ramped from room temperature (~ 20 ^{o}C) to 90 ^{o}C over a period of 3 hours. The temperature was held for 3 hours and then allowed to furnace cool.

3.1.6 Electrodeposition of Calcium Alginate on $PP_{17.5}$

Calcium alginate (CA) layers were electrodeposited onto $PP_{17.5}$ electrodes using the electrogelling method as described by Cheng *et al.* [31]. A 0.25 % w/v solution of $CaCO_3$ (99.5 % purity) (Alfa Aesar, USA) was made by mixing pulverised $CaCO_3$ granules in DI water. The solution was then passed through a stainless-steel sieve (pore diameter 0.5 mm) and any remnant clumps were crushed down and reconstituted. Sodium alginate powder (MW 10,000-600,000 g/mol) (PanReac AppliChem ITW Reagents, USA) was then added to make up a 1 wt% solution. Stirring was sustained by means of a PTFE stir bar until all the powder had dissolved, and the precursor solution was then stored at a temperature of 3±1 ^{o}C when not in use. The stir bar was left inside the solution. Whenever it was needed, the solutions would be stirred again to ensure homogeneity. A clean technique was applied in which no new foreign objects (pipettes, spatula, etc.) were ever inserted into the stock precursor solution to minimise bacterial contamination. The required amounts of solution were instead poured out into a separate vessel and the stock returned to storage.

For the electrogelling process, a few drops of precursor solution (~ 1 ml) were pipetted onto the surface of a clean $PP_{17.5}$ electrode (1 minute of ultrasonication at 45 kHz in IPA) and placed in a CitoVac vacuum impregnation unit (Struers, Denmark) at 0.1 bar for 10 minutes. A separate 25 ml were also placed in a glass beaker and subjected to the same vacuum. The purpose of this procedure was twofold, to impregnate the structure of PEDOT:PSS with the precursor solution, and to remove any trapped air pockets. Excess solution was then wiped off the non-targeted areas and the electrode was mounted into the electrogelling jig as shown in Figure 3.6. Type IV electrodes were mounted in an identical way as per the PEDOT:PSS electropolymerisation jig (Figure 3.5 b) and so they were not repeated in the diagram. The vacuumed solution was then slowly transferred into the vessel to avoid the reintroduction of air pockets.

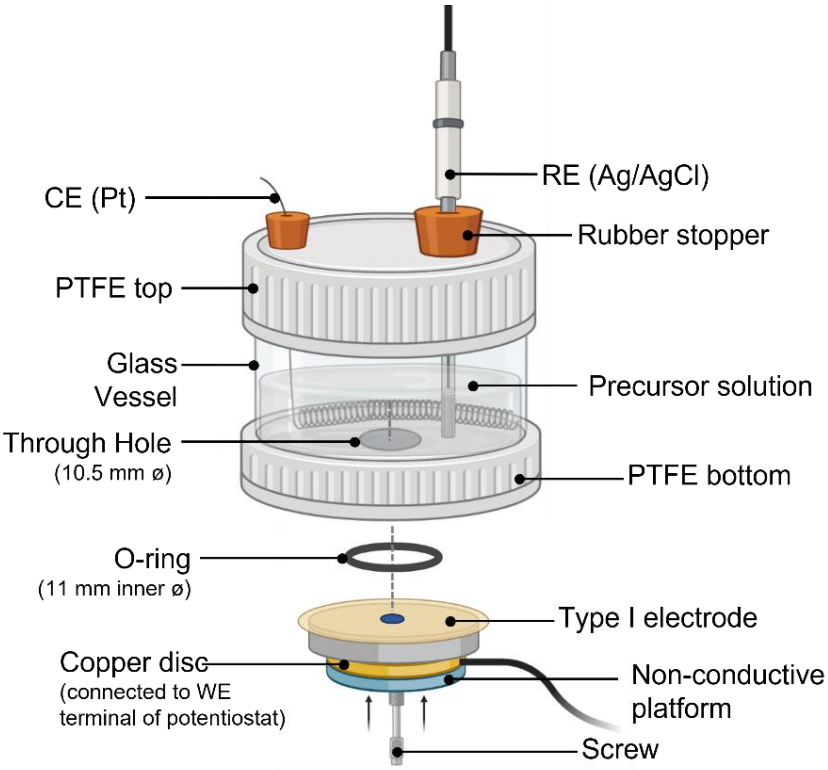

Figure 3.6: Illustration of the electrochemical set-up used to electrodeposit CA gels onto $PP_{17.5}$ electrodes. The set-up is shown with a Type I electrode in the process of being mounted. Diagram created on Biorender.com.

A three-electrode system with identical components as described in section 3.1.5 was established, with the $PP_{17.5}$ acting as the WE in place of the TiN_{IV}. Anodic galvanostatic electrogelling was then initiated by applying a current density of 0.85 $mAcm^{-2}$ for 60, 90, and 120 s to produce the CA_{60s}, CA_{90s}, and CA_{120s}, electrodes, respectively. This process was optimized through a sequence of trial experiments in which the current density and deposition time were varied.

After gelling was complete the electrode was dismounted from the jig and excess precursor solution was removed by rinsing (indirect spraying with DI water from a wash bottle). The electrode was then submerged in a 1 mM $CaCl_2$ (Avantor Performance Materials, USA) firming solution and left to soak for 30 minutes. Once the time had elapsed, the electrode was then removed from solution for testing or characterisation. In the case of Type IV electrodes, the silicone was carefully cut away with a scalpel and the hose clip removed.

3.2 Characterisation

3.2.1 Microscopy

Optical micrographs of the electrode surfaces were captured using an Axiocam 506 Colour microscope camera (Zeiss, Germany) mounted onto an Axioscope 5 Light Optical Microscope (Zeiss, Germany). Low-magnification images of CA electrodes were taken using a TV Lens C-0.6x stereo microscope (Nikon, Japan) equipped with a Leica DFC295 camera (Leica, Germany).

Scanning Electron Microscopy (SEM) was carried out on a Merlin field scanning electrode microscope (Zeiss, Germany) using Type II secondary electron (SE2) detection. An electron high tension (EHT) voltage of 15 kV was applied along with magnifications of up to 15,000x. Samples were affixed to Al stubs using conductive carbon tape before placing in the SEM chamber. In the case of CA electrodes, a fixing protocol based on the work of Santana *et al.* [362] was first carried out. The protocol is identical to that applied for fixing cells, and is described in detail in section 3.6.4.

3.2.2 X-Ray Diffraction

X-ray diffraction (XRD) data was collected for the TiN electrodes using a D8 Advance X-Ray diffractometer (Bruker, USA) set up in Bragg-Brentano configuration. A CuKα radiation source (λ = 1.5406 Å) was used, and measurements were carried out at an acceleration voltage of 40 kV and at room temperature (21 ^{o}C). Peaks were collected between the 2θ values of 20^{o} and 80^{o} with a step size of 0.01^{o} and a dwell time of 2 s. A PDXL integrated X-ray powder diffraction software (Rigaku, Japan) was then used to fit resultant peaks to their corresponding phases.

3.2.3 Micro-Raman Spectroscopy

An Xplora Plus Raman microscope (Horiba Scientific, Japan) operated at room temperature (21^{o}C) was used to identify the chemical structure of various materials in this work, namely TiN, PEDOT:PSS, calcium alginate, and $CaCO_3$ powder. All the materials were assessed in their air-dried state. The $CaCO_3$ powder was placed onto an opaque slide for ease of handling. In all cases, a 532 nm (green light) laser was used with a 10s acquisition time and an 1800 grating. For TiN_I electrodes, additional

measurements were made using a 785 nm (red light) laser while keeping the other parameters constant.

3.2.4 Energy Dispersive Spectroscopy

The SEM described in section 3.2.1 was equipped with an Octane Elect EDS system (EDAX, Japan) to perform energy dispersive spectroscopy (EDS). Carried out at an EHT of 15 kV, the technique was used to determine the atomic % of elements within specified spots.

3.2.5 Cross-Sectional Analysis and Thickness Measurements

3.2.5.1 TiN Electrodes

The TiN electrodes were mounted in room temperature curing EpoSet epoxy resin (Metprep, UK) and sectioned on an Accutom-10 precision cut-off machine (Struers, Denmark) with a SiC wheel (Metprep, UK). The exposed faces were then ground and polished using the same procedure as described in section 3.1.2. After cleaning (1 minute of ultrasonication at 45 kHz in IPA) and drying, the cross-sections were imaged using SEM. The average and standard deviation were based on 3 replicate electrodes of each electrode type.

3.2.5.2 PP Electrodes

PP electrodes were first given a protective Ni coating through an electroplating process. The electrode was connected to the cathodic port of a power supply and submerged in 250 ml of Watt's Bath solution (30 g/L Boric acid, 190 g/L Nickel Sulphate, and 40 g/L Nickel (II) Chloride Hexahydrate in DI water (Apollo Scientific, UK)) kept at 40^{o} C. A strip of 99.6% pure Nickel (0.15 x 8 x 100 mm) (US Solid, USA) acted as the anode. A current of 0.49 A was applied for 20 minutes, after which the electrode was rinsed with DI water and dried in air. The electrode was then mounted in room temperature curing EpoSet resin (Metprep, UK) and sectioned on an Accutom-10 precision cut-off machine (Struers, Denmark) with a SiC wheel (Metprep, UK). The exposed face was then finely ground with 1200 grit SiC paper (Metprep, UK) to preserve the structure of the polymer, rinsed with DI water, and dried in air. SEM images were then taken of the cross-sections and layer constituents confirmed via EDS (as detailed in section 3.2.4). The average and standard deviation were based on 3 replicate electrodes of each thickness type.

3.2.5.3 CA Electrodes

Thickness measurements were made on Type I electrodes, where the diameter of the exposed area was 5.5 mm (GSA = 0.238 cm^2). The PTFE mask was pre-cut for ease of removal (Figure 3.7 a), and the segments were carefully peeled off with tweezers without disturbing the gel (Figure 3.7 b). After removal, the gels were allowed to swell in PBS for 30 minutes before thickness measurements were made.

The barrel of a TV Lens C-0.6x stereo microscope (Nikon, Japan) was turned horizontal as shown in Figure 3.7 c, and a spirit level was used to ensure the barrel was parallel with the sliding platform underneath. The electrodes were placed on a level platform where the height and lateral position could be adjusted to bring the gel into focus. Measurements were made from apex to base of the gel, and the average and standard deviation derived from 5 replicates.

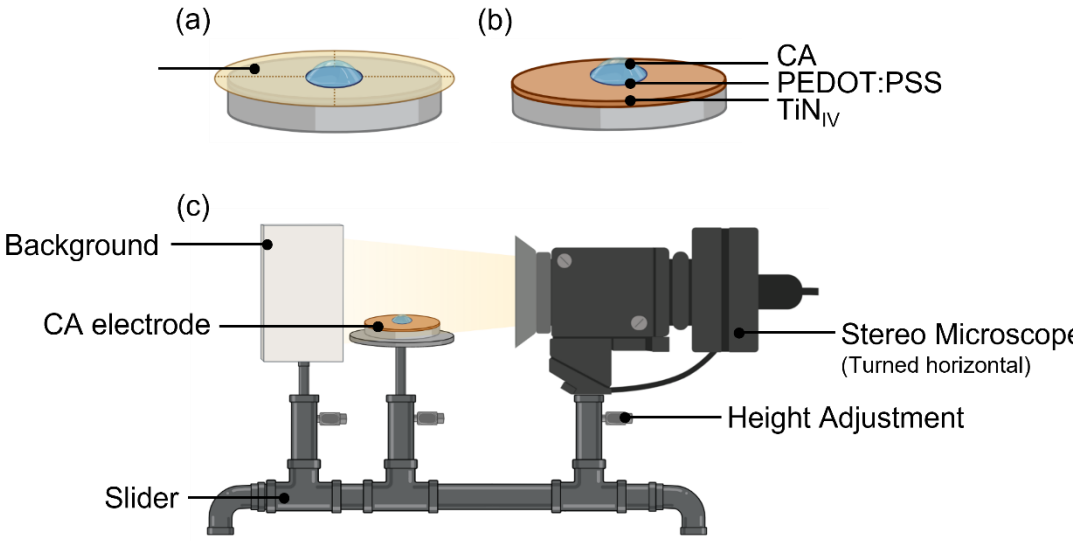

Figure 3.7: (a) Type I CA electrode, where the mask was pre-cut for ease of removal; (b) The same electrode with the mask removed, with labels identifying the 3 layers; (c) The set-up used to measure the thickness of the CA gels. Diagram created on Biorender.com.

3.2.6 Non-Contact Profilometry

Surface roughness measurements of TiN and PP electrodes were made on a non-contact XYRIS 3-dimensional optical profilometer with a sensor resolution of 0.010 µm (Taicaan Technologies, UK). Sampling areas of 10x10 mm and 2x2 mm were

established for TiN and PP electrodes, respectively. A grid spacing of 10 µm was established in both x and y dimensions, and interrogations were done at a maximum scan speed of 5 mm/s. The results, based on repeats of 3, were analysed on the surface metrology software BEX Boddies Extreme (TaiCaan Technology, UK) using a 0.8 mm gaussian cut-off limit.

3.3 Electrochemical Testing

The tests described in this section were carried out in 150 ml of one of the four electrolytes described hereunder:

- PBS - Phosphate Buffered Saline (Oxoid, UK) solution. Contents detailed in Appendix C.
- Et_4NBF_4 in AN - A 1M solution of ET_4NBF_4 (tetraethylammonium tetrafluoroborate salt) (Apollo Scientific, UK) in AN (acetonitrile) (Apollo Scientific, UK).
- PBS+ BSA+ Azide – PBS with 2.5g/dl of BSA (Bovine Serum Albumin) powder (Europa Bioproducts, UK) and 0.3 wt% sodium azide salt (Biochem Chemopharma, France).
- PBS+ BSA+ P/S – PBS with 2.5g/dl of BSA (bovine serum albumin) powder and 1 v% P/S (penicillin-streptomycin) (Sigma-Aldrich, USA).

The electrolytes were maintained at a physiological temperature of 37 ± 2 ^oC by means of a water jacket through which heated DI water was pumped. In all cases, a 3-electrode system was employed where the electrode under test acted as the WE and a 25 cm length of coiled Pt wire with 0.4 mm diameter (99.95% purity) (Advent Research Materials, UK) served as the CE. For aqueous electrolytes, the RE was a Saturated Calomel Electrode (SCE) (Gamry, USA), whereas for the organic electrolyte an Ag/Ag^+ electrode (Ossila, UK) was employed. A bridge probe was also included to bring the sensing tip of the RE closer to the surface of the WE. The bridge was filled with the same solution as the RE (3 M KCl in DI water, and 0.01 M $AgNO_3$ in acetonitrile for the SCE and Ag/Ag^+, respectively). All experiments were carried out using a computer-driven Reference600 potentiostat/galvanostat (Gamry, USA). A diagram of the electrochemical set-up is shown in Figure 3.8. Only Type I electrodes were used for these tests. Table

3.3 provides a summary of which tests (described in the ensuing subsections 3.3.1 to 3.3.4) each electrode was subjected to and in which electrolyte.

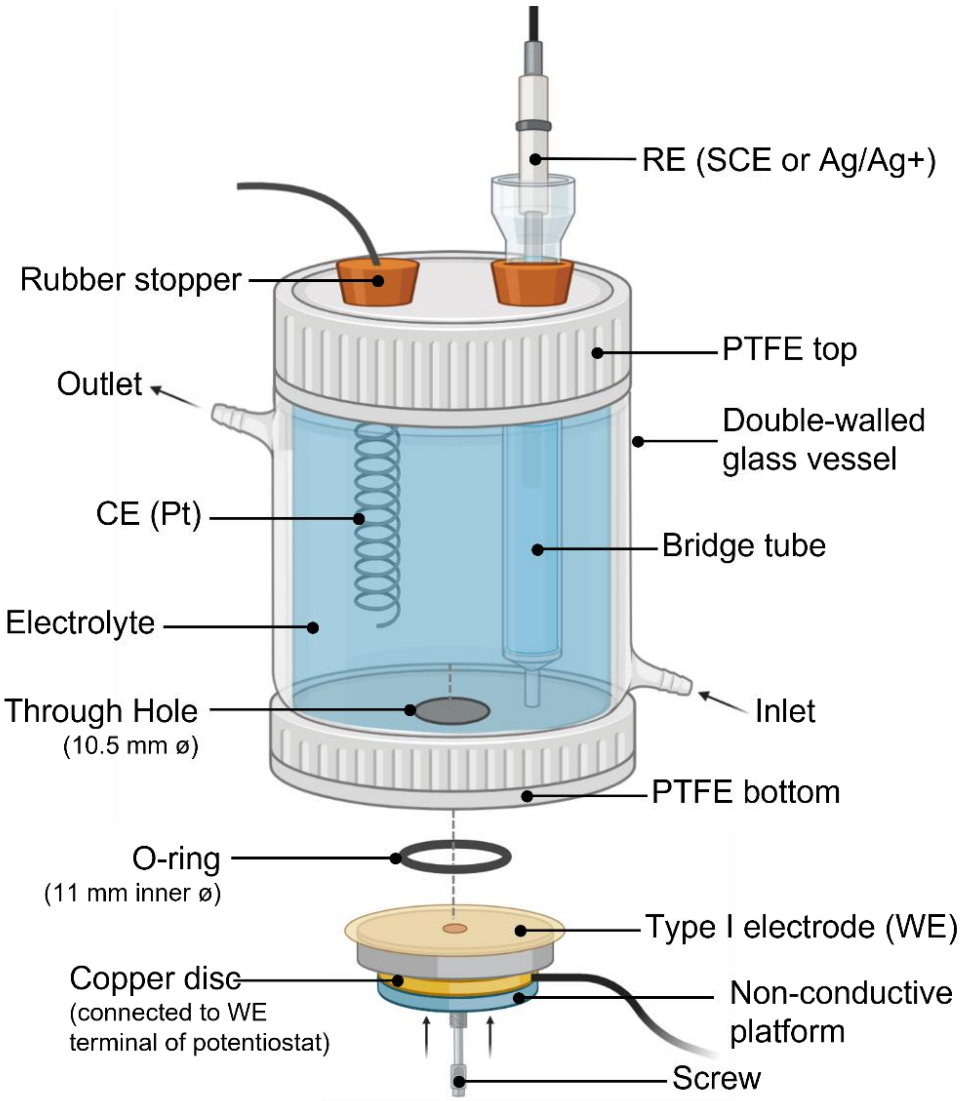

Figure 3.8: Schematic for the set-up used in electrochemical measurements The set-up is shown with a Type I electrode in the process of being mounted. Diagram created on Biorender.com.

Table 3.3: Summary of electrochemical tests in different electrolytes for each electrode.

	TiN Electrodes				**PP Electrodes**			**CA Electrodes**		
	TiN_{I}	**TiN_{II}**	**TiN_{III}**	**TiN_{IV}**	**$PP_{12.5}$**	**PP_{15}**	**$PP_{17.5}$**	**CA_{60s}**	**CA_{90s}**	**CA_{120s}**
EIS + CV in PBS	✓	✓	✓	✓	✓	✓	✓	✓	✓	✓
EIS + CV in Et_4NBF_4 in AN	✓									
EIS + CV in PBS+ BSA+ Azide	✓	✓	✓	✓						
EIS + CV in PBS+ BSA+P/S				✓			✓			
Cyclic Lifetime Assessment in PBS	✓			✓			✓*			
24-Hr Immersion Testing in PBS+ BSA+ Azide	✓	✓	✓	✓						
24-Hr Immersion Testing in PBS+ BSA+P/S				✓			✓			

*Tests at 1 Vs^{-1} were also repeated for an extended WW.

3.3.1 Electrochemical Impedance Spectroscopy (EIS)

EIS (electrochemical impedance spectroscopy) was carried out in potentiostatic mode after an hour of monitoring the OCP (open circuit potential). A sinusoidal waveform with amplitude 10 mV was applied about the OCP for the frequency range 0.1 – 10k Hz. Echem Analyst software (Gamry, USA) was then used to execute a Kramers-Kronig transform (KKT) on the obtained data and confirm it to be linear, stable, and causal. Only data sets that met this criterion were considered as viable repeats. The same software was then used to develop and fit an equivalent circuit model to the data. Models that did not return sufficient fits were discarded. The results are given as the average and standard deviation of 5 repeats.

3.3.2 Cyclic Voltammetry

CV (cyclic voltammetry) measurements were carried out by sweeping the electrode voltage between its electrolysis limits, i.e., within its water window (WW). The limits were established via linear sweep voltammetry, in which the potential was varied at a rate of 0.05 Vs^{-1} in the cathodic and anodic directions with respect to the OCP. The potentials at which rapidly increasing current was observed were taken to be the electrode's electrolysis limits. CV tests were then conducted at sweep rates of v = 0.05, 0.1, 0.5, and 1 Vs^{-1}. The last cycle from 10 consecutive cycles was chosen for analysis to ensure electrode stabilisation. The cathodic charge storage capacity (CSC_C) was then derived by integrating the area bounded by the cathodic sweep and the 0-current line as per Equation 2.10. The results are given as the average and standard deviation of 5 repeats.

3.3.3 Cyclic Lifetime Assessments

Cyclic lifetime assessments were carried out by subjecting the electrodes to 10,000 consecutive CV cycles at sweep rates of v = 0.1 and 1 Vs^{-1}, within the WW. EIS measurements were carried out at the beginning of the cycling regiment and after every 1,000 cycles according to the EIS test description given in section 3.3.1 (including OCP monitoring). The CSC_C (from CV tests) and the variables obtained from equivalent circuit modelling (from EIS tests) were plotted against cycle number to track electrode performance. Micro-Raman spectroscopy was then carried out on the cycled electrodes

to assess any changes imparted by cycling. The tests were carried out in repeats of 5, except for extended WW tests for $PP_{17.5}$, which were carried out in repeats of 3.

3.3.4 24-Hour Immersion Tests

24-Hour immersion tests were carried out in protein-containing electrolytes and consisted of EIS measurements made every 4-hour period. The measurements were taken as per the process description given in section 3.3.1 (including OCP monitoring). The variables obtained from equivalent circuit modelling were plotted against hours of immersion to track electrode performance. The results are given as the average and standard deviation of 5 repeats.

3.4 Assessing Adhesion of PEDOT:PSS to TiN_{IV}

$PP_{17.5}$ electrodes were subjected to 45 minutes of ultrasonication in order to assess the adhesion of the PEDOT:PSS layer to the underlying TiN_{IV}. An electrochemical cell was designed using a polypropylene (PP) vessel with a screw-on lid, into which 3 holes were drilled and fitted with hollow rubber stoppers (Figure 3.9). The insulated wire of a Type II electrode (here acting as the WE) was bent upwards and fed through one of the rubber stoppers as shown in the figure. The coiled Pt wire and SCE as described in section 3.3 were applied as the CE and RE, respectively. The bridge tube was not included in these experiments. The cell was filled with 80 ml of PBS and placed inside the DI water bath of a US-10SD ultrasonic cleaner (Biobase, China). The temperature of the DI water was maintained at 37 ± 2^{o} C, thus keeping the PBS solution at the same physiological temperature.

The experiment consisted of 45 minutes of ultrasonication at a frequency of 45 kHz with intermittent EIS measurements (section 3.3.1) carried out every 5 minutes. The OCP monitoring for these tests was limited to only 10 minutes. Optical micrographs were taken of the electrode surface after every 5 minutes of ultrasonication. It was ensured that the RE and CE were taken out of the assembly and that the WE was touching the bottom of the vessel whenever ultrasonication was underway.

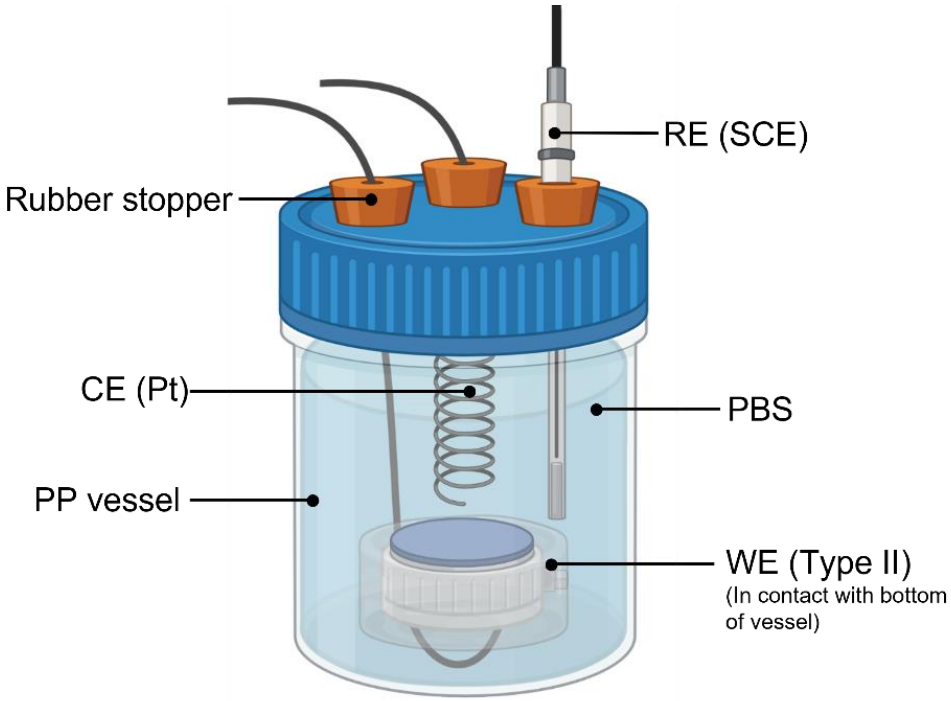

Figure 3.9: Diagram of the electrochemical cell used in ultrasonication experiments for $PP_{17.5}$ electrodes (Type II). Diagram created on Biorender.com.

3.5 CA Dissolution Assessment

Five CA_{60s} gels were developed onto Type III electrodes (method described in section 3.1.6) with an exposed area of diameter 10 mm (refer to Figure 3.3 c). After 30 minutes of immersion in the 0.1 mM $CaCl_2$ hardening solution, the electrodes were left to sit in DI water for a further 30 minutes to wash away any remaining unbound calcium ions. The electrodes were then sterilized by 1 hour of immersion in 70% IPA solution (Sigma Aldrich, USA), rinsed with sterile PBS (Oxoid, UK), and transferred to sterile 6-well plates (CytoOne, USA) under a Fast V laminar flow hood (Dasit Group, Italy). 3ml of sterile PBS (Oxoid, UK) was then added to the well of each electrode (herein referred to as CA Wells) and to 5 more blank wells to act as controls (herein referred to as BLNK Wells). The plates were then incubated (Leec, UK) at a temperature of 37°C, a relative humidity of 95%, and a CO_2 concentration of 5%.

The moles of Ca dissolved in solution were assessed every day for the first 5 days and then twice a week for up to 35 days. This was done using a solution of the Ca-sensitive dye Arsenazo III (1, 8-Dihydroxy-3, 6-disulpho-2, 7-naphthalene-bis(azo)-dibenzenearsonic acid) which changes colour from blue to dark purple when it complexes with calcium. Separate stock solutions were made of 1 mM Arsenazo III

(Tokyo Chemicals, Japan) and 0.1 M Imidazole buffer (Tokyo Chemicals, Japan). Reference molarity solutions of 0.0975 mM, 0.195 mM, 0.39 mM, 0.78 mM, and 1.56 mM were also made using $CaCl_2$ (Avantor Performance Materials, USA) dissolved in DI water. For each day that a reading was performed, a bulk solution was made up containing:

- 18.75 ml of the 0.1 M Imidazole Buffer solution
- 1.875 ml of the 1 mM Arsenazo III solution, and
- 24.375 ml of DI water

3 ml of solution was then pipetted into 15 fresh wells of 6-well plates (herein referred to as complexation wells). Closed plates containing the BLNK and CA wells were removed from the incubator and gently agitated on an orbital plate shaker (Eppendorf, USA) for 1 minute to ensure homogeneous distribution of Ca^{2+} ions in solution. Each well then had 125 µL of its solution sampled and transferred to one of the complexation wells under sterile conditions. A fresh 125 µL of sterile PBS was added back to the CA and BLNK wells to maintain a total volume of 3 ml throughout the experiment duration. 125 µL were also pipetted from each of the 5 calibration molarity solutions and transferred to the remaining 5 complexation wells. The plates were then gently agitated for 15 minutes using the same orbital plate shaker.

After the 15 minutes had elapsed, 5 samples of 120 µL were pipetted from each complexation well into a 96-well plate (CytoOne, USA) (herein referred to as spectro-wells, 75 total). The plates were then transferred to a SPECTROstar Nano spectrophotometer (BMG Labtech, Germany) where absorbance peaks were read at a wavelength of 650 nm. This process is illustrated in Figure 3.10. The average intensity from the 5x 120 µL spectrophotometry wells was calculated to account for experimental error, and constituted as the intensity reading for one of the repeats (i.e., one complexation well). The average and standard deviation for CA and Blank wells was then calculated from these values. The reference solutions of $CaCl_2$ were used to correlate the intensity measurements to moles of Ca.

Cumulative summation was used to account for the 125 µL of solution lost to sampling each day. The total moles on day N ($M_T\ on\ D_n$) were calculated using Equation 3.1:

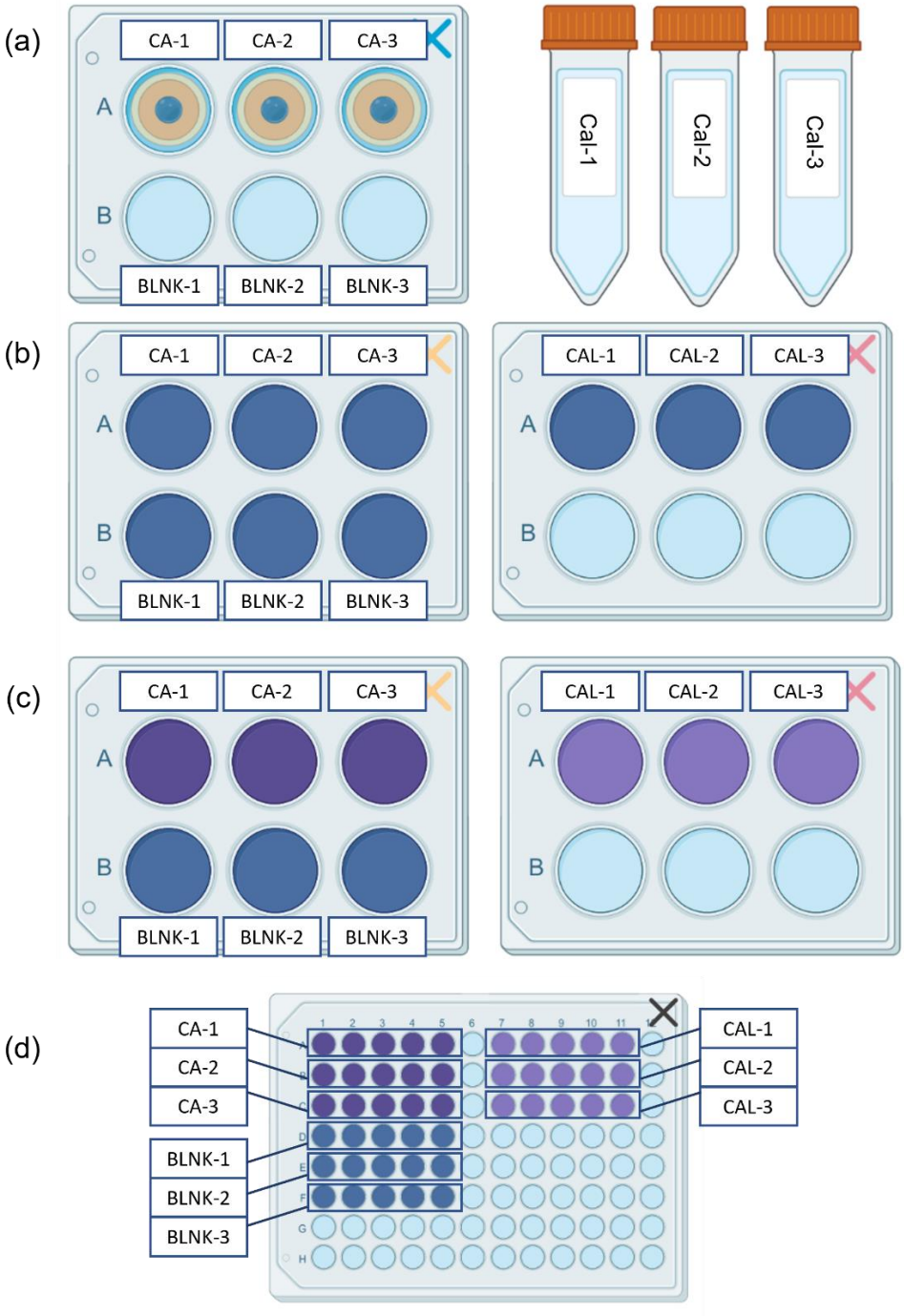

Figure 3.10: Schematic of the process by which the number of moles released from the CA_{60s} electrodes was quantified. The illustration shows the electrodes (CA) and blanks (BLNK) in repeats of 3 rather than 5. 3 calibration solutions (CAL) are also shown rather than 5: (a) The CA electrodes and the blanks (BLNK) in their wells, taken out of the incubator. The vials of calibration solutions (CAL) are also shown; (b) Nine new wells (complexation wells) are filled with Ca-indicator solution (Arsenazo III, Imidazole, and DI water); (c) 125 µL is then sampled from each CA well, BLNK well, and CAL tube, and added to their respective complexation well. Complexation is complete after 15 minutes. (d) Five 120 µL samples are taken from each complexation well and transferred to spectro-wells for absorbance measurements. Crosses of the same colour (top-right corners of wells) indicate the same plate at different timepoints. Diagram created on Biorender.com.

$$M_T \; on \; D_n = M_S \; on \; D_n + M_{125\mu L} \; on \; D_{n-1} + \; M_{125\mu L} \; on \; D_{n-2} + \cdots \qquad (3.1)$$

Where M_S is the number of moles detected in solution, and $M_{125\mu L}$ is the number of moles lost to the 125 µL sample. The moles of calcium were then plotted against number of days in solution to characterise the electrode's degradation profile.

At the end of the experiment, the CA_{60s} electrodes were imaged using stereo microscopy (refer to section 3.2.1) to identify any remaining gel on the surface. Residual gel was removed by 1 minute of ultrasonication in a 1M solution of NaCl and cleaned by another minute of ultrasonication in DI water. The electrodes were then dried in air and re-impregnated with PBS in vacuum (0.5 bar) for EIS measurements (refer to section 3.3.1).

3.6 Cell Culture Experiments

3.6.1 Protocols

3.6.1.1 General Cell Growth and Culture

Two different cell types were used in this work, both purchases from ATCC, USA:

1. Neonatal human dermal fibroblasts (NHDF), primary cells
2. SH-SY5Y human neuroblastoma cell line (a subline, thrice cloned from the SK-N-SH cell line)

The NHDF cells were received frozen and thawed into their culture media. The SH-SY5Y cells were donated by G. Vassallo Eminyan (University of Malta) and received at passage number 10 (P10) in a T75 flask (Orange Scientific, Belgium). Both cell types were grown for a number of weeks in T75 flasks in their respective media (Table 3.4) and subcultured every few days following a trypsinisation procedure (refer to section 3.6.1.2). The cells were kept in an incubator (Leec, UK) at a temperature of 37°C, a relative humidity of 95%, and a CO_2 concentration of 5%. A stock of NHDF cells at P14 was built up in this way, where the cells were then frozen at -80° C for short-term storage (< 2 months), or in liquid nitrogen for long-term cryogenic storage. A stock of SH-SY5Y cells at P12 was also developed, where the cells were kept frozen at -80° C for short-term storage only (< 2 months).

Table 3.4: Details on the cell culture media used for NHDF and SH-SY5Y cells. Media Formulations are given in Appendix A.

Cell Type	Culture Medium	Serum	Antibiotic
NHDF	Dulbecco's Modified Eagle's Medium (DMEM), high glucose (Sigma Aldrich, USA)	10% Foetal Bovine Serum (FBS) Solution (PAN Biotech, Germany)	0.1 % Penicillin-Streptomycin (P/S) (Sigma Aldrich, USA)
SH-SY5Y	1:1 ratio of DMEM:F12 Medium (Biowest, France)		

3.6.1.2 Subculture by Trypsinisation

Cells were subcultured when reaching a confluency of 90% and 70% for the NHDF and SH-SY5Y, respectively. An EVOS XL Core inverted microscope (Invitrogen, USA) was used to observe the cells for confluency and contamination. Inside a laminar flow hood (Dasit Group, Italy), the media in the flask was discarded and replaced with 5 ml of sterile PBS (Oxoid, UK). The PBS was gently swirled around the flask to wash the cells of any remaining media and then discarded. 5 ml of trypsin solution (1% in PBS) (Gibco, USA) was placed in the flask, which was then transferred to the incubator for 5 minutes. After the time had elapsed, the trypsin had broken down the cell-to-flask and cell-to-cell bonds, allowing the cells to lift into suspension. The trypsin was quenched with 5 ml of the cells' respective completed media and the contents of the flask transferred to a sterile centrifuge tube (Isolab, Germany). The cells were then spun at 1500 rpm for 5 minutes in a 5810 Centrifuge (Eppendorf, Germany). The supernatant liquid was discarded, and the pellet of cells resuspended in fresh completed medium. The NHDF were subcultured at a 1:2 ratio, whereas the SH-SY5Y were subcultured at a ratio of 1:10.

3.6.1.3 Freezing and Thawing

Cells were frozen down for storage in order to build up a stock supply of vials at the same passage. In this way, all the cell culture tests could be conducted with cells at the same passage, thus avoiding the introduction of unnecessary variability. Upon reaching confluency, the cells were collected using trypsinisation and the pellet resuspended in 1 ml of FBS liquid. After transferring to a cryovial, 100 µL of sterile cryoprotectant Di-methyl Sulfoxide (DMSO) (Sigma Aldrich, USA) was added and the vial was immediately placed in a -80 ^{o}C freezer (Fryka, Germany) for up to 2 months. For long-term storage, the frozen vials were moved to a liquid nitrogen tank (Taylore Wharton, USA).

When needed, a vial was brought out from freezing and thawed in a 37^{o} C water bath. The contents were then added to a centrifuge tube containing 10 ml of media. The tube was capped, gently agitated, and spun in a centrifuge (see section 3.6.1.2 for details). The pellet was then resuspended in fresh medium and the process repeated. This was done to ensure minimal amounts of cryoprotectant remained. The cells were then cultured in a T27 flask with their respective media.

3.6.1.4 Resazurin Reduction – Cell Viability Measurements

Cell viability was assessed using a resazurin reduction assay. In solution, resazurin appears blue and permeates cells where it gets metabolized by viable cells to resorufin, a red compound. The colour change is then measured using spectrophotometry and correlated with the relative number of viable cells in culture [363]. Resazurin solutions are non-toxic to viable cells, unlike tetrazolium dyes such as MTT, and do not require cell lysis steps like luciferase-based ATP assays [364]. A 1 L stock of resazurin solution was made by dissolving 0.15 mg of resazurin sodium salt (Tokyo Chemicals, Japan) per 1 ml of PBS. The solution was then split into 50 ml opaque bottles and stored frozen at -20^{o} C. The bottles were protected from light and thawed only when needed. Thawed solutions were either used up within a week or discarded.

To measure cell viability, the samples and/or electrodes with cell growth were transferred to fresh new wells under sterile conditions. This was done to exclude cells growing on the plastic of the wells from the measurement. Each well, plus 5 extra blank wells, were then filled with a 1:6 ratio of resazurin solution: culture medium. The plates were then placed in an incubator for 2 hours for resazurin reduction to take place. After the time had elapsed, the electrodes and/or samples were transferred back to their original wells and incubated if the experiment was still underway, or to PBS for rinsing and fixing if the experiment was at its end (section 3.6.4).

Five 120 µL samples could then be taken from each resazurin-containing well and transferred to a 96-well plate for spectrophotometry on a microplate reader (Tecan, Switzerland). The five samples were taken to obtain an average from each original resazurin well (i.e., electrode and/or sample) to account for experimental error, and act as technical replicates. The absorbance of the wells was read at wavelengths of 570 (the test wavelength) and 600 nm (the reference wavelength). For each well, the absorbance

at 600 nm ($Absorbance_{600}$) was subtracted from the absorbance at 570 nm ($Absorbance_{570}$) to get the absolute absorbance of the well ($AbsWell_x$), as per Equation 3.2:

$$AbsWell_x = (Absorbance_{570} - Absorbance_{600}) \qquad \text{Equation (3.2)}$$

The average absolute absorbance for blank wells (Avg_{blank}) was then calculated, and the corrected absorbance of each well ($CorrAbsWell_x$) could be found according to Equation 3.3:

$$CorrAbsWell_x = AbsWell_x - Avg_{blank} \qquad \text{Equation (3.3)}$$

From this, the average corrected absorbance value of each sample/electrode ($AbsSample_x$) could be calculated, along with the average and standard deviation for each sample/electrode category. When presented as a bar graph, the maximum average corrected absorbance value obtained throughout the experiment ($AbsSample_{max}$) was given a value of 1, and all other absorbance values (x) were normalised with respect to it according to Equation 3.4 [365]:

$$x = \frac{AbsSample_x \times 1}{AbsSample_{max}} \qquad \text{Equation (3.4)}$$

The absorbance spectrum for resazurin in its oxidised and reduced (resorufin) states is given in Appendix D.

3.6.1.5 Neural Differentiation with All-Trans Retinoic Acid

At ~ 70% confluency, the SH-SY5Y neuroblastomas could be differentiated into neural-like cells. The medium was first removed, and the cells rinsed with PBS. Special care was taken to direct the jet of liquid away from the adhered cells. DMEM:F12 medium was then added, containing the same 0.1% of P/S but no FBS. 1 µL of ATRA (all-trans-Retinoic acid) solution (10 mM concentration) (Sigma Aldrich, USA) was also added per 1 ml of medium. The cells were then incubated for 72 hours, after which they were assessed on an inverted microscope. This protocol was adapted from the works of Shipley *et al.* [366] and Kovalevich *et al.* [367].

3.6.2 Fibroblast Fouling Assessment

Fibroblast fouling assessments were carried out on the TiN, $PP_{17.5}$, and CA_{60s} electrodes. The electrodes were sterilized by immersion in 70% IPA solution for 30 minutes, followed by immersion in sterile PBS for a further 30 minutes to remove any alcohol remnants. The experimental set-up is summarized in Table 3.5. In each experiment, every electrode or sample was tested in repeats of 5. The experiment would then be replicated at a later date. The results from the 2 replicate experiments would then be pooled, basing the average and standard deviation on a sample size of n = 10. Electrodes of Type III were used with 6-well plates for test number 1 (and its replicate), whereas electrodes of Type IV were used with 12-well plates for tests number 2 and 3 (and their replicates).

Table 3.5: Summary of the experimental set-up for fibroblast fouling assessments.

Test No.	Electrodes Involved	No. of Each Electrode/ Sample	Electrode Type	Size of Well-Plate	Volume of Media/well (mL)	Total No. of Wells Used/ Experiment	Replicates of Experiment
1	TiN_I TiN_{II} TiN_{III} TiN_{IV}	5	III	6	3	20	2
2	TiN_{IV} $PP_{17.5}$	5	IV	12	2.5	10	2
3	$PP_{17.5}$ CA_{60s}	5	IV	12	2.5	10	2

NHDF cells at P14 were thawed and cultured until 90% confluent. The trypsinisation protocol was then performed and the pellet resuspended in 2ml of medium. Using a haemocytometer (Hirschmann, Germany), the cells were counted and pipetted onto the centre of the surface of the electrodes at a density of 8×10^4 cells/cm^2. After 5 minutes, in which the cells were given some time to adhere, a volume of culture medium was added depending on the size of the well plate (refer to Table 3.5). The plates were then moved to an incubator and cell viability measurements were performed after 24, 48, and 72 hours. A schematic showing this process is given in Figure 3.11.

In the case of test number 1 (and its replicate), the resazurin indicator solution was added in a different way than it was in tests number 2 and 3 (and their replicates). In the latter

cases, a bulk solution was made with a 1:6 ratio of resazurin solution: culture medium. The required volume (2.5 ml) was then pipetted into each well. In test number 1 (and its replicate), 2.5 ml of media and 0.5 ml of resazurin solution were separately added to each individual well, potentially introducing an additional source of error.

Statistical significance between groups was established using one-way ANOVA and a post-hoc Tukey test. Significance was considered if $p < 0.05$.

3.6.3 Neuroblastoma Adhesion and Differentiation Assessment

Neuroblastoma adhesion and differentiation assessments were carried out on the TiNIV, $PP_{17.5}$, and CA_{60s} electrodes. Thermanox cell culture plastic slips (TMO) (NUNC, USA) of the same area as the electrodes were also employed as controls. The electrodes and slips were sterilized by immersion in 70% IPA solution for 30 minutes, followed by immersion in sterile PBS for a further 30 minutes to remove any alcohol remnants. The experimental set-up is summarized in Table 3.5. In each experiment, every electrode or slip was tested in repeats of 5. The experiment would then be replicated at a later date. The results from the 2 replicate experiments would then be pooled, basing the average and standard deviation on a sample size of n = 10. Electrodes of Type IV were used.

Table 3.6: Summary of the experimental set-up for neuroblastoma adhesion and differentiation assessments.

Test No.	Electrodes Involved	No. of Each Electrode/ Sample	Electrode Type	Size of Well-Plate	Volume of Media/well (mL)	Total No. of Wells Used/ Experiment	Replicates of Experiment
1	TiN_{IV} $PP_{17.5}$ CA_{60s} TMO	5	IV	12	2.5	20	2

SH-SY5Y cells at P12 were thawed and cultured until confluent. The trypsinisation protocol was then performed and the pellet resuspended in 2ml of medium. Using a haemocytometer (Hirschmann, Germany), the cells were counted and pipetted onto the centre of the surface of the electrodes and TMO slips at a density of 1×10^5 cells/cm^2. After 5 minutes, in which the cells were given some time to adhere, a volume of culture medium was added depending on the size of the well plate (refer to Table 3.5). The plates were then moved to an incubator for 72 hours. The medium was refreshed at the 48-hour time-point.

After 72 hours the medium was removed, and the cells gently washed with PBS. New medium was mixed, containing the same 0.1% of P/S but no FBS. 1 µL of ATRA (all-trans-Retinoic acid) solution (10 mM concentration) (Sigma Aldrich, USA) was also added per 1 ml of medium. The medium was then pipetted and the plates put back in the incubator for another 72 hours. The medium was again refreshed at the 48-hour time-point. Cell viability measurements were performed after the 72 hours had elapsed.

3.6.4 Cell Fixing

The substrates used for fibroblast fouling and neural differentiation assessments (sections 3.6.2 and 3.6.3, respectively) were imaged using SEM (refer to section 3.2.1 for details on SEM imaging). The cells thus required a fixing process to preserve their morphology. The samples were first rinsed with PBS and then each immersed in 3 ml of fixing solution containing 1.2 ml of DI water, 1.5 ml of 0.2 M Sodium Cacodylate solution (Fisher Scientific, USA), and 0.3 ml of Glutaraldehyde (25 %) (Acros Organics, USA). After 10 minutes the solution was replaced with 3 ml of 0.1 M Sodium Cacodylate solution and left to sit for the same amount of time. Following this, a gradual dehydration procedure was performed in which the samples were sequentially immersed in aqueous solutions of ethanol (Fisher Scientific, USA) of increasing concentration (25, 50, 60, 70, 80, 90, and 100%). Each step lasted 10 minutes. In a fume hood, the samples were then placed in 1,1,1,3,3,3-Hexamethyldisilazane (Tokyo Chemicals, Japan) for another 10 minutes, and then left to dry for an hour. Once dried, the samples were mounted onto Al stubs using conductive carbon tape and sputtered with a nanometric coating of Au. This was done to avoid surface charging and to obtain higher resolution SEM images.

3.7 Statistical Methods

The statistical tests used in this work were carried out using SPSS software, version 20.0 (SPSS Inc., USA). Statistical significance between groups was established using one-way ANOVA and a post-hoc Tukey test in the case of three or more groups, and t-tests in the case of two groups. Trends of statistical significance were established using Pearson's Correlation coefficient. In both cases, significance was considered if $p < 0.05$. A summary of the analytical tests used to determine statistical significance is given in Table 3.7.

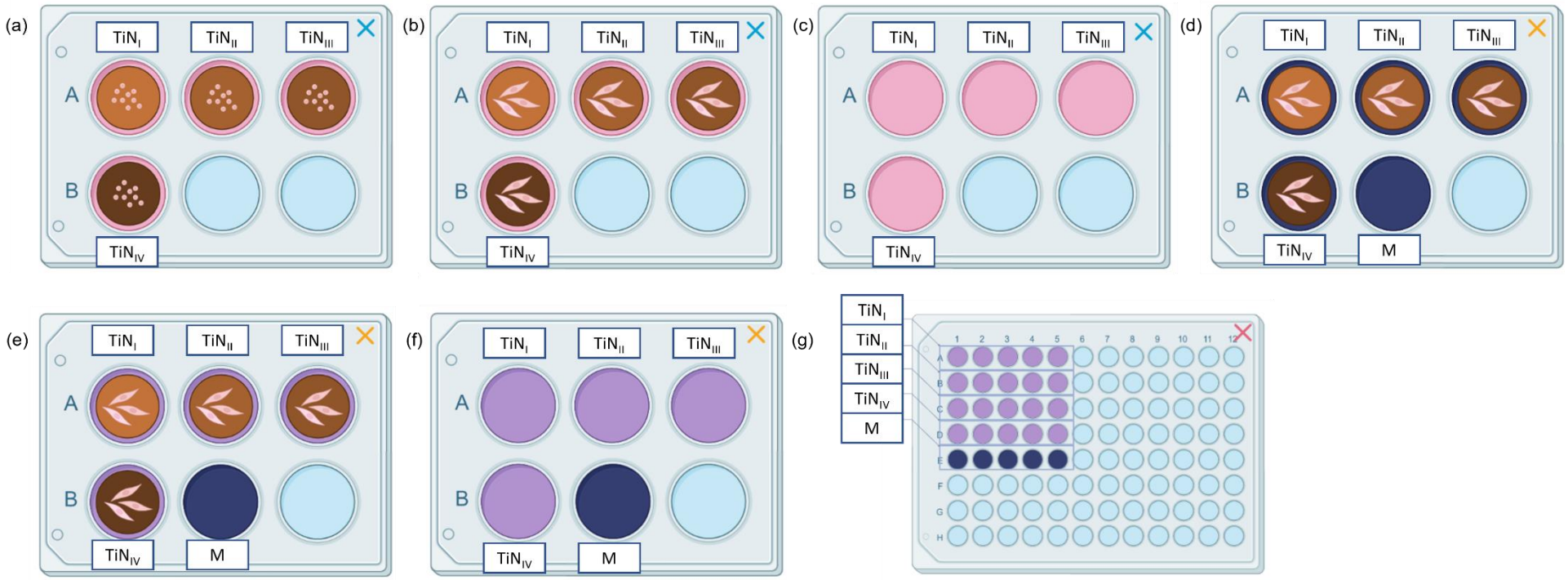

Figure 3.11: A schematic showing cell viability measurements. The example given illustrates a fibroblast fouling experiment on TiN electrodes: (a) Fibroblasts are cultured on the electrode surfaces and incubated; (b) After 24 hours the plate is taken out of the incubator and the cells have grown; (c) The electrodes are transferred to a new plate (d) and indicator solution (resazurin + medium) is added to the wells. An extra well labelled 'M' (i.e., medium only) is also filled; (e) After 2 hours in the incubator, the resazurin reduction reaction is complete; (f) The electrodes are removed from the indicator solution and placed back in their original wells; (g) Five 120 µL samples are taken from each well and transferred to a 96-well plate for spectrophotometry. Crosses of the same colour (top-right corners of wells) indicate the same plate at different timepoints during the experiment. For any given experiment, each condition is done in repeats of 5, and each experiment is replicated twice. Diagram created on Biorender.com.

Table 3.7: Summary of analytical tests used to determine statistical significance. In all cases, significance is considered if $p<0.05$.

Element being tested for Significance	**One-way ANOVA + Post-hoc Tukey Test (3 groups or more)**	**t-Test (2 groups)**	**Pearson's Correlation (Trend)**
Differences arising from electrochemical tests: • Values of |Z| and circuit model elements arising from EIS measurements; • Values of CSC_C arising from CV measurements	✓		
Differences in relative Raman intensity measurements (before and after 10,000 CV cycles)		✓	
Differences in relative intensity measurements (made using spectrophotometry) obtained from cell viability tests (representing relative number of viable cells)	✓		
Differences in surface roughness values from optical profilometry measurements	✓		
Differences in layer thickness values observed using SEM, optical, or stereo microscopy	✓		
Trends observed in the values of CSC_C, |Z|, and circuit model elements (from CV and EIS tests) made during: • 10,000 CV cycle analysis • 24 hours of immersion in protein-containing electrolyte • 45 minutes of ultrasonication			✓
Trends observed in relative intensity measurements (made using spectrophotometry) during CA gel dissolution experiments			✓

4 Results

4.1 Characterization of TiN_I

4.1.1 Topography and Imaging

Polished Ti6Al4V substrates were coated with a TiN layer using PVD (method outlined in section 3.1.3) to produce TiN_I electrodes. Optical profilometry measurements (method outlined in section 3.2.6) for the electrode surfaces are given in Table 4.1. SEM imaging revealed a uniform rough and porous morphology with sparse overgrowth defects, a few of which are visible in Figure 4.1 a. Pyramidal structures with maximum approximate dimensions of 500 nm (Figure 4.1 b and c) were observed to crown tapered, disaggregated columns. The columns exhibit a de-densification effect as the distance from the coating/substrate interface increases (Figure 4.1 d). The average coating thickness based on 5 electrodes (method outlined in section 3.2.5.1) was measured at 9.5 ± 0.8 µm.

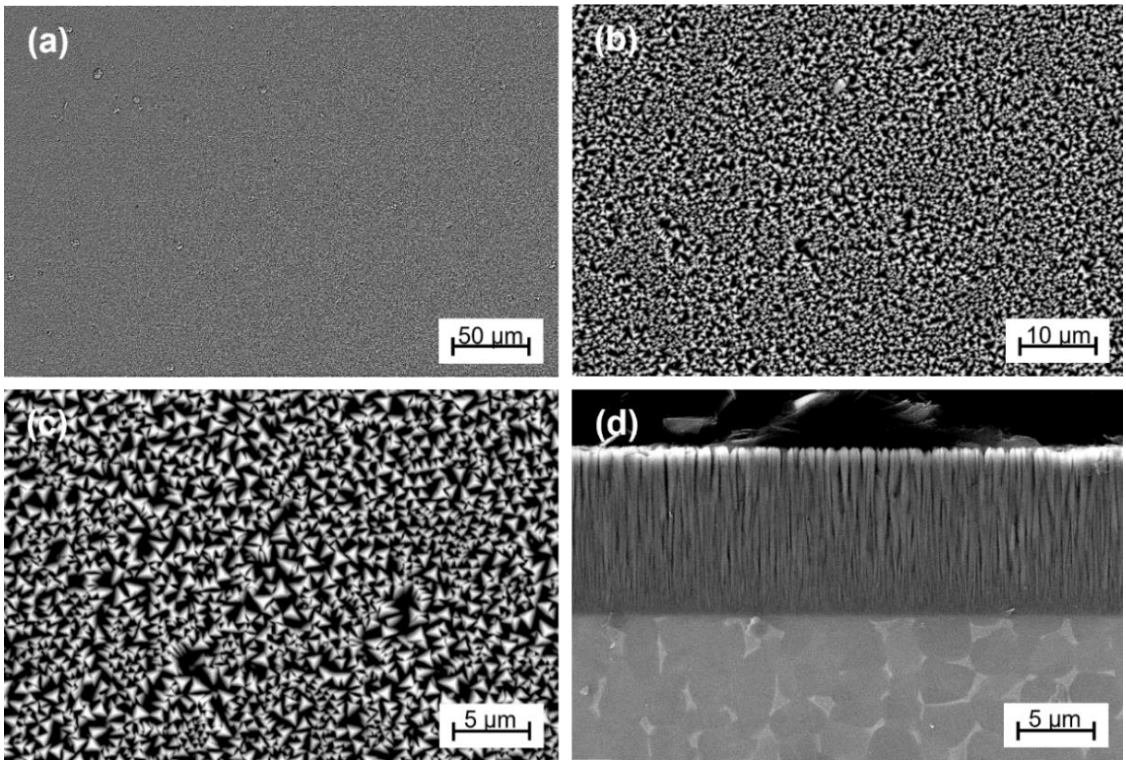

Figure 4.1: Topographic SEM images of TiN_I electrodes at 1k x (a), 5k x (b), and 10k x (c) magnification. A cross-section image of the electrode is also given at a magnification of 10k x (d). (b-d) adapted from Arpa *et al.* [368].

Table 4.1: Optical profilometry measurements for TiN_I electrode surfaces, based on a 10x10 mm sampling area and a 0.8 mm gaussian cut-off limit. The average and standard deviation of 3 electrode surfaces is given.

Variable (in µm)	TiN_I
Roughness Average, R_a	0.1 ± 0.02
RMS Roughness, R_q	0.2 ± 0.03
Max. Profile Peak Height, R_p	1.5 ± 0.4
Max. Profile Valley Depth, R_v	1.5 ± 0.2
Max. Total Height of the Profile, R_t	3.1 ± 1.0

4.1.2 X-Ray Diffraction and Micro-Raman Spectroscopy

A representative Bragg-Brentano XRD spectrum for TiNI electrodes is given in Figure 4.2 a for the range $30^o < 2\theta < 80^o$. Two sharp, distinct peaks (numbered 1 and 2 on the figure) were identified and their positions of 2θ are detailed in Table 4.2.

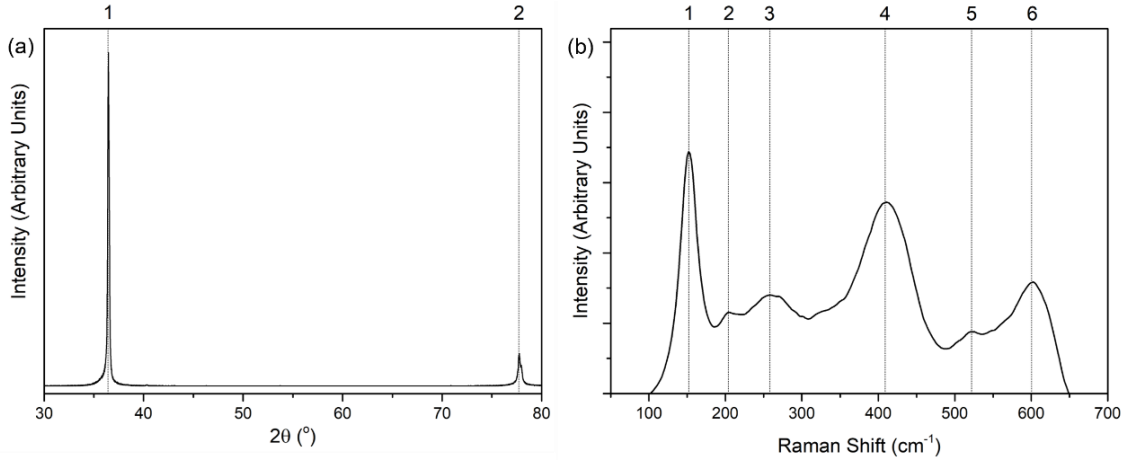

Figure 4.2: Representative (a) Bragg-Brentano X-ray diffractograms obtained using a CuKα radiation source (λ = 1.5406 Å) and; (b) Micro-Raman spectra of TiN_I electrodes obtained using a green light laser (λ = 532 nm). Numbered lines indicate notable peaks emerging from the spectra, where the corresponding 2θ angles and Raman shifts are given in Table 4.2 and Table 4.3, respectively. From Arpa *et al.* [368].

A representative micro-Raman spectrum for the TiNI electrodes, collected using a 532 nm λ green light laser, is shown in Figure 4.2 b for the range 50-700 cm^{-1}. Six prominent peaks (numbered 1-6 on the figure) were identified, and their respective Raman shifts are detailed in Table 4.3. The shifts were calculated from an average of 3 spectra for 5 different electrodes.

Table 4.2: XRD peaks and their respective angles of 2θ as identified in Figure 4.2 a.

Peak No.	2θ (°)
1	36.46
2	77.74

Table 4.3: Raman peaks and their respective shifts as identified in Figure 4.2 b.

Peak No.	Raman Shift (cm^{-1})
1	152
2	205
3	260
4	410
5	519
6	601

4.1.3 Electrochemical Testing in Physiological and Organic (Non-Protonated) Electrolytes

TiN_I electrodes were subjected to identical electrochemical tests in a protonated, physiological electrolyte (PBS), and a non-protonated, organic electrolyte (a 1M solution of Et_4NBF_4 in AN) to differentiate between double-layer and pseudocapacitive ability (method outlined in section 3.3). Representative Bode and Nyquist plots for both conditions are shown in Figure 4.3, where the values for impedance are normalised to 1 cm^2. The equivalent circuits used to model the spectra are given in Figure 4.4 a and b for tests conducted in PBS and AN, respectively. A simple Randles circuit was sufficient to model AN spectra made up of a parallel arrangement between resistance to faradaic charge transfer (R_f) and double-layer capacitance (CPE_{dl}), both in series with solution resistance (R_s). Rather than a standard capacitor, a constant phase element described by the variables Y_{dl} and α_{dl} was employed to account for non-ideal behaviour.

Due to incongruency in the low-frequency domain, an identical circuit could not be used to model spectra obtained in PBS. Initial trials in which a Warburg impedance (of both the bounded and infinite variety) was included in series with R_f did not return convergent fits ($\chi^2 >> 0.001$), and so the circuit model was discarded. The Warburg impedance was instead replaced by a constant phase element representing pseudocapacitance (CPE_{pseu}), further defined by the variables Y_{pseu} and α_{pseu}. Convergent fits were then successfully obtained using this model. The results obtained from fitting the equivalent circuits, as well as the $|Z|_{1Hz}$, are given in Table 4.4.

Cyclic voltammetry measurements at scan rates of 0.05, 0.1, 0.5, and 1 Vs^{-1} were also conducted in both electrolytes. The electrolysis limits were found to be -0.6 and 0.9 V *vs* SCE and all voltammetry scans were carried out within that window. Representative voltammograms are shown in Figure 4.5 where current density is plotted against the potential given with respect to the SCE. The corresponding average CSC_C measurements are listed in Table 4.5, where the values obtained in PBS are consistently higher than those measured in AN at all sweep rates.

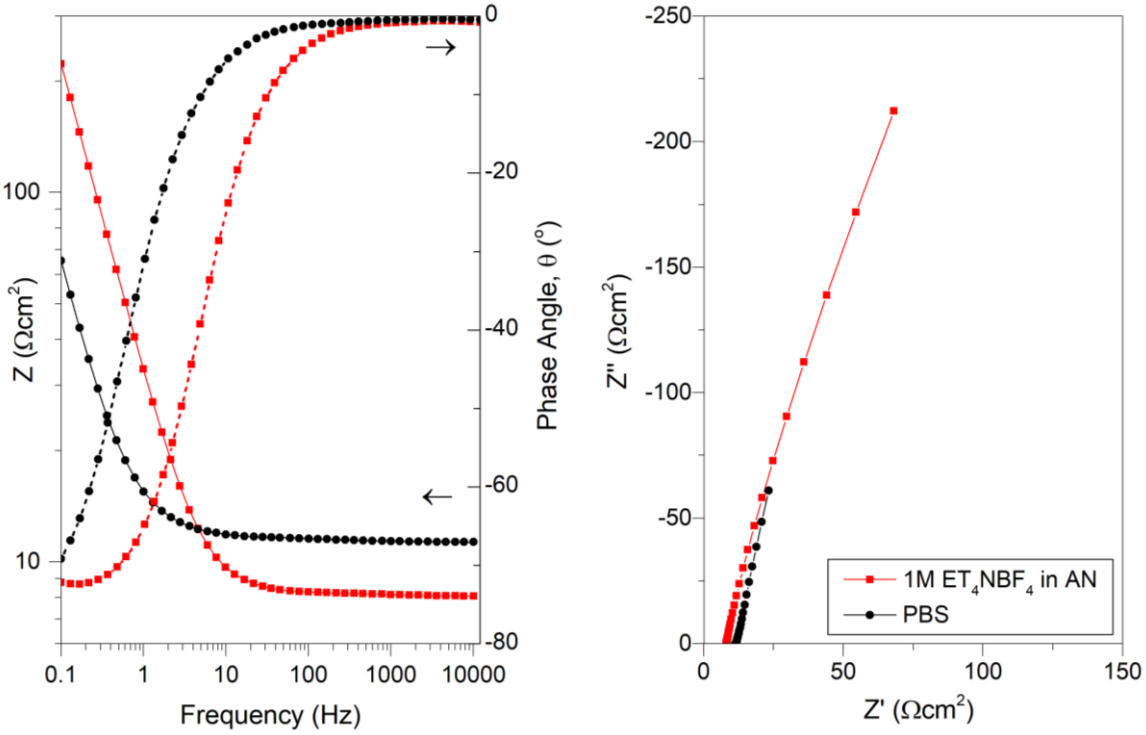

Figure 4.3: Representative impedance and phase angle Bode plots (left) and Nyquist plots (right) for TiN_I electrodes measured in PBS (black) and a 1M solution of Et_4NBF_4 in AN (red). From Arpa *et al.* [368].

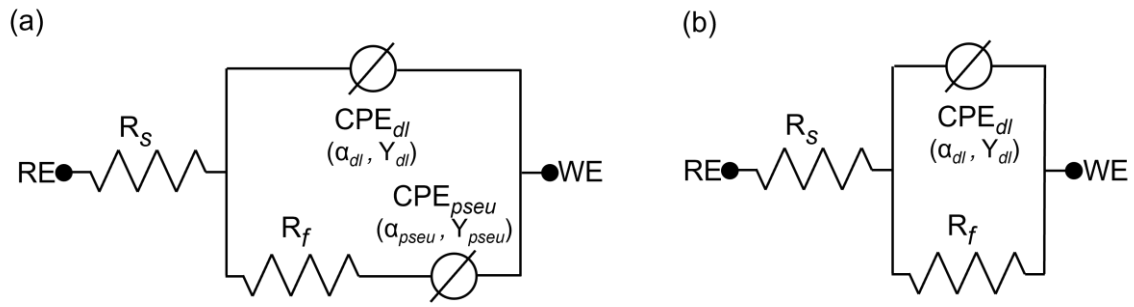

Figure 4.4: The equivalent circuit models used to fit the EIS spectra obtained for TiN_I electrodes tested in PBS (a) and in a 1M solution of Et_4NBF_4 in AN (b). From Arpa *et al.* [368].

Table 4.4: Results of fitting the EIS spectra obtained for TiN_I electrodes tested in PBS and 1M Et_4NBF_4 in AN (Figure 4.3) to the equivalent circuit model given in Figure 4.4 a and b, respectively. The $|Z|_{1Hz}$ is also given. Results are given as the average of 5 repeated readings with standard deviation from the mean.

Circuit Element	Units	PBS	1M Et4NBF4 in AN
R_s	Ωcm^2	14.9 ± 3.1	7.6 ± 0.4
R_f	Ωcm^2	1.5 ± 0.5	2537.9 ± 840
Y_{dl}	$mSs^{\alpha}cm^{-2}$	3.9 ± 0.7	7.1 ± 2.7
α_{dl}	/	0.855 ± 0.024	0.868 ± 0.019
Y_{pseu}	$mSs^{\alpha}cm^{-2}$	14.7 ± 3	/
α_{pseu}	/	0.879 ± 0.007	/
$\|Z\|_{1Hz}$	Ωcm^2	17.8 ± 2.1	30 ± 3.7

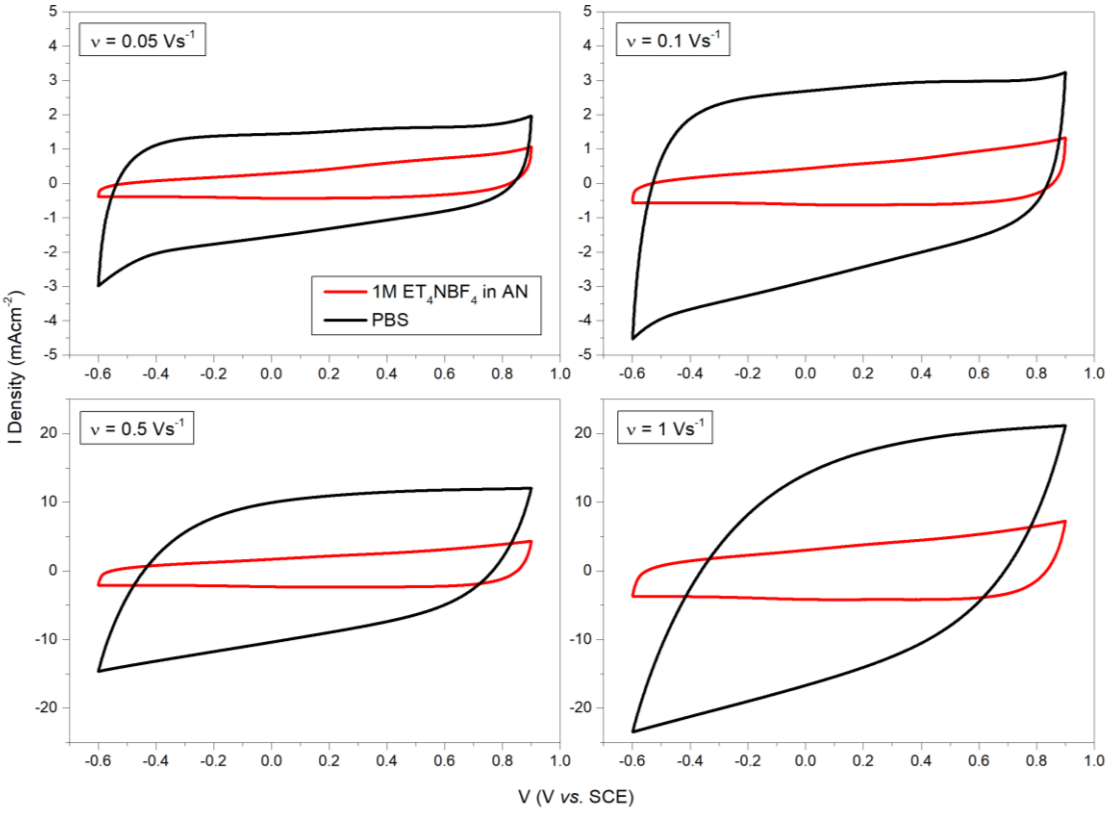

Figure 4.5: Representative voltammograms for TiN_I electrodes measured at different sweep rates of v in PBS (black) and a 1M solution of Et_4NBF_4 in AN (red). From Arpa *et al.* [368].

Table 4.5: The CSC_C for TiN_I electrodes measured at different sweep rates of v in PBS and a 1M solution of Et_4NBF_4 in AN. Results show the average and standard deviation of 5 repeated readings.

	CSC_C ($mCcm^{-2}$)	
v (Vs^{-1})	PBS	1M Et4NBF4 in AN
0.05	53 ± 6	11 ± 3
0.1	46 ± 5	9 ± 2
0.5	30 ± 3	7 ± 1
1	22 ± 3	6 ± 1

4.1.4 Cycling Lifetime

The cycling lifetime of TiN_I electrodes was assessed in PBS by subjecting them to 10,000 consecutive CV cycles at ν= 0.1 and 1 Vs^{-1} (method outlined in section 3.3.3). Figure 4.6 shows representative Bode and Nyquist plots for the electrodes before testing and after 10,000 cycles at each sweep rate. Only very minute changes are evident for electrodes tested at 1 Vs^{-1}, whereas a significant increase in $|Z|_{<10Hz}$ is apparent along with a positive shift in the phase angle for electrodes tested at 0.1 Vs^{-1}. Similarly, voltammograms plotted after 0 and 10,000 cycles (Figure 4.7) display no significant change in shape or volume for ν = 1 Vs^{-1}, whereas the voltammogram for ν = 0.1 Vs^{-1} becomes depressed and loses ~50% of its area by the end of the testing regiment.

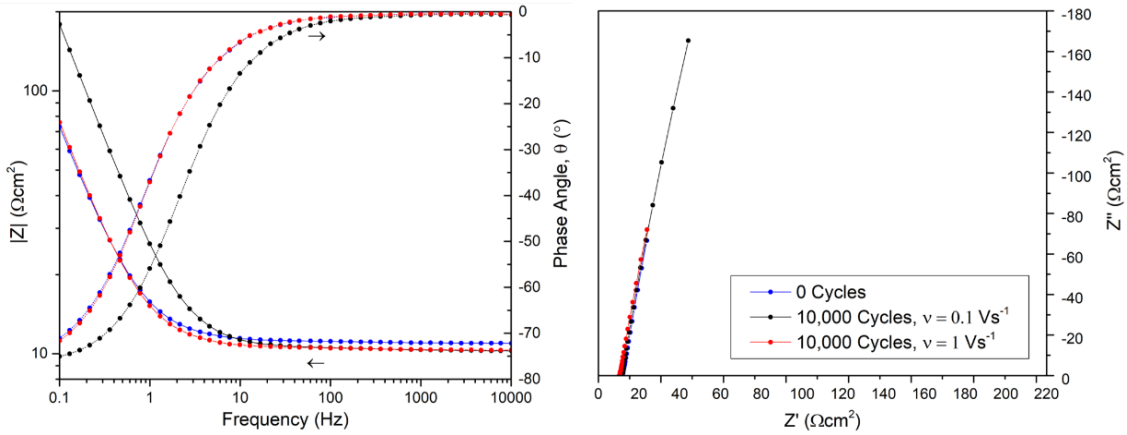

Figure 4.6: Representative impedance and phase angle Bode (left) and Nyquist (right) plots for TiN_I electrodes measured in PBS before (blue) and after 10,000 CV cycles at sweep rates of 0.1 Vs^{-1} (black) and 1 Vs^{-1} (red).

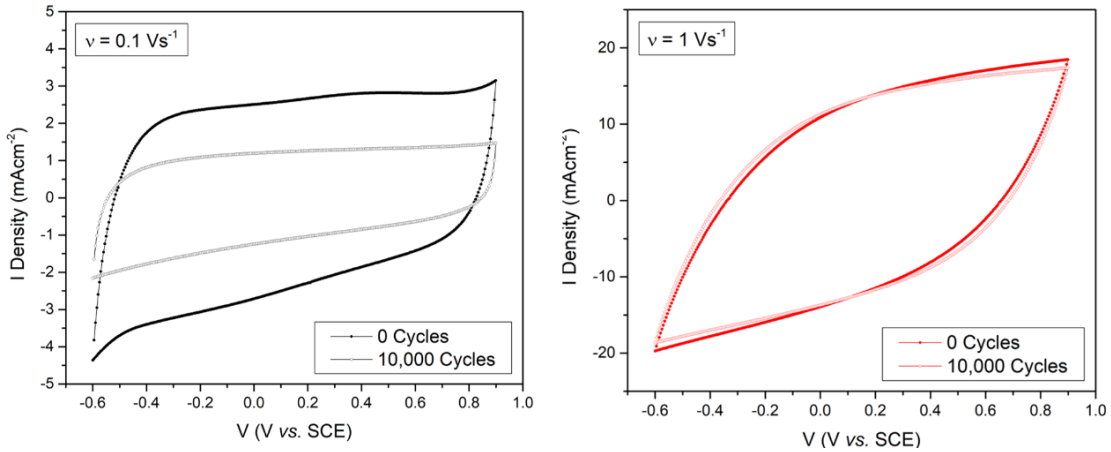

Figure 4.7: Representative voltammograms of TiN_I electrodes subjected to 10,000 CV cycles at sweep rates of 0.1 Vs^{-1} (left) and 1 Vs^{-1} (right), showing the response after 0 (solid symbol) and 10,000 (hollow symbol) cycles.

The EIS spectra obtained throughout the duration of the tests were fitted with the equivalent circuit shown in Figure 4.4 a, and the model variables are plotted as a function of cycle number in Figure 4.8. The model was able to produce convergent fits for all the spectra collected, suggesting that no fundamental change in the charge transfer mechanisms occurred as a result of cycling. The variations in R_f, Y_{dl}, α_{dl}, and α_{pseu} did not differ significantly between the two scan rates, whereas a steady drop in Y_{pseu} is apparent for electrodes tested at v = 0.1 Vs^{-1}. Conversely, this behaviour is absent for electrodes cycled at v = 1 Vs^{-1} and corresponds well with the unchanged Bode and Nyquist plots shown in Figure 4.6. Comparably, the charge retention percentage, which is also plotted in Figure 4.8 f, shows a negligible drop in the case of v = 1 Vs^{-1} (< 1.5% drop), whereas only ~ 54% of the charge is retained by the 10,000th cycle for v = 0.1 Vs^{-1}. These results reflect the unchanged and diminished area of the voltammograms shown in Figure 4.7 for v = 1 Vs^{-1} and v = 0.1 Vs^{-1}, respectively.

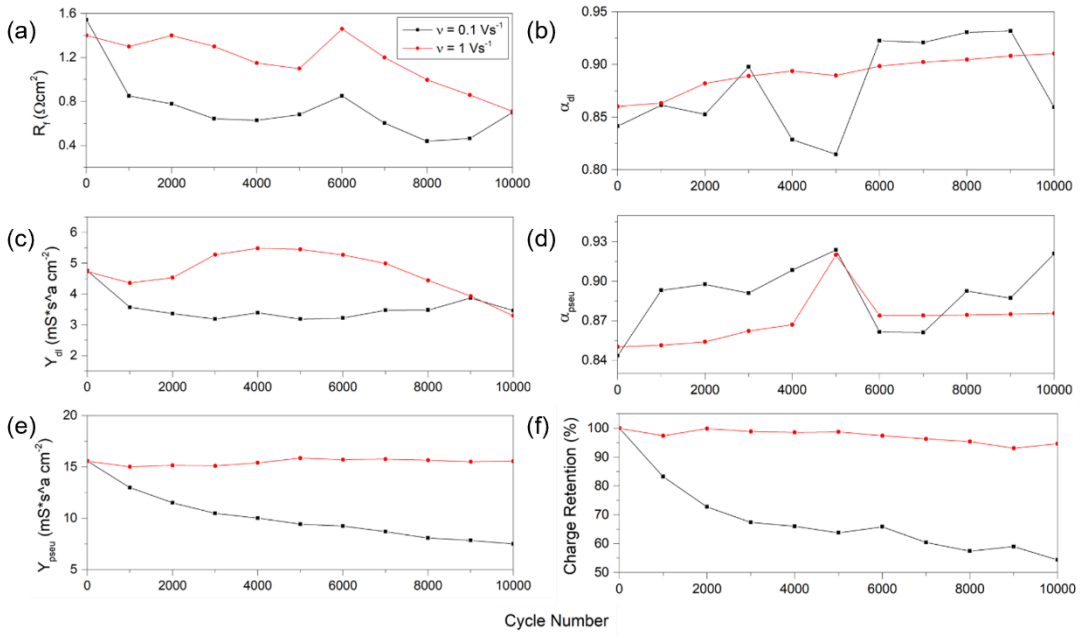

Figure 4.8: Plots of (a) R_F, (b) α_{dl}, (c) Y_{dl}, (d) α_{pseu}, (e) $Y_{pseu,}$, and (f) charge retention % as a function of cycle number for TiN_I electrodes subjected to 10,000 CV cycles at scan rates of 0.1 Vs^{-1} (black) and 1 Vs^{-1} (red), tested in PBS. EIS values were obtained by fitting the resultant EIS spectra to the equivalent circuit model shown in Figure 4.4 a.

Representative micro-Raman spectra of the electrode surfaces before and after cycling are given in Figure 4.9. The relative intensities of peaks numbered 1 and 6 were calculated from 5 measurements per electrode for 5 electrodes. No significant difference

($p > 0.05$) was observed for the I_6/I_1 ratio[12] when electrodes were cycled at v = 1 Vs^{-1}, whereas a significant increase was noted ($p < 0.05$) when cycling at v = 0.1 Vs^{-1}.

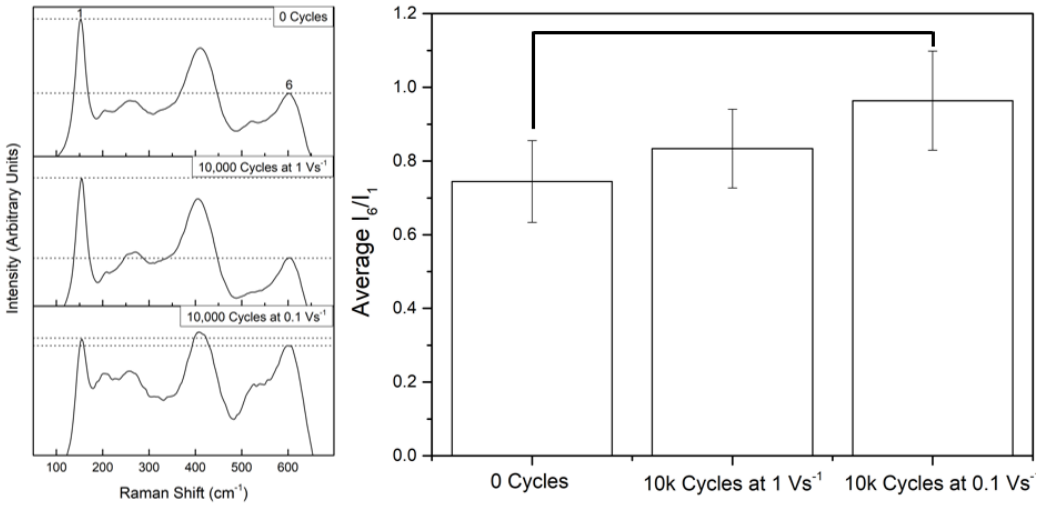

Figure 4.9: Representative micro-Raman spectra of TiN_I electrode surfaces after 0 cycles and 10,000 cycles at a scan rate of either v = 1 Vs^{-1} or v = 0.1 Vs^{-1} (left). Dotted lines show the relative intensities of peaks number 1 and 6, which are also computed and plotted as a bar graph (right). Black line connectors indicate a statistically significant difference ($p < 0.05$) between groups, determined using one-way ANOVA and a post-hoc Tukey test. From Arpa *et al.* [368].

4.2 Development of TiN_{II}, TiN_{III}, and TiN_{IV}

4.2.1 Topography and Imaging

Variations of the original TiN_I electrode were produced by sand blasting polished Ti6Al4V substrates with media of different diameters (method described in section 3.1.2). The roughened surfaces were then coated with a TiN layer using an identical PVD procedure as implemented for TiN_I (method described in section 3.1.3). Optical profilometry measurements for the resulting TiN_{II}, TiN_{III}, and TiN_{IV} electrodes are detailed in Table 4.6. Representative SEM images showing the topographies and cross-sections of the electrodes are also shown in Figure 4.10.

The roughness measurements corroborate visual observations made using SEM, where higher values were obtained in the order TiN_{IV}>TiN_{III}>TiN_{II}>TiN_I. Overgrowth clusters increase both in frequency and size, achieving maximal values in the TiN_{IV} electrodes.

[12] The significance of the I_6/I_1 ratio will be discussed in detail in section 5.2.

The size of the pyramidal structures also increases concurrently, and maximum diameters of 1.4, 1.7, and 2.8 µm were observed for TiN_{II}, TiN_{III}, and TiN_{IV} electrodes, respectively, with higher size variation being expressed in the same ascending order. Conversely, no significant change in coating thickness was observed, where the averages measured from 5 electrodes were found to be 9.3 ± 0.8 µm, 9.3 ± 0.6 µm and 9.5 ± 0.6 µm for TiN_{II}, TiN_{III}, and TiN_{IV} electrodes, respectively.

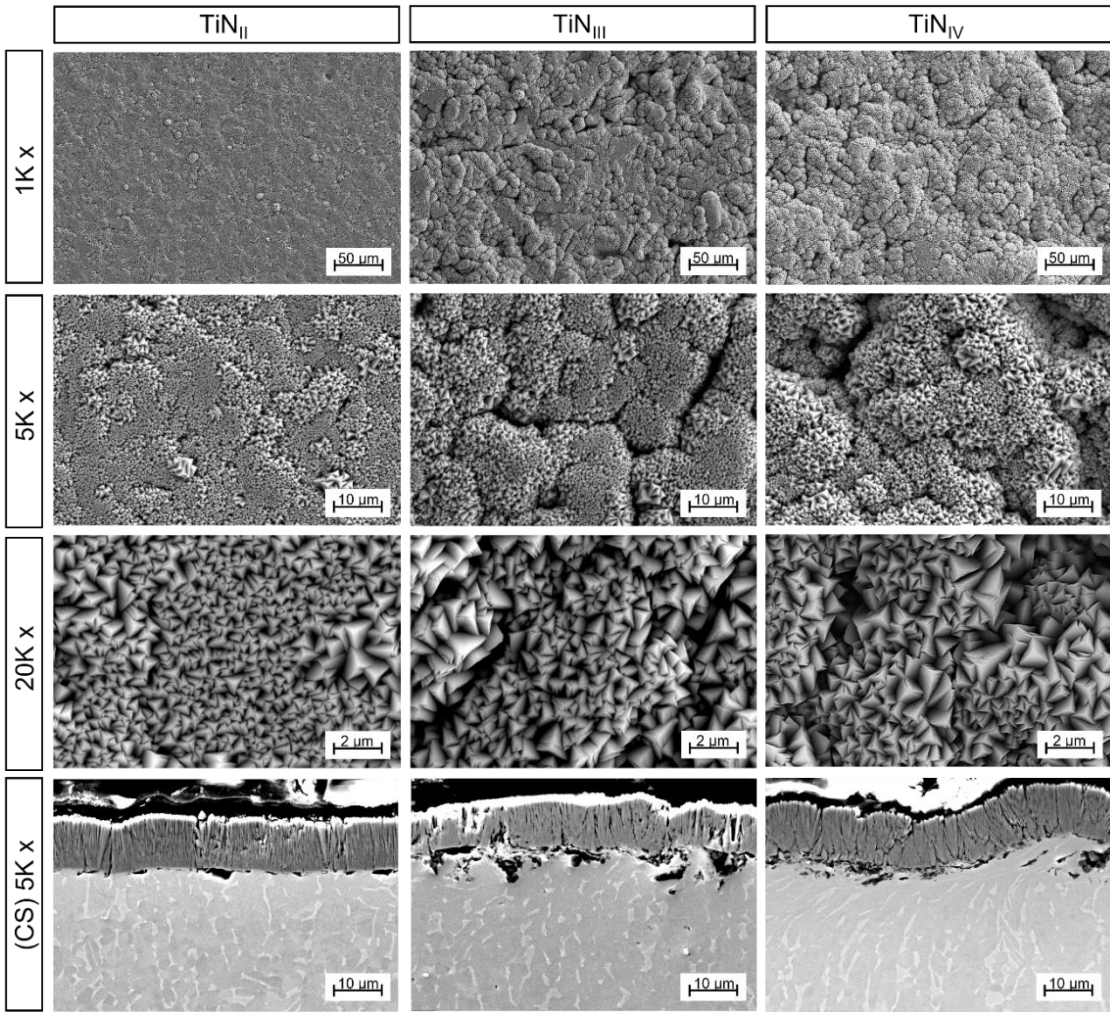

Figure 4.10: Topographic SEM images of TiN_{II}, TiN_{III}, and TiN_{IV} electrodes at 1k x, 5k x, and 20k x magnification. Cross-section images of each electrode are also given at a magnification of 5k x.

Table 4.6: Optical profilometry measurements for TiN_{II}, TiN_{III}, and TiN_{IV} electrode surfaces, based on a 10x10 mm sampling area and a 0.8 mm gaussian cut-off limit. The measurements for TiN_I electrodes are also shown for comparison. The average and standard deviation of three electrode surfaces is given.

Variable (in µm)	**TiN_I**	**TiN_{II}**	**TiN_{III}**	**TiN_{IV}**
Roughness Average, R_a	0.1 ± 0.02	0.5 ± 0.1	1.8 ± 0.4	3.1 ± 0.9
RMS Roughness, R_q	0.2 ± 0.03	0.6 ± 0.1	2.3 ± 0.6	4.0 ± 1.2
Max. Profile Peak Height, R_p	1.5 ± 0.4	4.2 ± 1.2	6.8 ± 0.7	12.1 ± 1.7
Max. Profile Valley Depth, R_v	1.5 ± 0.2	2.4 ± 0.4	9.9 ± 1.6	20.9 ± 2.7
Max. Total Height of the Profile, R_t	3.1 ± 1.0	6.7 ± 2.1	16.8 ± 3.0	33.0 ± 4.5

4.2.2 X-Ray Diffraction and Micro-Raman Spectroscopy

Representative Bragg-Brentano XRD patterns (method described in section 3.2.2) for TiN_{II}, TiN_{III}, and TiN_{IV}, electrodes are given in Figure 4.11 for the range $30^{o} < 2\theta < 80^{o}$. The diffractogram for TiN_{I} is also included for comparison. 2θ values for the peaks numbered 1 to 5 are detailed in Table 4.7. Peaks number 1 and 5 emerge in all four electrodes, whereas peaks number 2, 3, and 4 appear only in TiN_{III}, and TiN_{IV} electrodes. Values of 2θ for TiN_{I} and TiN_{II} electrodes are identical, whereas slight positive shifts of $\sim 0.15^{o}$ and 0.22^{o} are apparent for TiN_{III} and TiN_{IV} electrodes respectively, as compared to TiN_{I} and TiN_{II}. In all four electrodes, peak number 1 is dominant.

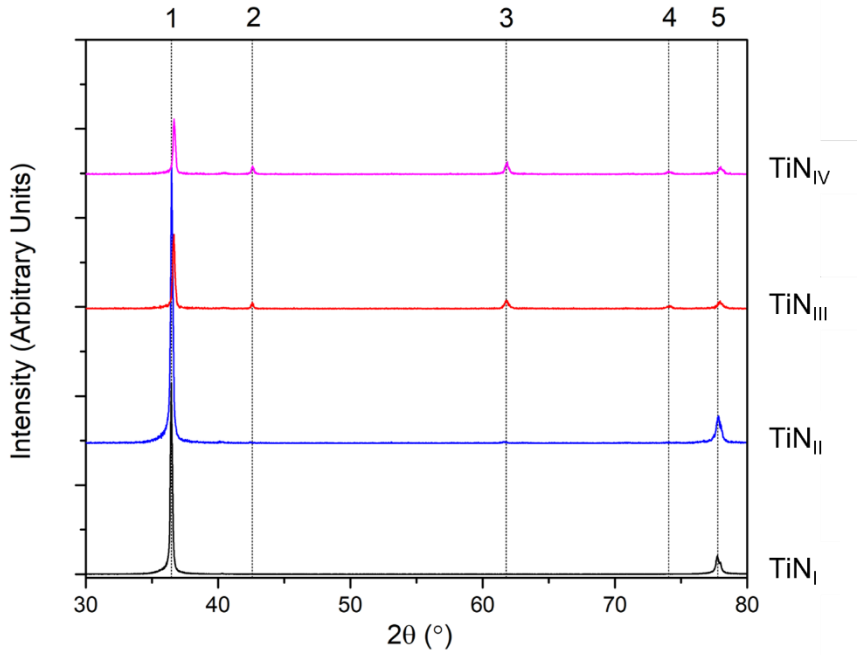

Figure 4.11: Representative Bragg-Brentano X-ray diffractograms for TiN_{II} (blue), TiN_{III} (red) and TiN_{IV} (pink) electrodes obtained using a CuKα radiation source (λ = 1.5406 Å). The spectrum for TiN_{I} (black) electrodes is also given for comparison. Numbered lines indicate peaks emerging from the spectra, where the corresponding 2θ angles are given in Table 4.7.

Table 4.7: XRD peaks and their respective angles of 2θ for TiN_{II}, TiN_{III}, and TiN_{IV} electrodes as identified in Figure 4.11. The results for TiNI electrodes are also shown for comparison.

	2θ (°)			
Peak No.	**TiN_{I}**	**TiN_{II}**	**TiN_{III}**	**TiN_{IV}**
1	36.46	36.46	36.61	36.68
2	/	/	42.52	42.59
3	/	/	61.77	61.84
4	/	/	74.05	74.12
5	77.74	77.74	77.89	77.96

Representative micro-Raman spectra collected using a 532 nm λ green light laser (method described in section 3.2.3) for TiN_{II}, TiN_{III}, and TiN_{IV} electrodes are given in Figure 4.12. The spectrum for TiN_I is also included for comparison. The six prominent peaks identified (numbered 1-6 on the figure) are consistent throughout all four electrodes, and no significant difference ($p > 0.05$) was found in the Raman shifts with respect to TiN_I. As such, the shifts are identical to those detailed in Table 4.3, and were likewise calculated from an average of 3 spectra for 5 different samples per electrode type.

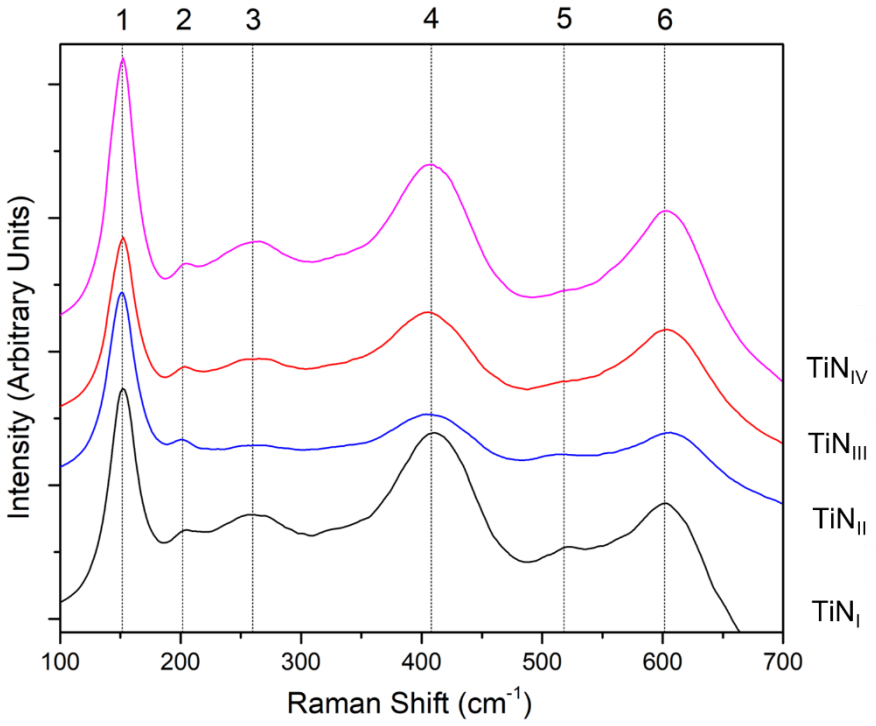

Figure 4.12: Representative Micro-Raman spectra for TiN_{II} (blue), TiN_{III} (red) and TiN_{IV} (pink) electrodes obtained using a green light laser (λ = 532 nm). The spectrum for TiN_I (black) electrodes is also given for comparison. Numbered lines indicate prominent peaks emerging from the spectra, where the corresponding Raman shifts are identical to those presented in Table 4.3.

4.2.3 Electrochemical Testing in Physiological Electrolytes

4.2.3.1 Testing in PBS

The electrodes were subjected to electrochemical measurements in PBS solution, using testing procedures identical to those implemented for TiN_I (method described in section 3.3). EIS Bode and Nyquist plots for TiN_{II}, TiN_{III}, and TiN_{IV} electrodes are given in Figure 4.13, where the plots for TiN_I are also included for comparison. No variability in electrochemical behaviour was identified between the four electrode types, producing

very similar EIS spectra that could all be modelled using the equivalent circuit shown in Figure 4.4 a. The results extracted from modelling are given in Table 4.8, where again no significant difference ($p > 0.05$) was observed between the four electrodes for any of the variables.

Similar results are obtained for CV testing, where no significant difference ($p > 0.05$) could be observed in the shape or volume of resultant voltammograms, shown in Figure 4.14. As with the EIS plots, voltammograms for TiNI electrodes are shown for comparison. Table 4.9 provides the values for the average CSC_C of electrodes, again indicating no statistically significant difference ($p > 0.05$) between the four electrode types.

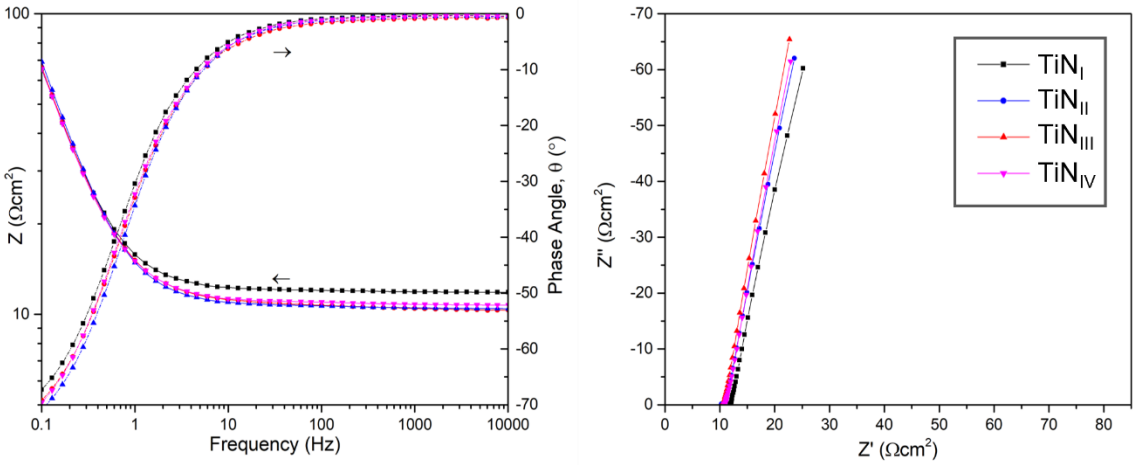

Figure 4.13: Representative impedance and phase angle Bode plots (left) and Nyquist plots (right) for TiN_{II} (blue), TiN_{III} (red), and TiN_{IV} (pink) electrodes measured in PBS. Plots for TiN_I (black) electrodes are also shown for comparison.

Table 4.8: Results of fitting the EIS spectra obtained for TiN_{II}, TiN_{III}, and TiN_{IV} electrodes tested in PBS (Figure 4.13) to the equivalent circuit model given in Figure 4.4 a. The $|Z|_{1Hz}$ is also given. Results are given as the average of 5 repeated readings with standard deviation from the mean. The results for TiN_I electrodes are included for comparison.

Circuit Element	Units	TiN_I	TiN_{II}	TiN_{III}	TiN_{IV}
R_s	Ωcm^2	14.9 ± 3.1	11.4 ± 0.8	12.3 ± 1.9	12.5 ± 1.9
R_f	Ωcm^2	1.5 ± 0.5	0.7 ± 0.4	1.0 ± 0.9	0.8 ± 0.6
Y_{dl}	$mSs^{\alpha}cm^{-2}$	3.9 ± 0.7	4.0 ± 0.7	4.8 ± 0.6	4.3 ± 0.4
α_{dl}	/	0.855 ± 0.024	0.876 ± 0.040	0.864 ± 0.018	0.835 ± 0.017
Y_{pseu}	$mSs^{\alpha}cm^{-2}$	14.7 ± 3	16.8 ± 2.0	15.6 ± 0.7	16.2 ± 1.5
α_{pseu}	/	0.879 ± 0.007	0.881 ± 0.006	0.875 ± 0.012	0.868 ± 0.047
$\|Z\|_{1Hz}$	Ωcm^2	17.8 ± 2.1	17.0 ± 2.2	17 ± 3.0	17.8 ± 2.0

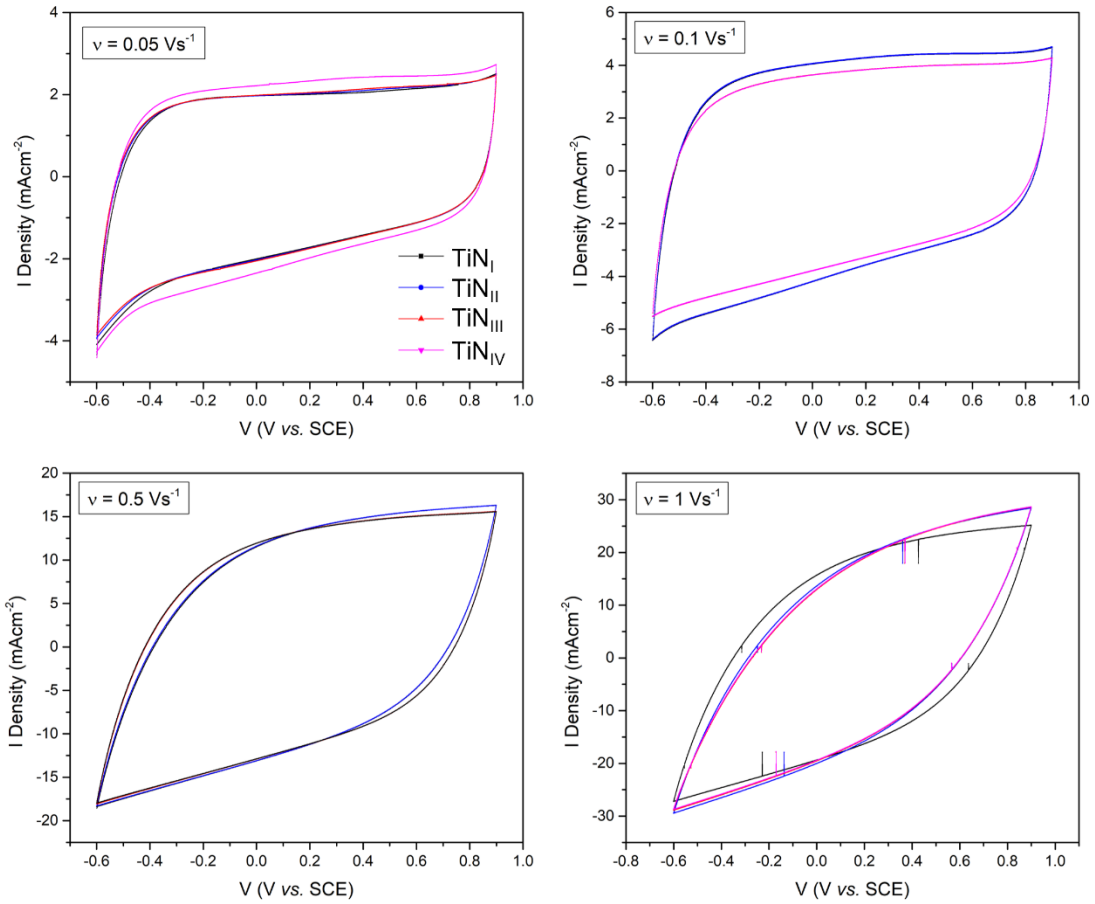

Figure 4.14: Representative voltammograms for TiN_{II} (blue), TiN_{III} (red), and TiN_{IV} (pink) electrodes measured at different sweep rates of ν in PBS. Voltammograms for TiN_I electrodes (black) are also given for comparison.

Table 4.9: The CSC_C for TiN_{II}, TiN_{III}, and TiN_{IV} electrodes measured at different sweep rates of ν in PBS. Results show the average and standard deviation of 5 repeated readings. Results for TiN_I are also included for comparison.

	CSC_C ($mCcm^{-2}$)			
ν (Vs^{-1})	**TiN_I**	**TiN_{II}**	**TiN_{III}**	**TiN_{IV}**
0.05	53 ± 6	53 ± 2	51 ± 5	53 ± 2
0.1	46 ± 5	48 ± 4	44 ± 4	46 ± 2
0.5	30 ± 3	30 ± 2	28 ± 2	29 ± 1
1	22 ± 3	20 ± 1	19 ± 2	21 ± 1

4.2.3.2 Testing in PBS+BSA

All four electrode types were tested in a protein-containing electrolyte comprising of PBS with an added 2.5g/dl of BSA and 0.3 wt% sodium azide salt. All other testing parameters were kept constant as per the tests in PBS (method described in section 3.3). Resulting impedance and phase angle Bode plots are given in Figure 4.15, including also

reference spectra of TiN_{IV} electrodes when tested in PBS. No fundamental change in the EIS response was noted, and the spectra were modelled using the equivalent circuit shown in Figure 4.4 a. The results are detailed in Table 4.10, where no statistically significant differences are apparent ($p > 0.05$) between the electrode types in the same medium.

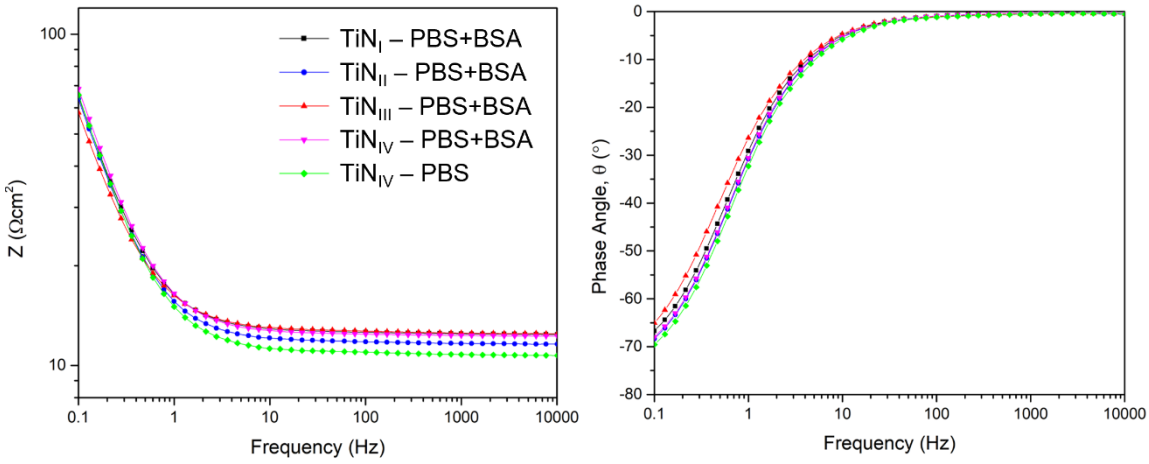

Figure 4.15: Representative impedance (left) and phase angle (right) Bode plots for TiN_I (black), TiN_{II} (blue), TiN_{III} (red), and TiN_{IV} (pink) electrodes measured in PBS+BSA electrolyte. Plots for TiN_{IV} electrodes measured in PBS (green) are also shown for comparison.

Table 4.10: Results of fitting the EIS spectra obtained for TiN_I, TiN_{II}, TiN_{III}, and TiN_{IV} electrodes (Figure 4.15) to the equivalent circuit model given in Figure 4.4 a, along with the $|Z|_{1Hz}$. Tests were conducted in PBS+BSA. Results are given as the average of 5 repeated readings with standard deviation from the mean. Results for the TiN_{IV} electrodes measured in PBS are also given for comparison.

		PBS+BSA				**PBS**
Circuit Element	**Units**	**TiN_I**	**TiN_{II}**	**TiN_{III}**	**TiN_{IV}**	**TiN_{IV}**
R_s	Ωcm^2	13.9 ± 0.2	15.9 ± 0.5	13.8 ± 1.8	14.9 ± 1.1	12.5 ± 1.9
R_f	Ωcm^2	0.9 ± 0.1	0.8 ± 0.4	0.7 ± 0.2	0.9 ± 0.1	0.8 ± 0.6
Y_{dl}	$mSs^{\alpha}cm^{-2}$	4.3 ± 0.8	4.1 ± 0.6	5.3 ± 2.1	4.3 ± 1.9	4.3 ± 0.4
α_{dl}	/	0.887 ± 0.016	0.859 ± 0.023	0.832 ± 0.037	0.886 ± 0.052	0.835 ± 0.017
Y_{pseu}	$Ss^{\alpha}cm^{-2}$	14.8 ± 0.8	15.4 ± 0.4	15.6 ± 2.4	14.3 ± 1.4	16.2 ± 1.5
α_{pseu}	/	0.876 ± 0.004	0.888 ± 0.011	0.914 ± 0.077	0.889 ± 0.018	0.868 ± 0.047
$\|Z\|_{1Hz}$	Ωcm^2	17.1 ± 1.7	17.0 ± 2.3	17.7 ± 2.4	17.5 ± 1.8	17.8 ± 2.0

Figure 4.16 shows representative voltammograms for all four electrodes tested in PBS+BSA electrolyte, while those for TiN_{IV} as measured in PBS are also included for reference. Although the average CSC_C's, given in Table 4.11, do not differ significantly

between the electrodes in the same electrolyte, a small but notable decrease in voltammogram area is evident when compared to the PBS plot (green in Figure 4.16) at all scan rates.

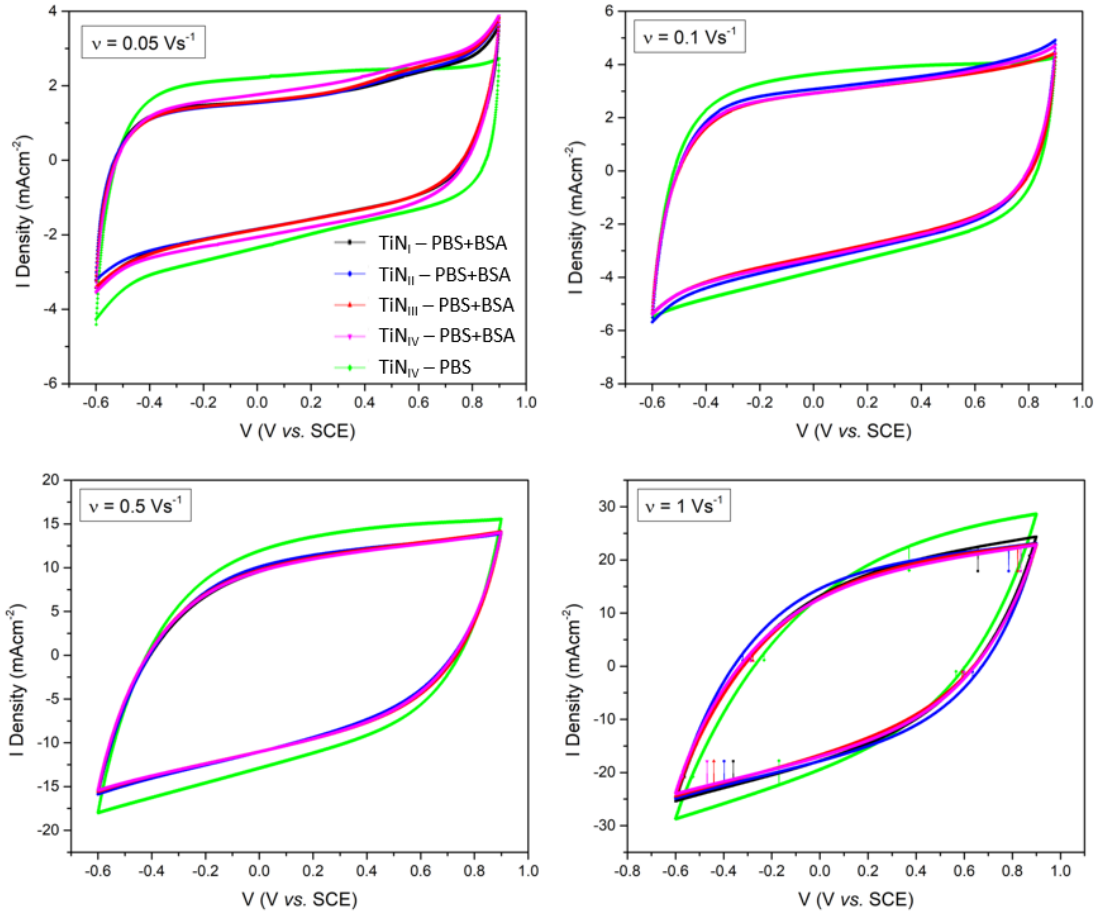

Figure 4.16: Representative voltammograms for TiN_I (black), TiN_{II} (blue), TiN_{III} (red), and TiN_{IV} (pink) electrodes measured at different sweep rates of v in PBS+BSA. Plots for TiN_{IV} electrodes measured in PBS (green) are also shown for comparison.

Table 4.11: The CSC_C for TiN_I, TiN_{II}, TiN_{III}, and TiN_{IV} electrodes measured at different sweep rates of v in PBS+BSA. Results show the average and standard deviation of 5 repeated readings. Results for the TiN_{IV} electrodes measured in PBS are also given for comparison.

	CSC_C ($mCcm^{-2}$)				
	PBS+BSA				**PBS**
v (Vs^{-1})	**TiN_I**	**TiN_{II}**	**TiN_{III}**	**TiN_{IV}**	**TiN_{IV}**
0.05	47 ± 2	47 ± 2	49 ± 1	48 ± 2	53 ± 2
0.1	41 ± 2	40 ± 3	41 ± 1	40 ± 1	46 ± 2
0.5	25 ± 3	24 ± 4	25 ± 2	24 ± 2	29 ± 1
1	17 ± 3	17 ± 2	17 ± 1	17 ± 1	21 ± 1

Tests in PBS+BSA were also conducted over a 24-hour period, where EIS measurements were made every 4 hours. Figure 4.17 shows representative impedance and phase angle Bode plots for TiN_{IV} electrodes collected at the 7 different time points. Very similar plots were acquired for TiN_I, TiN_{II}, and TiN_{III} electrodes, and so are not included here to avoid repetition.

Using the same equivalent circuit shown in Figure 4.4 a, the spectra for all four electrodes were fitted to the model and the variables plotted as a function of immersion time in Figure 4.18. No significant variation occurs to the variables as testing time progresses, with the exception of R_s and Y_{pseu}. The solution resistance consistently exhibited a small drop (~ 4 - 5 Ωcm^2) in the first four hours of testing followed by apparently random fluctuations, while pseudocapacitance exhibits a gradual decrease over time.

4.2.4 Assessing Attachment and Proliferation of NHDF

TiN_I, TiN_{II}, TiN_{III}, and TiN_{IV} electrodes were incubated with neonatal human dermal fibroblasts (NHDF) for a total of 72 hours to assess susceptibility towards fibrous encapsulation. The relative number of viable fibroblasts adhered to the electrode surfaces was determined through spectrophotometric detection of resazurin reduction (method described in section 3.6.2). The results of two replicate tests where 5 electrodes were assessed per electrode type per test (i.e., n=10), are shown in Figure 4.19 for 24, 48, and 72 hours. The largest average reduction value (TiN_1 after 72 hours) was given a value of '1', and all other values are given relative to it. Due to the large error bars, statistically significant differences ($p < 0.05$) were observed only between TiN_I electrodes after 24 and 72 hours (marked * in the figure), and between TiN_I and TiN_{IV} electrodes after 72 hours (marked ** in the figure). These results indicate that TiN_{IV} successfully reduced fibroblast proliferation over its surface by an average of 62% when compared to TiN_I.

SEM images of NHDF fixed on the electrode surfaces using glutaraldehyde after 72 hours of incubation are shown at various magnifications in Figure 4.20 and Figure 4.21. Cell coverage appears to decrease as the electrode roughness increases, with a very clear difference evident between Figure 4.20 a and d, representing TiN_I and TiN_{IV} surfaces, respectively. Fibroblast size and morphology also vary significantly, with large,

flattened and well-spread cells on TiN_I and TiN_{II} surfaces forming a confluent layer. On the other hand, cells on TiN_{III} and TiN_{IV} electrodes are smaller, narrower, and exhibit sections of no surface contact due to the feature-heavy 3D surfaces (Figure 4.21 g and h). Moreover, cells do not form a confluent layer on these latter electrodes.

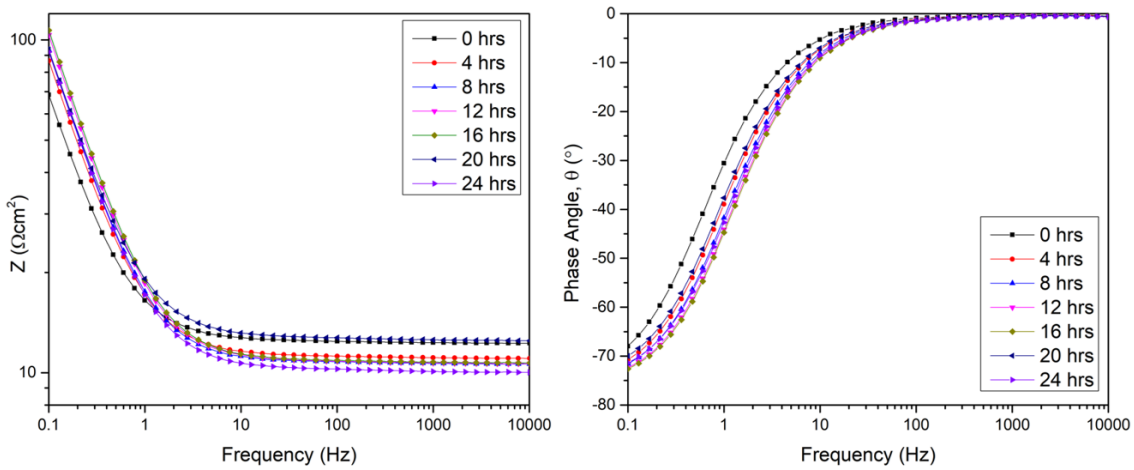

Figure 4.17: Representative impedance (left) and phase angle Bode plots (right) for TiN_{IV} electrodes measured in PBS+BSA electrolyte over 24 hours.

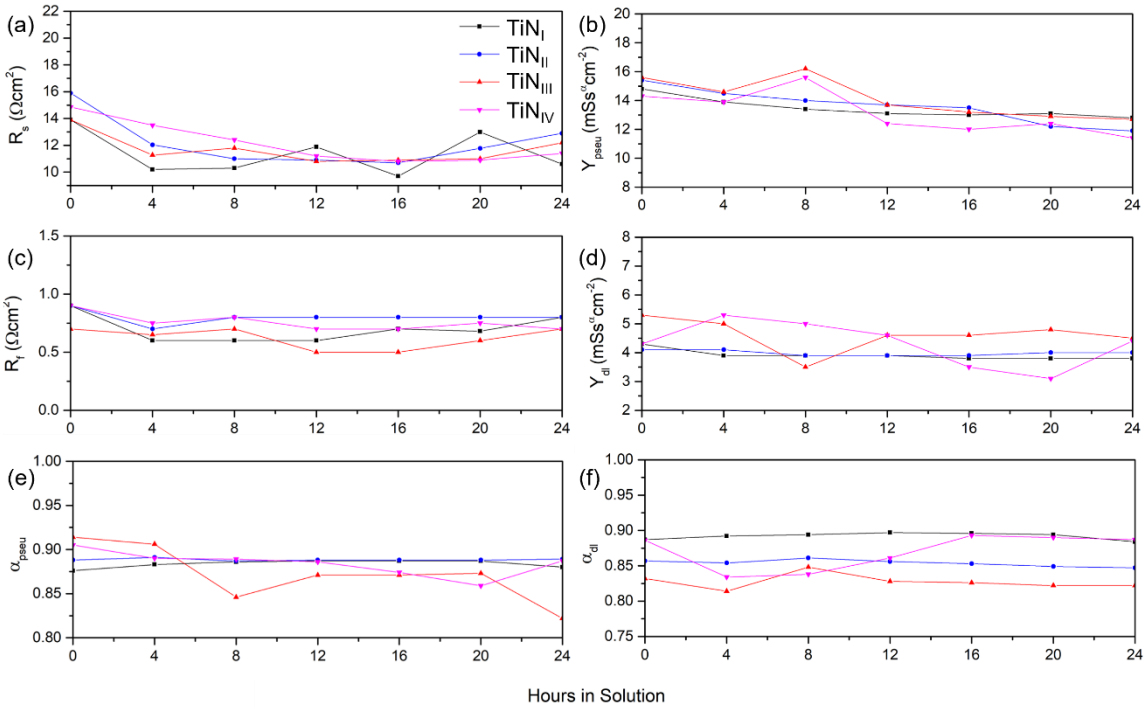

Figure 4.18: Plots showing the variation in (a) R_s, (b) Y_{pseu}, (c), R_f, (d) Y_{dl}, (e) α_{pseu}, and (f) α_{dl} as a function of time immersed in PBS+BSA solution for TiN_I (black), TiN_{II} (blue), TiN_{III} (red), and TiN (pink) electrodes.

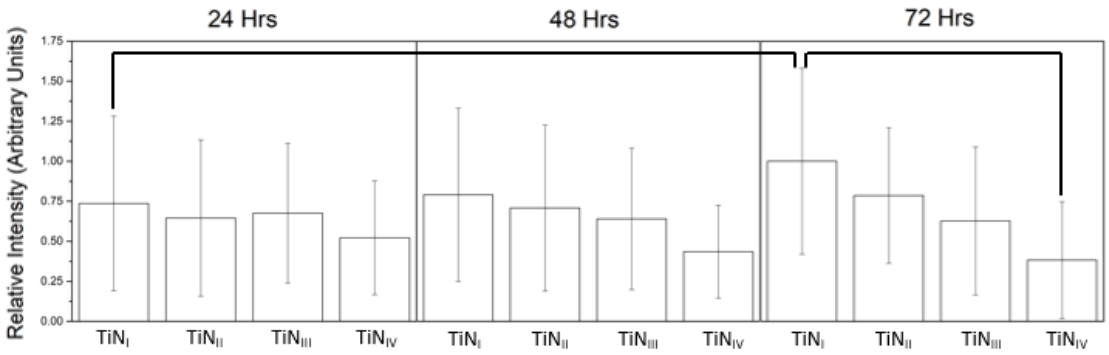

Figure 4.19: Average relative intensity of Resazurin reduction by NHDF cells measured on TiN_I, TiN_{II}, TiN_{III}, and TiN_{IV} electrodes. Cells were seeded at a density of 8×10^4 cells/cm^2. Measurements were made using spectrophotometry at wavelengths of 570 and 600 nm after 24, 48, and 72 hours of incubation. Results show the average with standard deviation of 2 replicate tests where 5 samples were employed per electrode type, per test (i.e., n=10). Black line connectors indicate statistically significant differences ($p < 0.05$) between groups, determined using one-way ANOVA and a post-hoc Tukey test. The largest average reduction value (TiN_1 after 72 hours) was given a value of '1', and all other values are given relative to it.

4.3 Development of TiN_{IV}/PEDOT:PSS

4.3.1 The Electrodeposition Process

TiN_{IV} electrodes were selected for subsequent development of TiN/PEDOT:PSS multi-layer systems (method described in section 3.1.5). Optimum current density for electrodeposition was determined to be 1.3 mAcm^{-2} through a series of trial experiments in which the current density was increased in increments of 0.1 mAcm^{-2} (1 – 1.4 mAcm^{-2}) until reaching threshold. Threshold was reached when PEDOT:PSS layer displayed blistering, cracking, and delamination. Another series of experiments was then carried out to determine viable deposition times (10 – 20 minutes) in increments of 2.5 minutes. The deposition time limit was determined when the PEDOT:PSS layer displayed cracking and delamination. Deposition times of 12.5, 15, and 17.5 minutes were chosen to produce TiN_{IV}/PEDOT:PSS electrodes labelled $PP_{12.5}$, PP_{15}, and $PP_{17.5}$, respectively. Figure 4.22 shows a representative plot of the electrodeposition process, in which a TiN_{IV} electrode with a GSA of 0.126 cm^2 undergoes PEDOT:PSS deposition for 17.5 minutes, producing a $PP_{17.5}$ electrode. The voltage response remains stable at ~ 0.9 V *vs* SCE for the duration of the process.

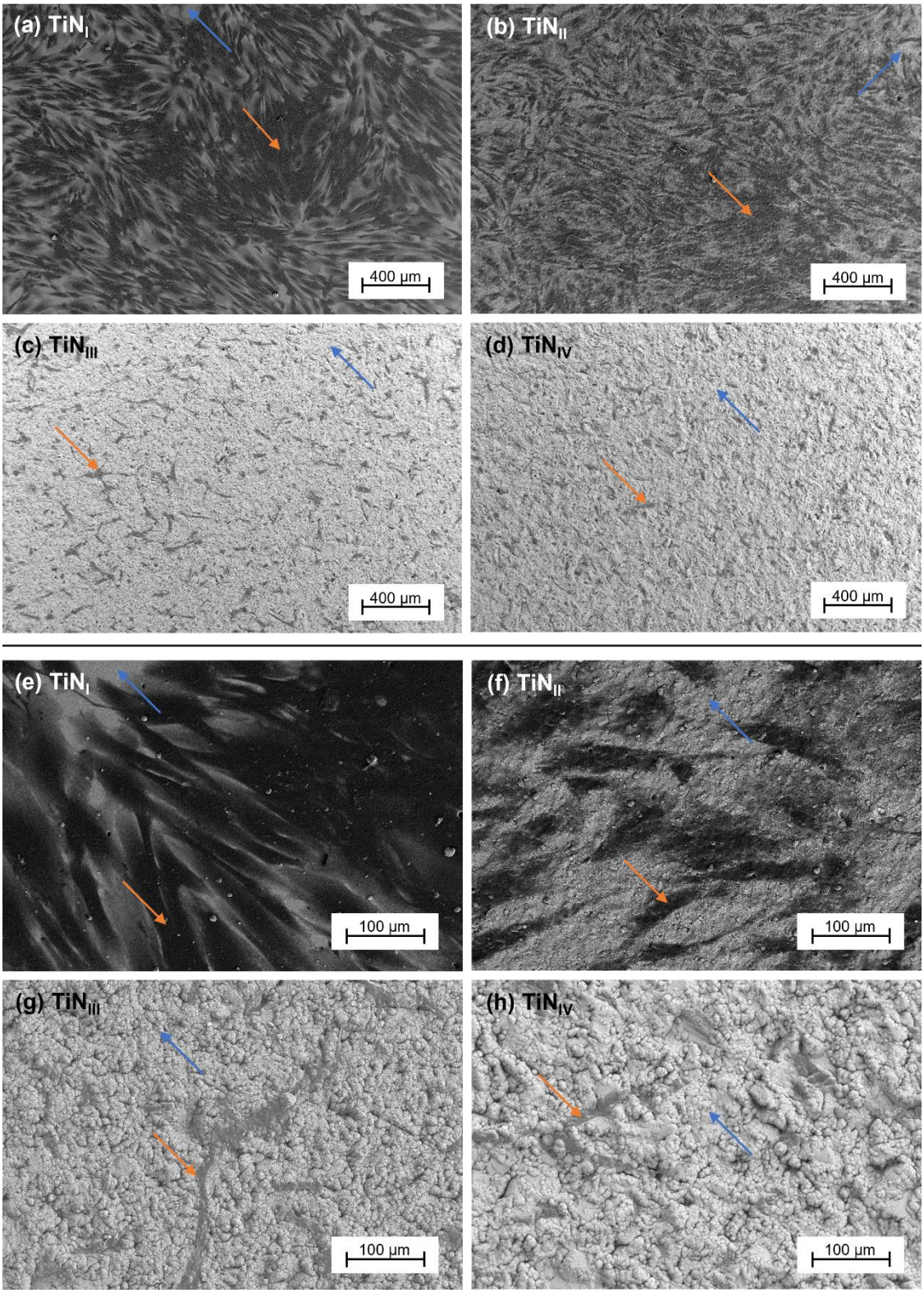

Figure 4.20: SEM images of HNDF on TiN_I (a, e), TiN_{II} (b, f), TiN_{III} (c, g), and TiN_{IV} (d, h) electrodes after 72 hours of culture and fixing in glutaraldehyde. Surfaces were sputter-coated with a nanometric layer of Au to improve conductivity. Images were taken at 100x (a-d) and 500x (e-h) magnification. Orange arrows indicate examples of fibroblast cells, whereas blue arrows indicate areas of the TiN surface not covered in cells.

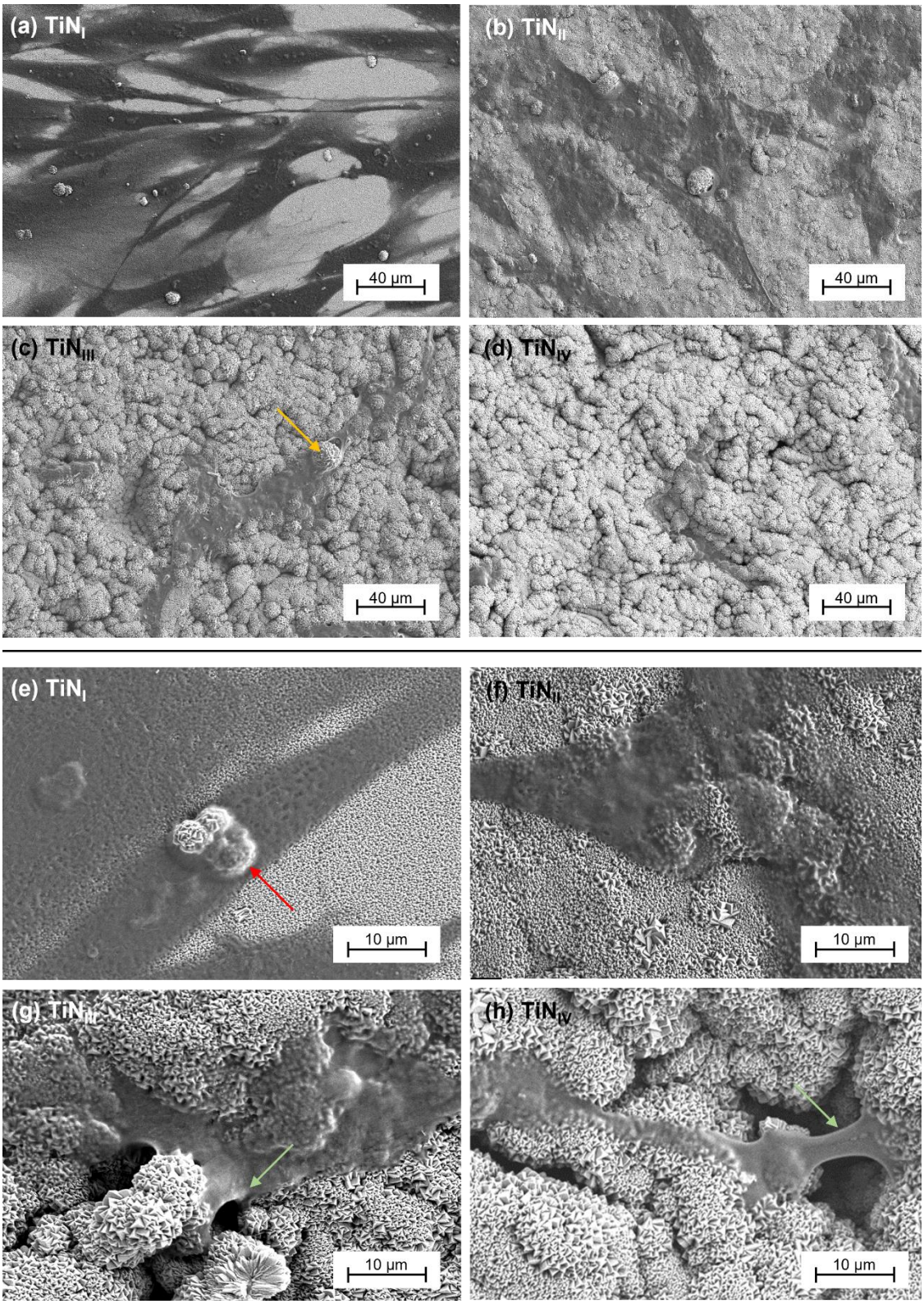

Figure 4.21: SEM images of HNDF on TiN_I (a, e), TiN_{II} (b, f), TiN_{III} (c, g), and TiN_{IV} (d, h) electrodes after 72 hours of culture and fixing in glutaraldehyde. Surfaces were sputter-coated with a nanometric layer of Au to improve conductivity. Images were taken at 1k x (a-d) and 5k x (e-h) magnification. Yellow arrow in (c) indicates overgrowth cluster disturbing cell morphology and causing stretching. Red arrow in (e) indicates cell growing over and around cluster. Green arrows in (g,h) show cells stretching across topographical features of the TiN.

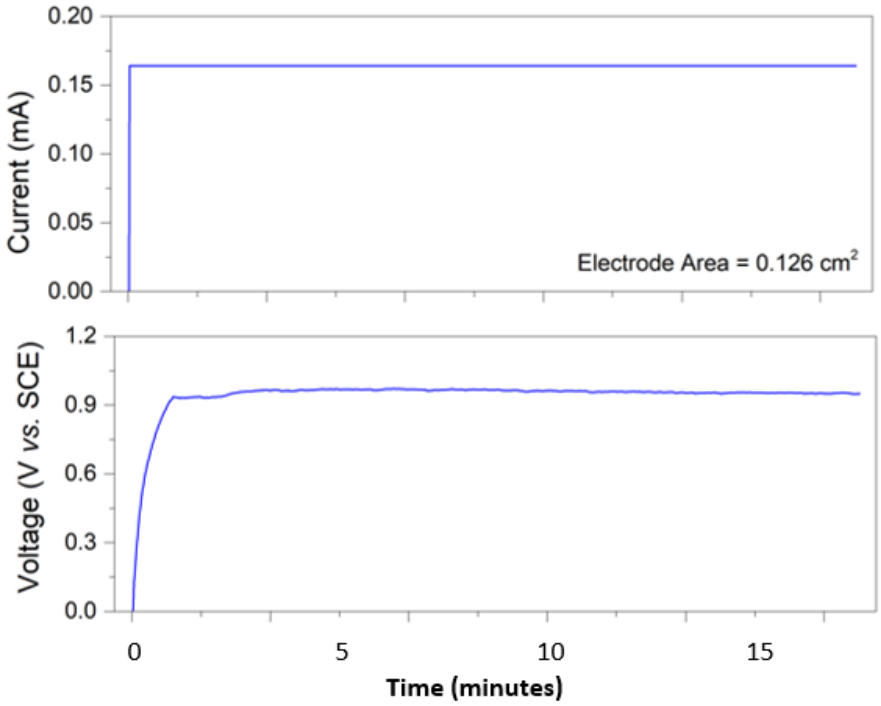

Figure 4.22: Representative plot of deposition current (density of 1.3 $mAcm^{-2}$) and voltage response against time, for a $PP_{17.5}$ electrode with a surface area of 0.126 cm^2.

4.3.2 Topography and Imaging

Optical profilometry measurements for the resulting $PP_{12.5}$, PP_{15}, and $PP_{17.5}$ electrodes (in the baked state) are detailed in Table 4.12, where no statistically significant difference ($p > 0.05$) was observed for any of the variables amongst the different electrodes. For this reason, representative topographic images are only shown for the $PP_{17.5}$ electrode. Figure 4.23 a is an optical micrograph, highlighting the characteristic blue colour of PEDOT:PSS, whereas Figure 4.23 b-d are SEM images at different magnifications, showing the high ESA and globular morphology of the polymer, including the nanometric spheres that make up its structure. All images are taken for electrodes having undergone a baking treatment at 90 °C for 3 hours.

Cross-sections of the $PP_{12.5}$, PP_{15}, and $PP_{17.5}$ electrodes (method described in section 3.2.5.2) are shown in Figure 4.24, where the 3 layers of interest are distinctly visible. EDS (method described in section 3.2.4) was used to confirm the electroplated Ni layer, the PEDOT:PSS coating, and the underlying TiN_{IV}. An example of this is given in Figure 4.24 c, where areas marked (i), (ii), and (iii) respectively correspond to these three layers. The thickness of the PEDOT:PSS coatings could thus be measured. The average and

standard deviation obtained from measuring 3 electrodes of each type were found to be 2.4 ± 0.4 µm, 4.6 ± 0.8 µm, and 8.7 ± 1.1 µm for $PP_{12.5}$, PP_{15}, and $PP_{17.5}$ electrodes, respectively.

Table 4.12: Optical profilometry measurements for $PP_{12.5}$, PP_{15}, and $PP_{17.5}$ electrode surfaces, based on a 2x2 mm sampling area and a 0.8 mm gaussian cut-off limit. The average and standard deviation of three electrode surfaces is given. The results for TiN_{IV} electrodes are also given for comparison.

Variable (in µm)	**$PP_{12.5}$**	**PP_{15}**	**$PP_{17.5}$**	**TiN_{IV}**
Roughness Average, R_a	3.1 ± 0.2	3.0 ± 0.3	3.7 ± 0.6	3.1 ± 0.9
RMS Roughness, R_q	4.0 ± 0.1	3.8 ± 0.4	4.4 ± 1.2	4.0 ± 1.2
Max. Profile Peak Height, R_p	10.6 ± 2.5	9.9 ± 3.5	9.5 ± 2.3	12.1 ± 1.7
Max. Profile Valley Depth, R_v	9.8 ± 1.9	8.3 ± 2.0	11.3 ± 4.1	20.9 ± 2.7
Max. Total Height of the Profile, R_t	21.4 ± 4.3	21.4 ± 2.7	22.1 ± 2.8	33.0 ± 4.5

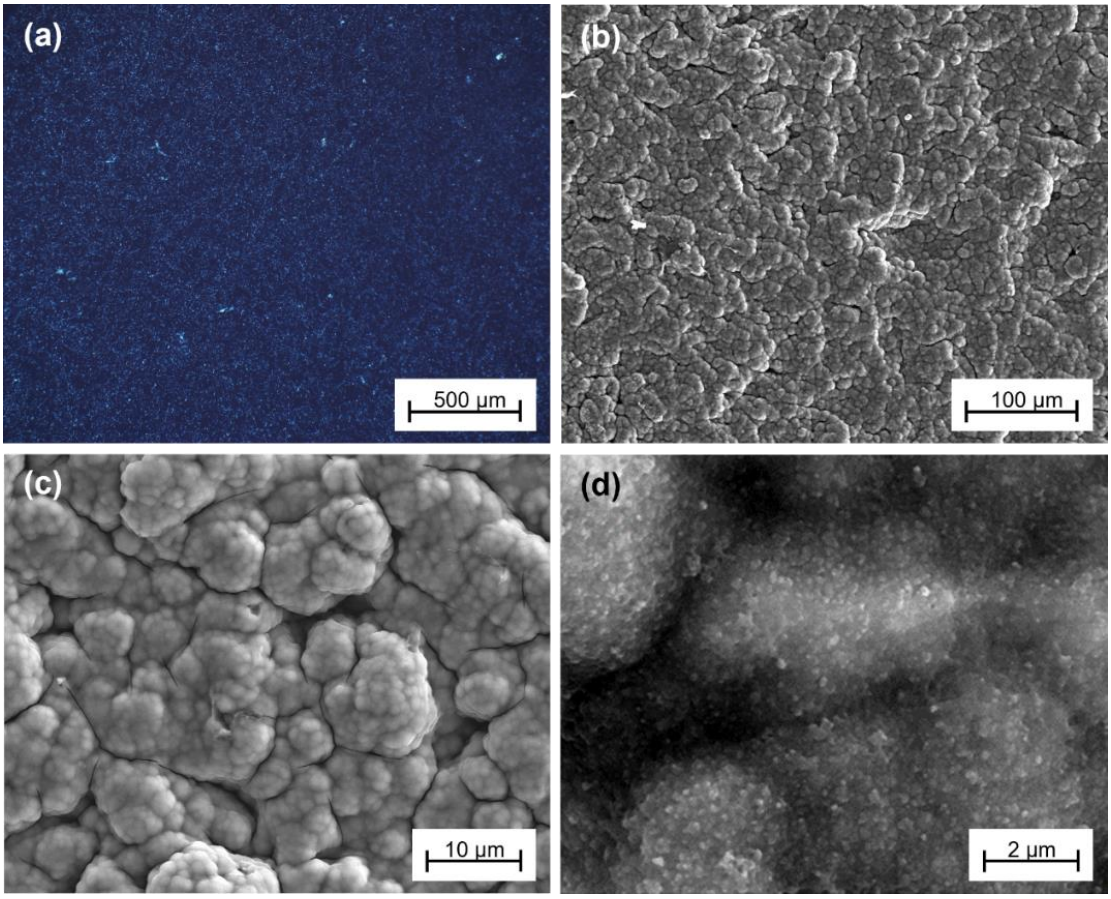

Figure 4.23: (a) Low-magnification optical microscope image of $PP_{17.5}$ electrode, showing the signature blue colour of PEDOT:PSS; (b-d) SEM images of $PP_{17.5}$ electrodes at higher magnifications.

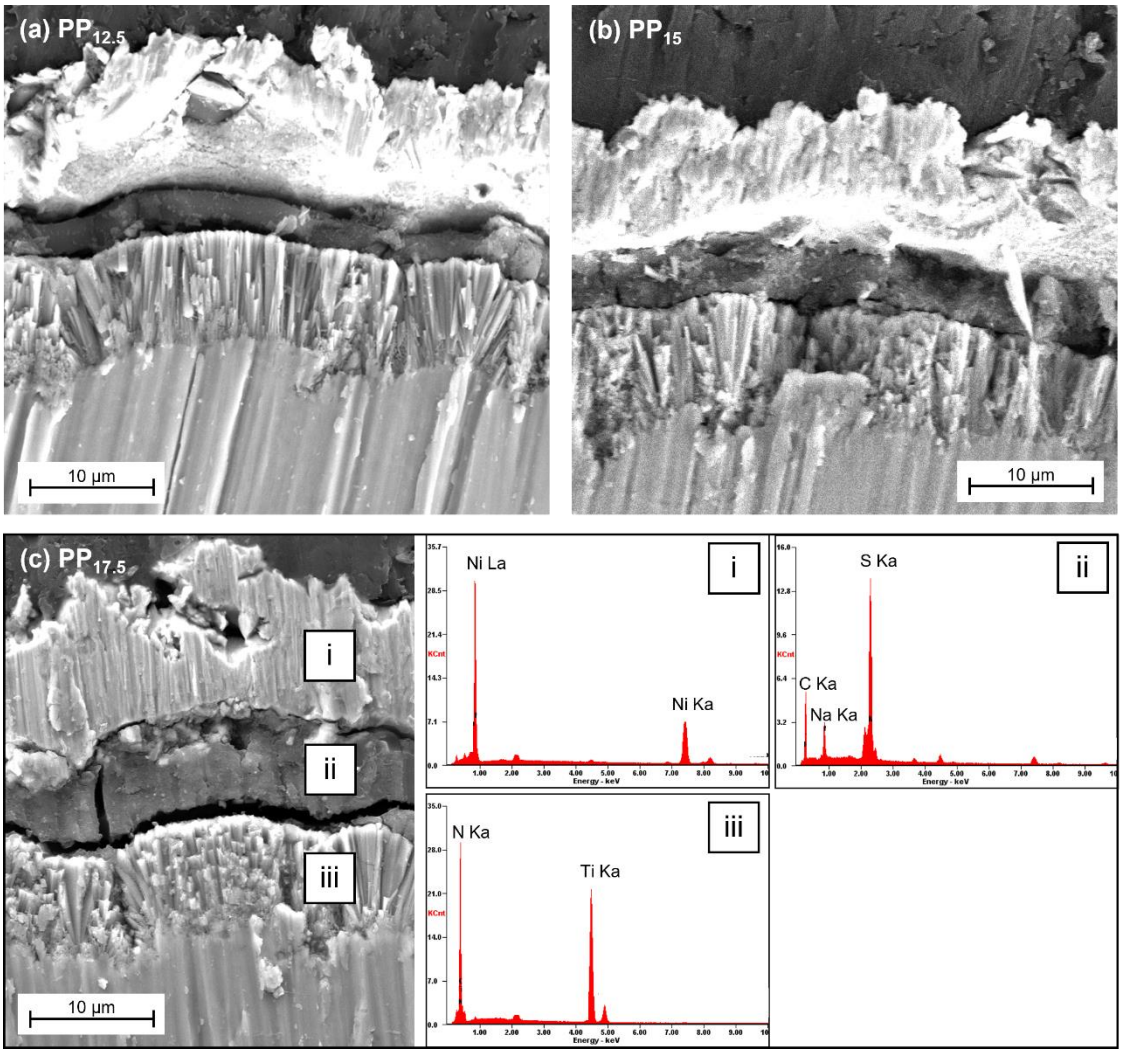

Figure 4.24: Representative cross-sectional SEM images of nickel-plated $PP_{12.5}$ (a), PP_{15} (b), and $PP_{17.5}$ (c) electrodes shown in cross-section. Layer elemental constituents were determined using EDS analysis, an example of which is given for $PP_{17.5}$ electrodes in (c), showing the nickel plating (i), PEDOT:PSS layer (ii) and TiN_{IV} (iii).

4.3.3 Micro-Raman Spectroscopy

Representative micro-Raman spectra collected using a 532 nm λ green light laser for $PP_{17.5}$ electrodes in the as-deposited and baked (90 °C for 3 hours) state are given in Figure 4.25. The Raman shifts of the seven prominent peaks identified (numbered 1-7 on the figure) for the baked specimen are given in Table 4.13.

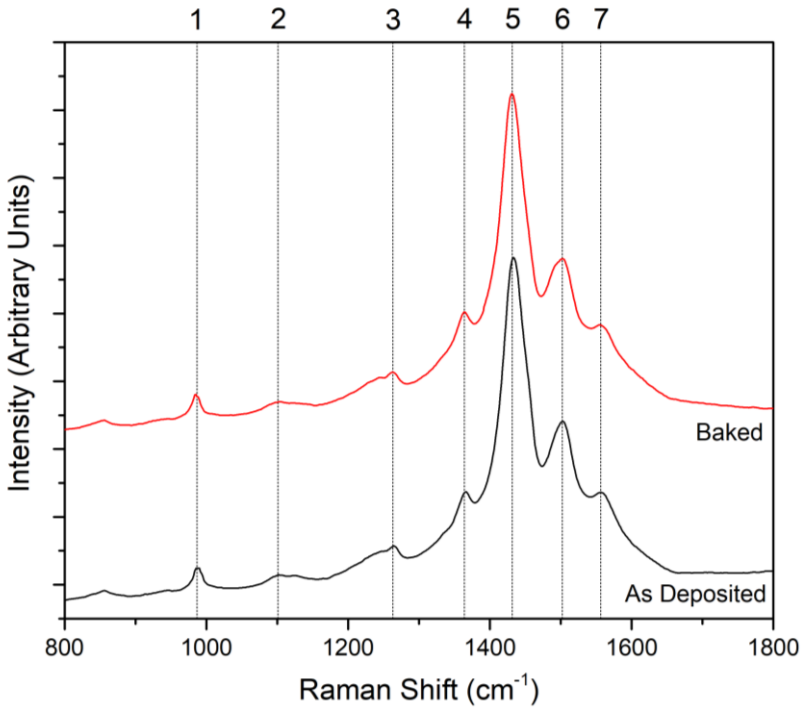

Figure 4.25: Representative micro-Raman spectra of $PP_{17.5}$ electrodes collected before and after heat treatment, shown in black and red respectively. Numbered lines indicate prominent peaks emerging from the baked spectrum, where the corresponding Raman shifts are given in Table 4.13.

Table 4.13: Raman peaks and their respective shifts as identified in Figure 4.25 for the baked specimen.

Peak No.	Raman Shift (cm^{-1})
1	986
2	1072-1162
3	1263
4	1363
5	1431
6	1501
7	1556

4.3.4 Electrochemical Testing in Physiological Electrolytes

4.3.4.1 Testing in PBS

The electrodes were subjected to electrochemical measurements in PBS solution, using testing procedures identical to those implemented for TiN electrodes (method described in section 3.3). EIS Bode and Nyquist plots for $PP_{12.5}$, PP_{15}, and $PP_{17.5}$ electrodes are given in Figure 4.26, where the plots for TiNIV are also included for comparison. A clear downward shift in $|Z|_{<10Hz}$ is apparent for the PEDOT:PSS electrodes, where the shift increases as polymer deposition time increases. When accounting for differences in solution resistance, an average 77% reduction in $|Z|_{1Hz}$ is achieved for $PP_{17.5}$ electrodes

as compared to TiN_{IV}. With regards to fitting an equivalent circuit, the spectra were successfully modelled using the circuit shown in Figure 4.4 a, achieving convergent fits for all three deposition times. The results are shown in Table 4.14.

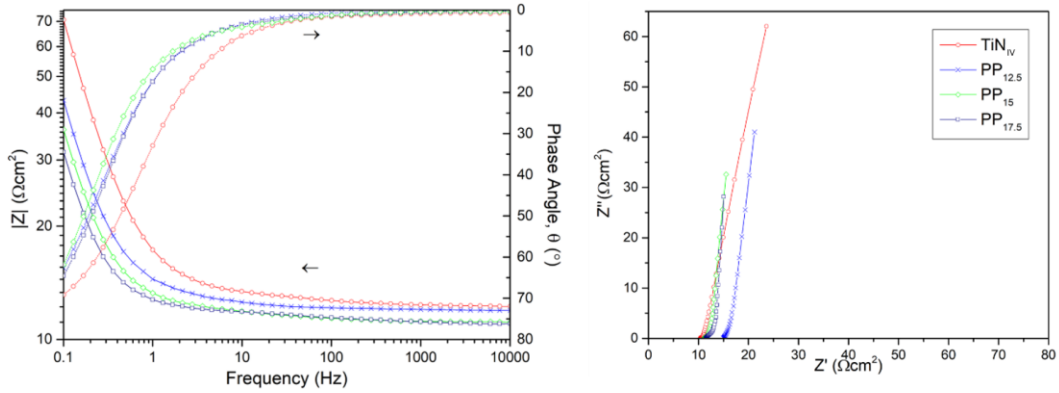

Figure 4.26: Representative impedance and phase angle Bode plots (left) and Nyquist plots (right) for $PP_{12.5}$ (blue), PP_{15} (green), and $PP_{17.5}$ (navy) electrodes measured in PBS. Plots for TiN_{IV} electrodes (red) are also shown for comparison.

Table 4.14: Results of fitting the EIS spectra obtained for $PP_{12.5}$, PP_{15}, and $PP_{17.5}$ electrodes tested in PBS (Figure 4.26) to the equivalent circuit model given in Figure 4.4 a. The $|Z|_{1Hz}$ is also given. Results are given as the average of 5 repeated readings with standard deviation from the mean. Results for TiN_{IV} electrodes are also given for comparison.

Circuit Element	Units	TiN_{IV}	$PP_{12.5}$	PP_{15}	$PP_{17.5}$
R_s	Ωcm^2	12.5 ± 1.9	11.9 ± 2.1	11.1 ± 1.0	11.0 ± 1.2
R_f	Ωcm^2	0.8 ± 0.6	3.4 ± 0.2	2.5 ± 0.6	1.6 ± 0.5
Y_{dl}	$mSs^{\alpha}cm^{-2}$	4.3 ± 0.4	14.0 ± 2.2	16.9 ± 3.2	19.3 ± 3.0
α_{dl}	/	0.835 ± 0.017	0.853 ± 0.050	0.882 ± 0.046	0.890 ± 0.007
Y_{pseu}	$mSs^{\alpha}cm^{-2}$	16.2 ± 1.5	29.0 ± 7.4	32.2 ± 5.3	41.4 ± 2.6
α_{pseu}	/	0.868 ± 0.047	0.960 ± 0.032	0.952 ± 0.014	0.964 ± 0.014
$\|Z\|_{1Hz}$	Ωcm^2	17.8 ± 2.0	14.5 ± 2.448	13.5 ± 1.1	12.2 ± 1.3

The electrolysis limits (i.e., water window, WW) for PEDOT:PSS were found to be -1.2 and 0.8 V *vs* SCE. However, when CV measurements were carried out between these limits, cracks were observed on the the PEDOT:PSS layer after testing. Subsequent CV measurements were thus made between the limits of -0.6 and 0.8 V *vs* SCE[13], and representative voltammograms for the PEDOT:PSS electrodes are shown in Figure 4.27. Voltammograms for TiN_{IV} electrodes are also included for comparison, where measurements were carried out between the limits of -0.6 to 0.9 V *vs* SCE. The CSC_C results are detailed in Table 4.15. Thicker PEDOT:PSS coatings produced higher

[13] The rationale behind this decision will be discussed in detail in section 5.4.3.

CSC_C's up until v = 0.1 Vs^{-1}. At higher scan rates there was no statistically significant difference ($p > 0.05$) in the measured CSC_C's for the three electrodes.

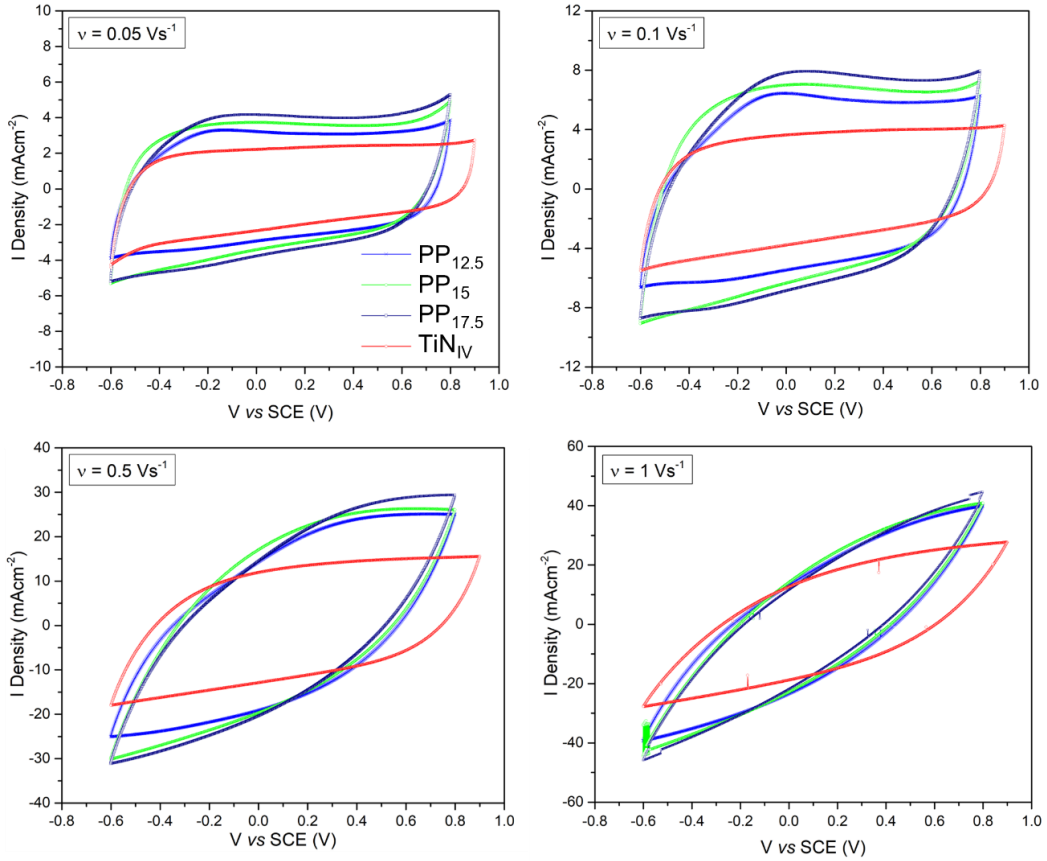

Figure 4.27: Representative voltammograms for $PP_{12.5}$, PP_{15}, and $PP_{17.5}$ electrodes measured at different sweep rates of v in PBS, scanned between the limits of -0.6 to 0.8 V *vs* SCE. Plots for TiN_{IV} electrodes are also shown for comparison, where the scan limits were set to -0.6 to 0.9 V *vs* SCE.

Table 4.15: The CSC_C for $PP_{12.5}$, PP_{15}, and $PP_{17.5}$ electrodes, measured at different sweep rates of v in PBS, scanned between the limits of -0.6 to 0.8 V *vs* SCE. The CSC_C for $PP_{17.5}$ electrodes measured at v = 1 Vs^{-1} using the full WW of PEDOT:PSS (-1.2 to 0.8 V *vs* SCE) is also given. Results show the average and standard deviation of 5 repeated readings. The CSC_C for TiN_{IV} electrodes (scanned between the limits of -0.6 to 0.9 V *vs* SCE) are also given for comparison.

	CSC_C ($mCcm^{-2}$)				
v (Vs^{-1})	**TiN_{IV}**	**$PP_{12.5}$**	**PP_{15}**	**$PP_{17.5}$**	**$PP_{17.5}$**
0.05	53 ± 2	75 ± 3	88 ± 2	94 ± 2	/
0.1	46 ± 2	67 ± 2	77 ± 1	81 ± 2	/
0.5	29 ± 1	37 ± 1	37 ± 1	38 ± 1	/
1	21 ± 1	20 ± 2	21 ± 1	20 ± 1	32 ± 2
WW (V *vs* SCE)	**-0.6 to 0.9**	**-0.6 to 0.8**			**-1.2 to 0.8**

It was further observed that cracking did not occur when conducting CV measurements within the full WW of PEDOT:PSS at high scan rates (1 $Vs^{-1} \leq \nu$). As such, CV measurements for $PP_{17.5}$ electrodes were also carried out for the range -1.2 to 0.8 V *vs* SCE at a scan rate of ν = 1 Vs^{-1}. A representative voltammogram for these testing conditions is shown in Figure 4.28, plotted along with the voltammogram for the same electrode using the restricted WW (-0.6 to 0.8 V *vs* SCE), and the TiN_{IV} electrode with its own WW (-0.6 to 0.9 V *vs* SCE). The CSC_C for this test condition is also included in Table 4.15, increasing by 60% over the original value of the restricted WW.

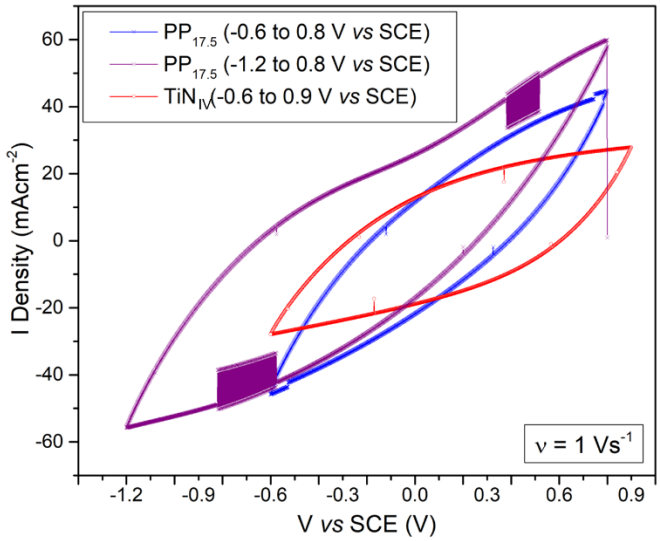

Figure 4.28: Representative voltammograms for tests conducted at ν = 1 Vs^{-1}. $PP_{17.5}$ electrodes were tested using the restricted WW (-0.6 to 0.8 V *vs* SCE) (blue) and the full WW (-1.2 to 0.8 V *vs* SCE) (purple). The voltammogram for TiN_{IV} electrodes (tested between -0.6 to 0.9 V *vs* SCE) (red) is also included for comparison.

4.3.4.2 Testing in PBS+BSA

As they returned the best electrochemical measurements in PBS, $PP_{17.5}$ electrodes were chosen to assess the behaviour of PEDOT:PSS in protein-containing electrolyte. Since sodium azide is incompatible with PEDOT:PSS, it was replaced with the antibiotic penicillin-streptomycin (P/S) to discourage bacterial growth in solution. Representative impedance and phase angle Bode plots for tests conducted in PBS+BSA electrolyte are shown in Figure 4.29, along with a plot for tests carried out in PBS for comparison. Only a slight increase in the impedance was observed with the changing electrolyte, and the

spectra could be successfully modelled using the equivalent circuit given in Figure 4.4 a, the results of which are outlined in

Table 4.16. CV tests conducted in the same electrolyte indicate a similar trend, where a slight decrease in voltammogram area (Figure 4.30) and measured CSC_C (Table 4.17) were observed when compared to scans done in PBS. For assessments done in PBS+BSA electrolyte, CV scans were only carried out for the WW of -0.6 and 0.8 V *vs* SCE.

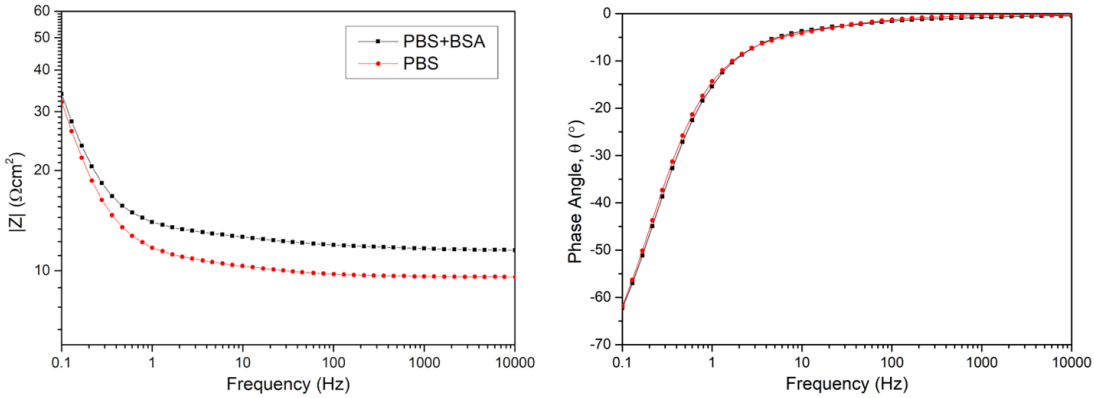

Figure 4.29: Representative impedance (left) and phase angle (right) Bode plots for $PP_{17.5}$ electrodes measured in PBS+BSA electrolyte (black). Plots for $PP_{17.5}$ electrodes measured in PBS (red) are also shown for comparison.

Table 4.16: Results of fitting the EIS spectra obtained for $PP_{17.5}$ electrodes (Figure 4.29, black) to the equivalent circuit model given in Figure 4.4 a, along with the $|Z|_{1Hz}$. Tests were conducted in PBS+BSA (with P/S) electrolyte. Results are given as the average of 5 repeated readings with standard deviation from the mean. Results for tests conducted in PBS are also shown for comparison.

Circuit Element	Units	PBS+BSA	PBS
R_s	Ωcm^2	12.0 ± 0.6	11.0 ± 1.2
R_f	Ωcm^2	1.4 ± 0.2	1.6 ± 0.5
Y_{dl}	$mSs^{\alpha}cm^{-2}$	14.5 ± 4.7	19.3 ± 3.0
α_{dl}	/	0.862 ± 0.018	0.890 ± 0.007
Y_{pseu}	$Ss^{\alpha}cm^{-2}$	40.3 ± 2.7	41.4 ± 2.6
α_{pseu}	/	0.942 ± 0.005	0.964 ± 0.014
$\|Z\|_{1Hz}$	Ωcm^2	14.8 ± 1.9	12.2 ± 1.3

Tests in PBS+BSA were also conducted over a 24-hour period, where EIS measurements were made every 4 hours. Figure 4.31 shows representative impedance and phase angle Bode plots for $PP_{17.5}$ electrodes collected at the 7 different time points. Using the same equivalent circuit as before, the spectra were fitted to the model and the variables plotted as a function of immersion time in Figure 4.32. The variables for similar tests conducted

on TiN_{IV} electrodes are also plotted on the same axes[14]. No significant variation occurs to the variables as testing time progresses bar for a slight increase in R_f of ~ 0.5 Ωcm^2. Y_{pseu}, Y_{dl}, and α_{pseu} remain consistently higher for $PP_{17.5}$ than for TiN_{IV} electrodes throughout the duration of the experiments.

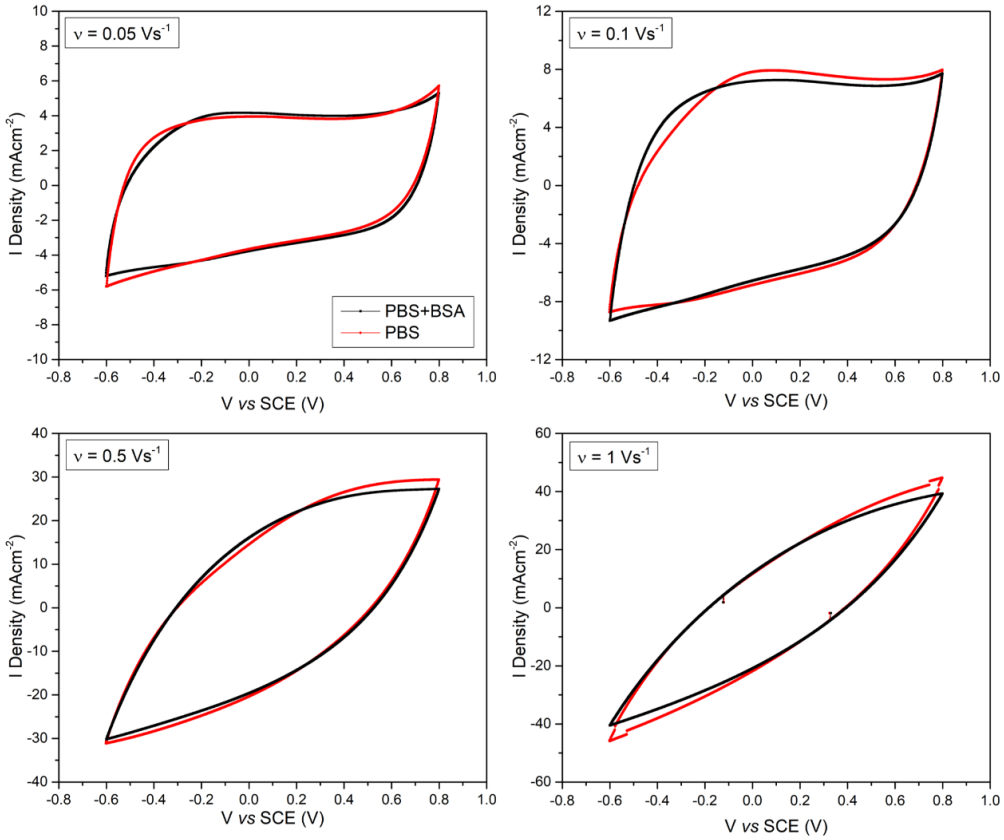

Figure 4.30: Representative voltammograms for $PP_{17.5}$ electrodes measured at different sweep rates of v in PBS+BSA (with P/S), scanned between the limits of -0.6 to 0.8 V *vs* SCE. Plots for $PP_{17.5}$ electrodes measured in PBS between the same limits are also shown for comparison.

Table 4.17: The CSC_C for $PP_{17.5}$ electrodes measured at different sweep rates of v in PBS+BSA (with P/S) electrolyte in the WW of -0.6 to 0.8 V *vs* SCE. Results show the average and standard deviation of 5 repeated readings. Results for tests conducted in PBS are also shown for comparison.

	CSC_C (mCcm^{-2})	
v (Vs^{-1})	**PBS+BSA**	**PBS**
0.05	90 ± 2	94 ± 2
0.1	78 ± 1	81 ± 2
0.5	35 ± 2	38 ± 1
1	18 ± 1	20 ± 1

[14] There was no observable difference between tests conducted in electrolyte supplemented with sodium azide versus penicillin/streptomycin for TiNIV electrodes, and plots demonstrating this finding may be viewed in Appendix E.

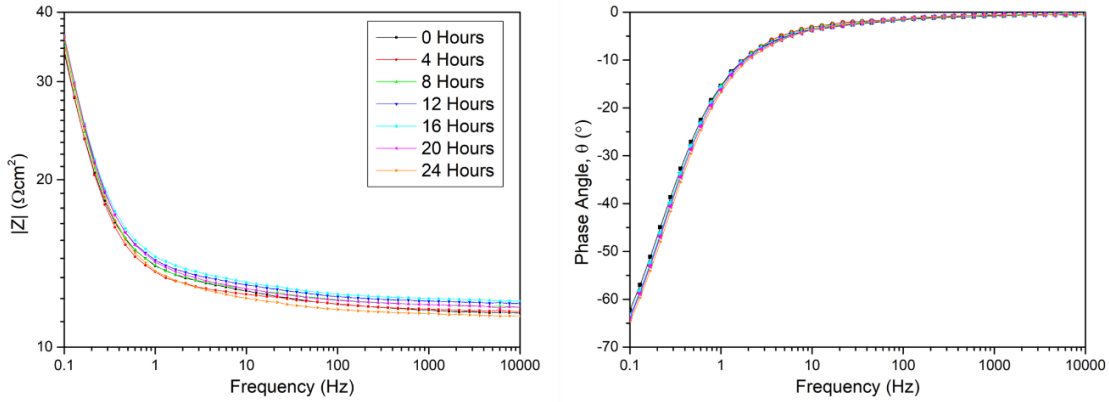

Figure 4.31: Representative impedance (left) and phase angle Bode plots (right) for $PP_{17.5}$ electrodes measured in PBS+BSA electrolyte over 24 hours.

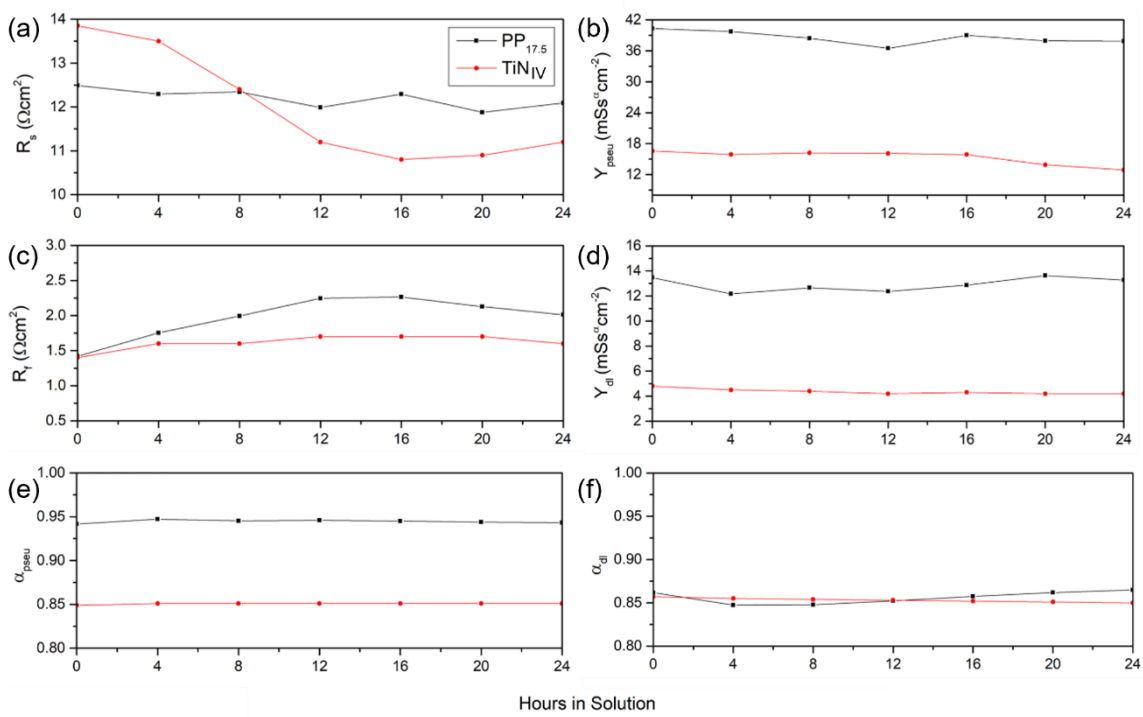

Figure 4.32: Plots showing the variation in (a) R_s, (b) Y_{pseu}, (c), R_f, (d) Y_{dl}, (e) α_{pseu}, and (f) α_{dl} as a function of time immersed in PBS+BSA solution (with P/S) for $PP_{17.5}$ electrodes (black). The values obtained for TiN_{IV} electrodes (red) are also given for comparison.

4.3.5 Assessing Cycling Lifetime in PBS

The cycling lifetime of $PP_{17.5}$ electrodes was assessed in PBS by subjecting them to 10,000 consecutive CV cycles at sweep rates of v= 0.1 and 1 Vs^{-1}, where tests at the latter scan rate were carried out for both the restricted and full WW of PEDOT:PSS. EIS measurements were made before the experiment initiated and after every 1000 cycles to monitor electrode performance. Experiments in which cycling was carried out using the restricted WW were done in replicates of 5, whereas those for the full WW were done

in replicates of 3. Figure 4.33 shows representative Bode and Nyquist plots for the electrodes before testing and after 10,000 cycles for the three testing conditions. Only very minute changes are evident for electrodes tested at 1 Vs^{-1} (both WW's), whereas a significant increase in $|Z|_{<10Hz}$ is apparent along with a positive shift in the phase angle for electrodes tested at 0.1 Vs^{-1}. The shape of the Nyquist plot also changes for electrodes tested at a slow scan rate. Similarly, voltammograms plotted after 0 and 10,000 cycles (Figure 4.34) display no significant change in shape or volume for v = 1 Vs^{-1} (both WW's), whereas the voltammogram for v = 0.1 Vs^{-1} becomes depressed and loses ~60% of its area by the end of the testing regiment.

The EIS spectra obtained throughout the duration of the tests were fitted with the equivalent circuit shown in Figure 4.4 a, and the model variables are plotted as a function of cycle number in Figure 4.35. The model was able to produce convergent fits for all the spectra collected when testing at a scan rate of 1 Vs^{-1}, suggesting that no fundamental change in the charge transfer mechanisms occurred as a result of cycling. However, the model efficiency declined after 6,000 cycles at a scan rate of 0.1 Vs^{-1}. Since plausible results were still obtained using this model, it was retained. Included in the plots are also the results for the assessment of cyclic stability of TiN_{IV} electrodes[15], carried out at scan rates of 0.1 and 1 Vs^{-1}.

The most notable change occurs in the value of R_f for $PP_{17.5}$ electrodes cycled at a scan rate of 0.1 Vs^{-1}, increasing considerably to ~ 37 Ωcm^2 by the end of 10,000 cycles. A large decrease in the Y_{pseu} and α_{pseu} are also evident for this condition, with values approaching those of TiNIV by the end of the experiment. Y_{dl} also undergoes slight degradation, although α_{dl} remains consistent. The charge retention % also reflects this drop in electrochemical performance, where only ~ 40% of the original CSC_C is measured after 10,000 cycles. None of these issues present in the $PP_{17.5}$ electrodes tested at a scan rate of 1 Vs^{-1}, for either voltage range. The results indicate no significant changes to any of the variables, and charge retention is maintained at values upwards of 99%.

[15] There was no observable difference between the lifetime cycling tests of TiNI and TiNIV electrodes. Plots demonstrating this finding may be viewed in Appendix G.

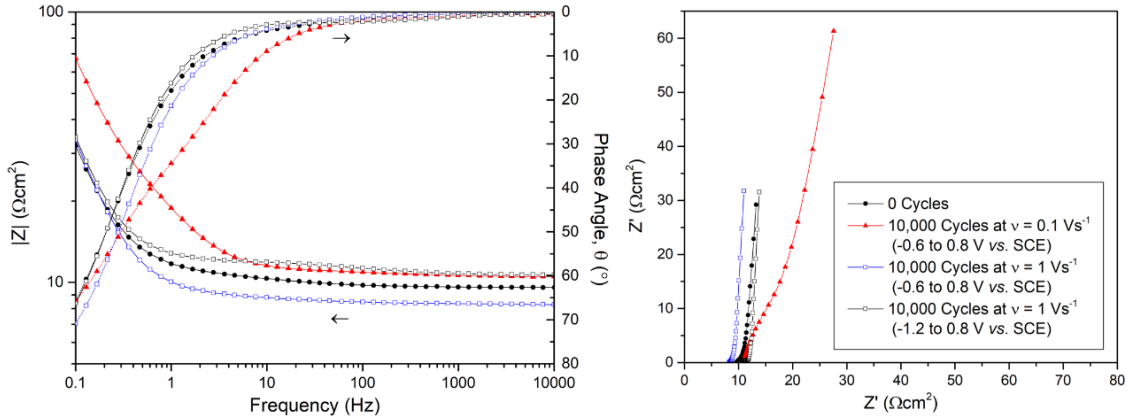

Figure 4.33: Representative impedance and phase angle Bode plots (left) and Nyquist plots (right) for $PP_{17.5}$ electrodes measured in PBS before and after 10,000 CV cycles at sweep rates of 0.1 Vs^{-1} and 1 Vs^{-1} using cycling limits of -0.6 to 0.8 V *vs.* SCE and -1.2 to 0.8 V *vs.* SCE.

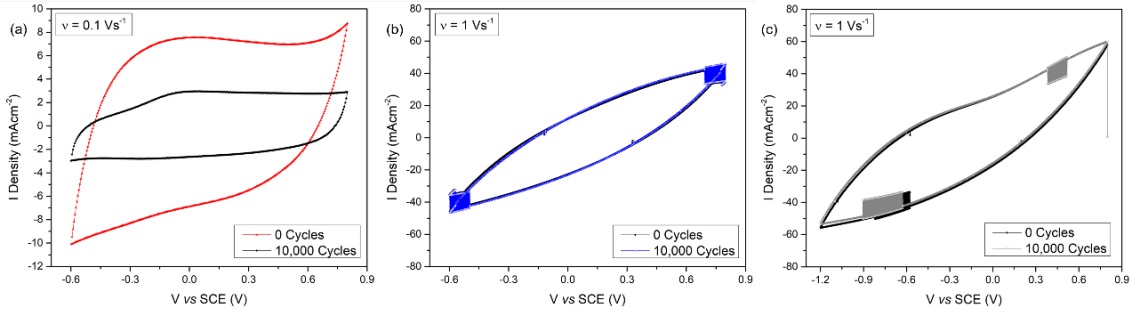

Figure 4.34: Representative voltammograms of $PP_{17.5}$ electrodes subjected to 10,000 CV cycles at (a) 0.1 Vs^{-1} (limits between -0.6 to 0.8 V *vs.* SCE), (b) 1 Vs^{-1} (limits between -0.6 to 0.8 V *vs.* SCE), (c) 1 Vs^{-1} (limits between -1.2 to 0.8 V *vs.* SCE), showing the response after 0 and 10,000 cycles.

The $PP_{17.5}$ electrode surfaces were analysed following cyclic lifetime assessment. Figure 4.36 shows micrographs of the surfaces after 10,000 cycles at 1 Vs^{-1} (reduced WW) and 0.1 Vs^{-1}, along with micro-Raman spectra collected before and after cycling. No cracks, delaminations, or other indications of damage could be identified on the electrodes cycled at 1 Vs^{-1} for either the reduced or full (not shown) WW. No discernible change could be detected in the micro-Raman spectra for these electrodes either. With regards to electrodes tested at 0.1 Vs^{-1}, large areas of the PEDOT:PSS coating were observed to be missing, exposing the TiN_{IV} material underneath. However micro-Raman spectra obtained on sections of remaining PEDOT:PSS were found to be identical to those obtained before cycling. Moreover, spectra obtained on the exposed TiN_{IV} also appear identical to those collected on pristine TiN surfaces.

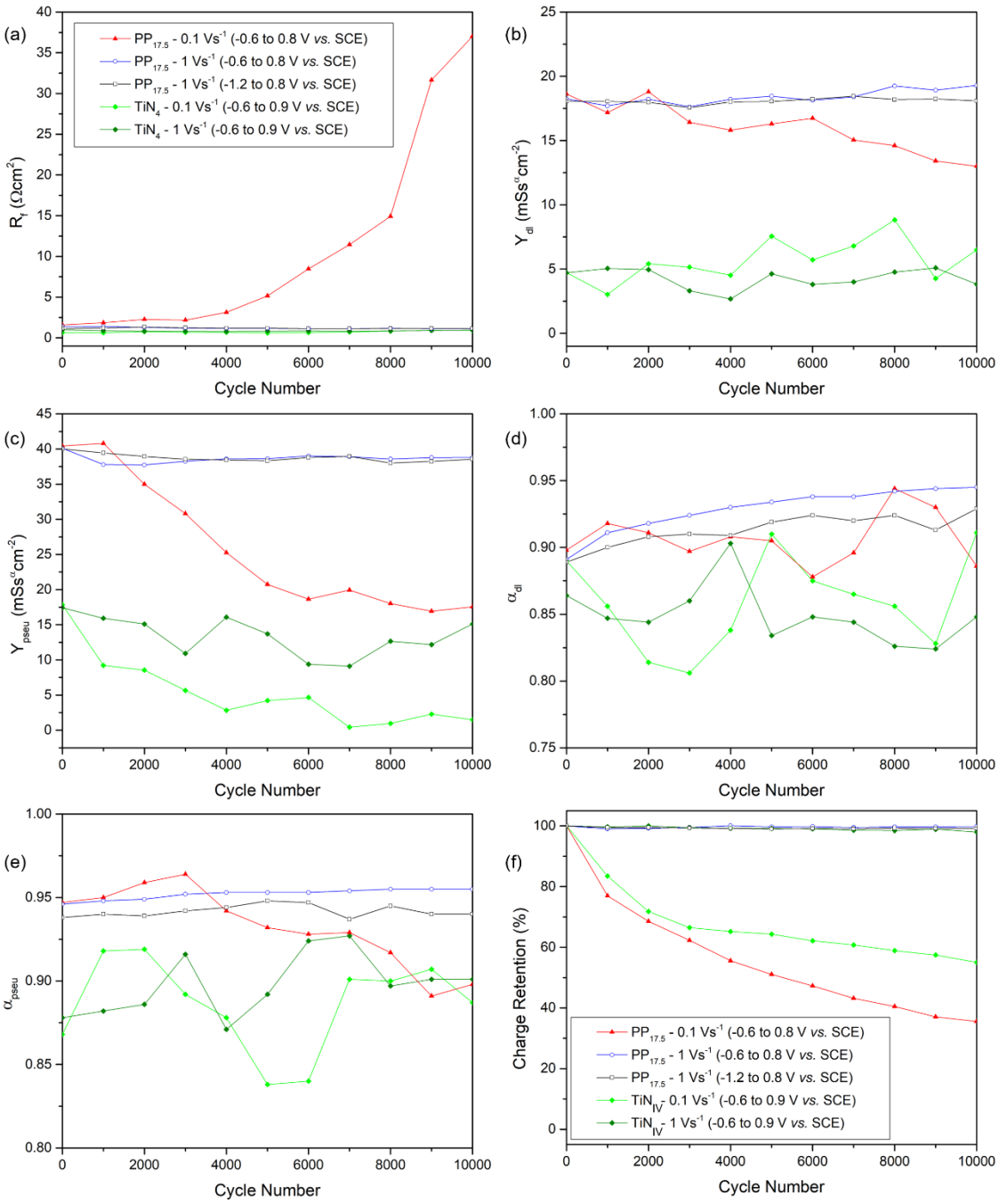

Figure 4.35: Plots of (a) R_f, (b) Y_{dl}, (c) Y_{pseu}, (d) α_{dl}, (e) $\alpha_{pseu,}$ and (f) charge retention % as a function of cycle number for $PP_{17.5}$ electrodes subjected to 10,000 CV cycles at scan rates of 0.1 Vs^{-1} (limits between -0.6 to 0.8 V *vs.* SCE), 1 Vs^{-1} (limits between -0.6 to 0.8 V *vs.* SCE), and 1 Vs^{-1} (limits between -1.2 to 0.8 V *vs.* SCE). Plots for lifetime cycling tests carried out on TiN_{IV} electrodes are also shown for comparison and were obtained at scan rates of 0.1 Vs^{-1} (limits between -0.6 to 0.9 V *vs.* SCE), and 1 Vs^{-1} (limits between -0.6 to 0.9 V *vs.* SCE).

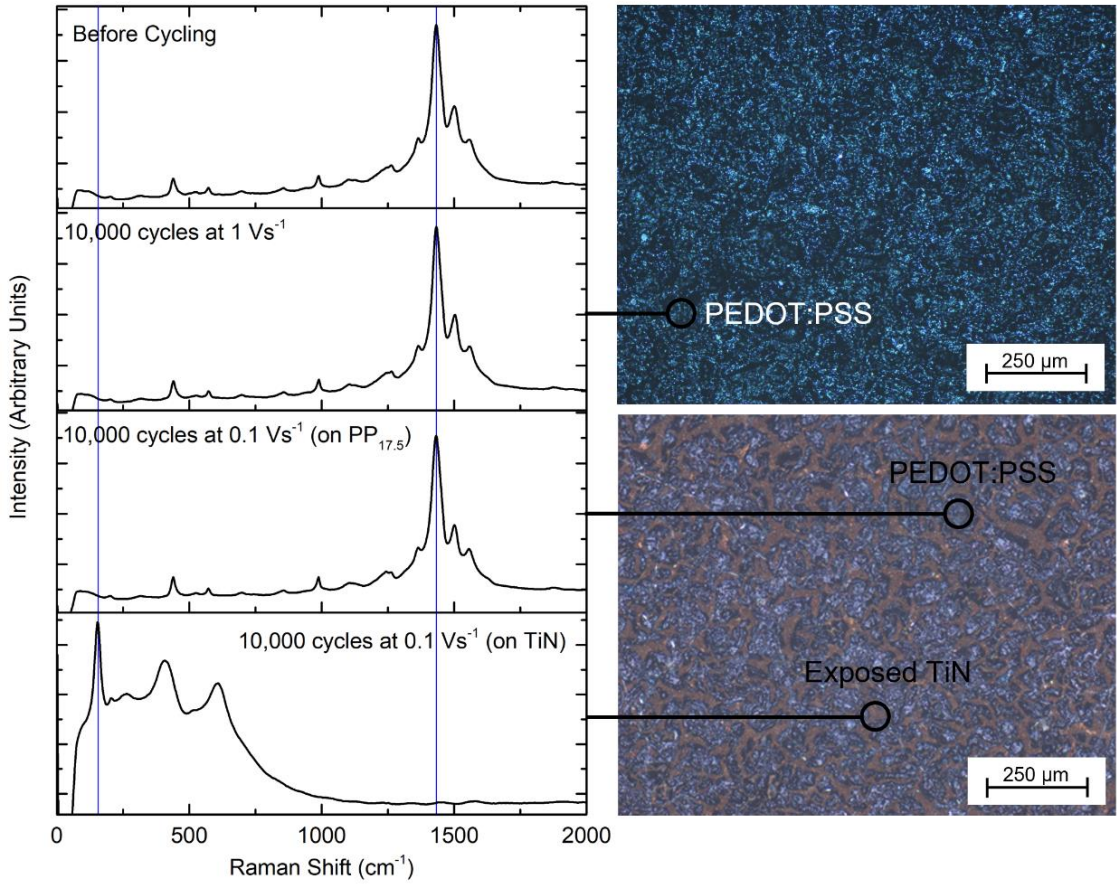

Figure 4.36: Representative micro-Raman spectra of $PP_{17.5}$ electrodes before cycling and after 10,000 CV cycles at scan rates v of 1 and 0.1 Vs^{-1}. Measurements were also made on the sections of TiN that became exposed after cycling at 0.1 Vs^{-1}. Optical microscope images of the surfaces after cycling are also given for context.

4.3.6 Assessing Adhesion of PEDOT:PSS to TiN using Ultrasonication

The adhesion strength of PEDOT:PSS layers to the underlying TiN was assessed by subjecting $PP_{17.5}$ electrodes to 45 kHz ultrasonication in PBS (method described in section 3.4). EIS measurements and microscope imaging were performed every 5 minutes. Representative impedance Bode plots from the experiment are shown in Figure 4.37 a. Minute changes to the electrochemical behaviour were observed in the first 20 minutes of testing, and the EIS spectra were successfully modelled using the equivalent circuit shown in Figure 4.4 a. With reference to Figure 4.37 b, no significant upward trend in the $|Z|_{1Hz}$ was in fact observed up to this time point, and results of circuit fitting (Figure 4.37 c) show stable values for all the variables. Correspondingly, no signs of physical damage could be observed on the electrode surfaces for the first 20 minutes (Figure 4.38).

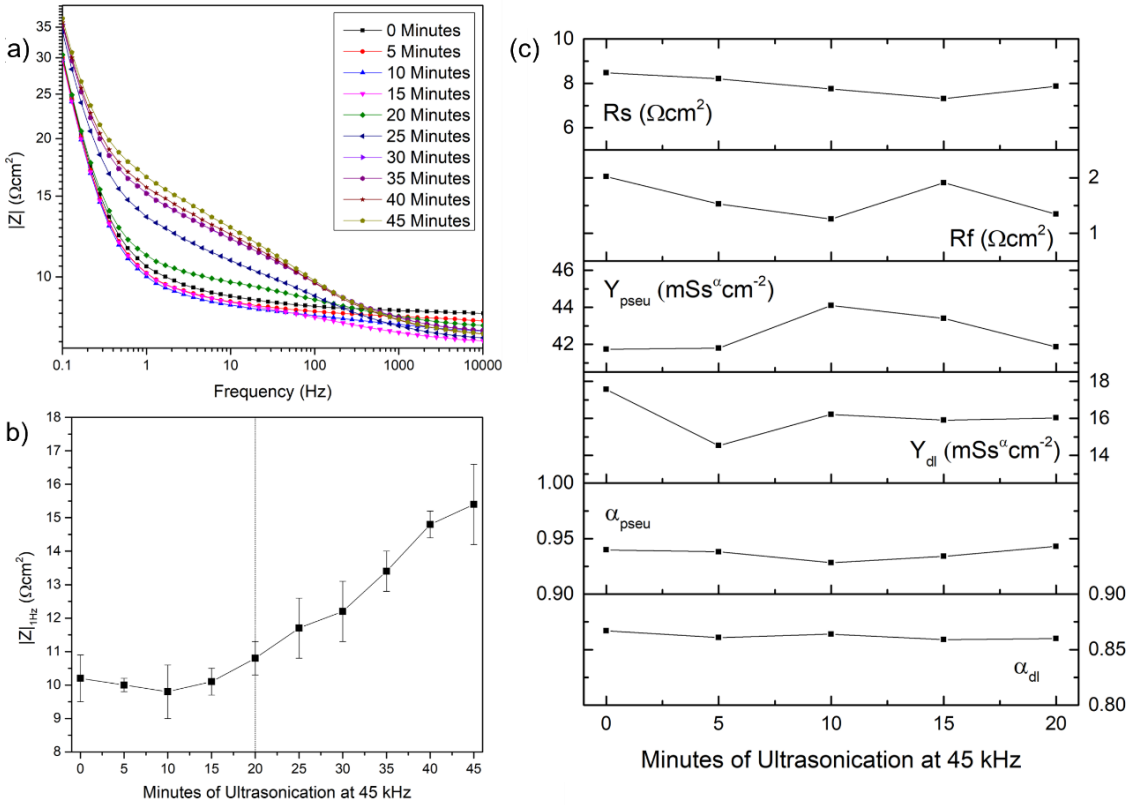

Figure 4.37: (a) Representative Bode impedance plots for $PP_{17.5}$ electrodes subjected to 45 kHz ultrasonication in PBS. EIS measurements were made every 5 minutes for a total of 45 minutes; (b) Plot of the average $|Z|_{1Hz}$ with minutes of ultrasonication. The error bars show standard deviation from the mean of 3 repeated readings. Dotted line indicates timepoint beyond which visual damage was observed on the electrode, and; (c) Plots of R_s, R_f, Y_{pseu}, Y_{dl}, α_{pseu}, and α_{dl} with minutes of ultrasonication up to 20 minutes, as derived from fitting the equivalent circuit model shown in Figure 4.4 a.

Significant changes appeared on the electrodes after 20 minutes of testing, where the impedance measurements between ~ 0.3 and 100 Hz increased gradually until the end of the experiment (Figure 4.37 a and b). The equivalent circuit used previously in fact did not return satisfactory convergent fits beyond this timepoint and so no modelling was performed between timepoints of 25-45 minutes. Visible damage was also observed when the electrode surfaces were assessed under optical microscope following experiment termination. Figure 4.38 shows areas of exposed TiN_{IV} (green circles), emergent cracks (white circles), and instances where sections of the PEDOT:PSS appear to have come off (red circle).

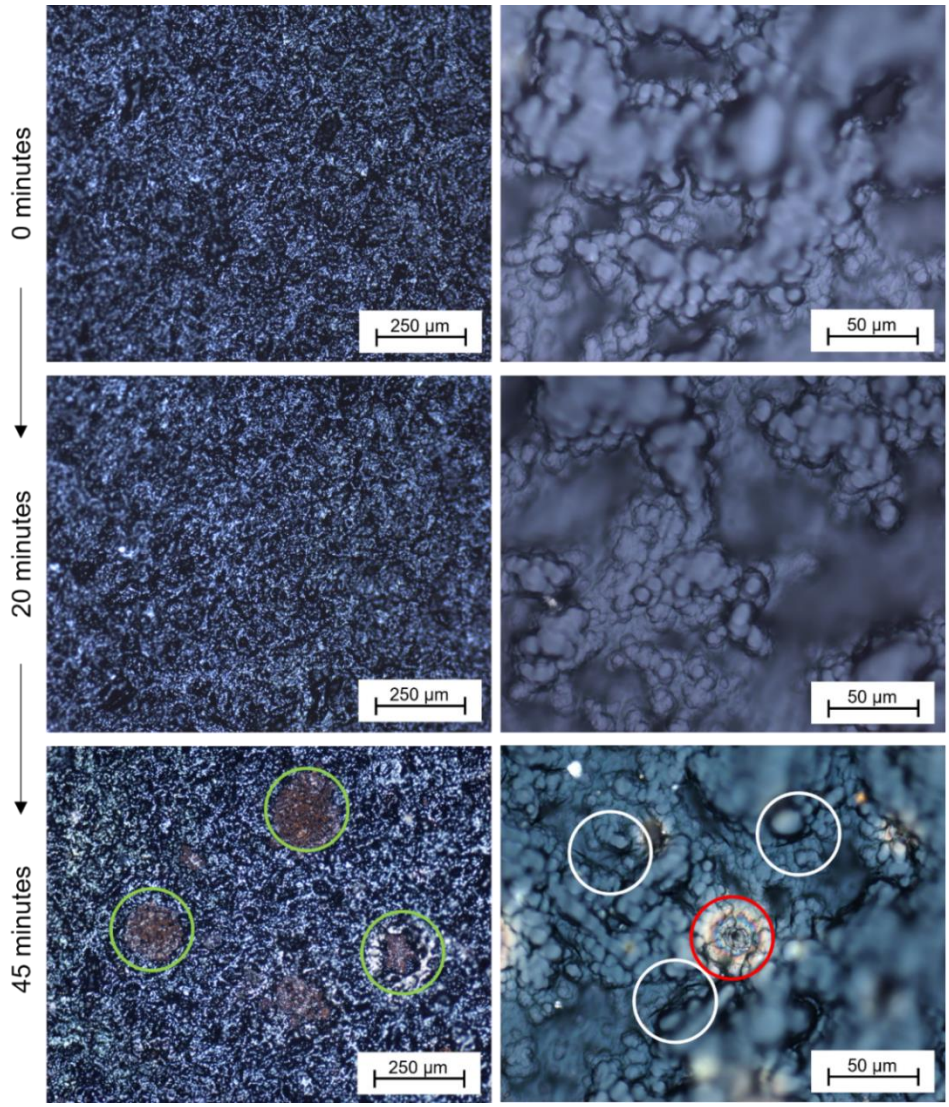

Figure 4.38: Representative optical microscopy images at 2 magnifications of $PP_{17.5}$ electrodes before and after 20 and 45 minutes of ultrasonication in PBS. Green circles show areas of TiN_{IV} exposure, white circles highlight cracks, and the red circle shows an instance where sections of the PEDOT:PSS appear to have come off after 45 minutes of testing.

4.3.7 Assessing Attachment and Proliferation of NHDF

$PP_{17.5}$ and TiN_{IV} electrodes were incubated with neonatal human dermal fibroblasts (NHDF) at a density of 8×10^4 cells/cm^2 for a total of 72 hours to assess susceptibility towards fibrous encapsulation. The relative number of viable fibroblasts adhering to the electrode surfaces was determined through spectrophotometric detection of resazurin reduction (method described in section 3.6.2). The results of two replicate tests where 5 electrodes were assessed per electrode type per test (i.e., n=10), are shown in Figure 4.39 for 24, 48, and 72 hours. The largest average reduction value ($PP_{17.5}$ after 72 hours) was given a value of '1', and all other values are given relative to it. Statistically significant

differences ($p < 0.05$) were observed on every day between TiN_{IV} and $PP_{17.5}$ electrodes (marked *, ***, and ***** in the figure), where $PP_{17.5}$ electrode surfaces had higher numbers of NHDF cells. After 72 hours, the $PP_{17.5}$ electrodes had 1.67 times more viable fibroblasts than the TiN_{IV}.

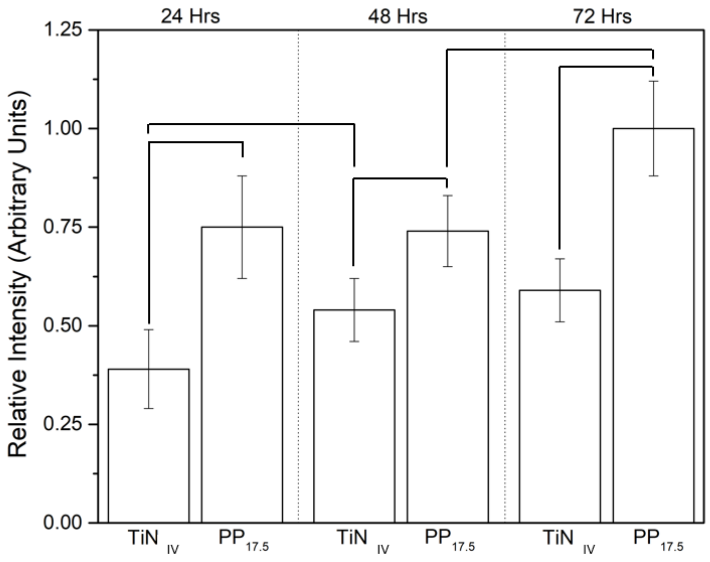

Figure 4.39: Average relative intensity of Resazurin reduction by NHDF cells measured on TiN_{IV} and $PP_{17.5}$ electrodes. Cells were seeded at a density of 8×10^4 cells/cm^2. Measurements were made using spectrophotometry at wavelengths of 570 and 600 nm after 24, 48, and 72 hours of incubation. Results show the average with standard deviation from the mean of duplicate tests where a sample size of 5 was employed per electrode type per test (i.e., n=10). The reduction value for $PP_{17.5}$ after 72 hours was given a value of '1', and all other values are given relative to it. Black line connectors indicate statistically significant differences ($p < 0.05$) between groups, determined using one-way ANOVA and a post-hoc Tukey test.

SEM images of NHDF fixed on the electrode surfaces using glutaraldehyde after 72 hours of incubation are shown at various magnifications in Figure 4.40 and Figure 4.41. Cell coverage is visually very different between TiN_{IV} and $PP_{17.5}$ electrodes, where the latter features a confluent layer. An inset showing the original PEDOT:PSS surface at the same magnification is in fact provided in Figure 4.40 b, for reference. Conversely, cells on TiN_{IV} surfaces do not form a confluent layer. Fibroblast size and morphology also vary significantly, with large, flattened and well-spread cells on $PP_{17.5}$ surfaces (Figure 4.41 d-f), while cells on the TiN_{IV} electrodes are smaller, narrower, and exhibit sections of no surface contact due to the feature-heavy 3D surfaces (Figure 4.41 a-c).

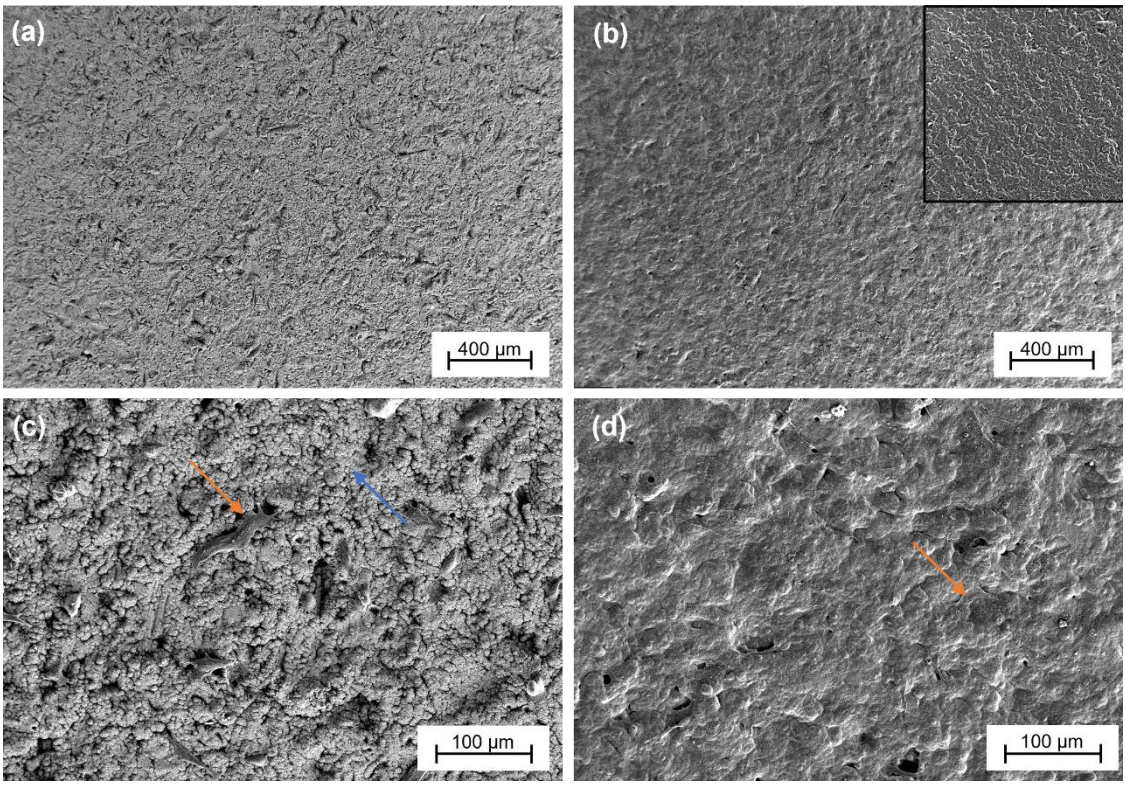

Figure 4.40: SEM images of NHDF on TiN_{IV} (a, c) and $PP_{17.5}$ (b, d) electrodes after 72 hours of culture and fixing in glutaraldehyde. Surfaces were sputter-coated with a nanometric layer of Au to improve conductivity. Inset in (b) shows a PEDOT:PSS surface before culturing at the same magnification for comparison. Orange arrows indicate fibroblasts, whereas blue arrow indicates uncovered electrode surface.

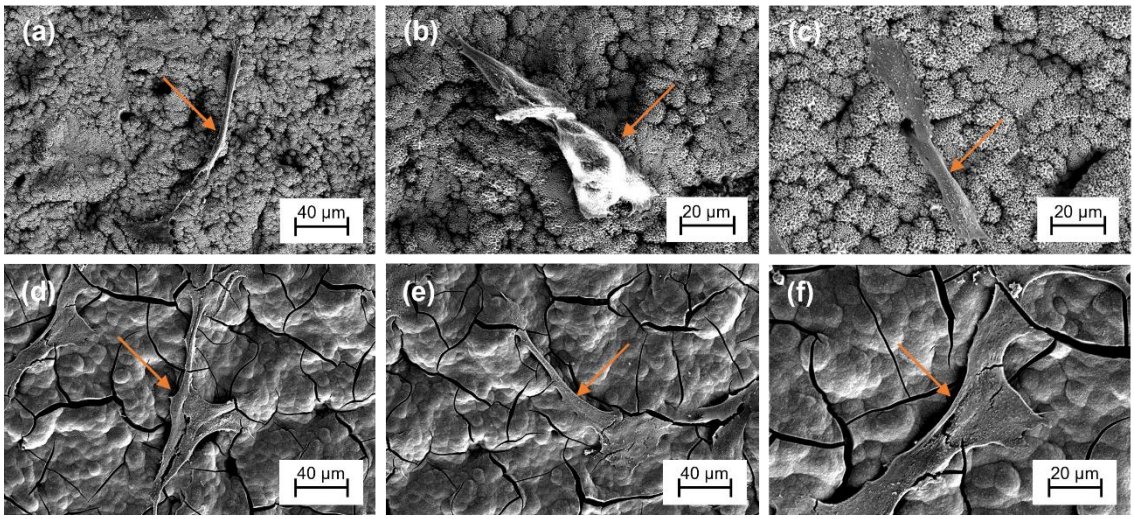

Figure 4.41: High magnification SEM images of NHDF on TiN_4 (a-c) and $PP_{17.5}$ (d-f) electrodes after 72 hours of culture and fixing in glutaraldehyde. Surfaces were sputter-coated with a nanometric layer of Au to improve conductivity. Images on $PP_{17.5}$ were taken on the periphery of the electrode surface where cell density was lowest. Orange arrows indicate fibroblasts growing on the electrode surface.

4.4 Development of TiN/PEDOT:PSS/Alginate Electrodes

4.4.1 The Electrogelling Process

$PP_{17.5}$ electrodes were selected for the subsequent development of TiN/PEDOT:PSS/Alginate multi-layer electrode systems (method described in section 3.1.6). Optimum current density for the electrogelling procedure was determined to be 0.85 $mAcm^{-2}$ through a series of trial experiments in which the current density was increased in increments of 0.05 $mAcm^{-2}$ (starting from 0.8 $mAcm^{-2}$) until reaching an acceptable gel. Current densities at which the gel became dislodged from the electrode, at which large bubbles were observed in the gel (Figure 4.42 a), or at which the PEDOT:PSS suffered damage such as cracking (Figure 4.42 b) or delamination (Figure 4.42 c) were abandoned.

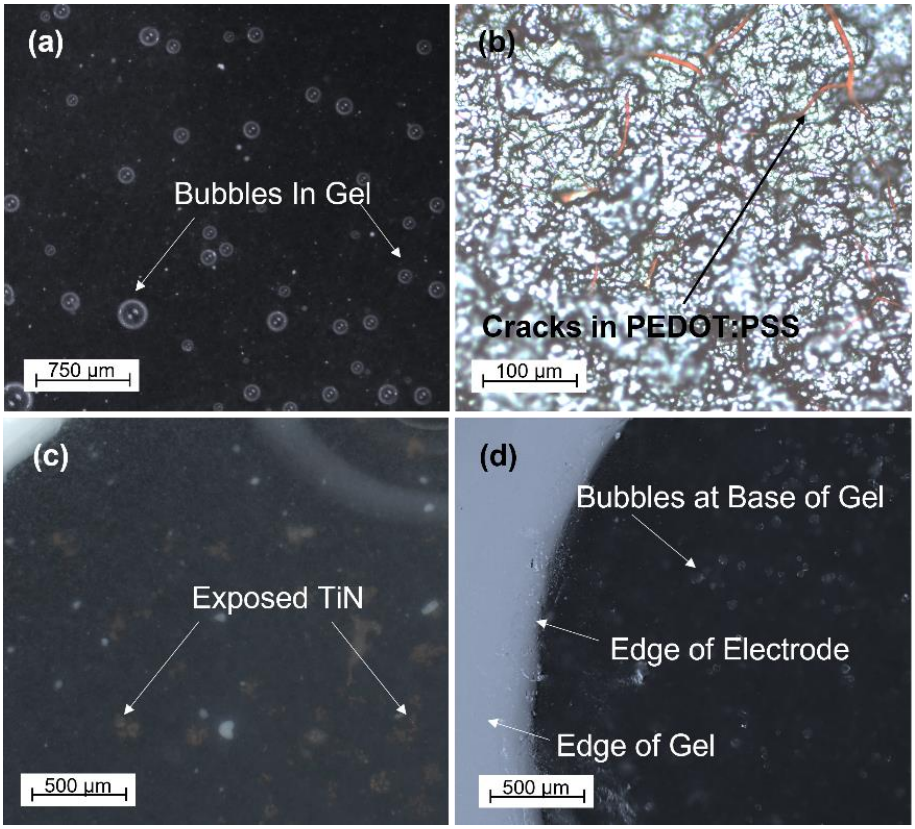

Figure 4.42: Optical microscope images showing: (a) Bubbles in a gel grown using a current density of 1 $mAcm^{-2}$ for 60s; (b) Cracks in the PEDOT:PSS layer after depositing a gel at 1.1 $mAcm^{-2}$ for 60s. Image taken after drying gel in air and removing it with tweezers; (c) Areas of TiN exposed under the PEDOT:PSS layer, viewed through a gel deposited using a current density of 1.1 $mAcm^{-2}$ for 60s; (d) Gel formation over PTFE mask and bubbles at the base of the gel. Observed in a gel deposited at a current density of 0.85 $mAcm^{-2}$ for 180s.

Another series of experiments were then carried out to determine viable deposition times (30 – 180 s) in increments of 30s. Thresholds were determined when the calcium alginate layer lacked sufficient structural integrity to withstand washing (indirect spraying with DI water from a wash bottle) (lower threshold) or dislodged from the electrode (upper threshold). An example is also given in Figure 4.42 d of a gel grown at 0.85 $mAcm^{-2}$ for 180 s that resisted complete delamination. Bubbles at the base of the gel and spill-over growth were observed and are labelled in the image. Deposition times of 60, 90, and 120s were ultimately chosen to produce TiN/PEDOT:PSS/Alginate electrodes labelled CA_{60s}, CA_{90s}, and CA_{120s}, respectively.

Figure 4.43 shows a representative plot of the electrodeposition process, in which a $PP_{17.5}$ electrode (GSA 0.126 cm^2, Ø 4 mm) undergoes calcium alginate deposition for 120s, producing a CA_{120s} electrode. The voltage magnitude rises steeply for the first 30s and then gradually for the duration of the process.

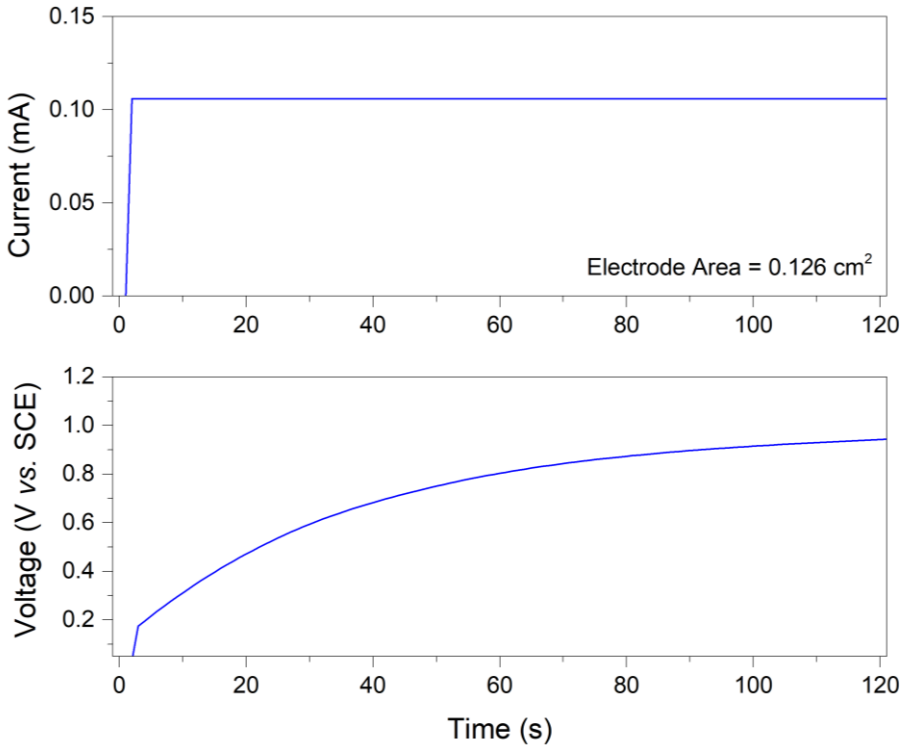

Figure 4.43: Representative plot of deposition current (density of 0.85 $mAcm^{-2}$) and voltage response against time, for a CA_{120s} electrode with a surface area of 0.126 cm^2 and diameter 4 mm.

4.4.2 Imaging and Thickness Measurements

After being immersed in a 1 mM $CaCl_2$ hardening solution for 30 minutes, the gels were transferred to PBS solution and allowed to swell for 30 minutes. After the time had elapsed the electrodes were removed from the electrolyte, the excess liquid dabbed away with filter paper and imaging was carried out at different magnifications using optical microscopy. The technique used produced clear gels (Figure 4.44 a) which were largely free of any residual $CaCO_3$ particles. Higher magnification reveals the multi-scale porous structure of the gel, evident in both the optical microscope image and in the SEM image (method for SEM analysis of hydrogels is described in sections 3.2.1 and 3.6.4), labelled b and c in Figure 4.44, respectively.

The stereo micrographs shown in Figure 4.45 a were taken in side-view to determine the shape and thickness of the three different calcium alginate coatings (method described in section 3.2.5.3). In all cases the coatings take on the form of spherical caps, reminiscent of sessile drops. Thickness measurements were made from apex to base on five replicate coatings. The results with standard deviation were found to be 405 ± 21 µm, 581 ± 44 µm, and 650 ± 101 µm for CA_{60s}, CA_{90s}, and CA_{120s}, respectively. The relationship between coating thickness and electrogelling time is therefore not linear (Figure 4.45 b).

4.4.3 Micro-Raman Spectroscopy

Representative micro-Raman spectra collected using a 532 nm λ green light laser for $CaCO_3$ powder and CA_{60s} electrodes are given in Figure 4.46 (method described in section 3.2.3). The spectrum for a pristine $PP_{17.5}$ electrode is also given for comparison. The Raman shifts of the nine prominent peaks identified (numbered 1-9 on the figure) for the CA_{60s} electrode are given in Table 4.18, where peaks number 6, 7, and 9 also emerge in the spectrum for $CaCO_3$ powder. No peaks associated with PEDOT:PSS emerged.

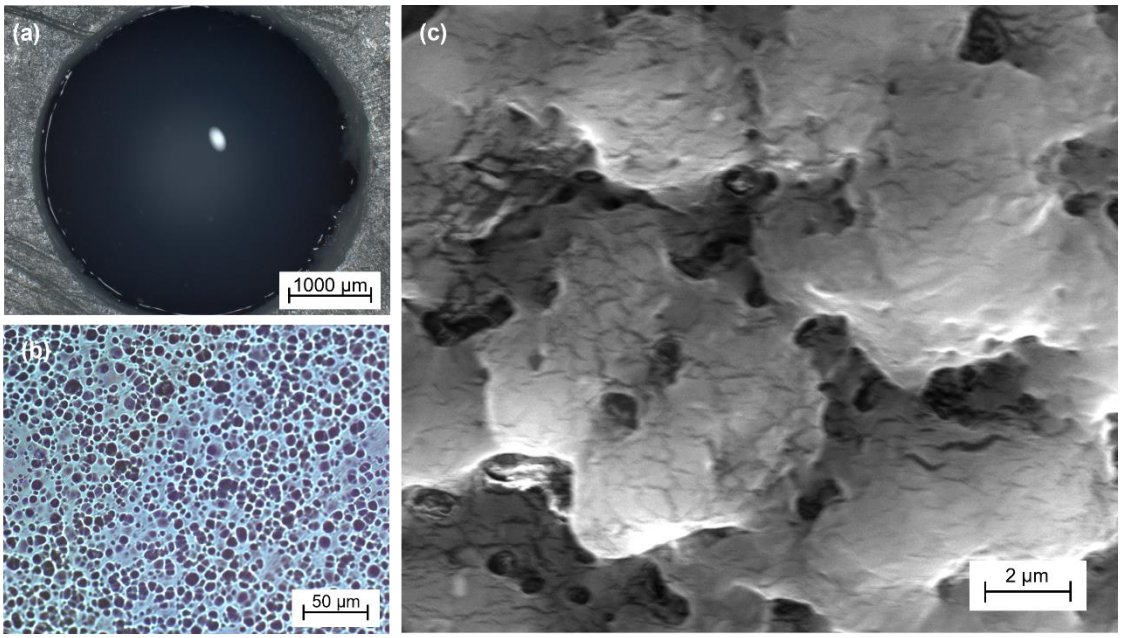

Figure 4.44: (a, b) Optical microscope images of a CA_{120s} electrode at different magnifications. Images taken after 30 minutes of swelling in PBS; (c) High magnification SE-SEM image of a CA_{120s} electrode after fixation with glutaraldehyde and sputter-coating with Au.

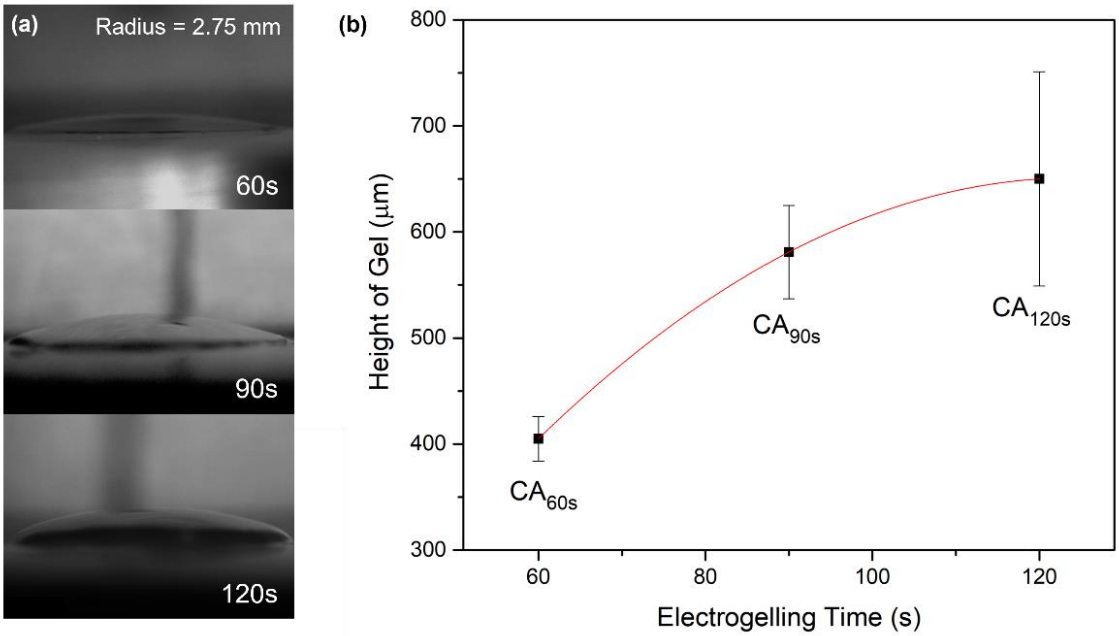

Figure 4.45: (a) Stereo microscope images taken in side profile of CA_{60s}, CA_{90s}, and CA_{120s} electrodes (surface area of 0.238 cm^2 and diameter 5.5 mm); (b) Plot showing the relationship between deposition time and alginate layer thickness. Images taken after 30 minutes of swelling in PBS.

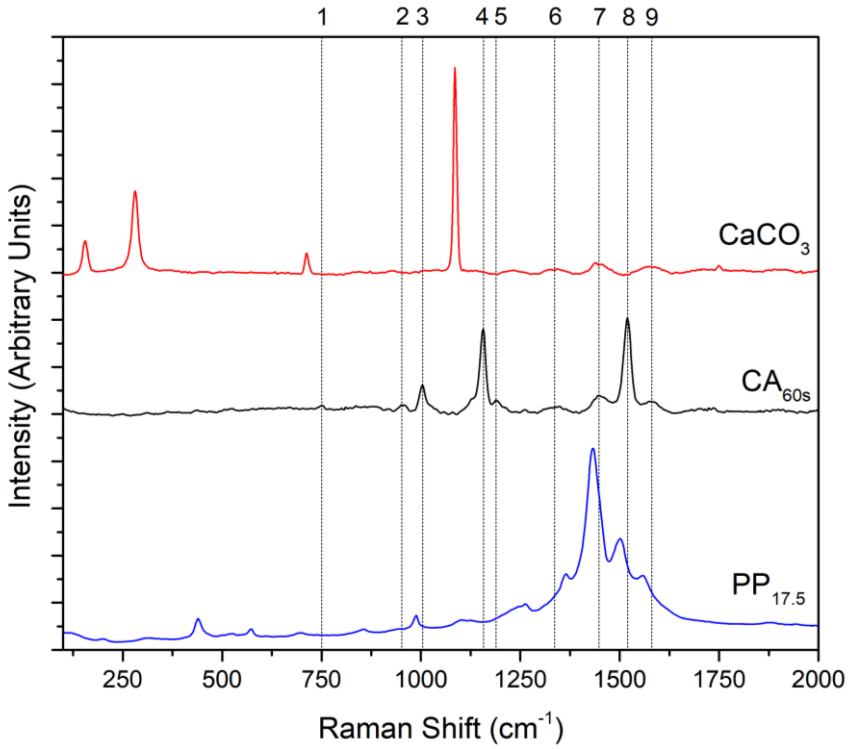

Figure 4.46: Representative micro-Raman spectra for $CaCO_3$ powder (red), CA_{60s} electrodes (black), and $PP_{17.5}$ electrodes (blue). Numbered lines indicate notable peaks emerging from the CA_{60s} measurements. Corresponding Raman shifts are given in Table 4.18.

Table 4.18: Raman peaks and their respective shifts as identified in Figure 4.46. The associated spectra are also indicated (CA_{60s} or $CaCO_3$). No peaks associated with $PP_{17.5}$ material were identified in the CA_{60s} measurements.

Peak No.	Raman Shift (cm^{-1})	Associated Spectra
1	751	CA_{60s}
2	955	CA_{60s}
3	1004	CA_{60s}
4	1157	CA_{60s}
5	1188	CA_{60s}
6	1345	$CaCO_3$, CA_{60s}
7	1441	$CaCO_3$, CA_{60s}
8	1520	CA_{60s}
9	1585	$CaCO_3$, CA_{60s}

4.4.4 Electrochemical Testing in Physiological Electrolytes

4.4.4.1 Testing in PBS

CA_{60s}, CA_{90s}, and CA_{120s} electrodes were subjected to electrochemical measurements in PBS solution, using testing procedures identical to those implemented for PEDOT:PSS and TiN electrodes (method described in section 3.3). EIS Bode and Nyquist plots are

given in Figure 4.47, where the plots for $PP_{17.5}$ are also included for comparison. A clear positive shift in |Z| is apparent for the alginate-coated electrodes, predominantly due to a large increase in the solution resistance at high frequencies (~ 7 Ωcm^2). With regards to fitting an equivalent circuit, the spectra were successfully modelled using the circuit shown in Figure 4.4 a, achieving convergent fits for all three deposition times The results are shown in Table 4.19.

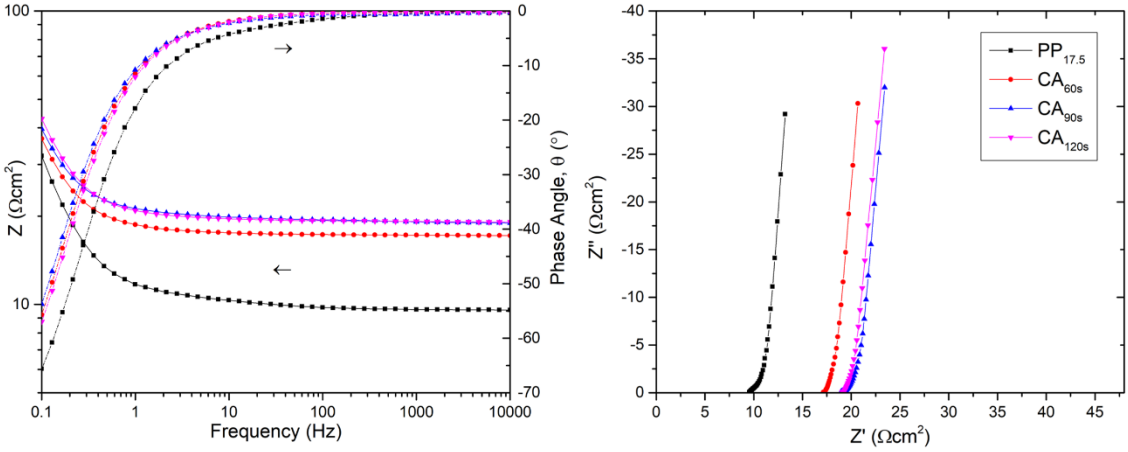

Figure 4.47: Representative impedance and phase angle Bode plots (left) and Nyquist plots (right) for CA_{60s} (red), CA_{90s} (blue), and CA_{120s} (pink) electrodes measured in PBS. Plots for $PP_{17.5}$ electrodes (black) are also shown for comparison.

Table 4.19: Results of fitting the EIS spectra obtained for CA_{60s}, CA_{90s}, and CA_{120s} electrodes (Figure 4.47 to the equivalent circuit model given in Figure 4.4 a, along with the $|Z|_{1Hz}$. Results for $PP_{17.5}$ electrodes are also provided for comparison. Tests were conducted in PBS. Results are given as the average of 5 repeated readings with standard deviation from the mean.

Circuit Element	Units	$PP_{17.5}$	CA_{60s}	CA_{90s}	CA_{120s}
R_s	Ωcm^2	11.0 ± 1.2	17.6 ± 0.3	18.8 ± 0.6	18.7 ± 0.4
R_f	Ωcm^2	1.6 ± 0.5	1.9 ± 0.3	2.1 ± 0.3	2.0 ± 0.4
Y_{dl}	$mSs^{\alpha}cm^{-2}$	19.3 ± 3.0	13.5 ± 2.4	13.9 ± 2.2	12.3 ± 0.6
α_{dl}	/	0.890 ± 0.007	0.861 ± 0.037	0.848 ± 0.037	0.854 ± 0.025
Y_{pseu}	$Ss^{\alpha}cm^{-2}$	41.4 ± 2.6	35.3 ± 3.4	34.8 ± 3.9	33.3 ± 6
α_{pseu}	/	0.964 ± 0.014	0.913 ± 0.006	0.910 ± 0.005	0.912 ± 0.005
$\|Z\|_{1Hz}$	Ωcm^2	12.2 ± 1.3	18.6 ± 0.5	20.4 ± 0.5	21.1 ± 0.5

The electrodes were also subjected to CV testing, where resulting voltammograms are shown in Figure 4.48 and the measured CSC_C listed in Table 4.20. Voltammograms for $PP_{17.5}$ electrodes are also shown for comparison. The water window limits were not observed to change with the addition of an alginate layer, and so scans were carried out

between the voltage limits of -0.6 to 0.8 V *vs* SCE. Significant ($p < 0.05$) drops in CSC_C were recorded for all CA electrodes with respect to the original $PP_{17.5}$, where the drop increases with alginate deposition time. This pattern disappears at high scan rates ($\nu = 1$ Vs^{-1}) as the CSC_C is equal for all CA electrodes. The error bars for CA_{120s} electrodes are notably high at all scan rates.

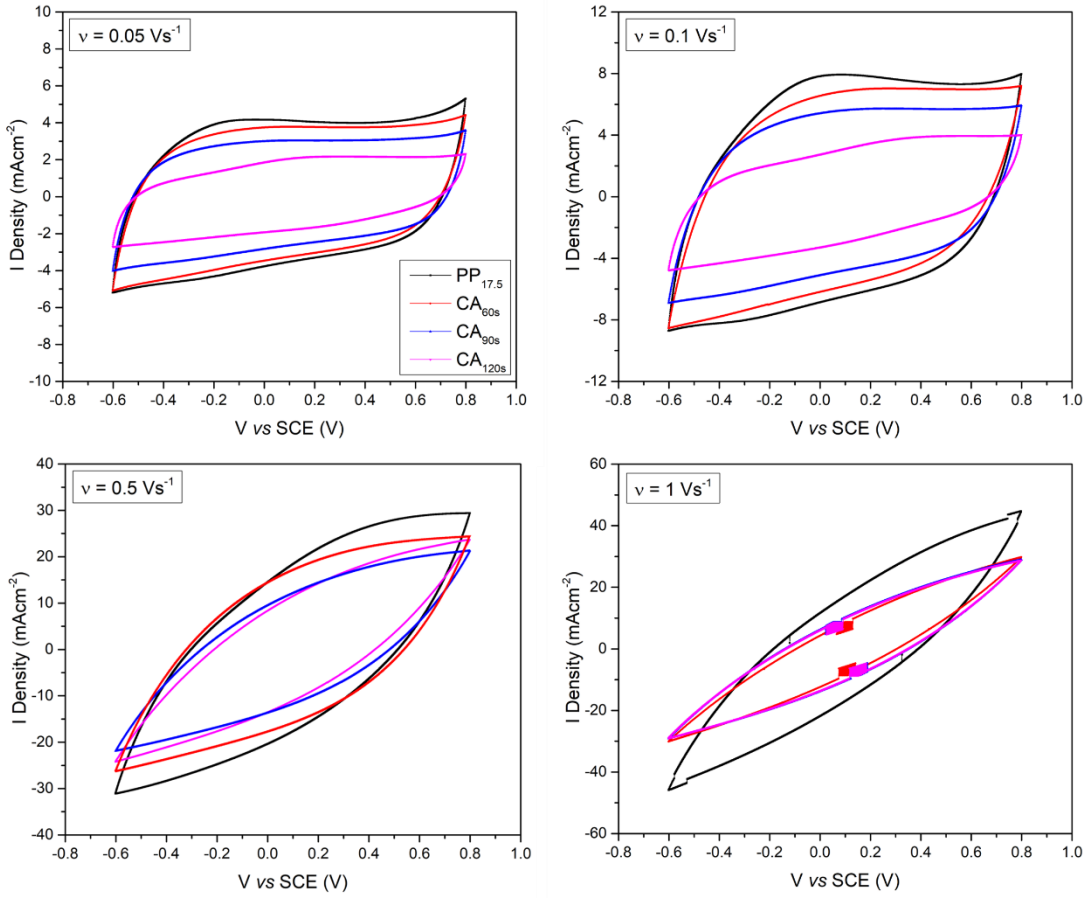

Figure 4.48: Representative voltammograms for CA_{60s} (red), CA_{90s} (blue), and CA_{120s} (pink) electrodes measured at different sweep rates of ν in PBS. Voltammograms for $PP_{17.5}$ electrodes (black) are also plotted for comparison.

Table 4.20: The CSC_C for CA_{60s}, CA_{90s}, and CA_{120s} electrodes, measured at different sweep rates of ν in PBS. Results show the average and standard deviation of 5 repeated readings. Results for $PP_{17.5}$ electrodes are also provided for comparison.

	CSC_C ($mCcm^{-2}$)			
ν (Vs^{-1})	**$PP_{17.5}$**	**CA_{60s}**	**CA_{90s}**	**CA_{120s}**
0.05	94 ± 2	84 ± 5	73 ± 2	52 ± 14
0.1	81 ± 2	70 ± 4	61 ± 1	47 ± 15
0.5	38 ± 1	24 ± 1	20 ± 1	18 ± 6
1	20 ± 1	10 ± 1	10 ± 1	10 ± 3

4.4.5 Calcium Alginate Degradation Assessment

CA_{60s} electrodes with a 10 mm diameter were developed, resulting in calcium alginate layers measuring 485 ± 67 µm. The electrodes were immersed in sterile PBS solution and the degradation of the alginate layers was monitored via the release of calcium using Arsenazo III (method described in section 3.5). The average results based on the measurements of 5 electrodes, are shown in Figure 4.49 a. Readings taken from blank wells containing PBS only are also included for reference. The absence of a molarity plateau indicates that calcium ions were still being released into solution after 35 days of immersion. Figure 4.49 b shows a stereo micrograph of one of the electrode surfaces immediately following the experiment. A thin, sparse layer of calcium alginate may still be observed. In many areas the underlying PEDOT:PSS is exposed.

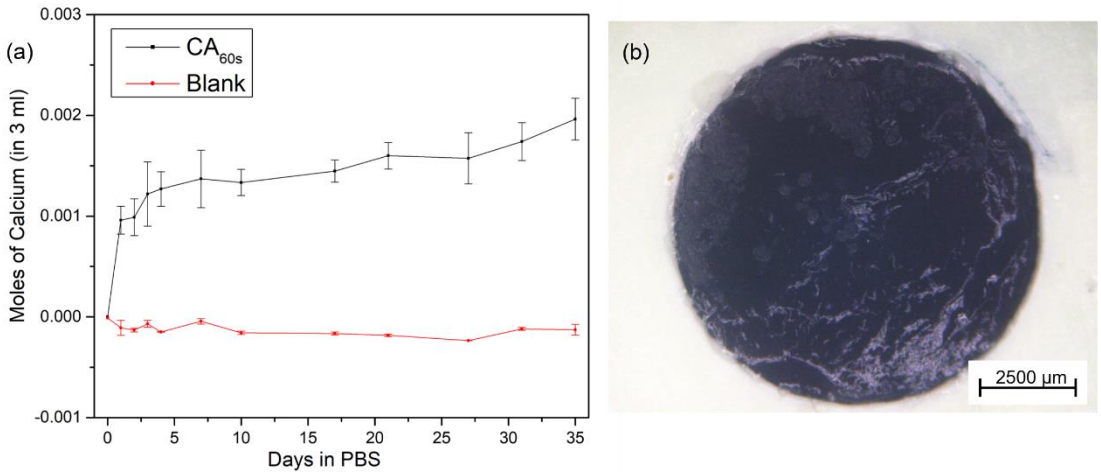

Figure 4.49: (a) Moles of calcium released from CA_{60s} electrodes (5 mm radius) into 3ml of PBS, plotted against number of days immersed in solution. Readings taken from blank wells (PBS only) are also included. Error bars show standard deviation from the mean, calculated from 5 repeats; (b) Stereo micrograph of one of the CA_{60s} electrode surfaces following 35 days of immersion in PBS.

After the remaining alginate films had been removed via ultrasonication (in a 1M solution of NaCl), cleaned (1 minute of ultrasonication in DI water), dried in air, and reimpregnated with PBS (under 0.5 bar of vacuum) the electrodes were subjected to EIS tests to assess whether the alginate deposition process had an adverse effect on the electrochemical response of the electrodes. Representative impedance and phase angle Bode plots for CA_{60s} electrodes on day 0 and day 35 (after alginate removal) are shown in Figure 4.50, along with the plots for a $PP_{17.5}$ electrode for reference. EIS modelling done using the equivalent circuit shown in Figure 4.4 a, and the results are given in Table

4.21. Only a slight degradation of electrochemical properties was observed, and an incomplete drop in the R_s to pre-alginate deposition conditions.

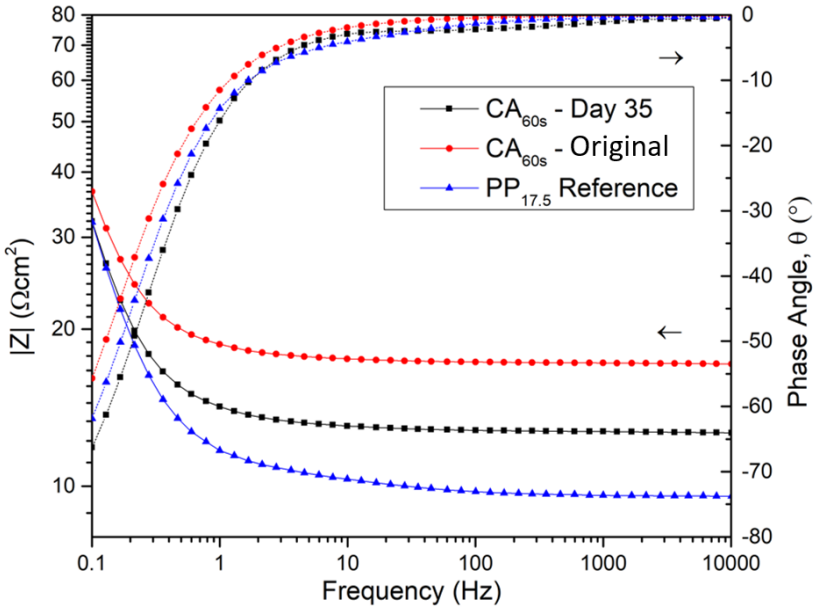

Figure 4.50: Impedance and phase angle Bode plots for CA_{60s} electrodes before (red) and after 35 days of immersion in PBS (after alginate removal) (black). The plots for a $PP_{17.5}$ electrode (blue) are also given for reference.

Table 4.21: Results of fitting the EIS spectra obtained for CA_{60s} electrodes after 35 days of immersion in PBS and removal of alginate layer (Figure 4.50, black) to the equivalent circuit model given in Figure 4.4 a, along with the $|Z|_{1Hz}$. Tests were conducted in PBS. Results are given as the average of 5 repeated readings with standard deviation from the mean. Results for the original CA_{60s} and $PP_{17.5}$ electrodes are also included for reference.

Circuit Element	Units	$PP_{17.5}$	CA_{60} – Original	CA_{60} – Removed
R_s	Ωcm^2	11.0 ± 1.2	17.6 ± 0.3	12.9 ± 2.7
R_f	Ωcm^2	1.6 ± 0.5	1.9 ± 0.3	1.4 ± 0.3
Y_{dl}	$mSs^{\alpha}cm^{-2}$	19.3 ± 3.0	13.5 ± 2.4	16.3 ± 3.4
α_{dl}	/	0.890 ± 0.007	0.861 ± 0.037	0.842 ± 0.010
Y_{pseu}	$Ss^{\alpha}cm^{-2}$	41.4 ± 2.6	35.3 ± 3.4	37.2 ± 3.0
α_{pseu}	/	0.964 ± 0.014	0.913 ± 0.006	0.947 ± 0.009
$\|Z\|_{1Hz}$	Ωcm^2	12.2 ± 1.3	18.6 ± 0.5	14.5 ± 1.7

4.4.6 Assessing Attachment and Proliferation of NHDF

$PP_{17.5}$ and CA_{60s} electrodes (5 mm radius, 464 ± 51 µm height) were incubated with neonatal human dermal fibroblasts (NHDF) at a density of 8×10^4 cells/cm^2 for a total of 72 hours to assess susceptibility to fibrous encapsulation (method described in section

3.6.2). The results of two tests, where 5 electrodes were assessed per electrode type per test (i.e., n=10), are shown in Figure 4.51 for 24, 48, and 72 hours. The largest average reduction value ($PP_{17.5}$ after 72 hours) was given a value of '1', and all other values are given relative to it. Statistically significant differences ($p < 0.05$) were observed on every day between CA_{60s} and $PP_{17.5}$ electrodes (marked *, **, and *** in the figure), where $PP_{17.5}$ electrode surfaces had higher numbers of NHDF cells. No statistically significant growth ($p > 0.05$) in number of fibroblasts was detected on the CA_{60s} electrodes over 3 days, whereas significant growth ($p < 0.05$) was detected on the $PP_{17.5}$ electrodes between the first and last days of testing (marked **** in the figure). After 72 hours, the CA_{60s} electrodes had an average of 72% less fibroblast adhesion as compared to the $PP_{17.5}$ electrode surfaces.

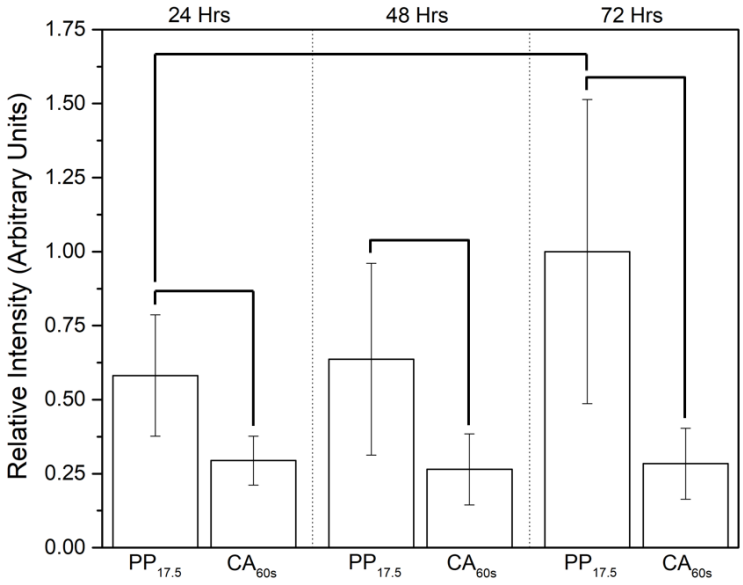

Figure 4.51: Average relative intensity of Resazurin reduction by NHDF cells measured on $PP_{17.5}$ and CA_{60s} electrodes. Cells were seeded at a density of 8×10^4 cells/cm^2. Measurements were made using spectrophotometry at wavelengths of 570 and 600 nm after 24, 48, and 72 hours of incubation. Results show the average with standard deviation from duplicate tests where a sample size of 5 was employed per condition per test (i.e., n=10). The reduction value for $PP_{17.5}$ after 72 hours was given a value of '1', and all other values are given relative to it. Black line connectors indicate statistically significant differences ($p < 0.05$) between groups, determined using one-way ANOVA and a post-hoc Tukey test.

SEM images of NHDF fixed on the electrode surfaces (method described in section 3.6.4) using glutaraldehyde after 72 hours of incubation are shown at two magnifications in Figure 4.52. Cell coverage is visually very different between $PP_{17.5}$ and CA_{60s} electrodes, where the former features a confluent layer. An inset showing the original

PEDOT:PSS surface at the same magnification is in fact provided in Figure 4.52 a, for reference. Conversely, no adherent fibroblasts could be identified on the CA_{60s} electrodes, save for some globular matter resembling cellular debris (yellow arrows in Figure 4.52 b).

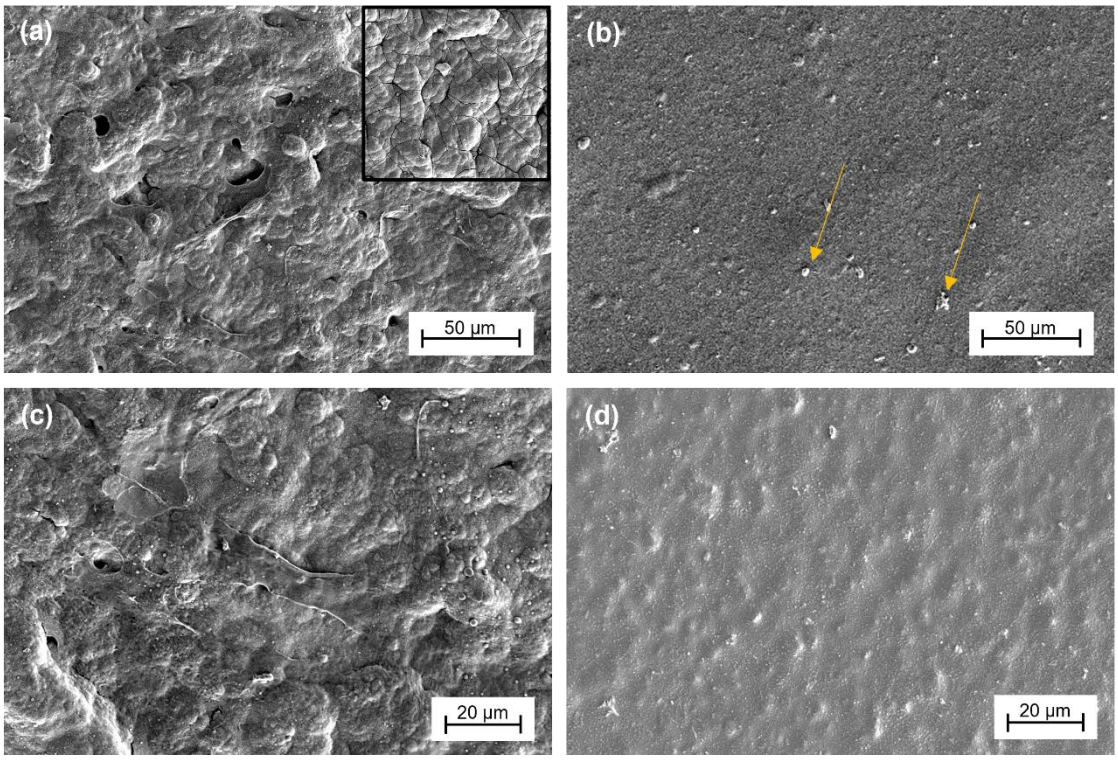

Figure 4.52: SEM images of HNDF on $PP_{17.5}$ (a, c) and CA_{60s} (b, d) electrodes after 72 hours of culture and fixing in glutaraldehyde. Surfaces were sputter-coated with a nanometric layer of Au to improve conductivity. Inset in (a) shows a PEDOT:PSS surface before culturing at the same magnification for comparison. Yellow arrows in (b) indicate examples of globular matter.

4.5 Assessing Adhesion and Differentiation of SH-SY5Y Neural Cells

The three prominent electrodes featured in this work, TiN_{IV}, $PP_{17.5}$, and CA_{60s}, were assessed for the attachment and differentiation of SH-SY5Y neuroblastoma cells into neural-like cells using ATRA (all-trans retinoic acid). An example of successful differentiation is shown in Figure 4.53, where SH-SY5Y cells were seeded and cultured in 6-well plates for 72 hours, and then treated with ATRA for a further 72 hours before the image was taken. The most prominent distinctions are the extension of neural processes (Figure 4.53 b, blue arrow) and the change from a flat to a fusiform morphology (Figure 4.53 b, red arrow) following ATRA treatment

The same process (72 hours of culture followed by 72 hours of treatment with ATRA) was repeated on TiN_{IV}, $PP_{17.5}$, and CA_{60s} electrodes, as well as Thermanox (TMO) cell culture slides (method described in section 3.6.3). The results of two tests, where 5 electrodes/ slides were assessed per condition per test (i.e., n=10), are shown in Figure 4.54 after 72 hours of treatment. No statistically significant difference ($p > 0.05$) was detected between the TMO and CA_{60s} samples. Significant differences were however observed between TMO and TiN_{IV} samples, between TMO and $PP_{17.5}$ samples, and between TiN_{IV} and $PP_{17.5}$ electrodes (marked * in the figure). In addition, statistically significant differences were also observed between CA_{60s} and TiN_{IV} electrodes, and between CA_{60s} and $PP_{17.5}$ electrodes (marked * in the figure).

SEM images of the SH-SY5Y cells fixed on the tested surfaces using glutaraldehyde at the end of the experiment are shown at various magnifications in Figure 4.55 for the TMO slides, Figure 4.56 for the CA_{60s} electrodes, Figure 4.57 for the TiN_{IV} electrodes, and Figure 4.58 for the $PP_{17.5}$ electrodes. Cells cultured on the TMO surfaces were observed to have extended neural processes (neurite extensions) (red arrows) and attained a fusiform morphology (blue arrows), similar to those observed on the CA_{60s} electrodes. Very few neurite extensions are visible on TiN_{IV} electrodes, and most cells appear to have a flattened morphology (green arrows). Conversely, many fusiform-shaped cells with long, neural processes are visible on the $PP_{17.5}$ electrodes, along with some remaining flat cells.

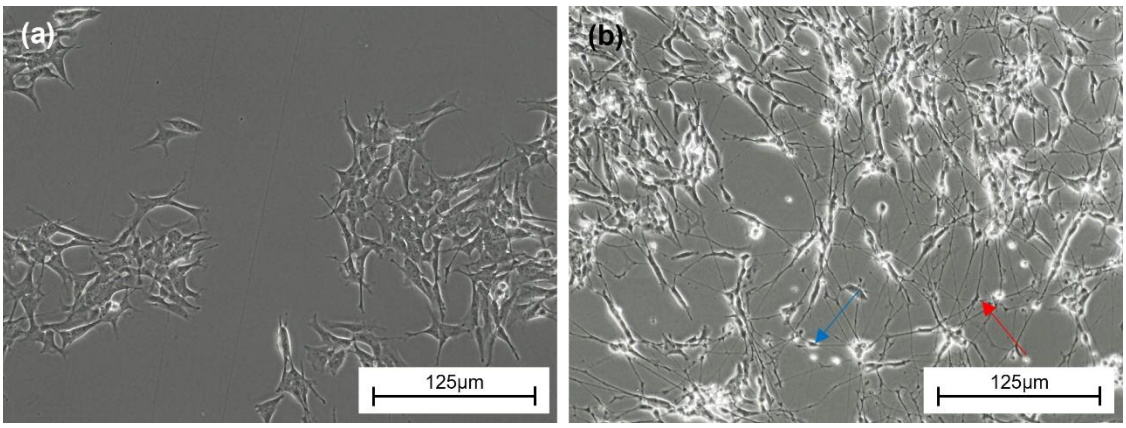

Figure 4.53: Optical microscope images of (a) SH-SY5Y cells with a flattened morphology growing in cell culture wells 72 hours after seeding, and; (b) after 72 hours of ATRA treatment. Cells take on a fusiform morphology (blue arrow shows example) and extend neural processes (red arrow shows example).

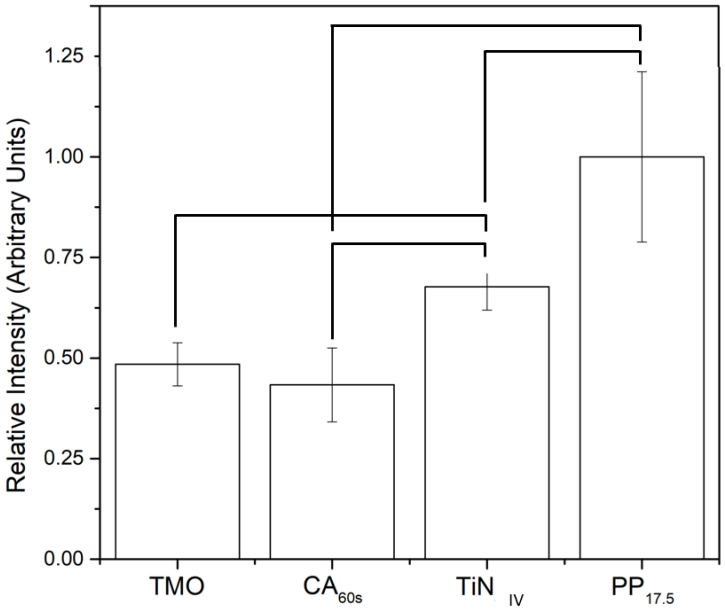

Figure 4.54: Average relative intensity of Resazurin reduction by SH-SY5Y cells measured on different electrodes and control (TMO) surfaces. Cells were cultured at a density of 1×10^5 cells/cm^2. Measurements were made using spectrophotometry at wavelengths of 570 and 600 nm after 72 hours of cell growth and a further 72 hours of treatment with ATRA. Results show the average with standard deviation from the mean of duplicate tests where a sample size of 5 was employed per condition per test (i.e., n=10). The reduction value for $PP_{17.5}$ after 72 hours was given a value of '1', and all other values are given relative to it. Black line connectors indicate statistically significant differences ($p < 0.05$) between groups, determined using one-way ANOVA and a post-hoc Tukey test.

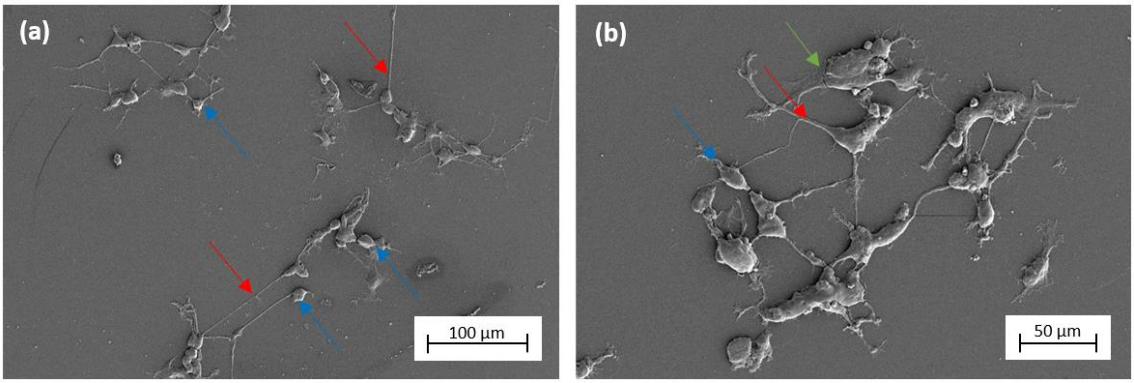

Figure 4.55: SEM images of SH-SY5Y cells on TMO slips after 72 hours of culture and a further 72 hours of treatment with ATRA. Blue arrows show cell bodies with a fusiform morphology, whereas green arrows show a flattened morphology. Red arrows indicate neural processes. Cells were fixed in glutaraldehyde and sputter-coated with a nanometric layer of Au to improve conductivity.

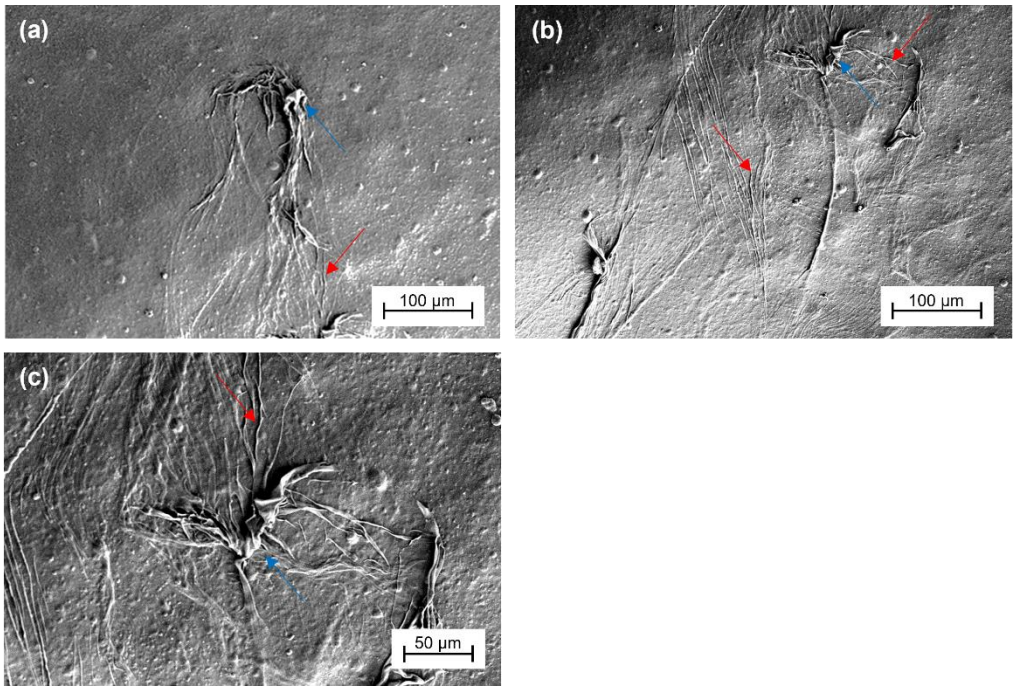

Figure 4.56: SEM images of SH-SY5Y cells on CA_{60s} electrodes after 72 hours of culture and a further 72 hours of treatment with ATRA. Blue arrows show cell bodies with a fusiform morphology, whereas red arrows indicate neural processes. Cells were fixed in glutaraldehyde and sputter-coated with a nanometric layer of Au to improve conductivity.

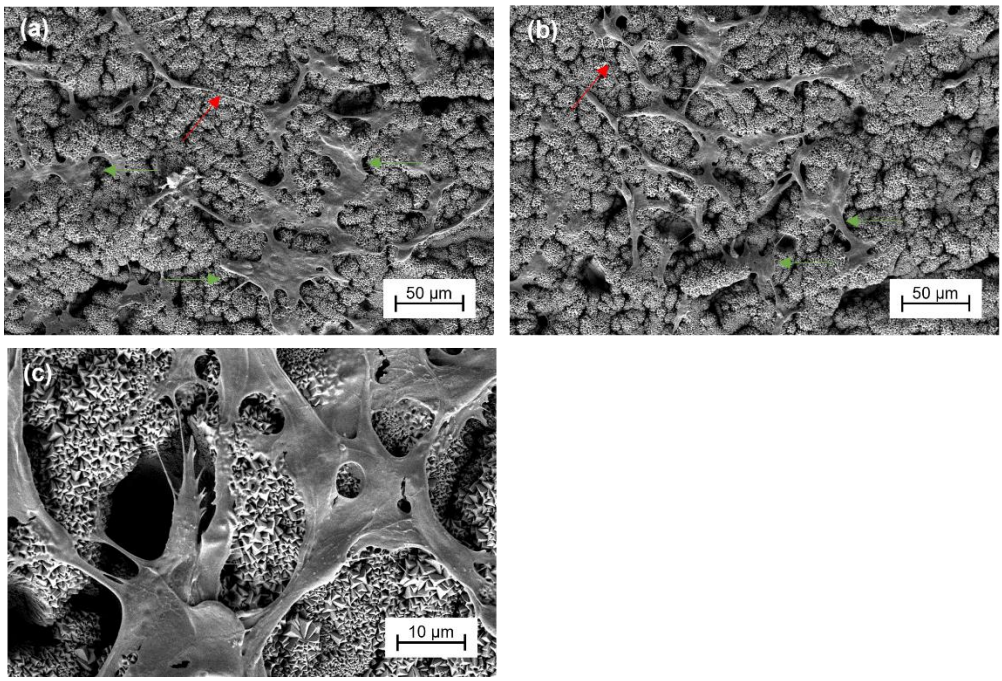

Figure 4.57: SEM images of SH-SY5Y cells on TiN_{IV} electrodes after 72 hours of culture and a further 72 hours of treatment with ATRA. Blue arrows show cell bodies with a fusiform morphology, whereas green arrows show a flattened morphology. Red arrows indicate neural processes. Cells were fixed in glutaraldehyde and sputter-coated with a nanometric layer of Au to improve conductivity.

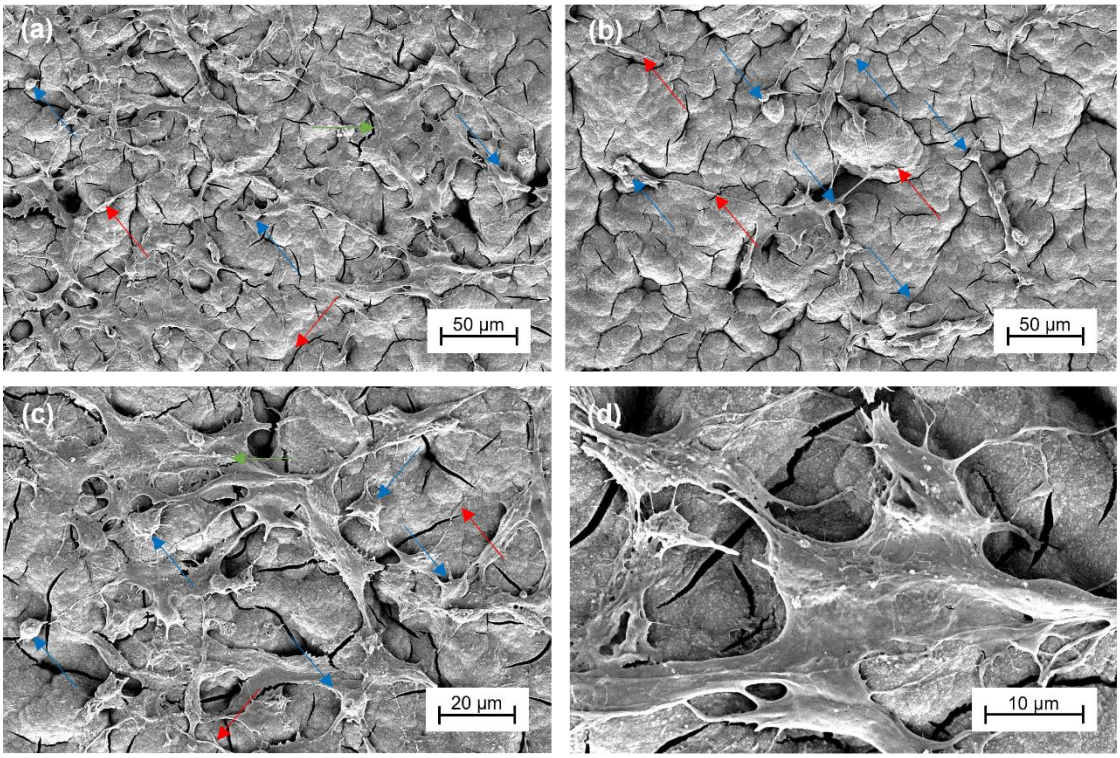

Figure 4.58: SEM images of SH-SY5Y cells on $PP_{17.5}$ electrodes after 72 hours of culture and a further 72 hours of treatment with ATRA. Blue arrows show cell bodies with a fusiform morphology, whereas green arrows show a flattened morphology. Red arrows indicate neural processes. Cells were fixed in glutaraldehyde and sputter-coated with a nanometric layer of Au to improve conductivity.

5 Discussion

5.1 Introduction - Summary of Results

In this work, neural electrodes based on overstoichiometric TiN (TIN_I, TIN_{II}, TIN_{III}, TIN_{IV}) were developed with different surface roughnesses through sand blasting of the substrate, followed by PVD. The electrochemical performance of the electrodes was similar despite variations in surface morphology, and EIS modelling revealed an additional capacitance besides double layer capacitance. The electrode with the highest surface roughness (TiN_{IV}) proved more resistant to fibrous encapsulation than the original electrode (TiN_I) after 72 hours of incubation with NHDFs. To improve electrochemical performance, a layer of PEDOT:PSS was electrodeposited onto the surface of TiN_{IV}. The PP electrodes produced higher values of CSC_C and reduced values of |Z| as compared to the TiN, which remained stable with sequential cycling and ultrasonication. A larger number of adhered fibroblasts was observed on the PP electrodes as compared to the TiN_{IV} after 72 hours of incubation. The PP electrodes were coated with a layer of calcium alginate to render the surface antifouling, resulting in reduced number of adhered fibroblasts on the CA electrode as compared to PP. A slight deterioration in the electrochemical properties was observed with the addition of the hydrogel, but the properties were quasi-completely restored after the gel's dissolution. When SH-SY5Y neuroblastoma cells were incubated on the electrodes and treated with ATRA, only cells on the PP, CA, and control (Thermanox slides) surfaces underwent morphological changes consistent with differentiation.

5.2 Overstoichiometric TiN_I as a Combined Double-Layer and Pseudocapacitor

The TiN_I electrodes developed in this work feature a highly porous and columnar microstructure, whereby the apparent grain structure is almost exclusively pyramidal (Figure 4.1 a-c). Moreover, the quasi-unidirectional growth pattern of the columns, a perpendicular arrangement with respect to the Ti6Al4V substrate (Figure 4.1 d), suggests a highly textured coating. Indexing the Bragg-Brentano XRD spectrum in Figure 4.2 a using PDF no. 04-015-0336 in fact reveals peaks no.1 and 2 as the (111) and (222) orientations respectively of FCC-like (rock-salt prototype crystal structure)

Osbornite TiN with space group Fm-3m(225). This result corroborates the visual observations made via SEM, confirming the presence of texture along the (111) plane.

As the plane of lowest strain energy, (111) prevalence is expected in TiN films of a certain thickness [177], [226]. In these cases, the condition of $E_{strain} > E_{surface}$ arises, and so the (111) texture develops as a means to lower the system's overall energy [177], [221], [368]. The measured average height of the TiN_I electrodes developed in this work (9.5 ± 0.8 μm) well exceed the threshold of 212 nm beyond which (111) dominated growth is expected, as determined by Liang *et al.* [177]. Crystal lattice distortion of TiN by way of skewing the Ti/N ratio in favour of the N atoms also places a high level of strain on the grains, further favouring the evolution of a (111) texture and the signature pyramidal appearance [226], [369]. In their work, Cunha *et al.* [226] demonstrate the correlation between TiN films with a strong (111) texture and over-stoichiometry, where under and near-stoichiometric films are shown to have dense, compact structures whilst lacking a (111) texture. The works of Ponon *et al.* [220], Chuang *et al.* [227], and Penilla *et al.* [224] further lend credence to the relationship between over-stoichiometry and the observed microstructure.

Micro-Raman spectroscopy was carried on the TiN_I electrodes to investigate their over-stoichiometry. The 6 emergent peaks, seen Figure 4.2 b and identified in Table 4.3, are related in literature with either Ti or N ions depending on their respective Raman shifts. Acoustic range scattering, falling within the range of ~ 150 to 350 cm^{-1}, is associated with heavy Ti ions, whereas those within the range of ~ 550 to 650 cm^{-1} are associated with lighter N ions [370]. With reference to the works of various research groups [220], [236], [240], [371]–[373], the emergent peaks at 152, 260, and 601 cm^{-1} were assigned to the first-order transverse acoustic (TA), longitudinal acoustic (LA), and transverse optical (TO) modes of TiN. Inferring the premise that structures such as stoichiometric TiN cannot produce first-order scattering in micro-Raman analysis due to perfect inversion symmetry, the emergent peaks necessarily represent the defects that induced them [167], [370], [374]. For the stoichiometric deviation theorised in this work, acoustic peaks may thus be related to N-vacancies (nitrogen vacancies), while optical peaks may be related to Ti-vacancies (titanium vacancies) [220], [234], [235], [371]. When applying the qualitative analysis I_{TO}/I_{TA} (I_6/I_1), in which the ratio of TO and TA

peak intensities are compared, a value of $I_{TO}/I_{TA} < 1$ (0.74 ± 0.11) is obtained, suggesting that N-vacancies are the more frequently occurring defect [234], [375].

Despite the apparent inconsistency of an over-stoichiometric TiN film having an abundance of N-vacancies, there have been multiple reports in literature in which this phenomenon arose [233]–[235], [376], [377]. Given the high propensity for over-stoichiometric TiN films to oxidize at ambient conditions [237], [238], the presence of varied transitional oxides (TiO_x, NO_x, Ti_xO_y, and TiO_xN_y) that stabilize in the form of anatase TiO_2 have come to be expected on these films [167], [234], [239]. The concomitant detection of N-vacancies in the TiN bulk and N-dopants in the oxide were thus connected to the act of substitutional doping, where excess N-atoms undergo outward diffusion to generate the aforementioned N-vacancies [167], [234]. As a sub-surface characterisation technique, the micro-Raman analysis carried out on the TiNI electrodes in this work is well-suited to the identification of such diffusion-generated N-vacancies [378]. For the congruent detection of substitutional dopants in the oxide, attention is drawn to the three peaks with Raman shifts of 205, 410, and 519 cm^{-1} in Figure 4.2 b. It is theorised by Achour *et al.* [235] that a resonance effect occurs from the intersection of a 532 nm laser wavelength (~ energy 2.33 eV) and the band gap of N-TiO_2 (N-doped TiO_2) (2.2-2.6 eV [379]), thus allowing detection of these peaks. Adopting their methodology, in which Raman measurements are repeated using non-green light laser wavelengths (refer to section 2.4.3), these three peaks in fact did not emerge when the surface was interrogated with a 785 nm wavelength, shown in Figure 5.1. As such, the peaks were ascribed to N-TiO_2, validating the presence of N-vacancies in the bulk TiN, and linking their evolution as part of the same mechanism.

The significance of identifying N-dopants in the oxide becomes apparent when considering the electrochemical behaviour of TiN_I. It has been widely demonstrated that the presence of β-N (substitutional Nitrogen) in TiO_2 gives rise to O-vacancies through the act of charge compensation. In turn, these O-vacancies can participate in reversible faradaic reactions, giving rise to pseudocapacitive charge transfer [215], [233], [376], [380]. To assess the validity of this hypothesis, a series of exclusionary experiments were devised to distinguish between faradaic and non-faradaic charge transfer mechanisms. Such experiments required that identical electrochemical measurements be made in two electrolytes; one that enables both double-layer capacitance and

pseudocapacitance, and another which supresses one of these mechanisms. PBS solution was chosen as the former, conveniently doubling as a representative for physiological conditions. An electrolyte comprising a 1M solution of Et_4NBF_4 in acetonitrile was chosen to suppress faradaic reactions. As acetonitrile is aprotic and the Et_4N^+ ion experiences severe spatial limitations due to its bulkiness, pseudocapacitive reactions are heavily restricted. For consistency, both solutions were kept at a temperature of 37 ± 2°C.

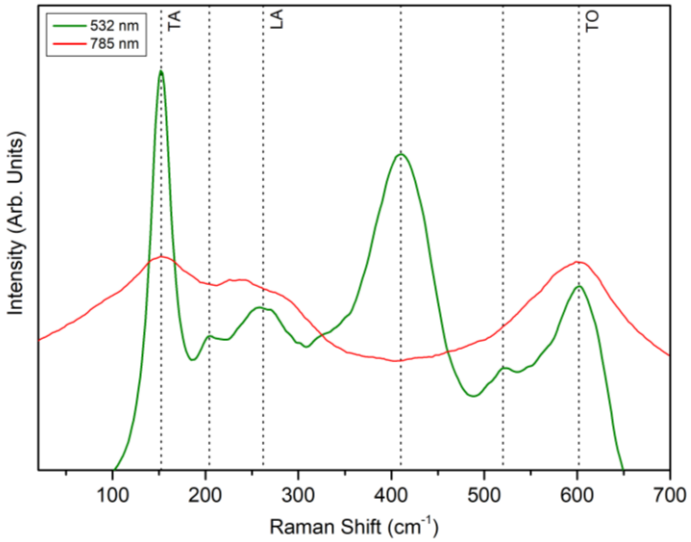

Figure 5.1: Representative micro-Raman spectrum measured on TiNI electrode surfaces using a wavelength of 785 nm (red), superimposed on the original spectrum measured using a 532 nm laser wavelength (green). Peaks associated with TiN are labelled TA, LA, and TO. From Arpa *et al.* [368].

The resultant EIS spectra, which are given in Figure 4.3, show a clear difference between the two electrolytes. While a simple Randles circuit (Figure 4.4 b) was sufficient to model the spectra collected in acetonitrile, the circuit was not applicable to spectra obtained in PBS. Following the trend in literature whereby porous electrodes typically require the inclusion of a diffusional element in the model circuit, both an infinite and bounded Warburg were sequentially assessed for their suitability [173], [178], [226]. However, neither of these circuits, featuring the respective Warburg element in series with the resistance to faradaic charge transfer, returned convergent fits ($\chi^2 > 0.001$). In many cases, the errors associated with the individual circuit elements were in fact several order of magnitude larger than the values themselves. Moreover, the signature feature of an electrochemical system under diffusional control, i.e., the ~ 45° angle in the low-frequency region of the Nyquist plot, was notably absent (Figure 4.3). For these reasons, the mixed kinetic and diffusion control circuit was discarded. Canillas *et al.* [217]

experienced similar issues when attempting to include a Warburg element in their model for porous TiN, and likewise discarded it.

The second equivalent circuit model that was assessed for conformity was the so-called 'porous coating model', in which the Warburg element is replaced by a parallel arrangement of pore resistance (R_p) and coating capacitance (C_c) [381], [382]. This circuit, sequentially modelled both with an ideal and leaky capacitor (CPE) for C_c, also failed to return convergent fits ($\chi^2 > 0.001$), again producing very large errors. Although this model is also in widespread use for electrochemical systems involving a porous coating, its applicability hinges on the presence of coating defects [383], [384]. For the TiN_I electrodes, this would necessitate significant electrolyte interaction with the Ti substrate. When considering the highly dense morphology of the TiN layer at the TiN/substrate interface (Figure 4.1 d), electrolyte penetration was judged to be only of very low possibility. Combined with the incongruity of the electrochemical model, it was determined that the TiN layer was sufficient in isolating the Ti6Al4V substrate from the electrolyte, and so the model was discarded.

Having reliably eliminated diffusion limitations and through-coating porosity as major influential factors, the circuit was instead amended to account for pseudocapacitive behaviour (Figure 4.4 a). A constant phase element, CPE_{pseu}, was included in place of a Warburg impedance to represent capacitive contribution of faradaic origin. A similar equivalent circuit was chosen by Brezesinski *et al.* [180] to model a combined double-layer and pseudocapacitive material, where the shape of the Nyquist plot closely resembles that of TiN_I (Figure 4.3). The works of Bryan *et al.* [385], Pauli *et al.* [386], and Yan *et al.* [387] also employ the same circuit, so providing a reliable method through which to distinguish capacitive contribution. Consistent convergent fits ($\chi^2 < 0.001$) were obtained when this model was applied to spectra collected in PBS, and thus it was adopted.

Beyond the necessity of adopting different models for the two electrolytes, the results obtained from fitting the equivalent circuits (Table 4.4) make further apparent the differing electrochemical response of TiNI electrodes. Y_{dl} and α_{dl} both returned slightly higher values for acetonitrile than PBS (7.1 ± 2.7 *vs* 3.9 ± 0.7 $mSs^{\alpha}cm^{-2}$ and 0.868 ± 0.019 *vs* 0.855 ± 0.024, respectively), reliably excluding double-layer capacitance as an influential factor behind the significant impedance increase observed in organic

electrolyte. A similar statement may be made in the case of R_s. The main contributor towards the large impedance measured in acetonitrile is evidently R_f, where the 2.5 $k\Omega cm^2$ value far exceeds the 1.5 Ωcm^2 obtained in PBS by 3 orders of magnitude. Given that the organic electrolyte was chosen to supress faradaic reactions, it follows that R_f would increase when compared to PBS, an electrolyte which permits such reactions to occur. Assessing the ratio Y_{pseu}/Y_{dl} in PBS further reveals that reversible faradaic reactions constitute the majority of the electrode's capacitive function, surpassing double-layer capacitance by an approximate factor of 3.8.

Similar conclusions may be reached through the analysis of CV measurements, where CSC_C values obtained in PBS were consistently higher than those obtained in acetonitrile (Table 4.5). The results of Achour *et al.* [235] and Hasegawa *et al.* [236] are comparable, as both studies report a drop in the measured capacitance of their respective TiN electrodes when moving from protonated to non-protonated electrolytes. Moreover, the trend is consistent for a variety of scan rates, including the 0.05, 0.1, 0.5, and 1 V^{-1} as applied in this work. Although no accompanying EIS measurements and circuit modelling was conducted, the authors attribute this drop to suppression of faradaic charge transfer, asserting the prominent role of pseudocapacitance in the electrochemical performance of over-stoichiometric TiN.

Assessing the shape of voltammograms collected in PBS (Figure 4.5) may provide further insight into electrode behaviour with varying charge/discharge rates. At low scan rates (0.05 and 0.1 Vs^{-1}), the voltammograms exhibit quasi-perfect rectangular shapes, an electrochemical signature that is typically associated with pure EDLCs [160]. Coupled with the absence of any discernible redox peaks, these two factors comprise the most frequently cited rationale for the classification of TiN as a double-layer capacitor [3], [101], [229], [388], [389]. However, this phenomenon is not unique to TiN, and is in fact observable in other well-known pseudocapacitive materials, most notably oxides such as MnO_2 (manganese dioxide) [390], [391] and RuO_2 (ruthenium dioxide) [161], [392]. In fact, this behaviour is intricately tied to the surface-formed TiO_2 rather than the TiN itself, and is contingent on a large ESA and a highly defective crystal structure. In typical pseudocapacitive bulk materials like Pt and Au, voltammograms exhibit obvious and well-defined redox peaks due to an equal distribution of energy amongst the rigidly ordered redox-active sites. Conversely, active sites (defects) in porous

pseudocapacitors are simultaneously more available (due to the high ESA) and variably distributed over the surface (Figure 5.2 a). Moreover, these sites can be of different energy requirements, leading to under- and over-potentials for sites requiring less and more energy to perform a redox reaction, respectively. The overlap of such peaks results in a broadening effect, which in combination with charge evolving from double-layer capacitance, can result in a smooth CV profile similar to that of a pure EDLC (Figure 5.2 b) [161], [393], [394]. Hypothetical redox reaction peaks for TiN_I electrodes are shown in Figure 5.2 c superimposed on a voltammogram measured at 0.1 Vs^{-1}.

As the scan rate is increased (0.5 $Vs^{-1} < v$), the shape of the voltammogram changes and becomes oblique, deviating from a capacitive to a more resistive response reminiscent of an ohmic-type conductor. Accordingly, the measured CSC_C also decreases as the scan rate increases [101]. Cunha *et al.* [226] recorded similar results when testing porous TiN electrodes at v = 0.1 *vs* 1 Vs^{-1} (Figure 2.25 e), as did many other research groups when measuring TiN at different scan rates [167], [233], [388], [395]. One of the major contributing factors to this effect is pore resistance, in which a delay line with a large time constant forms inside a pore (Figure 2.12 a) and renders the bottom segments of the ESA inaccessible [101]. When considering the strong dependence that extrinsic pseudocapacitance has on available surface area, this effect is likely to affect both double-layer and faradaic charge transfer [394]. Moreover, pseudocapacitance is further limited by the kinetics of the redox reactions themselves, as the ad- and de-sorption of cations is a comparatively time-consuming process when compared to the formation of a double layer [236], [396]. It is possible that this effect accounts for the disappearance of the broad faradaic peaks at high scan rates [394]. That being said, the impact of kinetic limitation is evidently small, as the semi-circular component of the Nyquist plot in the high-frequency region is supressed to the point of being indistinguishable (Figure 4.3). This corresponds to the small R_f obtained from fitting the equivalent circuit (1.5 ± 0.5 Ωcm^2), rendering the system kinetically facile [397]. Therefore, despite the shift towards more resistive behaviour at high scan rates, the overall performance of the TiN_I electrode is still majorly capacitive and is capable of transferring sufficient charge even at 1 Vs^{-1} (22 ± 3 $mCcm^{-2}$).

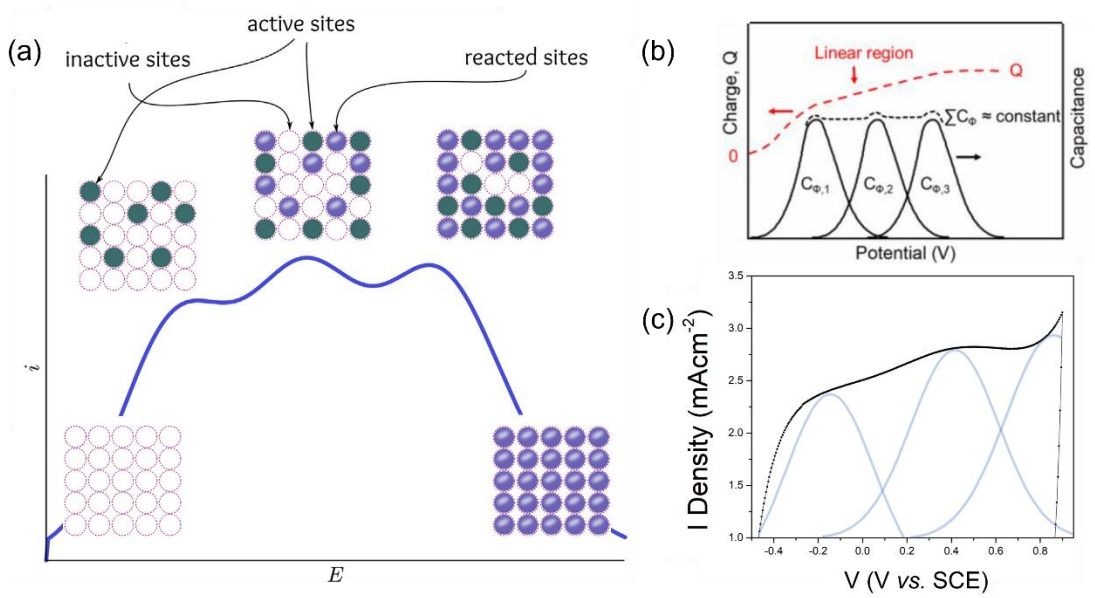

Figure 5.2: (a) CV profile at the redox potentials of an extrinsic pseudocapacitor, showing the recruitment of redox-reactive sites as the potential is swept. Adapted from [394]; (b) Multiple redox reactions ($C_{\Phi,1}$, $C_{\Phi,2}$, and $C_{\Phi,3}$) occurring sequentially, resulting in a quasi-constant total capacitance (ΣC_{Φ}). The total charge (shown in red) appears linear, with only broad and diminished peaks emerging. From [161]; (c) A close-up of the anodic portion of a CV curve for TiN_I electrodes measured at ν = 0.1 Vs^{-1}. Superimposed curves in blue are the hypothesised redox reactions causing the visible broad peaks.

A testing regiment involving the sequential application of 10,000 CV cycles with intermittent EIS measurements was applied to assess faradaic reaction reversibility over numerous charge/discharge cycles. In line with the recommendations of Hou *et al.* [187], the two contrasting scan rates of 0.1 and 1 Vs^{-1} were chosen to assess the electrode under high and low capacitive demand, respectively. Tests conducted at 0.1 Vs^{-1} were intended to exhaust the electrode's pseudocapacitive mechanism, wherein a large number of redox-active sites (O-vacancies) would be engaged in each cycle. Any change in the electrochemical performance of the electrode could then be correlated to changes in the material chemistry. Conversely, the 1 Vs^{-1} scan rate was considered closer to conditions of intended use. However, it should be noted that the typical stimulation and/or recording pulse exchanges far less charge per cycle (refer to Table 2.3), and as such the testing conditions may still be considered somewhat aggressive [12], [101].

The electrochemical results clearly reflect the anticipated response of the TiN_I electrodes under the two different cycling rates. Considering first the electrodes cycled at 1 Vs^{-1}, the EIS plots shown in Figure 4.6 reveal no observable changes in the phase and impedance Bode plots, while the Nyquist plot retains an identical shape without increase

in either the real or imaginary components. Fitting the equivalent circuit to the EIS spectra and plotting the model variables with cycle number (Figure 4.8) corroborates these results, as no significant variation ($p > 0.05$) was found to occur in any of the model variables that would negatively impact the electrochemical performance. Most notably, Y_{pseu} and α_{pseu} maintain constant values, suggesting no degradation effects were imparted to the pseudocapacitive mechanisms from cycling. The voltammograms collected at the start and end of the testing regiment (Figure 4.7) in fact show very minor changes in area, and a charge retention percentage upwards of 98.5% was recorded at termination of experiment.

Pseudocapacitance in TiN_I electrodes thus appears to be highly reversible for the conditions applied. Moreover, the relative number of Ti and N vacancies in the material was also revealed to be unchanged when using micro-Raman spectroscopy. No statistically significant difference ($p > 0.05$) was observed in the I_{TO}/I_{TA} ratio before and after testing (Figure 4.9), suggesting that the number of N-vacancies in the TiN bulk remained constant. By extension, this would imply that the relative number of β-N and subsequently generated O-vacancies in the oxide was also maintained. These observations are in keeping with the theory of Achour *et al.* [235], in which over-stoichiometric TiN acts as a bulk reservoir for N-dopants. With each cycle a number of O-vacancies are consumed to oxidation reactions, followed by concomitant diffusion of atomic oxygen and β-N into and out from the bulk TiN, respectively. Newly-generated N-vacancies are thus 'healed' by atomic oxygen, and new O-vacancies are formed in the oxide by N-doping. The relative number of O- and N-vacancies is therefore kept stable, and pseudocapacitive ability does not degrade.

The starkly different results obtained when cycling at 0.1 Vs^{-1} serve to reinforce this hypothesis. A significant increase in $|Z|_{f<10Hz}$ is shown on the Bode plot along with a positive shift in $f_{cut\text{-}off}$ (Figure 4.6). Although the overall shape of the Nyquist plot is retained and the same circuit model could be used ($\chi^2 < 0.001$), both the real and imaginary parts were observed to increase at low frequencies. These changes were revealed to originate almost exclusively from degradation of Y_{pseu}, as none of the other variables exhibited any significant negative changes with test progression (Figure 4.8). Critically, the stability of Y_{dl} and α_{dl} reliably excludes phenomena like pore blockage or structural collapse from having any influence on the observed impedance increase [186],

[398]. It is interesting to note that the drop in Y_{pseu} begins immediately and continues to occur gradually with cycle number rather than experiencing a sudden drop at some threshold value, and therefore matches the behaviour of similar pseudocapacitive electrodes [186], [376], [399]. The voltammogram (Figure 4.7) also evidently changes, with an approximate 50% loss in area and the apparent disappearance of the muted faradaic peaks. The CSC_C in fact degrades to only 54% of its original value by the $10{,}000^{th}$ cycle (Figure 4.8 f).

In dealing with PANi (polyaniline) electrodes (a pseudocapacitive material), Hou *et al.* [187] observed very similar results when testing cyclic stability at a scan rate of 0.5 versus 0.02 Vs^{-1}. Only a 0.4% decrease in CSC was recorded at the higher sweep rate after 5000 successive cycles, whereas a 21.7% decrease was measured at 0.02 Vs^{-1}. The authors link these findings to an extended diffusion time in the case of slower scan rates, where the time window afforded under these testing conditions allows a higher volume of redox-active sites to be engaged. Since no faradaic system is perfectly reversible, a large number of sites fail to regenerate for the ensuing cycle, thus degrading pseudocapacitance in a quasi-linear manner. Liu *et al.* [186] describe such behaviour as also being typical of non-stoichiometric metal oxides, wherein oxygen defects fail to regenerate from one cycle to another for whichever reason. Indeed, micro-Raman analysis of TiN_I electrodes tested at 0.1 Vs^{-1} returned a statistically significant change ($p < 0.05$) in the I_{TO}/I_{TA} ratio (Figure 4.9), unlike the previous case of cycling at 1 Vs^{-1}. Rather than remaining stable, the relative number of N-vacancies in the TiN sub-surface is here presumed to have decreased, which by extension links to a similar decrease in β-N and O-vacancies for the oxide [235]. The correlation between over-stoichiometry and pseudocapacitance is thus made stronger through these experiments, linking Y_{pseu}, CSC_C, and incidence of N-vacancies in the material.

Based on the results and observations made in sections 4.1 and 5.2, a graphical summary of the hypothesised mechanism behind the electrochemical behaviour of TiN_I is presented in Figure 5.3. The work in these sections has also been published in a peer reviewed journal [400].

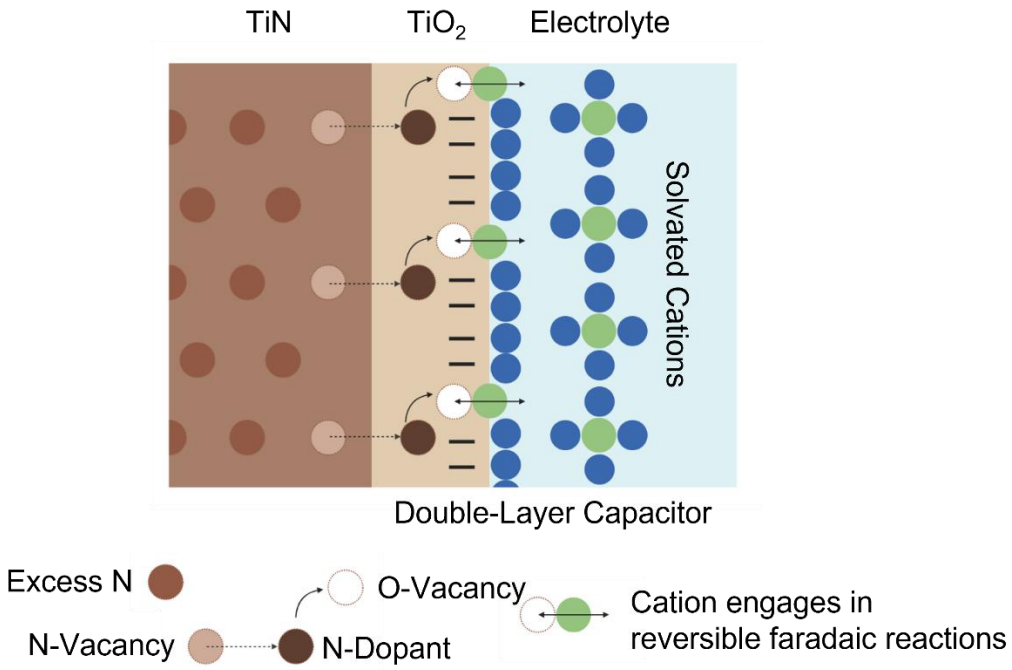

Figure 5.3: The hypothesised mechanisms behind the capacitive behaviour of TiNI electrodes. Excess N in the bulk of TiN diffuses out towards the surface and dopes the TiO_2, leaving behind an N-vacancy. The N-dopant causes the formation of an O-vacancy through the act of charge compensation. Cations can then engage in reversible faradaic reactions while double-layer capacitance is also active. Diagram created with BioRender.com

5.3 Modified Porous TiN Electrodes

5.3.1 Development and Characterisation of TiN_{II}, TiN_{III}, and TiN_{IV}

A strategy was devised to lower the susceptibility of porous TiN to fibrous encapsulation as reported in literature [228]–[230]. It was desired for this segment of the investigation that an abiotic approach be employed to tackle the issue of fibroblast attachment, whilst maintaining over-stoichiometric, porous TiN as the primary electrode material. This required that the electrochemical properties of TiN_I also be retained. With reference to the works of Bourkoula *et al.* [296], Pennisi *et al.* [299], Choi *et al.* [297], and Cyster *et al.* [298], in which fibroblast attachment and proliferation were controlled via surface roughening, a similar approach was chosen to reach this objective.

It is well-documented that the topography of a PVD coating may be controlled by the surface roughness of its underlying substrate [401]–[403]. Close replication of the substrate profile is possible for features in the 10 µm scale [402], whereas peaks and valleys encourage shadowing, overgrowth defects, and clustering of grains [401], [403].

To achieve these effects, the Ti6Al4V substrates were textured with three different diameters of media in a sand blasting treatment prior to PVD. Identical deposition conditions as those employed for TiN_I could thus be maintained, allowing direct comparisons to be made between the electrodes.

The resultant coatings, termed TiN_{II}, TiN_{III}, and TiN_{IV} (Figure 4.10), were sufficiently distinct from the original TiN_I (Figure 4.1) and from each other. Optical profilometry measurements revealed increasing values for all the roughness parameters (Table 4.6) in the order $TiN_I < TiN_{II} < TiN_{III} < TiN_{IV}$. As expected, the highest degree of three-dimensionality was observed in TiN_{IV} electrodes, reaching average maximum profile heights of 33.0 ± 4.5 µm. Maximal pyramidal diameters (Figure 4.10 at 20k x magnification) also followed this trend, as did the variation in pyramid size for each respective coating. Panjan *et al.* [404] make similar observations in their work involving PVD TiN coatings, and attribute these characteristics to competing growth profiles of adjacent grains. Geometric shadowing effects brought on by roughened surfaces result in preferential growth for grains in favourable positions. These grains thus grow faster and larger than their shadowed counterparts, and results in grain size variability as observed.

When viewed in cross-section (Figure 4.10) it may be observed that all the modified coatings retained the columnar microstructure of TiN_I, and no significant differences were found in coating thicknesses ($p > 0.05$). However, instances of re-nucleation events appear to increase along the same trend described above, with a smaller fraction of full-length grains occurring in TiN_{IV} than for TiN_I. Even so, the TiN_{IV} coating averaged only 1 re-nucleation event through the coating thickness at any given point.

The X-ray diffractograms collected for the different coatings (Figure 4.11) match the pattern for PDF file no. 04-015-0336, confirming a TiN Osbornite FCC-like crystal structure. Like the TiN_I electrodes, the most prominent peak was found to be the (111) orientation, suggesting highly textured coatings in all the variations. This was also corroborated by the SEM images, in which the distinct pyramidal shape of the grains could be observed. No distinguishing features could be identified in the XRD scans when comparing TiN_I and TiN_{II} electrodes, with the latter also returning a distinct (222) peak at the 2θ value of 36.46°. In the case of the TiN_{III} and TiN_{IV} electrodes, three other peaks emerged (labelled numbers 2, 3, and 4 in Figure 4.11) which were identified as the (200),

(220), and (311) orientations, respectively. Trends in literature suggest these minute peaks to be associated with re-nucleation events, as initial grain growth at nucleation sites is more likely to be of random orientation [227], [368], [405]. The dominant plane, in this case the (111) orientation, is re-established once the $E_{strain} > E_{surface}$ threshold is crossed, and the texture is maintained [177], [221], [368].

It was further observed that slight positive shifts emerged in the spectra for TiN_{III} and TiN_{IV} electrodes with respect to that of TiN_I, where the offsets were approximately of 0.15^o and 0.22^o, respectively. These calculations were based on the (111) and (222) peaks, which emerge in all four of the electrode measurements. Conventionally, a positive shift in the value of 2θ denotes some form of compression in the crystal lattice [406], [407]. Although some speculation regarding the relative content of lattice defects may be entertained based on these results, there was no way to corroborate any of the hypotheses. Chiefly, no significant discrepancies were observed for the micro-Raman spectra (Figure 4.12), and all four electrodes were similarly designated to be over-stoichiometric TiN. For this reason, the minor differences in the crystal structures (i.e., the 2θ shifts and emergence of (200), (220), and (311) orientations) were deemed to be inconsequential for the scope of this work. Hereafter, the electrodes will therefore be considered of identical crystal structure and chemical makeup.

5.3.2 TiN_I, TiN_{II}, TiN_{III}, and TiN_{IV} Electrodes have Identical Electrochemical Properties in PBS

The modified TiN electrodes were subjected to electrochemical measurements in PBS under testing conditions identical to those applied for TiN_I. All the electrodes were impregnated with the electrolyte prior to testing by submersion and application of moderate vacuum (0.5 bar) for 10 minutes. No significant difference was observed ($p > 0.05$) for any of the measurements made under these conditions. Bode and Nyquist plots (Figure 4.13) are of identical shape and magnitude, with no evident trend of increasing or decreasing impedance with electrode roughness. Consequently, the same equivalent circuit (Figure 4.4 a) could be used to model the spectra, returning similar results for all the variables derived (Table 4.8). The same trend was observed for cyclic voltammetry (Figure 4.14) and the CSC_C values computed at all four scan rates (Table 4.9) One of the major concerns arising for the modified TiN electrodes, electrolyte interaction with

the underlying Ti6Al4V substrate, was therefore reliably dispelled based on these results. Changes in the Bode and Nyquist plots, errors in the equivalent circuit model fitting, and the evolution of gas bubbles during CV measurements[16] would have otherwise been expected in the case of electrolyte infiltration [381], [410], [411].

To establish whether electrochemical similarities would break down during chronic applications, the TiN_{IV} electrodes were subjected to a regiment of 10,000 consecutive cycles at scan rates of 0.1 and 1 Vs^{-1}. In fact, the TiN_{IV} electrodes responded in a quasi-identical manner to the original material (Appendix F), wherein gradual decay of the Y_{pseu} and CSC_C values were the only notable changes with cycle number at 0.1 Vs^{-1}. Micro-Raman analysis, including comparisons of the I_{TA}/I_{TO} ratio before and after cycling, were also consistent for TiN_I and TiN_{IV}. Based on these results, it was determined that the substrate roughening procedures did not induce any electrochemical disadvantage to the TiN_{II}, TiN_{III}, and TiN_{IV} electrodes as compared to TiN_I. It is speculated that any potential negative effects arising from re-nucleation were either not significant enough to translate into the electrochemical response, or were offset by some small increase in the ESA gained by substrate roughening [412]–[414].

5.3.3 The Impact of Protein on the Electrochemical Properties of TiN Electrodes

It is common for neural electrodes to register a significant decline in their electrochemical properties upon introduction to a biological environment. This is true for many materials in current use, including Pt, Pt/Ir alloys, and Au, where the observation is made within the acute phases of implantation, and thus excludes cell attachment as a viable influence at this stage [415]–[417]. Rather, protein adsorption is thought to be the main contributor towards this phenomenon, disrupting charge transfer mechanisms along the ESA and raising the overall impedance [416]. Although there exists a great body of work concerning the influence of protein on the aforementioned materials [418]–[421], the literature regarding porous TiN is lacking. It has been reported by Meijs *et al.* [292] that smooth TiN electrode surfaces are susceptible to

[16] Water electrolysis limits for bare Ti6Al4V were found to be -0.3 to 0.7 V *vs* SCE in PBS. An example is given in Appendix E.

albumin adsorption, which in turn reduces the CSC_C as compared to measurements made in PBS (Figure 2.47 d). In other work [228], it is theorised that similar protein adsorption diminishes the electrochemical properties of porous TiN (broadly analogous to TiN_I in its crystal structure and morphology) by blocking the pores. This postulation was deduced from acute EIS measurements made upon implantation in rats, although no circuit modelling is performed to consolidate the hypothesis.

The electrochemical tests (EIS and CV measurements) previously conducted in PBS were thus repeated in a protein-containing electrolyte (PBS + 2.5g/dl BSA) to characterise its influence. The concentration of BSA was chosen based on the amounts typically found in healthy interstitial fluid rather than the CSF, as the former carries a higher percentage and represents a more adverse testing condition [68]–[70]. Sodium azide was also added to the electrolyte (0.3 wt%) to prevent bacterial growth and subsequent alterations of the test conditions. Since the eventual testing of PEDOT:PSS electrodes was not foreseen at the time of these experiments, the same set of measurements were conducted on TiN_{IV} using a 1% (by volume) solution of penicillin-streptomycin (P/S) in place of the sodium azide[17] (Figure 4.32). In all cases the electrodes were impregnated with the electrolyte prior to testing using the same vacuum method described previously (section 5.3.2).

The four electrodes produced very similar Bode plots (Figure 4.15) to one another, with no significant discrepancies in the measured impedance or phase angle. Moreover, the similarity extends to measurements made in PBS, and so the same equivalent circuit was employed to model the spectra (results shown in Table 4.10). A slight increase in the R_s is the only apparent change following addition of albumin (and sodium azide) to the testing solution. While this is true for TiN_{II}, TiN_{III}, and TiN_{IV} electrodes, the trend does not hold for TiN_I (14.9 ± 3.1 versus 13.9 ± 0.2 Ωcm^2 in PBS and PBS+BSA respectively). This was attributed to the fact that measurements of TiN_I electrodes in PBS were carried out in a separate set of experiments that preceded the rest by a number of months. The value of R_s is very sensitive to the relative distance between the tip of the reference electrode and the surface of the working electrode [422], [423]. Although efforts were made to replicate the testing set-up between experimental sets, the

[17] Sodium azide is a strong reducing agent and nucleophile, and thus has the potential to reduce PEDOT:PSS and affect its electrochemical properties.

electrochemical cell had to be disassembled between the first and second batch of experiments[18] for cleaning and maintenance. For these reasons, R_s values for TiN_I in PBS were excluded from the group analysis. In doing so, a significant 18.8% increase in solution resistance ($p < 0.05$) was reliably established when comparing the collective average measured in PBS and protein-containing electrolyte (12.1 ± 0.6 and 14.9 ± 1 Ωcm^2 respectively). Different studies [417], [424]–[426] have likewise reported an increase in R_s when adding albumin to saline electrolyte, even at lower concentrations than those employed here.

The cyclic voltammetry scans (Figure 4.16, Table 4.11) make more obvious the disparity in measurements when albumin is added to the electrolyte. All the electrodes exhibit significant reductions in their voltammogram areas when comparing results in PBS and PBS+BSA, accompanied by drops in the CSC_C. The shift towards more resistive behaviour is particularly visible at a scan rate of 0.05 Vs^{-1}, where the current response (i.e., the shape of the CV curve) assumes higher diagonality in correspondence with an ohmic drop [101].

These observations do not concur with the hypothesis developed by Meijs *et al.* [230] in their analysis of similar porous TiN electrodes. Following subcutaneous implantation in the backs of Wistar rats, acute EIS measurements revealed higher impedance measurements within the high frequency domain as compared to *in vitro* measurements made in PBS. Although no circuit modelling is carried out, the authors correlate $|Z|_{1kHz}$ with electrolyte and/or tissue resistance, and thus propose pore blockage from proteins as the underlying cause. This position is restated in another publication from the same authors [228], where porous TiN electrodes are subjected to similar *in vitro* and *in* vivo testing conditions with comparable results. Despite the similarities in the results of the current work and those reported by Meijs *et al.* [228], [230], it is here understood that large-scale pore blockage is not likely to be a factor of influence. Such a phenomenon typically affects the electrode's capacitive mechanisms as a result of decreased access to the full ESA [418], [420], [425], [427], [428]. This behaviour was not recorded for any of the four TiN electrodes upon acute measurements.

[18] Refer to Appendix G for Experimental batches.

A significant effect on the electrodes' capacitive properties only appears with prolonged immersion time in the protein-containing solution (Figure 4.18). Y_{pseu} undergoes a gradual decay over the course of the experiment, losing approximately 13% of its initial value on average. The value of R_s exhibits a concurrent drop and reaches values equivalent to those obtained in PBS. Albumin blocking is thus time-dependent in the case of porous TiN electrodes, with initial effects manifesting in the electrolyte resistance before impacting capacitive mechanisms. Interestingly, no decay appears in the case of Y_{dl}, further strengthening the argument against large-scale pore blockage by the proteins. Harris *et al.* [418] posit an alternative effect, in which the addition of BSA to test electrolytes can result in a phenomenon known as micro-blocking. In this case, only partial, discontinuous points of the ESA are impacted rather than the formation of a continuous affected layer. Such a phenomenon might not disrupt double-layer formation, but interrupt reversible faradaic reactions that require access to specific sites on the material surface for operation. Incomplete protein saturation of the surface with respect to the time window of immersion may also be a factor [429]. It is however worth noting that saturation is typically reached within 2 hours of immersion in solutions of physiologically-relevant concentrations of albumin (bovine or human) [429]–[431].

Finally, in comparing measurements obtained for TiNIV using P/S in place of sodium azide (Appendix D), no significant differences ($p > 0.05$) were revealed for any of the variables derived. These results were used to establish any influence that sodium azide might have had on boosting the electrochemical performance (reducing R_s, increasing Y_{pseu}, etc.) via introduction of additional ionic species as being minimal.

5.3.4 TiN_{IV} Electrodes Reduce Fibroblast Attachment

NHDF cells were cultured on the surfaces of the modified TiN electrodes and incubated for a total of 72 hours in DMEM. Cell viability measurements were carried out using a resazurin indicator on the same samples every 24 hours. The results of these measurements are given in Figure 4.19. It is speculated that the large error associated with the results is tied to the experiment methodology as described in section 3.6.1.4. For this specific batch of experiments the resazurin indicator was added to each well individually rather than mixing the indicator with the media in a bulk solution prior to pipetting. As such, due to the small volumes being pipetted, additional random error was introduced into the experiment. However, the methodology was kept consistent between

replicate experiments, and statistical analysis revealed no significant difference ($p > 0.05$) between the means for the same condition across replicates. The average and standard deviation shown were thus calculated from the pooled results of 5 repeats across 2 replicate experiments (i.e., n =10).

The only statistically significant difference ($p < 0.05$) to emerge from the experiments is between the number of cells on TiN_I electrodes after 24 and 72 hours, and between TiN_I and TiN_{IV} electrodes after 72 hours. Similar numbers of fibroblasts appear to be present on the electrodes after 24 hours, suggesting that the initial stages of cell attachment are insensitive to surface topography. Moreover, no significant proliferation ($p > 0.05$) seemingly occurs on any of the electrodes over the culture period with the exception of TiN_I samples. Over 72 hours, the average number of fibroblasts on TiN_I surfaces had increased by 36%, and by the end of the experiment, TiN_I electrodes had more than double (~ 2.6 times) the number of viable fibroblasts as compared to TiN_{IV}.

These findings are congruent with the work of Bourkoula *et al.* [296], in which HDF cells were cultured on PMMA substrates of varying roughness values. As in this case, no difference in the number of fibroblasts was observed on the substrates after 24 hours. Similar observations were made by Canullo *et al.* [432] and Miao *et al.* [433], wherein both groups were assessing the influence of surface roughness on fibroblast attachment. As key mediators of cell attachment, protein adsorption and subsequent formation of an ECM are crucial in determining the amount of fibroblasts detected on a surface in the initial stages of testing [434], [435]. This process is intimately tied to surface wettability, which by extension depends on material chemistry and roughness [436]. With respect to the latter, research points towards nanotopographical features as having the most impact on protein adsorption [433], [435], [437], whereas the process appears largely insensitive to changes in micro-scale texturing [433], [438], [439]. Albumin, the most abundant serum protein in completed DMEM solutions, has recorded diameters of less than 10 nm [440]. Micro-scale features thus appear flat, and no distinction is made between pyramidal diameters of 0.5 µm (TiN_I) and 2.8 µm (TiN_{IV}) [439]. Moreover, no evidence of differential protein adsorption was observed from the analysis of 24-hour EIS measurements in PBS+BSA electrolyte (section 5.3.3). In conjunction with the evidence for identical material chemistry amongst the four electrode types (section

5.3.1), it is thus theorised that similar levels of protein adsorption led to an equivalent number of fibroblast attachment at 24 hours.

Following the initial stages of cell adhesion, micrometre surface features evidently played a large role in hindering fibroblast growth and proliferation. Cell spreading and enlargement, both prerequisites for proliferation of fibroblasts, are made more difficult with the introduction of physical obstacles [296], [441]. Compared to the size of fibroblasts in culture (> 100 µm), the porous surface of TiN_I electrodes appears planar, and cells express typical flattened morphologies (Figure 4.21 a), good spread (Figure 4.21 a), and quasi-complete surface coverage (Figure 4.20 a and e). Infrequent overgrowth defects present maximal surface protrusions of only 1.5 µm (Table 4.6), which the fibroblasts either bypass or grow over (Figure 4.21 e).

Conversely, an abundance of pits, valleys, and overgrowths (as found on TiN_{IV} and TiN_{III}) directly interfere with the cells' ability to establish and mature essential focal adhesion points, effectively impeding their spreading and growth [296], [441]. A notable decrease in the average cell size is in fact apparent in Figure 4.21 a-d, as the surfaces change from TiN_I to TiN_{IV}. Fibroblasts also adopt an elongated shape and extend more membrane projections, becoming isolated and so failing to form a confluent layer (Figure 4.20 c and d) . These factors combine to arrest the cell cycle and block proliferation processes [299], [441], correlating to the absence of significant growth between day 1 and 3 for TiN_{II}, TiN_{III}, and TiN_{IV} electrodes. The bridging of fibroblasts in between contact points of high elevation was further observed on TiN_{III} and TiN_{IV} electrodes (Figure 4.21 g and h). Excessive stretching of the cell membrane occurs as a result, deteriorating cellular function and threatening viability. Bourkoula *et al.* [296] present this phenomenon as being highly influential in determining a relationship between fibroblast viability and surface roughness. A threshold roughness is reached when the geometry of surface features causes cellular stretching that exceeds membrane elasticity limit. It is possible to apply this hypothesis to the current work, whereby threshold roughness is achieved on the TiN_{IV} electrodes, producing the statistically significant difference in cell number after 72 hours with respect to TiN_I.

5.4 TiN/PEDOT:PSS Dual-Layer Electrodes

5.4.1 Development and Characterisation

An expansive body of work from the last decade has made clear the electrochemical benefits to be gained from adding CP layers onto roughened electrode surfaces [98], [253], [258]–[260], [282], [288], [442]. PEDOT:PSS films have been previously deposited onto nanostructured Pt [259], etched Au [282], and porous IrO_x [260] with the intention of securing good mechanical adhesion. TiN_{IV} electrodes were thus considered to be optimal candidates for a similar line of investigation, providing a feature-heavy structure on which to establish physical anchoring. Electropolymerisation was chosen as a means of deposition to exploit the porous architecture of TiN_{IV}, wherein the precursor solution could be impregnated into its structure using vacuum (0.1 bar). With the exception of Wang *et al.* [129], no previous research has explored the deposition of PEDOT:PSS onto TiN electrodes, and none have done so on porous TiN, at time of writing.

Using a process of sequential trials, the current density of 1.3 $mAcm^{-2}$ was chosen to carry out all ensuing depositions. Further increase to the current density resulted in cracked and blistered coatings, possibly due to an excess current pushing the TiN_{IV} past its electrolysis limits and into initiating water splitting [101]. In order to observe the possible effects of volumetric capacitance [244], [252], [266], three deposition times were chosen (12.5, 15, and 17.5 minutes) for study. The upper limit was capped at 17.5 minutes as any further charge delivered resulted in sections of polymer delamination and cracking. Similar occurrences have been described in literature [443], [444] for PEDOT:PSS films, demonstrating the existence of a thickness threshold beyond which the structure cannot support itself, resulting in excessive stress, cracking, and coating lift-off.

The resultant coatings closely match the descriptions given in literature for PEDOT:PSS [252], [260], [269]. The signature blue colour (Figure 4.23 a), typical of PEDOT:PSS films measuring in the µm scale [241], emerged in all three electrode variations ($PP_{12.5}$, PP_{15}, and $PP_{17.5}$). Cross-sectional imaging and thickness measurements of the CP layers (Figure 4.24) accordingly reveal them to be well outside the range in which transparency is expected [244], [445]. The relationship between layer thickening and increased

deposition time was also established in line with other reports [252], [266]. It should be here noted that the thickness measurements given reflect only the polymer layer superficial to the TiN. However, close observation of the SEM images in Figure 4.24 reveal PEDOT:PSS material to also exist within the columnar structure of the TiN. The empty spaces between individual columns, very evident in pristine TiN_{IV} coatings (Figure 4.10), are here absent, and the spaces appear to be occupied. As such, the voluminal content of PEDOT:PSS is expected to be higher than the simple calculation of electrode GSA multiplied by thickness of the measured layer.

Planar SEM images taken of $PP_{17.5}$ electrodes reveal the nodular texture of PEDOT:PSS (Figure 4.23 b and c), consisting of aggregated spheres measuring less than 10 nm in diameter (Figure 4.23 d). The morphology is synonymous with that presented by Chikar *et al.* [252], in which a very similar galvanostatic electrodeposition process was employed to develop the polymer (Figure 2.30 a). This texture provides the basis for the porosity of PEDOT:PSS, whereby an electrolyte should, in theory, be able to penetrate between the spherical agglomerates [143]. It was not possible to view the polymer morphology in cross-section, as the process of sample preparation (cutting and grinding) could not preserve the morphology of the soft material.

The polymerisation of PEDOT:PSS onto the TiN_{IV} electrodes was also confirmed via micro-Raman spectroscopy. Spectra were collected before and after the baking treatment at 90^{o} C, a process intended to introduce regions of PEDOT crystallites within the polymer whilst drying off any residual precursor solution [241], [272]. Particularly, it was desired that this procedure occur without any significant PSS burn-off, maintaining the PEDOT:PSS ratio and its related benefits of biofunctionality [268]. The baking parameters were chosen based on the reports of research groups specifically designing PEDOT:PSS electrodes for neural interfacing [139], [269], [330]. The obtained spectra (Figure 4.25) were in line with those of numerous other works in literature [273]–[276], returning the 7 major peaks associated with the material. With reference to the these studies [273]–[276], peaks number 1, 2, and 7 (refer to Table 4.13 for peak positions) were assigned to C-C, SO_3^-, and C-C-H bonds of PSS, respectively. On the other hand, peaks numbered 3 – 6 were assigned to C_α- $C_{\alpha'}$ inter-ring stretching, C_β - $C_{\beta'}$ stretching, symmetrical $C_\alpha = C_\beta$, and asymmetrical $C_\alpha = C_\beta$ vibrations of the PEDOT chain, respectively. In comparing the spectra before and after baking, no significant change in

the intensity ratio of PEDOT:PSS peaks is evident. A relative drop in peak intensity for PSS-associated shifts is expected when significant dopant removal occurs [268], [273], [446]. The absence of this phenomenon therefore suggests no significant degradation to the PSS component occurred as a result of the chosen treatment. This result was anticipated, as PSS burn-off is expected to commence only at temperatures in excess of 120 °C [447].

5.4.2 Crack Damage in PEDOT:PSS Layers

A number of small cracks may be observed on SEM images of PP electrodes (examples are given in Figure 5.4). Conversely, no such cracks could be identified on the polymer surface when using optical microscopy prior to SEM analysis, even at high magnifications (Figure 4.23 a and Figure 4.38). Moreover, it was determined that cracking was not occurring as a result of the baking process, as surfaces were inspected via optical microscopy before and after baking to no effect. Care was taken to avoid thermal shock, ramping up the temperature from RT to 90 °C over a period of 3 hours, and then allowing the electrodes to cool overnight in the furnace after a holding period of 3 hours. SEM images of the electrodes from cell culture experiments further show identical cracks propagating through the cell structure, matching those on the polymer. An example of this is shown in Figure 5.4. From this it was deduced that cracking of PP electrodes was occurring only upon their placement in the SEM chamber for analysis.

Wegler *et al.* [448] reported issues with cracking of PEDOT:PSS films confined in between layers of glass and alumina. Through a series of controlled climate experiments, the PEDOT:PSS was observed to expand upon exposure to humidity, resulting in crack formation due to the confined space of the layered assembly. Owing to the hygroscopic nature of the PSS component, PEDOT:PSS films readily adsorb moisture from the environment, and swell in volume to accommodate the water molecules [449]–[451]. Although highly desirable in the context of electrolyte adsorption and electrochemical performance, this feature can pose some issues with characterisation. The absolute vacuum employed for SEM analysis in the current work drops the humidity in the chamber to 0%, causing rapid contraction of the polymer as a consequence of moisture loss. This causes a build-up of tensile stress within the polymer, which is subsequently relieved by crack formation. Moreover, the rigid TiN is unaffected by this process. The mismatch caused by the unchanging TiN and contracting PEDOT:PSS may have further

contributed to the observed cracks in SEM images (process illustrated in Figure 5.5). It is also possible that volume shrinkage brought on by the SEM vacuum caused the PEDOT:PSS films to separate from the Ni and TiN in the cross-section SEM analysis (Figure 4.24). A layer of empty space is in fact visible in the images, possibly representing volume previously occupied by the adsorbed water molecules. It is thus critical to specify that the measured thickness of PEDOT:PSS layers is representative only of their dried state.

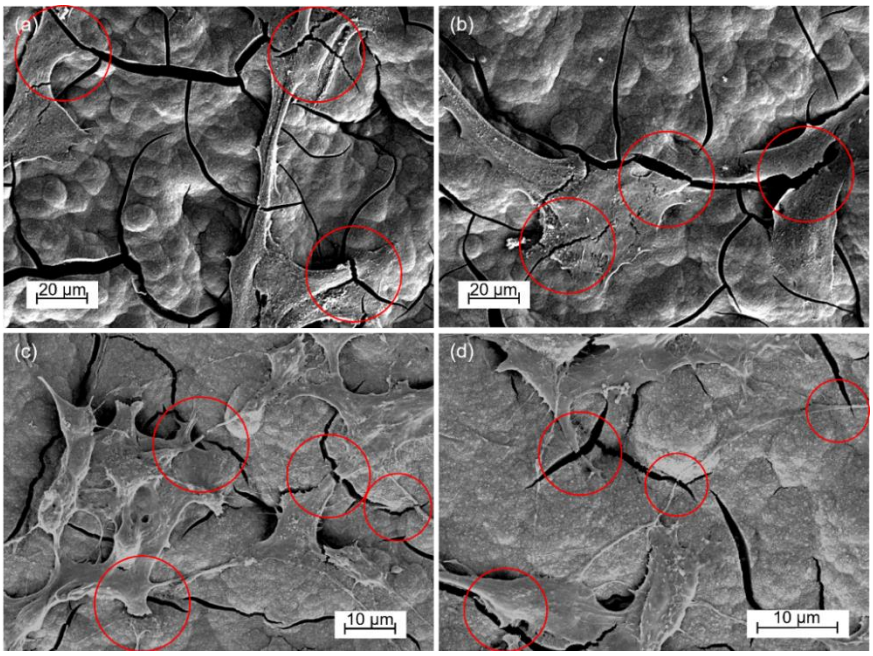

Figure 5.4: SEM images of $PP_{17.5}$ electrodes with (a, b) NHDF after 72 hours of culture, and; (c, d) SH-SY5Y cells after 72 hours of culture and a further 72 hours of treatment with ATRA. Cells were fixed in glutaraldehyde and sputter-coated with a nanometric layer of Au to improve conductivity. Red circles highlight cracks in the PEDOT:PSS layer that propagate through the cells as well.

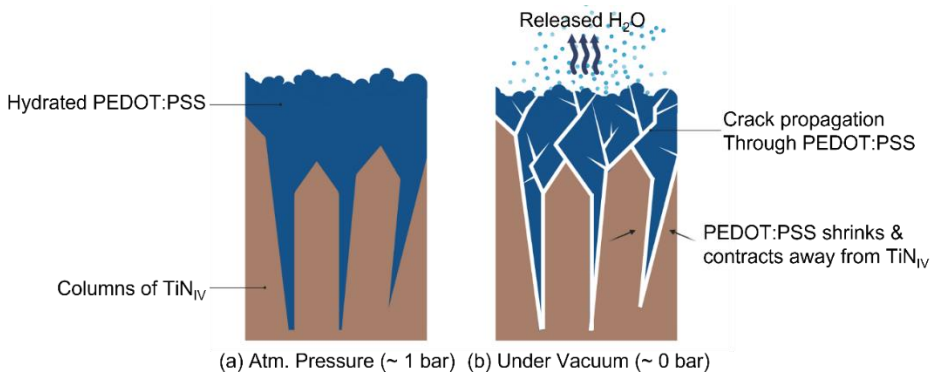

Figure 5.5: Illustration showing (a) The hydrated PEDOT:PSS at atmospheric pressure, adhered to the TiN_{IV} columns in the PP electrodes; (b) The vacuum in the SEM chamber is turned on (~ 0 bar) and the water molecules are rapidly pulled out of the PEDOT:PSS. The sudden loss in volume causes the polymer to contract away from the TiN_{IV}, causing cracks to form and propagate. Diagram created with BioRender.com.

5.4.3 PEDOT:PSS Layer Improves Electrochemical Properties of TiN_{IV} Electrodes

$PP_{12.5}$, PP_{15}, and $PP_{17.5}$ electrodes were subjected to electrochemical measurements in PBS, where testing conditions were maintained identical to those applied for TiN. The electrodes were also impregnated with the electrolyte prior to testing by submersion and application of moderate vacuum (0.5 bar) for 10 minutes.

Representative Bode and Nyquist plots for all three electrodes are compared with the typical spectra for TiN_{IV} in Figure 4.26. It is immediately evident that the addition of a PEDOT:PSS layer on the TiN_{IV} electrodes reduces the measured impedance, the effect of which is more pronounced as deposition time is increased. $PP_{17.5}$ electrodes in fact register the lowest impedance in comparison to TiN_{IV}. These findings are in line with those of other researchers; PEDOT:PSS films have been deposited onto a variety of different electrode materials, notably Pt [252], [259], Au [143], [198], [444], and IrOx [259], [260], with significant reductions to the impedance occurring as a result. This is attributed in part to the polymer's high ESA, where the nano-structured porous architecture and hygroscopic nature facilitates electrolyte adsorption into the material's bulk and hence increase the double-layer capacitance [244], [266]. Cations from the electrolyte may then also participate in sequential doping and de-doping processes, made possible by the $PEDOT^+$ component, resulting in additional capacitive action [101], [128]. Congruently, a strong capacitive response may be evidenced in the low frequency domain of the Nyquist plots (Figure 4.26) [161], [180]. Higher angles are generated for the PP electrodes as compared to the original TiN_{IV}, and although subtle, the angle also increases with increased deposition time. This suggests that the capacitive contribution increases as the PEDOT:PSS layer thickens.

To gain a better understanding of the capacitive mechanisms at play, the EIS spectra were fitted with an equivalent circuit model. Given the similarities in the overall shape of the Bode and Nyquist plots, as well as identical hypothesised capacitive mechanisms (i.e., combined double-layer and pseudocapacitance), the same model (Figure 4.4 a) was adopted for the PP electrodes as was for the TiN_{IV}. In addition to separating the two capacitive components [161], adopting the same model as the TiN_{IV} electrodes is doubly advantageous in that it allows direct comparisons to be made between the two materials. Convergent fits were successfully obtained for all PP electrodes using this circuit (χ^2 <

0.001), and results from modelling are shown in Table 4.14. It can be seen that both Y_{dl} and Y_{pseu} increase with the introduction of a PEDOT:PSS layer. Moreover, both values follow the same trend of increasing with layer thickness, corresponding to the observed impedance drops in the Bode plots. These findings compare well to the works of Bianchi *et al.* [266], Chikar *et al.* [252], and Gerwin *et al.* [444], in which thicker PEDOT:PSS coatings resulted in lower impedance measurements and higher values of capacitance. The authors attribute this phenomenon to volumetric capacitance, a feature tied to the intrinsic nature of the material's pseudocapacitance [162], [163]. It is interesting to note that both Y_{pseu} and Y_{dl} have an approximately linear relationship with layer thickness, although there is some ambiguity in the case of Y_{dl} due linear fitting across only three data points (Figure 5.6 a and b). Nevertheless, these results indicate that the saturation effect as described by Bianchi *et al.* [266] was not yet reached with the layer thicknesses explored in this work. Although it is possible that higher capacitance values could be obtained with thicker coatings, deposition times beyond 17.5 minutes were producing defective PEDOT:PSS films (as discussed in section 5.4.1). For this reason, the limiting factor in the electrode system is physical rather than electrochemical.

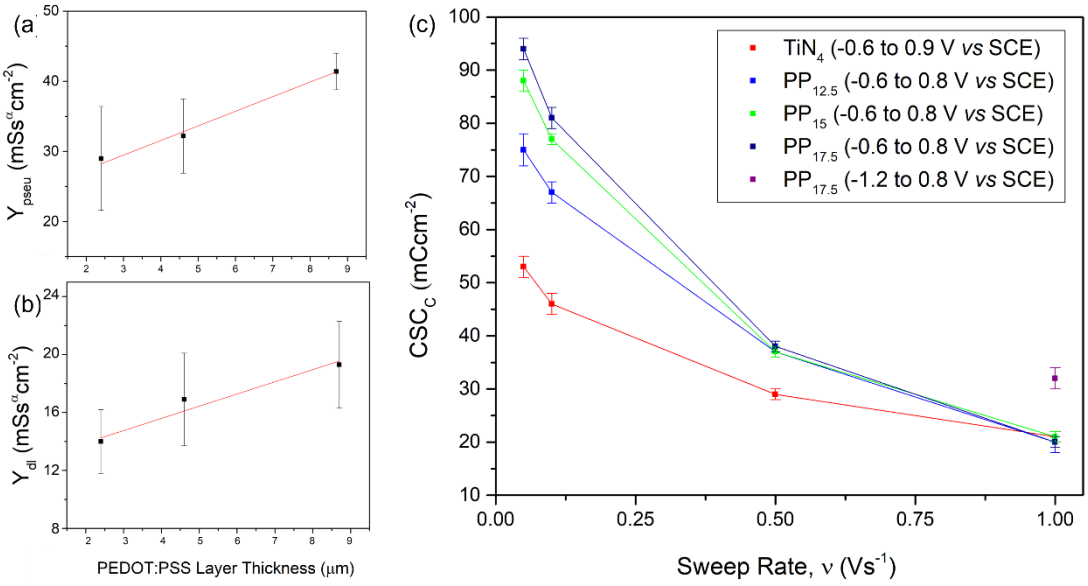

Figure 5.6: The relationship between PEDOT:PSS layer thickness with (a) Y_{pseu}, and (b) Y_{dl}, including linear fit; (c) The CSC_C of TiN_{IV} (red), $PP_{12.5}$ (blue), PP_{15} (green), and $PP_{17.5}$ (navy) electrodes at different sweep rates. The CSC_C of $PP_{17.5}$ electrodes at 1 Vs^{-1} is also given for the extended WW (purple).

In addition to improvement in the Y_{pseu} and Y_{dl}, the corresponding value of α for pseudocapacitance is significantly higher in PP electrodes than for TiN_{IV}. This variable may be considered as an empirical measurement of how 'good' or 'bad' the capacitive

mechanism is. When applied to pseudocapacitance, the value of α_{pseu} reflects the material's efficiency in carrying out reversible faradaic reactions [157]. From this it may be inferred that the doping and de-doping process carried out by PEDOT:PSS is superior to the redox reaction occurring at the sites of O-vacancies in over-stoichiometric TiN_{IV}. This may be due to better cation adsorption kinetics, and/or a more homogeneous distribution of the $PEDOT^+$ sites in comparison to the O-vacancy sites [452]–[454].

The electrochemical advantage of the deposited PEDOT:PSS layer is also reflected in the cyclic voltammetry measurements (Figure 4.27). At low scan rates ($v \leq 0.1$ Vs^{-1}) in particular, the increase in CSC_C over TiN_{IV} electrodes is evident (Table 4.15), despite adopting a smaller scanning window (-0.6 to 0.9 and -0.6 to 0.8 V *vs* SCE for TiN_{IV} and PP electrodes, respectively). At these values of v, kinetic limitations and effects of pore resistance are minimal, and so the aforementioned volumetric capacitance may be maximally exploited [101], [236], [396]. $PP_{17.5}$ thus measures a higher CSC_C than PP_{15}, and higher still than $PP_{12.5}$ (Figure 5.6 c). This effect disappears at a scan rate of v = 0.5 Vs^{-1}, as no statistically significant difference is measured in CSC_C for the three PP electrodes, although the value for polymer electrodes is notably still higher than for TiN_{IV}. No significant difference remains at 1 Vs^{-1}, and all 4 electrodes return equal values of CSC_C. At high charge/discharge rates, only a portion of the available surface area is utilized due to the delay-line effect as described by Cogan [101]. As such, film thicknesses beyond 2.4 µm are inconsequential for the scope of CSC_C. Moreover, the advantage over TiN_{IV} electrodes is lost.

This shortcoming was attributed to the restricted WW that was being applied to the PP electrodes. Despite identifying the electrolysis limits for PEDOT:PSS to be -1.2 and 0.8 V *vs* SCE in accordance with the work of others [243], [269], [282], [455], cracks were emerging on the electrode surfaces after CV testing in this window. Initially it was thought that the electrolyte was penetrating through the PEDOT:PSS layer and interacting with the underlying TiN_{IV}. As the cathodic limit for TiN was previously determined to lie within this window (-0.6 V *vs* SCE), it was speculated that the CV scan was initiating hydrogen evolution on the surface of the ceramic [101], thus resulting in the cracking observed. As such, the testing limits for PP electrodes were adapted to lie within the WW of both materials. No cracks were identified following this procedure.

However, it was later recognized that cracking did not occur on the PP electrodes when running CV tests within the extended water window at high scan rates ($v \geq 1$ Vs^{-1}). Moreover, similar to the rationale applied for PBS contact with the underlying Ti substrate, there was little evidence to support the theory of significant electrolyte contact with the TiN. Boehler *et al.* [259] observed significant bubbling on their Pt/PEDOT:PSS electrode due to electrolyte contact with the Pt, resulting in complete delamination of the polymer film with a number of cycles. No such bubbling was observed on the PP electrodes during testing, nor did the CP films delaminate in spite of cracking. Thus, the cracking was alternatively speculated to be a consequence of the doping/de-doping process. As described by Liu and Li [186], PEDOT:PSS expands during the cathodic sweep (reduction), as cations from the electrolyte are adsorbed into the material to dope $PEDOT^{+}$. During the anodic sweep (oxidation), the PEDOT is de-doped, and the cations return to the electrolyte with an accompanying contraction of polymer material (Figure 2.36). A similar issue to that resulting from SEM analysis is hence thought to arise. Namely, stress build-up and elastic mismatch between the TiN and the PEDOT:PSS (restricting the polymer's expansion) during the doping stage produces the observed cracks. In accordance with the electrochemical theory behind the charge transfer mechanism of PEDOT:PSS, reducing the testing window should reduce the number of cations doping $PEDOT^{+}$ [128], [241], [444]. In turn, the amount of volumetric expansion should also decrease, mitigating the formation and propagation of cracks.

Conversely, this problem is not expected to occur at high scan rates, where the amount of adsorbed dopants is already restricted due to kinetic limitations [187], [236], [396]. This is a plausible reason as to why the PP electrodes do not crack when tested within the full WW at 1 Vs^{-1}. The voltammograms for the $PP_{17.5}$ electrodes were thus also recorded between the limits of -1.2 and 0.8 V *vs* SCE at this sweep rate, resulting in a CSC_C of 32 ± 2 $mCcm^{-2}$ (purple in Figure 4.28). This represents a 52% increase over the original TiN_{IV}. Moreover, since the typical stimulation pulse employs much faster charge/discharge rates than the 1 Vs^{-1} tested here (refer to Table 2.3), limits for measuring the CIC may be reliably based on the full WW of PEDOT:PSS rather than the restricted one [21].

As the PEDOT:PSS electrode with the lowest measured impedance, the $PP_{17.5}$ was chosen to carry out all ensuing tests and further electrode development. In order to test

the theory of v-dependant cracking as outlined above, and to assess the charge retention capacity of the PEDOT:PSS coating, $PP_{17.5}$ electrodes were subjected to 10,000 charge/discharge cycles under three different conditions. The electrodes were cycled at sweep rates of 0.1 and 1 Vs^{-1} using the restricted WW, while tests at 1 Vs^{-1} were also carried out using the full WW. No detrimental impact to electrochemical performance was observed for the electrodes tested at high scan rate, for both the full and restricted WW. No significant drop ($p > 0.05$) in any of the equivalent circuit variables was recorded, and charge retention was maintained upwards of 99% (Figure 4.35) This represents an advantage over TiN_{IV} electrodes, whereby the CSC_C is both numerically higher (in the case of the extended WW) and has a higher retention rate for $PP_{17.5}$. No evidence of cracks or delaminations was observed on any of the electrodes tested, nor any significant change in the micro-Raman measurements (Figure 4.36). The $PP_{17.5}$ electrode was thus judged to be highly efficient in its charge transfer mechanism, displaying quasi-complete reversibility at clinically-relevant charge/discharge rates.

On the other hand, electrodes tested at 0.1 Vs^{-1} displayed antipodal behaviour to those tested at 1 Vs^{-1}. Y_{pseu}, Y_{dl}, and α_{pseu} all experience significant degradation, the onset of which appears to be around the 3,000 cycle mark for the latter two variable (Figure 4.35). The R_f mirrors this behaviour, remaining comparatively stable for the first 3,000 cycles before initiating a large, gradual increase until the end of the experiment. The electrodes also lose the majority of their CSC_C, with only 32 ± 2 $mCcm^{-2}$ remaining from the original 81± 2 $mCcm^{-2}$. It was revealed via microscope analysis (Figure 4.36) that the underlying cause of this electrochemical degradation is significant loss of PEDOT:PSS coverage on the electrode surface. The CP layer had become fragmented, although the remnants maintained their adhesion to the TiN_{IV} surface even during the rinsing process (gentle squirting with DI water from a wash bottle). Micro-Raman spectra were then collected on both the PEDOT:PSS fragments and on the exposed TiN_{IV}, both of which compare well to the respective material in its pristine state (Figure 4.36).

In the absence of any detectable chemical change to either the PEDOT:PSS or the underlying TiN_{IV}, the results suggest some form of mechanical degradation to the polymer coating. Osmotic stress is a known contributor to the physical breakdown of CP electrodes, particularly when they are deposited as films onto rigid substrates [186], [187], [260]. The sequential adsorption and desorption of cations with each progressive

cycle results in material fatigue that initiates cracking and subsequent delamination. A relevant example of this effect was demonstrated by Hou *et al.* [187] in their investigation into the cyclic stability of PANi (polyaniline) CP electrodes. Following 5,000 consecutive cycles at a sweep rate of 0.5 Vs^{-1}, PANi electrodes retained 99.6% of their initial capacitive function, whereas only 78.4% was retained when scanning at 0.02 Vs^{-1}. These results were corroborated by microscope analysis, showing undamaged and cracked surfaces for electrodes tested at high and low scan rates, respectively. This was attributed to osmotic stress resulting from sequential expansion and contraction of the material; a process which occurs to a smaller degree at high scan rates due to the kinetic limitations of doping.

It is possible that the $PP_{17.5}$ electrodes were subjected to similar effects from osmotic stress, leading to the degradation of electrochemical properties as measured. Cracking and delamination of the PEDOT:PSS film would correspond to lower Y_{pseu} and Y_{dl} as the volume of polymer is reduced with coating loss, whereas their capacitive efficiency (the empirical variable α) becomes hindered due to discontinuities in the surface. The α_{pseu} appears more sensitive to these effects than α_{dl}, possibly due to the simultaneous action of the TiN and PEDOT:PSS capacitive mechanisms. Moreover, sections of dislodged polymer resting on the electrode surface could further disrupt the charge transfer process, contributing to the large increase in R_f. Similar effects have been observed in electrode surfaces blocked by obstructive material [425], [456]. It is worth noting that after 6,000 cycles, the fitting efficiency of the equivalent circuit model had dropped. The Nyquist plot at the end of the 10,000 cycles (Figure 4.33) is in fact notably different from those of pristine and undamaged electrodes. An additional time constant appears to have been introduced [386], possibly as a result of TiN exposure to electrolyte and subsequent engagement in the charge transfer process. Significant participation of TiN_{IV} to charge transfer however seems to only have occurred in the latter part of the experiment, as micro-Raman analysis did not reveal any changes to the I_{TO}/I_{TA} ratio. A shift in the ratio, similar to that observed in Figure 4.9, would have otherwise been expected [235]. These tests therefore served their intended purpose in demonstrating the effects of osmotic stress as they manifest in $PP_{17.5}$ electrodes, and further highlighting their absence under clinically-relevant experimental conditions.

5.4.4 Adhesion of PEDOT:PSS to TiN_{IV}

A prevalent issue limiting the application of CP films in neural interfacing is poor adhesion to the underlying electrode surface [259], [282], [283]. It is possible that strong mechanical interlocking between PEDOT:PSS and the porous architecture of the TiN_{IV} provides sufficient adhesion between the two materials in the $PP_{17.5}$ electrode system. To test this hypothesis, the electrodes were subjected to ultrasonic vibrations at 45 kHz with intermittent EIS measurements and optical analysis. Such an experiment imparts physical stress on the electrode in excess of what is expected to be encountered *in vivo*, and thus provides an accelerated means to test the integrity of the film [198].

The results (Figure 4.37) indicate excellent mechanical stability under the testing conditions for the first 20 minutes of ultrasonication. No significant changes ($p > 0.05$) were identified in any of the variables from the equivalent circuit model, nor in the value of $|Z|_{1Hz}$. Moreover, no signs of physical damage were observed on the surface of the electrode (Figure 4.38). In this regard, the $PP_{17.5}$ electrodes displayed a higher resistance to mechanical agitation than the electrodes studied by Pranti *et al.* [198] (iodide-etched Au electrodes coated with a PEDOT:PSS layer). After 11 minutes of ultrasonication, the $|Z|_{1Hz}$ had registered a small yet significant increase, attributed by the authors to structural changes in the polymer rather than cracking or delamination. Neither effect was present in the $PP_{17.5}$ electrodes at the 20-minute mark.

The experiment was extended beyond this timepoint to observe what mode of failure the $PP_{17.5}$ electrodes would experience. After 20 minutes the impedance undergoes a significant 'jump' to higher values and continues to increase gradually with testing. It was not possible to fit the equivalent circuit model for the acquired spectra, as the fits did not converge ($\chi^2 > 0.001$). As this coincided with the emergence of cracks, delaminations, and TiN exposure (Figure 4.38) it is possible to attribute this occurrence with a change in charge transfer mechanism. Contact of the underlying TiN_{IV} with the electrolyte introduces new time constants into the model, whereby double-layer formation is non-homogenous, and two competing pseudocapacitive mechanisms are acting in tandem [454]. A very similar effect (shape of the Bode plot) emerges in the work of Boehler *et al.* [259], in which cracking and delamination of the PEDOT:PSS film exposes the Pt electrode underneath.

From these results it was possible to ascertain that sufficient adhesion exists between the TiN_{IV} ceramic and the electrodeposited PEDOT:PSS layer. Critically, no delamination is expected to occur from regular use, and the electrode was further shown capable of enduring forces excessive to those encountered *in vivo.*

5.4.5 The Impact of Protein on the Electrochemical Properties of $PP_{17.5}$ Electrodes and Implications for Cell Adhesion

The $PP_{17.5}$ electrodes were tested in protein-containing electrolyte using an identical experimental procedure as that employed for TiN_{IV} (section 4.2.3.2). The antibiotic P/S was added to solution to prevent bacterial growth in place of sodium azide. The comparisons drawn in this section are against TiN_{IV} electrodes tested using the same electrolyte rather than the original one containing sodium azide. Results demonstrating the similarities between TiN_{IV} electrodes tested in protein-containing electrolyte with either P/S or sodium azide may be viewed in Appendix D.

EIS measurements reveal that $PP_{17.5}$ electrodes maintain their electrochemical advantage over TiN_{IV} even in protein-containing solutions. A very minute increase in impedance was recorded (Figure 4.29), revealed through circuit modelling to stem from a 25% drop in Y_{dl}. Cyclic voltammetry measurements, which were carried out only within the restricted WW (Figure 4.30), echo these results. Unlike the TiN_{IV} electrodes, no significant reductions emerge in either the pseudo- or double-layer capacitance over the course of the 24-hour experiments. Rather, a slight increase in the R_f component appears to be the only change observed (Figure 4.32). In their work related to PEDOT:PSS electrodes, Marzocchi *et al.* [300] report similar findings, wherein the effect is attributed to spontaneous reorganization of the polymer chains, and is triggered by contact with the electrolyte (DMEM). This lowers carrier mobility, thus leading to a gradual increase in resistance in the early stages of the experiment. The value of R_f in fact does not continue to rise after 12 hours of immersion. At the end of the experiment, both the electrodes appear similarly impacted by the solution's protein content, with $PP_{17.5}$ maintaining its advantage due to having superior initial properties.

Although systemic electrochemical studies comparing the performance of PEDOT:PSS with and without protein in the electrolyte are lacking in the current literature, there is an abundance of work dealing with the material's propensity for protein adsorption

[306], [457]–[459]. Interestingly, PEDOT:PSS often displays electrostatic repulsion towards negatively charged species in solution, amongst them the protein albumin. This is due to the oft-adopted molar ratios of the precursor solution constituents (i.e., EDOT and PSS), resulting in a polymer with a theoretical excess of negative charge in its unpolarised state [306], [457], [458]. Substantial charge transfer suppression is thus avoided, a possible reason as to why adverse electrochemical effects are relatively low in PEDOT:PSS when compared to other materials like Pt [460], [461], Au [430], [461], or anodized Ti [462]. Unlike these materials, the $PP_{17.5}$ electrodes did not display significant depressions in the cyclic voltammogram when albumin was added to the electrolyte.

Static repulsion notwithstanding, the $PP_{17.5}$ electrodes are evidently still capable of adsorbing some amount of protein, as reflected by the drop in Y_{dl}. Moreover, a variety of studies have shown PEDOT:PSS to be highly adept at supporting cellular growth [41], [329], [463], [464], for which the adsorption of protein is a necessary pre-requisite [434], [435]. In this regard, the $PP_{17.5}$ electrodes were shown to be at a disadvantage in terms of fibroblast fouling. Cell culture experiments using NHDF on TiNIV and $PP_{17.5}$ electrodes were carried out using the same protocol previously adopted for the modified TiN surfaces. For this experimental set, the resazurin indicator was added to the media in bulk before pipetting into the wells, therefore eliminating the pipetting error associated with the previous experimental set (section 4.2.4). It is possible that the adoption of this methodology resulted in the smaller error bars seen in Figure 4.39 as compared to Figure 4.19. Nevertheless, inter-experimental results demonstrate good consistency for TiN_{IV}, wherein a number of fibroblasts are recorded to have attached within the first 24 hours and express only small rates of proliferation over three days. When viewed under SEM, the fibroblasts had once again failed to form a confluent layer (Figure 4.40 a and c), and the majority of cells were isolated, small, and elongated in shape (Figure 4.41 a-c).

In contrast, a higher number of fibroblasts had adhered to $PP_{17.5}$ electrodes after 24 hours, reaching confluency by the end of the experiment. Large sections of the $PP_{17.5}$ surface were in fact obscured by the growth, and the polymer topography could not be identified (Figure 4.40 b and d). Fibroblast morphology had to be assessed from the periphery of the electrode surface where cell coverage was lowest. Figure 4.41 d-f shows

the fibroblasts as they contrast with those observed on the TiN_{IV} (Figure 4.41 a-c). The cells are larger, have good spread, and appear flattened, in line with the descriptions provided in literature of healthy, well-adherent cells [299], [432], [433]. Correspondingly, the PEDOT:PSS layer increased the number of adherent fibroblasts by a factor of 1.67 in comparison to the TiN_{IV} electrodes.

One of the possible contributors towards this outcome is the smoothening effect brought about by the electrodeposited polymer. Comparing the optical profilometry measurements of $PP_{17.5}$ and TiN_{IV} electrodes reveals a significant drop in the average profile height with the addition of a PEDOT:PSS layer (Table 4.12). As already established via the fibroblast studies on the modified TiN electrodes (section 5.3.4), as well as through the findings of other research groups [296], [441], [465], micro-surface topography can have a large influence on cell proliferation. The polymer effectively levelled the physical features that originally acted as deterrents to fibroblast growth, creating a comparatively smooth surface on which the cells could spread. The phenomenon of stretched and bridging cells, in which a large portion of the fibroblast makes no physical contact with the electrode surface [296] (see Figure 4.21 g and h as example), was in fact notably absent on $PP_{17.5}$ electrodes. Comparisons may be drawn with the works of Marzocchi *et al.* [300], Rauer *et al.* [457], and Amorini *et al.* [41], in which fibroblasts are similarly shown to adhere and proliferate on PEDOT:PSS surfaces.

Deposition of a PEDOT:PSS layer is thus double-edged, providing superior electrochemical properties in the way of lower impedance, higher charge storage capacity, and a wider water window, but leaves the electrode more susceptible to fibrous encapsulation in comparison to TiN_{IV}.

5.5 Calcium Alginate Hydrogels for Selective Cell Growth

5.5.1 Development and Characterisation

The $PP_{17.5}$ electrodes were found to be at a disadvantage for chronic applications in relation to the original TiN_{IV} surfaces due to higher rates of fouling. It was thus determined that the electrochemical benefits gained through the PEDOT:PSS layer were at risk of negation by a high rise in tissue impedance once implanted. For this reason, an

antifouling coating was developed in the form of a reversible hydrogel. The methodology for the anodic electrodeposition of calcium alginate [31] was adopted.

The parameters for the procedure were optimized in such a way as to induce a controlled amount of water splitting, thereby generating the necessary H^+ protons for gelling without excessive bubble formation or damage to the electrode (refer to Figure 2.51). It was found through sequential experimentation that 0.85 $mAcm^{-2}$ could be applied for a maximum of 120s and a minimum of 60s to achieve gels that met the required criteria; well-adhered gels with good structural integrity and a perimeter defined by that of the underlying PEDOT:PSS electrode. Higher current densities were observed to cause physical damage to the $PP_{17.5}$ electrodes in the form of crack formation and polymer delamination (Figure 4.42 b and c). Although not in the context of calcium alginate deposition, the breakdown of CPs and electrode materials in general is expected when they are subjected to large current densities, causing irreversible damage that degrades their physical integrity and charge transfer capacity [101], [151].

With regards to gelling duration, alginates prepared with a 30s gelation time lacked the structural integrity necessary to withstand rinsing (indirect spraying with DI water from a wash bottle) and were too thin for accurate characterisation. Conversely, when gelling time exceeded 120s the alginate layer would occasionally detach from the underlying PEDOT:PSS. One of the possible contributors towards detachment is thought to be excessive gaseous bubble formation (Figure 4.44 d) [343], [466]. With reference to Figure 2.51, it may be seen that gas generation is a necessary corollary of the gelling process. It is possible that over extended periods of time (i.e., > 120 s), a significant number of gas bubbles (O_2 and/or CO_2) form at the electrode/gel interface, creating areas of separation between the two materials. In large enough quantities this phenomenon could lead to hydrogel detachment. This process is in fact a recorded method through which hydrogels may be removed from an electrode surfaces [343]. Another possible contributor is spill-over growth, in which excessive gelling time grows the alginate beyond the electrode's defined edge. In doing so the extremities of the gel form over the PTFE mask, establish no physical anchorage, and thus leave the gel more susceptible to detachment. Both these phenomena were observed in gels that had resisted complete delamination (Figure 4.44 d). The hypotheses are illustrated in Figure 5.7. It was thus

decided that further analysis be restricted to gels of 60, 90, and 120s electrodeposition time (CA_{60s}, CA_{90s}, and CA_{120s}, respectively).

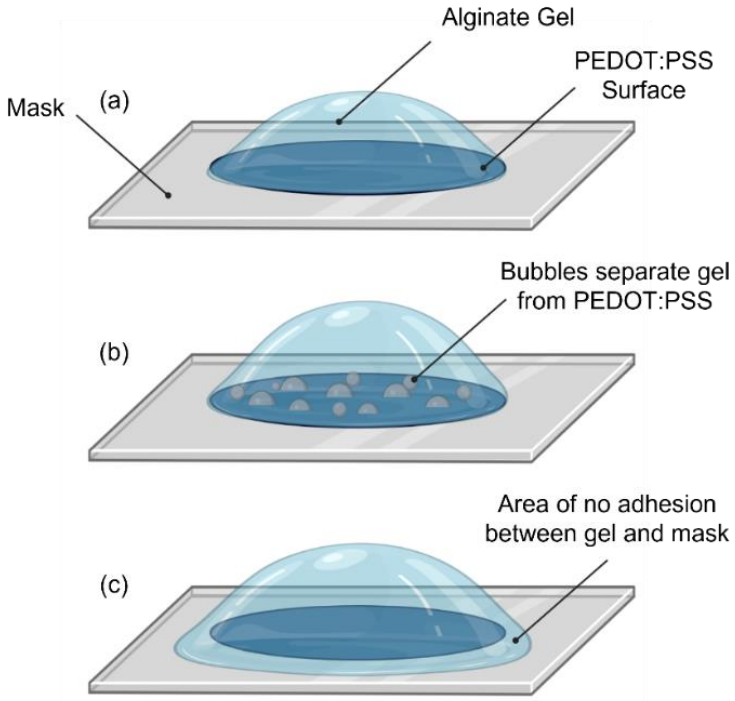

Figure 5.7: Illustration of calcium alginate developed using electrodeposition (0.85 $mAcm^{-2}$) showing (a) a well-adhered gel with maximum deposition time of 120s; (b) a gel with long deposition time (>120s), with bubble formation separating gel from PEDOT:PSS, and; (c) a gel with long deposition time (>120s), growing over the perimeter of the electrode and onto the PTFE mask. Diagram created with BioRender.com

In the work of Cheng *et al.* [31] it was observed that calcium alginate gels produced via anodic electrodeposition possess a cross-linking density gradient. This is correlated with calcium ion distribution, where the number of Ca^{2+} ions available for gelling drops with distance from the electrode surface. As a consequence, the outer limits of the gel should theoretically contain a lower density of cross-linked material. To obtain more homogenous gels, Ferlauto *et al.* [269] allowed the alginates to soak in a $CaCl_2$ hardening solution following polymerisation. This methodology was adopted, and the electrodes were immersed in a 1 mM $CaCl_2$ solution and left to soak for 30 minutes after polymerisation. The timing was strictly controlled, as longer periods of immersion lead to excessive cross-linking, polymer shrinkage, and layer detachment.

The observed morphology of the calcium alginate layers (Figure 4.44 b) is well in accordance with those documented in literature [362], [467], [468], possessing a mesh-like structure with a high incidence of porosity when swollen. Attempts to take high-

magnification SEM images of the gel were only partially successful due to the brittle nature of dehydrated calcium alginate. Small cracks can in fact be seen over the surface of the material in Figure 4.44 c, a well-documented occurrence in the works of other research groups regardless of the sample preparation method [467], [469], [470]. The specimen in this work were prepared in line with the procedure as outlined by Santana *et al.* [362], whereby the gels were fixed in glutaraldehyde, dehydrated in ethanol, and finally desiccated before sputtering with gold. The authors report some loss in alginate morphology and inability to distinguish individual pores. Although this was true to some extent in the present work, enough of the gel's structure was left intact to observe a 3-D network of porous material.

In assessing the relationship between deposition time and thickness of gel, the rate of layer thickening was observed to be non-linear (Figure 4.45). In response to similar findings, Cheng *et al.* [31] posit a saturation effect that slows down growth rate at prolonged deposition times. Newly generated H^+ ions at the electrode surface are subject to diffusion limitations, having to travel longer distances to reach the dissolution front at the edge of the gel. Moreover, H^+ ions could preferentially liberate new Ca^{2+} ions from partially dissolved $CaCO_3$ particles within the existing gel. This creates a steeper crosslinking gradient along the thickness of the gel, as less ions are available at the dissolution front to initiate new gel formation. From this it may be inferred that gels produced with longer deposition times are denser (i.e., less porous) at the electrode/gel interface than those with shorter deposition times (illustrated in Figure 5.8).

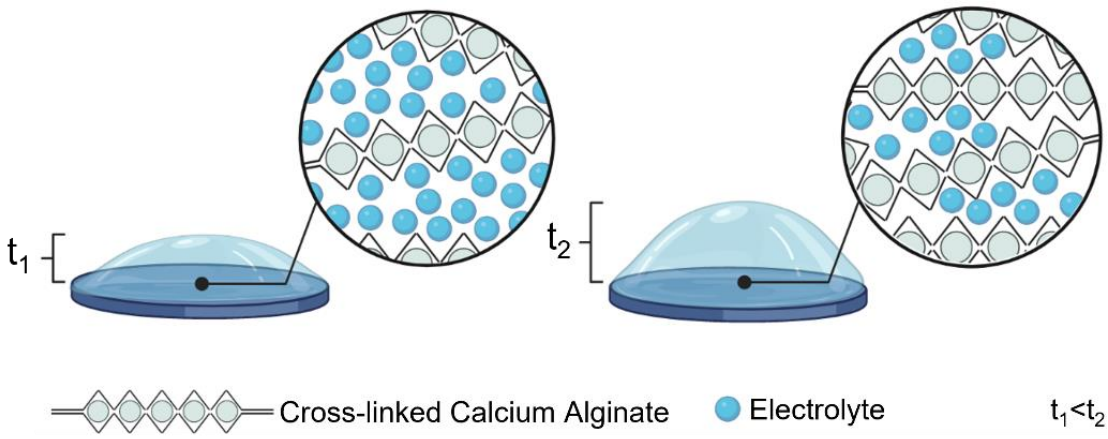

Figure 5.8: Illustration showing the theoretical difference in cross-linking density for alginates produced under different gelling times, where $t_1<t_2$. Diagram created with BioRender.com.

It was further noted that CA_{120s} gels had significant variations in layer thickness, resulting in a comparatively large standard deviation value of 101 µm. Studies dealing with electrodeposited calcium alginates are very few, with the work of Cheng *et al.* [31] being the foremost source on the subject. As such, it is difficult to correlate this finding with some known phenomenon. However, a tentative hypothesis was developed. It is possible that in some gels, more of the newly liberated H^+ protons manage to diffuse out towards the dissolution front before liberating new Ca^{2+} ions closer to the electrode. This could be due to subtle differences in the homogeneity of precursor solution, and they may not produce notable variations in the gels until some threshold gelling time is reached. This would effectively cause variation in the resulting thicknesses as some gels grow thicker while other increase the crosslinking density at the gel/electrode interface.

Imaging was also employed to assess whether remnants of undissolved $CaCO_3$ were present in the gelled material. The majority of the CA layers were clear, with only small and infrequent instances of undissolved powder being visible (Figure 4.44). This was further confirmed via micro-Raman spectroscopy. Gels dried in air were analysed whilst still attached to the underlying $PP_{17.5}$ electrodes, while samples of $CaCO_3$ powder were placed on opaque slides. The resulting spectra for both materials (Figure 4.46) were corroborated with other work [31], [341], [345], [471], [472], confirming the emergence of all the major peaks necessary for accurate characterisation. Table 5.1 details possible assignments of the emergent Raman bands with reference to these studies [31], [341], [345], [471], [472]. Notably, only 3 peaks associated with $CaCO_3$ were detected in the gels (numbered 6, 7, and 9 in Table 5). When comparing these results to the work of Cheng et al. [31], closer association may be made with gels of low residual $CaCO_3$ content rather than high (Figure 2.52). Carbonate-associated peaks are of low-intensity in the CA_{60} spectra, and the 3 major bands (shifts of 155, 281, and 1087 cm^{-1}) that emerge in the $CaCO_3$ spectra are completely absent. The micro-Raman results thus suggest no incidence of residual $CaCO_3$ powder in the gels' interrogated areas. Moreover, none of the peaks associated with PEDOT:PSS emerged in any of the CA spectra, suggesting that polymer dissolution as a result electrogelling did not occur in significant enough quantities (if at all) to be detected in the alginate.

Table 5.1: Emergent peaks from the micro-Raman spectra of CA electrodes shown in Figure 4.46. Possible assignments are listed with reference to relevant literature.

Peak No.	Raman Shift (cm^{-1})	Associated Material	Possible Assignments	References
1	751	CA_{60s}	C-C Stretching C-O Stretching C-C-H Bending C-C-O Bending	[31], [341], [345]
2	955	CA_{60s}		
3	1004	CA_{60s}		
4	1157	CA_{60s}	Glycosidic Ring Breathing	
5	1188	CA_{60s}	Carboxylate Stretching Vibration (symmetric or C-O bond stretching)	
6	1345	$CaCO_3$	Asymmetric Stretching of CO_3^{2-} ions	[471], [472]
7	1441	$CaCO_3$		
8	1520	CA_{60s}	Symmetric or Asymmetric Carboxylate Stretching Vibration	[31], [341], [345]
9	1585	$CaCO_3$	Asymmetric Stretching of CO_3^{2-} ions	[471], [472]

5.5.2 Effect of CA on the Electrochemical Properties of PEDOT:PSS

The introduction of a non-conductive hydrogel layer onto the $PP_{17.5}$ electrodes was expected to cause some form of negative impact on the electrochemical properties. Literature suggests these effects are to be partially mitigated by the alginate's porous structure, wherein the electrolyte can permeate through the gel and interact with the underlying electrode [252], [269], [332]. The CA electrodes were thus subjected to EIS and CV measurements to assess this impact. Unlike previous tests, the CA electrodes were not impregnated with the PBS under vacuum to prevent damaging the material. The samples were instead immersed in the electrolyte for 1 hour prior to testing.

The shapes of the EIS Bode and Nyquist plots (Figure 4.47) remain largely unchanged by the CA layer, and do not suggest any fundamental alteration to the electrode's charge transfer methods. The most significant effects are apparent at frequencies larger than the $f_{cut\text{-}off}$. Fitting the equivalent circuit model (Figure 4.4 a) to the data confirms a significant jump in the value of R_s for all three electrodes ($p < 0.05$), with C_{60} returning the smallest increase (Table 4.19). All the other circuit elements are similarly impacted with respect to the $PP_{17.5}$ electrode. Y_{dl} and Y_{pseu} respectively drop by an average of 32 and 15% when considering the CA_{60s} electrodes. Their associated empirical values of α (α_{dl} and α_{pseu}) also decrease ($p < 0.05$), signifying a drop in the mechanisms' efficiency.

This may be tied to a reduction of PEDOT:PSS ESA following hydrogel formation (Figure 5.9), wherein a percentage of the CP surface is covered by non-conductive hydrogel. These areas cannot interact with the electrolyte, and so the capacitance values decrease [28], [473].

It is interesting to note that no clear trend in any of the model variables emerges with increasing gel thickness. The issue in this regard appears to be the CA_{120s} electrodes, wherein excessive variability in gel thickness (Figure 4.45 b) produces large error bars. This is evident for Y_{pseu}, as well as for the CSC_C measurements (Table 4.20) and brings the repeatability of such electrodes into question. Although sustaining the electrogelling process up to 120s was not observed to impart any physical damage to the PEDOT:PSS, the unpredictability of both the physical dimensions and the electrochemical properties of the resulting gel are highly undesirable. Wide margins of error can lead to over- or under-estimations of charge injection and impedance, affecting such parameters as the stimulation pulse magnitude or device placement from target neurons [39], [130]. On these bases, the CA_{120s} electrodes were deemed to be unfit for the intended application.

When comparing the CA_{60s} and CA_{90s} electrodes, the values of R_f and R_s differ significantly ($p < 0.05$) (Table 4.19). The thicker layer of hydrogel in the case of the CA_{90s} electrodes is a logical origin for this increase, as it provides more dielectric material between the working and counter electrodes. There is also the possibility that CA_{90s} electrodes have a higher cross-linking density at the electrode/gel interface in addition to having a larger volume of material (Figure 5.8). This would stem from proton mobility issues and preferential dissolution adjacent to the anode, as previously discussed [31]. However, if present, the extent to which this phenomenon has influence on the electrolyte resistance is uncertain. A higher cross-linking density at the electrode/gel interface would imply a higher surface fraction of conductive polymer that is covered by non-conductive hydrogel (Figure 5.9). It follows that capacitive mechanisms along the ESA would be disrupted, producing lower measurements of capacitance (CPE_{dl} and CPE_{pseu}) in addition to a higher resistance to charge transfer (R_f) [473], [474]. Since no statistically significant difference ($p > 0.05$) was observed in any of the capacitance values for the CA_{60s} and CA_{90s} electrodes, the influence of cross-linking density could not be definitively determined.

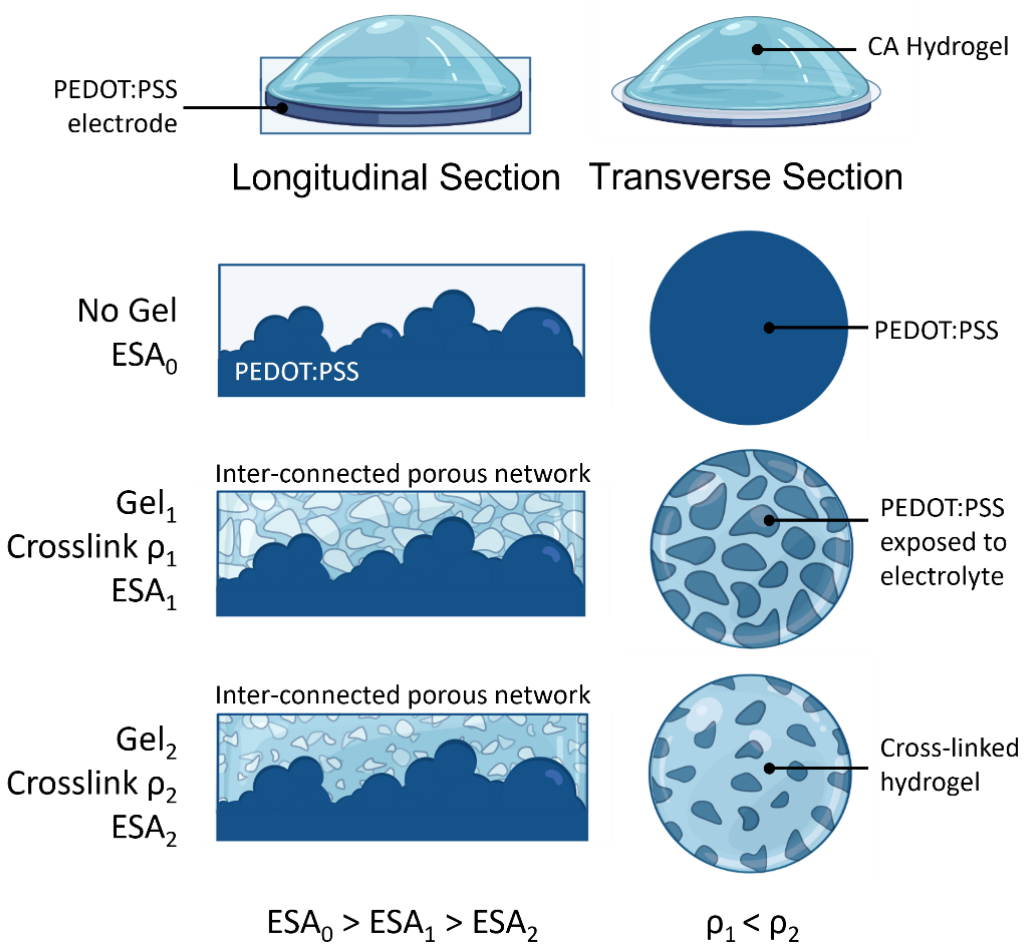

Figure 5.9: Illustration showing theoretical longitudinal (left) and transverse (right) cross-sections of a $PP_{17.5}$ electrode (ESA_0) and two CA electrodes. Gel_1 and Gel_2 have crosslink densities of ρ_1 and ρ_2 respectively, where $\rho_1 < \rho_2$. The transverse sections are shown close to the electrode/gel interface. More of the PEDOT:PSS surface is in direct contact with the electrolyte for Gel_1 than Gel_2, and thus $ESA_0 > ESA_1 > ESA_2$. Diagram created with BioRender.com.

The differences between CA_{60s} and CA_{90s} electrodes were rendered inconsequential from the aspect of charge injection, as both return identical values of CSC_C (10 $mCcm^{-2}$) at high charge/discharge rates ($\upsilon = 1\ V^{-1}$) (Table 4.20). The delay-line effect (refer to Figure 2.12), already in action due to electrode porosity [101], is aggravated by the large interfacial resistance caused by the hydrogel. It is possible that a saturation effect occurs at such high scan rates, wherein the thickness of the hydrogel has little impact on the overall charge transfer capacity. Owing to the time restriction, only ions within a certain distance of the PEDOT:PSS electrode participate in pseudo- and double-layer capacitance. Ions outside of this range do not have time to diffuse through the gel, and so the impact of a thicker layer is minimized. The opposite is true at slower sweep rates ($\upsilon \leq 0.5\ Vs^{-1}$) where ions have more time to migrate towards the CP [175], [473]. Under

these conditions the gel thickness has a greater impact on the CSC_C, with the effect being most pronounced at $\upsilon = 0.05\ V^{-1}$.

5.5.3 CA Reversibility Restores Electrochemical Properties of PEDOT:PSS

To determine whether the original electrochemical properties of PEDOT:PSS could be recovered following alginate dissolution, the CA_{60} electrodes were chosen for a degradation assessment. The degradation profile was mapped using a Ca^{2+} ion detector solution containing Arsenazo III and Imidazole buffer. The moles of calcium released into PBS solution were measured periodically over a span of 35 days using spectrophotometry. The resulting plot, given in Figure 4.49 a, matches the degradation profiles of typical alginate gels in literature [475]–[478]. When immersed PBS, Ca^{2+} ions are expelled from the hydrogel due to preferential bonding with monovalent ions such as Na^+ and K^+. This exchange breaks down the egg-box structure of the gel, and the polymer gradually disintegrates [132], [332]. The burst release of calcium over the first 24 hours is a distinct feature in these studies [475]–[478], where the sudden influx of electrolyte through the gel initiates the calcium release process. This brings up the Ca^{2+} ion count from 0 (refer to Appendix C for contents of PBS) to the initial measured value. The degradation then progressed gradually over the 35-day period, remaining incomplete by the end of the experiment. No plateau in calcium molarity was reached, and visual observations revealed sparse, thin segments of hydrogel still attached to the electrodes (Figure 4.49 b).

These results suggest that hydrogel degradation rate is not uniform across the entire structure. Had this been the case, layer detachment from the electrode surface would have been observed. Gel present in the porous structure of the PEDOT:PSS would have dissolved, compromising the layer's anchorage points and separating the two materials [479]. One of the possible contributing factors is differing ion accessibility throughout the hydrogel [473]. Crosslinked material that is closer to the gel/electrolyte interface has higher accessibility to unbound monovalent ions than material found at the bottom of the gel [360], [480]. Disassociated alginate chains may also become trapped within the crosslinked gel due to their structural rigidity [481], further hindering the inward diffusion of PBS ions. Calcium alginate formed within the pores of PEDOT:PSS is

additionally subject to the limitations of geometrically confined diffusion [361], thus increasing its resistivity to dissolution. It is also possible that the theorised cross-linking density gradient that exists along the thickness of the gel as described by Cheng *et al.* [31] contributed towards this effect. Ionic movement is made more difficult approaching the electrode/gel interface if a higher cross-linking density exists [360]. Moreover, a higher cross-linking density implies a larger number of Ca^{2+} ions to be liberated, leading to a slower rate of degradation as compared to the outer regions of the gel [473], [478].

At termination of experiment, remnants of the gel were removed by 1 minute of ultrasonication in a 1M solution of NaCl and cleaned by another minute of ultrasonication in DI water. The electrodes were then dried in air and re-impregnated with PBS in vacuum (0.5 bar) for electrochemical measurements. EIS results (Figure 4.50) demonstrate a quasi-complete restoration of the electrode's modelled variables, with a prominent large drop in the R_s. Faradaic resistance R_f was completely down to pre-alginate levels, whereas the pseudo- and double-layer capacitances (Y_{pseu} and Y_{dl}) regained 90 and 85% of their initial values on average, respectively (Table 4.21). Owing to the value of R_s (12.9 Ωcm^2), it is possible to attribute the incomplete reversal to some remnant of calcium alginate in the pores of PEDOT:PSS. This would effectively prevent full reclamation of the original ESA, leading to the supressed values of Y_{pseu} and Y_{dl} [473], [474]. It is also possible that some small amount of damage was delivered to the CP layer during the electrogelling process, though there were no physical indications to suggest this occurred. In spite of this, the resorbed CA_{60s} electrodes delivered excellent electrochemical properties comparable to $PP_{17.5}$ and maintaining the advantage over TiN_{IV} electrodes.

5.5.4 CA Reduces Fibroblast Attachment and Benefits Neural Integration

The primary objective of the calcium alginate layer was to provide anti-fouling properties to the $PP_{17.5}$ electrodes. The efficacy of this strategy was demonstrably proven via NHDF cell culture experiments. CA_{60s} electrodes were chosen for analysis since they affected the electrochemical properties of PEDOT:PSS the least and so provided the best opportunity for a combined low-impedance and low-fouling electrode. The pattern of fibroblast adhesion and growth for $PP_{17.5}$ electrodes was found to be consistent with earlier tests (section 5.4.5), resulting in a confluent layer of cells by the end of the 72-

hour period (Figure 4.52 a and c). The fibroblasts were again observed to cover the polymer surface, attaining a flat and well-spread morphology that obscured the topography of PEDOT:PSS.

Contrastingly, cell growth appeared to be completely absent on the surfaces of CA_{60s} electrodes (Figure 4.52 b and d). Instances of small, spherical matter were identified in place of fibroblasts having typical viable morphologies [299], [432], [433]. Concurrently, resazurin reduction measurements made over the testing period revealed some amount of cell viability after 24 hours, but no significant proliferation was recorded during 72 hours of culture (Figure 4.51). Machida *et al.* [346] and Singh *et al.* [347] report similar findings when assessing the adhesion of fibroblasts to calcium alginate gels (refer to Table 2.10 for gelation methodology). The results are even consistent with works on other antifouling surfaces such as nano-cellulose films [482] and carboxyl-functionalised polystyrene colloids [483]. In all cases, samples with the lowest measured cell viability had no discernible fibroblast growth, instead featuring some small, rounded specimens similar to those found on the CA_{60} surfaces. The authors speculate these to be fibroblasts arrested in the sedimentation stage, where weak (if any) adhesion to the test surface preserves their spherical shape. Despite contributing to viability measurements, such cells fail to flatten, stretch, and form focal adhesion sites, and thus cannot grow and proliferate [484]. The calcium alginate layer thus rendered exceptional resistance to fibrous fouling, simultaneously allowing $PP_{17.5}$ electrodes to retain most of their electrochemical properties.

As the hydrogel layer on the CA_{60s} electrode was shown to be reversible (section 5.5.3), the calcium alginate is expected to degrade over its time *in vivo* and bring the PEDOT:PSS in direct contact with the biological environment [338]. It was theorised that this feature could be put to advantage by way of promoting direct integration of device and neural tissue. Calcium alginate hydrogels and PEDOT:PSS have both shown potential as scaffolds for neural growth [328]–[330], [353], [354], [356], [357]. The hypothesis proposed is thus, that the calcium alginate layer may simultaneously prevent fibrous encapsulation whilst providing a platform for neural development *in vivo*. The hydrogel degrades as neural growth progresses towards the PEDOT:PSS, evading fibrous attachment and finally establishing direct physical contact with the target tissue. Such developments are in their infancy within the field of neural integration, although a

number of studies [357], [485]–[487] have already demonstrated the capacity to regenerate and/or repopulate the nervous system with neural tissue using calcium alginate scaffolds.

Preliminary cell culture experiments were thus carried out to assess whether the $PP_{17.5}$ and CA_{60s} surfaces as developed had the potential to support neural growth. The SH-SY5Y neuroblastoma line, in widespread use as a neuronal cell model [488], was chosen for this application. Trials were carried out in well-plates prior to the electrodes. The cells were cultured for 72 hours, during which an approximate 70% confluency would be reached. At this point, the neuroblastomas have a flattened phenotype and lack any substantial neurite extensions (processes) (Figure 4.53 a), matching descriptions given elsewhere in literature [366], [489]. To initiate differentiation into neuron-type cells, fresh culture medium was prepared to include retinoic acid (ATRA) while excluding any protein content. After 72 hours the cells had come to resembles neurons, attaining a new fusiform morphology (Figure 4.53 b) and extending long, branching processes [366], [489], [490]. This process was repeated on CA_{60s}, $PP_{17.5}$, and TiN_{IV} electrode surfaces, with TMO (Thermanox) slides acting as a positive growth control. Resazurin reduction measurements were taken after 72 hours of treatment with ATRA, and the cells were fixed using glutaraldehyde for SEM imaging. It is worth noting that the intensity measurements (Figure 4.54) cannot distinguish between neuroblastoma and neuroblast-like cells, and so only provide an indication of the total number of viable cells [364].

Results from the viability assessments indicate that cell growth was successful on all surfaces with respect to TMO (Figure 4.54). The highest numbers were detected on the $PP_{17.5}$ surfaces, with a statistically significant difference ($p < 0.05$) existing with respect to all other sample type. The average measurement for $PP_{17.5}$ was found to be approximately 2.1 times larger when compared to TMO slides. For both $PP_{17.5}$ and TMO, the imaged cells show indications of having responded to the retinoic acid treatment, differentiating from neuroblastomas to neuron-like cells. Cells with the typical flattened morphology of the SH-SY5Y cell line [366], [489], [490] are mostly absent on TMO slides, although some instances could still be identified (Figure 4.55 b). The majority of observed cells adopted a fusiform morphology and extended long processes, although a relatively small percentage of the sample surface is covered when compared to the $PP_{17.5}$ electrodes (Figure 4.58). It is possible that some damage was

caused to the cells on TMO slides whilst they were mounted onto the SEM stubs. Subjecting the slides to some bending stress was unavoidable during this process, as the thin samples had to be firmly affixed to the stubs via conductive tape. This necessitated some pressure be applied, although efforts were made to confine this to the edges of the sample where cell growth is typically most sparse.

The high viability measurements made on the $PP_{17.5}$ electrodes match the visual observations made using SEM (Figure 4.58). A larger percentage of the surface is covered by neuron-like cells, where several long neural processes are extended over the polymer. Some remnant neuroblastoma-like cells were also identified. The abundant growth of neural-crest derived cells onto PEDOT:PSS surfaces is a common trend in literature [317], [328], [329]. As discussed in section 2.5.2, cells within this category have a reportedly high affinity for textured surfaces, and multiple studies have demonstrated higher growth and proliferation rates on rough materials as compared to smoother ones [202], [312]–[314]. This might contribute towards the obtained results, in which more viable cells were found on the $PP_{17.5}$ than the TMO slides. Pisciotta *et al.* [328] made similar observations in comparing the growth of neural crest-derived stem cells on plastic culture plates, electrodeposited PEDOT:PSS (RMS ~25 nm) and spin-coated PEDOT:PSS (RMS ~2 nm) films. The electrodeposited polymer registered the highest number of viable cells after 7 days of culture by a large, significant margin, while also having the highest measured amount of neuronal markers. The differing RMS values were attributed by the authors as the main driving force between these differences.

Surface roughness is however not the sole influential factor determining growth. Neuron and neuron-like cells are highly sensitive to mechanical cues from the substrate, and preferentially adhere and growth on low-stiffness materials [1], [44], [139], [316], [491]. This might have contributed to the larger number ($p < 0.05$) of viable cells detected on $PP_{17.5}$ surfaces as compared to TiN_{IV} (Figure 4.54), despite the latter being significantly rougher (refer to Table 4.12). Unlike the NHDFs (refer to section 5.3.4), the SH-SY5Y cells successfully adhered to the TiN_{IV} surface and have the typical flattened morphology (Figure 4.57). This may be attributed to the differing stiffnesses of the two cell lines. The average Young's Modulus for SH-SY5Y cells lies within the range of 1-10 kPa [492], whereas NHDF's can have values up to 24 kPa [493]. As demonstrated

by Bourkoula *et al.* [296], stiff cells are more sensitive to surface features, as they cannot stretch over obstacles with the same ease as cells of higher elasticity. It may be for this reason that neuroblastoma cells spread so readily over the TiN_{IV} surfaces. In spite of this, very limited markers of ATRA-induced differentiation were observed in these cells. The morphologies are evidently flat and lack any substantial neurite process extensions. Ozgun *et al.* [491] demonstrated that SH-SY5Y cells more readily undergo ATRA-induced differentiation into neuron-like cells when cultured on softer polyacrylamide gels (0.1 kPa) rather than stiffer ones (50 kPa). Considering the Young's Modulus of TiN can be up to 3 orders of magnitude higher than PEDOT:PSS (refer to Table 2.9), the higher observed number of neural-type cells on $PP_{17.5}$ as compared to TiNIV may be explained on this basis.

Interestingly, no statistically significant difference was observed in cell viability when comparing CA_{60s} surfaces with the control TMO (Figure 4.54). A number of neuron-like cells with long, branching processes were observed on the electrodes (Figure 4.56), although the cell morphology is difficult to describe accurately due to hydrogel warping. Santana *et al.* [362] report similar issues when conducting SEM imaging of cells fixed on calcium alginate gels with glutaraldehyde. Nevertheless, the neurites are clearly visible in the micrographs, and in some instances even cell bodies that are suspected as collapsed may be evidenced (Figure 4.56). Although neural cell growth on alginate gels is greatly enhanced through methods like functionalization, pre-conditioning, or drug-loading [252], [356], [357], there are numerous studies in which pure gels are shown to support neural growth [353], [354], [494]. Despite lacking cell adhesion ligands [487], calcium alginate gels provide favourable conditions for neural growth through their tissue-comparable stiffnesses [334], [354], [468], [491]. Moreover, the gel formulation for CA_{60s} was simultaneously capable of supporting the growth of neural-like cells whilst resisting hydrolytic degradation throughout the experiment's duration. This was one of the challenges faced by Ayar *et al.* [356] when searching for a crosslinking density that produced alginate gels with sufficient structural integrity that could also support neural growth. As shown in section 5.5.3, the hydrogel degrades gradually over 35 days. Moreover, the gel was evidently still present on the electrodes after the 6-day cell culture period (Figure 4.56). In combination with its demonstrated resistance to fibrous growth, and the possibility of increasing neural adhesion via one of the

aforementioned methods, the CA_{60s} electrode has great potential as a chronic, bio-integrative device.

A graphical summary of the cellular interactions explored in this work on TiN_I, TiN_{IV}, $PP_{17.5}$, and CA_{60s} electrodes is given in Figure 5.10. The hypothesised bio-integrative function of CA_{60s} is also illustrated in Figure 5.11.

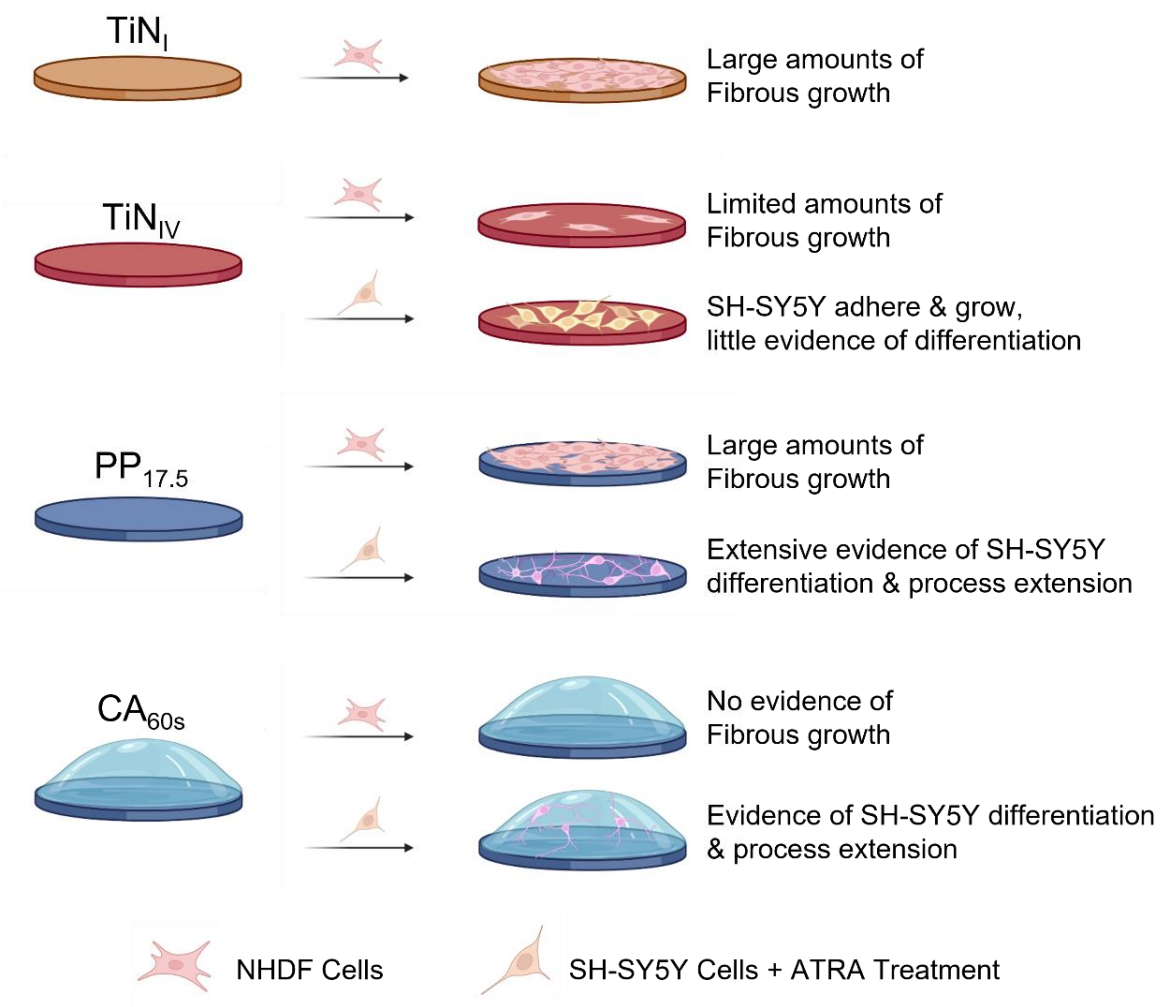

Figure 5.10: Graphical summary of the obtained results from cell culture work conducted on TiN_I, TiN_{IV}, $PP_{17.5}$, and CA_{60s} electrodes. Diagram created with BioRender.com.

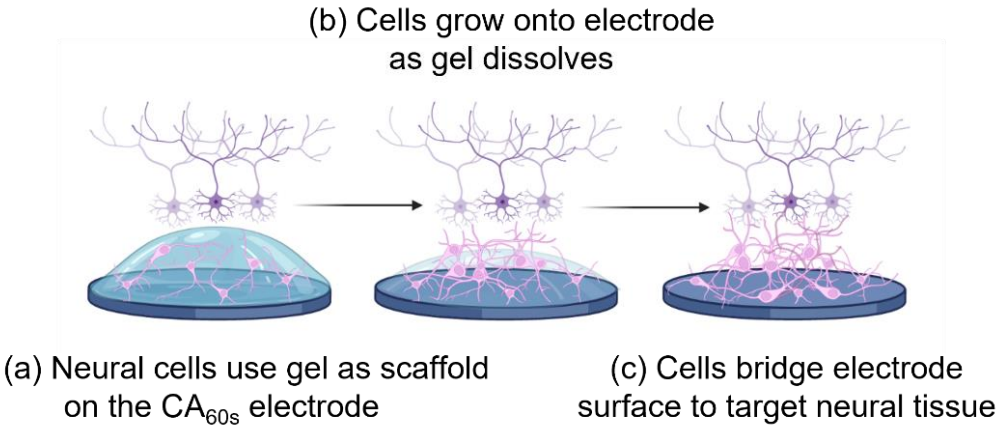

Figure 5.11: An illustration of the hypothesised bio-integrative potential of CA_{60s} electrodes, where (a) neural cells use the gel as a scaffold. Fibrous growth is simultaneously mitigated; (b) the gel dissolves as the cells grow, until; (c) the cells establish a bridge between the PEDOT:PSS surface and the target neural tissue. Diagram created with BioRender.com.

5.6 Electrochemical Comparisons

The TiN_{IV}, $PP_{17.5}$, and CA_{60s} electrodes developed in this work were compared on the basis of their electrochemical performance with other prominent electrodes in literature (see Table 2.8 for references). When available, the measurements for CA_{60s} electrodes after alginate degradation were also provided. Results for TiN_I were omitted due to similarities with TiN_{IV}. Comparisons were made on the value of $|Z|_{1Hz}$ (Figure 5.12 a) and the CSC_C at sweep rates of $v = 0.05$ (Figure 5.12 b) and 0.1 Vs^{-1} (Figure 5.12 c). Comparisons could not be made at higher scan rates as the data is not available in literature.

It is evident from the plots that the TiN_{IV}, $PP_{17.5}$ and CA_{60s} electrodes provide a large advantage over many industry-established smooth materials such as Pt [162], [184], [191] and its alloys with Ir [197]. Given its low incidence of fouling *in vitro*, the TiN_{IV} electrode has the potential to outperform these materials even within the biological environment, as all have an extensive history of fibrous encapsulation [197], [283], [299]. TiN_{IV} even surpasses some of the PEDOT:PSS multi-layered electrodes in terms of both impedance and CSC_C [198], [252], [259], [260], and has comparable CSC_C measurements to SIROF [200] and AIROF [205], two materials that are considered the gold standard in neural interfacing.

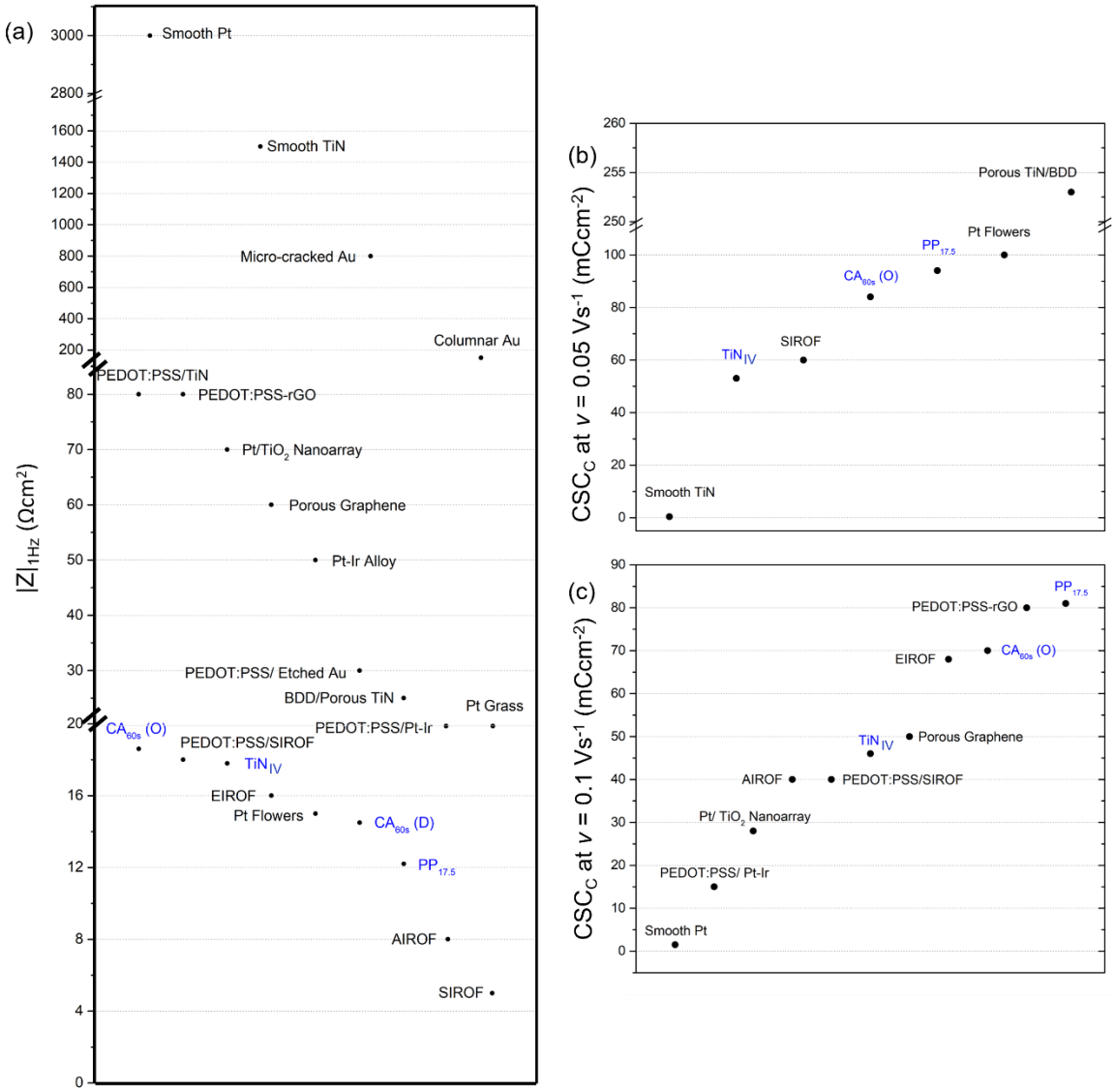

Figure 5.12: Comparing the electrochemical properties of TiN_{IV}, $PP_{17.5}$, and CA_{60s} (in blue) with prominent electrodes in literature (in black) on the basis of (a) the $|Z|_{1Hz}$; (b) the CSC_C at $v = 0.05$ Vs^{-1}, and; (c) the CSC_C at $v = 0.1$ Vs^{-1}. CA_{60s} (O) denotes the original values whereas CA_{60s} (D) denotes the values measured after removal of the alginate layer. Refer to Table 2.8 for citations on the data from literature.

$PP_{17.5}$ electrodes on the other hand are at the very top of the performance scale, being outdone only by AIROF [205] and SIROF [200] in terms of impedance, but regaining the advantage by a wide margin in terms of the CSC_C. The electrode is also on par with nanostructured platinum [295] and PEDOT:PSS-rGO composite [265] for the CSC_C and has a lower impedance than both. This latter point is true even for CA_{60s} electrodes following dissolution of the alginate. The only material that outdoes the $PP_{17.5}$ and CA_{60s} electrodes by a wide margin in terms of the CSC_C is the dual-layer BDD/ Porous TiN [176], measuring a large 253 $mCcm^{-2}$ at $v = 0.05$ Vs^{-1}. It is unclear whether this

advantage is sustained at higher scan rates as the authors do not perform such measurements, although it is worth noting that the WW of this material is exceedingly large (-1.3 to 1.2 V *vs* Ag/AgCl). With respect to impedance, the BDD/TiN material is at a disadvantage, having a $|Z|_{1Hz}$ value that is double that of $PP_{17.5}$.

The $PP_{17.5}$ thus offer a balanced repertoire, whereby the electrode is simultaneously able to deliver high charge transfer capacity at low impedance values, properties that are sustained with tens of thousands of charge/discharge cycles. The addition of a calcium alginate layer only partially affects these properties in comparison to other leading electrode materials, the majority of which are apparently regained once the hydrogel dissolves. The hydrogel additionally renders superior resistance to fibroblast attachment and, having shown its potential to support neural growth, opens the door towards a better bio-integrated device.

6 Conclusions

Three electrode variations based on TiN, PEDOT:PSS, and calcium alginate were developed in this work for their application in neural interfacing. Hereunder is a summary of the conclusions reached throughout the study:

1. An over-stoichiometric porous TiN layer having pyramidal grains, columnar microstructure, and a (111) texture was successfully developed on Ti6Al4V substrates using magnetron sputtering PVD.

2. Micro-Raman spectroscopy revealed N-vacancies in the material sub-surface. It was further deduced through semi-quantitative comparison of peak intensities that N-vacancies make up the majority of point defects and dominate over Ti-vacancies. Concomitant detection of peaks associated with N-doped TiO_2 prompted a hypothesis in which these two phenomena are linked. Oxide formation is thermodynamically facile in over-stoichiometric TiN and occurs upon the material's exposure to air. Meanwhile, excess N in the sub-surface diffuse out towards the oxide, leaving behind N-vacancies in the nitride. The N are then incorporated into the oxide as substitutional dopants, triggering the formation of O-vacancies through the act of charge compensation.

3. Pseudocapacitance in TiN films has been reported within the context of their application as supercapacitors and fuel cells. However, within the field of neural interfacing, TiN is generally regarded exclusively as an electrochemical double layer capacitor. Exclusionary electrochemical tests were devised in this work to study the capacitive mechanisms of the porous TiN. EIS and CV measurements in protonated and non-protonated electrolytes revealed a large, significant drop in the material's charge transfer abilities, resulting in higher impedances and lower CSC_C when faradaic reactions were suppressed. Equivalent circuit modelling established a higher percentage contribution to charge transfer from pseudocapacitance (~ 79%) than double-layer capacitance (~ 21%).

4. Unlike double-layer capacitance, pseudocapacitance is known to degrade with electrochemical cycling. This can pose a significant issue in chronic neural electrodes, rendering them potentially ineffective with time. Cyclic stability testing

at a clinically-relevant charge/discharge rate ($1 Vs^{-1}$) revealed only minimal drop (< 1.5%) in electrode capacity over 10,000 cycles. This may indicate some mechanism through which O-vacancies in the oxide are renewed, possibly by further outwards diffusion and substitutional doping of N. Micro-Raman measurements revealed no significant change in the relative frequency of N and Ti vacancies. The opposite was true at scan rates of higher faradaic demand ($0.1 Vs^{-1}$), resulting in a significant drop in the frequency of N vacancies along with degradation of electrochemical properties, specifically pseudocapacitance.

5. In terms of electrochemical properties, the TiN electrode well outperforms established materials such as Pt, Pt/Ir, and Au, and some forms of IrOx. It is even comparable to some frontier materials currently under consideration such as graphene. However, one of its drawbacks is reportedly fibrous encapsulation. To tackle this, the Ti6Al4V substrates were roughened via surface blasting prior to PVD coating. This resulted in electrodes with differing surfaces roughnesses but identical chemical makeup, crystal structure, and electrochemical properties. The similarities also extended when measurements were made in protein-containing electrolytes, although a slight drop (~ 13%) in Y_{pseu} was measured over 24 hours.

6. TiN_{IV} electrodes (where R_a, R_q and R_t for TiN_{IV} >> TiN_I) successfully reduced fibroblast growth by 62% as compared to TiN_I, indicating that surface roughness can be an effective tool for mitigating fibrous encapsulation. The results further suggest the existence of a roughness threshold, whereby fibroblast growth is only impeded by surface features in excess of a critical dimension. TiN_{II} and TiN_{III} surfaces in fact did not influence cell growth to significant degrees. TiN_{IV} electrodes thus have great potential as a replacement for TiN_I, delivering the same electrochemical properties with greater resistance to fouling.

7. In applications of spatial limitation such as intracranial, intraspinal, and intraneural electrodes, the requirement for high charge transfer density and low impedance is critical. Moreover, the growing trend of biofunctionalized devices favours electrodes with mechanical properties that more closely mimic the neural environment. As a hard, stiff ceramic engineered to resist cellular growth, TiN_{IV} cannot meet these criteria. As a potential solution to both issues, a layer of the conductive polymer PEDOT:PSS was grown onto TiN_{IV} electrodes using a

galvanostatic electrodeposition process. The thickness of the layer could be increased up to ~ 9 µm, beyond which the structure would collapse and be unable to support itself.

8. EIS measurements in PBS prove the strategy of a CP layer efficacious, as the Y_{dl} and Y_{pseu} increase by the approximate factors of 4.5 and 2.5 respectively for $PP_{17.5}$. The CSC_C was also improved at all the investigated scan rates. Chiefly, the extended WW of PEDOT:PSS could be fully utilized at high charge/discharge rates ($v = 1$ Vs^{-1}) without incurring physical damage to the electrode through osmotic stress. A 1.6 factor increase in CSC_C was obtained at 1 Vs^{-1} in this manner.

9. The PP electrodes exhibit volumetric capacitance, whereby the capacitance measurements (Y_{dl} and Y_{pseu}) increase with layer thickness. Saturation of the effect is not observed at the thicknesses explored (~ 2-9 µm).

10. Cyclic stability testing at 1 Vs^{-1} revealed only minimal drop (< 1 %) in electrode capacity over 10,000 cycles, thus performing better than the TiN electrodes in both projected charge retention and absolute charge transfer values. This was true for both the restricted and full WW. The effects of osmotic stress were demonstrated via cycling at 0.1 Vs^{-1}, where electrode performance experienced a significant decline after ~ 3,000 cycles. The PEDOT:PSS layer exhibited damage in the form of cracks and partial delamination after testing. Micro-Raman spectroscopy revealed no significant changes to the chemical structure of either the conductive polymer or the underlying TiN_{IV}. This suggests that participation of TiN in pseudocapacitance did not occur to significant amounts, and that damage to the PEDOT:PSS was of a physical rather than chemical origin.

11. The electrochemical characteristics of $PP_{17.5}$ electrodes are only minimally affected by the presence of proteins in solution, stemming mostly from a drop in the Y_{dl}, and maintain their electrochemical advantage over TiN electrodes even after 24 hours of immersion.

12. A prominent point of concern in multi-layered electrodes is the integrity of the adhesive mechanism that keeps the structure together. This was assessed via ultrasonication tests, representing excessive mechanical force which neural

electrodes are unlikely to encounter *in vivo*. The $PP_{17.5}$ electrodes are demonstrably capable of withstanding 20 minutes of ultrasonication without significant detriment to their electrochemical properties nor any changes to their physical state. This is attributed to excellent mechanical interlocking of the PEDOT:PSS layer with the underlying $TiN_{IV.}$

13. NHDF cell culture experiments reveal $PP_{17.5}$ electrodes as being more susceptible to fouling when compared with TiN_{IV}. The PEDOT:PSS layer increased the number of adhering fibroblasts by ~ 67%, bringing them back on par with the TiN_1. A calcium alginate hydrogel layer deposited onto the $PP_{17.5}$ electrode effectively resolves this issue. No indications of fibroblast adhesion, growth, or proliferation could be identified on the CA_{60s} electrode surfaces.

14. The CA layer was developed using anodic electrogelling directly onto the $PP_{17.5}$ surface. A deposition time of 60s is sufficient to produce a well-adhered, porous gel with repeatable thickness values (405 ± 21 µm) that only marginally reduces the electrochemical properties of $PP_{17.5}$. As a bioresorbable material, the CA dissolves over time, and the majority of EIS-derived values (Y_{dl}, $Y_{pseu,}$ $|Z|_{1Hz}$, etc.) are restored to the original values of $PP_{17.5}$.

15. The degradation profile of CA_{60s} electrodes was mapped using a Ca^{2+} ion detector, and it was found to degrade from the outside-in, possibly due to differences in cross-linking density and ion accessibility across the structure. This allows the gel to degrade without detaching from the PEDOT:PSS layer.

16. The $PP_{17.5}$ and CA_{60s} electrodes (after dissolution) compare well with other prominent materials currently under consideration for neural interfacing. In addition to superseding the electrochemical properties of established materials like Pt, Pt/Ir, and Au, the electrodes also rank very high in both their measured impedance and CSC_C with frontier proposals in recent publications. Nano-structured Pt flowers, PEDOT:PSS-rGO composite, porous graphene, and some forms of IrOx are notable examples.

17. As the hydrogel dissolves, the PEDOT:PSS will eventually be brought in direct contact with the biological environment *in vivo*. This feature may be exploited to

promote direct integration of device and neural tissue. $PP_{17.5}$ and CA_{60s} electrode surfaces can both support the adherence, growth, and differentiation of SH-SY5Y neuroblastomas into neural-type cells with process extensions. Conversely, TiN_{IV} surfaces are unable to support neural differentiation, possibly due to high material stiffness.

18. The calcium alginate layer on CA_{60s} electrodes may serve a dual role, preventing fibrous encapsulation whilst providing a platform for neural development *in vivo*. The hydrogel degrades as neural growth progresses towards the PEDOT:PSS, evading fibrous attachment and finally establishing direct physical contact with the target tissue.

7 Further Work

The following are recommendations to further progress the discoveries made in this work:

1. The potential of CA_{60s} electrodes to support neural growth makes it interesting to further pursue the hypothesis presented in section 5.5.4. The gels may be made more hospitable to neural cells either through pre-conditioning (such as with neurotrophic factors or ligands) or drug-loading (with DEX, for example), and the experiment (neural cell culture) sustained through their dissolution period.

2. Research in which neural cells are incorporated directly into the alginate during its gelation is already underway. Given the relative scarcity of electrodeposited gels in literature, it might be a viable avenue of exploration to perform anodic electrodeposition with neural cells mixed in with the precursor solution.

3. As the biological environment is more complex than any simulated *in vitro* experiment, it is recommended that the electrodes be subjected to *in vivo* tests in an animal model such as rats. Chronic electrochemical measurements may be made to monitor the effects of fibrous fouling and/or neural integration, followed by histological analysis to compare the electrodes on the grounds of their biological performance.

8 References

[1] U. A. Aregueta-Robles, A. J. Woolley, L. A. Poole-Warren, N. H. Lovell, and R. A. Green, "Organic electrode coatings for next-generation neural interfaces," *Front. Neuroeng.*, vol. 7, no. MAY, pp. 1–18, 2014, doi: 10.3389/fneng.2014.00015.

[2] P. L. Gildenberg, "History of electrical neuromodulation for chronic pain," *Pain Med.*, vol. 7, no. SUPPL. 1, 2006, doi: 10.1111/j.1526-4637.2006.00118.x.

[3] N. Chen *et al.*, "Neural interfaces engineered via micro- and nanostructured coatings," *Nano Today*, vol. 14, pp. 59–83, 2017, doi: 10.1016/j.nantod.2017.04.007.

[4] V. Vedam-Mai *et al.*, "Proceedings of the Eighth Annual Deep Brain Stimulation Think Tank: Advances in Optogenetics, Ethical Issues Affecting DBS Research, Neuromodulatory Approaches for Depression, Adaptive Neurostimulation, and Emerging DBS Technologies," *Front. Hum. Neurosci.*, vol. 15, no. April, pp. 1–24, 2021, doi: 10.3389/fnhum.2021.644593.

[5] C. A. Megerian, G. S. Murray, and N. F. Manzoor, "Cochlear Implant Surgery," *Medscape*, 2022. https://emedicine.medscape.com/article/857242-overview (accessed Feb. 06, 2023).

[6] L. N. Ayton *et al.*, "An update on retinal prostheses," *Clin. Neurophysiol.*, vol. 131, no. 6, pp. 1383–1398, 2020, doi: 10.1016/j.clinph.2019.11.029.

[7] A. D. Sdrulla, Y. Guan, and S. N. Raja, "Spinal Cord Stimulation: Clinical Efficacy and Potential Mechanisms," *Pain Pract.*, vol. 18, no. 8, pp. 1048–1067, 2018, doi: 10.1111/papr.12692.

[8] A. Rowald *et al.*, "Activity-dependent spinal cord neuromodulation rapidly restores trunk and leg motor functions after complete paralysis," *Nat. Med.*, vol. 28, no. 2, pp. 260–271, 2022, doi: 10.1038/s41591-021-01663-5.

[9] J. Li, X. Liu, W. Mao, T. Chen, and H. Yu, "Advances in Neural Recodring and Stimulation Integrated Circuits," *Front. Neurosci.*, vol. 15, 2021, doi: 10.3389/fnins.2021.663204.

[10] WHO, "WHO methods and data sources for global burden of disease estimates 2000-2019," no. December, p. 86, 2020, [Online]. Available: http://www.who.int/healthinfo/statistics/GlobalDALYmethods_2000_2011.pdf?ua=1

[11] H. Niu, I. Alvarez-Alvarez, F. Guillen-Grima, and I. Aguinaga-Ontoso, "Prevalence and incidence of Alzheimer's disease in Europe: A meta-analysis," *Neurologia*, vol. 32, no. 8, 2017.

[12] S. F. Cogan, S. Hara, and K. A. Ludwig, *The Safe Delivery of Electrical Currents and Neuromodulation*, Second Edi. Elsevier Ltd, 2018. doi: 10.1016/b978-0-12-805353-9.00007-3.

[13] J. H. Lee, H. Kim, J. H. Kim, and S. H. Lee, "Soft implantable microelectrodes for future medicine: Prosthetics, neural signal recording and neuromodulation," *Lab Chip*, vol. 16, no. 6, pp. 959–976, 2016, doi: 10.1039/c5lc00842e.

[14] R. D. Goodwin, L. C. Dierker, M. Wu, S. Galea, C. Hoven, and A. H. Weinberger, "Trends in U.S. Depression Prevalence From 2015 to 2020: The Widening Treatment Gap," *Am. Journa Prev. Med.*, vol. 63, no. 5, pp. 726–733, 2022.

[15] J. Lin *et al.*, "Projection of the future diabetes burden in the United States through 2060," *Popul. Health Metr.*, vol. 16, no. 1, pp. 1–9, 2018, doi: 10.1186/s12963-018-0166-4.

[16] B. Gunasekera, T. Saxena, R. Bellamkonda, and L. Karumbaiah, "Intracortical recording interfaces: Current challenges to chronic recording function," *ACS Chem. Neurosci.*, vol. 6, no. 1, pp. 68–83, 2015, doi: 10.1021/cn5002864.

[17] C. Liang *et al.*, "Strategies for interface issues and challenges of neural electrodes," *Nanoscale*, vol. 14, no. 9, pp. 3346–3366, 2022, doi: 10.1039/d1nr07226a.

[18] D. J. Tyler, "Electrodes for the Neural Interface," in *Neuromodulation*, Second Edi., Elsevier Ltd, 2018, pp. 239–274. doi: 10.1016/b978-0-12-805353-9.00020-6.

[19] C. J. Hartmann, S. Fliegen, S. J. Groiss, L. Wojtecki, and A. Schnitzler, “An update on best practice of deep brain stimulation in Parkinson’s disease,” *Ther. Adv. Neurol. Disord. Rev.*, vol. 12, no. 0, pp. 1–20, 2019, doi: 10.1177/https.

[20] P. Oldroyd and G. G. Malliaras, “Achieving long-term stability of thin-film electrodes for neurostimulation,” *Acta Biomater.*, vol. 139, pp. 65–81, 2022, doi: 10.1016/j.actbio.2021.05.004.

[21] J. J. Pancrazio *et al.*, “Thinking Small: Progress on Microscale Neurostimulation Technology,” *Neuromodulation*, vol. 20, no. 8, pp. 745–752, 2017, doi: 10.1111/ner.12716.

[22] B. Ghane-Motlagh and M. Sawan, “Design and Implementation Challenges of Microelectrode Arrays: A Review,” *Mater. Sci. Appl.*, vol. 04, no. 08, pp. 483–495, 2013, doi: 10.4236/msa.2013.48059.

[23] C. M. Tringides and D. J. Mooney, “Materials for Implantable Surface Electrode Arrays: Current Status and Future Directions,” *Adv. Mater.*, vol. 34, no. 20, pp. 1–25, 2022, doi: 10.1002/adma.202107207.

[24] D. H. Kim, J. A. Wiler, D. J. Anderson, D. R. Kipke, and D. C. Martin, “Conducting polymers on hydrogel-coated neural electrode provide sensitive neural recordings in auditory cortex,” *Acta Biomater.*, vol. 6, no. 1, pp. 57–62, 2010, doi: 10.1016/j.actbio.2009.07.034.

[25] M. S. Hirmaz, “Fundamental Aspects of Surface Engineering: A Review,” *Int. J. Sci. Res.*, vol. 9, no. 6, pp. 18–22, 2018, [Online]. Available: www.ijsr.net

[26] H. Xiao, F. Di, J. Che, and Y. Xiao, “Surface Modification and Functionalization of Neural Electrodes,” *Prog. Chem.*, vol. 25, no. 11, pp. 1962–1972, 2013.

[27] D. H. Kim and D. C. Martin, “Sustained release of dexamethasone from hydrophilic matrices using PLGA nanoparticles for neural drug delivery,” *Biomaterials*, vol. 27, no. 15, pp. 3031–3037, 2006, doi: 10.1016/j.biomaterials.2005.12.021.

[28] H. Dechiraju, M. Jia, L. Luo, and M. Rolandi, “Ion-Conducting Hydrogels and Their Applications in Bioelectronics,” *Adv. Sustain. Syst.*, vol. 6, no. 2, pp. 1–10, 2022, doi: 10.1002/adsu.202100173.

[29] P. Fattahi, G. Yang, G. Kim, and M. Reza Abidian, “A Review of Organic and Inorganic Biomaterials for Neural Interfaces,” *Adv. Mater.*, vol. 26, no. 12, pp. 1846–1885, 2014.

[30] M. R. Abidian and D. C. Martin, “Multifunctional nanobiomaterials for neural interfaces,” *Adv. Funct. Mater.*, vol. 19, no. 4, pp. 573–585, 2009, doi: 10.1002/adfm.200801473.

[31] Y. Cheng, X. Luo, J. Betz, G. F. Payne, W. E. Bentley, and G. W. Rubloff, “Mechanism of anodic electrodeposition of calcium alginate,” *Soft Matter*, vol. 7, no. 12, pp. 5677–5684, 2011, doi: 10.1039/c1sm05210a.

[32] F. H. Martini, J. L. Nath, and E. F. Bartholomew, *Fundamentals of Anatomy & Physiology*, 10th ed. San Francisco: Pearson Education, Inc., 2015.

[33] P. Rea, *Overview of the nervous system*. 2015. doi: 10.1016/b978-0-443-06684-9.50023-8.

[34] L. Jennes, “Cytology of the Central Nervous System,” *Conn’s Transl. Neurosci.*, pp. 1–10, 2017, doi: 10.1016/B978-0-12-802381-5.00001-4.

[35] Y. Lei, H. Han, F. Yuan, A. Javeed, and Y. Zhao, “The brain interstitial system: Anatomy, modeling, in vivo measurement, and applications,” *Prog. Neurobiol.*, vol. 157, pp. 230–246, 2017, doi: 10.1016/j.pneurobio.2015.12.007.

[36] P. Rea, “Introduction to the Nervous System,” in *Essential Clinical Anatomy of the Nervous System*, Academic Press, 2015. doi: 10.1016/B978-0-12-802030-2/00001-7.

[37] C. Kolluru *et al.*, “Imaging peripheral nerve micro-anatomy with MUSE, 2D and 3D approaches,” *Sci. Rep.*, vol. 12, no. 1, pp. 1–8, 2022, doi: 10.1038/s41598-022-14166-1.

[38] T. Yang, Y. J. Dai, G. Chen, and S. Sen Cui, “Dissecting the Dual Role of the Glial Scar and

Scar-Forming Astrocytes in Spinal Cord Injury," *Front. Cell. Neurosci.*, vol. 14, no. April, 2020, doi: 10.3389/fncel.2020.00078.

[39] C. Keogh, "Optimizing the neuron-electrode interface for chronic bioelectronic interfacing," *Neurosurg. Focus*, vol. 49, no. 1, pp. 1–8, 2020, doi: 10.3171/2020.4.FOCUS20178.

[40] W. Chang, T. Berta, Y. H. Kim, S. Lee, S. Y. Lee, and R. R. Ji, "Expression and Role of Voltage-Gated Sodium Channels in Human Dorsal Root Ganglion Neurons with Special Focus on Nav1.7, Species Differences, and Regulation by Paclitaxel," *Neurosci. Bull.*, vol. 34, no. 1, pp. 4–12, 2018, doi: 10.1007/s12264-017-0132-3.

[41] F. Amorini *et al.*, "Electrically Controlled 'sponge Effect' of PEDOT:PSS Governs Membrane Potential and Cellular Growth," *ACS Appl. Mater. Interfaces*, vol. 9, no. 8, pp. 6679–6689, 2017, doi: 10.1021/acsami.6b12480.

[42] N. Bhadra, T. L. Vrabec, N. Bhadra, and K. L. Kilgore, "Reversible conduction block in peripheral nerve using electrical waveforms," *Bioelectron. Med.*, vol. 1, no. 1, pp. 39–54, 2018, doi: 10.2217/bem-2017-0004.

[43] B. Wang *et al.*, "Firing frequency maxima of fast-spiking neurons in human, monkey, and mouse neocortex," *Front. Cell. Neurosci.*, vol. 10, no. OCT2016, pp. 1–13, 2016, doi: 10.3389/fncel.2016.00239.

[44] J. Rivnay, H. Wang, L. Fenno, K. Deisseroth, and G. G. Malliaras, "Next-generation probes, particles, and proteins for neural interfacing," *Sci. Adv.*, vol. 3, no. 6, 2017, doi: 10.1126/sciadv.1601649.

[45] Molecular Devices LLC, "What is an action potential?" https://www.moleculardevices.com/applications/patch-clamp-electrophysiology/what-action-potential (accessed Oct. 31, 2022).

[46] T. E. of E. Brittanica, "Action Potential," *Encyclopaedia Brittanica*, 2022. https://www.britannica.com/science/action-potential (accessed Oct. 31, 2022).

[47] K. Y. Lee *et al.*, "Low-intensity, Kilohertz Frequency Spinal Cord Stimulation Differently Affects Excitatory and Inhibitory Neurons in the Rodent Superficial Dorsal Horn," *Neuroscience*, vol. 428, pp. 132–139, 2020, doi: 10.1016/j.neuroscience.2019.12.031.

[48] H. Miyawaki, B. O. Watson, and K. Diba, "Neuronal firing rates diverge during REM and homogenize during non-REM," *Sci. Rep.*, vol. 9, no. 1, pp. 1–14, 2019, doi: 10.1038/s41598-018-36710-8.

[49] A. Burroughs *et al.*, "The dynamic relationship between cerebellar Purkinje cell simple spikes and the spikelet number of complex spikes," *J. Physiol.*, vol. 595, no. 1, pp. 283–299, 2017, doi: 10.1113/JP272259.

[50] P. Alcami, R. Franconville, I. Llano, and A. Marty, "Measuring the firing rate of high-resistance neurons with cell-attached recording," *J. Neurosci.*, vol. 32, no. 9, pp. 3118–3130, 2012, doi: 10.1523/JNEUROSCI.5371-11.2012.

[51] K. A. Nave and H. B. Werner, "Myelination of the nervous system: Mechanisms and functions," *Annu. Rev. Cell Dev. Biol.*, vol. 30, pp. 503–533, 2014, doi: 10.1146/annurev-cellbio-100913-013101.

[52] G. Palmer, T. J. Hibberd, T. Roose, S. J. H. Brookes, and M. Taylor, "Measurement of strains experienced by viscerofugal nerve cell bodies during mechanosensitive firing using digital image correlation," *Am. J. Physiol. - Gastrointest. Liver Physiol.*, vol. 311, no. 5, pp. G869–G879, 2016, doi: 10.1152/ajpgi.00397.2015.

[53] T. Kudo, D. H. Loh, D. Kuljis, C. Constance, and C. S. Colwell, "Fast delayed rectifier potassium current: Critical for input and output of the circadian system," *J. Neurosci.*, vol. 31, no. 8, pp. 2746–2755, 2011, doi: 10.1523/JNEUROSCI.5792-10.2011.

[54] A. A. Jiman *et al.*, "Multi-channel intraneural vagus nerve recordings with a novel high-density carbon fiber microelectrode array," *Sci. Rep.*, vol. 10, no. 1, pp. 1–13, 2020, doi:

10.1038/s41598-020-72512-7.

[55] A. A. Grace, D. J. Lodge, and D. M. Buffalari, “Dopamine-CNS pathways and neurophysiology,” *Encycl. Neurosci.*, pp. 549–555, 2009, doi: 10.1016/B978-008045046-9.01140-2.

[56] L. K. Kaczmarek and Y. Zhang, “Kv3 channels: Enablers of rapid firing, neurotransmitter release, and neuronal endurance,” *Physiol. Rev.*, vol. 97, no. 4, pp. 1431–1468, 2017, doi: 10.1152/physrev.00002.2017.

[57] E. A. Rancz, T. Ishikawa, I. Duguid, P. Chadderton, S. Mahon, and M. Häusser, “High-fidelity transmission of sensory information by single cerebellar mossy fibre boutons,” *Nature*, vol. 450, no. 7173, pp. 1245–1248, 2007, doi: 10.1038/nature05995.

[58] F. Z. Xiu-Lin Wu, Qiu-Jin Yan, “Abnormal synaptic plasticity and impaired cognition in schizophrenia,” vol. 3206, no. 4, 2022, [Online]. Available: 10.5498/wjp.v12.i4.541

[59] E. A. Martin, A. M. Lasseigne, and A. C. Miller, “Understanding the Molecular and Cell Biological Mechanisms of Electrical Synapse Formation,” *Front. Neuroanat.*, vol. 14, no. April, pp. 1–13, 2020, doi: 10.3389/fnana.2020.00012.

[60] C. S. Thomas, “The Presynaptic Active Zone,” *Neuron*, vol. 75, no. 1, pp. 11–25, 2012, doi: 10.1016/j.neuron.2012.06.012.The.

[61] D. S. Faber and A. E. Pereda, “Two forms of electrical transmission between neurons,” *Front. Mol. Neurosci.*, vol. 11, no. November, pp. 1–11, 2018, doi: 10.3389/fnmol.2018.00427.

[62] J. Kandel and D. Pokharel, “Mean Brain Weight among Autopsy Cases at the Department of Forensic Medicine of a Tertiary Care Centre: A Descriptive Cross-sectional Study,” *J. Nepal Med. Assoc.*, vol. 60, no. 247, pp. 274–277, 2022, doi: 10.31729/jnma.7162.

[63] A. Frostell, R. Hakim, E. P. Thelin, P. Mattsson, and M. Svensson, “A review of the segmental diameter of the healthy human spinal cord,” *Front. Neurol.*, vol. 7, no. DEC, pp. 1–13, 2016, doi: 10.3389/fneur.2016.00238.

[64] T. O. Wichmann, H. H. Damkier, and M. Pedersen, “A Brief Overview of the Cerebrospinal Fluid System and Its Implications for Brain and Spinal Cord Diseases,” *Front. Hum. Neurosci.*, vol. 15, no. January, pp. 1–7, 2022, doi: 10.3389/fnhum.2021.737217.

[65] H. McCann, G. Pisano, and L. Beltrachini, “Variation in Reported Human Head Tissue Electrical Conductivity Values,” *Brain Topogr.*, vol. 32, no. 5, pp. 825–858, 2019, doi: 10.1007/s10548-019-00710-2.

[66] C. Bédard, H. Kröger, and A. Destexhe, “Modeling Extracellular Field Potentials and the Frequency-Filtering Properties of Extracellular Space,” *Biophys. J.*, vol. 86, no. 3, pp. 1829–1842, 2004, doi: 10.1016/S0006-3495(04)74250-2.

[67] M. I. Altaf, M. Reddy, and A. Ahmad, “Dielectric properties of human blood of patients suffering from renal failure,” *AIP Conf. Proc.*, vol. 2200, no. December, 2019, doi: 10.1063/1.5141206.

[68] D. L. Felten, M. K. O’Banion, and M. S. Maida, “Ventricles and the Cerebrospinal Fluid,” *Netter’s Atlas Neurosci.*, pp. 85–91, 2016, doi: 10.1016/b978-0-323-26511-9.00006-0.

[69] T. Yajima, H. Takahashi, and K. Yasuda, “Comparison of Interstitial Fluid Glucose Levels Obtained by Continuous Glucose Monitoring and Flash Glucose Monitoring in Patients With Type 2 Diabetes Mellitus Undergoing Hemodialysis,” *J. Diabetes Sci. Technol.*, vol. 14, no. 6, pp. 1088–1094, 2019, doi: 10.1177/1932296819882690.

[70] M. mohan Bajaj and S. Ibrahim, “The Body Fluid Compartments: Extracellular and Intracellular Fluids; Edema,” in *Human physiology, BIS processes, & biomedical disorders*, 2005, pp. 305–321.

[71] E. Aurand, J. Wagner, C. Lanning, and K. Bjugstad, “Building Biocompatible Hydrogels for Tissue Engineering of the Brain and Spinal Cord,” *J. Funct. Biomater.*, vol. 3, no. 4, pp. 839–863, 2012, doi: 10.3390/jfb3040839.

[72] R. V. Haberberger, C. Barry, N. Dominguez, and D. Matusica, “Human dorsal root ganglia,” *Front. Cell. Neurosci.*, vol. 13, no. June, pp. 1–17, 2019, doi: 10.3389/fncel.2019.00271.

[73] R. Chen, A. Canales, and P. Anikeeva, “Neural recording and modulation technologies,” *Nat. Rev. Mater.*, vol. 2, no. 2, pp. 1–16, 2017, doi: 10.1038/natrevmats.2016.93.

[74] C. R. Foundation, “Understanding CMT and The Peripheral Nervous System.” https://cmtrf.org/cmt-101-video-cmt-the-peripheral-nervous-system/ (accessed Jul. 26, 2022).

[75] S. Di Cataldo *et al.*, “Automated 3D immunofluorescence analysis of Dorsal Root Ganglia for the investigation of neural circuit alterations: a preliminary study.,” *Position Pap. 2016 Fed. Conf. Comput. Sci. Inf. Syst.*, vol. 9, pp. 65–70, 2016, doi: 10.15439/2016f569.

[76] J. Scheib and A. Höke, “Advances in peripheral nerve regeneration,” *Nat. Rev. Neurol.*, vol. 9, no. 12, pp. 668–676, 2013, doi: 10.1038/nrneurol.2013.227.

[77] H. C. Lehmann, G. Wunderlich, G. R. Fink, and C. Sommer, “Diagnosis of peripheral neuropathy,” *Neurol. Res. Pract.*, vol. 2, no. 1, 2020, doi: 10.1186/s42466-020-00064-2.

[78] C. R. Carvalho, J. M. Oliveira, and R. L. Reis, “Modern Trends for Peripheral Nerve Repair and Regeneration: Beyond the Hollow Nerve Guidance Conduit,” *Front. Bioeng. Biotechnol.*, vol. 7, no. November, pp. 1–30, 2019, doi: 10.3389/fbioe.2019.00337.

[79] L. M. Y. Yu, N. D. Leipzig, and M. S. Shoichet, “Promoting neuron adhesion and growth,” *Mater. Today*, vol. 11, no. 5, pp. 36–43, 2008, doi: 10.1016/S1369-7021(08)70088-9.

[80] M. Anderson, N. B. Shelke, O. S. Manoukian, X. Yu, L. D. McCullough, and S. G. Kumbar, “Peripheral nerve regeneration strategies: Electrically stimulating polymer based nerve growth conduits,” *Crit. Rev. Biomed. Eng.*, vol. 43, no. 2–3, pp. 131–149, 2015, doi: 10.1615/critrevbiomedeng.2015014015.

[81] S. Guo and L. A. DiPietro, “Factors affecting wound healing,” *J. Dent. Res.*, vol. 89, no. 3, pp. 219–229, 2010, doi: 10.1177/0022034509359125.

[82] S. Hall, “The response to injury in the peripheral nervous system,” *J. Bone Jt. Surg. - Ser. B*, vol. 87, no. 10, pp. 1309–1319, 2005, doi: 10.1302/0301-620X.87B10.16700.

[83] L. Ottoboni, B. von Wunster, and G. Martino, “Therapeutic Plasticity of Neural Stem Cells,” *Front. Neurol.*, vol. 11, no. March, 2020, doi: 10.3389/fneur.2020.00148.

[84] D. M. Thompson, A. N. Koppes, J. G. Hardy, and C. E. Schmidt, “Electrical stimuli in the central nervous system microenvironment,” *Annu. Rev. Biomed. Eng.*, vol. 16, pp. 397–430, 2014, doi: 10.1146/annurev-bioeng-121813-120655.

[85] E. S. Donkor, “Stroke in the 21st Century: A Snapshot of the Burden, Epidemiology, and Quality of Life,” *Stroke Res. Treat.*, vol. 2018, 2018, doi: 10.1155/2018/3238165.

[86] M. Tabusi *et al.*, *Neuronal death in pneumococcal meningitis is triggered by pneumolysin and RrgA interactions with β-actin*, vol. 17, no. 3. 2021. doi: 10.1371/JOURNAL.PPAT.1009432.

[87] M. A. Anderson *et al.*, “Astrocyte scar formation aids CNS axon regeneration,” *Nature*, vol. 532, no. 7598, pp. 195–200, 2016, doi: 10.1038/nature17623.Astrocyte.

[88] D. B. Popovi and R. Chapter, “1 Central Nervous System Leading To Sensory – Motor Neuron Injury,” no. d, pp. 3–20.

[89] J. Clark, Z. Zhu, J. Chuckowree, T. Dickson, and C. Blizzard, “Efficacy of epothilones in central nervous system trauma treatment: What has age got to do with it?,” *Neural Regen. Res.*, vol. 16, no. 4, pp. 618–620, 2021, doi: 10.4103/1673-5374.295312.

[90] L. Zhao, H. Y. Shi, Y. M. Ma, and J. W. Liu, “Neural stem cell therapy for brain disease,” *World J. Stem Cells*, vol. 13, no. 9, pp. 1278–1292, 2021, doi: 10.4252/wjsc.v13.i9.1278.

[91] A. C. Boese, Q. S. E. Le, D. Pham, M. H. Hamblin, and J. P. Lee, “Neural stem cell therapy for subacute and chronic ischemic stroke,” *Stem Cell Res. Ther.*, vol. 9, no. 1, pp. 1–17, 2018, doi: 10.1186/s13287-018-0913-2.

[92] A. P. Tran, P. M. Warren, and J. Silver, “New insights into glial scar formation after spinal cord injury,” *Cell Tissue Res.*, vol. 387, no. 3, pp. 319–336, 2022, doi: 10.1007/s00441-021-03477-w.

[93] J. Silver and J. H. Miller, “Regeneration beyond the glial scar,” *Nat. Rev. Neurosci.*, vol. 5, no. 2, pp. 146–156, 2004, doi: 10.1038/nrn1326.

[94] J. Cregg, M. A DePaul, R. F. Angela, and B. T. Lang, “Functional Regeneration Beyond the Glial Scar,” *Exp. Neurol.*, vol. 253, pp. 197–207, 2014, doi: https://doi.org/10.1016/j.expneurol.2013.12.024.

[95] E. P. and the C. of 5 S. 2007, “Council Directive 93/42/EEC (The Medical Devices Directive).” 2007. doi: 10.4324/9780080523156-6.

[96] M. A. González-González *et al.*, “Thin Film Multi-Electrode Softening Cuffs for Selective Neuromodulation,” *Sci. Rep.*, vol. 8, no. 1, pp. 1–15, 2018, doi: 10.1038/s41598-018-34566-6.

[97] C. Günter, J. Delbeke, and M. Ortiz-Catalan, “Safety of long-term electrical peripheral nerve stimulation: Review of the state of the art,” *J. Neuroeng. Rehabil.*, vol. 16, no. 1, pp. 1–16, 2019, doi: 10.1186/s12984-018-0474-8.

[98] A. A. Guex, N. Vachicouras, A. E. Hight, M. C. Brown, D. J. Lee, and S. P. Lacour, “Conducting polymer electrodes for auditory brainstem implants,” *J. Mater. Chem. B*, vol. 3, no. 25, pp. 5021–5027, 2015, doi: 10.1039/c5tb00099h.

[99] K. A. Yildiz, A. Y. Shin, and K. R. Kaufman, “Interfaces with the peripheral nervous system for the control of a neuroprosthetic limb: A review,” *J. Neuroeng. Rehabil.*, vol. 17, no. 1, pp. 1–19, 2020, doi: 10.1186/s12984-020-00667-5.

[100] K. Woeppel, Q. Yang, and X. T. Cui, “Recent advances in neural electrode–tissue interfaces,” *Curr. Opin. Biomed. Eng.*, vol. 4, pp. 21–31, 2017, doi: 10.1016/j.cobme.2017.09.003.

[101] S. F. Cogan, “Neural stimulation and recording electrodes,” *Annu. Rev. Biomed. Eng.*, vol. 10, pp. 275–309, 2008, doi: 10.1146/annurev.bioeng.10.061807.160518.

[102] S. M. Wellman *et al.*, “A Materials Roadmap to Functional Neural Interface Design,” *Adv. Funct. Mater.*, vol. 28, no. 12, pp. 1–38, 2018, doi: 10.1002/adfm.201701269.

[103] I. Dones and V. Levi, “Spinal cord stimulation for neuropathic pain: Current trends and future applications,” *Brain Sci.*, vol. 8, no. 8, 2018, doi: 10.3390/brainsci8080138.

[104] J. F. Baizabal-Carvallo and M. Alonso-Juarez, “Low-frequency deep brain stimulation for movement disorders,” *Park. Relat. Disord.*, vol. 31, pp. 14–22, 2016, doi: 10.1016/j.parkreldis.2016.07.018.

[105] M. Gulino, D. Kim, S. Pané, S. D. Santos, and A. P. Pêgo, “Tissue response to neural implants: The use of model systems toward new design solutions of implantable microelectrodes,” *Front. Neurosci.*, vol. 13, no. JUL, pp. 1–24, 2019, doi: 10.3389/fnins.2019.00689.

[106] M. Freeberg, G. C. J. Pinault, D. J. Tyler, R. J. Triolo, and R. Ansari, “Chronic nerve health following implantation of nerve cuff electrodes designed for the proximal femoral nerve,” *Neurology*, vol. 90, no. 15, pp. 1–17, 2018, [Online]. Available: http://www.embase.com/search/results?subaction=viewrecord&from=export&id=L622308859

[107] S. C. Payne *et al.*, “Blood glucose modulation and safety of efferent vagus nerve stimulation in a type 2 diabetic rat model,” *Physiol. Rep.*, vol. 10, no. 8, pp. 1–12, 2022, doi: 10.14814/phy2.15257.

[108] M. G. Sarr *et al.*, “The EMPOWER Study: Randomized, prospective, double-blind, multicenter trial of vagal blockade to induce weight loss in morbid obesity,” *Obes. Surg.*, vol. 22, no. 11, pp. 1771–1782, 2012, doi: 10.1007/s11695-012-0751-8.

[109] R. T. Hassarati, W. F. Dueck, C. Tasche, P. M. Carter, L. A. Poole-Warren, and R. A. Green, “Improving cochlear implant properties through conductive hydrogel coatings,” *IEEE Trans. Neural Syst. Rehabil. Eng.*, vol. 22, no. 2, pp. 411–418, 2014, doi: 10.1109/TNSRE.2014.2304559.

[110] C. Neudorfer *et al.*, “Kilohertz-frequency stimulation of the nervous system: A review of underlying mechanisms,” *Brain Stimul.*, vol. 14, no. 3, pp. 513–530, 2021, doi: 10.1016/j.brs.2021.03.008.

[111] F. He, R. Lycke, M. Ganji, C. Xie, and L. Luan, “Ultraflexible Neural Electrodes for Long-Lasting Intracortical Recording,” *iScience*, vol. 23, no. 8, p. 101387, 2020, doi: 10.1016/j.isci.2020.101387.

[112] D. Nguyen *et al.*, “Novel Graphene Electrode for Retinal Implants: An in vivo Biocompatibility Study,” *Front. Neurosci.*, vol. 15, no. March, pp. 1–10, 2021, doi: 10.3389/fnins.2021.615256.

[113] B. Thielen and E. Meng, “A comparison of insertion methods for surgical placement of penetrating neural interfaces,” *J. Neural Eng.*, vol. 18, no. 4, 2021, doi: 10.1088/1741-2552/abf6f2.

[114] K. Bradley, “The technology: The anatomy of a spinal cord and nerve root stimulator: The lead and the power source,” *Pain Med.*, vol. 7, no. SUPPL. 1, 2006, doi: 10.1111/j.1526-4637.2006.00120.x.

[115] S. Oribe *et al.*, “Hydrogel-Based Organic Subdural Electrode with High Conformability to Brain Surface,” *Sci. Rep.*, vol. 9, no. 1, pp. 1–10, 2019, doi: 10.1038/s41598-019-49772-z.

[116] C. Russell, A. D. Roche, and S. Chakrabarty, “Peripheral nerve bionic interface: a review of electrodes,” *Int. J. Intell. Robot. Appl.*, vol. 3, no. 1, pp. 11–18, 2019, doi: 10.1007/s41315-019-00086-3.

[117] M. Schiefer, K. H. Polasek, R. J. Triolog, G. C. J. Pinault, and D. J. Tyler, “Selective stimulation of the human femoral nerve with a flat interface nerve electrode,” *J. Neural Eng.*, vol. 7, no. 2, 2010, doi: 10.1088/1741-2560/7/2/026006.

[118] D. J. Tyler and D. M. Durand, “A slowly penetrating intrafascicular nerve elctrode for selective activation of peripheral nerves,” vol. 5, no. 1, pp. 51–61, 1997.

[119] T. Boretius *et al.*, “A transverse intrafascicular multichannel electrode (TIME) to interface with the peripheral nerve,” *Biosens. Bioelectron.*, vol. 26, no. 1, pp. 62–69, 2010, doi: 10.1016/j.bios.2010.05.010.

[120] M. R. MacEwan, E. R. Zellmer, J. J. Wheeler, H. Burton, and D. W. Moran, “Regenerated sciatic nerve axons stimulated through a chronically implanted macro-sieve electrode,” *Front. Neurosci.*, vol. 10, no. DEC, pp. 1–12, 2016, doi: 10.3389/fnins.2016.00557.

[121] J. W. Salatino, K. A. Ludwig, T. D. Y. Kozai, and E. K. Purcell, “Glial responses to implanted electrodes in the brain,” *Nat. Biomed. Eng.*, vol. 1, no. 11, pp. 862–877, 2017, doi: 10.1038/s41551-017-0154-1.

[122] A. Carnicer-Lombarte, S. T. Chen, G. G. Malliaras, and D. G. Barone, “Foreign Body Reaction to Implanted Biomaterials and Its Impact in Nerve Neuroprosthetics,” *Front. Bioeng. Biotechnol.*, vol. 9, no. April, pp. 1–22, 2021, doi: 10.3389/fbioe.2021.622524.

[123] J. L. Skousen, M. J. Bridge, and P. A. Tresco, “A strategy to passively reduce neuroinflammation surrounding devices implanted chronically in brain tissue by manipulating device surface permeability,” *Biomaterials*, vol. 36, pp. 33–43, 2015, doi: 10.1016/j.biomaterials.2014.08.039.

[124] N. Noskovicova, B. Hinz, and P. Pakshir, “Implant fibrosis and the underappreciated role of myofibroblasts in the foreign body reaction,” *Cells*, vol. 10, no. 7, 2021, doi: 10.3390/cells10071794.

[125] A. Campbell and C. Wu, “Chronically implanted intracranial electrodes: Tissue reaction and electrical changes,” *Micromachines*, vol. 9, no. 9, pp. 1–14, 2018, doi: 10.3390/mi9090430.

[126] G. Rosso, I. Liashkovich, P. Young, D. Röhr, and V. Shahin, “Schwann cells and neurite outgrowth from embryonic dorsal root ganglions are highly mechanosensitive,” *Nanomedicine Nanotechnology, Biol. Med.*, vol. 13, no. 2, pp. 493–501, 2017, doi: 10.1016/j.nano.2016.06.011.

[127] E. A. Cuttaz, C. A. R. Chapman, O. Syed, J. A. Goding, and R. A. Green, “Stretchable, Fully Polymeric Electrode Arrays for Peripheral Nerve Stimulation,” *Adv. Sci.*, vol. 8, no. 8, pp. 1–14, 2021, doi: 10.1002/advs.202004033.

[128] M. Demelas, E. Scavetta, L. Basiricò, R. Rogani, and A. Bonfiglio, “A deeper insight into the operation regime of all-polymeric electrochemical transistors,” *Appl. Phys. Lett.*, vol. 102, no. 19, pp. 1–6, 2013, doi: 10.1063/1.4804423.

[129] A. Wang, D. Jung, D. Lee, and H. Wang, “Impedance Characterization and Modeling of Subcellular to Micro-sized Electrodes with Varying Materials and PEDOT:PSS Coating for Bioelectrical Interfaces,” *ACS Appl. Electron. Mater.*, vol. 3, no. 12, pp. 5226–5239, 2021, doi: 10.1021/acsaelm.1c00687.

[130] S. Nag and N. V. Thakor, “Implantable neurotechnologies: electrical stimulation and applications,” *Med. Biol. Eng. Comput.*, vol. 54, no. 1, pp. 63–76, 2016, doi: 10.1007/s11517-015-1442-0.

[131] G. K. K. Chik *et al.*, “Flexible Multichannel Neural Probe Developed by Electropolymerization for Localized Stimulation and Sensing,” *Adv. Mater. Technol.*, vol. 2200143, pp. 1–12, 2022, doi: 10.1002/admt.202200143.

[132] E. Redolfi Riva and S. Micera, “Progress and challenges of implantable neural interfaces based on nature-derived materials,” *Bioelectron. Med.*, vol. 7, no. 1, 2021, doi: 10.1186/s42234-021-00067-7.

[133] A. Karimi, A. Shojaei, and P. Tehrani, “Mechanical properties of the human spinal cord under the compressive loading,” *J. Chem. Neuroanat.*, vol. 86, pp. 15–18, 2017, doi: 10.1016/j.jchemneu.2017.07.004.

[134] J. Kerns, H. Piponov, C. Helder, F. Amirouche, G. Solitro, and M. Gonzalez, “Mechanical Properties of the Human Tibial and Peroneal Nerves Following Stretch With Histological Correlations,” *Anat. Rec.*, vol. 302, no. 11, pp. 2030–2039, 2019, doi: 10.1002/ar.24250.

[135] S. Yilmaz-Bayraktar, K. Foremny, M. Kreienmeyer, A. Warnecke, and T. Doll, “Medical-Grade Silicone Rubber–Hydrogel-Composites for Modiolar Hugging Cochlear Implants,” *Polymers (Basel).*, vol. 14, no. 9, pp. 1–19, 2022, doi: 10.3390/polym14091766.

[136] W. Y. Chang, T. H. Fang, and Y. C. Lin, “Physical characteristics of polyimide films for flexible sensors,” *Appl. Phys. A Mater. Sci. Process.*, vol. 92, no. 3, pp. 693–701, 2008, doi: 10.1007/s00339-008-4623-y.

[137] A. Weltman, J. Yoo, and E. Meng, “Flexible, penetrating brain probes enabled by advances in polymer microfabrication,” *Micromachines*, vol. 7, no. 10, 2016, doi: 10.3390/mi7100180.

[138] M. David-Pur, L. Bareket-Keren, G. Beit-Yaakov, D. Raz-Prag, and Y. Hanein, “All-carbon-nanotube flexible multi-electrode array for neuronal recording and stimulation,” *Biomed. Microdevices*, vol. 16, no. 1, pp. 43–53, 2014, doi: 10.1007/s10544-013-9804-6.

[139] M. Shur *et al.*, “Soft Printable Electrode Coating for Neural Interfaces,” *ACS Appl. Bio Mater.*, vol. 3, no. 7, pp. 4388–4397, 2020, doi: 10.1021/acsabm.0c00401.

[140] J. Jeong, N. Chou, and S. Kim, “Fabrication of flexible electrode array based on PDMS for long-term in-vivo use,” *Int. IEEE/EMBS Conf. Neural Eng. NER*, no. 0, pp. 911–914, 2013, doi: 10.1109/NER.2013.6696083.

[141] S. Zhang *et al.*, “A Removable Insertion Shuttle for Ultraflexible Neural Probe Implantation with Stable Chronic Brain Electrophysiological Recording,” *Adv. Mater. Interfaces*, vol. 7, no. 6, pp. 1–8, 2020, doi: 10.1002/admi.201901775.

[142] J. Pas *et al.*, “A bilayered PVA/PLGA-bioresorbable shuttle to improve the implantation of flexible neural probes,” *J. Neural Eng.*, vol. 15, no. 6, 2018, doi: 10.1088/1741-2552/aadc1d.

[143] C. Cointe *et al.*, “Scalable batch fabrication of ultrathin flexible neural probes using a bioresorbable silk layer,” *Microsystems Nanoeng.*, vol. 8, no. 1, 2022, doi: 10.1038/s41378-022-00353-7.

[144] Y. H. An *et al.*, “Effects of sterilization on implant mechanical property and biocompatibility,” *Int. J. Artif. Organs*, vol. 28, no. 11, pp. 1126–1137, 2005, doi: 10.1177/039139880502801110.

[145] M. Haim Zada, A. Kumar, O. Elmalak, G. Mechrez, and A. J. Domb, “Effect of Ethylene Oxide and Gamma (γ-) Sterilization on the Properties of a PLCL Polymer Material in Balloon Implants,” *ACS Omega*, vol. 4, no. 25, pp. 21319–21326, 2019, doi: 10.1021/acsomega.9b02889.

[146] T. Chung, J. Q. Wang, J. Wang, B. Cao, Y. Li, and S. W. Pang, “Electrode modifications to lower electrode impedance and improve neural signal recording sensitivity,” *J. Neural Eng.*, vol. 12, no. 5, 2015, doi: 10.1088/1741-2560/12/5/056018.

[147] W. Franks, I. Schenker, P. Schmutz, and A. Hierlemann, “Impedance characterization and modeling of electrodes for biomedical applications,” *IEEE Trans. Biomed. Eng.*, vol. 52, no. 7, pp. 1295–1302, 2005, doi: 10.1109/TBME.2005.847523.

[148] E. S. Ereifej *et al.*, “Implantation of neural probes in the brain elicits oxidative stress,” *Front. Bioeng. Biotechnol.*, vol. 6, no. FEB, 2018, doi: 10.3389/fbioe.2018.00009.

[149] E. R. Whittemore, D. T. Loo, J. A. Watt, and C. W. Cotmans, “A detailed analysis of hydrogen peroxide-induced cell death in primary neuronal culture,” *Neuroscience*, vol. 67, no. 4, pp. 921–932, 1995.

[150] R. K. Shepherd *et al.*, “Platinum dissolution and tissue response following long-term electrical stimulation at high charge densities,” *J. Neural Eng.*, vol. 18, no. 3, 2020, doi: 10.1088/1741-2552/abe5ba.

[151] S. Negi, R. Bhandari, L. Rieth, R. Van Wagenen, and F. Solzbacher, “Neural electrode degradation from continuous electrical stimulation: Comparison of sputtered and activated iridium oxide,” *J. Neurosci. Methods*, vol. 186, no. 1, pp. 8–17, 2010, doi: 10.1016/j.jneumeth.2009.10.016.

[152] A. Shah Idil and N. Donaldson, “The use of tungsten as a chronically implanted material,” *J. Neural Eng.*, vol. 15, no. 2, 2018, doi: 10.1088/1741-2552/aaa502.

[153] K. Wissel *et al.*, “Effects of the in vitro corroded platinum electrode contacts in human cochlear implants on cell culture models,” *PLoS One*, pp. 1–20, 2018.

[154] K. T. Kim, M. Y. Eo, T. T. H. Nguyen, and S. M. Kim, “General review of titanium toxicity,” *Int. J. Implant Dent.*, vol. 5, no. 1, 2019, doi: 10.1186/s40729-019-0162-x.

[155] A. B. Seabra, A. J. Paula, R. De Lima, O. L. Alves, and N. Durán, “Nanotoxicity of graphene and graphene oxide,” *Chem. Res. Toxicol.*, vol. 27, no. 2, pp. 159–168, 2014, doi: 10.1021/tx400385x.

[156] P. Bhojane, “Recent advances and fundamentals of Pseudocapacitors: Materials, mechanism, and its understanding,” *J. Energy Storage*, vol. 45, no. October 2021, p. 103654, 2022, doi: 10.1016/j.est.2021.103654.

[157] C. Boehler, S. Carli, L. Fadiga, T. Stieglitz, and M. Asplund, “Tutorial: guidelines for standardized performance tests for electrodes intended for neural interfaces and bioelectronics,” *Nat. Protoc.*, vol. 15, no. 11, pp. 3557–3578, 2020, doi: 10.1038/s41596-020-0389-2.

[158] J. Liu *et al.*, “Advanced Energy Storage Devices: Basic Principles, Analytical Methods, and Rational Materials Design,” *Adv. Sci.*, vol. 5, no. 1, 2018, doi: 10.1002/advs.201700322.

[159] M. Endo, T. Takeda, Y. J. Kim, K. Koshiba, and K. Ishii, “High Power Electric Double Layer Capacitor (EDLC ’ s); from Operating Principle to Pore Size Control in Advanced Activated Carbons,” *Carbon Sci.*, vol. 1, no. 3, pp. 117–128, 2001.

[160] N. R. Chodankar *et al.*, “True Meaning of Pseudocapacitors and Their Performance Metrics: Asymmetric versus Hybrid Supercapacitors,” *Small*, vol. 16, no. 37, pp. 1–35, 2020, doi: 10.1002/smll.202002806.

[161] S. Fleischmann *et al.*, “Pseudocapacitance: From Fundamental Understanding to High Power Energy Storage Materials,” *Chem. Rev.*, vol. 120, no. 14, pp. 6738–6782, 2020, doi:

10.1021/acs.chemrev.0c00170.

[162] C. Boehler, T. Stieglitz, and M. Asplund, “Nanostructured platinum grass enables superior impedance reduction for neural microelectrodes,” *Biomaterials*, vol. 67, pp. 346–353, 2015, doi: 10.1016/j.biomaterials.2015.07.036.

[163] A. Sekretaryova, *Powering wearable bioelectronic devices*. Elsevier Ltd., 2019. doi: 10.1016/B978-0-08-102407-2.00005-9.

[164] Y. Jiang and J. Liu, “Definitions of Pseudocapacitive Materials: A Brief Review,” *Energy Environ. Mater.*, vol. 2, no. 1, pp. 30–37, 2019, doi: 10.1002/eem2.12028.

[165] S. H. Lee, K. S. Lee, S. Sorcar, A. Razzaq, M. G. Lee, and S. Il In, “Novel porous brain electrodes for augmented local field potential signal detection,” *Materials (Basel).*, vol. 12, no. 3, pp. 1–8, 2019, doi: 10.3390/ma12030542.

[166] H. K. Song, Y. H. Jung, K. H. Lee, and L. H. Dao, “Electrochemical impedance spectroscopy of porous electrodes: The effect of pore size distribution,” *Electrochim. Acta*, vol. 44, no. 20, pp. 3513–3519, 1999, doi: 10.1016/S0013-4686(99)00121-8.

[167] A. Achour *et al.*, “Titanium nitride films for micro-supercapacitors: Effect of surface chemistry and film morphology on the capacitance,” *J. Power Sources*, vol. 300, pp. 525–532, 2015, doi: 10.1016/j.jpowsour.2015.09.012.

[168] I. Yang, S. G. Kim, S. H. Kwon, M. S. Kim, and J. C. Jung, “Relationships between pore size and charge transfer resistance of carbon aerogels for organic electric double-layer capacitor electrodes,” *Electrochim. Acta*, vol. 223, pp. 21–30, 2017, doi: 10.1016/j.electacta.2016.11.177.

[169] D. D. Stupin *et al.*, “Bioimpedance Spectroscopy: Basics and Applications,” *ACS Biomater. Sci. Eng.*, vol. 7, no. 6, 2021, doi: 10.1021/acsbiomaterials.0c01570.

[170] G. Schiavone, X. Kang, F. Fallegger, J. Gandar, G. Courtine, and S. P. Lacour, “Guidelines to Study and Develop Soft Electrode Systems for Neural Stimulation,” *Neuron*, vol. 108, no. 2, pp. 238–258, 2020, doi: 10.1016/j.neuron.2020.10.010.

[171] A. Weltin and J. Kieninger, “Electrochemical methods for neural interface electrodes,” *J. Neural Eng.*, vol. 18, no. 5, 2021, doi: 10.1088/1741-2552/ac28d5.

[172] A. Norlin, J. Pan, and C. Leygraf, “Electrochemical Behavior of Stimulation⁄Sensing Materials for Pacemaker Electrode Applications,” *J. Electrochem. Soc.*, vol. 152, no. 9, p. J110, 2005, doi: 10.1149/1.1972981.

[173] J. Huang, “Diffusion impedance of electroactive materials, electrolytic solutions and porous electrodes: Warburg impedance and beyond,” *Electrochim. Acta*, vol. 281, pp. 170–188, 2018, doi: 10.1016/j.electacta.2018.05.136.

[174] S. Feliu, “Electrochemical impedance spectroscopy for the measurement of the corrosion rate of magnesium alloys: Brief review and challenges,” *Metals (Basel).*, vol. 10, no. 6, pp. 1–23, 2020, doi: 10.3390/met10060775.

[175] L. Pan *et al.*, “Hierarchical nanostructured conducting polymer hydrogel with high electrochemical activity,” *Proc. Natl. Acad. Sci. U. S. A.*, vol. 109, no. 24, pp. 9287–9292, 2012, doi: 10.1073/pnas.1202636109.

[176] S. Meijs *et al.*, “Diamond/porous titanium nitride electrodes with superior electrochemical performance for neural interfacing,” *Front. Bioeng. Biotechnol.*, vol. 6, no. November, pp. 1–10, 2018, doi: 10.3389/fbioe.2018.00171.

[177] H. Liang, J. Xu, D. Zhou, X. Sun, S. Chu, and Y. Bai, “Thickness dependent microstructural and electrical properties of TiN thin films prepared by DC reactive magnetron sputtering,” *Ceram. Int.*, vol. 42, no. 2, pp. 2642–2647, 2016, doi: 10.1016/j.ceramint.2015.10.070.

[178] S. J. Cooper, A. Bertei, D. P. Finegan, and N. P. Brandon, “Simulated impedance of diffusion in porous media,” *Electrochim. Acta*, vol. 251, pp. 681–689, 2017, doi: 10.1016/j.electacta.2017.07.152.

[179] J. Song and M. Z. Bazant, “Effects of Nanoparticle Geometry and Size Distribution on Diffusion Impedance of Battery Electrodes,” *J. Electrochem. Soc.*, vol. 160, no. 1, pp. A15–A24, 2013, doi: 10.1149/2.023301jes.

[180] T. Brezesinski, J. Wang, R. Senter, K. Brezesinski, B. Dunn, and S. H. Tolbert, “On the Correlation between Mechanical Flexibility, Nanoscale Structure, and Charge Storage in Periodic Mesoporous CeO2 Thin Films,” *ACS Nano*, vol. 4, no. 2, pp. 967–977, 2010.

[181] G. Piret *et al.*, “3D-nanostructured boron-doped diamond for microelectrode array neural interfacing,” *Biomaterials*, vol. 53, pp. 173–183, 2015, doi: 10.1016/j.biomaterials.2015.02.021.

[182] S. Elyahoodayan *et al.*, “Stimulation and Recording of the Hippocampus Using the Same Pt-Ir Coated Microelectrodes,” *Front. Neurosci.*, vol. 15, no. February, 2021, doi: 10.3389/fnins.2021.616063.

[183] A. Frommhold and E. Tarte, “Effect of film structure on the electrochemical properties of gold electrodes for neural implants,” *Electrochim. Acta*, vol. 56, no. 17, pp. 6001–6007, 2011, doi: 10.1016/j.electacta.2011.04.100.

[184] Y. J. Wu *et al.*, “Conformal deposition of Pt on titania nanotubes to produce a bio-electrode for neuro-stimulating applications,” *Electrochem. commun.*, vol. 88, no. November 2017, pp. 61–66, 2018, doi: 10.1016/j.elecom.2018.01.019.

[185] W. Hasenkamp, S. Musa, A. Alexandru, W. Eberle, and C. Bartic, “Electrodeposition and characterization of iridium oxide as electrode material for neural recording and stimulation,” *IFMBE Proc.*, vol. 25, no. 9, pp. 472–475, 2009, doi: 10.1007/978-3-642-03889-1_126.

[186] T. Liu and Y. Li, “Addressing the Achilles’ heel of pseudocapacitive materials: Long-term stability,” *InfoMat*, vol. 2, no. 5, pp. 807–842, 2020, doi: 10.1002/inf2.12105.

[187] L. Hou, H. Zhou, and H. J. Zhai, “Cycling stability depends closely on scan rate: the case of polyaniline supercapacitor electrodes,” *Soft Mater.*, vol. 19, no. 4, pp. 452–456, 2021, doi: 10.1080/1539445X.2020.1856872.

[188] Blackrock Neurotech, “Utah ArrayTM.” https://blackrockneurotech.com/research/products/?gclid=Cj0KCQjwyOuYBhCGARIsAIdGQRO6RuH4tiWs6kofXYOLVA8iS1UpwF0mU9FIIN7sIpv9BdRNXmlDNY0aAlssEALw_wcB#electrodes (accessed Sep. 09, 2022).

[189] NeuroNexus, “Deep Brain Stimulation.” https://www.neuronexus.com/products/electrode-arrays/deep-brain-stimulation (accessed Sep. 09, 2022).

[190] NeuroNexus, “Peripheral Nerve Cuffs.” https://www.neuronexus.com/products/electrode-arrays/peripheral-nerve-cuffs (accessed Sep. 09, 2022).

[191] E. M. Hudak, D. W. Kumsa, H. B. Martin, and J. T. Mortimer, “Electron transfer processes occurring on platinum neural stimulating electrodes: Calculated charge-storage capacities are inaccessible during applied stimulation,” *J. Neural Eng.*, vol. 14, no. 4, 2017, doi: 10.1088/1741-2552/aa6945.

[192] M. Schweigmann, F. Kirchhoff, and K. P. Koch, “Comparative study of platinum electroplating to improve micro gold electrode arrays with LCP laminate,” *Biomed. Tech.*, vol. 67, no. 1, pp. 33–42, 2022, doi: 10.1515/bmt-2021-0020.

[193] Q. Zeng, Y. Zhang, T. Wu, B. Sun, K. Xia, and S. Mark Humayun, “3D Nano-crystal Platinum for High-performance Neural Electrode,” *Proc. Annu. Int. Conf. IEEE Eng. Med. Biol. Soc. EMBS*, vol. 2018-July, pp. 4217–4220, 2018, doi: 10.1109/EMBC.2018.8513278.

[194] ASTM International, “ASTM B684/B684M-22: Standard Specification for Platinum-Iridium Electrical Contact Materials.” 2022.

[195] Medtronic, “Sensite™ Directional Leads for Deep Brain Stimulation (DBS),” 2022. https://europe.medtronic.com/xd-en/healthcare-professionals/products/neurological/deep-brain-stimulation-systems/sensight-lead.html (accessed Sep. 09, 2022).

[196] Plexon, “Neural Electrodes, Probes and Arrays.” https://plexon.com/products/plexon-electrodes-

probes-and-arrays/ (accessed Sep. 09, 2022).

[197] A. N. Dalrymple *et al.*, “Electrochemical and biological characterization of thin-film platinum-iridium alloy electrode coatings: A chronic in vivo study,” *J. Neural Eng.*, vol. 17, no. 3, 2020, doi: 10.1088/1741-2552/ab933d.

[198] A. S. Pranti, A. Schander, A. Bödecker, and W. Lang, “PEDOT: PSS coating on gold microelectrodes with excellent stability and high charge injection capacity for chronic neural interfaces,” *Sensors Actuators, B Chem.*, vol. 275, no. March, pp. 382–393, 2018, doi: 10.1016/j.snb.2018.08.007.

[199] F. Decataldo *et al.*, “Stretchable Low Impedance Electrodes for Bioelectronic Recording from Small Peripheral Nerves,” *Sci. Rep.*, vol. 9, no. 1, pp. 1–9, 2019, doi: 10.1038/s41598-019-46967-2.

[200] J. Maeng *et al.*, “High-charge-capacity sputtered iridium oxide neural stimulation electrodes deposited using water vapor as a reactive plasma constituent,” *J. Biomed. Mater. Res. - Part B Appl. Biomater.*, vol. 108, no. 3, pp. 880–891, 2020, doi: 10.1002/jbm.b.34442.

[201] Q. Zeng, K. Xia, B. Sun, Y. Yin, T. Wu, and M. S. Humayun, “Electrodeposited Iridium Oxide on Platinum Nanocones for Improving Neural Stimulation Microelectrodes,” *Electrochim. Acta*, vol. 237, pp. 152–159, 2017, doi: 10.1016/j.electacta.2017.03.213.

[202] C. Chen, S. Ruan, X. Bai, C. Lin, C. Xie, and I. S. Lee, “Patterned iridium oxide film as neural electrode interface: Biocompatibility and improved neurite outgrowth with electrical stimulation,” *Mater. Sci. Eng. C*, vol. 103, no. June, p. 109865, 2019, doi: 10.1016/j.msec.2019.109865.

[203] Q. Zeng, Z. Huang, G. Cai, and T. Wu, “Platinum Nanocrystal Assisted by Low-Content Iridium for High-Performance Flexible Electrode: Applications on Neural Interface, Water Oxidation, and Anti-Microbial Contamination,” *Adv. Mater. Interfaces*, vol. 8, no. 22, pp. 1–16, 2021, doi: 10.1002/admi.202100965.

[204] X. Y. Kang, J. Q. Liu, H. C. Tian, B. Yang, Y. Nuli, and C. S. Yang, “Fabrication and electrochemical comparison of SIROF-AIROF-EIROF microelectrodes for neural interfaces,” *2014 36th Annu. Int. Conf. IEEE Eng. Med. Biol. Soc. EMBC 2014*, vol. 1, pp. 478–481, 2014, doi: 10.1109/EMBC.2014.6943632.

[205] R. A. Frederick, I. Y. Meliane, A. Joshi-Imre, P. R. Troyk, and S. F. Cogan, “Activated iridium oxide film (AIROF) electrodes for neural tissue stimulation,” *J. Neural Eng.*, vol. 17, no. 5, 2020, doi: 10.1088/1741-2552/abb9bf.

[206] Y. Lu, T. Wang, Z. Cai, Y. Cao, H. Yang, and Y. Y. Duan, “Anodically electrodeposited iridium oxide films microelectrodes for neural microstimulation and recording,” *Sensors Actuators, B Chem.*, vol. 137, no. 1, pp. 334–339, 2009, doi: 10.1016/j.snb.2008.11.036.

[207] S. Negi, R. Bhandari, and F. Solzbacher, “Morphology and Electrochemical Properties of Activated and Sputtered Iridium Oxide Films for Functional Electrostimulation,” *J. Sens. Technol.*, vol. 02, no. 03, pp. 138–147, 2012, doi: 10.4236/jst.2012.23020.

[208] Y. Zhong, X. H. Xia, F. Shi, J. Y. Zhan, J. P. Tu, and H. J. Fan, “Transition metal carbides and nitrides in energy storage and conversion,” *Adv. Sci.*, vol. 3, no. 5, 2015, doi: 10.1002/advs.201500286.

[209] B. Gao *et al.*, “Recent progress in nanostructured transition metal nitrides for advanced electrochemical energy storage,” *J. Mater. Chem. A*, vol. 7, no. 1, pp. 14–37, 2019, doi: 10.1039/c8ta05760e.

[210] A. Pathak and A. K. Singh, “Transition Metal Nitrides: A First Principles Study,” *High Temp. Mater. Process.*, vol. 35, no. 4, pp. 389–398, 2016, doi: 10.1515/htmp-2014-0169.

[211] I. Gotman and Gutmanas EY, “Titanium nitride-based coatings on implantable medical devices,” *Adv. Biomater. Devices Med.*, pp. 53–73, 2014.

[212] R. P. Van Hove, I. N. Sierevelt, B. J. Van Royen, and P. A. Nolte, “Titanium-Nitride Coating of

Orthopaedic Implants: A Review of the Literature," *Biomed Res. Int.*, vol. 2015, 2015, doi: 10.1155/2015/485975.

[213] M. Schaldach, M. Hubmann, R. Hardt, and A. Weikl, "Titannitrid-Herzschrittmacher-Elektroden - Pacemaker Electrodes Made of Titanium Nitride," *Biomed. Tech. Eng.*, vol. 34, no. 7–8, pp. 185–190, 2009, doi: 10.1515/bmte.1989.34.7-8.185.

[214] M. N. Solovan, V. V. Brus, E. V. Maistruk, and P. D. Maryanchuk, "Electrical and optical properties of TiN thin films," *Inorg. Mater.*, vol. 50, no. 1, pp. 40–45, 2014, doi: 10.1134/S0020168514010178.

[215] A. Poursaee, G. Najaf-Tomaraei, and M. S. Kennedy, "Electronic behavior of native oxide films on Ti and TiN during 90-day immersion in electrolytes with different pH levels," *Rare Met.*, vol. 40, no. 3, pp. 582–589, 2021, doi: 10.1007/s12598-020-01386-5.

[216] G. Chen, M. Gatti, and M. M. C. Cheng, "Titanium Nitride Nanotubes Electrodes for Chronic Neural Stimulation," *2019 20th Int. Conf. Solid-State Sensors, Actuators Microsystems Eurosensors XXXIII, TRANSDUCERS 2019 EUROSENSORS XXXIII*, no. June, pp. 1662–1665, 2019, doi: 10.1109/TRANSDUCERS.2019.8808585.

[217] M. Canillas, B. Moreno, M. Carballo-Vila, J. R. Jurado, and E. Chinarro, "Bulk Ti nitride prepared from rutile TiO 2 for its application as stimulation electrode in neuroscience," *Mater. Sci. Eng. C*, vol. 96, no. February 2018, pp. 295–301, 2019, doi: 10.1016/j.msec.2018.11.030.

[218] B. Chang, "The Effective Capacitance of a Constant Phase Element with Resistors in Series and Parallel," 2022, doi: https://papers.ssrn.com/sol3/papers.cfm?abstract_id=4079679.

[219] R. Sait, S. Govindarajan, and R. Cross, "Nitridation of optimised TiO2 nanorods through PECVD towards neural electrode application," *Materialia*, vol. 4, no. September, pp. 127–138, 2018, doi: 10.1016/j.mtla.2018.09.015.

[220] N. K. Ponon *et al.*, "Effect of deposition conditions and post deposition anneal on reactively sputtered titanium nitride thin films," *Thin Solid Films*, vol. 578, pp. 31–37, 2015, doi: 10.1016/j.tsf.2015.02.009.

[221] Z. Wang, D. Zhang, P. Ke, X. Liu, and A. Wang, "Influence of Substrate Negative Bias on Structure and Properties of TiN Coatings Prepared by Hybrid HIPIMS Method," *J. Mater. Sci. Technol.*, vol. 31, no. 1, pp. 37–42, 2015, doi: 10.1016/j.jmst.2014.06.002.

[222] B. Subramanian, R. Ananthakumar, V. S. Vidhya, and M. Jayachandran, "Influence of substrate temperature on the materials properties of reactive DC magnetron sputtered Ti / TiN multilayered thin films," vol. 176, pp. 1–7, 2011, doi: 10.1016/j.mseb.2010.08.004.

[223] A. V. Rane, K. Kanny, V. K. Abitha, and S. Thomas, *Methods for Synthesis of Nanoparticles and Fabrication of Nanocomposites*. Elsevier Ltd., 2018. doi: 10.1016/B978-0-08-101975-7.00005-1.

[224] E. Penilla and J. Wang, "Pressure and Temperature Effects on Stoichiometry and Microstructure of Nitrogen-Rich TiN Thin Films Synthesized via Reactive Magnetron DC-Sputtering," *J. Nanomater.*, vol. 2008, pp. 1–9, 2008, doi: 10.1155/2008/267161.

[225] N. Sun *et al.*, "Sputtered titanium nitride films with finely tailored surface activity and porosity for high performance on-chip micro-supercapacitors," *J. Power Sources*, vol. 489, no. June 2020, p. 229406, 2021, doi: 10.1016/j.jpowsour.2020.229406.

[226] L. T. Cunha, P. Pedrosa, C. J. Tavares, E. Alves, F. Vaz, and C. Fonseca, "The role of composition, morphology and crystalline structure in the electrochemical behaviour of TiNx thin films for dry electrode sensor materials," *Electrochim. Acta*, vol. 55, no. 1, pp. 59–67, 2009, doi: 10.1016/j.electacta.2009.08.004.

[227] K. L. Chuang, M. T. Tsai, and F. H. Lu, "Morphology control of conductive TiN films produced by air-based magnetron sputtering," *Surf. Coatings Technol.*, vol. 350, no. February, pp. 1091–1097, 2018, doi: 10.1016/j.surfcoat.2018.02.020.

[228] S. Meijs, C. Sørensen, S. Sorensen, K. Rechendorff, M. Fjorback, and N. J. M. Rijkhoff,

"Comparison of the electrochemical properties of smooth and porous TiN electrode coatings in rats," *Int. IEEE/EMBS Conf. Neural Eng. NER*, vol. 2015-July, pp. 486–489, 2015, doi: 10.1109/NER.2015.7146665.

[229] S. Meijs, M. Fjorback, C. Jensen, S. Sørensen, K. Rechendorff, and N. J. M. Rijkhoff, "Influence of fibrous encapsulation on electro-chemical properties of TiN electrodes," *Med. Eng. Phys.*, vol. 38, no. 5, pp. 468–476, 2016, doi: 10.1016/j.medengphy.2016.02.010.

[230] S. Meijs, C. SØrensen, S. SØrensen, K. Rechendorff, M. Fjorback, and N. J. M. Rijkhoff, "Influence of implantation on the electrochemical properties of smooth and porous TiN coatings for stimulation electrodes," *J. Neural Eng.*, vol. 13, no. 2, 2016, doi: 10.1088/1741-2560/13/2/026011.

[231] S. Meijs, M. Fjorback, C. Jensen, S. Sørensen, K. Rechendorff, and N. J. M. Rijkhoff, "Electrochemical properties of titanium nitride nerve stimulation electrodes: An in vitro and in vivo study," *Front. Neurosci.*, vol. 9, no. JUL, pp. 1–11, 2015, doi: 10.3389/fnins.2015.00268.

[232] S. Meijs, S. Sørensen, K. Rechendorff, and N. Rijkhoff, "In vivo charge injection limits increased after 'unsafe' stimulation," *NEUROTECHNIX 2015 - Proc. 3rd Int. Congr. Neurotechnology, Electron. Informatics*, no. Neurotechnix, pp. 101–105, 2015, doi: 10.5220/0005606301010105.

[233] E. Kao, C. Yang, R. Warren, A. Kozinda, and L. Lin, "ALD titanium nitride on vertically aligned carbon nanotube forests for electrochemical supercapacitors," *Sensors Actuators, A Phys.*, vol. 240, pp. 160–166, 2016, doi: 10.1016/j.sna.2016.01.044.

[234] A. Achour *et al.*, "Role of nitrogen doping at the surface of titanium nitride thin films towards capacitive charge storage enhancement," *J. Power Sources*, vol. 359, pp. 349–354, 2017, doi: 10.1016/j.jpowsour.2017.05.074.

[235] A. Achour *et al.*, "Hierarchical nanocomposite electrodes based on titanium nitride and carbon nanotubes for micro-supercapacitors," *Nano Energy*, vol. 7, pp. 104–113, 2014, doi: 10.1016/j.nanoen.2014.04.008.

[236] G. Hasegawa *et al.*, "Impact of Electrolyte on Pseudocapacitance and Stability of Porous Titanium Nitride (TiN) Monolithic Electrode," *J. Electrochem. Soc.*, vol. 162, no. 1, pp. A77–A85, 2015, doi: 10.1149/2.0491501jes.

[237] S. Logothetidis, E. I. Meletis, G. Stergioudis, and A. A. Adjaottor, "Room temperature oxidation behavior of TiN thin films," *Thin Solid Films*, vol. 338, no. 1–2, pp. 304–313, 1999, doi: 10.1016/S0040-6090(98)00975-4.

[238] S. Logothetidis and A. Barborica, "In-situ and real time room temperature oxidation studies of fee TiN thin films," *Microelectron. Eng.*, vol. 33, no. 1–4, pp. 309–316, 1997, doi: 10.1016/s0167-9317(96)00059-7.

[239] V. Augustyn, P. Simon, and B. Dunn, "Pseudocapacitive oxide materials for high-rate electrochemical energy storage," *Energy Environ. Sci.*, vol. 7, no. 5, pp. 1597–1614, 2014, doi: 10.1039/c3ee44164d.

[240] I. G. Morozov, O. V. Belousova, O. A. Belyakov, I. P. Parkin, S. Sathasivam, and M. V. Kuznetcov, "Titanium nitride room-temperature ferromagnetic nanoparticles," *J. Alloys Compd.*, vol. 675, pp. 266–276, 2016, doi: 10.1016/j.jallcom.2016.03.111.

[241] M. N. Gueye, A. Carella, J. Faure-Vincent, R. Demadrille, and J. P. Simonato, "Progress in understanding structure and transport properties of PEDOT-based materials: A critical review," *Prog. Mater. Sci.*, vol. 108, no. October 2018, 2020, doi: 10.1016/j.pmatsci.2019.100616.

[242] Q. Li, Q. Zhou, L. Wen, and W. Liu, "Enhanced thermoelectric performances of flexible PEDOT:PSS film by synergistically tuning the ordering structure and oxidation state," *J. Mater.*, vol. 6, no. 1, pp. 119–127, 2020, doi: 10.1016/j.jmat.2020.01.001.

[243] K. Trzciński, M. Szkoda, A. P. Nowak, M. Łapiński, and A. Lisowska-Oleksiak, "Widening of the electroactivity potential range by composite formation - capacitive properties of TiO2/BiVO4/PEDOT:PSS electrodes in contact with an aqueous electrolyte," *Beilstein J.*

Nanotechnol., vol. 10, pp. 483–493, 2019, doi: 10.3762/BJNANO.10.49.

[244] S. M. Kim *et al.*, "High-performance, polymer-based direct cellular interfaces for electrical stimulation and recording," *NPG Asia Mater.*, vol. 10, no. 4, pp. 255–265, 2018, doi: 10.1038/s41427-018-0014-9.

[245] K. Sun *et al.*, "Review on application of PEDOTs and PEDOT:PSS in energy conversion and storage devices," *J. Mater. Sci. Mater. Electron.*, vol. 26, no. 7, pp. 4438–4462, 2015, doi: 10.1007/s10854-015-2895-5.

[246] J. Song *et al.*, "High-Conductivity , Flexible and Transparent PEDOT : PSS Electrodes for High Performance Semi-Transparent Supercapacitors," *Polymers (Basel).*, vol. 12, no. 450, 2020.

[247] Z. Rahimzadeh, S. M. Naghib, Y. Zare, and K. Y. Rhee, "An overview on the synthesis and recent applications of conducting poly(3,4-ethylenedioxythiophene) (PEDOT) in industry and biomedicine," *J. Mater. Sci.*, vol. 55, no. 18, pp. 7575–7611, 2020, doi: 10.1007/s10853-020-04561-2.

[248] C. Boehler, Z. Aqrawe, and M. Asplund, "Applications of PEDOT in bioelectronic medicine," *Bioelectron. Med.*, vol. 2, no. 2, pp. 89–99, 2019, doi: 10.2217/bem-2019-0014.

[249] R. Kroon *et al.*, "Thermoelectric plastics: From design to synthesis, processing and structure-property relationships," *Chem. Soc. Rev.*, vol. 45, no. 22, pp. 6147–6164, 2016, doi: 10.1039/c6cs00149a.

[250] J. Rivnay *et al.*, "Structural control of mixed ionic and electronic transport in conducting polymers," *Nat. Commun.*, vol. 7, pp. 11287–11289, 2016, doi: 10.1038/ncomms11287.

[251] B. Bessaire *et al.*, "Synthesis of continuous conductive PEDOT: PSS nanofibers by electrospinning: A conformal coating for optoelectronics," *ACS Appl. Mater. Interfaces*, vol. 9, no. 1, pp. 950–957, 2017, doi: 10.1021/acsami.6b13453.

[252] J. A. Chikar, J. L. Hendricks, S. M. Richardson-Burns, Y. Raphael, B. E. Pfingst, and D. C. Martin, "The use of a dual PEDOT and RGD-functionalized alginate hydrogel coating to provide sustained drug delivery and improved cochlear implant function," *Biomaterials*, vol. 33, no. 7, pp. 1982–1990, 2012, doi: 10.1016/j.biomaterials.2011.11.052.

[253] H. S. Mandal *et al.*, "Improving the performance of poly(3,4-ethylenedioxythiophene) for brain-machine interface applications," *Acta Biomater.*, vol. 10, no. 6, pp. 2446–2454, 2014, doi: 10.1016/j.actbio.2014.02.029.

[254] A. Luraghi, F. Peri, and L. Moroni, "Electrospinning for drug delivery applications: A review," *J. Control. Release*, vol. 334, pp. 463–484, 2021, doi: 10.1016/j.jconrel.2021.03.033.

[255] Y. Liang, A. Offenhäusser, S. Ingebrandt, and D. Mayer, "PEDOT:PSS-Based Bioelectronic Devices for Recording and Modulation of Electrophysiological and Biochemical Cell Signals," *Adv. Healthc. Mater.*, vol. 10, no. 11, pp. 1–24, 2021, doi: 10.1002/adhm.202100061.

[256] X. Tracy Cui and D. Daomin Zhou, "Poly (3,4-ethylenedioxythiophene) for chronic neural stimulation," in *IEEE Transactions on Neural Systems and Rehabilitation Engineering*, 2007, vol. 15, no. 4, pp. 502–508. doi: 10.1097/00004691-198701000-00012.

[257] W. Li, J. Chen, J. Zhao, J. Zhang, and J. Zhu, "Application of ultrasonic irradiation in preparing conducting polymer as active materials for supercapacitor," *Mater. Lett.*, vol. 59, no. 7, pp. 800–803, 2005, doi: 10.1016/j.matlet.2004.11.024.

[258] K. Siuzdak, M. Sawczak, and A. Lisowska-Oleksiak, "Fabrication and properties of electrode material composed of ordered titania nanotubes and pEDOT:PSS," *Solid State Ionics*, vol. 271, pp. 56–62, 2015, doi: 10.1016/j.ssi.2014.09.041.

[259] C. Boehler, F. Oberueber, S. Schlabach, T. Stieglitz, and M. Asplund, "Long-Term Stable Adhesion for Conducting Polymers in Biomedical Applications: IrOx and Nanostructured Platinum Solve the Chronic Challenge," *ACS Appl. Mater. Interfaces*, vol. 9, no. 1, pp. 189–197, 2017, doi: 10.1021/acsami.6b13468.

[260] J. Leal, N. Jedrusik, S. Shaner, C. Boehler, and M. Asplund, "SIROF stabilized PEDOT/PSS

allows biocompatible and reversible direct current stimulation capable of driving electrotaxis in cells," *Biomaterials*, vol. 275, 2021, doi: 10.1016/j.biomaterials.2021.120949.

[261] V. A. Bhanu and K. Kishore, "Role of Oxygen in Polymerization reactions," *Chem. Rev.*, vol. 91, no. 2, pp. 99–117, 1991, doi: 10.1201/b16743-12.

[262] P. Cheah, C. N. Bhikha, J. H. O'Haver, and A. E. Smith, "Effect of Oxygen and Initiator Solubility on Admicellar Polymerization of Styrene on Silica Surfaces," *Int. J. Polym. Sci.*, vol. 2017, 2017, doi: 10.1155/2017/6308603.

[263] S. Nie, Z. Li, Y. Yao, and Y. Jin, "Progress in Synthesis of Conductive Polymer Poly(3,4-Ethylenedioxythiophene)," *Front. Chem.*, vol. 9, no. December, pp. 1–8, 2021, doi: 10.3389/fchem.2021.803509.

[264] D. Minudri *et al.*, "Water Soluble Cationic Poly(3,4-Ethylenedioxythiophene) PEDOT-N as a Versatile Conducting Polymer for Bioelectronics," *Adv. Electron. Mater.*, vol. 6, no. 10, 2020, doi: 10.1002/aelm.202000510.

[265] M. H. Wang *et al.*, "Direct electrodeposition of Graphene enhanced conductive polymer on microelectrode for biosensing application," *Biosens. Bioelectron.*, vol. 99, no. July 2017, pp. 99–107, 2018, doi: 10.1016/j.bios.2017.07.030.

[266] M. Bianchi *et al.*, "Scaling of capacitance of PEDOT : PSS : volume vs. area," *J. Mater. Chem. C*, vol. 8, pp. 11252–11262, 2020, doi: 10.1039/d0tc00992j.

[267] L. Cao, Q. Tang, and G. Wang, "Synthesis and performance of cross-linked PEDOT:MOI-P(SS-HEA) transparent conductive films by UV irradiation," *RSC Adv.*, vol. 6, pp. 29592–29597, 2016, doi: 10.1039/C6RA02859D.

[268] X. Huang, L. Deng, F. Liu, Q. Zhang, and G. Chen, "Effect of Crystalline Microstructure Evolution on Thermoelectric Performance of PEDOT : PSS Films," *Energy Mater. Adv.*, vol. 2021, pp. 1–10, 2021, doi: 10.34133/2021/1572537.

[269] L. Ferlauto *et al.*, "Development and Characterization of PEDOT : PSS / Alginate Soft Microelectrodes for Application in Neuroprosthetics Electrode Arrays Used in the Study," *Front. Neurosci.*, vol. 12, pp. 648–658, 2018, doi: 10.3389/fnins.2018.00648.

[270] P. Sakunpongpitiporn, K. Phasuksom, N. Paradee, and A. Sirivat, "Facile synthesis of highly conductive PEDOT : PSS via surfactant templates," *RSC Adv.*, vol. 9, pp. 6363–6378, 2019, doi: 10.1039/c8ra08801b.

[271] Z. Liu *et al.*, "Tuned Transport Behavior of the IPA-Treated PEDOT:PSS Flexible Temperature Sensor via Screen Printing," *J. Electron. Mater.*, vol. 50, no. 4, pp. 2356–2364, 2021, doi: 10.1007/s11664-021-08740-y.

[272] C. M. Palumbiny, F. Liu, T. P. Russell, A. Hexemer, C. Wang, and P. Müller-Buschbaum, "The crystallization of PEDOT:PSS polymeric electrodes probed in situ during printing," *Adv. Mater.*, vol. 27, no. 22, pp. 3391–3397, 2015, doi: 10.1002/adma.201500315.

[273] S. H. Chang, C. H. Chiang, F. S. Kao, C. L. Tien, and C. G. Wu, "Unraveling the Enhanced Electrical Conductivity of PEDOT:PSS Thin Films for ITO-Free Organic Photovoltaics," *IEEE Photonics J.*, vol. 6, no. 4, 2014, doi: 10.1109/JPHOT.2014.2331254.

[274] J. Yang *et al.*, "Modulating resistive switching by diluted additive of poly(vinylpyrrolidone) in poly(3,4-ethylenedioxythiophene): poly(styrenesulfonate)," *J. Appl. Phys.*, vol. 110, no. 11, 2011, doi: 10.1063/1.3666057.

[275] Q. Zhao, R. Jamal, L. Zhang, M. Wang, and T. Abdiryim, "The structure and properties of PEDOT synthesized by template-free solution method," *Nanoscale Res. Lett.*, vol. 9, no. 1, pp. 1–9, 2014, doi: 10.1186/1556-276X-9-557.

[276] T. A. Yemata *et al.*, "Modulation of the doping level of PEDOT:PSS film by treatment with hydrazine to improve the Seebeck coefficient," *RSC Adv.*, vol. 10, no. 3, pp. 1786–1792, 2020, doi: 10.1039/c9ra07648d.

[277] M. S. Mahajan, D. M. Marathe, S. S. Ghosh, V. Ganesan, and J. V. Sali, "Changes in in-plane

electrical conductivity of PEDOT:PSS thin films due to electric field induced dipolar reorientation," *RSC Adv.*, vol. 5, no. 105, pp. 86393–86401, 2015, doi: 10.1039/c5ra13610e.

[278] A. J. Olivares *et al.*, "Nanostructural modification of PEDOT:PSS for high charge carrier collection in hybrid frontal interface of solar cells," *Polymers (Basel).*, vol. 11, no. 6, pp. 1–17, 2019, doi: 10.3390/polym11061034.

[279] E. Noormohammadi, F. Poli, C. Durante, M. Lunardon, S. Sanjabi, and F. Soavi, "Electrodeposition of Cobalt-Copper Oxides Decorated with Conductive Polymer for Supercapacitor Electrodes with High Stability," vol. 202200102, pp. 1–11, 2022, doi: 10.1002/celc.202200102.

[280] A. Elschner and W. Lövenich, "Solution-deposited PEDOT for transparent conductive applications," *MRS Bull.*, vol. 36, no. 10, pp. 794–798, 2011, doi: 10.1557/mrs.2011.232.

[281] P. V. Almeidaa, C. M. S. Izumia, H. F. Dos Santosa, and and A. C. Sant'Anaa, "Spectroscopic characterization of pedot:pss conducting polymer by resonance raman and serrs spectroscopies," *Quim. Nova*, vol. 42, no. 9, pp. 1073–1080, 2019.

[282] A. S. Pranti, A. Schander, A. Bödecker, and W. Lang, "PEDOT: PSS coating on gold microelectrodes with excellent stability and high charge injection capacity for chronic neural interfaces," *Sensors Actuators, B Chem.*, vol. 275, no. March, pp. 382–393, 2018, doi: 10.1016/j.snb.2018.08.007.

[283] S. Venkatraman *et al.*, "In vitro and in vivo evaluation of PEDOT microelectrodes for neural stimulation and recording," *IEEE Trans. Neural Syst. Rehabil. Eng.*, vol. 19, no. 3, pp. 307–316, 2011, doi: 10.1109/TNSRE.2011.2109399.

[284] A. Inoue, H. Yuk, B. Lu, and X. Zhao, "Strong adhesion of wet conducting polymers on diverse substrates," *Sci. Adv.*, vol. 6, no. 12, pp. 1–11, 2020, doi: 10.1126/sciadv.aay5394.

[285] X. Fan *et al.*, "High-efficiency robust organic solar cells using transfer-printed PEDOT:PSS electrodes through interface bonding engineering," *Mater. Chem. Front.*, vol. 3, no. 5, pp. 901–908, 2019, doi: 10.1039/c8qm00614h.

[286] Y. Lu, H. Lyu, A. G. Richardson, T. H. Lucas, and D. Kuzum, "Flexible Neural Electrode Array Based-on Porous Graphene for Cortical Microstimulation and Sensing," *Sci. Rep.*, vol. 6, no. September, pp. 1–9, 2016, doi: 10.1038/srep33526.

[287] T. Zhang *et al.*, "Comparison of cytotoxic and inflammatory responses of pristine and functionalized multi-walled carbon nanotubes in RAW 264.7 mouse macrophages," *J. Hazard. Mater.*, vol. 219–220, pp. 203–212, 2012, doi: 10.1016/j.jhazmat.2012.03.079.

[288] V. S. Vajrala, V. Saunier, L. G. Nowak, E. Flahaut, C. Bergaud, and A. Maziz, "Nanofibrous PEDOT-Carbon Composite on Flexible Probes for Soft Neural Interfacing," *Front. Bioeng. Biotechnol.*, vol. 9, no. November, pp. 1–15, 2021, doi: 10.3389/fbioe.2021.780197.

[289] K. Fraser *et al.*, "Histopathology of the broad class of carbon nanotubes and nanofibers used or produced in U.S. facilities in a murine model," *Part. Fibre Toxicol.*, vol. 18, no. 1, pp. 1–26, 2021, doi: 10.1186/s12989-021-00440-z.

[290] E. R. Kisin *et al.*, "Genotoxicity of carbon nanofibers: Are they potentially more or less dangerous than carbon nanotubes or asbestos?," *Toxicol. Appl. Pharmacol.*, vol. 252, no. 1, pp. 1–10, 2011, doi: 10.1016/j.taap.2011.02.001.

[291] X. Wang *et al.*, "Multi-walled carbon nanotubes induce apoptosis via mitochondrial pathway and scavenger receptor," *Toxicol. Vitr.*, vol. 26, no. 6, pp. 799–806, 2012, doi: 10.1016/j.tiv.2012.05.010.

[292] S. Meijs *et al.*, "Biofouling resistance of boron-doped diamond neural stimulation electrodes is superior to titanium nitride electrodes in vivo," *J. Neural Eng.*, vol. 13, no. 5, 2016, doi: 10.1088/1741-2560/13/5/056011.

[293] C. P. Pennisi, "Diamond / Porous Titanium Nitride Electrodes With Superior Electrochemical Performance for Neural Interfacing," vol. 6, no. November, pp. 1–10, 2018, doi:

10.3389/fbioe.2018.00171.

[294] M. Alcaide, A. Taylor, M. Fjorback, V. Zachar, and C. P. Pennisi, “Boron-doped nanocrystalline diamond electrodes for neural interfaces: In vivo biocompatibility evaluation,” *Front. Neurosci.*, vol. 10, no. MAR, pp. 1–9, 2016, doi: 10.3389/fnins.2016.00087.

[295] C. Köhler, A. Kloke, A. Drzyzga, R. Zengerle, and S. Kerzenmacher, “Fabrication of highly porous platinum electrodes for micro-scale applications by pulsed electrodeposition and dealloying,” *J. Power Sources*, vol. 242, pp. 255–263, 2013, doi: 10.1016/j.jpowsour.2013.05.035.

[296] A. Bourkoula *et al.*, “Roughness threshold for cell attachment and proliferation on plasma micro-nanotextured polymeric surfaces: The case of primary human skin fibroblasts and mouse immortalized 3T3 fibroblasts,” *J. Phys. D. Appl. Phys.*, vol. 49, no. 30, p. 304002, 2016, doi: 10.1088/0022-3727/49/30/304002.

[297] C. H. Choi, S. H. Hagvall, B. M. Wu, J. C. Y. Dunn, R. E. Beygui, and C. J. CJ Kim, “Cell interaction with three-dimensional sharp-tip nanotopography,” *Biomaterials*, vol. 28, no. 9, pp. 1672–1679, 2007, doi: 10.1016/j.biomaterials.2006.11.031.

[298] L. A. Cyster, K. G. Parker, T. L. Parker, and D. M. Grant, “The effect of surface chemistry and nanotopography of titanium nitride (TiN) films on 3T3-L1 fibroblasts,” *J. Biomed. Mater. Res. - Part A*, vol. 67, no. 1, pp. 138–147, 2003, doi: 10.1002/jbm.a.10087.

[299] C. P. Pennisi *et al.*, “Nanoscale topography reduces fibroblast growth, focal adhesion size and migration-related gene expression on platinum surfaces,” *Colloids Surfaces B Biointerfaces*, vol. 85, no. 2, pp. 189–197, 2011, doi: 10.1016/j.colsurfb.2011.02.028.

[300] M. Marzocchi *et al.*, “Physical and Electrochemical Properties of PEDOT:PSS as a Tool for Controlling Cell Growth,” *ACS Appl. Mater. Interfaces*, vol. 7, no. 32, pp. 17993–18003, 2015, doi: 10.1021/acsami.5b04768.

[301] H. M. Alishah *et al.*, “Effect of UV exposure of ITO/PEDOT:PSS substrates on the performance of inverted-type perovskite solar cells,” *J. Mater. Sci. Mater. Electron.*, vol. 31, no. 10, pp. 7968–7980, 2020, doi: 10.1007/s10854-020-03336-4.

[302] L. V. Lingstedt *et al.*, “Effect of DMSO Solvent Treatments on the Performance of PEDOT:PSS Based Organic Electrochemical Transistors,” *Adv. Electron. Mater.*, vol. 5, no. 3, pp. 1–8, 2019, doi: 10.1002/aelm.201800804.

[303] I. Song, N. Yeon Park, G. Seung Jeong, J. Hwan Kang, J. Hwa Seo, and J. Y. Choi, “Conductive channel formation for enhanced electrical conductivity of PEDOT:PSS with high work-function,” *Appl. Surf. Sci.*, vol. 529, no. July, 2020, doi: 10.1016/j.apsusc.2020.147176.

[304] T. D. Y. Kozai *et al.*, “Chronic in vivo evaluation of PEDOT/CNT for stable neural recordings,” in *IEEE Trans Biomed Eng*, 2016, vol. 63, no. 1, pp. 111–119. doi: 10.1109/TBME.2015.2445713.Chronic.

[305] G. Filho, C. Júnior, B. Spinelli, I. Damasceno, F. Fiuza, and E. Morya, “All-Polymeric Electrode based on PEDOT:PSS for In-Vivo Neural Recording,” *Biosensors*, vol. 12, no. 10, 2022, doi: 10.20944/preprints202209.0222.v1.

[306] C. C. Hsu *et al.*, “Anti-fouling and anti-coagulation capabilities of PEDOT-biopolymer coating by in-situ electrochemical copolymerization,” *Surf. Coatings Technol.*, vol. 397, no. May, p. 125963, 2020, doi: 10.1016/j.surfcoat.2020.125963.

[307] D. O. Meredith, L. Eschbach, M. A. Wood, M. O. Riehle, A. S. G. Curtis, and R. G. Richards, “Human fibroblast reactions to standard and electropolished titanium and Ti-6Al-7Nb, and electropolished stainless steel,” *J. Biomed. Mater. Res. - Part A*, vol. 75, no. 3, pp. 541–555, 2005, doi: 10.1002/jbm.a.30457.

[308] D. O. Meredith, L. Eschbach, M. O. Riehle, A. S. G. Curtis, and R. G. Richards, “Microtopography of Metal Surfaces Influence Fibroblast Growth by Modifying Cell Shape, Cytoskeleton, and Adhesion,” *J. Orthop. Res. Sept.*, vol. 25, no. June, pp. 1121–1127, 2007, doi: 10.1002/jor.

[309] Z. Deng, R. Zhu, L. Ma, K. Zhou, Z. Yu, and Q. Wei, “Diamond for antifouling applications: A review,” *Carbon N. Y.*, vol. 196, no. April 2021, pp. 923–939, 2022, doi: 10.1016/j.carbon.2022.05.015.

[310] O. Dunseath *et al.*, “Studies of Black Diamond as an antibacterial surface for Gram Negative bacteria: the interplay between chemical and mechanical bactericidal activity,” *Sci. Rep.*, vol. 9, no. 1, pp. 1–10, 2019, doi: 10.1038/s41598-019-45280-2.

[311] N. Torres-martinez *et al.*, “Evaluation of chronically implanted subdural boron doped diamond / CNT recording electrodes in miniature swine brain To cite this version : HAL Id : hal-03487040 Evaluation of Chronically implanted Subdural Boron Doped Diamond / CNT recording electrodes i,” 2021.

[312] R. Ding, N. C. Miller, K. M. Woeppel, X. T. Cui, and T. D. B. Jacobs, “Surface Area and Local Curvature: Why Roughness Improves the Bioactivity of Neural Implants,” *Langmuir*, vol. 38, no. 24, pp. 7512–7521, 2022, doi: 10.1021/acs.langmuir.2c00473.

[313] A. Domínguez-Bajo *et al.*, “Nanostructured gold electrodes promote neural maturation and network connectivity,” *Biomaterials*, vol. 279, 2021, doi: 10.1016/j.biomaterials.2021.121186.

[314] C. A. R. Chapman *et al.*, “Nanoporous gold as a neural interface coating: Effects of topography, surface chemistry, and feature size,” *ACS Appl. Mater. Interfaces*, vol. 7, no. 13, pp. 7093–7100, 2015, doi: 10.1021/acsami.5b00410.

[315] D. Koch, W. J. Rosoff, J. Jiang, H. M. Geller, and J. S. Urbach, “Strength in the periphery: Growth cone biomechanics and substrate rigidity response in peripheral and central nervous system neurons,” *Biophys. J.*, vol. 102, no. 3, pp. 452–460, 2012, doi: 10.1016/j.bpj.2011.12.025.

[316] A. P. Balgude, X. Yu, A. Szymanski, and R. V. Bellamkonda, “Agarose gel stiffness determines rate of DRG neurite extension in 3D cultures,” *Biomaterials*, vol. 22, no. 10, pp. 1077–1084, 2001, doi: 10.1016/S0142-9612(00)00350-1.

[317] G. Cellot *et al.*, “PEDOT:PSS interfaces support the development of neuronal synaptic networks with reduced neuroglia response in vitro,” *Front. Neurosci.*, vol. 9, no. JAN, pp. 1–11, 2016, doi: 10.3389/fnins.2015.00521.

[318] B. Liu, C. Pavlou, Z. Wang, Y. Cang, C. Galiotis, and G. Fytas, “Determination of the elastic moduli of CVD graphene by probing graphene/polymer Bragg stacks,” *2D Mater.*, vol. 8, no. 3, 2021, doi: 10.1088/2053-1583/abfedb.

[319] J. W. Jiang, J. S. Wang, and B. Li, “Young’s modulus of graphene: A molecular dynamics study,” *Phys. Rev. B - Condens. Matter Mater. Phys.*, vol. 80, no. 11, 2009, doi: 10.1103/PhysRevB.80.113405.

[320] X. Wang, X. Shen, F. Sun, and B. Shen, “Influence of boron doping level on the basic mechanical properties and erosion behavior of boron-doped micro-crystalline diamond (BDMCD) film,” *Diam. Relat. Mater.*, vol. 73, pp. 218–231, 2017, doi: 10.1016/j.diamond.2016.09.025.

[321] H. Issele, D. Mercier, L. Vignoud, and C. Olagnon, “Determination of the young’s modulus of a TiN thin Film by Nanoindentation: Analytical models and FEM simulation,” *e-Journal Surf. Sci. Nanotechnol.*, vol. 10, no. September 2016, pp. 624–629, 2012, doi: 10.1380/ejssnt.2012.624.

[322] T. H. Fang, S. R. Jian, and D. S. Chuu, “Nanomechanical properties of TiC, TiN and TiCN thin films using scanning probe microscopy and nanoindentation,” *Appl. Surf. Sci.*, vol. 228, no. 1–4, pp. 365–372, 2004, doi: 10.1016/j.apsusc.2004.01.053.

[323] M. Rivas, “Iridium Oxide (IrO2) as a Top Electrode for Ferroelectric Micro-Electro-Mechanical Systems (MEMS) Devices for Radiation Rich Environments,” 2018.

[324] K. Abbas, “Characterization of the mechanical properties of freestanding platinum thin films,” p. 121, 2013.

[325] A. Mathur and J. Erlebacher, “Size dependence of effective Young’s modulus of nanoporous

gold," *Appl. Phys. Lett.*, vol. 90, no. 6, pp. 2005–2008, 2007, doi: 10.1063/1.2436718.

[326] N. Kim *et al.*, "Elastic conducting polymer composites in thermoelectric modules," *Nat. Commun.*, vol. 11, no. 1, 2020, doi: 10.1038/s41467-020-15135-w.

[327] U. Lang, N. Naujoks, and J. Dual, "Mechanical characterization of PEDOT:PSS thin films," *Synth. Met.*, vol. 159, no. 5–6, pp. 473–479, 2009, doi: 10.1016/j.synthmet.2008.11.005.

[328] A. Pisciotta *et al.*, "PEDOT: PSS promotes neurogenic commitment of neural crest-derived stem cells," *Front. Physiol.*, vol. 13, no. August, pp. 1–17, 2022, doi: 10.3389/fphys.2022.930804.

[329] F. Pires, Q. Ferreira, C. A. V. Rodrigues, J. Morgado, and F. C. Ferreira, "Neural stem cell differentiation by electrical stimulation using a cross-linked PEDOT substrate: Expanding the use of biocompatible conjugated conductive polymers for neural tissue engineering," *Biochim. Biophys. Acta - Gen. Subj.*, vol. 1850, no. 6, pp. 1158–1168, 2015, doi: 10.1016/j.bbagen.2015.01.020.

[330] L. Ferlauto *et al.*, "All-polymeric transient neural probe for prolonged in-vivo electrophysiological recordings," *Biomaterials*, vol. 274, no. November 2020, 2021, doi: 10.1016/j.biomaterials.2021.120889.

[331] A. S. Hoffman, "Hydrogels for biomedical applications," *Adv. Drug Deliv. Rev.*, vol. 64, no. SUPPL., pp. 18–23, 2012, doi: 10.1016/j.addr.2012.09.010.

[332] K. Y. Lee and D. J. Mooney, "Alginate: Properties and biomedical applications," *Prog. Polym. Sci.*, vol. 37, no. 1, pp. 106–126, 2012, doi: 10.1016/j.progpolymsci.2011.06.003.

[333] Q. Chen, X. Tian, J. Fan, H. Tong, Q. Ao, and X. Wang, "An Interpenetrating Alginate/Gelatin Network for Three-Dimensional (3D) Cell Cultures and Organ Bioprinting," *Molecules*, vol. 25, no. 756, 2020.

[334] J. Goding, C. Vallejo-Giraldo, O. Syed, and R. Green, "Considerations for hydrogel applications to neural bioelectronics," *J. Mater. Chem. B*, vol. 7, no. 10, pp. 1625–1636, 2019, doi: 10.1039/c8tb02763c.

[335] C. J. Wright *et al.*, "Synthesis and 3D printing of conducting alginate–polypyrrole ionomers," *Gels*, vol. 6, no. 2, pp. 1–12, 2020, doi: 10.3390/gels6020013.

[336] M. Mahinroosta, Z. Jomeh Farsangi, A. Allahverdi, and Z. Shakoori, "Hydrogels as intelligent materials: A brief review of synthesis, properties and applications," *Mater. Today Chem.*, vol. 8, pp. 42–55, 2018, doi: 10.1016/j.mtchem.2018.02.004.

[337] F. Abasalizadeh *et al.*, "Alginate-based hydrogels as drug delivery vehicles in cancer treatment and their applications in wound dressing and 3D bioprinting," *J. Biol. Eng.*, vol. 14, no. 8, pp. 1–22, 2020, doi: 10.1186/s13036-020-00239-0.

[338] M. I. Neves, L. Moroni, and C. C. Barrias, "Modulating Alginate Hydrogels for Improved Biological Performance as Cellular 3D Microenvironments," *Front. Bioeng. Biotechnol.*, vol. 8, no. June, 2020, doi: 10.3389/fbioe.2020.00665.

[339] M. Szekalska, A. Puciłowska, E. Szymańska, P. Ciosek, and K. Winnicka, "Alginate: Current Use and Future Perspectives in Pharmaceutical and Biomedical Applications," *Int. J. Polym. Sci.*, vol. 2016, 2016, doi: 10.1155/2016/7697031.

[340] B. Sarker *et al.*, "Evaluation of fibroblasts adhesion and proliferation on alginate-gelatin crosslinked hydrogel," *PLoS One*, vol. 9, no. 9, pp. 1–12, 2014, doi: 10.1371/journal.pone.0107952.

[341] M. M. Campos-Vallette *et al.*, "Characterization of sodium alginate and its block fractions by surface-enhanced Raman spectroscopy," *J. Raman Spectrosc.*, vol. 41, no. 7, pp. 758–763, 2010, doi: 10.1002/jrs.2517.

[342] E. A. Nunamaker, E. K. Purcell, and D. R. Kipke, "In vivo stability and biocompatibility of implanted calcium alginate disks," *J. Biomed. Mater. Res. Part A*, vol. 83, pp. 1128–1137, 2007, doi: 10.1002/jbm.a.

[343] V. Lakshminarayanan, L. Poltorak, E. J. R. Sudhölter, E. Mendes, and J. van Esch, "Electrochemically assisted hydrogel deposition, shaping and detachment," *Electrochim. Acta*, vol. 350, 2020, doi: 10.1016/j.electacta.2020.136352.

[344] W. Chen, B. Zhu, L. Ma, and X. Hua, "Shape-controlled fabrication of cell-laden calcium alginate-PLL hydrogel microcapsules by electrodeposition on microelectrode," *J. Biomater. Appl.*, vol. 32, no. 4, pp. 504–510, 2017, doi: 10.1177/0885328217726439.

[345] T. Schmid, A. Messmer, B. S. Yeo, W. Zhang, and R. Zenobi, "Towards chemical analysis of nanostructures in biofilms II: Tip-enhanced Raman spectroscopy of alginates," *Anal. Bioanal. Chem.*, vol. 391, no. 5, pp. 1907–1916, 2008, doi: 10.1007/s00216-008-2101-1.

[346] I. MacHida-Sano, Y. Matsuda, and H. Namiki, "In vitro adhesion of human dermal fibroblasts on iron cross-linked alginate films," *Biomed. Mater.*, vol. 4, no. 2, 2009, doi: 10.1088/1748-6041/4/2/025008.

[347] R. Singh *et al.*, "Evaluation of hydrogel matrices for vessel bioplotting: Vascular cell growth and viability," *J. Biomed. Mater. Res. - Part A*, vol. 104, no. 3, pp. 577–585, 2016, doi: 10.1002/jbm.a.35590.

[348] J. Zhang *et al.*, "Novel Balanced Charged Alginate/PEI Polyelectrolyte Hydrogel that Resists Foreign-Body Reaction," *ACS Appl. Mater. Interfaces*, vol. 10, no. 8, pp. 6879–6886, 2018, doi: 10.1021/acsami.7b17670.

[349] B. L. Strand *et al.*, "Poly-L-lysine induces fibrosis on alginate microcapsules via the induction of cytokines," *Cell Transplant.*, vol. 10, no. 3, pp. 263–275, 2001, doi: 10.3727/000000001783986800.

[350] T. Hickey, D. Kreutzer, D. J. Burgess, and F. Moussy, "In vivo evaluation of a dexamethasone/PLGA microsphere system designed to suppress the inflammatory tissue response to implantable medical devices," *J. Biomed. Mater. Res.*, vol. 61, no. 2, pp. 180–187, 2002, doi: 10.1002/jbm.10016.

[351] T. D. Y. Kozai, A. S. Jaquins-Gerstl, A. L. Vazquez, A. C. Michael, and X. T. Cui, "Dexamethasone retrodialysis attenuates microglial response to implanted probes in vivo," *Biomaterials*, vol. 87, pp. 157–169, 2016, doi: 10.1016/j.biomaterials.2016.02.013.

[352] N. De la Oliva, X. Navarro, and J. del Valle, "Dexamethasone Reduces the Foreign Body Reaction to Intraneural Electrode Implants in the Peripheral Nerve of the Rat," *Anat. Rec.*, vol. 301, no. 10, pp. 1722–1733, 2018, doi: 10.1002/ar.23920.

[353] M. Matyash, F. Despang, R. Mandal, D. Fiore, M. Gelinsky, and C. Ikonomidou, "Novel soft alginate hydrogel strongly supports neurite growth and protects neurons against oxidative stress," *Tissue Eng. - Part A*, vol. 18, no. 1–2, pp. 55–66, 2012, doi: 10.1089/ten.tea.2011.0097.

[354] A. Banerjee *et al.*, "The influence of hydrogel modulus on the proliferation and differentiation of encapsulated neural stem cells," *Biomaterials*, vol. 30, no. 27, pp. 4695–4699, 2009, doi: 10.1016/j.biomaterials.2009.05.050.

[355] J. Kurowiak, A. Kaczmarek-Pawelska, A. G. Mackiewicz, and R. Bedzinski, "Analysis of the degradation process of alginate-based hydrogels in artificial urine for use as a bioresorbable material in the treatment of urethral injuries," *Processes*, vol. 8, no. 3, 2020, doi: 10.3390/pr8030304.

[356] Z. Ayar, M. Shafieian, O. Sabzevari, and Z. Hassannejad, "Modification of the alginate hydrogel with fibroblast- and Schwann cell-derived extracellular matrix potentiates differentiation of mesenchymal stem cells toward neuron-like cells," *J. Appl. Polym. Sci.*, vol. 139, no. 33, 2022, doi: 10.1002/app.52501.

[357] E. Ansorena *et al.*, "Injectable alginate hydrogel loaded with GDNF promotes functional recovery in a hemisection model of spinal cord injury," *Int. J. Pharm.*, vol. 455, no. 1–2, pp. 148–158, 2013, doi: 10.1016/j.ijpharm.2013.07.045.

[358] E. K. Purcell, A. Singh, and D. R. Kipke, "Alginate composition effects on a neural stem cell-seeded scaffold," *Tissue Eng. - Part C Methods*, vol. 15, no. 4, pp. 541–550, 2009, doi:

10.1089/ten.tec.2008.0302.

[359] J. P. Frampton, M. R. Hynd, M. L. Shuler, and W. Shain, “Fabrication and optimization of alginate hydrogel constructs for use in 3D neural cell culture,” *Biomed. Mater.*, vol. 6, no. 1, 2011, doi: 10.1088/1748-6041/6/1/015002.

[360] M. Golmohamadi and K. J. Wilkinson, “Diffusion of ions in a calcium alginate hydrogel-structure is the primary factor controlling diffusion,” *Carbohydr. Polym.*, vol. 94, no. 1, pp. 82–87, 2013, doi: 10.1016/j.carbpol.2013.01.046.

[361] D. M. Tartakovsky and M. Dentz, “Diffusion in Porous Media: Phenomena and Mechanisms,” *Transp. Porous Media*, vol. 130, no. 1, pp. 105–127, 2019, doi: 10.1007/s11242-019-01262-6.

[362] B. P. Santana *et al.*, “Comparing different methods to fix and to dehydrate cells on alginate hydrogel scaffolds using scanning electron microscopy,” *Microsc. Res. Tech.*, vol. 78, no. 7, pp. 553–561, 2015, doi: 10.1002/jemt.22508.

[363] S. Ansar Ahmed, R. M. Gogal, and J. E. Walsh, “A new rapid and simple non-radioactive assay to monitor and determine the proliferation of lymphocytes: an alternative to [3H]thymidine incorporation assay,” *J. Immunol. Methods*, vol. 170, no. 2, pp. 211–224, 1994, doi: 10.1016/0022-1759(94)90396-4.

[364] T. L. Riss *et al.*, “Cell Viability Assays,” *Assay Guid. Man.*, no. Md, pp. 1–25, 2004, [Online]. Available: http://www.ncbi.nlm.nih.gov/pubmed/23805433

[365] Life Technologies Corporation, “PrestoBlue™ Cell Viability Reagent Protocol - Product Information Sheet,” 2010. [Online]. Available: http://tools.thermofisher.com/content/sfs/manuals/PrestoBlue_Reagent_PIS_15Oct10.pdf

[366] M. M. Shipley, C. A. Mangold, and M. L. Szpara, “Differentiation of the SH-SY5Y human neuroblastoma cell line,” *J. Vis. Exp.*, vol. 2016, no. 108, pp. 1–12, 2016, doi: 10.3791/53193.

[367] J. Kovalevich and D. Langford, “Considerations for the Use of SH-SY5Y Neuroblastoma Cells in Neurobiology,” *Methods Mol Biol.*, vol. 1078, pp. 35–44, 2013, doi: 10.1007/978-1-62703-640-5.

[368] J. Arpa, K. Rechendorff, P. S. Wismayer, and B. Mallia, “Ultra-porous titanium nitride as a dual-action supercapacitor for implantable neural interfacing electrodes,” *Mater. Chem. Phys.*, vol. 289, no. June, p. 126435, 2022, doi: 10.1016/j.matchemphys.2022.126435.

[369] G. Abadias, “Stress and preferred orientation in nitride-based PVD coatings,” *Surf. Coatings Technol.*, vol. 202, no. 11, pp. 2223–2235, 2008, doi: 10.1016/j.surfcoat.2007.08.029.

[370] C. S. Shin *et al.*, “Growth, surface morphology, and electrical resistivity of fully strained substoichiometric epitaxial TiNx ($0.67 \leq x < 1.0$) layers on MgO(001),” *J. Appl. Phys.*, vol. 95, no. 1, pp. 356–362, 2004, doi: 10.1063/1.1629155.

[371] W. Spengler, R. Kaiser, A. N. Christensen, and G. Müller-Vogt, “Raman scattering, superconductivity, and phonon density of states of stoichiometric and nonstoichiometric TiN,” *Phys. Rev. B*, vol. 17, no. 3, pp. 1095–1101, Feb. 1978, doi: 10.1103/PhysRevB.17.1095.

[372] Z. H. Ding, B. Yao, L. X. Qiu, and T. Q. Lv, “Raman scattering investigation of nanocrystalline δ-TiNx synthesized by solid-state reaction,” *J. Alloys Compd.*, vol. 421, no. 1–2, pp. 247–251, 2006, doi: 10.1016/j.jallcom.2005.11.017.

[373] C. C. Kuo, Y. T. Lin, A. Chan, and J. T. Chang, “High temperature wear behavior of titanium nitride coating deposited using high power impulse magnetron sputtering,” *Coatings*, vol. 9, no. 9, pp. 1–13, 2019, doi: 10.3390/coatings9090555.

[374] S. Sedira, S. Achour, A. Avci, and V. Eskizeybek, “Physical deposition of carbon doped titanium nitride film by DC magnetron sputtering for metallic implant coating use,” *Appl. Surf. Sci.*, vol. 295, pp. 81–85, 2014, doi: 10.1016/j.apsusc.2014.01.010.

[375] H. C. Barshilia and K. S. Rajam, “Raman spectroscopy studies on the thermal stability of TiN, CrN, TiAlN coatings and nanolayered TiN/CrN, TiAlN/CrN multilayer coatings,” *J. Mater. Res.*, vol. 19, no. 11, pp. 3196–3205, 2004, doi: 10.1557/JMR.2004.0444.

[376] C. C. Chen, N. Liang, W. Tse, I. Chen, and J. Duh, “Raman Spectra of Titanium Nitride Thin Films,” *Chinese J. Phys.*, vol. 32, pp. 205–210, 1994.

[377] T. Zheng *et al.*, “Sputtered Titanium Nitride Films on Titanium Foam Substrates as Electrodes for High-Power Electrochemical Capacitors,” *ChemElectroChem*, vol. 5, no. 16, pp. 2199–2207, 2018, doi: 10.1002/celc.201800467.

[378] A. Calzolari and A. Catellani, “Controlling the TiN Electrode Work Function at the Atomistic Level: A First Principles Investigation,” *IEEE Access*, vol. 8, pp. 156308–156313, 2020, doi: 10.1109/ACCESS.2020.3017726.

[379] Z. Xu *et al.*, “Topic review: Application of raman spectroscopy characterization in micro/nano-machining,” *Micromachines*, vol. 9, no. 7, 2018, doi: 10.3390/mi9070361.

[380] A. Fujishima, X. Zhang, and D. A. Tryk, “TiO2 photocatalysis and related surface phenomena,” *Surf. Sci. Rep.*, vol. 63, no. 12, pp. 515–582, 2008, doi: 10.1016/j.surfrep.2008.10.001.

[381] A. K. Rumaiz, J. C. Woicik, E. Cockayne, H. Y. Lin, G. H. Jaffari, and S. I. Shah, “Oxygen vacancies in N doped anatase TiO2: Experiment and first-principles calculations,” *Appl. Phys. Lett.*, vol. 95, no. 26, pp. 1–4, 2009, doi: 10.1063/1.3272272.

[382] A. U. Chaudhry, B. Mansoor, T. Mungole, G. Ayoub, and D. P. Field, “Corrosion mechanism in PVD deposited nano-scale titanium nitride thin film with intercalated titanium for protecting the surface of silicon,” *Electrochim. Acta*, vol. 264, pp. 69–82, 2018, doi: 10.1016/j.electacta.2018.01.042.

[383] P. Pedrosa *et al.*, “TiN x coated polycarbonate for bio-electrode applications,” *Corros. Sci.*, vol. 56, pp. 49–57, 2012, doi: 10.1016/j.corsci.2011.11.008.

[384] S. K. Dhoke and A. S. Khanna, “Electrochemical impedance spectroscopy (EIS) study of nano-alumina modified alkyd based waterborne coatings,” *Prog. Org. Coatings*, vol. 74, no. 1, pp. 92–99, 2012, doi: 10.1016/j.porgcoat.2011.11.020.

[385] N. Waters, R. Connolly, D. W. Brown, and B. Lakowski, “Electrochemical Impedance Spectroscopy for Coating Evaluation using a Micro Sensor,” 2014.

[386] A. M. Bryan, L. M. Santino, Y. Lu, S. Acharya, and J. M. D’Arcy, “Conducting Polymers for Pseudocapacitive Energy Storage,” *Chem. Mater.*, vol. 28, no. 17, pp. 5989–5998, 2016, doi: 10.1021/acs.chemmater.6b01762.

[387] M. de Pauli *et al.*, “Capacitance spectra extracted from EIS by a model-free generalized phase element analysis,” *Electrochim. Acta*, vol. 320, p. 134366, 2019, doi: 10.1016/j.electacta.2019.06.059.

[388] B. Yan *et al.*, “Facile synthesis of MnPO4·H2O nanowire/graphene oxide composite material and its application as electrode material for high performance supercapacitors,” *Catalysts*, vol. 6, no. 12, 2016, doi: 10.3390/catal6120198.

[389] P. Yang *et al.*, “Ultrafast-charging supercapacitors based on corn-like titanium nitride nanostructures,” *Adv. Sci.*, vol. 3, no. 6, pp. 1–7, 2015, doi: 10.1002/advs.201500299.

[390] B. M. Gray, A. L. Hector, M. Jura, J. R. Owen, and J. Whittam, “Effect of oxidative surface treatments on charge storage at titanium nitride surfaces for supercapacitor applications,” *J. Mater. Chem. A*, vol. 5, no. 9, pp. 4550–4559, 2017, doi: 10.1039/C6TA08308K.

[391] M. Toupin, T. Brousse, and D. Bélanger, “Charge storage mechanism of MnO2 electrode used in aqueous electrochemical capacitor,” *Chem. Mater.*, vol. 16, no. 16, pp. 3184–3190, 2004, doi: 10.1021/cm049649j.

[392] S. Fleischmann *et al.*, “Continuous transition from double-layer to Faradaic charge storage in confined electrolytes,” *Nat. Energy*, vol. 7, no. 3, pp. 222–228, 2022, doi: 10.1038/s41560-022-00993-z.

[393] J. Wang *et al.*, “Pseudocapacitive materials for electrochemical capacitors: From rational synthesis to capacitance optimization,” *Natl. Sci. Rev.*, vol. 4, no. 1, pp. 71–90, 2017, doi: 10.1093/nsr/nww072.

[394] S. Dsoke, K. Pfeifer, and Z. Zhao, *The role of nanomaterials for supercapacitors and hybrid devices*, 1st ed., vol. 19. Elsevier Ltd., 2021. doi: 10.1016/B978-0-12-821434-3.00001-6.

[395] A. Eftekhari and M. Mohamedi, "Tailoring pseudocapacitive materials from a mechanistic perspective," *Mater. Today Energy*, vol. 6, pp. 211–229, 2017, doi: 10.1016/j.mtener.2017.10.009.

[396] Y. Xie, Y. Wang, and H. Du, "Electrochemical capacitance performance of titanium nitride nanoarray," *Mater. Sci. Eng. B Solid-State Mater. Adv. Technol.*, vol. 178, no. 20, pp. 1443–1451, 2013, doi: 10.1016/j.mseb.2013.09.005.

[397] N. Vicente, M. Haro, and G. Garcia-Belmonte, "New approaches to the lithiation kinetics in reaction-limited battery electrodes through electrochemical impedance spectroscopy," *Chem. Commun.*, vol. 54, no. 9, pp. 1025–1040, 2018, doi: 10.1039/c7cc08373d.

[398] B. Wei, H. Liang, D. Zhang, Z. Qi, H. Shen, and Z. Wang, "Magnetron sputtered TiN thin films toward enhanced performance supercapacitor electrodes," *Mater. Renew. Sustain. Energy*, vol. 7, no. 2, pp. 1–9, 2018, doi: 10.1007/s40243-018-0117-9.

[399] H. Ji *et al.*, "Capacitance of carbon-based electrical double-layer capacitors," *Nat. Commun.*, vol. 5, no. Cmcm, 2014, doi: 10.1038/ncomms4317.

[400] X. Cai, Y. Song, S. Q. Wang, X. Sun, and X. X. Liu, "Extending the cycle life of high mass loading MoOx electrode for supercapacitor applications," *Electrochim. Acta*, vol. 325, p. 134877, 2019, doi: 10.1016/j.electacta.2019.134877.

[401] P. Panjan, A. Drnovšek, P. Gselman, M. Čekada, and M. Panjan, *Review of growth defects in thin films prepared by PVD techniques*, vol. 10, no. 5. 2020. doi: 10.3390/COATINGS10050447.

[402] M. A. Taha, N. A. El-Mahallawy, R. M. Hammouda, and S. I. Nassef, "PVD coating of Mg-AZ31 by thin layer of Al and Al-Si," *J. Coatings Technol. Res.*, vol. 7, no. 6, pp. 793–800, 2010, doi: 10.1007/s11998-010-9252-7.

[403] P. Panjan, A. Drnovšek, N. Mahne, M. Čekada, and M. Panjan, "Surface topography of pvd hard coatings," *Coatings*, vol. 11, no. 11, 2021, doi: 10.3390/coatings11111387.

[404] P. Panjan, A. Drnovšek, P. Terek, A. Miletić, M. Čekada, and M. Panjan, "Comparative Study of Tribological Behavior of TiN Hard Coatings Deposited by Various PVD Deposition Techniques," *Coatings*, vol. 12, no. 3, 2022, doi: 10.3390/coatings12030294.

[405] G. Abadias, Y. Y. Tse, P. Guérin, and V. Pelosin, "Interdependence between stress, preferred orientation, and surface morphology of nanocrystalline TiN thin films deposited by dual ion beam sputtering," *J. Appl. Phys.*, vol. 99, no. 11, 2006, doi: 10.1063/1.2197287.

[406] C. Ducu, S. Moga, D. Negrea, V. Malinovschi, and M. Balaceanu, "Stress and texture in titanium nitride thin films by X-ray diffraction techniques," *J. Optoelectron. Adv. Mater.*, vol. 12, no. 5, pp. 1078–1082, 2010.

[407] R. Bavadi and S. Valedbagi, "Physical properties of titanium nitride thin film prepared by DC magnetron sputtering," *Mater. Phys. Mech.*, vol. 15, no. 2, pp. 167–172, 2012.

[408] D. Zhang and G. Nagayama, "Effective Wetting Area Based on Electrochemical Impedance Analysis: Hydrophilic Structured Surface," *Langmuir*, vol. 35, no. 50, pp. 16508–16513, 2019, doi: 10.1021/acs.langmuir.9b03349.

[409] A. Shodiev *et al.*, "Insight on electrolyte infiltration of lithium ion battery electrodes by means of a new three-dimensional-resolved lattice Boltzmann model," *Energy Storage Mater.*, vol. 38, no. December 2020, pp. 80–92, 2021, doi: 10.1016/j.ensm.2021.02.029.

[410] D. Yang, C. Liu, X. Liu, M. Qi, and G. Lin, "EIS diagnosis on the corrosion behavior of TiN coated NiTi surgical alloy," *Curr. Appl. Phys.*, vol. 5, no. 5, pp. 417–421, 2005, doi: 10.1016/j.cap.2004.11.002.

[411] V. M. C. A. Oliveira, C. Aguiar, A. M. Vazquez, A. Robin, and M. J. R. Barboza, "Improving corrosion resistance of Ti-6Al-4V alloy through plasma-assisted PVD deposited nitride

coatings," *Corros. Sci.*, vol. 88, pp. 317–327, 2014, doi: 10.1016/j.corsci.2014.07.047.

[412] F. Reshadi, S. Khorasani, and G. Faraji, "Surface characterization of nanostructured commercially pure titanium modified by sandblasting and acid-etching for implant applications," *Proc. Inst. Mech. Eng. Part J J. Eng. Tribol.*, vol. 234, no. 3, pp. 414–423, 2020, doi: 10.1177/1350650119864246.

[413] N. Arroyo-Currás, K. Scida, K. L. Ploense, T. E. Kippin, and K. W. Plaxco, "High Surface Area Electrodes Generated via Electrochemical Roughening Improve the Signaling of Electrochemical Aptamer-Based Biosensors," *Anal. Chem.*, vol. 89, no. 22, pp. 12185–12191, 2017, doi: 10.1021/acs.analchem.7b02830.

[414] A. Zintler *et al.*, "Enhanced Conductivity and Microstructure in Highly Textured TiN1- x/ c-Al2O3Thin Films," *ACS Omega*, vol. 7, no. 2, pp. 2041–2048, 2022, doi: 10.1021/acsomega.1c05505.

[415] L. Li *et al.*, "Electrochemical and biological performance of hierarchical platinum-iridium electrodes structured by a femtosecond laser," *Microsystems Nanoeng.*, vol. 8, no. 1, 2022, doi: 10.1038/s41378-022-00433-8.

[416] I. R. Cassar *et al.*, "Electrodeposited platinum-iridium coating improves in vivo recording performance of chronically implanted microelectrode arrays," *Biomaterials*, vol. 205, pp. 120–132, 2019, doi: 10.1016/j.biomaterials.2019.03.017.Electrodeposited.

[417] S. Sommakia, J. L. Rickus, and K. J. Otto, "Effects of adsorbed proteins, an antifouling agent and long-duration DC voltage pulses on the impedance of silicon-based neural microelectrodes," *Proc. 31st Annu. Int. Conf. IEEE Eng. Med. Biol. Soc. Eng. Futur. Biomed. EMBC 2009*, pp. 7139–7142, 2009, doi: 10.1109/IEMBS.2009.5332456.

[418] A. R. Harris, P. Carter, R. Cowan, and G. G. Wallace, "Impact of Protein Fouling on the Charge Injection Capacity, Impedance, and Effective Electrode Area of Platinum Electrodes for Bionic Devices," *ChemElectroChem*, vol. 8, no. 6, pp. 1078–1090, 2021, doi: 10.1002/celc.202001574.

[419] J. Selvakumaran, J. L. Keddie, D. J. Ewins, and M. P. Hughes, "Protein adsorption on materials for recording sites on implantable microelectrodes," *J. Mater. Sci. Mater. Med.*, vol. 19, no. 1, pp. 143–151, 2008, doi: 10.1007/s10856-007-3110-x.

[420] C. Newbold *et al.*, "Changes in biphasic electrode impedance with protein adsorption and cell growth," *J. Neural Eng.*, vol. 7, no. 5, pp. 1741–1766, 2010, doi: 10.1088/1741-2560/7/5/056011.Changes.

[421] B. Guo, J.-I. Anzai, and T. Oza, "Adsorption Behavior of Serum Albumin on Electrode Surfaces and the Effects of Electrode Potential," *Chem. Pharm. Bull.*, vol. 44, no. 4, pp. 800–803, 1996, [Online]. Available: http://www.mendeley.com/research/geology-volcanic-history-eruptive-style-yakedake-volcano-group-central-japan/%0Ahttps://www.sciencedirect.com/science/article/pii/S0038080620318011%0Ahttps://www.jstage.jst.go.jp/article/jjshs1925/72/6/72_6_525/_article/-c

[422] H. S. Magar, R. Y. A. Hassan, and A. Mulchandani, "Electrochemical impedance spectroscopy (Eis): Principles, construction, and biosensing applications," *Sensors*, vol. 21, no. 19, 2021, doi: 10.3390/s21196578.

[423] J.-Q. Chen, X.-X. Ye, L.-W. Liao, Z. Wei, M.-L. Xu, and Y.-X. Chen, "Ohmic Drop Compensation in Electrochemical Measurement," *J. Electrochem.*, vol. 27, no. 3, pp. 291–300, 2021.

[424] M. A. Siddiqui, I. Ullah, H. Liu, S. Zhang, L. Ren, and K. Yang, "Preliminary study of adsorption behavior of bovine serum albumin (BSA) protein and its effect on antibacterial and corrosion property of Ti-3Cu alloy," *J. Mater. Sci. Technol.*, vol. 80, no. January, pp. 117–127, 2021, doi: 10.1016/j.jmst.2020.11.046.

[425] S. Grant *et al.*, "Label-free and reversible immunosensor based upon an ac impedance interrogation protocol," *Anal. Chim. Acta*, vol. 537, no. 1–2, pp. 163–168, 2005, doi: 10.1016/j.aca.2005.01.003.

[426] Z. Mardina, J. Venezuela, M. S. Dargusch, Z. Shi, and A. Atrens, “The influence of the protein bovine serum albumin (BSA) on the corrosion of Mg, Zn, and Fe in Zahrina’s simulated interstitial fluid,” *Corros. Sci.*, vol. 199, no. February, p. 110160, 2022, doi: 10.1016/j.corsci.2022.110160.

[427] J. Wegener, M. Sieber, and H. J. Galla, “Impedance analysis of epithelial and endothelial cell monolayers cultured on gold surfaces,” *J. Biochem. Biophys. Methods*, vol. 32, no. 3, pp. 151–170, 1996, doi: 10.1016/0165-022X(96)00005-X.

[428] S. Karimi, T. Nickchi, and A. Alfantazi, “Effects of bovine serum albumin on the corrosion behaviour of AISI 316L, Co-28Cr-6Mo, and Ti-6Al-4V alloys in phosphate buffered saline solutions,” *Corros. Sci.*, vol. 53, no. 10, pp. 3262–3272, 2011, doi: 10.1016/j.corsci.2011.06.009.

[429] R. A. Green, H. Toor, C. Dodds, and N. H. Lovell, “Variation in performance of platinum electrodes with size and surface roughness,” *Sensors Mater.*, vol. 24, no. 4, pp. 165–180, 2012, doi: 10.18494/sam.2012.821.

[430] S. E. Moulton, J. N. Barisci, A. Bath, R. Stella, and G. G. Wallace, “Investigation of protein adsorption and electrochemical behavior at a gold electrode,” *J. Colloid Interface Sci.*, vol. 261, no. 2, pp. 312–319, 2003, doi: 10.1016/S0021-9797(03)00073-0.

[431] H. Heli, N. Sattarahmady, A. Jabbari, A. A. Moosavi-Movahedi, G. H. Hakimelahi, and F. Y. Tsai, “Adsorption of human serum albumin onto glassy carbon surface - Applied to albumin-modified electrode: Mode of protein-ligand interactions,” *J. Electroanal. Chem.*, vol. 610, no. 1, pp. 67–74, 2007, doi: 10.1016/j.jelechem.2007.07.005.

[432] C. L. *et al.*, “Fibroblast interaction with different abutment surfaces: In vitro study,” *Int. J. Mol. Sci.*, vol. 21, no. 6, 2020, [Online]. Available: http://www.embase.com/search/results?subaction=viewrecord&from=export&id=L2004006609%0Ahttp://dx.doi.org/10.3390/ijms21061919

[433] X. Miao *et al.*, “The response of human osteoblasts, epithelial cells, fibroblasts, macrophages and oral bacteria to nanostructured titanium surfaces: A systematic study,” *Int. J. Nanomedicine*, vol. 12, pp. 1415–1430, 2017, doi: 10.2147/IJN.S126760.

[434] P. Aliuos *et al.*, “Evaluation of single-cell force spectroscopy and fluorescence microscopy to determine cell interactions with femtosecond-laser microstructured titanium surfaces,” *J. Biomed. Mater. Res. - Part A*, vol. 101 A, no. 4, pp. 981–990, 2013, doi: 10.1002/jbm.a.34401.

[435] E. Ngandu Mpoyi, M. Cantini, P. M. Reynolds, N. Gadegaard, M. J. Dalby, and M. Salmerón-Sánchez, “Protein Adsorption as a Key Mediator in the Nanotopographical Control of Cell Behavior,” *ACS Nano*, vol. 10, no. 7, pp. 6638–6647, 2016, doi: 10.1021/acsnano.6b01649.

[436] V. R. Kearns, R. J. McMurray, and M. J. Dalby, “Biomaterial surface topography to control cellular response: Technologies, cell behaviour and biomedical applications,” *Surf. Modif. Biomater. Methods Anal. Appl.*, pp. 169–201, 2011, doi: 10.1533/9780857090768.1.169.

[437] Z. Adamczyk, A. Pomorska, M. Nattich-Rak, M. Wytrwal-Sarna, and A. Bernasik, “Protein adsorption mechanisms at rough surfaces: Serum albumin at a gold substrate,” *J. Colloid Interface Sci.*, vol. 530, pp. 631–641, 2018, doi: 10.1016/j.jcis.2018.06.063.

[438] S. K. Nishimoto *et al.*, “The effect of titanium surface roughening on protein absorption, cell attachment, and cell spreading.,” *Int. J. Oral Maxillofac. Implants*, vol. 23, no. 4, pp. 675–80, 2008, [Online]. Available: http://www.ncbi.nlm.nih.gov/pubmed/18807564

[439] E. Luong-Van *et al.*, “Review: Micro-and nanostructured surface engineering for biomedical applications,” *J. Mater. Res.*, vol. 28, no. 2, pp. 165–174, 2013, doi: 10.1557/jmr.2012.398.

[440] M. A. Kiselev, I. A. Gryzunov, G. E. Dobretsov, and M. N. Komarova, “Size of a human serum albumin molecule in solution,” *Biofizika*, vol. 46, no. 3, pp. 423–7, 2001, [Online]. Available: http://www.ncbi.nlm.nih.gov/pubmed/11449540

[441] F. Robotti *et al.*, “A micron-scale surface topography design reducing cell adhesion to implanted materials,” *Sci. Rep.*, vol. 8, no. 1, pp. 1–13, 2018, doi: 10.1038/s41598-018-29167-2.

[442] V. Castagnola *et al.*, “Parylene-based flexible neural probes with PEDOT coated surface for brain stimulation and recording,” *Biosens. Bioelectron.*, vol. 67, pp. 450–457, 2015, doi: 10.1016/j.bios.2014.09.004.

[443] J. McQuade and L. T. Vuong, “Solvent Retention and Crack Evolution in Dropcast PEDOT:PSS and Dependence on Surface Wetting,” *ACS Omega*, vol. 3, no. 4, pp. 3868–3873, 2018, doi: 10.1021/acsomega.8b00085.

[444] G. Dijk, H. J. Ruigrok, and R. P. O’Connor, “Influence of PEDOT:PSS Coating Thickness on the Performance of Stimulation Electrodes,” *Adv. Mater. Interfaces*, vol. 7, no. 16, pp. 1–9, 2020, doi: 10.1002/admi.202000675.

[445] B. Friedel *et al.*, “Effects of layer thickness and annealing of PEDOT:PSS layers in organic photodetectors,” *Macromolecules*, vol. 42, no. 17, pp. 6741–6747, 2009, doi: 10.1021/ma901182u.

[446] H. Park, S. H. Lee, F. S. Kim, H. H. Choi, I. W. Cheong, and J. H. Kim, “Enhanced thermoelectric properties of PEDOT:PSS nanofilms by a chemical dedoping process,” *J. Mater. Chem. A*, vol. 2, no. 18, pp. 6532–6539, 2014, doi: 10.1039/c3ta14960a.

[447] E. Vitoratos *et al.*, “Thermal degradation mechanisms of PEDOT:PSS,” *Org. Electron.*, vol. 10, no. 1, pp. 61–66, 2009, doi: 10.1016/j.orgel.2008.10.008.

[448] B. Wegler, O. Schmidt, and B. Hensel, “Influence of PEDOT:PSS on the effectiveness of barrier layers prepared by atomic layer deposition in organic light emitting diodes,” *J. Vac. Sci. Technol. A Vacuum, Surfaces, Film.*, vol. 33, no. 1, p. 01A147, 2015, doi: 10.1116/1.4904500.

[449] Q. Wei, M. Mukaida, W. Ding, and T. Ishida, “Humidity control in a closed system utilizing conducting polymers,” *RSC Adv.*, vol. 8, no. 23, pp. 12540–12546, 2018, doi: 10.1039/c8ra01776j.

[450] Y. Xia, G. Yan, and J. Lin, “Review on tailoring pedot:Pss layer for improved device stability of perovskite solar cells,” *Nanomaterials*, vol. 11, no. 11, pp. 1–16, 2021, doi: 10.3390/nano11113119.

[451] X. Fan *et al.*, “PEDOT:PSS for Flexible and Stretchable Electronics: Modifications, Strategies, and Applications,” *Adv. Sci.*, vol. 6, no. 19, 2019, doi: 10.1002/advs.201900813.

[452] P. Córdoba-Torres, T. J. Mesquita, O. Devos, B. Tribollet, V. Roche, and R. P. Nogueira, “On the intrinsic coupling between constant-phase element parameters α and Q in electrochemical impedance spectroscopy,” *Electrochim. Acta*, vol. 72, pp. 172–178, 2012, doi: 10.1016/j.electacta.2012.04.020.

[453] M. H. Martin and A. Lasia, “Influence of experimental factors on the constant phase element behavior of Pt electrodes,” *Electrochim. Acta*, vol. 56, no. 23, pp. 8058–8068, 2011, doi: 10.1016/j.electacta.2011.02.068.

[454] J. B. Jorcin, M. E. Orazem, N. Pébère, and B. Tribollet, “CPE analysis by local electrochemical impedance spectroscopy,” *Electrochim. Acta*, vol. 51, no. 8–9, pp. 1473–1479, 2006, doi: 10.1016/j.electacta.2005.02.128.

[455] D. Levasseur, I. Mjejri, T. Rolland, and A. Rougier, “Color tuning by oxide addition in PEDOT:PSS-based electrochromic devices,” *Polymers (Basel).*, vol. 11, no. 1, pp. 1–12, 2019, doi: 10.3390/polym11010179.

[456] M. H. M. Zaid, J. Abdullah, N. Rozi, A. A. M. Rozlan, and S. A. Hanifah, “A sensitive impedimetric aptasensor based on carbon nanodots modified electrode for detection of 17ß-estradiol,” *Nanomaterials*, vol. 10, no. 7, pp. 1–14, 2020, doi: 10.3390/nano10071346.

[457] S. B. Rauer *et al.*, “Porous PEDOT:PSS Particles and their Application as Tunable Cell Culture Substrate,” *Adv. Mater. Technol.*, vol. 7, no. 1, pp. 1–13, 2022, doi: 10.1002/admt.202100836.

[458] C.-C. Hsu, Y.-W. Cheng, C.-C. Liu, X.-Y. Peng, M.-C. Yung, and T.-Y. Liu, “Anti-Bacterial and Anti-Fouling Capabilities of Poly(3,4-Ethylenedioxythiophene) Derivative Nanohybrid Coatings on SUS316L Stainless Steel by Electrochemical Polymerization,” *Polymers (Basel).*,

vol. 12, pp. 1467–1479, 2020.

[459] Y. S. Hsiao *et al.*, “Manipulating location, polarity, and outgrowth length of neuron-like pheochromocytoma (PC-12) cells on patterned organic electrode arrays,” *Lab Chip*, vol. 11, no. 21, pp. 3674–3680, 2011, doi: 10.1039/c1lc20675c.

[460] P. Bernabeu, L. Tamisier, A. De Cesare, and A. Caprani, “Study of the adsorption of albumin on a platinum rotating disk electrode using impedance measurements,” *Electrochim. Acta*, vol. 33, no. 8, pp. 1129–1136, 1988, doi: 10.1016/0013-4686(88)80204-4.

[461] Q. Xie, C. Xiang, Y. Yuan, Y. Zhang, L. Nie, and S. Yao, “A novel dual-impedance-analysis EQCM system - Investigation of bovine serum albumin adsorption on gold and platinum electrode surfaces,” *J. Colloid Interface Sci.*, vol. 262, no. 1, pp. 107–115, 2003, doi: 10.1016/S0021-9797(03)00196-6.

[462] F. Y. Oliva, O. R. Cámara, and L. B. Avalle, “Adsorption of human serum albumin on electrochemical titanium dioxide electrodes: Protein-oxide surface interaction effects studied by electrochemical techniques,” *J. Electroanal. Chem.*, vol. 633, no. 1, pp. 19–34, 2009, doi: 10.1016/j.jelechem.2009.04.024.

[463] E. Šafaríková, J. Ehlich, S. Stríteský, M. Vala, L. Kubala, and J. Vítecek, “Conductive Polymer PEDOT : PSS-Based Platform for Embryonic Stem-Cell Differentiation,” *Int. J. Mol. Sci.*, vol. 23, pp. 1107–1123, 2022.

[464] J. G. Hardy *et al.*, “Conducting polymer-based multilayer films for instructive biomaterial coatings Dip coating direction Weakly aligned broblasts on multilayer lms: Glass-conducting polymer-chitosan-gelatin Passage of a DC current through the lm enhances cell alignment DC cu,” *Futur. Sci. OA*, vol. 1, no. 4, p. 79, 2015, [Online]. Available: www.future-science.com

[465] M. A. Rausch *et al.*, “Impact of implant surface material and microscale roughness on the initial attachment and proliferation of primary human gingival fibroblasts,” *Biology (Basel).*, vol. 10, no. 5, 2021, doi: 10.3390/biology10050356.

[466] M. Warcaba, K. Kowalski, A. Kopia, and T. Moskalewicz, “Impact of Surface Topography, Chemistry and Properties on the Adhesion of Sodium Alginate Coatings Electrophoretically Deposited on Titanium Biomaterials,” *Metall. Mater. Trans. A Phys. Metall. Mater. Sci.*, vol. 52, no. 10, pp. 4454–4467, 2021, doi: 10.1007/s11661-021-06397-0.

[467] R. Aston, K. Sewell, T. Klein, G. Lawrie, and L. Grøndahl, “Evaluation of the impact of freezing preparation techniques on the characterisation of alginate hydrogels by cryo-SEM,” *Eur. Polym. J.*, vol. 82, pp. 1–15, 2016, doi: 10.1016/j.eurpolymj.2016.06.025.

[468] J. Jang, Y. J. Seol, H. J. Kim, J. Kundu, S. W. Kim, and D. W. Cho, “Effects of alginate hydrogel cross-linking density on mechanical and biological behaviors for tissue engineering,” *J. Mech. Behav. Biomed. Mater.*, vol. 37, pp. 69–77, 2014, doi: 10.1016/j.jmbbm.2014.05.004.

[469] M. M. Elnashar, M. A. Yassin, A. E. F. A. Moneim, and E. M. A. Bary, “Investigating the unexpected behavior for the release kinetics of brilliant blue encapsulated into calcium alginate beads,” *Eurasian Chem. J.*, vol. 12, no. 1, pp. 69–77, 2010, doi: 10.18321/ectj209.

[470] A. Kulamarva *et al.*, “In vitro cytotoxicity of functionalized single walled carbon nanotubes for targeted gene delivery applications,” *Nanotoxicology*, vol. 2, no. 4, pp. 184–188, 2008, doi: 10.1080/17435390802464994.

[471] L. Bayarjargal, C. J. Fruhner, N. Schrodt, and B. Winkler, “CaCO3 phase diagram studied with Raman spectroscopy at pressures up to 50 GPa and high temperatures and DFT modeling,” *Phys. Earth Planet. Inter.*, vol. 281, no. May, pp. 31–45, 2018, doi: 10.1016/j.pepi.2018.05.002.

[472] J. Gao, Y. Liu, X. Wu, X. Yuan, Y. Liu, and W. Su, “Structural Modifications of Single-Crystal Aragonite,” *Minerals*, vol. 10, pp. 924–942, 2020.

[473] Y. Wu, S. Joseph, and N. R. Aluru, “Effect of cross-linking on the diffusion of water, ions, and small molecules in hydrogels,” *J. Phys. Chem. B*, vol. 113, no. 11, pp. 3512–3520, 2009, doi: 10.1021/jp808145x.

[474] G. Kaklamani, D. Kazaryan, J. Bowen, F. Iacovella, S. H. Anastasiadis, and G. Deligeorgis, “On the electrical conductivity of alginate hydrogels,” *Regen. Biomater.*, vol. 5, no. 5, pp. 293–301, 2018, doi: 10.1093/rb/rby019.

[475] E. Barka, D. K. Papayannis, T. M. Kolettis, and S. Agathopoulos, “Optimization of Ca2+ content in alginate hydrogel injected in myocardium,” *J. Biomed. Mater. Res. - Part B Appl. Biomater.*, vol. 107, no. 2, pp. 223–231, 2019, doi: 10.1002/jbm.b.34113.

[476] W. P. Voo, B. B. Lee, A. Idris, A. Islam, B. T. Tey, and E. S. Chan, “Production of ultra-high concentration calcium alginate beads with prolonged dissolution profile,” *RSC Adv.*, vol. 5, no. 46, pp. 36687–36695, 2015, doi: 10.1039/c5ra03862f.

[477] J. Su, H. Xu, J. Sun, X. Gong, and H. Zhao, “Dual delivery of BMP-2 and bFGF from a new nano-composite scaffold, loaded with vascular stents for large-size mandibular defect regeneration,” *Int. J. Mol. Sci.*, vol. 14, no. 6, pp. 12714–12728, 2013, doi: 10.3390/ijms140612714.

[478] Y. H. Lee, J. J. Chang, W. F. Lai, M. C. Yang, and C. T. Chien, “Acceleration of wound healing in diabetic rats by layered hydrogel dressing,” *Carbohydr. Polym.*, vol. 88, no. 2, pp. 809–819, 2012, doi: 10.1016/j.colsurfb.2011.04.002.

[479] Y. Pang, F. Xi, J. Luo, G. Liu, T. Guo, and C. Zhang, “An alginate film-based degradable triboelectric nanogenerator,” *RSC Adv.*, vol. 8, no. 12, pp. 6719–6726, 2018, doi: 10.1039/c7ra13294h.

[480] E. Axpe *et al.*, “A Multiscale Model for Solute Diffusion in Hydrogels,” *Macromolecules*, vol. 52, no. 18, pp. 6889–6897, 2019, doi: 10.1021/acs.macromol.9b00753.

[481] H. Nie, A. He, J. Zheng, S. Xu, J. Li, and C. C. Han, “Effects of chain conformation and entanglement on the electrospinning of pure alginate,” *Biomacromolecules*, vol. 9, no. 5, pp. 1362–1365, 2008, doi: 10.1021/bm701349j.

[482] R. Kummala *et al.*, “Human Dermal Fibroblast Viability and Adhesion on Cellulose Nanomaterial Coatings: Influence of Surface Characteristics,” *Biomacromolecules*, vol. 21, no. 4, pp. 1560–1567, 2020, doi: 10.1021/acs.biomac.0c00107.

[483] P. Y. Wang, P. Koegler, H. Thissen, and P. Kingshott, “Fibroblast Responses Toward Colloidal Assembles and Plasma Polymer Coating,” *IEEE Trans. Nanotechnol.*, vol. 17, no. 3, pp. 385–388, 2018, doi: 10.1109/TNANO.2017.2767081.

[484] A. A. Khalili and M. R. Ahmad, “A Review of cell adhesion studies for biomedical and biological applications,” *Int. J. Mol. Sci.*, vol. 16, no. 8, pp. 18149–18184, 2015, doi: 10.3390/ijms160818149.

[485] J. Zhou *et al.*, “Alginate hydrogel cross-linked by Ca2+ to promote spinal cord neural stem/progenitor cell differentiation and functional recovery after a spinal cord injury,” *Regen. Biomater.*, no. August, 2022, doi: 10.1093/rb/rbac057.

[486] M. I. Günther, N. Weidner, R. Müller, and A. Blesch, “Cell-seeded alginate hydrogel scaffolds promote directed linear axonal regeneration in the injured rat spinal cord,” *Acta Biomater.*, vol. 27, pp. 140–150, 2015, doi: 10.1016/j.actbio.2015.09.001.

[487] D. Joung, N. S. Lavoie, S.-Z. Guo, S. H. Park, A. M. Parr, and M. C. McAlpine, “3D Printed Neural Regeneration Devices,” *Adv. Fun*, vol. 30, no. 1, pp. 139–148, 2020, doi: 10.1002/adfm.201906237.

[488] M. Şahin, G. Öncü, M. A. Yılmaz, D. Özkan, and H. Saybaşılı, “Transformation of SH-SY5Y cell line into neuron-like cells: Investigation of electrophysiological and biomechanical changes,” *Neurosci. Lett.*, vol. 745, no. December 2020, 2021, doi: 10.1016/j.neulet.2021.135628.

[489] A. P. Kalinovskii *et al.*, “Retinoic Acid-Differentiated Neuroblastoma SH-SY5Y Is an Accessible In Vitro Model to Study Native Human Acid-Sensing Ion Channels 1a (ASIC1a),” *Biology (Basel).*, vol. 11, no. 2, 2022, doi: 10.3390/biology11020167.

[490] L. Strother, G. B. Miles, A. R. Holiday, Y. Cheng, and G. H. Doherty, “Long-term culture of SH-SY5Y neuroblastoma cells in the absence of neurotrophins: A novel model of neuronal ageing,” *J. Neurosci. Methods*, vol. 362, no. December 2019, p. 109301, 2021, doi: 10.1016/j.jneumeth.2021.109301.

[491] A. Ozgun, F. Z. Erkoc-Biradlı, O. Bulut, and B. Garipcan, “Substrate stiffness effects on SH-SY5Y: The dichotomy of morphology and neuronal behavior,” *J. Biomed. Mater. Res. - Part B Appl. Biomater.*, vol. 109, no. 1, pp. 92–101, 2021, doi: 10.1002/jbm.b.34684.

[492] Z. Bednarikova, Z. Gazova, F. Valle, and E. Bystrenova, “Atomic force microscopy as an imaging tool to study the bio/nonbio complexes,” *J. Microsc.*, vol. 280, no. 3, pp. 241–251, 2020, doi: 10.1111/jmi.12936.

[493] C. C. Lien, M. C. Wu, and H. I. Chang, “The influence of UVB radiation on proliferation and young’s modulus of dermal fibroblasts,” *Appl. Mech. Mater.*, vol. 195–196, pp. 424–428, 2012, doi: 10.4028/www.scientific.net/AMM.195-196.424.

[494] L. S. Yao, T. Q. Liu, D. Ge, Z. F. Cui, and X. H. Ma, “Culture of neural stem cells in alginate microbeads,” *Biotechnol. Prog.*, vol. 22, no. 0, pp. 1683–1689, 2006.

[495] J. Narvaez-Monroy, E. Villalobos-Portillo, L. Fuentes-Cobas, and L. Fuentes-Montero, “Polycrystal X-ray diffraction modelling: Grazing incidence versus Bragg-Brentano,” *J. Phys. Conf. Ser.*, vol. 1723, no. 1, pp. 1–6, 2021, doi: 10.1088/1742-6596/1723/1/012047.

[496] E. Ruoslahti, “RGD and other recognition sequences for integrins,” *Annu. Rev. Cell Dev. Biol.*, vol. 12, pp. 697–715, 1996, doi: 10.1146/annurev.cellbio.12.1.697.

Appendix A - Cell Culture Media Formulations

Typical formulations of Neurobasal Medium (NB) (Gibco, UK) and Eagle's Minimum Essential Medium (EMEM) (Gibco, UK). Formulations for Dulbecco's Modified Eagle Medium (DMEM) (Sigma Aldrich, USA) and DMEM:F12 medium (Biowest, France) used for cell culture experiments in this work are also included.

	Concentration (mg/L)			
Components	**NB**	**EMEM**	**DMEM**	**DMEM:F12**
Glycine	30.0	/	30.0	18.75
L-Akanyl-L-Glutamine	/	/	862.0	/
L-Alanine	2.0	/	/	4.45
L-Arginine hydrochloride	84.0	126.0	84.0	147.5
L-Asparagine-H_2O	0.83	/	/	7.5
L-Aspartic Acid	/	/	/	6.65
L-Cysteine hydrochloride-H_2O	/	/	/	17.56
L-Cysteine	31.5	/	/	/
L-Cysteine 2HCl	/	313.0	63.0	31.29
L-Glutamic Acid	/	/	/	7.35
L-Glutamine	/	292.0	/	365.0
L-Histidine hydrochloride-H_2O	42.0	42.0	42.0	31.48
L-Isoleucine	105.0	52.0	105.0	54.47
L-Leucine	105.0	52.0	105.0	59.05
L-Lysine hydrochloride	146.0	73.0	30.0	91.25
L-Methionine	30.0	15.0	30.0	17.24
L-Phenylalanine	66.0	32.0	66.0	35.48
L-Proline	7.76	/	/	17.25
L-Serine	42.0	/	42.0	26.25
L-Threonine	95.0	48.0	95.0	53.45
L-Tryptophan	16.0	10.0	16.0	9.02
L-Tyrosine	72.0	52.0	72.0	55.79
L-Valine	94.0	117.0	94.0	52.85
Biotin	/	/	/	0.0035
Choline chloride	4.0	1.0	4.0	8.98
D-Calcium pantothenate	4.0	1.0	4.0	2.24

Folic Acid	4.0	1.0	4.0	2.65
Niacinamide	4.0	1.0	4.0	2.02
Pyridoxal hydrochloride	4.0	1.0	4.0	2.013
Riboflavin	0.4	1.0	0.4	0.219
Thiamine hydrochloride	4.0	0.1	4.0	2.17
Vitamin B12	0.0068	/	/	0.68
i-Inositol	7.2	2.0	7.2	12.6
Calcium Chloride ($CaCl_2$)	200.0	140.0	264.0	116.6
Cupric sulfate ($CuSO_4$•$5H_2O$)	/	/	/	0.0013
Ferric Nitrate ($Fe(NO_3)_3$• $(H_2O)_9$	0.1	/	0.1	0.05
Ferric sulfate ($FeSO_4$•$7H_2O$)	/	/	/	0.417
Magnesium Chloride ($MgCl_2$)	77.3	/	/	28.64
Magnesium Sulfate ($MgSO_4$)	/	98.0	200.0	48.84
Potassium Chloride (KCl)	400.0	400.0	400.0	311.8
Sodium Bicarbonate ($NaHCO_3$)	2200.0	350.0	3700.0	2438
Sodium Chloride (NaCl)	3000.0	8000.0	6400.0	6995.5
Sodium Phosphate monobasic (NaH_2PO_4-H_2O)	125.0	/	141.0	71.02
Sodium Phosphate dibasic (Na_2HPO_4)	/	48.0	/	/
Zinc Sulfate ($ZnSO_4$-$7H_2O$)	0.194	/	/	0.432
D-Glucose (Dextrose)	4500.0	1000.0	4500.0	3151
HEPES	2600.0	/	/	/
Phenol Red	8.1	376.4	15.0	8.1
Sodium Pyruvate	25.0	/	110.0	55
Hypoxanthine Na	/	/	/	2.39
Linoleic Acid	/	/	/	0.042
Lipoic Acid	/	/	/	0.105
Putrescine 2HCl	/	/	/	0.081
Thymidine	/	/	/	0.365

Appendix B - Material Certificate for Ti6Al4V Alloy (Brindley Metals, UK)

BAOJI TONGRUN METAL MATERIAL LIMITED COMPANY

MILL TEST CERTIFICATE №: 20170102

EN10204 3.1 DATE:9.Jan.2017

Commodity: GR5 TITANIUM BAR								Finish:ANNEALED		
Specification:ASTM B348/ASTM B381/NACE MR0175								Order No.: TT03187		
Size [mm]			Heat NO.		Quantity [pc]		Net Weight [kg]		Lot No.	
Dia.2″ x3000-3100mm			20161128		30		839.2		1611-5	
Heat Temperature:	750℃	Heat Insulation:		90minutes		Air Cooling:			4hours	
Chemical Composition(WT%)										
Requirement		Ti	Al	V	Fe	C	N	O	H	Residual element	
			≤	≤	≤	≤	≤	≤	≤	Each	Total
		Remainder	5.5-6. 75	3.5-4.5	0.30	0.08	0.05	0.20	0.0125	≤ 0.10	≤ 0.40
Result	Top	Remainder	6.42	4.26	0.205	0.009	0.022	0.18	0.001	≤ 0.10	≤ 0.40
	Bottom	Remainder	6.18	4.18	0.202	0.009	0.022	0.18	0.001		

Tensile Test				
Requirement Min	Tensile Strength [Mpa]	Yield Strength 0.2% [Mpa]	Elongation [%]	Area of Reduction [%]
	895MIN	825MIN	10MIN	25MIN
	1013	959	15.5	41

Other Test			
Visual Inspection	Dimensional Inspection	DPI	Hardness
Acceptable	Acceptable	Acceptable	32.5(HRC)
Micro Structure	Surface Contamination Test	Ultrasonic Test	
Acceptable	Acceptable	Acceptable AMS2631B classA and AMS2154 classA	

I hereby certify product conforms to all specifically listed technical requirements, and other requirements for these specifications. Furthermore, I certify the above quantitative were derived from testing and analysis and are in accordance with the reference specification(s) requirements.

VICE-MANAGER OF QUALITY DEPARTEMENT
BAOJI TONGRUN METAL MATERIAL LIMITED COMPANY

Appendix C- Formulation of Phosphate Buffered Saline (PBS) (Oxoid, UK)

	Concentration (g/L)
Potassium Chloride (KCl)	0.2
Potassium Phosphate Monobasic (KH_2PO_4)	0.2
Sodium Chloride (NaCl)	8.0
Sodium Phosphate Dibasic (Anhydrous) (Na_2HPO_4)	1.15

Appendix D- The absorbance spectrum for resazurin in its oxidised and reduced (resorufin) states (Tip Biosystems, Singapore)

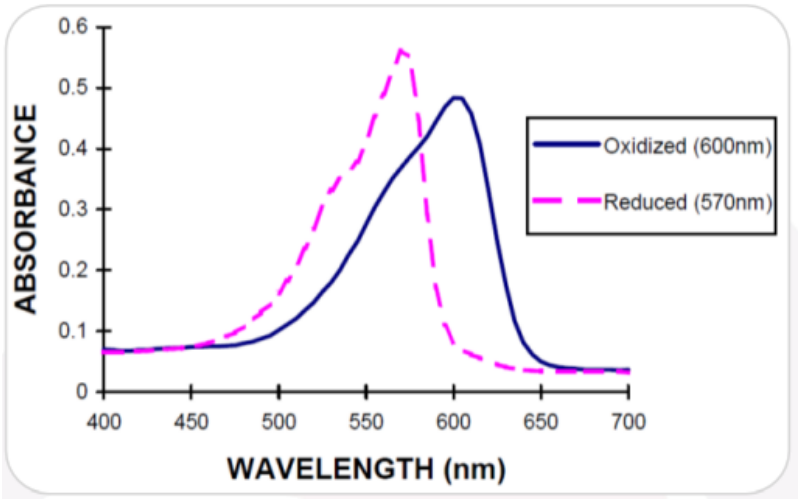

Appendix E - EIS Measurements on TiN_{IV} in Protein Containing Electrolytes

Plots showing the variation in (a) R_s, (b) Y_{pseu}, (c), R_f, (d) Y_{dl}, (e) α_{pseu}, and (f) α_{dl} as a function of time for TiN_{IV} electrodes immersed in PBS+BSA solution with P/S (black) and sodium azide (red). No statistically significant difference ($p > 0.5$) was observed in the two electrolytes.

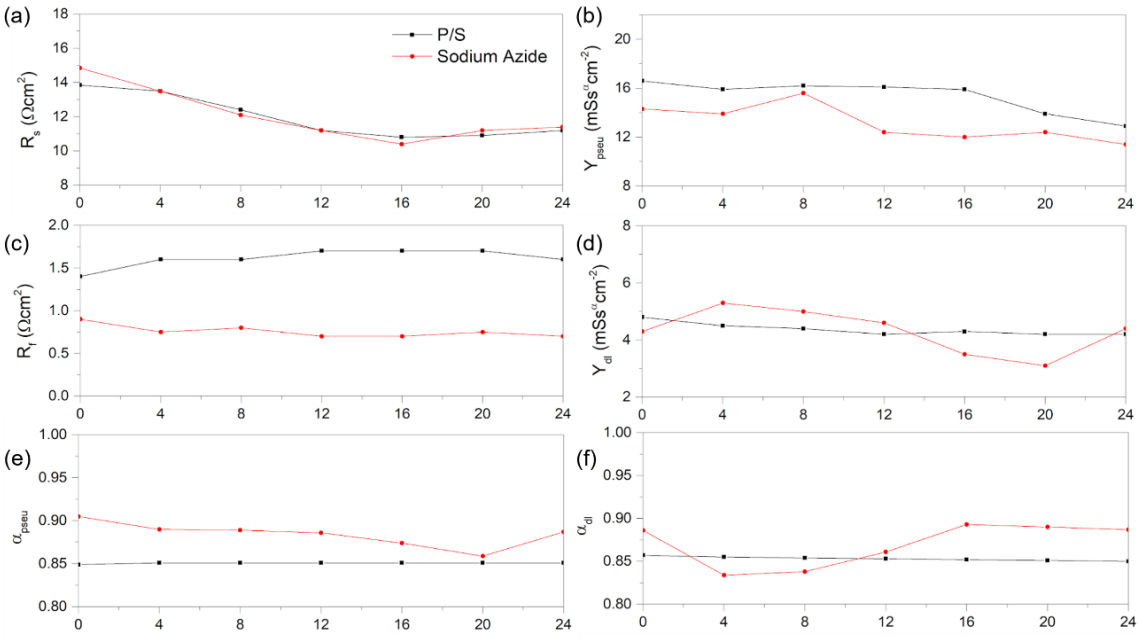

Appendix F - Representative Voltammogram of Ti6Al4V Alloy

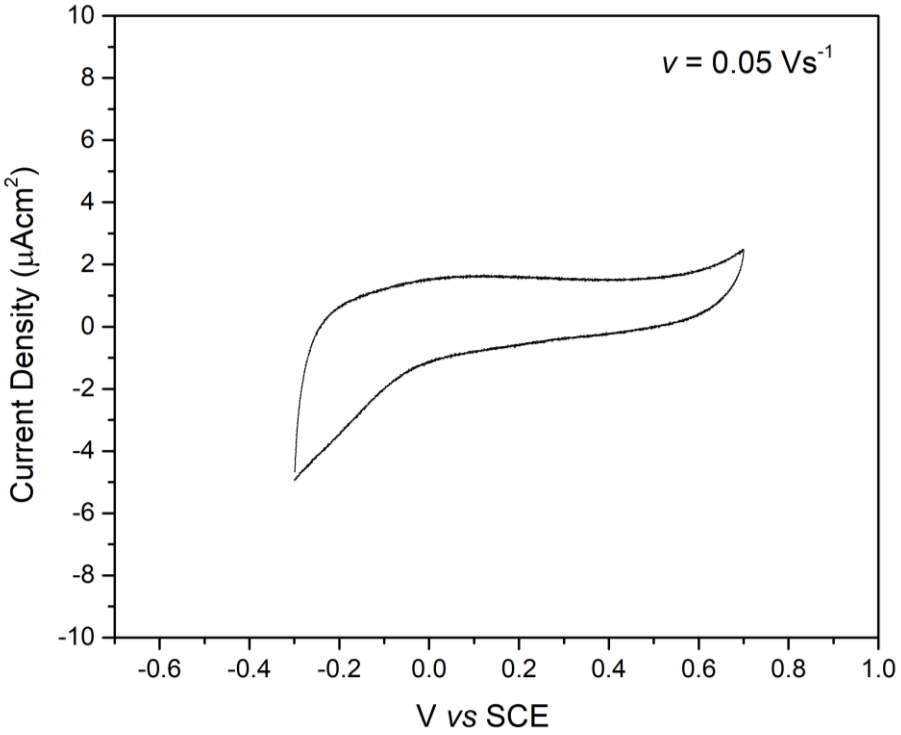

Appendix G - 10,000 Cyclic Voltammetry Cycle Assessments

Plots showing the variation in (a) R_f, (b) Y_{dl}, (c), Y_{pseu}, (d) α_{dl}, (e) α_{pseu}, and (f) charge retention percentage as a function of cycle number for TiN_I and TiN_{IV} electrodes. Cycling was carried out at scan rates of v = 0.1 and 1 Vs^{-1}. No statistically significant difference ($p > 0.5$) was observed between the two electrodes at the same scan rate.

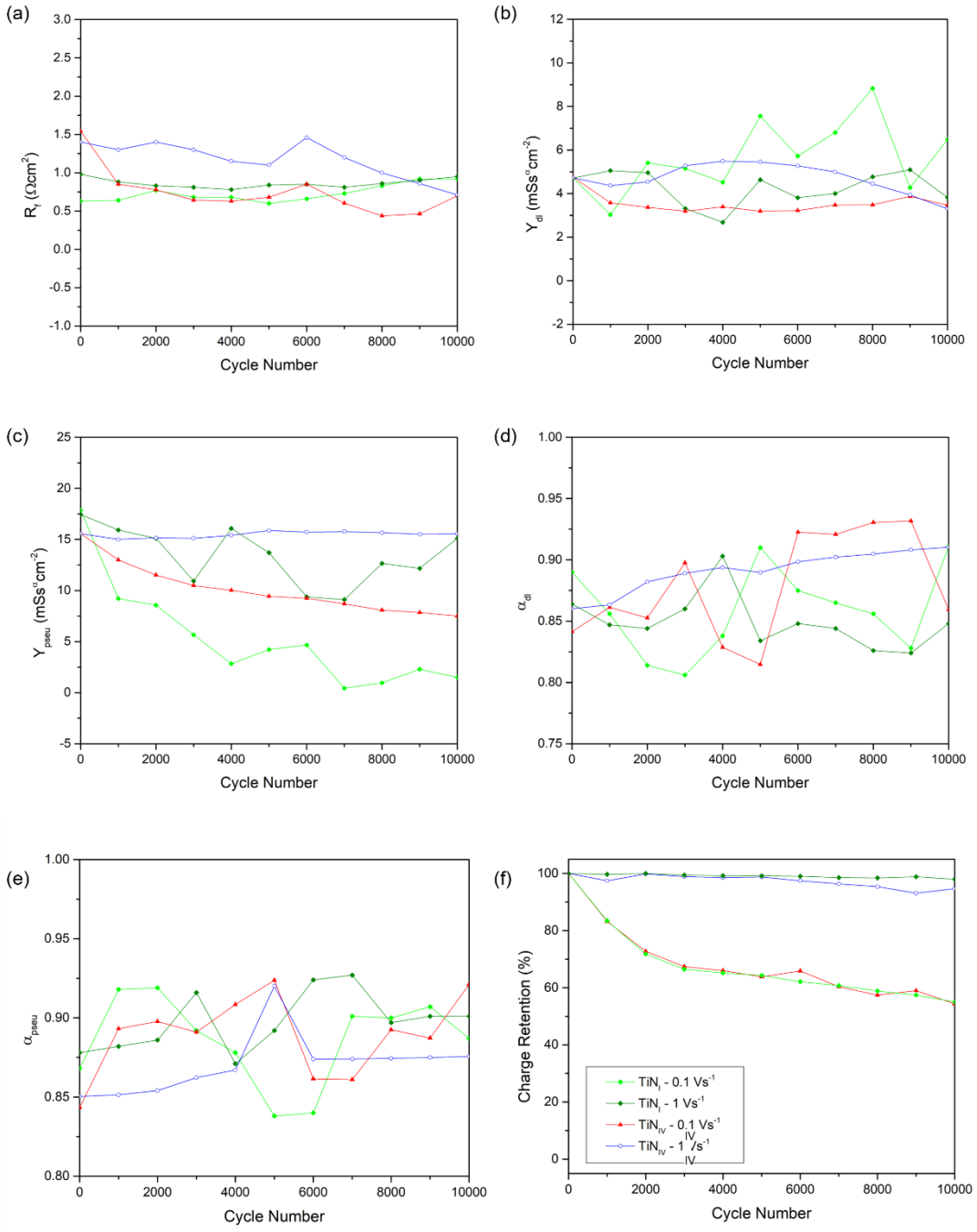

Appendix H - Experimental Batches

Batch number identification for grouped electrochemical tests. A batch number change was issued if more than three months elapsed between subsequent intra-batch test groups (demarcated by bullet points), if electrochemical cell was disassembled for cleaning and/or maintenance, or in the case of no. 4, if a different electrochemical cell was used.

Batch Number	Electrochemical Tests
1	• EIS, CV, and Cycling Lifetime tests on TiN_1 electrodes in PBS and 1M Et4NBF4 in AN
2	• EIS and CV tests on TiN_2, TiN_3, and TiN_4 electrodes in PBS • Cycling Lifetime tests on TiN_4 electrodes in PBS • EIS, CV, and 24-hour Immersion Tests on TiN_1, TiN_2, TiN_3, and TiN_4 electrodes in PBS+BSA with Sodium Azide
3	• EIS and CV tests on $PP_{12.5}$, PP_{15}, and $PP_{17.5}$ electrodes in PBS • Cycling Lifetime tests on $PP_{17.5}$ electrodes in PBS • EIS, CV, and 24-hour Immersion Tests on $PP_{17.5}$ electrodes in PBS+BSA with P/S • EIS, CV, and 24-hour Immersion Tests on TiN_4 electrodes in PBS+BSA with P/S
4	• Mechanical Adhesion (Ultrasonication + EIS) Tests on $PP_{17.5}$ electrodes in PBS
5	• EIS and CV tests on CA_{60s}, CA_{90s}, and CA_{120s} electrodes in PBS
6	• EIS, CV, and 24-hour Immersion Tests on CA_{60s} electrodes in PBS+BSA with P/S
7	• EIS measurements on CA_{60s} electrodes after 35 days of immersion in PBS and dissolution of alginate layer
8	• CV and Cyclic Lifetime tests at 1 Vs^{-1} on $PP_{17.5}$ electrodes in PBS for extended WW (-1.2 to 0.8 V *vs* SCE)